

ADVANCES IN POROUS SEMICONDUCTOR RESEARCH

EDITED BY: Thierry Djenizian and Nicolas Hans Voelcker
PUBLISHED IN: Frontiers in Chemistry





frontiers

Frontiers eBook Copyright Statement

The copyright in the text of individual articles in this eBook is the property of their respective authors or their respective institutions or funders. The copyright in graphics and images within each article may be subject to copyright of other parties. In both cases this is subject to a license granted to Frontiers.

The compilation of articles constituting this eBook is the property of Frontiers.

Each article within this eBook, and the eBook itself, are published under the most recent version of the Creative Commons CC-BY licence.

The version current at the date of publication of this eBook is CC-BY 4.0. If the CC-BY licence is updated, the licence granted by Frontiers is automatically updated to the new version.

When exercising any right under the CC-BY licence, Frontiers must be attributed as the original publisher of the article or eBook, as applicable.

Authors have the responsibility of ensuring that any graphics or other materials which are the property of others may be included in the CC-BY licence, but this should be checked before relying on the CC-BY licence to reproduce those materials. Any copyright notices relating to those materials must be complied with.

Copyright and source acknowledgement notices may not be removed and must be displayed in any copy, derivative work or partial copy which includes the elements in question.

All copyright, and all rights therein, are protected by national and international copyright laws. The above represents a summary only. For further information please read Frontiers' Conditions for Website Use and Copyright Statement, and the applicable CC-BY licence.

ISSN 1664-8714

ISBN 978-2-88963-649-5

DOI 10.3389/978-2-88963-649-5

About Frontiers

Frontiers is more than just an open-access publisher of scholarly articles: it is a pioneering approach to the world of academia, radically improving the way scholarly research is managed. The grand vision of Frontiers is a world where all people have an equal opportunity to seek, share and generate knowledge. Frontiers provides immediate and permanent online open access to all its publications, but this alone is not enough to realize our grand goals.

Frontiers Journal Series

The Frontiers Journal Series is a multi-tier and interdisciplinary set of open-access, online journals, promising a paradigm shift from the current review, selection and dissemination processes in academic publishing. All Frontiers journals are driven by researchers for researchers; therefore, they constitute a service to the scholarly community. At the same time, the Frontiers Journal Series operates on a revolutionary invention, the tiered publishing system, initially addressing specific communities of scholars, and gradually climbing up to broader public understanding, thus serving the interests of the lay society, too.

Dedication to Quality

Each Frontiers article is a landmark of the highest quality, thanks to genuinely collaborative interactions between authors and review editors, who include some of the world's best academicians. Research must be certified by peers before entering a stream of knowledge that may eventually reach the public - and shape society; therefore, Frontiers only applies the most rigorous and unbiased reviews.

Frontiers revolutionizes research publishing by freely delivering the most outstanding research, evaluated with no bias from both the academic and social point of view. By applying the most advanced information technologies, Frontiers is catapulting scholarly publishing into a new generation.

What are Frontiers Research Topics?

Frontiers Research Topics are very popular trademarks of the Frontiers Journals Series: they are collections of at least ten articles, all centered on a particular subject. With their unique mix of varied contributions from Original Research to Review Articles, Frontiers Research Topics unify the most influential researchers, the latest key findings and historical advances in a hot research area! Find out more on how to host your own Frontiers Research Topic or contribute to one as an author by contacting the Frontiers Editorial Office: researchtopics@frontiersin.org

ADVANCES IN POROUS SEMICONDUCTOR RESEARCH

Topic Editors:

Thierry Djenizian, MINES Saint-Etienne, France

Nicolas Hans Voelcker, Monash University, Australia

Citation: Djenizian, T., Voelcker, N. H., eds. (2020). Advances in Porous Semiconductor Research. Lausanne: Frontiers Media SA.

doi: 10.3389/978-2-88963-649-5

Table of Contents

- 05 Editorial: Advances in Porous Semiconductor Research**
Thierry Djenizian and Nicolas H. Voelcker
- 07 Toward Multi-Parametric Porous Silicon Transducers Based on Covalent Grafting of Graphene Oxide for Biosensing Applications**
Rosalba Moretta, Monica Terracciano, Principia Dardano, Maurizio Casalino, Luca De Stefano, Chiara Schiattarella and Ilaria Rea
- 17 Porous Silicon Bragg Reflector/Carbon Dot Hybrids: Synthesis, Nanostructure, and Optical Properties**
Naama Massad-Ivanir, Susanta Kumar Bhunia, Raz Jelinek and Ester Segal
- 27 High Anodic-Voltage Focusing of Charge Carriers in Silicon Enables the Etching of Regularly-Arranged Submicrometer Pores at High Density and High Aspect-Ratio**
Chiara Cozzi, Giovanni Polito, Lucanos M. Strambini and Giuseppe Barillaro
- 36 Hyperspectral and Color Imaging of Solvent Vapor Sorption Into Porous Silicon**
Soohyun Chun and Gordon M. Miskelly
- 48 Impregnation of High-Magnetization FeCo Nanoparticles in Mesoporous Silicon: An Experimental Approach**
Mathieu Lepasant, Benjamin Bardet, Lise-Marie Lacroix, Pierre Fau, Cyril Garnerio, Bruno Chaudret, Katerina Soulantica, Thomas Defforge, Damien Valente, Caroline Andreazza, Jérôme Billoué, Patrick Poveda and Gaël Gautier
- 54 Structural and Optical Properties of Silicon Nanowire Arrays Fabricated by Metal Assisted Chemical Etching With Ammonium Fluoride**
Kirill A. Gonchar, Veronika Y. Kitaeva, George A. Zharik, Andrei A. Eliseev and Liubov A. Osminkina
- 61 Crystallographically Determined Etching and Its Relevance to the Metal-Assisted Catalytic Etching (MACE) of Silicon Powders**
Kurt W. Kolasinski, Bret A. Unger, Alexis T. Ernst and Mark Aindow
- 77 Electrodeposition of Polymer Electrolyte Into Porous $\text{LiNi}_{0.5}\text{Mn}_{1.5}\text{O}_4$ for High Performance All-Solid-State Microbatteries**
Girish D. Salian, Chrystelle Lebouin, Alina Galeyeva, Andrey P. Kurbatov and Thierry Djenizian
- 85 Magnetic Characteristics of Ni-Filled Luminescent Porous Silicon**
Petra Granitzer, Klemens Rumpf, Peter Poelt and Michael Reissner
- 91 TiO_2 ALD Coating of Amorphous TiO_2 Nanotube Layers: Inhibition of the Structural and Morphological Changes Due to Water Annealing**
Siowwoon Ng, Hanna Sopha, Raul Zazpe, Zdenek Spotz, Vijay Bijalwan, Filip Dvorak, Ludek Hromadko, Jan Prikryl and Jan M. Macak
- 103 Optical and Electrochemical Properties of Self-Organized TiO_2 Nanotube Arrays From Anodized Ti–6Al–4V Alloy**
Henia Fraoucene, Vinsensia Ade Sugiawati, Djedjiga Hatem, Mohammed Said Belkaid, Florence Vacandio, Marielle Eyraud, Marcel Pasquinelli and Thierry Djenizian

- 112** *Formation of Si/SiO₂ Luminescent Quantum Dots From Mesoporous Silicon by Sodium Tetraborate/Citric Acid Oxidation Treatment*
Maxim B. Gongalsky, Julia V. Kargina, Jose F. Cruz, Juan F. Sánchez-Royo, Vladimir S. Chirvony, Liubov A. Osminkina and Michael J. Sailor
- 124** *Gold-Sensitized Silicon/ZnO Core/Shell Nanowire Array for Solar Water Splitting*
Fu-Qiang Zhang, Ya Hu, Rui-Nan Sun, Haoxin Fu and Kui-Qing Peng
- 131** *Emerging Functions of Nanostructured Porous Silicon—With a Focus on the Emissive Properties of Photons, Electrons, and Ultrasound*
Nobuyoshi Koshida and Toshihiro Nakamura
- 146** *3D Patterning of Si by Contact Etching With Nanoporous Metals*
Stéphane Bastide, Encarnacion Torralba, Mathieu Halbwax, Sylvain Le Gall, Elias Mpogui, Christine Cachet-Vivier, Vincent Magnin, Joseph Harari, Dmitri Yarekha and Jean-Pierre Vilcot
- 159** *Cavitation Induced by Janus-Like Mesoporous Silicon Nanoparticles Enhances Ultrasound Hyperthermia*
Andrey Sviridov, Konstantin Tamarov, Ivan Fesenko, Wujun Xu, Valery Andreev, Victor Timoshenko and Vesa-Pekka Lehto
- 171** *Magnetic Nanoparticles Enhance Pore Blockage-Based Electrochemical Detection of a Wound Biomarker*
Gayathri Rajeev, Allison J. Cowin, Nicolas H. Voelcker and Beatriz Prieto Simon



Editorial: Advances in Porous Semiconductor Research

Thierry Djenizian^{1,2*} and Nicolas H. Voelcker^{3,4}

¹ Mines Saint-Etienne, Center of Microelectronics in Provence, Department of Flexible Electronics, Gardanne, France,

² Al-Farabi Kazakh National University, Center of Physical-Chemical Methods of Research and Analysis, Almaty, Kazakhstan,

³ Department of Materials Science and Engineering, Monash University, Clayton, VIC, Australia, ⁴ Melbourne Centre for Nanofabrication, Victorian Node of the Australian National Fabrication Facility, Clayton, VIC, Australia

Keywords: semiconductor, porous material, microfabrication, nanomaterials, nanotechnologies

Editorial on the Research Topic

OPEN ACCESS

Edited by:

Steve Suib,
University of Connecticut,
United States

Reviewed by:

Wee-Jun Ong,
Xiamen University Malaysia, Malaysia

*Correspondence:

Thierry Djenizian
thierry.djenizian@emse.fr

Specialty section:

This article was submitted to
Chemical and Process Engineering,
a section of the journal
Frontiers in Chemistry

Received: 11 December 2019

Accepted: 10 February 2020

Published: 06 March 2020

Citation:

Djenizian T and Voelcker NH (2020)
Editorial: Advances in Porous
Semiconductor Research.
Front. Chem. 8:122.
doi: 10.3389/fchem.2020.00122

Advances in Porous Semiconductor Research

Since the discovery of the luminescent properties of porous silicon by Canham (1990), the anodization process has attracted renewed interest for the fabrication of porous semiconductors. To date, this technique is widely used to design new materials with advanced physico-chemical properties for many applications in optics, microelectronics, energy, biomedicine, etc. . .

This Research Topic features the most important and recent exciting results related to all aspects of manufacturing, characterization, properties, and applications of porous semiconductors (Si, Ge, III-V compounds, TiO₂ nanotubes, etc.).

This Research Topic is a collection of articles carefully selected from 200 abstracts submitted to the 2018 Porous Semiconductors Science and Technology Conference. All abstracts were peer-reviewed by a panel composed of 6 co-chairs and 16 senior researchers from the scientific advisory board. The peer-reviewed papers have been chosen based on novelty of the work, fair representation of the scientific topics, and geographical considerations. Thus, this Research Topic involves co-authors from 31 academic institutions established in 15 countries from Europe, North America, Asia, and Australia.

The topical areas cover electrochemical and metal-assisted chemical etching, surface chemistry and functionalization, pore filling and nanoparticle decoration, novel nanostructures and microfabrication techniques, micro photonics and luminescence, micro systems and electronics, biomedical applications including diagnostics, bioimaging and drug delivery, energy harvesting, storage and conversion, sensors, as well as emerging applications.

We encourage readers to explore the review by Koshida and Nakamura who gives a broad overview of the emerging functions of nanostructured porous silicon for physical applications. There are also several examples of original articles covering the fabrication (Bastide et al.; Kolasinski et al.) and use of advanced properties of porous silicon for emerging applications like

magnetic and electronic features (Granitzer et al.; Lepesant et al.), optical properties (Gonchar et al.), biosensing (Gongalsky et al.; Rajeev et al.; Segal et al.; Cozzi et al.), energy storage and harvesting (Djenizian et al.).

REFERENCES

Canham, L. T. (1990). Silicon quantum wire array fabrication by electrochemical and chemical dissolution of wafers. *Appl. Phys. Lett.* 57:1046. doi: 10.1063/1.103561

Conflict of Interest: The authors declare that the research was conducted in the absence of any commercial or financial relationships that could be construed as a potential conflict of interest.

AUTHOR CONTRIBUTIONS

All authors listed have made a substantial, direct and intellectual contribution to the work, and approved it for publication.

Copyright © 2020 Djenizian and Voelcker. This is an open-access article distributed under the terms of the Creative Commons Attribution License (CC BY). The use, distribution or reproduction in other forums is permitted, provided the original author(s) and the copyright owner(s) are credited and that the original publication in this journal is cited, in accordance with accepted academic practice. No use, distribution or reproduction is permitted which does not comply with these terms.



Toward Multi-Parametric Porous Silicon Transducers Based on Covalent Grafting of Graphene Oxide for Biosensing Applications

Rosalba Moretta^{1,2}, Monica Terracciano¹, Principia Dardano¹, Maurizio Casalino¹, Luca De Stefano^{1*}, Chiara Schiattarella^{1,3} and Ilaria Rea¹

¹ Institute for Microelectronics and Microsystems, Unit of Naples, Naples, Italy, ² Department of Chemical Sciences, "Federico II" University of Naples, Naples, Italy, ³ Department of Physics, "Federico II" University of Naples, Naples, Italy

OPEN ACCESS

Edited by:

Thierry Djenizian,
École des Mines de
Saint-Étienne–Campus Georges
Charpak Provence, France

Reviewed by:

Rabah Boukherroub,
UMR8520 Institut D'électronique, de
Microélectronique et de
Nanotechnologie (IEMN), France
Ciro Chiappini,
King's College London,
United Kingdom

*Correspondence:

Luca De Stefano
luca.destefano@na.imm.cnr.it

Specialty section:

This article was submitted to
Chemical Engineering,
a section of the journal
Frontiers in Chemistry

Received: 10 September 2018

Accepted: 08 November 2018

Published: 22 November 2018

Citation:

Moretta R, Terracciano M, Dardano P,
Casalino M, De Stefano L,
Schiattarella C and Rea I (2018)
Toward Multi-Parametric Porous
Silicon Transducers Based on
Covalent Grafting of Graphene Oxide
for Biosensing Applications.
Front. Chem. 6:583.
doi: 10.3389/fchem.2018.00583

Graphene oxide (GO) is a two-dimensional material with peculiar photoluminescence emission and good dispersion in water, that make it an useful platform for the development of label-free optical biosensors. In this study, a GO-porous silicon (PSi) hybrid device is realized using a covalent chemical approach in order to obtain a stable support for biosensing applications. Protein A, used as bioprobe for biosensing purposes, is covalently linked to the GO, using the functional groups on its surface, by carbodiimide chemistry. Protein A bioconjugation to GO-PSi hybrid device is investigated by atomic force microscopy (AFM), scanning electron microscopy (SEM), water contact angle (WCA) measurements, Fourier transform infrared (FTIR) spectroscopy, steady-state photoluminescence (PL), and fluorescence confocal microscopy. PSi reflectance and GO photoluminescence changes can thus be simultaneously exploited for monitoring biomolecule interactions as in a multi-parametric hybrid biosensing device.

Keywords: porous silicon, graphene oxide, covalent grafting, photoluminescence, optical device

INTRODUCTION

Graphene oxide (GO) is the oxidized counterpart of graphene, characterized by oxygen-bearing functional groups in the form of epoxy, hydroxyl, and carboxyl acids groups on both the basal plane and edges (Dreyer et al., 2010). The oxygen-containing functional groups on the GO sheets make this material more hydrophilic than graphene. In the last decade, GO has attracted great attention because of its unique electronic, mechanical, thermal, and optical properties (Park and Ruoff, 2009; Loh et al., 2010). Moreover, GO can be functionalized with biomolecules without using cross-linkers in aqueous solution, so that this material is particularly interesting for biosensing applications (Jung et al., 2010; Loh et al., 2010; Liu et al., 2012; Zhang et al., 2013).

Several strategies have been published to functionalize GO. In particular, carboxylic acid groups on the GO sheets can be used as reactant sites for immobilization or conjugation of several biological molecules such as proteins, peptides, antibodies, DNA, and so on (Zhang et al., 2010; Wu et al., 2011). Furthermore, GO exhibits steady-state photoluminescence (PL) particular features, such as a broad PL emission from 500 to 900 nm on exposure to near UV radiation, that have been proposed for the development of a new class of optoelectronic devices (Chien et al., 2012). Unfortunately, the PL of a thin layer of GO nanosheets is too weak, mainly due to the oxygen-functional groups producing non-radiative recombination between their electrons

and holes present in sp^2 clusters (Gupta et al., 2014). Oxygen plasma treatment can be used to get higher PL emission from GO (Gokus et al., 2009; Eda et al., 2010). An alternative approach based on the infiltration of GO into large surface area substrate is a valid strategy to enhance the light generation from the resulting composite material, and porous silicon (PSi) is optimal candidate for this task. PSi is a nanostructured material produced by electrochemical anodization of doped crystalline silicon in hydrofluoric acid (HF)-based solution. Pores size and morphology of PSi samples can be properly tuned changing the etching parameters (HF concentration, current density) and the characteristics of the silicon substrate (dopant type, resistivity, crystal orientation). Due to its sponge-like morphology, characterized by a specific surface area of hundreds of $m^2\ cm^{-3}$, PSi is definitely an ideal transducer for the development of several kinds of biosensors (Sailor, 2012; Canham, 2017). In recent papers, hybrid devices constituted by GO electrostatically immobilized on amino-modified mesoporous silicon (i.e., PSi with a pores size $<50\ nm$) were described. In particular, homogeneous monolayer and aperiodic Thue-Morse multi-layered structure made of 64 layers were used in order to infiltrate GO nanosheets by spin-coating. The enhancement and the modulation of the PL signal emitted from GO adsorbed on both the hybrid structures were highlighted, while these phenomena were not observed in the case of GO on crystalline flat silicon (Rea et al., 2014, 2016).

In this work, a chemical procedure to covalently bind GO to PSi surface has been developed in order to realize a stable hybrid device for biosensing purposes. Macroporous silicon, characterized by pores size $>50\ nm$, has been used in infiltrating the GO sheets inside the pores of material. The GO-PSi hybrid device has been covalently conjugated to FITC-labeled protein A (PrA*) derived from *Staphylococcus aureus* as a model bioprobe. The effective covalent interaction between GO-PSi and PrA* demonstrates the possibility to realize a robust system for biosensing whose operating mechanism is based on the changes of PSi reflectance and GO photoluminescence.

The development of GO-PSi hybrid device and its interaction with the PrA* have been investigated by Fourier transform infrared spectroscopy (FTIR), spectroscopic reflectometry, steady-state photoluminescence (PL), atomic force microscopy (AFM), scanning electron microscopy (SEM), water contact angle (WCA) measurements, and fluorescence confocal microscopy.

MATERIALS AND METHODS

Chemicals

Hydrofluoric acid (HF), undecylenic acid (UDA), N-(3-Dimethylaminopropyl)-N'-ethylcarbodiimide hydrochloride (EDC), N-hydroxysuccinimide (NHS), MES hydrate, tert-Butyloxycarbonyl-NH-PEG-Amine (BOC-NH-PEG-NH₂), trifluoroacetic acid (TFA), chloroform, tetrahydrofuran, FITC-labeled Protein A (PrA*) from *S. aureus* were purchased from Sigma Aldrich (St. Louis, MO, USA). Graphene oxide (GO) nanosheets were purchased from Biotool.com (Houston, TX,

USA) as a batch of 2 mg/mL in water with a nominal sheets size between 50 and 200 nm.

Preparation of Graphene Oxide

Graphene oxide (GO), 1 mg ml^{-1} , was sonicated using an ultrasonic processor for 1 h in ice at 50% of available power amplitude.

Porous Silicon (PSi) Layer Fabrication and Hydrosilylation Process

PSi was fabricated by electrochemical etching of *n*-type crystalline silicon ($0.01\text{--}0.02\ \Omega\ cm$ resistivity, (100) oriented and $500\ \mu m$ thick) in HF (5% in weight)/ethanol solution at room temperature (RT). Before the etching process, the silicon substrate was immersed in HF solution for 2 min to remove the oxide native layer. A current density of $20\ mA\ cm^{-2}$ for 90 s, was applied to obtain a single layer of PSi with a porosity of 61% ($n_{PSi} = 1.83$ at $\lambda = 1.2\ \mu m$), a thickness *L* of $2.1\ \mu m$ and a pores dimension between 50 and 250 nm, determined by ellipsometry and SEM imaging (Terracciano et al., 2016). The as-etched PSi was placed in a Schlenk tube containing deoxygenated neat UDA (99% v/v) and allowed to react at $110^\circ C$ for 18 h under a stream of argon. The treated chip was extensively washed in tetrahydrofuran and chloroform in order to remove the excess of reagent (Shabir et al., 2017).

Pegylation of PSi Layer and Covalent Grafting of GO

UDA-modified PSi sample was placed in a Schlenk tube containing freshly prepared EDC/NHS aqueous mixture (0.005 M in MES 0.1 M) for 90 min at RT. Sample was rinsed in deionized water three times and dried under nitrogen stream. PEGylation was performed dipping the sample in BOC-NH-PEG-NH₂ solution (0.4 M, overnight, at $4^\circ C$) (Harris et al., 1992; Sam et al., 2010); the excess of reagent was removed rinsing the sample in MES buffer and in deionized water. The *t*-butyloxycarbonyl (BOC) protecting group of amine portion was removed from the PEG covalently bound to PSi surface incubating the sample in a solution of TFA (95% v/v, 90 min, at RT): sample was then washed in deionized water so as to remove the excess of TFA. GO was covalently bound to the PSi surface incubating the sample in sonicated GO (1 mg/ml) in presence of EDC/NHS (0.020 M EDC and 0.016 M NHS in MES 0.1 M, overnight, at RT).

Covalent Grafting of FITC-Labeled Protein a on PSi Layer

GO-modified PSi was incubated in 0.33 mg/ml of FITC-labeled Protein A (PrA*) in presence of EDC/NHS (0.020 M EDC and 0.016 M NHS in MES 0.1 M, overnight, at RT). The reaction was conducted over-night at RT.

Atomic Force Microscopy

A XE-100 AFM (Park Systems) was used for the imaging of PSi sample before and after functionalization with GO. Surface imaging was obtained in non-contact mode using silicon/aluminum coated cantilevers (PPP-NCHR 10 M; Park

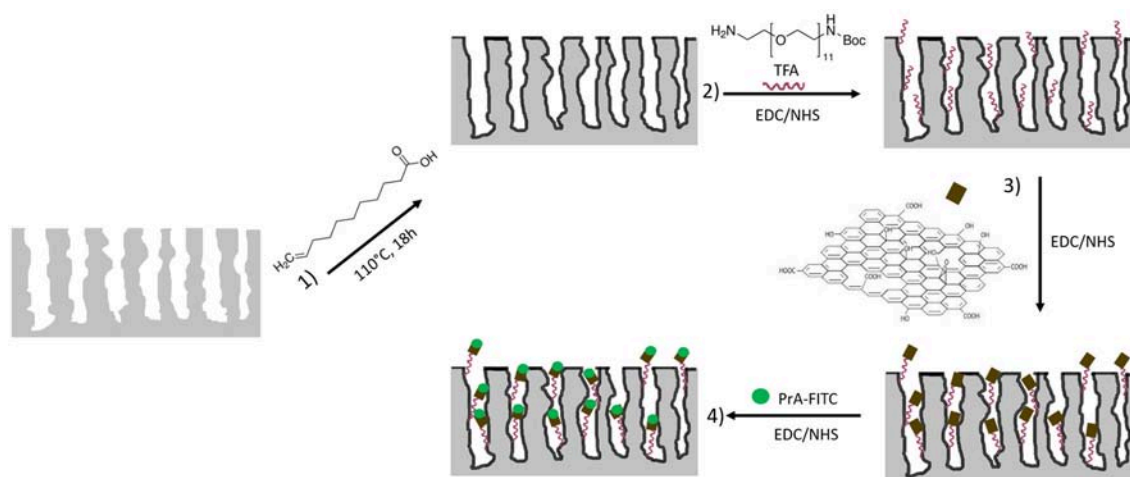


FIGURE 1 | Functionalization scheme of macroporous silicon. **Reaction 1:** hydrosilylation process of PSi using undecylenic acid, 18 h at 110°C . **Reaction 2:** PEGylation process of PSi by EDC/NHS and deprotection of NH-BOC by TFA treatment. **Reaction 3:** immobilization of GO by EDC/NHS on PEGylated PSi. **Reaction 4:** immobilization of PrA* on hybrid device.

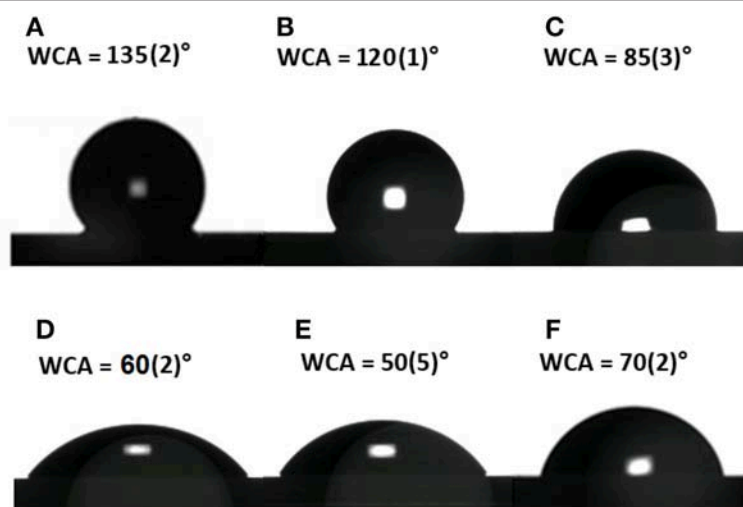


FIGURE 2 | Water contact angle measurement performed on bare PSi (A), after hydrosilylation (B), after PEGylation (C), after TFA treatment (D), after GO functionalization (E), and after PrA* immobilization (F).

Systems) $125\ \mu\text{m}$ long with resonance frequency of 200 to $400\ \text{kHz}$ and nominal force constant of $42\ \text{N/m}$. The scan frequency was typically $1\ \text{Hz}$ per line. AFM images were analyzed by the program XEI 1.8.1.build214 (Park Systems).

Scanning Electron Microscopy

SEM characterization of PSi sample was performed before and after GO functionalization. Images were acquired at $5\ \text{kV}$ accelerating voltage and $30\ \mu\text{m}$ wide aperture by a Field Emission Scanning Electron Microscope (Carl Zeiss NTS GmbH 1500 Raith FESEM). InLens detector was used. Samples were tilted at 90° in order to perform SEM analysis in lateral view.

Water Contact Angle Measurements

Sessile drop technique was used for WCA measurements on a First Ten Angstroms FTA 1000 C Class coupled with drop shape analysis software. Results of WCA are expressed as mean \pm standard deviation (s.d.) of at least three measurements on the same sample of three independent experiments (i.e., at least nine measurements for each result).

Fourier Transform Infrared Spectroscopy

The FTIR spectra of all samples were obtained using a Nicolet Continuum XL (Thermo Scientific) microscope in the wavenumber region of $4,000\text{--}650\ \text{cm}^{-1}$ with a resolution of $4\ \text{cm}^{-1}$.

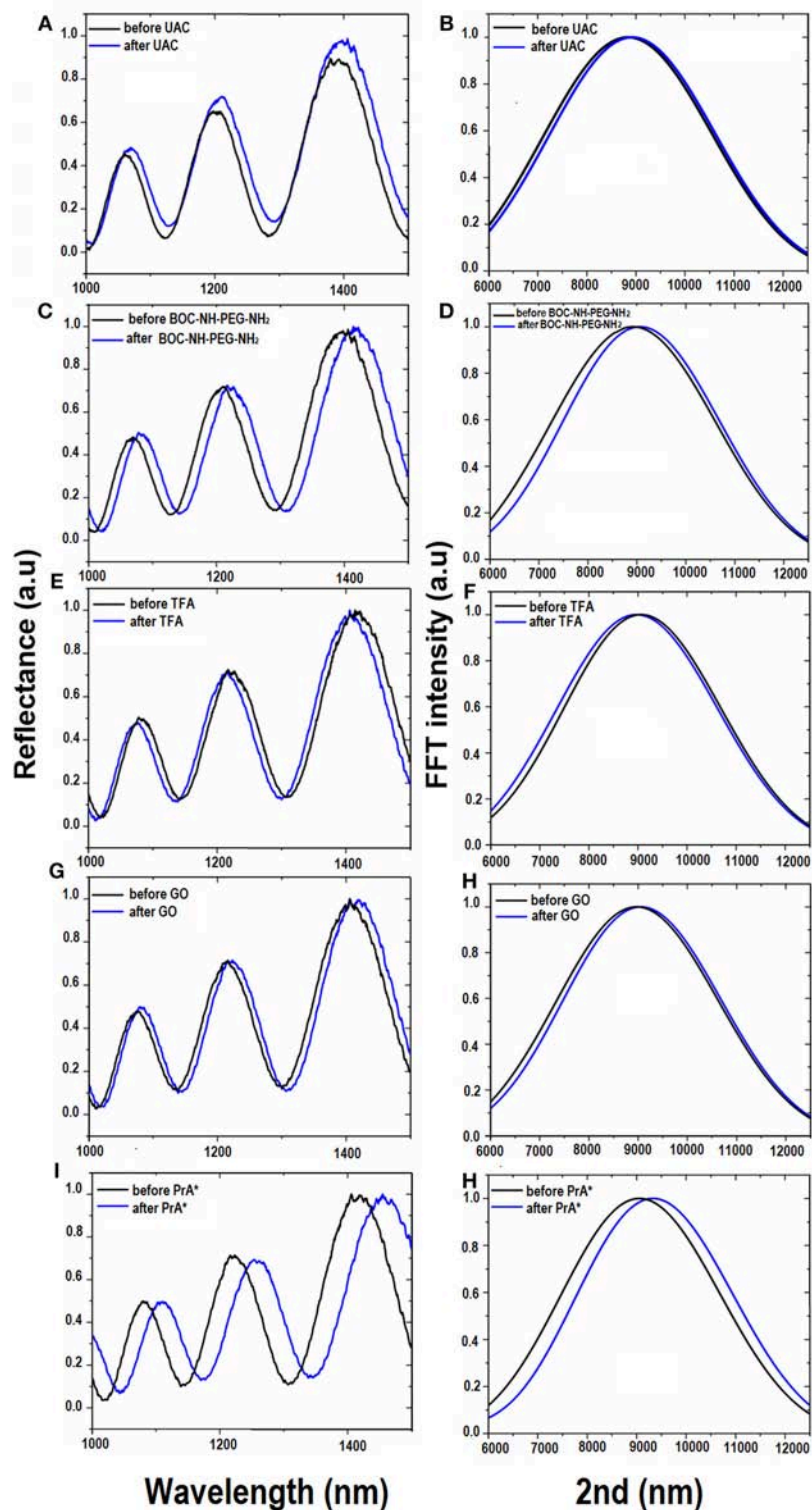


FIGURE 3 | Reflectivity spectra (A) and corresponding Fourier transforms (B) of PSi before (black line), and after (blue line) UDA treatment. Reflectivity spectra (C) and corresponding Fourier transforms (D) of UDA-PSi before and after PEGylation with BOC-NH-PEG-NH₂ (blue line). Reflectivity spectra (E) and corresponding Fourier transforms (F) of PEGylated PSi before (black line) and after selective deprotection of -NH-BOC by TFA treatment (blue line). Reflectivity spectra (G) and corresponding Fourier transforms (H) of deprotected PEG-PSi before (black line) and after GO immobilization (blue line). Reflectivity spectra (I) and corresponding Fourier transforms (J) after PrA* functionalization.

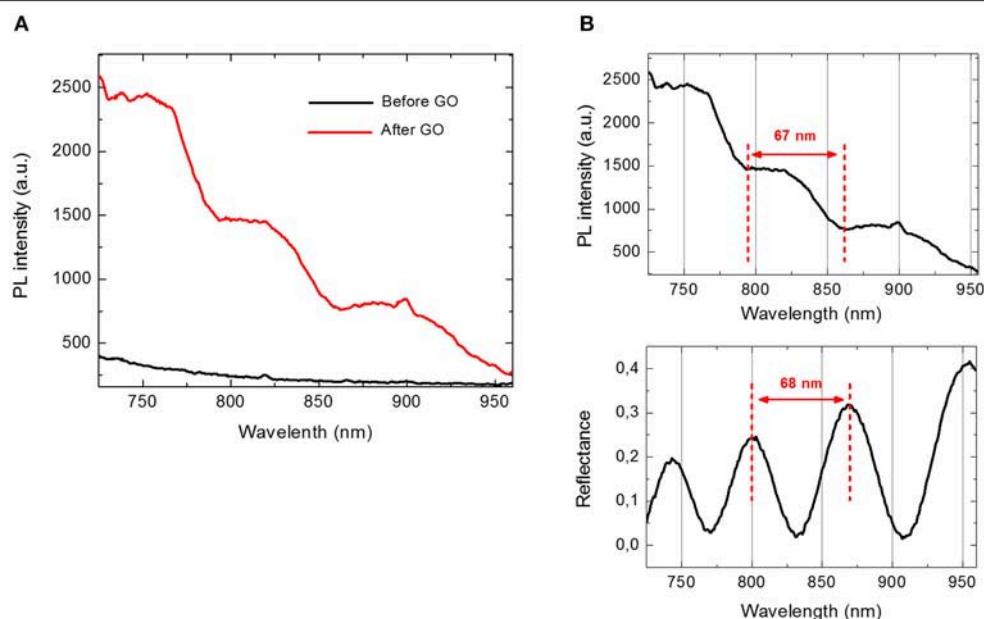


FIGURE 4 | (A) Photoluminescence spectra of PSi before (black line) and after GO covalent immobilization (red line) at an excitation wavelength of 442 nm. **(B)** Comparison between photoluminescence spectrum (upper graph) and reflectivity spectrum (lower graph) of GO-PSi device.

Spectroscopic Reflectometry

The reflectivity spectra of PSi sample were measured at normal incidence by means of a Y optical reflection probe (Avantes), connected to a white light source and to an optical spectrum analyser (Ando, AQ6315B). The spectra were collected over the range 600–1,600 nm with a resolution of 1 nm. Reflectivity spectra shown in the work are the average of three measurements.

Steady-State Photoluminescence (PL)

Steady-state photoluminescence (PL) spectra were excited by a continuous wave He-Cd laser at 442 nm (KIMMON Laser System). PL was collected at normal incidence to the surface of samples through a fiber, dispersed in a spectrometer (Princeton Instruments, SpectraPro 300i), and detected using a Peltier cooled charge coupled device (CCD) camera (PIXIS 100F). A long pass filter with a nominal cut-on wavelength of 458 nm was used to remove the laser line at monochromator inlet.

Laser Scanning Confocal Microscopy

Fluorescent samples were imaged using an inverted fully automated confocal Nikon AR-1 microscope. The NIS elements software was used for image acquisition/elaboration.

RESULTS AND DISCUSSION

The structure of GO is characterized by a large amount of hydroxyl, epoxy, and carboxyl groups distributed on the whole surface, which makes this material much more hydrophilic than graphene (Dreyer et al., 2010). GO can be thus processed in aqueous solution in order to directly link biomolecules to its surface for the realization of a biosensor, whose sensing

mechanism could be based on changes of GO photoluminescence (Morales-Narváez and Merkoçi, 2012).

The fabrication of a multiparametric hybrid transducer, based on GO covalently immobilized on macroporous PSi surface, required the optimization of GO infiltration, and, before this step, a proper characterization of its behavior in aqueous solutions. GO solubility could be not assured in presence of a biological molecule, so that in **Supplementary Information** (SI) the interaction of free GO sheets and a FITC labeled PrA*, dispersed in demineralized water, is reported. The formation of the complex GO-PrA* was evaluated by DLS (Figure S1), ζ -potential measurements, UV-Vis (Figure S2), and photoluminescence (Figure S3). These results evidenced slight aggregation after GO-PrA* conjugation by EDC/NHS chemistry and a strong interaction between the two systems, which led to changes in UV-Vis absorbance and PL emission. Before infiltration, GO nanosheets had been sonicated until sheets size showed values lower than 100 nm to DLS (data not showed here). After size reduction, GO was covalently bound to the PSi surface following the functionalization scheme reported in **Figure 1**. Since the main drawback of PSi is its chemical instability in oxidizing environment, such as biological conditions (Ghulinyan et al., 2008), a method to stabilize the surface is mandatory in biosensing applications. A hydrosilylation process has thus been used as a valid strategy to make the PSi a more stable platform. After hydrosilylation, the Si-H surface bonds, typical of as-etched PSi, were converted in Si-C bonds, making the material more robust and resistant to hydrolysis and oxidation (**Figure 1**, Reaction 1). The thermal reaction between UDA and as-etched PSi induced the formation of an organic monolayer covalently attached to the surface through the formation of Si-C bonds

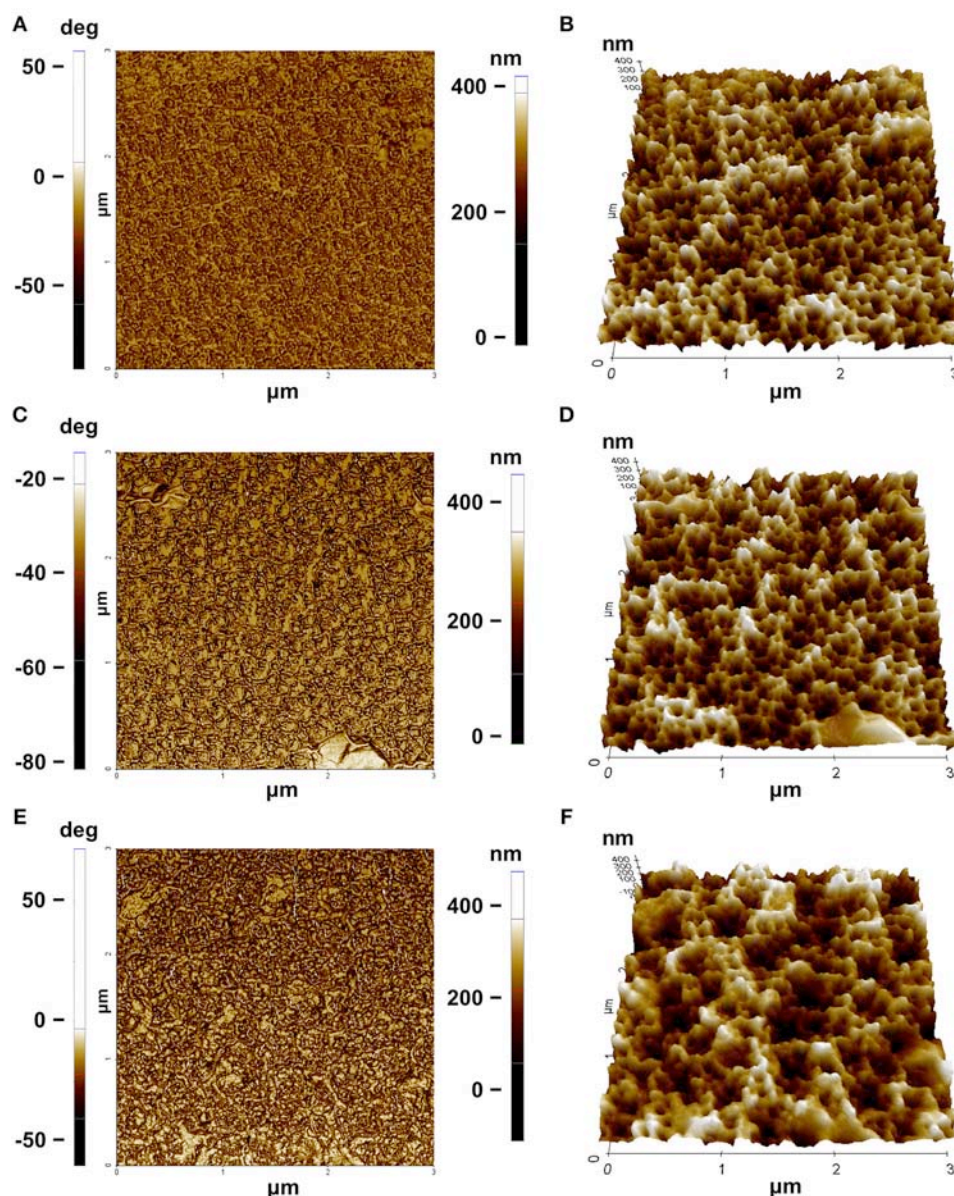


FIGURE 5 | AFM characterization: **(A)** phase and **(B)** three-dimensional rendering of PSI before GO functionalization; **(C)** phase and **(D)** three-dimensional rendering of PSI after GO functionalization; **(E)** phase and **(F)** three-dimensional rendering of PSI after PrA* functionalization.

(Boukherroub et al., 2002). The carboxyl acid groups exposed on the surface could be used for further functionalization steps.

The GO grafting to the hydrosilylated-PSi surface required a cross-linker with exposed amino groups. In this study, the PEG molecule was used as bi-functional cross-linker. The covalent grafting of the BOC-NH-PEG-NH₂ was achieved by carbodiimide chemistry and, after amine group deprotection by acid hydrolysis of BOC with TFA (Figure 1, Reaction 2), the GO sheets were bound on amino-terminal PSi by essentially using the same chemistry (Figure 1, Reaction 3) (Harris et al., 1992). A biosensor transducer always includes a specific bioprobe that recognizes a ligand of interest. Placing a biomolecule into

a complex matrix, leaving its properties untouched, requires proper design and stability test of the final hybrid device. In this frame, the interaction between the GO-PSi architecture and a model biological molecule, the Protein A [pure and in its FITC labeled form (PrA*)] was studied. The PrA* was covalently bound to the hybrid device using same EDC/NHS chemistry (Figure 1, Reaction 4). In order to verify the effective covalent bond between GO-nanosheets/amino-modified PSi and PrA/GO-modified PSi promoted by carbodiimide chemistry, two negative control samples (NH₂-PSi_CTR and GO-PSi_CTR) were incubated with GO and PrA (pure and in its FITC labeled form), respectively, without EDC/NHS treatment. Since

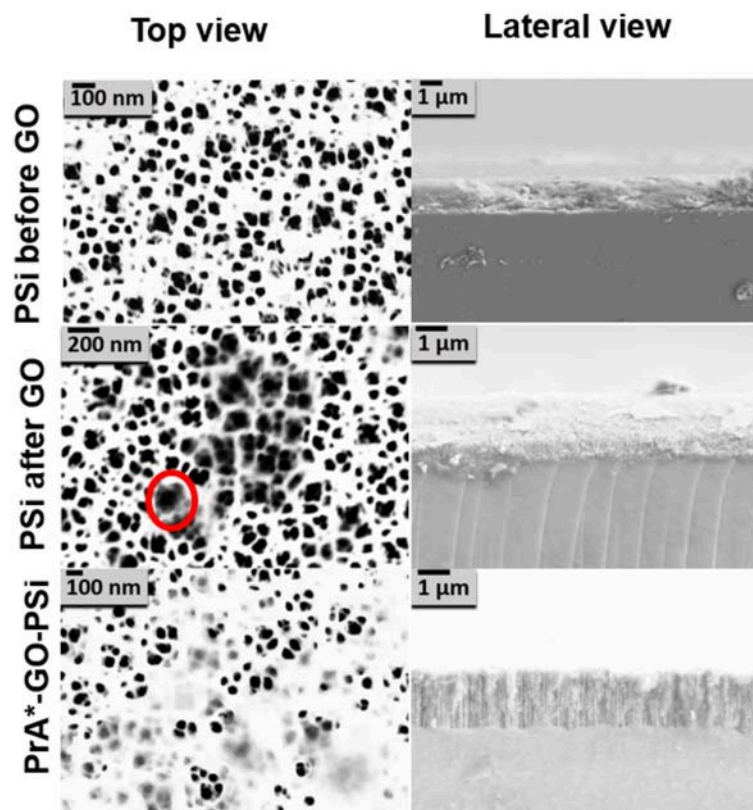


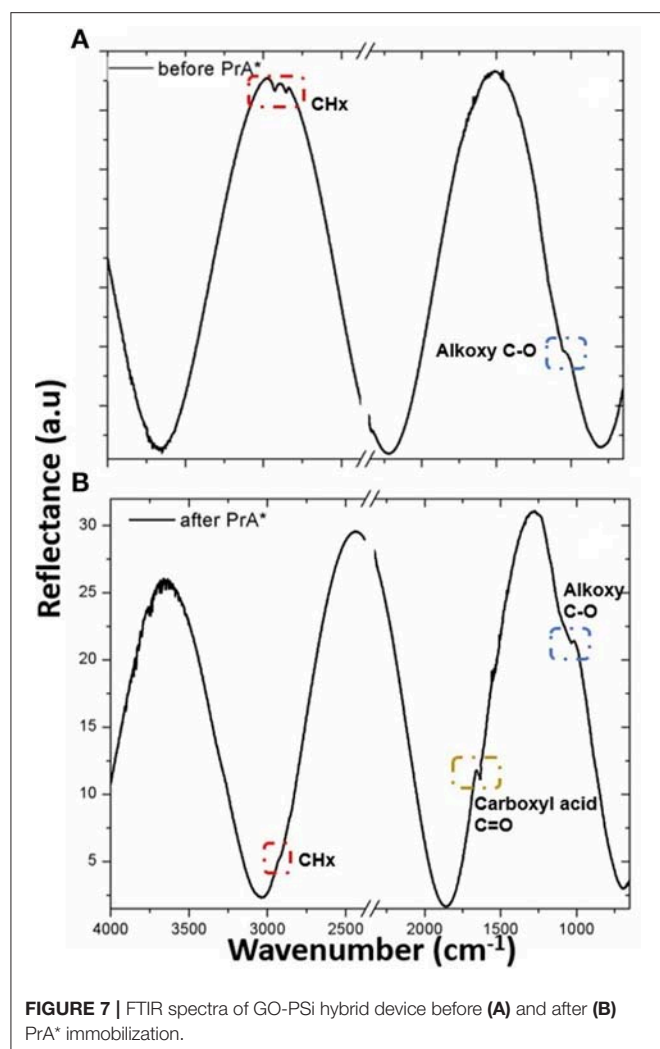
FIGURE 6 | SEM images of PSi before and after GO covalent immobilization, and after PrA functionalization. The red circle indicates the presence of GO.

carbodiimide conjugation should activate carboxyl groups by direct reaction with primary amines via amide bond formation, without EDC/NHS surface treatment, it was not possible to obtain any experimental evidence of covalently bonded GO and PrA on control samples.

Evaluation of surface wettability is a fundamental analysis in the development of such hybrid devices. After each functionalization step, different functional groups were exposed on the GO-PSi chip causing a change in the surface wettability. The as-etched PSi showed a hydrophobic surface quantified by a WCA value of $135 \pm 2^\circ$ (**Figure 2A**); a weak decrease of wettability value was evaluated after the hydrosilylation process ($\text{WCA} = 120 \pm 1^\circ$), mainly due to carboxyl-terminal chain (**Figure 2B**); the introduction of the hydrophilic group BOC-NH-PEG-NH₂ induced a further decrease of WCA value to $85 \pm 3^\circ$ (**Figure 2C**); the removal of the BOC group and the exposure of the hydrophilic amino group, present in the PEG chain, was responsible of a WCA value of $60 \pm 2^\circ$ (**Figure 2D**); after the GO sheets binding, the presence of the oxygen functional groups made the PSi substrate more hydrophilic with a WCA of $50 \pm 5^\circ$ (**Figure 2E**); finally, the PrA* bioconjugation on GO-PSi surface increased the wettability of the surface up to a WCA of $70 \pm 2^\circ$ due to the presence of hydrophobic amino acids in the protein structure (**Figure 2F**). No change of surface wettability was observed in the case of negative

control samples (NH₂-PSi_CTRL and GO-PSi_CTRL, data not shown).

Since chemical functionalization and bioconjugation are additive processes from the material point of view, the optical thickness (i.e., the product of physical thickness, d , by the average refractive index n of the layer) of the obtained GO-PSi hybrid device, calculated by the FFT of the reflectivity spectrum, was expected to increase. The FFT peak position along the x-axis corresponds to two times the optical thickness (2OT) of the layer (Rea et al., 2014). In **Figure 3** are reported the normal incidence reflectivity spectra of PSi before and after hydrosilylation (**Figure 3A**), and PEGylation process (**Figure 3C**) together with their corresponding FFTs (**Figures 3B,D**). Since the physical thickness d of PSi layer was fixed, the FFT peak shifts of about 90 nm, after UDA treatment, and of 145 nm after the PEGylation process were due to the increase of the average refractive index of the composite material. This result clearly indicated the two chemical functionalization steps added material layers to the PSi matrix. **Figure 3D** shows the reflectivity spectrum with the corresponding FFTs (**Figure 3E**) after the removal of the BOC protector group. The optimization of the reaction was confirmed as a blue shift of the peak of -100 nm (**Figure 3F**), since the chemical substance has been removed. The GO functionalization and the PrA* conjugation on GO-PSi surface is reported in **Figures 3G–J**. A FFT peak shift of 90 nm after



the PSi surface grafting by GO was an evidence of the occurred functionalization. Finally, the PrA* covalently linked to the hybrid surface induced a further red shift of 275 nm. The analysis of reflectivity spectra of negative control samples (NH₂-PSi_CTRL and GO-PSi_CTRL) showed no significant change before and after treatment with GO and PrA solution, respectively, (data not shown).

The infiltration of GO into PSi was also analyzed by PL measurements. As it can be noted in **Figure 4A**, in the case of bare PSi, no signal of PL could be detected; on the contrary, the covalent grafting of GO into GO-PSi structure was revealed by a modulation of the PL signal. This was a clear evidence of the GO infiltration into the PSi matrix. The concentration of GO covalently conjugated to PSi was estimated as about 7.5 μg/mL; this value was obtained by comparing the PL spectrum of GO-PSi device with those of some solutions containing different concentrations of GO (**Figure S4**).

Figure 4B shows a comparison between PL and reflectivity spectra recorded by GO infiltrated in PSi monolayer. The modulation of PL intensity could be explained by considering

the optical theory of Fabry-Perot interferometer. Among all the wavelengths, λ_{em} emitted by GO infiltrated in PSi, only those fulfilling the relationship $L = m (\lambda_{em}/2n_{PSi})$, with L thickness of the PSi layer and m integer, could constructively interfere producing maxima in the PL spectrum of the hybrid structure. The distance between two consecutive photoluminescence maxima was about 67 nm, which well matched the free spectral range of the GO-PSi hybrid structure. In a previous work, we demonstrated that the presence of an interferometer under the GO layer was able to modulate GO photoluminescence (Rea et al., 2014). No change of PL spectra was observed in the case of negative control samples (NH₂-PSi_CTRL and GO-PSi_CTRL).

Morphological features of the surface were highlighted by AFM (**Figures 5A–F**). The AFM images of bare PSi revealed the presence of hillocks and voids (black zones) of about 100 nm distributed on the whole surface; after the functionalization of the PSi chip with GO, partial pore blocking was evident due to the presence of big GO nano-sheets (white zones) on the PSi surface and some coverage of the surface was visible after the PrA* bioconjugation. The roughnesses of the sample surfaces were calculated by analyzing the AFM images obtaining values of roughness statistical media (Rsm) equal to $0.22 \pm 0.01 \mu\text{m}$ for PSi sample before GO, $Rsm = 0.45 \pm 0.03 \mu\text{m}$ after GO, and $Rsm = 0.34 \pm 0.02 \mu\text{m}$ after PrA*. SEM images of conjugated sample are reported in **Figure 6**. In the top view, traces of GO (highlighted by red circle) on the PSi surface could be seen, and, in the lateral views, the few GO sheets into the porous matrix were visible. The final PrA*-GO-PSi hybrid device had quite almost covered surface and partially blocked pores.

A further analysis of GO-PSi hybrid device functionalization with PrA* was obtained by FTIR spectroscopy (**Figure 7**). The presence of GO onto hybrid device was confirmed by the presence of CH_x at 2,929–2,851 cm⁻¹ of carbon networks and the alkoxy C–O at 1,024 cm⁻¹ (Yang et al., 2009). After the incubation with the PrA*, the hybrid device PrA*-GO-PSi showed the stretching bands of CH_x at 2,924 cm⁻¹ peak, the amide I band at 1,651 cm⁻¹ associated with C=O stretching vibration and the alkoxy C–O band at 1,037 cm⁻¹ (Socrates, 2007). These data confirmed the covalent bonding of PrA* onto GO-PSi hybrid device.

Confocal microscopy was used for a deeper characterization of the PrA* infiltration process. In particular, **Figure 8A** is a 3D representation of all focal planes fluorescence recorded by the instrument, confirming the covalent bioconjugation of PrA*. In case of the negative control, the corresponding 3D image was completely dark (**Figure 8B**), and there was not any evidence of aspecific absorption to sample surface. **Figure 8C** shows the sequence of confocal laser scanning microscope images of the PSi monolayer infiltrated by the PrA*: the first image was the one of the top surface while the last was the one recorded at the bottom. **Figure 8D** quantifies the intensity profiles of the average fluorescence signal and it could be clearly seen that the labeled protein was distributed as a Gaussian function having its maximum value close to the center of the layer. This result

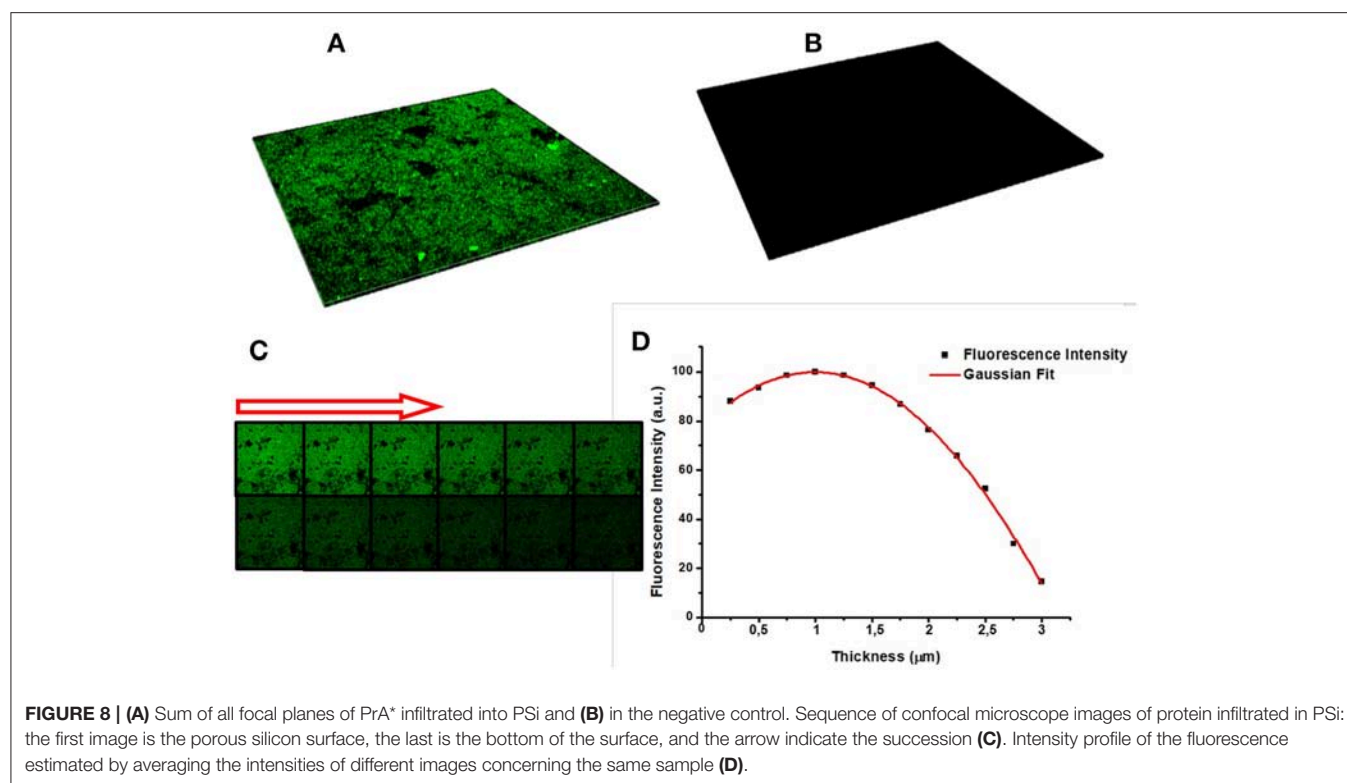


FIGURE 8 | (A) Sum of all focal planes of PrA* infiltrated into PSi and (B) in the negative control. Sequence of confocal microscope images of protein infiltrated in PSi: the first image is the porous silicon surface, the last is the bottom of the surface, and the arrow indicate the succession (C). Intensity profile of the fluorescence estimated by averaging the intensities of different images concerning the same sample (D).

further confirm that the protein was penetrated inside the pores (De Stefano and D'Auria, 2007).

CONCLUSIONS

A robust and chemically stable hybrid transducer for biosensing application based on GO, Psi, and PrA*, as a model bioprobes, has been designed and demonstrated. EDC/NHS coupling chemistry has efficiently grafted GO to PSi and PrA* to the GO-PSi matrix. Changes in reflectivity optical spectrum and in photoluminescence have been used to characterize the fabrication process but also the transducing features. AFM, SEM, and confocal imaging revealed the main features of the composite

structure. The results highlighted promising performances for next generation of multi-parametric biosensors.

AUTHOR CONTRIBUTIONS

All authors listed have made a substantial, direct and intellectual contribution to the work, and approved it for publication.

SUPPLEMENTARY MATERIAL

The Supplementary Material for this article can be found online at: <https://www.frontiersin.org/articles/10.3389/fchem.2018.00583/full#supplementary-material>

REFERENCES

- Boukherroub, R., Wojtyk, J. T. C., Wayner, D. D. M., and Lockwood, D. J. (2002). Thermal hydrosilylation of undecylenic acid with porous silicon. *J. Electrochem. Soc.* 149, H59–H63. doi: 10.1149/1.1432679
- Canham, L. (2017). *Properties of Porous Silicon*. Available online at: <http://trove.nla.gov.au/work/20545070?selectedversion=NBD13544299> (accessed August 2, 2017).
- Chien, C. T., Li, S. S., Lai, W. J., Yeh, Y. C., Chen, H. A., Chen, I. S., et al. (2012). Tunable Photoluminescence from graphene oxide. *Angew. Chemie Int. Ed.* 51, 6662–6666. doi: 10.1002/anie.201200474
- De Stefano, L., and D'Auria, S. (2007). Confocal imaging of protein distributions in porous silicon optical structures. *J. Phys. Condens. Matter* 19:395009. doi: 10.1088/0953-8984/19/39/395009
- Dreyer, D. R., Park, S., Bielawski, C. W., and Ruoff, R. S. (2010). The chemistry of graphene oxide. *Chem. Soc. Rev.* 39, 228–240. doi: 10.1039/B917103G
- Eda, G., Lin, Y. Y., Mattevi, C., Yamaguchi, H., Chen, H. A., Chen, I. S., et al. (2010). Blue photoluminescence from chemically derived graphene oxide. *Adv. Mater.* 22, 505–509. doi: 10.1002/adma.200901996
- Ghulinyan, M., Geloz, B., Ohta, T., Pavesi, L., Lockwood, D. J., and Koshida, N. (2008). Stabilized porous silicon optical superlattices with controlled surface passivation. *Appl. Phys. Lett.* 93:061113. doi: 10.1063/1.2969294
- Gokus, T., Nair, R. R., Bonetti, A., Böhmeler, M., Lombardo, A., Novoselov, K. S., et al. (2009). Making graphene luminescent by oxygen plasma treatment. *ACS Nano* 3, 3963–3968. doi: 10.1021/nn9012753
- Gupta, A., Shaw, B. K., and Saha, S. K. (2014). Bright green photoluminescence in aminoazobenzene-functionalized graphene oxide. *J. Phys. Chem. C* 118, 6972–6979. doi: 10.1021/jp412156x
- Harris, J. M., Sedaghat-Herati, M. R., Sather, P. J., Brooks, D. E., and Fyles, T. M. (1992). "Synthesis of new poly(ethylene glycol) derivatives," in *Poly(Ethylene Glycol) Chemistry*, ed J. M. Harris (Boston, MA: Springer US), 371–381.

- Jung, J. H., Cheon, D. S., Liu, F., Lee, K. B., and Seo, T. S. (2010). A graphene oxide based immuno-biosensor for pathogen detection. *Angew. Chemie Int. Ed.* 49, 5708–5711. doi: 10.1002/anie.201001428
- Liu, Y., Dong, X., Chen, P. et al. (2012). Biological and chemical sensors based on graphene materials. *Chem. Soc. Rev.* 41, 2283–2307. doi: 10.1039/C1CS15270J
- Loh, K. P., Bao, Q., Eda, G., and Chhowalla, M. (2010). Graphene oxide as a chemically tunable platform for optical applications. *Nat. Chem.* 2, 1015–1024. doi: 10.1038/nchem.907
- Morales-Narváez, E., and Merkoçi, A. (2012). Graphene oxide as an optical biosensing platform. *Adv. Mater.* 24, 3298–3308. doi: 10.1002/adma.201200373
- Park, S., and Ruoff, R. S. (2009). Chemical methods for the production of graphenes. *Nat. Nanotechnol.* 4, 217–224. doi: 10.1038/nnano.2009.58
- Rea, I., Casalino, M., Terracciano, M., Sansone, L., Politi, J., and De Stefano, L. (2016). Photoluminescence enhancement of graphene oxide emission by infiltration in an aperiodic porous silicon multilayer. *Opt. Exp.* 24, 24413–24421. doi: 10.1364/OE.24.024413
- Rea, I., Sansone, L., Terracciano, M., De Stefano, L., Dardano, P., Giordano, M., et al. (2014). Photoluminescence of graphene oxide infiltrated into mesoporous silicon. *J. Phys. Chem. C* 118, 27301–27307. doi: 10.1021/jp506539n
- Sailor, M. J. (2012). *Porous Silicon in Practice: Preparation, Characterization and Applications*. San Diego, CA: Wiley-VCH.
- Sam, S., Touahir, L., Salvador Andresa, J., Allongue, P., Chazalviel, J. N., Gouget-Laemmel, A. C., et al. (2010). Semiquantitative study of the EDC/NHS activation of acid terminal groups at modified porous silicon surfaces. *Langmuir* 26, 809–814. doi: 10.1021/la902220a
- Shabir, Q., Webb, K., Nadarassan, D. K., Loni, A., Canham, L. T., Terracciano, M., et al. (2017). Quantification and reduction of the residual chemical reactivity of passivated biodegradable porous silicon for drug delivery applications. *Silicon* 10:349. doi: 10.1007/s12633-016-9454-4
- Socrates, G. (2007). *Infrared and Raman Characteristic Group Frequencies: Tables and Charts*. John Wiley & Sons. Available online at: <https://www.wiley.com/en-us/Infrared+and+Raman+Characteristic+Group+Frequencies%3A+Tables+and+Charts%2C+3rd+Edition-p-9780470093078> (accessed April 14, 2018).
- Terracciano, M., De Stefano, L., Borbone, N., Politi, J., Oliviero, G., Nici, F., et al. (2016). Solid phase synthesis of a thrombin binding aptamer on macroporous silica for label-free optical quantification of thrombin. *RSC Adv.* 6, 86762–86769. doi: 10.1039/C6RA18401D
- Wu, M., Kempaiah, R., Huang, P. J., Maheshwari, V., and Liu, J. (2011). Adsorption and desorption of DNA on graphene oxide studied by fluorescently labeled oligonucleotides. *Langmuir* 27, 2731–2738. doi: 10.1021/la1037926
- Yang, X., Zhang, X., Ma, Y., Huang, Y., Wang, Y., and Chen, Y. (2009). Superparamagnetic graphene oxide-Fe₃O₄ nanoparticles hybrid for controlled targeted drug carriers. *J. Mater. Chem.* 19, 2710–2714. doi: 10.1039/b821416f
- Zhang, J., Zhang, F., Yang, H., Huang, X., Liu, H., Zhang, J., et al. (2010). Graphene oxide as a matrix for enzyme immobilization. *Langmuir* 26, 6083–6085. doi: 10.1021/la904014z
- Zhang, Y., Wu, C., Guo, S., and Zhang, J. (2013). Interactions of graphene and graphene oxide with proteins and peptides. *Nanotechnol. Rev.* 2, 27–45. doi: 10.1515/ntrev-2012-0078

Conflict of Interest Statement: The authors declare that the research was conducted in the absence of any commercial or financial relationships that could be construed as a potential conflict of interest.

Copyright © 2018 Moretta, Terracciano, Dardano, Casalino, De Stefano, Schiattarella and Rea. This is an open-access article distributed under the terms of the Creative Commons Attribution License (CC BY). The use, distribution or reproduction in other forums is permitted, provided the original author(s) and the copyright owner(s) are credited and that the original publication in this journal is cited, in accordance with accepted academic practice. No use, distribution or reproduction is permitted which does not comply with these terms.



Porous Silicon Bragg Reflector/Carbon Dot Hybrids: Synthesis, Nanostructure, and Optical Properties

Naama Massad-Ivanir^{1†}, Susanta Kumar Bhunia^{2,3†}, Raz Jelinek^{3,4*} and Ester Segal^{1,5*}

¹ Department of Biotechnology and Food Engineering, Technion–Israel Institute of Technology, Haifa, Israel, ² Schulich Faculty of Chemistry, Technion–Israel Institute of Technology, Haifa, Israel, ³ Department of Chemistry, Ben Gurion University of the Negev, Beer Sheva, Israel, ⁴ Ilse Katz Institute for Nanotechnology, Ben Gurion University of the Negev, Beer Sheva, Israel, ⁵ The Russell Berrie Nanotechnology Institute, Technion–Israel Institute of Technology, Haifa, Israel

OPEN ACCESS

Edited by:

Nicolas Hans Voelcker,
Monash University, Australia

Reviewed by:

Abel Santos,
University of Adelaide, Australia
Raul J. Martin-Palma,
Universidad Autónoma de Madrid,
Spain

*Correspondence:

Ester Segal
esegal@technion.ac.il
Raz Jelinek
razj@bgu.ac.il

[†]These authors have contributed
equally to this work

Specialty section:

This article was submitted to
Chemical Engineering,
a section of the journal
Frontiers in Chemistry

Received: 18 September 2018

Accepted: 05 November 2018

Published: 23 November 2018

Citation:

Massad-Ivanir N, Bhunia SK, Jelinek R
and Segal E (2018) Porous Silicon
Bragg Reflector/Carbon Dot Hybrids:
Synthesis, Nanostructure, and Optical
Properties. *Front. Chem.* 6:574.
doi: 10.3389/fchem.2018.00574

Carbon dots (C-dots) exhibit unique fluorescence properties, mostly depending upon their physical environments. Here we investigate the optical properties and nanostructure of Carbon dots (C-dots) which are synthesized *in situ* within different porous Silicon (PSi) Bragg reflectors. The resulting hybrids were characterized by photoluminescence, X-ray photoelectron, and Fourier Transform Infrared spectroscopies, as well as by confocal and transmission electron microscopy. We show that by tailoring the location of the PSi Bragg reflector photonic bandgap and its oxidation level, the C-dots emission spectral features can be tuned. Notably, their fluorescence emission can be significantly enhanced when the high reflection band of the PSi host overlaps with the confined C-dots' peak wavelength, and the PSi matrix is thermally oxidized at mild conditions. These phenomena are observed for multiple compositions of PSi Bragg reflectors/C-dots hybrids.

Keywords: porous silicon, carbon dots, Bragg reflectors, photoluminescence, fluorescence, Fabry–Pérot, optical properties

INTRODUCTION

In recent years, carbon dots (C-dots) have attracted considerable attention as a promising green nanomaterial for applications in sensing, bio-imaging, and optical devices owing to their unique optical properties (Lim et al., 2015; Tuerhong et al., 2017; Wang et al., 2017). Specifically, C-dots exhibit excitation-dependent emission, bright luminescence, low bleaching, and biocompatibility (Baker and Baker, 2010; Ding et al., 2014; Bhunia et al., 2016a; Sun and Lei, 2017). C-dots are small carbonaceous nanoparticles, with a typical size below 10 nm, and they are easily synthesized from various inexpensive and available precursors (Bhunia et al., 2016a,b). A notable feature of C-dots is the dependence of their optical properties upon their surface structure and proximate physical environments (Kwon et al., 2013; Zhang et al., 2013; Nandi et al., 2014).

Porous silicon (PSi)-based nanostructures have been widely reported as potential host matrices for light emitting materials, including organic dyes (Palestino et al., 2008; Jenie et al., 2014, 2015; Krismastuti et al., 2014; Mo et al., 2017) and quantum dots (QDs) (DeLouise Lisa and Ouyang, 2009; Qiao et al., 2010; Gaur et al., 2011, 2013; Dovzhenko et al., 2015, 2018a; Liu et al., 2015; Dovzhenko D. S. et al., 2016; Li et al., 2017; Zhang et al., 2017). PSi-based photonic crystals hosts

[e.g., Bragg reflector (Liu et al., 2015; He et al., 2017; Li et al., 2017) and microcavities (Jenie et al., 2014, 2015)] have been shown to affect the propagation and distribution of the light emitted by the guest fluorophores (Pacholski, 2013; Dovzhenko D. et al., 2016; Dovzhenko D. S. et al., 2016). Specifically, PSi-based microcavities have been shown to improve the spectral properties of emitting molecules, e.g., quantum yield, photostability and luminescence lifetime, by alignment between the reflectance spectrum dip of the microcavity and the emission of the fluorophores (Jenie et al., 2016).

We have recently synthesized a new hybrid host-guest material, consisting of a Fabry-Pérot PSi thin film encapsulating C-dots (Massad-Ivanir et al., 2018). In particular, we showed that the PSi/C-dots hybrid can be used for designing label-free optical sensors using two orthogonal signals i.e., the reflectivity of the PSi nanostructure and the fluorescence of the confined C-dots. Moreover, we demonstrated that these two signal modalities can be simultaneously detected and collected. Importantly, we have also demonstrated the sensing performance of the PSi/C-dots system is superior when compared to that of the individual components.

Here, we present a new composite system comprising C-dots embedded within PSi-based Bragg reflector, designed to explore the interrelation between the optical properties of the confined C-dots and the PSi host. Bragg reflectors are constructed by a simple anodization process in which the current density is alternated between two distinct values in a stepwise manner and the resulting multilayered porous film displays alternating layers of high and low refractive index (Vincent, 1994; Pavese and Dubos, 1997; Bisi et al., 2000). The optical thickness of the reflector layers is defined as $\lambda/4$, where λ is the center wavelength of the high reflectivity region (called photonic bandgap or stop band) over a desired spectral region (Bisi et al., 2000; Jane et al., 2009; Kilian et al., 2009; Pacholski, 2013). The position of the photonic bandgap is easily tuned by changing the electrochemical etching conditions (Sailor, 2011; Ning et al., 2014). The use of Bragg reflectors as the host matrix allows to control the propagation and distribution of the light emitted from the imbedded C-dots.

Bragg reflector/C-dots hybrids were constructed through a simple synthesis, in which a carbon precursor (such as glucose or sucrose solutions) was allowed to infiltrate into the PSi-based Bragg reflector matrix, and subsequent heating step generated the entrapped C-dots. We studied diverse types of C-dots with different emission spectra (blue, green, yellow and red) within various nanostructured Bragg reflectors with different photonic bandgap centers (425, 530, and 600 nm) and oxidation levels (freshly-etched, partially- and fully-oxidized). We demonstrate that by tuning the Bragg reflector photonic bandgap center to match the confined C-dots fluorescence emission, we can control the emission spectra properties. To the best of our knowledge, there is no study regarding optical properties of C-dots confined within photonic crystals. The present study can open up opportunities to design advanced nanomaterials with highly-tunable optical properties.

MATERIALS AND METHODS

Materials

Single-side polished and heavily-doped p-type Si wafers (0.001 Ω -cm resistivity, $\langle 100 \rangle$ oriented, B-doped) were obtained from Sil'tronix Silicon Technologies, France. Aqueous 48% hydrofluoric acid (HF) and ethanol (99.9%) were purchased from Merck, Germany. D-(+)-Glucose, Sucrose, Sodium tripolyphosphate, and O,O'-Bis (2-aminopropyl) polypropylene glycol-block-polyethylene glycol-block-polypropylene glycol (PEG-diNH₂) were supplied by Sigma-Aldrich Chemicals, Israel.

Fabrication of PSi Bragg Reflectors and Fabry-Pérot Films

A two-step anodization process was applied to produce a highly-porous nanostructures with pores of 25–40 nm to allow accommodation the C-dots. First, a sacrificial layer was etched in the Si wafer at a constant current density of 385 mA cm⁻² for 30 s (electrolyte composition: aqueous solution of HF and ethanol at 3:1 (v/v) ratio), using a ring of platinum as a counter electrode. Next, the resulting PSi layer was dissolved in an aqueous NaOH solution (0.1 M) followed by exposure to a solution composed of 1:3:1 (v/v/v) HF, ethanol and deionized water, respectively. Then, a second etching step was performed; the detailed etching conditions are summarized in **Table 1**. Finally, the freshly-etched films were thermally oxidized in a tube furnace (Thermo Scientific, Lindberg/Blue M™ 1,200°C Split-Hinge, USA) at 400°C or at 800°C for 1 h in ambient air, to form porous SiO₂ (PSiO₂) nanostructures.

Scanning Electron Microscopy

The morphology, i.e., thickness and average pore diameter, of the PSi Bragg reflectors and Fabry-Pérot thin films were characterized by high resolution scanning electron microscopy (HRSEM), using a Carl Zeiss Ultra Plus instrument, operated at an accelerating voltage of 1 keV.

Fourier Transform Infrared (FTIR) Spectroscopy

Freshly-etched and thermally-oxidized Bragg reflector films were characterized by FTIR spectroscopy at attenuated total reflectance (ATR) mode, utilizing a Thermo 6700 FTIR instrument, equipped with a Smart iTR diamond ATR device.

In situ Synthesis of C-Dots Within PSi Films

Various C-dots (blue, green, yellow and red) were incorporated into the porous films by *in situ* synthesis within the nanostructures. Different carbonaceous precursor solutions were introduced onto the upper surface of the PSi film and allowed to infiltrate into the pores. Subsequently, the samples were placed in an oven and mildly heated. **Table 2** summarizes the composition of the different precursor solutions and the pyrolysis conditions for each type of C-dots.

Synthesis of C-Dots Dispersions

Green C-dots dispersions, termed as “free” C-dots, were synthesized by a mild slow heating (at 150°C for 6 h) using the

TABLE 1 | Etching conditions of the different PSi films and their structural characteristics (i.e., average pore diameter and porous layer thickness as determined by high-resolution Scanning electron microscopy, HRSEM).

Photonic bandgap (nm)	Etching conditions (mA/cm ² , s)			Porous film characteristics			
	High refractive index layer	Low refractive index layer	No. of repeats	Pore diameter ^a (nm)		Pore diameter ^b (nm)	Thickness (nm)
				High refractive index layer	Low refractive index layer		
425	77, 1.37	385, 0.48	40	25 ± 3	38 ± 7	50 ± 6	6,360 ± 20
530	77, 1.59	385, 0.56	40				
600	77, 1.93	385, 0.65	40				
Single layer		385, 30		42 ± 10		54 ± 10	4,920 ± 40

The PSi Bragg reflectors with bandgap centers at 425, 530, and 600 nm were prepared from highly doped p-type single-crystal Si wafers anodized at alternating current densities of 77 and 385 mA cm⁻². The etching time of each layer slightly differ from wafer to wafer, due to small variations in the wafer resistivity and the following oxidation process. PSi Fabry-Pérot films, termed as single-layers, were fabricated at a constant current density of 385 mA cm⁻² for 30 s. ^aAverage pore diameter was measured from cross-sectional SEM images. ^bAverage pore diameter was measured from top-view SEM images.

TABLE 2 | Precursor aqueous solution composition and pyrolysis conditions for each type of C-dots.

C-dots	Precursor solution concentration (mg mL ⁻¹)	Pyrolysis conditions	
		Temperature (°C)	Time (h)
Blue	Glucose, 200	125	6
Green	Glucose, 400	150	6
Yellow	Sucrose, 400	150	6
Red	Glucose, 40 Na ₅ P ₃ O ₁₀ , 0.4 PEG-diNH ₂ , 20	150	7

aqueous precursor (400 mg glucose in 1 mL of double-distilled-H₂O) in a Teflon-lined autoclave chamber.

Measurement of Fluorescence Emission Spectra

The PSi/C-dot hybrid's fluorescence emission spectra were recorded at different excitation wavelengths using a spectrofluorimeter (FL920, Edinburgh Instruments, UK). The emission spectra were measured at different excitation wavelengths ranging from 300 to 600 nm.

Confocal Laser Scanning Microscopy (CLSM)

Following the *in situ* synthesis of C-dots within the PSi films, the resulting hybrids were characterized using an LSM 700 (Carl Zeiss, Germany) confocal laser scanning microscope (CLSM) connected to a Zeiss inverted microscope equipped with a Zeiss × 63 oil immersion objective. Laser lined at 405 and 555 nm were used to excite the PSi and the C-dots, respectively. Three-dimensional projection images of the hybrids were obtained using ZEN 2009 (Carl Zeiss, Germany) software;

where z-scans in 0.5 μm increments were taken over a depth of ~8 μm and projected and stacked. Imaris software (Bitplane AG, Zurich, Switzerland) was used for subsequent image analysis.

Transmission Electron Microscopy

The nanostructure of “confined” (extracted from the hybrids) and “free” (prepared in solution) C-dots was studied by a JEOL JEM-2100F high-resolution transmission electron microscope (HRTEM), at an accelerating voltage of 200 keV. Confined C-dots were collected from PSiO₂/C-dots hybrids after dissolution of the PSiO₂ matrix in a solution of HF and ethanol (3:1 v/v, respectively), followed by extraction of C-dots in absolute ethanol. Subsequently, the resulting C-dots solution was drop-casted on a graphene-coated copper grid.

X-Ray Photoelectron Spectroscopy (XPS)

Thermo Scientific ECSALAB X-ray photoelectron spectrometer with an AlKα x-ray source and a monochromator was used to characterize the “confined” (extracted from the hybrids) and “free” (prepared in solution) C-dots. The X-ray beam size was 500 μm and survey spectra were recorded with pass energy of 150 eV; high-energy resolution spectra were recorded with pass energy of 20 eV. XPS data was processed using the AVANTGE software.

Measurement of Interferometric Reflectance Spectra

Interferometric reflectivity spectra of the different PSi/C-dots hybrids were collected using a USB4000 (Ocean Optics, USA) charge-coupled device (CCD) spectrometer, which is fitted with a microscope objective lens coupled to a bifurcated fiber optic cable. A tungsten light source was focused onto the center of the sample surface with a spot size of 1–2 mm²; where both illumination of the surface and collection of the reflected light were performed along an axis coincident with the surface normal. The reflectivity data were recorded in a

wavelength range of 350–850 nm, with a spectral acquisition time of 25 ms.

RESULTS AND DISCUSSION

Preparation and Characterization of Porous Silicon Bragg Reflectors

Porous Silicon (PSi) Bragg reflector films with photonic bandgap centers at 425, 530, and 600 nm were fabricated by Si anodization and the detailed etching conditions are summarized in **Table 1** (Materials and Methods section). In general, 40 pairs of alternating high ($n_H = 1.87$) and low ($n_L = 1.12$) refractive index layers were constructed. **Figures 1A–C** presents characteristic images of the resulting PSi Bragg reflectors and their corresponding reflectivity spectra. The detailed structure of the films, in terms of their porous layer thickness and pore diameter, was studied by HRSEM. **Figure 1D** depicts cross-sectional micrographs of a typical PSiO₂ Bragg reflector, revealing the periodic nanostructure, which consists of a series of thin layers of alternating high and low refractive indices. The thickness of the resulting porous layer is $\sim 6.3 \mu\text{m}$ with interconnecting cylindrical pores (Bisi et al., 2000; Zhang, 2004), ranging in diameter from 25 to 40 nm. The average diameter of the pores' entrance is ~ 50 nm (see **Figure 1E**, top-view micrograph), which is somewhat larger than the bulk pores owing to the two-step anodization process. **Table 1** summarizes the detailed structural features for the three types of Bragg reflector films.

In the next step, the freshly-etched PSi films were thermally oxidized at 400°C or at 800°C for 1 h (denoted as partially- and fully-oxidized PSi, respectively). The photonic bandgap centers of the Bragg reflectors were tuned to values of 425, 530, and 600 nm after the thermal oxidation step. In order to do so, the freshly-etched PSi Bragg reflectors were fabricated to higher photonic bandgap centers, while after oxidation the bandgap wavelengths were blue-shifted to the desired mentioned values. The chemical properties of the different porous films were characterized by FTIR-ATR spectroscopy and the obtained spectra are presented in **Figure S1 (Supplementary Material)**. The spectrum of a freshly-etched PSi surface (**Figure S1**, trace A) depicts typical Si-H_x bending modes at 625, 661, and 920 cm⁻¹ (Socrates, 2001; Xia et al., 2006). Two small peaks related to the Si-OH stretching modes are also observed at 820 and 883 cm⁻¹ (Socrates, 2001; Xia et al., 2006). The latter are possibly attributed to the very thin native oxide layer that forms on the surface upon exposure to air. The spectrum of a partially-oxidized PSi surface (**Figure S1**, trace B) depicts small peaks that are related to Si-H_x bending modes at 625 and 900 cm⁻¹. An intense broad peak at 1,056 cm⁻¹, which is not observed for the freshly-etched surface, is ascribed to the Si-O-Si stretching mode (Socrates, 2001; Xia et al., 2006; Massad-Ivanir et al., 2011). Furthermore, an additional peak related to -(O_ySiH_x) vibration mode is observed at 802 cm⁻¹ (Shtenberg et al., 2014). The spectrum of the fully-oxidized PSi surface (**Figure S1**, trace C) depicts a larger Si-O-Si stretching mode peak at 1,056 cm⁻¹ and -(O_ySiH_x) vibration mode peak at 800 cm⁻¹. The latter are in

correlation with the disappearance of the Si-H_x peaks (at 625 and 900 cm⁻¹), owing to complete oxidation of hydrogen-terminated Si species (Shtenberg et al., 2014).

Synthesis of Bragg Reflectors/C-Dots Hybrid

PSi/C-dot hybrids were synthesized by allowing the carbonaceous precursor solution (see **Table 2** for details) to infiltrate into the porous nanostructure, followed by a mild pyrolysis process. In order to tune the photonic bandgap centers of Bragg reflectors to overlap with the fluorescence emission of the C-dots, we first characterized the emission spectra of C-dots embedded within Fabry-Pérot PSiO₂ thin films and representative results are presented in **Figure 2** (for blue, green, yellow and red C-dots). According to obtained spectra, the etching conditions of the different Bragg reflectors were further tuned to adjust their photonic bandgap center to overlap with the wavelength at which maximum fluorescence emission from the C-dots was attained. These values are marked by arrows in **Figure 2** and correspond to 425, 505, 535, and 600 nm of blue, green, yellow and red C-dots, respectively. In the next step, the C-dots precursors (see details in **Table 2**) were introduced into their corresponding PSi Bragg reflectors substrates. The latter included freshly-etched, partially-oxidized and fully-oxidized PSi and thus, three types of PSi/C-dots were prepared for each Bragg reflector.

Characterization of the Confined C-Dots

The detailed nanostructure and composition of the C-dots, confined within the PSiO₂ Bragg reflectors, were characterized by HRTEM and XPS, respectively. The confined C-dots were extracted from the PSiO₂ by dissolving the porous scaffold in HF and compared to “free” C-dots, which were prepared in solution from the same carbonaceous precursors.

The XPS data shown in **Figure 3** depicts the atomic species present in confined and “free” green C-dots (as representative C-dots). These results confirm minor differences between C-dots prepared *in situ* from confined precursor within the PSiO₂ Bragg reflector matrix and C-dots synthesized in solution. Specifically, the deconvoluted C 1s spectrum displays peaks at 284.7 eV, corresponding to sp² carbon atoms (C=C), 286.1 eV, assigned to C-OH groups and 287.6 eV, for -COOH and/or -COOR groups (Bhunia et al., 2016a,b; Massad-Ivanir et al., 2018). The O 1s spectrum shows peaks at 532.3 eV for O=C=OH and/or C-OH groups. The same XPS C1s and O1s signature peak positions were observed for C-dots extracted from PSiO₂ Fabry-Pérot thin films (**Figure 3A**), C-dots extracted from PSiO₂ Bragg reflectors with different photonic bandgap centers (**Figures 3B,C**) and “free” C-dots (**Figure 3D**). It is important to note that the “free” C-dots demonstrate the same XPS C1s and O1s signature peak positions. However, different deconvoluted XPS peak intensities were obtained, confirming that distinctive C-dots were formed within the porous nanostructures, in agreement with our previous work (Massad-Ivanir et al., 2018).

The representative TEM and HRTEM images shown in **Figures 4, S2 (Supplementary Material)** reveal the structural features of green C-dots prepared *in situ* within the Bragg

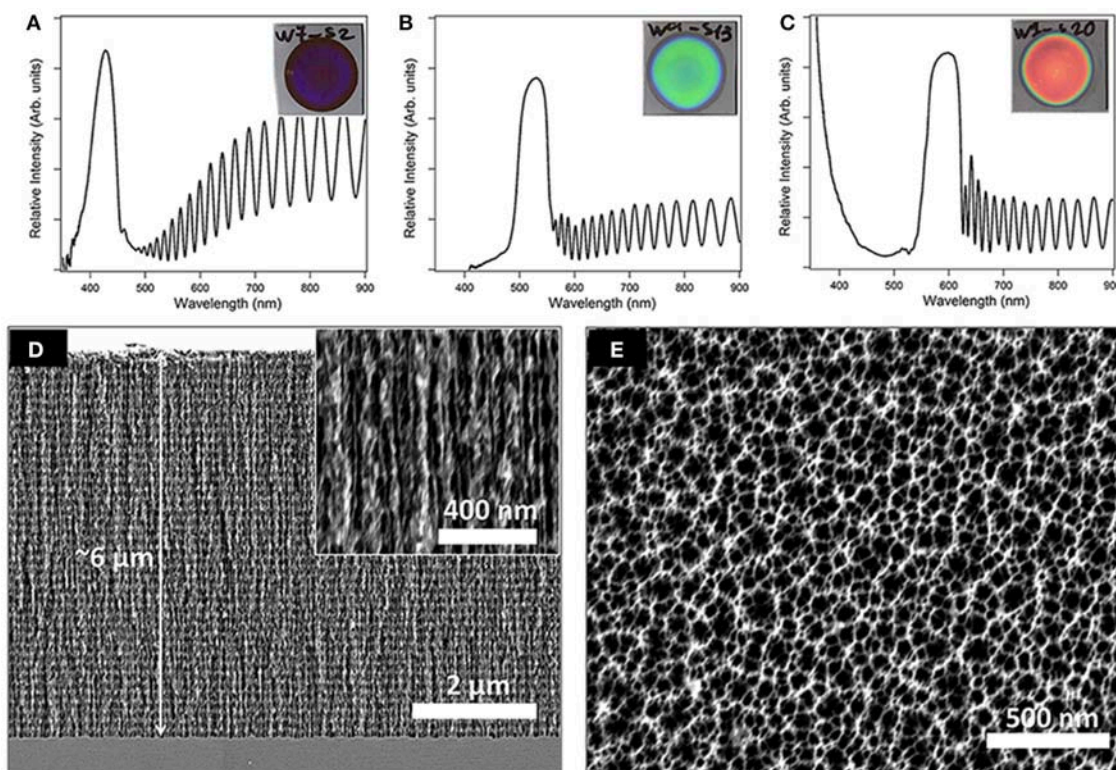


FIGURE 1 | Upper panel presents images and corresponding reflectivity spectra of the different PSi Bragg reflectors with bandgap centers at (A) 425, (B) 530, and (C) 600 nm. Lower panel depicts characteristic HRSEM images of a PSiO₂ Bragg reflector (D) cross-sectional and (E) top-view.

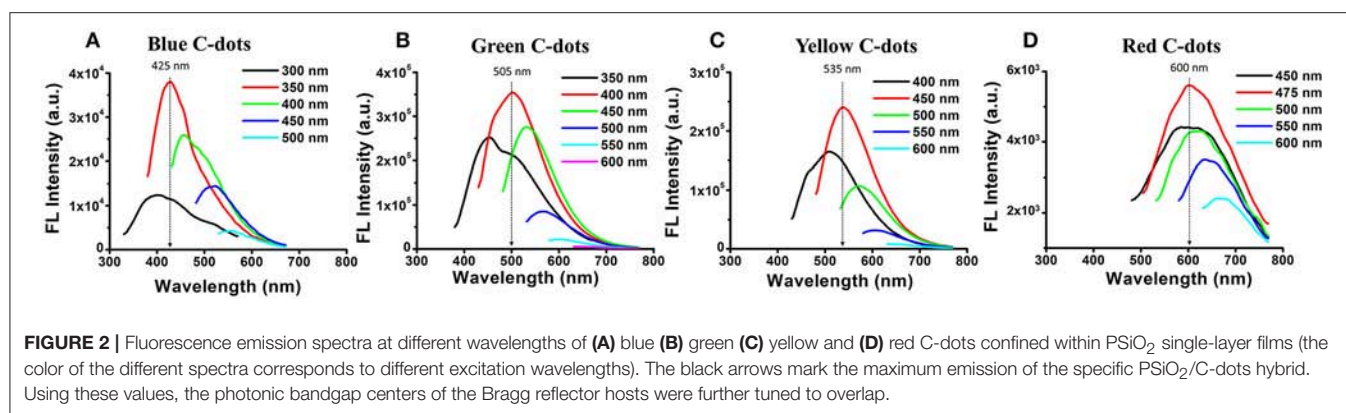
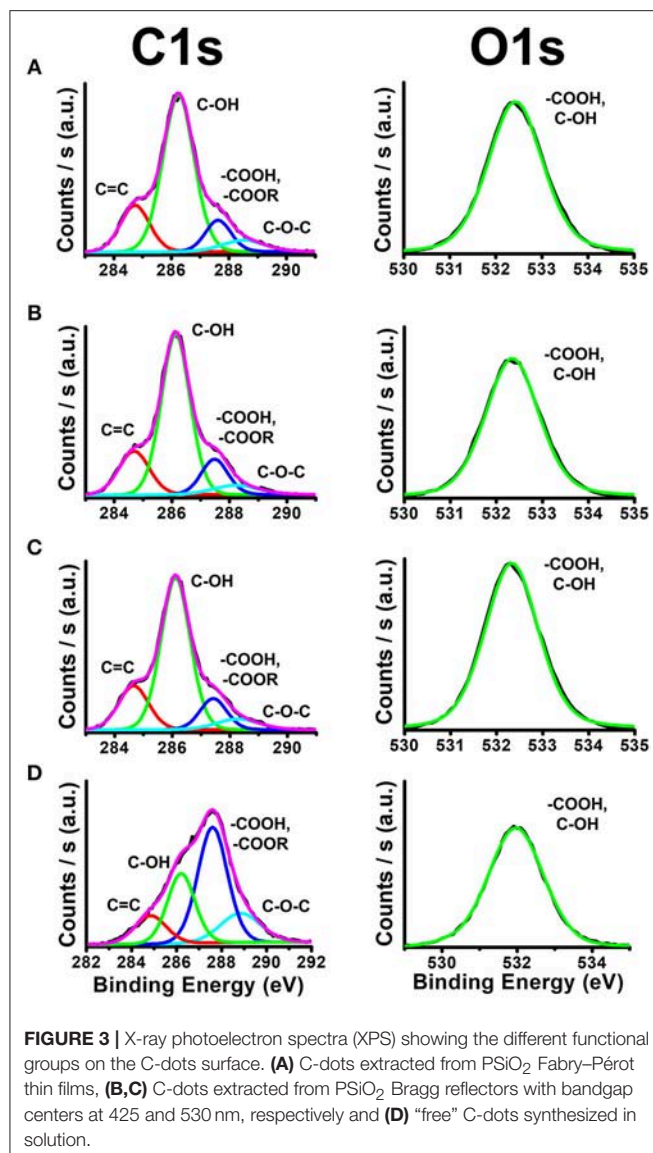


FIGURE 2 | Fluorescence emission spectra at different wavelengths of (A) blue (B) green (C) yellow and (D) red C-dots confined within PSiO₂ single-layer films (the color of the different spectra corresponds to different excitation wavelengths). The black arrows mark the maximum emission of the specific PSiO₂/C-dots hybrid. Using these values, the photonic bandgap centers of the Bragg reflector hosts were further tuned to overlap.

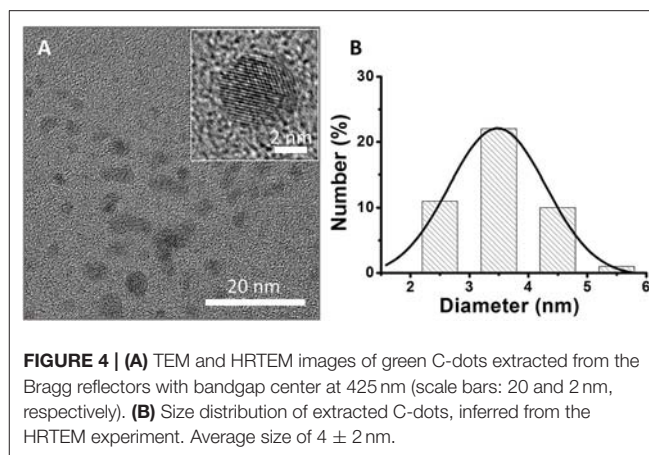
reflector nanoscale pores. The C-dots extracted from the different PSiO₂ matrices (Bragg reflectors with bandgap centers at 425 nm, 530 nm and PSiO₂ Fabry-Pérot thin film) exhibit a uniform spherical shape (see **Figures 4, S2, S3**, respectively) with a typical size of ~ 3.5 nm, as determined by size distribution analysis. The inset in **Figure 4** (as well as insets in **Figures S2, S3**) depicts detailed nanostructure of the collected nanoparticles. The crystalline graphite cores of the extracted C-dots are clearly observed with an in-plane lattice spacing of 0.215 nm, corresponding to the [110] plane of graphite (Dolai et al., 2017). The “free” green C-dots, prepared in solution, exhibit an average diameter of ~ 3.2 nm and a similar nanostructure, see

Figure S4 (Supplementary Material). These results confirm that the surface chemistry and size distribution of the confined C-dots are similar, regardless the nanostructures architecture and the location of Bragg reflector photonic bandgap center.

To validate the location of the C-dots within the porous layer, the reflectance spectra of the Bragg reflectors were recorded, before and after the C-dots synthesis. For partially- and full-oxidized PSi reflectors, significant red-shifts of the photonic bandgap, in the range of 75–125 nm, were observed following the *in situ* synthesis of the C-dots (**Figure 5A**), suggesting formation of the C-dots within the porous nanostructure. While, for the freshly-etched PSi reflectors, no change in the photonic



bandgap was detected (Figure S5), indicating that the C-dots did not penetrate into the nanostructure. Confocal laser scanning microscopy (CLSM) is used as a complementary tool to follow the distribution of the C-dots within the oxidized layers and clearly reveal the dispersion of C-dots within the pores, see Figures 5B–D. Specifically, the blue photoluminescence (PL) signal (Figure 5B), which is ascribed to the PSiO₂ scaffold ($\lambda_{\text{ex}} = 405 \text{ nm}$, $\lambda_{\text{em}} \geq 420 \text{ nm}$, long pass filter; Sa'ar, 2009), allows for the analysis of the host matrix and can be spatially correlated to the fluorescence of the red C-dots ($\lambda_{\text{ex}} = 555 \text{ nm}$, $\lambda_{\text{em}} \geq 560 \text{ nm}$, long pass filter) within the porous film (Figure 5C). Note that the C-dots fluorescence was recorded in z direction from the upper surface into the pores over a depth of $\sim 8 \mu\text{m}$, where z-scans in $0.5 \mu\text{m}$ increments were taken, projected and stacked as presented in Figures 5B–D. The overlay image (Figure 5D) confirms that fluorescence of the C-dots was observed throughout the entire depth of the porous scaffold over



a distance of $\sim 6 \mu\text{m}$. These results also indicate that the laser beam penetrated into the porous layer and induced excitation of the embedded C-dots, resulting in a substantial emission from entire depth of the PSiO₂. Residual fluorescence signals of the C-dots were also detected in a region slightly above the PSiO₂ interface (Figure 5D), likely because of attachment of the nanoparticles to the PSiO₂ surface.

Optical Properties of Bragg Reflector/C-Dots Hybrids

The optical properties of the confined C-dots were investigated while embedded within different PSi optical nanostructures (Fabry-Pérot thin film vs. Bragg reflectors with diverse photonic bandgap centers) at varied oxidation levels (none, partially, and fully). It is worth noting that the Bragg reflector hosts provide very high surface areas that are accessible to UV irradiation, thus capable of exciting the C-dot fluorescence. Figure 6 underscores the changes in emission spectra recorded for different PSi/blue C-dots hybrids. Importantly, the fluorescence emission spectra clearly depended upon the nanostructure architecture, the location of the Bragg reflector bandgap centers, and the oxidation level of the porous surface. Upon elevating the oxidation level, a decrease in the fluorescence quenching was apparent (i.e., the freshly-etched PSi induced the most significant quenching effect, which diminishes with oxidation). This phenomenon is ascribed to energy transfer between the Silicon and the C-dots, which results in the quenching of C-dots fluorescence signal (DeLouise Lisa and Ouyang, 2009). Moreover, enhancement, narrowing, and red shift (of 10–25 nm) of the emission spectra were achieved when the emission wavelength of the C-dots ($\sim 420 \text{ nm}$ for blue C-dots) matched the photonic bandgap center of the nanostructure (Bragg reflector with bandgap center at 425 nm), see highlighted spectra in Figure 6. The enhancement of the C-dots emission spectra can be related to the high reflection band of the Bragg reflector, which reflect upwards the C-dots' fluorescence. This enhancement cannot occur when the Bragg reflector bandgap is far beyond the C-dots fluorescence emission. Similar behavior was demonstrated for QDs embedded within PSi-based Bragg reflectors (or deposited

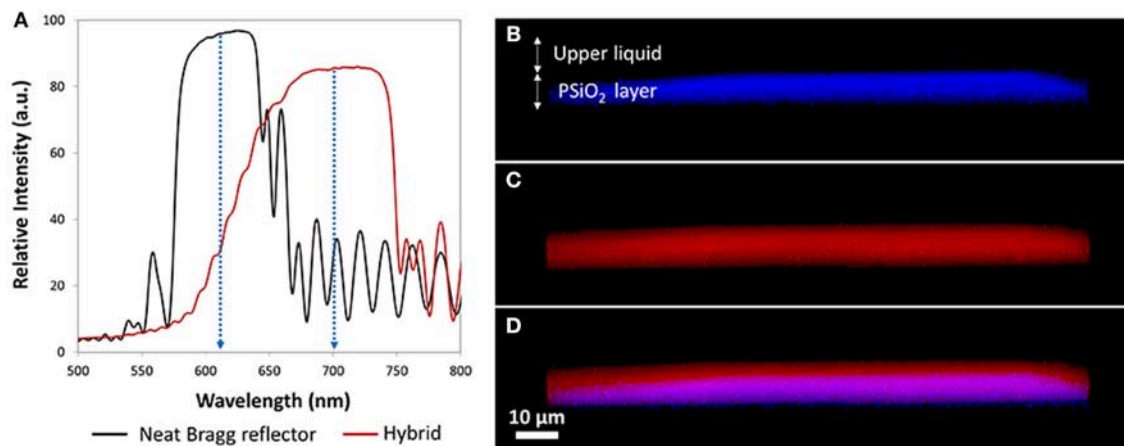


FIGURE 5 | Reflectivity spectra of the PSiO₂ (i.e., fully-oxidized) Bragg reflector before and after *in-situ* synthesis of the C-dots and the corresponding CLSM 3D projection images of the resulting PSiO₂ Bragg reflector/C-dots hybrid. **(A)** Reflectivity spectra of PSiO₂ Bragg reflector before (neat; black trace) and after (hybrid; red trace) *in situ* synthesis of red C-dots. **(B)** Photoluminescence of the PSiO₂ Bragg reflector; **(C)** fluorescence signal of confined red C-dots; **(D)** combined view of **(A,B)**, demonstrates the location of the C-dots within the porous layer in the z-direction.

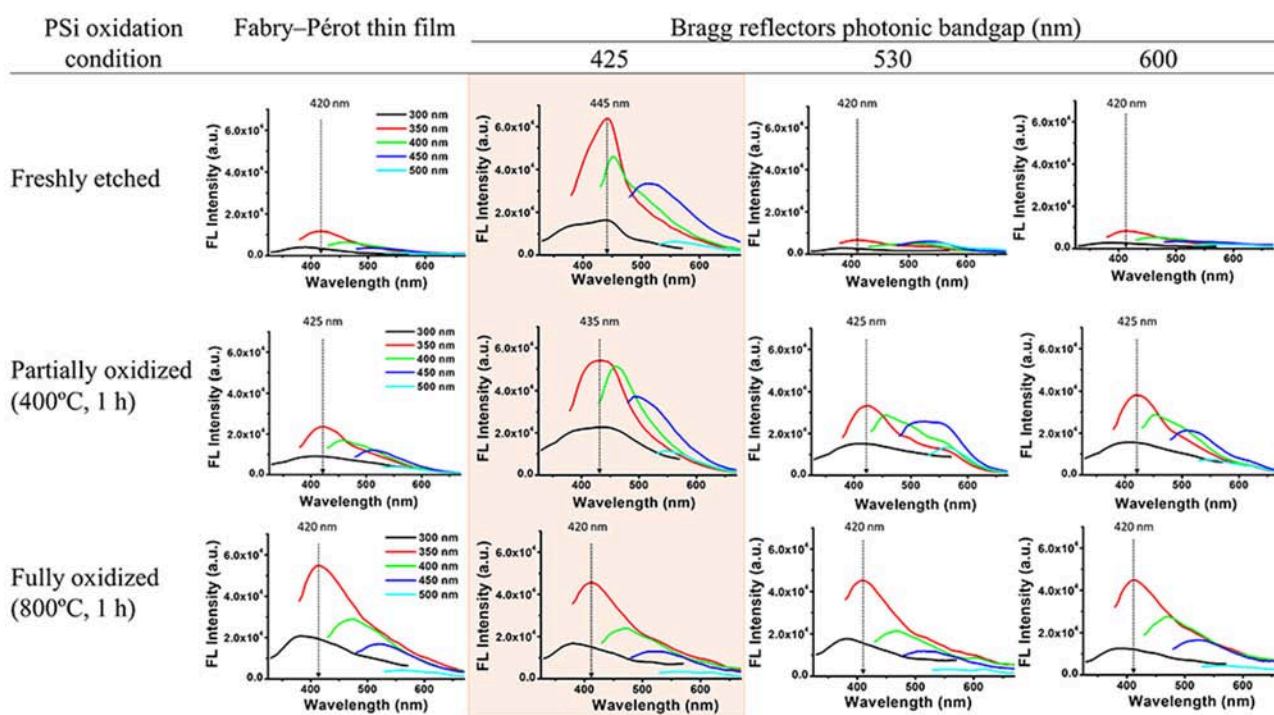
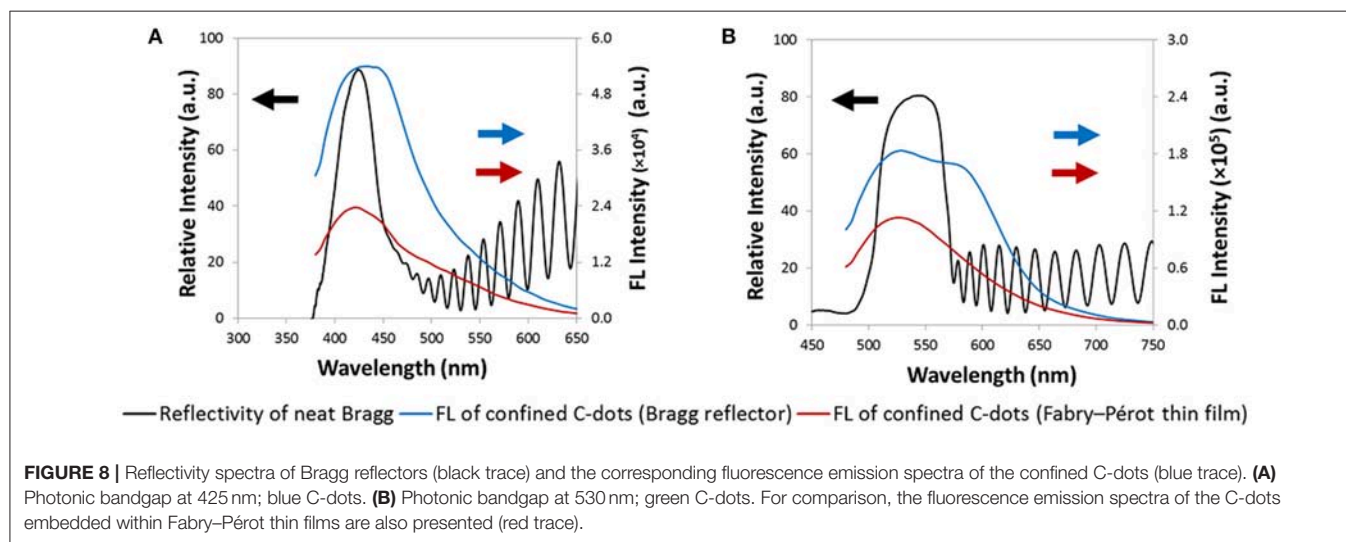
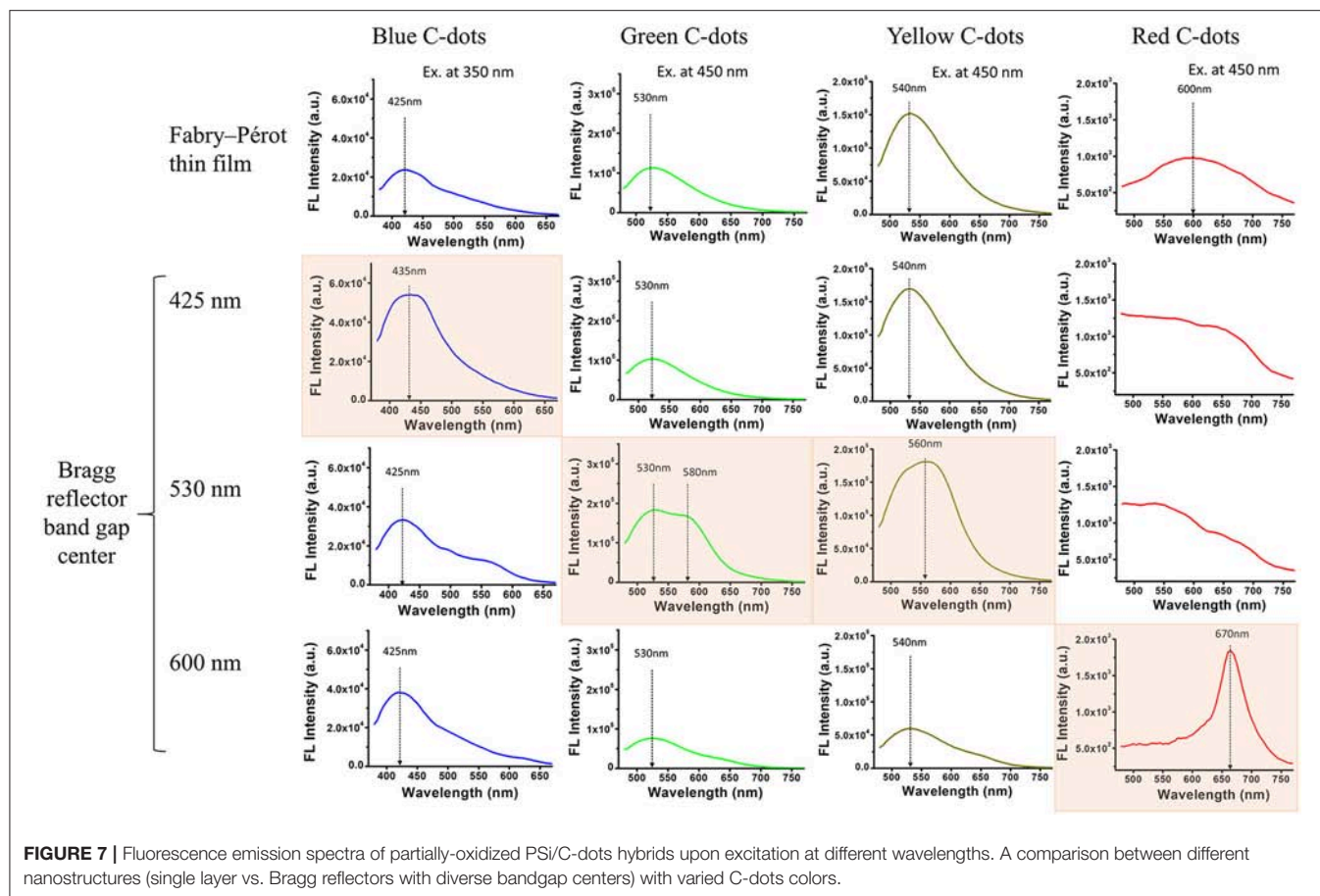


FIGURE 6 | Fluorescence emission spectra of PSi/blue C-dots hybrids at different excitation wavelengths (indicated by the different colors). A comparison between different nanostructures (Fabry–Pérot thin film vs. Bragg reflectors with diverse bandgap centers) with varied oxidation states (none, partially and fully).

on top of PSi Bragg reflectors; Liu et al., 2015; He et al., 2017; Li et al., 2017). Narrowing and shift of the emission spectra were also observed in similar hybrid systems in which QDs were confined within the pores of PSi photonic crystals (Dovzhenko et al., 2018a,b). For fully oxidized surfaces, this effect is not observed and this behavior may be attributed to the poor contrast between the alternating layers. Moreover,

in some cases, following the C-dots synthesis within the fully-oxidized Bragg reflectors, the characteristic reflectivity of the Bragg reflectors is distorted as presented in **Figure S6 (Supplementary Material)**.

Next, all four types of C-dots were synthesized within the partially-oxidized PSi structures (reflectors and Fabry–Pérot thin films) and **Figure 7** depicts the fluorescence emission spectra of



these hybrids. It can be clearly seen that the fluorescence emission spectra depend upon the location of the respective Bragg reflector bandgap center. For blue C-dots, the fluorescence signal intensity was enhanced only when the emission wavelength of the C-dots (~ 420 nm) overlapped with the Bragg reflector bandgap center (at 425 nm), and a red shift of 10 nm was apparent,

see highlighted spectrum in **Figure 7** (left panel). This behavior was also observed for the yellow and green C-dots, as seen in the highlighted spectra in **Figure 7** (middle panels). Notably, in the case of the PSi/green C-dots hybrids, the spectrum also broadened and a shoulder at 580 nm is apparent. The red C-dots exhibit the most pronounced enhancement and narrowing effect

of all studied hybrids, as highlighted in **Figure 7** (right panel). In addition, in the latter case, the C-dots fluorescence peak has red-shifted by ~ 70 nm. To summarize, the fluorescence intensity enhancement can be explained as spatial redistribution of the emitted light into a narrow cone normal to the surface (Baba et al., 1991; Qiao et al., 2010). Thus, the reflector's structure prevents the isotropic propagation of the C-dots fluorescence, and as a result their emission is preferentially directed toward the detector. Similarly, in previous studies on QDs embedded within PSi-based Bragg reflectors, a significant enhancement of the fluorescent emission was observed when their fluorescence peak overlaps with the reflector's bandgap (Liu et al., 2015; He et al., 2017; Li et al., 2017). Essentially, the Bragg reflector modified the optical mode density of the C-dots confined within the porous nanostructure, therefore enhancing emitted wavelengths inside the resonance wavelengths (Baba et al., 1991; Yamamoto et al., 1991; Qiao et al., 2010).

To further study the specific effect of the PSi Bragg reflectors reflectivity on the fluorescence properties of the confined C-dots, we present in **Figure 8** both the reflectivity spectra of neat Bragg reflectors (with no C-dots) and the corresponding fluorescence emission spectra of the confined C-dots. For comparison, the fluorescence emission spectra of the C-dots embedded within Fabry-Pérot thin films are also presented. For blue C-dots, the significant enhancement of the fluorescence intensity (in comparison to that observed for hybrids based on Fabry-Pérot thin films) corresponds to the right edge of the photonic bandgap (**Figure 8A**). Also, for green C-dots the fluorescence enhancement is manifested by a new shoulder at 580 nm, which overlaps with right edge of the host's photonic bandgap (**Figure 8B**). **Figure S7 (Supplementary Material)** presents the respective spectra also for yellow and red C-dots, exhibiting a similar trend. Dovzhenko et al. (2015) have also shown that the PL spectrum of QDs embedded within PSi is affected by the shape of the Bragg reflectivity spectrum. Specifically, the QDs PL was enhanced at a wavelength which corresponds to the edge of the photonic bandgap of the Bragg reflector host. This behavior is apparent also in the studied hybrids.

In conclusion, a hybrid system consisting of a PSi Bragg reflector matrix and encapsulated fluorescent C-dots enabled unique tunability of the C-dots' fluorescence, depending upon coupling between the C-dots' optical properties and the Bragg

reflectors' bandgaps. Thus, by careful design of the porous host, in terms of the Bragg reflector photonic bandgap and the PSi oxidation state, the PL properties of the embedded C-dots can be modulated and fine-tuned. Notably, we have found that the fluorescence emission spectrum of the confined C-dots is dependent upon the porous host nanostructure architecture, the shape and the location of the Bragg reflector photonic bandgap, and the oxidation level of the porous surface. For the best of our knowledge, this is the first time that FL optical properties of C-dots are characterized within PSi Bragg reflector matrix. The ability to this hybrid system to specifically modulate the photophysical properties of C-dots may advance the design of sophisticated nanomaterials for sensing and bioimaging.

AUTHOR CONTRIBUTIONS

NM-I fabricated and characterized the Bragg reflectors, conducted the HRSEM analyses and carried out the reflectivity measurements. SB synthesized and characterized the Bragg reflectors/C-dots hybrids, conducted the HRTEM and XPS analyses. All authors discussed the results and implications at all stages. ES and RJ have conceived the research, designed the study, and analyzed data. All authors wrote the manuscript.

ACKNOWLEDGMENTS

This research was supported by the Israel Science Foundation (grant No. 704/17). SB is grateful to the Planning and Budgeting Committee (PBC) of the Israeli Council for Higher Education for an Outstanding Post-Doctoral Fellowship. Particular acknowledgment is made of the use of the LS&E Infrastructure Unit of the Lorry I. Lokey Interdisciplinary Center for Life Sciences and Engineering. We gratefully acknowledge the fruitful discussions and the advice of Dr. Amit Nahor.

SUPPLEMENTARY MATERIAL

The Supplementary Material for this article can be found online at: <https://www.frontiersin.org/articles/10.3389/fchem.2018.00574/full#supplementary-material>

REFERENCES

- Baba, T., Hamano, T., Koyama, F., and Iga, K. (1991). Spontaneous emission factor of a microcavity DBR surface-emitting laser. *IEEE J. Quantum Electron.* 27, 1347–1358. doi: 10.1109/3.89951
- Baker, S. N., and Baker, G. A. (2010). Luminescent carbon nanodots: emergent nanolights. *Angew. Chem. Int. Ed.* 49, 6726–6744. doi: 10.1002/anie.200906623
- Bhunia, S. K., Maity, A. R., Nandi, S., Stepensky, D., and Jelinek, R. (2016a). Imaging cancer cells expressing the folate receptor with carbon dots produced from folic acid. *ChemBiochem* 17, 614–619. doi: 10.1002/cbic.201500694
- Bhunia, S. K., Nandi, S., Shikler, R., and Jelinek, R. (2016b). Tuneable light-emitting carbon-dot/polymer flexible films prepared through one-pot synthesis. *Nanoscale* 8, 3400–3406. doi: 10.1039/C5NR08400H
- Bisi, O., Ossicini, S., and Pavesi, L. (2000). Porous silicon: a quantum sponge structure for silicon based optoelectronics. *Surf. Sci. Rep.* 38, 1–126. doi: 10.1016/S0167-5729(99)00012-6
- DeLouise Lisa, A., and Ouyang, H. (2009). Photoinduced fluorescence enhancement and energy transfer effects of quantum dots porous silicon. *Phys. Stat. Sol. C* 6, 1729–1735. doi: 10.1002/pssc.200881089
- Ding, C. Q., Zhu, A. W., and Tian, Y. (2014). Functional surface engineering of C-dots for fluorescent biosensing and *in vivo* bioimaging. *Acc. Chem. Res.* 47, 20–30. doi: 10.1021/ar400023s
- Dolai, S., Bhunia, S. K., Zeiri, L., Paz-Tal, O., and Jelinek, R. (2017). Thenoyltrifluoroacetone (TTA)-carbon dot/aerogel fluorescent sensor for lanthanide and actinide ions. *ACS Omega* 2, 9288–9295. doi: 10.1021/acsomega.7b01883

- Dovzhenko, D., Osipov, E., Martynov, I., Samokhvalov, P., Eremin, I., Kotkovskii, G., et al. (2016). Porous silicon microcavity modulates the photoluminescence spectra of organic polymers and quantum dots. *Mater. Today Proc.* 3, 485–490. doi: 10.1016/j.matpr.2016.01.048
- Dovzhenko, D., Osipov, E., Martynov, T., Linkov, P., and Chistyakov, A. (2015). Enhancement of spontaneous emission from CdSe/CdS/ZnS quantum dots at the edge of the photonic band gap in a porous silicon Bragg mirror. *Phys. Proc.* 73, 126–130. doi: 10.1016/j.phpro.2015.09.132
- Dovzhenko, D. S., Chistyakov, A. A., and Nabiev, I. R. (2018a). “Modeling and optimization of the porous silicon photonic structures,” in *KnE Energy and Physics; The 2nd International Symposium Physics, Engineering and Technologies for Biomedicine* (Moscow).
- Dovzhenko, D. S., Chistyakov, A. A., and Nabiev, I. R. (2018b). “Porous silicon photonic crystal as a substrate for high efficiency biosensing,” in *KnE Energy and Physics; The 2nd International Symposium Physics, Engineering and Technologies for Biomedicine* (Moscow).
- Dovzhenko, D. S., Martynov, I. L., Samokhvalov, P. S., Mochalov, K. E., Chistyakov, A. A., and Nabiev, I. (2016). “Modulation of quantum dot photoluminescence in porous silicon photonic crystals as a function of the depth of their penetration,” in *Proceedings Photonic Crystal Materials and Devices XII* (Brussels: SPIE).
- Gaur, G., Koktysh, D., and Weiss, S. M. (2011). Integrating colloidal quantum dots with porous silicon for high sensitivity biosensing. *MRS Proc.* 1301:mrsf10-1301-pp06-03. doi: 10.1557/opl.2011.554
- Gaur, G., Koktysh, D. S., and Weiss, S. M. (2013). Immobilization of quantum dots in nanostructured porous silicon films: characterizations and signal amplification for dual-mode optical biosensing. *Adv. Funct. Mater.* 23, 3604–3614. doi: 10.1002/adfm.201202697
- He, L., Jia, Z., Zhou, J., Zhang, H., Lv, X., and Sun, D. (2017). Enhancement of the quantum dot fluorescence intensity by Au nanoparticle decoration of a porous silicon photonic crystal. *Appl. Phys. B* 123:153. doi: 10.1007/s00340-017-6723-x
- Jane, A., Dronov, R., Hodges, A., and Voelcker, N. H. (2009). Porous silicon biosensors on the advance. *Trends Biotechnol.* 27, 230–239. doi: 10.1016/j.tibtech.2008.12.004
- Jenie, S. N. A., Du, Z., McInnes, S. J. P., Ung, P., Graham, B., Plush, S. E., et al. (2014). Biomolecule detection in porous silicon based microcavities via europium luminescence enhancement. *J. Mater. Chem. B* 2, 7694–7703. doi: 10.1039/C4TB01409J
- Jenie, S. N. A., Plush, S. E., and Voelcker, N. H. (2016). Recent advances on luminescent enhancement-based porous silicon biosensors. *Pharm. Res.* 33, 2314–2336. doi: 10.1007/s11095-016-1889-1
- Jenie, S. N. A., Prieto-Simon, B., and Voelcker, N. H. (2015). Development of l-lactate dehydrogenase biosensor based on porous silicon resonant microcavities as fluorescence enhancers. *Biosens. Bioelectron.* 74, 637–643. doi: 10.1016/j.bios.2015.07.025
- Kilian, K. A., Böcking, T., and Gooding, J. J. (2009). The importance of surface chemistry in mesoporous materials: lessons from porous silicon biosensors. *Chem. Commun.* 630–640. doi: 10.1039/B815449J
- Krismastuti, F. S. H., Pace, S., and Voelcker, N. H. (2014). Porous silicon resonant microcavity biosensor for matrix metalloproteinase detection. *Adv. Funct. Mater.* 24, 3639–3650. doi: 10.1002/adfm.201304053
- Kwon, W., Do, S., Lee, J., Hwang, S., Kim, J. K., and Rhee, S.-W. (2013). Freestanding luminescent films of nitrogen-rich carbon nanodots toward large-scale phosphor-based white-light-emitting devices. *Chem. Mater.* 25, 1893–1899. doi: 10.1021/cm400517g
- Li, Y., Jia, Z., Lv, G., Wen, H., Li, P., Zhang, H., et al. (2017). Detection of *Echinococcus granulosus* antigen by a quantum dot/porous silicon optical biosensor. *Biomed. Opt. Express* 8, 3458–3469. doi: 10.1364/BOE.8.003458
- Lim, S. Y., Shen, W., and Gao, Z. (2015). Carbon quantum dots and their applications. *Chem. Soc. Rev.* 44, 362–381. doi: 10.1039/C4CS00269E
- Liu, C., Jia, Z., Lv, X., Lv, C., and Shi, F. (2015). Enhancement of QDs' fluorescence based on porous silicon Bragg mirror. *Physica B Condens. Matter* 457, 263–268. doi: 10.1016/j.physb.2014.10.005
- Massad-Ivanir, N., Bhunia, S. K., Raz, N., Segal, E., and Jelinek, R. (2018). Synthesis and characterization of a nanostructured porous silicon/carbon dot-hybrid for orthogonal molecular detection. *NPG Asia Mater.* 10:e463. doi: 10.1038/am.2017.233
- Massad-Ivanir, N., Shtenberg, G., Tzur, A., Krepker, M. A., and Segal, E. (2011). Engineering nanostructured porous SiO₂ surfaces for bacteria detection via “direct cell capture”. *Anal. Chem.* 83, 3282–3289. doi: 10.1021/ac200407w
- Mo, J. Q., Jiang, J., Zhai, Z. G., Shi, F. G., and Jia, Z. H. (2017). Enhancement of R6G fluorescence by N-type porous silicon deposited with gold nanoparticles. *Optoelectron. Lett.* 13, 10–12. doi: 10.1007/s11801-017-6269-5
- Nandi, S., Malishev, R., Parambath Kootery, K., Mirsky, Y., Kolusheva, S., and Jelinek, R. (2014). Membrane analysis with amphiphilic carbon dots. *Chem. Commun.* 50, 10299–10302. doi: 10.1039/C4CC03504F
- Ning, H., Krueger, N. A., Sheng, X., Keum, H., Zhang, C., Choquette, K. D., et al. (2014). Transfer-printing of tunable porous silicon microcavities with embedded emitters. *ACS Photon.* 1, 1144–1150. doi: 10.1021/ph500230j
- Pacholski, C. (2013). Photonic crystal sensors based on porous silicon. *Sensors (Basel)* 13, 4694–4713. doi: 10.3390/s130404694
- Palestino, G., Agarwal, V., Aulombard, R., Pérez, E., and Gergely, C. (2008). Biosensing and protein fluorescence enhancement by functionalized porous silicon devices. *Langmuir* 24, 13765–13771. doi: 10.1021/la8015707
- Pavesi, L., and Dubos, P. (1997). Random porous silicon multilayers: application to distributed Bragg reflectors and interferential Fabry-Perot filters. *Semicond. Sci. Technol.* 12, 570–575. doi: 10.1088/0268-1242/12/5/009
- Qiao, H., Guan, B., Böcking, T., Gal, M., Gooding, J. J., and Reece, P. J. (2010). Optical properties of II–VI colloidal quantum dot doped porous silicon microcavities. *Appl. Phys. Lett.* 96:161106. doi: 10.1063/1.3404183
- Sa'ar, A. (2009). Photoluminescence from silicon nanostructures: the mutual role of quantum confinement and surface chemistry. *J. Nanophotonics* 3:42. doi: 10.1117/1.3111826
- Sailor, M. J. (2011). *Porous Silicon in Practice*. Weinheim: Wiley-VCH.
- Shtenberg, G., Massad-Ivanir, N., Fruk, L., and Segal, E. (2014). Nanostructured porous Si optical biosensors: effect of thermal oxidation on their performance and properties. *ACS Appl. Mater. Interfaces* 6, 16049–16055. doi: 10.1021/am503987j
- Socrates, G. (2001). *Infrared and Raman Characteristic Group Frequencies: Tables and Charts, 3rd Edn*. Wiley.
- Sun, X., and Lei, Y. (2017). Fluorescent carbon dots and their sensing applications. *TrAC Trends Anal. Chem.* 89, 163–180. doi: 10.1016/j.trac.2017.02.001
- Tuerhong, M., Xu, Y., and Yin, X.-B. (2017). Review on carbon dots and their applications. *Chinese J. Anal. Chem.* 45, 139–150. doi: 10.1016/S1872-2040(16)60990-8
- Vincent, G. (1994). Optical-properties of porous silicon superlattices. *Appl. Phys. Lett.* 64, 2367–2369. doi: 10.1063/1.111982
- Wang, R., Lu, K.-Q., Tang, Z.-R., and Xu, Y.-J. (2017). Recent progress in carbon quantum dots: synthesis, properties and applications in photocatalysis. *J. Mater. Chem. A* 5, 3717–3734. doi: 10.1039/C6TA08660H
- Xia, B., Xiao, S.-J., Guo, D.-J., Wang, J., Chao, J., Liu, H.-B., et al. (2006). Biofunctionalisation of porous silicon (PS) surfaces by using homobifunctional cross-linkers. *J. Mater. Chem.* 16, 570–578. doi: 10.1039/B511175G
- Yamamoto, Y., Machida, S., and Bjork, G. (1991). Microcavity semiconductor-laser with enhanced spontaneous emission. *Phys. Rev. A* 44, 657–668. doi: 10.1103/PhysRevA.44.657
- Zhang, H. Y., Lv, J., and Jia, Z. H. (2017). Efficient fluorescence resonance energy transfer between quantum dots and gold nanoparticles based on porous silicon photonic crystal for DNA detection. *Sensors* 17: E1078. doi: 10.3390/s17051078
- Zhang, X., Zhang, Y., Wang, Y., Kalytchuk, S., Kershaw, S. V., Wang, Y., et al. (2013). Color-switchable electroluminescence of carbon dot light-emitting diodes. *ACS Nano* 7, 11234–11241. doi: 10.1021/nn405017q
- Zhang, X. G. (2004). Morphology and formation mechanisms of porous silicon. *J. Electrochem. Soc.* 151, C69–C80. doi: 10.1149/1.1632477

Conflict of Interest Statement: The authors declare that the research was conducted in the absence of any commercial or financial relationships that could be construed as a potential conflict of interest.

Copyright © 2018 Massad-Ivanir, Bhunia, Jelinek and Segal. This is an open-access article distributed under the terms of the Creative Commons Attribution License (CC BY). The use, distribution or reproduction in other forums is permitted, provided the original author(s) and the copyright owner(s) are credited and that the original publication in this journal is cited, in accordance with accepted academic practice. No use, distribution or reproduction is permitted which does not comply with these terms.



High Anodic-Voltage Focusing of Charge Carriers in Silicon Enables the Etching of Regularly-Arranged Submicrometer Pores at High Density and High Aspect-Ratio

Chiara Cozzi^{1†}, Giovanni Polito^{1†}, Lucanos M. Strambini² and Giuseppe Barillaro^{1,2*}

¹ Dipartimento di Ingegneria dell'Informazione, Università di Pisa, Pisa, Italy, ² Istituto di Elettronica e di Ingegneria dell'Informazione e delle Telecomunicazioni, Consiglio Nazionale delle Ricerche, Pisa, Italy

OPEN ACCESS

Edited by:

Thierry Djenizian,
École des Mines de
Saint-Étienne—Campus Georges
Charpak Provence, France

Reviewed by:

Luis F. Marsal,
University of Rovira i Virgili, Spain
Luca De Stefano,
Istituto per la Microelettronica e
Microsistemi (CNR), Italy

*Correspondence:

Giuseppe Barillaro
g.barillaro@iet.unipi.it

[†]These authors have contributed
equally to this work

Specialty section:

This article was submitted to
Chemical Engineering,
a section of the journal
Frontiers in Chemistry

Received: 21 September 2018

Accepted: 08 November 2018

Published: 30 November 2018

Citation:

Cozzi C, Polito G, Strambini LM and
Barillaro G (2018) High
Anodic-Voltage Focusing of Charge
Carriers in Silicon Enables the Etching
of Regularly-Arranged Submicrometer
Pores at High Density and High
Aspect-Ratio. *Front. Chem.* 6:582.
doi: 10.3389/fchem.2018.00582

The anodic dissolution of silicon in acidic electrolytes is a well-known technology enabling the silicon machining to be accurately controlled down to the micrometer scale in low-doped *n*-type silicon electrodes. Attempts to scale down this technology to the submicrometer scale has shown to be challenging, though it premises to enable the fabrication of meso and nano structures/systems that would greatly impact the fields of biosensors and nanomedicine. In this work, we report on the electrochemical etching at high anodic voltages (up to 40 V) of two-dimensional regular arrays of millions pores per square centimeter (up to $30 \times 10^6 \text{ cm}^{-2}$) with sub-micrometric diameter (down to $\sim 860 \text{ nm}$), high depth (up to $\sim 40 \mu\text{m}$), and high aspect-ratio (up to ~ 45) using low-doped *n*-type silicon electrodes (resistivity $3\text{--}8 \Omega \text{ cm}$). The use of high anodic voltages, which are over one order of magnitude higher than that commonly used in electrochemical etching of silicon, tremendously improves hole focusing at the pore tips during the etching and enables, in turn, the control of electrochemical etching of submicrometer-sized pores when spatial period reduces below $2 \mu\text{m}$. A theoretical model allows experimental results to be interpreted in terms of an electric-field-enhanced focusing of holes at the tip apex of the pores at high anodic voltages, with respect to the pore base, which leads to a smaller curvature radius of the tip apex and enables, in turn, the etching of pore tips to be preferentially sustained over time and space.

Keywords: nanostructuring, anodization, porous silicon, submicrometer pores, carrier focusing, high voltage

INTRODUCTION

From first discovery to modern days, the possibility of controlling the electrochemical preparation of pores in silicon at nano to micro scales in terms of both size and pattern has fascinated scientists for more than 50 years (Uhlir, 1956).

In 1990, Lehmann and Föll reported for the first time on how to control the anodic dissolution of *n*-type silicon electrodes in low concentration HF-based aqueous electrolytes by back-side illumination, so enabling the etching of regular two-dimensional lattices of pores at the micrometer scale (Lehmann and Föll, 1990). Once a lattice of pits is pre-defined on the silicon surface, size, position, and morphology of pores etched by back-side illumination electrochemical etching

(BIEE) on low-doped (i.e., a few Ω cm) *n*-type silicon electrodes was shown to be finely controlled by tuning the etching parameters, such as for instance, doping concentration of silicon, electrolyte composition and temperature, anodic voltage, and current density (Lehmann, 1993; Föll et al., 2002; Matthias et al., 2005; Barillaro and Strambini, 2010). A decade later, Barillaro et al. reported on how to broaden BIEE of silicon to fabricate lattices of linear trenches (Barillaro et al., 2002b), so enabling the fabrication of a multitude of microstructures besides pores (Barillaro et al., 2002a, 2005). In 2012, Barillaro et al. further pushed the BIEE of silicon ahead, showing how to control anodic dissolution anisotropy/isotropy in real-time to enable the fabrication of free-standing microstructures (Polito et al., 2013) and complex microsystems (Bassu et al., 2012) at the micrometer scale. Nowadays, the BIEE of silicon has evolved into a highly versatile microstructuring technology, namely electrochemical micromachining (ECM), with unique features, among which there are high aspect-ratio of etched structures (>100), low roughness of etched surfaces (<10 nm), high etching rate of high aspect-ratio structures (up to $10 \mu\text{m min}^{-1}$) (Cozzi et al., 2017). As a matter of fact, applications of ECM encompass today a broad range of research fields, from microelectronics (Kemell et al., 2007) and photonics (Surdo et al., 2013), to (bio)sensing (Surdo et al., 2012, 2014) and (nano)medicine (Harding et al., 2016; Delalat et al., 2018).

In spite of the significant technological advancement that has been achieved over the last two decades, the controlled etching of pores with either very large (i.e., $>20 \mu\text{m}$) or very small (i.e., $<1 \mu\text{m}$) diameter/spacing has not been achieved yet with BIEE on low-doped *n*-type silicon (Barillaro, 2015). Specifically, maximum diameter and spacing of lattice of pores was shown to have an upper boundary value of about 10 and $20 \mu\text{m}$, respectively; on the other hand, minimum size and spacing was reported to be restricted to about 1 and $2 \mu\text{m}$, respectively. Both upper and lower boundary values can be ascribed to a poor focusing of photogenerated charge carriers at the pore tips, as both diameter and spacing of pores increase/decrease above/below these values. Moreover, using an anodization voltage value of about 1 V, it was shown that a minimum current density value exists, for a given spacing, setting the minimum diameter value above which the etching of pore lattice can be finely controlled, at least for low-doped *n*-type silicon electrodes (Barillaro and Strambini, 2010).

In this work, the controlled etching of regular arrays of pores with submicrometric diameter ($<1 \mu\text{m}$) was successfully addressed by back-side illumination electrochemical etching of silicon electrodes with low-resistivity ($3\text{--}8 \Omega$ cm), using high anodization voltage values (up to 40 V) to effectively focus charge carriers to the pore tips when the spacing of pores is below $2 \mu\text{m}$. A theoretical model allowed experimental results to be interpreted in terms of an electric-field enhanced focusing of holes at the tip apex of the pores at high anodic voltages, with respect to the pore base, when pore spacing is smaller than the depletion region width in the silicon electrode. Although the use of high anodization voltages for the electrochemical etching of regular lattices of pores in silicon was already reported (Rönnebeck et al., 1999; Cozzi et al., 2015), this work represents

the first report on the controlled etching of sub-micrometric pores with high-density and high aspect-ratio.

MATERIALS AND METHODS

Materials and Chemicals

CZ-grown *n*-type (100)-oriented silicon wafers with a resistivity of $3\text{--}8 \Omega$ cm and covered with a 298-nm-thick silicon dioxide layer, either flat (i.e., without any pattern) or patterned with a two-dimensional (2D) lattice ($1 \times 1 \text{ cm}^2$) of square holes with side of $1 \mu\text{m}$ and spacing (*s*) of $1.8 \mu\text{m}$ (hole density $\sim 30 \times 10^6 \text{ cm}^{-2}$), were provided by STMicroelectronics (Milan, Italy). Acetone 99 wt%, pentane 99 wt%, 2-propanol 99.8 wt%, and hydrofluoric acid (HF) 48 wt% were purchased from Sigma-Aldrich. Ethanol 99.8 wt% and potassium hydroxide (KOH), pure powder at 85%, were purchased from Fluka Analytical. Sodium lauryl sulfate (SLS) powder was purchased from Carlo Erba Reagents.

Electrochemical Characterization of *n*-Type Silicon Electrode in Aqueous HF-Based Electrolyte by Linear Sweep Voltammetry

A thorough electrochemical characterization (>3 replicates) of flat (i.e., not patterned) *n*-type silicon electrodes in contact with an aqueous HF-based electrolyte (5 vol% HF:95 vol% H_2O , with 1,000 ppm of Sodium Lauryl Sulfate—SLS—as wetting agent) was carried out by linear sweep voltammetry. Flat silicon electrodes were achieved by cutting the flat silicon wafers in slabs of $2 \times 2 \text{ cm}^2$ and removing the silicon dioxide layer using a solution of HF:ethanol (1:1 by vol.) for 60 s at room temperature. Flat silicon electrodes were loaded in a three-electrodes electrochemical cell containing the HF-based electrolyte (details are provided in the **Supplementary Material**), and the current flowing through the etch-cell was monitored upon application of voltages varying from 2 to -1.5 V with a sweep rate of -0.1 V s^{-1} , under back-side illumination (halogen lamp, 250W) of silicon. Experimental current density-voltage (*J*-*V*) curves (**Figure S1, Supplementary Material**) highlight the presence of an electropolishing current density peak $J_{\text{peak}} = 78 \pm 3 \text{ mA cm}^{-2}$, occurring at a voltage $V_{\text{peak}} = 1.2 \text{ V}$, in good agreement with the literature (Lehmann and Föll, 1990; Barillaro and Strambini, 2010).

Potentiostatic Etching of Regular Arrays of Pores at High Anodic Voltage in Aqueous HF-Based Electrolyte

Pre-patterned *n*-type silicon electrodes were achieved starting from square silicon slabs ($2 \times 2 \text{ cm}^2$) cut from the patterned silicon wafers. The pattern was transferred onto the silicon surface by KOH etching, which yielded an array of inverted pyramid-shaped pits. The KOH etching was performed at 50°C for 750 s with a 20 wt% solution of KOH in deionized water, using the patterned silicon dioxide as a masking material. 2-Propanol was added to the KOH solution to increase wetting capability and to improve, in turn, etching uniformity. The silicon dioxide layer

was then dissolved using a solution of HF:ethanol (1:1 by vol.) for 60 s at room temperature.

The pre-patterned silicon electrodes were loaded in a three-electrodes electrochemical cell (details are provided in **Supplementary Material**) containing a HF-based electrolyte (5 vol% HF:95 vol% H₂O, with 1000 ppm of SLS as wetting agent), and etched for 2,000 s at different anodic voltage values, under back-side illumination of silicon.

The photogenerated etching current density (J_{etch}) was set to a given initial value J_{etch0} and linearly decreased over time to maintain the pore diameter constant with depth. Three different J_{etch0} values were tested, namely 13.4, 16.8, and 20.2 mA cm⁻², which were linearly reduced over time with a rate (α) of -0.938, -1.219, and -1.453 $\mu\text{A s}^{-1}\text{cm}^{-2}$, respectively, by decreasing the back-side illumination intensity through a reduction of the lamp power (Bassu et al., 2012). The different J_{etch0} values correspond to different expected porosity (i.e., dissolved silicon to total silicon volumetric ratio) values P_e :

$$P_e = \frac{J_{etch0}}{J_{peak}} \quad (1)$$

namely, 17.2, 21.5, and 25.8%, and, in turn, to different expected pore diameters d_e :

$$d_e = \sqrt{P_e \frac{4A_C}{\pi}} \quad (2)$$

namely, 0.842, 0.942, and 1.032 μm (**Table S1, Supplementary Material**), being $A_C = 1.8 \times 1.8 \mu\text{m}^2$ the unit cell area. For each J_{etch0} value, six different anodization voltage values (V_{etch}) were investigated, namely 1.2, 15, 20, 25, 35, and 40 V. The anodization voltage value is kept constant throughout the whole etching time. For $V_{etch} = 40$ V a further current density value $J_{etch0} = 10.07 \text{ mA cm}^{-2}$ ($P_e = 12.8\%$, $d_e = 0.644 \mu\text{m}$) was investigated, with J_{etch0} linearly reduced over time with $\alpha = -0.710 \mu\text{A s}^{-1}\text{cm}^{-2}$. Each experiment was replicated at least 3 times for each given J_{etch0} - V_{etch} pair.

After etching, pre-patterned silicon slabs underwent an overnight static bath in a HF:ethanol (1:4 by vol.) solution to fully remove SLS. A static rinse in ethanol and pentane, respectively, for 300 s followed by drying at 100°C on a hot plate was eventually performed.

All the etched slabs were then diced to allow morphological investigation of the longitudinal cross-section of the pores in the array to be carried out.

Morphological Characterization of Regular Arrays of Pores by SEM Microscopy

The morphological characterization of regular arrays of pores resulting from the electrochemical etching of pre-patterned silicon electrodes, at different anodic voltages and current densities, was performed by scanning electron microscope (SEM) using a JEOL JSM-6390. Top-view and cross-section images at different magnifications were acquired at an acceleration voltage of 3 kV. Five different cross-section images were acquired per

each slab at both 2,000 \times and 5,000 \times magnifications, from which pore depth and diameter were experimentally measured. The cross-section images were exploited to perform a statistical analysis using a home-made software routine implemented using Matlab (Mathworks, Inc.), so as to obtain average value and standard deviation of both depth (h_m) and diameter (d_m) of the etched pores.

Experimental porosity P_m values were obtained from h_m and d_m values through the use of Equation (3), as the ratio between pore cross-sectional area (i.e., A_{CS}) and the unit cell area A_C , assuming all pores featuring circular cross-section and constant diameter over depth:

$$P_m = \frac{A_{CS}}{A_C} = \frac{\pi \left(\frac{d_m}{2}\right)^2}{A_C} \quad (3)$$

Experimental data on pore geometrical features (i.e., h_m , d_m) were also used to analytically evaluate the total silicon volume dissolved during each etching experiment (M_m). In particular, experimental M_m values were evaluated through the use of Equation (4), as the number of pores involved during the etching ρ_P (i.e., ratio between the etching area E_A of $\sim 0.64 \text{ cm}^2$ and the unit cell area A_C) times the average pore volume (M_P):

$$M_m = \rho_P M_P = \frac{E_A}{A_C} \pi \left(\frac{d_m}{2}\right)^2 h_m \quad (4)$$

The experimental values obtained for the main pore parameters, i.e., diameter (d_m), depth (h_m), porosity (P_m), and volume (M_m), resulting from the above described morphological analysis of the SEM images, were compared with the expected values, i.e., d_e , h_e , P_e , and M_e , respectively, obtained from the etching parameters, i.e., etching time (t_{etch}) and etching current density (J_{etch}), on the basis of the model proposed by Barillaro and Pieri (2005). In particular, expected diameter (d_e) and porosity (P_e) were already reported in section Potentiostatic Etching of Regular Arrays of Pores at High Anodic Voltage in Aqueous HF-Based Electrolyte (Equations 1, 2). The expected silicon volume M_e dissolved for any J_{etch0} value was evaluated through the use of Equation (5), as the ratio of the total charge Q supplied during the whole etching experiment ($Q = E_A \int_0^{t_{etch}} J_{etch} dt$) and the product of silicon dissolution valence $n_v = 2.66$ (i.e., number of charges needed to dissolve a single silicon atom) (Barillaro and Pieri, 2005), elementary charge e (i.e., $e = 1.602 \times 10^{-19} \text{ C}$), and atomic density of silicon N_{Si} (i.e., $N_{Si} = 5 \times 10^{22} \text{ cm}^{-3}$):

$$M_e = \frac{Q}{n_v e N_{Si}} = \frac{E_A \int_0^{t_{etch}} J_{etch} dt}{n_v e N_{Si}} \quad (5)$$

Eventually, the expected pore depth (h_e) was evaluated using M_e and d_e values according to Equation (6):

$$h_e = \frac{M_e}{P_e E_A} \quad (6)$$

RESULTS AND DISCUSSION

High Anodic-Voltage Controlled Etching of Regular Arrays of High-Density High-Aspect-Ratio Pores in *n*-Type Silicon With Diameter Down to the Sub-micrometric Scale

Figure 1a (left side) shows a typical top-view SEM image of an array of pores prepared by anodic etching under back-side illumination at $V_{etch} = 1.2$ V and $P_e = 17.2\%$ ($J_{etch0} = 13.4$ mA cm⁻²) of low-doped *n*-type silicon pre-patterned with regular lattices of square holes with size of 1 μ m and pitch of 1.8 μ m. The etching results in randomly-organized pores with non-constant spacing and average diameter of about 2 μ m, which are uncorrelated from the pre-patterned layout, as confirmed by SEM analysis of the cross-section of the pore array (**Figure S2a**). Increasing the expected porosity value to 21.5 and 25.8% (etching current density value J_{etch0} to 16.8 and 20.2 mA cm⁻², respectively), while keeping the V_{etch} value unchanged (1.2 V), does not significantly improve the etching outcome (**Figures S2b,c**). This agrees with the state-of-the-art literature on the BIEE of pores in low-doped silicon at low anodic voltage (Barillaro and Strambini, 2010), according to which both minimum diameter and spacing exist for the controlled dissolution of silicon in acidic electrolytes, which depend on silicon resistivity, below which the anodic etching of regular patterns of square holes cannot be controlled to achieve a regular array of pores. For instance, for *n*-type silicon electrodes with resistivity of a few Ω cm, typically used in microelectronics, minimum values for diameter and spacing of pores above which the anodic etching can be fully controlled are about 1 and 2 μ m, respectively. Below these boundary values, competition for collection of holes, photogenerated on the silicon back-side, at the tips of adjacent pores is very high. In fact, after an initial nucleation phase, during which silicon dissolution proceeds with the formation of pits in correspondence of defect sites pre-patterned at the silicon surface, photogenerated hole collection is no longer uniform over time and space, so that some pits collect more holes than others within the array. The former keep growing and increase their diameter to reach a roughly constant steady-state value over depth; the latter stop growing after a given depth, which depends on the growth of neighbor pores (**Figures S2a–c**).

Intense electric-field establishing across the depletion region at the pore tips (defects, in the nucleation phase) is known to induce an effective hole-focusing at low V_{etch} values when diameter and spacing of pores (defects) is >2 μ m. We argue that severe overlap of space charge regions of adjacent pores occurring when the pore spacing reduces below 2 μ m leads to a defocusing of electric-field lines at the pore tips, which affects the collection of photogenerated holes and enhances surface non-homogeneities, giving rise to a non-uniform sharing of photogenerated holes and, in turn, to an uncontrolled etching/growth of the pores.

Experiments at higher anodic voltage values V_{etch} , namely from 15 to 40 V, using the same current density values above reported for 1.2 V, were carried out to investigate the effect

of an increasing electric-field on the focusing at the pore tips of holes photogenerated on the silicon back-side. Experimental results on the electrochemical etching of pores at increased anodic voltages are reported in **Figures 1b,c** and **Figures S2d–t**. Increasing the V_{etch} value turned out to have a beneficial effect on the controlled anodic etching of pre-patterned lattices of square holes with spacing < 2 μ m. In fact, the number of dying pores significantly reduces as the etching voltage increases from 1.2 to 15 and 20 V, for any given etching current density value, and the correlation between etched/growing pores and surface pattern greatly improves (**Figures S2d–i**). Remarkably, for a given anodic voltage value, the number of dying pores reduces as the etching current density increases, then becomes zero at 20 V and 20.2 mA cm⁻² ($P_e = 25.8\%$), so enabling the fabrication of a regular array of pores with uniform depth and diameter and without missing pores (**Figure S2i**). A further increase of the V_{etch} value to 25, 35, and 40 V (**Figures S2l–t**) highlights that, as the anodic voltage increases the etching of pores can be fully controlled also at smaller J_{etch0} values, namely 13.4 ($P_{theo} = 17.2\%$) and 16.8 mA cm⁻² ($P_{theo} = 21.5\%$). Notice that, at V_{etch} of 35 and 40 V, arrays of regular pores with no missing pores were successfully prepared with a submicrometric diameter of about 860 nm at $J_{etch0} = 13.4$ mA cm⁻² (**Figures 1b,c**).

Effect of High Anodic-Voltage on Geometrical Features of Regular Arrays of High-Density High-Aspect-Ratio Pores Etched in *n*-Type Silicon

A thorough morphological investigation of regular arrays of pores (with no missing pores) etched at different high anodic voltages/current densities was carried out to infer into the effect of etching parameters on pore diameter, porosity, and depth. **Figure 1d** shows experimental values (average value and standard deviation, sd) of pore diameter (d_m , left axis) and array porosity (P_m , right axis) vs. pore depth (h_m), achieved at anodic voltages of 25, 35, and 40 V and current densities of 13.4, 16.8, and 20.2 mA cm⁻². Coefficient of variation %CV (by definition, the ratio between standard deviation and mean values) values average 3.4 and 0.7% for diameter/porosity and depth, respectively, highlighting that the etched pores are uniform over the whole array both in the in-plane and out-of-plane directions. For a given anodic voltage, an increase of both pore diameter d_m and array porosity P_m occurs as the etching current density J_{etch0} increases. Remarkably, once etching current density and etching time are given, both diameter/porosity and depth of the pores strongly depend on the anodic voltage value. For instance, at $J_{etch0} = 13.4$ mA cm⁻² ($t_{etch} = 2,000$ s) the anodic etching of the pre-patterned square hole lattice gives rise to a regular array of sub-micrometric pores with diameter of 870 nm (sd = 35 nm) and depth of 39.5 μ m (sd = 131 nm) at 40 V, and diameter of 863 nm (sd = 27 nm) and depth of 38.3 μ m (sd = 335 nm) at 35 V, whereas pores etched at 25 V feature a diameter of 1.14 μ m (sd = 50 nm) and depth of 36.7 μ m (sd = 331 nm).

This differs from what expected for pores prepared in silicon through electrochemical etching at anodic voltage values close to the electropolishing voltage peak (i.e., a few Volts). In this case, once both etching current density and etching time are

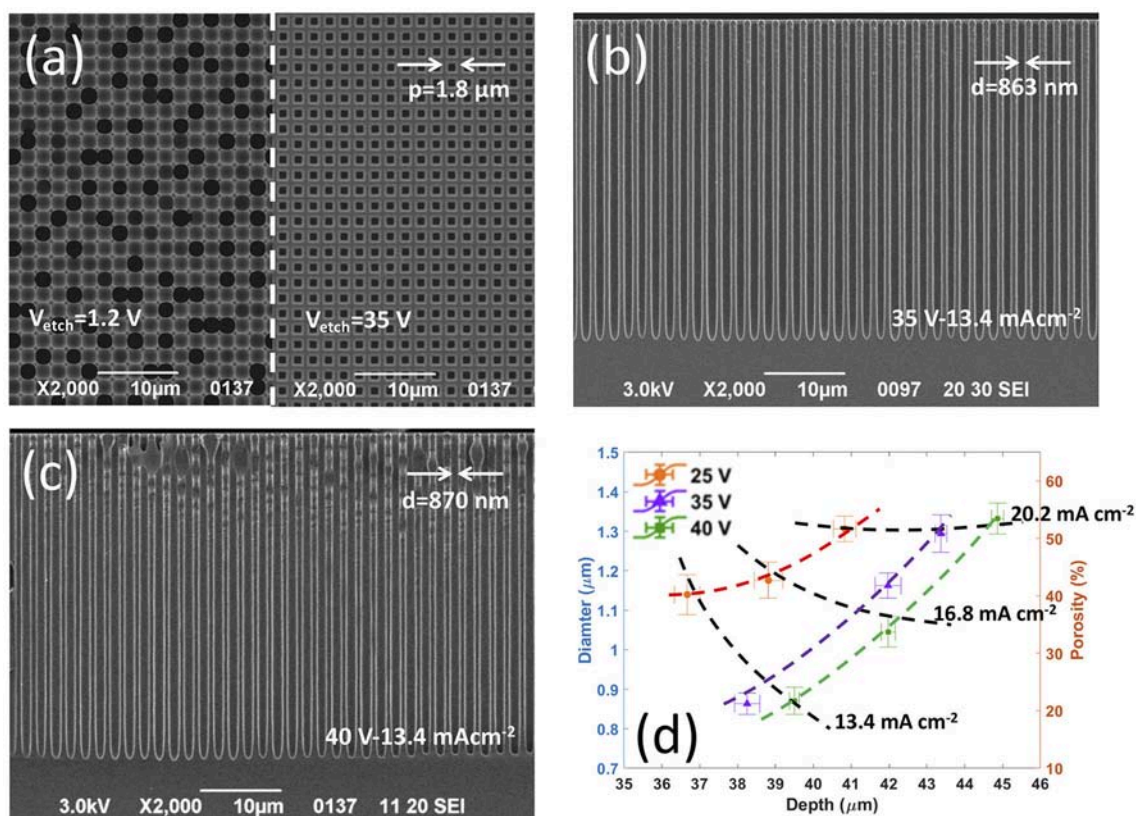


FIGURE 1 | Influence of etching voltage V_{etch} and etching current density J_{etch0} value on the controlled etching of pores with sub-micrometric diameter and spacing of $1.8\text{ }\mu\text{m}$. **(a)** Top-view SEM images showing (left side) the uncontrolled etching resulting by performing the BIEE with $V_{etch} = 1.2\text{ V}$ and $J_{etch0} = 13.4\text{ mA cm}^{-2}$, and (right side) a uniform array of sub-micrometric ordered pores featuring same diameter and depth, successfully achieved increasing the V_{etch} value to 35 V ; **(b,c)** cross section SEM images showing uniform arrays of sub-micrometric ordered pores featuring same diameter and depth successfully obtained by BIEE performed with **(b)** $V_{etch} = 35\text{ V}$ and $J_{etch0} = 13.4\text{ mA cm}^{-2}$, and **(c)** $V_{etch} = 40\text{ V}$ and $J_{etch0} = 13.4\text{ mA cm}^{-2}$. **(d)** Morphological investigation of fully-uniform arrays of ordered pores etched at high anodic voltages, in terms of pore diameter, porosity, and depth: average values and standard deviations (error bars) of pore diameter (left axis) with corresponding experimental porosity (right axis) as a function of pore depth (average values and standard deviations) for each of the V_{etch} and J_{etch0} values investigated.

chosen, the electrochemical etching leads to pores with same diameter/porosity and depth, regardless of the anodic voltage value, if diameter and spacing of the etched pores are above 1 and $2\text{ }\mu\text{m}$, respectively. **Figure S3a** shows expected values for diameter, porosity, and depth (calculated using Equations 1, 2, 6, respectively) of pores etched at current densities of 13.4 , 16.8 , and 20.2 mA cm^{-2} , regardless of the anodic voltage value. From the comparison between **Figure 1d** and **Figure S3a**, we can infer that, despite a properly controlled etching, a significant deviation of pore diameter and, in turn, array porosity from the expected values occurs at high anodic voltages for J_{etch0} values of 16.8 and 20.2 mA cm^{-2} , regardless of the V_{etch} value. On the contrary, the arrays etched at the lowest J_{etch0} value (i.e., 13.4 mA cm^{-2}) and highest V_{etch} values (i.e., 35 and 40 V) featured experimental diameter and porosity of about 870 nm and $\sim 20\%$, respectively, in good agreement with expected values (**Figure S3a**). Moreover, the comparison between **Figures 1d**, **S3a** also highlights a marked mismatch between measured and expected pore depths, thus pointing out that the growth rate depends on both J_{etch0} and V_{etch} values when the etching is performed at high anodic voltages.

Experimental results on pore depth, diameter, and porosity were further used to calculate the total amount of silicon dissolved (**Figure S3b**), for which a good agreement with expected values was obtained (dashed line in **Figure S3b**) when the electrochemical etching was performed at the highest J_{etch0} value (i.e., 20.2 mA cm^{-2}), regardless of the V_{etch} value. On the other hand, the mismatch between calculated and expected amount of silicon dissolved increased as the etching current density decreased, with a maximum mismatch obtained for fully uniform arrays of sub-micrometric pores etched at 13.4 mA cm^{-2} with 35 and 40 V . We argue that, such a mismatch can be ascribed to a variation of the silicon dissolution valence at high anodic voltages, when low etching current densities are employed.

Physics of High Anodic-Voltage Etching of High-Density Pores in *n*-Type Silicon Electrodes

The back-side illumination electrochemical etching of low-doped *n*-type silicon electrodes involves the flow of photogenerated holes through the depletion region establishing within the silicon

electrode, at the electrolyte/silicon interface. Therefore, a steady etching of pores within a silicon electrode pre-patterned with a regular lattice of defects requires that a steady flow of holes is established and sustained both in time and space through the space charge region at the pore tip. Both flow intensity and collection area of holes at the pore tip define, at a given etching time, the geometrical features of the resulting array of pores, namely diameter/porosity and length. Specifically, the flow intensity is mainly set by the electric-field establishing within the depletion region, while the collection area is mainly affected by the depletion region width establishing at the pore tip. Therefore, experimental results achieved on the electrochemical etching of high-density pores were tentatively interpreted in terms of the depletion region establishing at the pore tip at low and high anodic voltages.

The radius of curvature of the electrolyte/silicon interface is one of the key parameters affecting the depletion region developing within the silicon electrode, both in terms of width of the space charge region and intensity of the electric-field inside it. From SEM cross-sections of pores fabricated at low and high anodic voltages (Figures S2a–t), it is apparent that the pore tips become more elongated as the anodic voltage increases, so that the curvature radius at the apex of the pore tips is smaller at higher anodic voltage, with respect to that a low anodic voltage. This is sketched in Figure 2a, which shows as the curvature radius of the pore tip, and, in turn, of the electrolyte/silicon interface, increases monotonically moving from the tip apex, minimum value r_{min} , to the pore base, maximum value $r_{max} = d/2$, assuming for the pore a circular cross-section with a diameter d . A simplified theoretical model was implemented that takes variation of the curvature radius along the pore tip into account and allows the effect of anodic voltage on depletion region width and, in turn, electric-field intensity along the pore tip to be investigated. In the model, the tip surface is schematized with independent spherical surfaces/junctions with radius of curvature r_0 variable between r_{min} and the tip apex and r_{max} at the pore base (Figure 2a). One single pore/tip is analyzed, neglecting possible contributions of neighbor pores to depletion region and, in turn, electric-field at the pore tip. Also, the anodic voltage V_{etch} is assumed to fully drop across the space charge region formed in the silicon electrode, neglecting possible voltage drops across the space charge region established in the electrolyte and along the resistive paths between voltage source and electrolyte/silicon interface.

For a spherical electrolyte/silicon interface with curvature radius r_0 (Figure 2b), the following relations for electric-field $E(r)$ and electric potential $V(r)$ as a function of r_0 can be obtained by solving the Poisson equation in the silicon electrode (Muller and Kamins, 1977):

$$E(r) = \frac{qN_D}{3\epsilon_s} \left[-r + \frac{(r_0 + w_d)^3}{r^2} \right] \quad (7)$$

$$V(r) = \frac{qN_D}{6\epsilon_s} \left[r^2 + \frac{2(r_0 + w_d)^3}{r} - 3(r_0 + w_d)^2 \right] \quad (8)$$

being r the distance from center of the spherical surface, ϵ the dielectric constant of silicon, N_D the ionized donor

density, q the elementary electron charge, and w_d the width of the depletion region. Figure 2b shows a cross-section of a spherical electrolyte/silicon interface with curvature radius r_0 , also highlighting the depletion region w_d established within the silicon electrode.

For a given voltage difference V_d applied between electrolyte and silicon, a relationship between depletion region width w_d and applied voltage V_d is obtained by assuming $V(r_0) = -V_d$ in Equation (8) (see **Supplementary Material**). This relationship was used to plot the depletion region width w_d in the silicon electrode as a function of the voltage V_d applied across the silicon/electrolyte interface and of the curvature radius r_0 of the silicon/electrolyte interface (Figure 3a). Figure 3a shows a contour plot of the depletion region width w_d in the silicon electrode, as a function of the anodic voltage V_d (between 0 and 50 V) applied across the silicon/electrolyte interface and of the curvature radius r_0 (between 100 and 1,000 nm) of the silicon/electrolyte interface. Figure 3b shows the relationship between depletion region width w_d and curvature radius r_0 for increasing values of V_d (corresponding to the dashed lines in Figure 3a).

By replacing w_d into Equation (7) with its expression derived above, a relationship between the maximum electric-field $E_{max} = E(r_0)$ establishing within the depletion region in the silicon electrode and the voltage V_d applied is obtained (see **Supplementary Material**). This was used to plot the maximum value of the electric-field $E_{max} = E(r_0)$ within the depletion region in the silicon electrode as a function of the anodic voltage V_d applied across the silicon/electrolyte interface and of the curvature radius r_0 of the silicon/electrolyte interface (Figure 3c). Figure 3c shows a contour plot of the maximum value of the electric-field $E_{max} = E(r_0)$ establishing within the depletion region in the silicon electrode, as a function of the anodic voltage V_d (between 0 and 50 V) applied across the silicon/electrolyte interface and of the curvature radius r_0 (between 100 and 1,000 nm) of the silicon/electrolyte interface. Figure 3d shows the relationship between maximum electric-field E_{max} and curvature radius r_0 for increasing values of the applied voltage V_d (corresponding to dashed lines in Figure 3d). As expected, an increase of both depletion region width w_d and electric-field intensity E_{max} at the pore tip occurs as the anodic voltage V_d is augmented, regardless of the curvature radius at the tip. However, the degree by which both depletion region width w_d and electric-field intensity E_{max} are augmented, depends on the curvature radius value. For instance, as the curvature radius at the tip reduces from 500 nm (i.e., pore base) to 100 nm (i.e., pore apex), the ratio between width of the depletion region at the pore base and tip apex increases from 3.1 to 3.4 (Figure S4a), and the ratio between maximum electric-field intensity at the tip apex and pore base increases from 27 to 42 (Figure S4b), as the anodic voltage is augmented from 2 to 40 V.

We argue that, for array of pores with spacing much larger than twice the depletion region, the pores of the array can be considered isolated from each other, so that low values (e.g., 2 V) of the anodic voltage V_{etch} are enough to sustain an effective hole focusing at the pore tip apex, where the curvature radius of the electrolyte/silicon interface is smaller than that at the pore base,

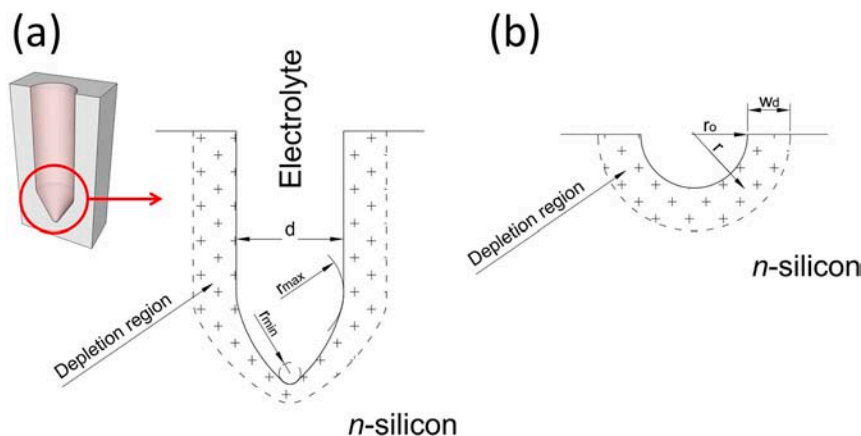


FIGURE 2 | Sketch of the electrolyte/silicon interface of a pore, with depletion region establishing into the silicon substrate highlighted. **(a)** Pore-shaped electrolyte/silicon interface; **(b)** hemispherical-shaped electrolyte-silicon interface. The radius of curvature of the electrolyte/silicon interface at the pore tip raises monotonically from the tip apex, minimum value r_{min} , to the pore radius, maximum value $r_{max} = d/2$, assuming for the pore a circular cross-section with a diameter d .

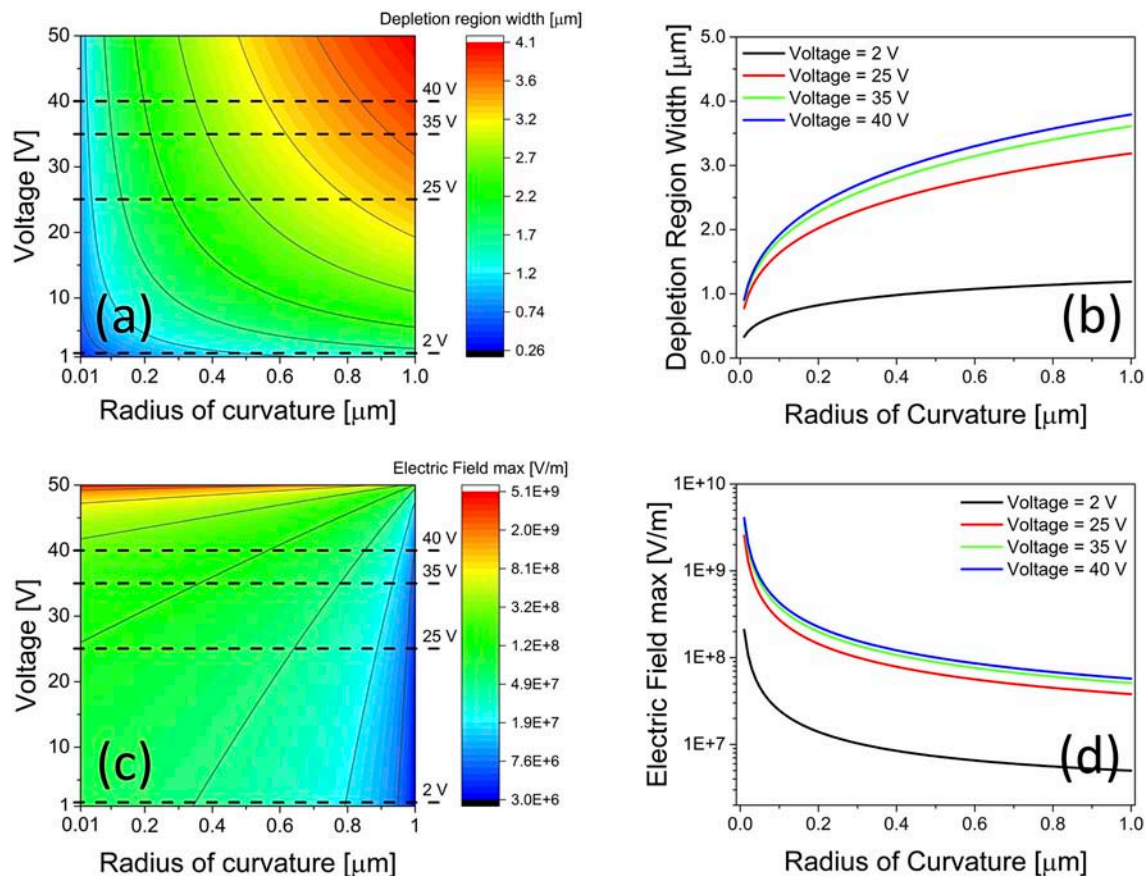


FIGURE 3 | Theoretical results on depletion region width and maximum electric-field intensity at the electrolyte/silicon interface of a pore, as a function of both anodic voltage and curvature radius values. **(a,c)** Contour plot of depletion region width w_d and maximum intensity of electric-field E_{max} in the silicon substrate as a function of electrolyte/silicon interface anodic voltage and curvature radius; **(b,d)** depletion region width w_d and maximum intensity of electric-field E_{max} in the silicon substrate as a function of electrolyte/silicon interface curvature radius, for different anodic voltage values, namely 2, 25, 35, and 40 V, corresponding to dashed lines in **(a,b)**.

thanks to the simultaneous lower value of w_d and higher value of E_{max} at the tip apex with respect to the pore base. This allows all pores of the arrays to develop and grow steadily. On the other hand, for array of pores with spacing of the same order of the depletion region or smaller (i.e., high-density array of pores), the pores in the array cannot be considered isolated anymore. In this case, the overlap of the depletion region between adjacent pores sensibly reduces the differences between curvature radius at the tip apex and pore base and, in turn, hole focusing efficiency at the tip apex. Tip apex and pore base now share photogenerated holes, thus producing morphologically-driven instabilities in the electrochemical etching of pores, for low anodic voltage values. Conversely, the use of high values (e.g., >20 V) for the anodic voltage V_{etch} allows the ratios between depletion region widths w_d at the tip apex and pore base (Figure S4a) and between maximum electric-field intensities E_{max} at the tip apex and pore base (Figure S4b) to be further enhanced with respect to those at low anodic voltage. This enables an efficient electric-field driven focusing of holes at the tip apex also for high-density array of pores with spacing smaller than the depletion region width, and, in turn, a stable pore growth/etching, in agreement with experimental results obtained at high anodic voltage in this work. Indeed, for a given etching current density value, whereas randomly-distributed pores were obtained from low-doped silicon substrates pre-patterned with a lattice of holes with spacing of $1.8\text{ }\mu\text{m}$ using a low anodic voltage (1.2 V), perfect arrays of pores were achieved at high anodic voltages (>20 V) using the same pre-patterned silicon substrates, thanks to the enhanced electric-field focusing of holes at the tip apex of the pores, with respect to the pore base, which allowed the etching of pore tips to be preferentially initiated and steadily sustained.

CONCLUSIONS

In conclusion, the controlled fabrication of high-density ($\sim 30 \times 10^6\text{ cm}^{-2}$) regular arrays of pores featuring high-depth (up to $\sim 45\text{ }\mu\text{m}$), high-aspect-ratio (from ~ 35 to ~ 45), and spacing of $1.8\text{ }\mu\text{m}$ was successfully achieved by back-side illumination

electrochemical etching at high anodic voltage (from 20 to 40 V) of low-doped (resistivity $3\text{--}8\text{ }\Omega\text{ cm}$) n -type silicon using low-HF-concentration etchants (5% by vol. in deionized water). Regular arrays of sub-micrometric pores featuring a diameter of 863 nm ($sd = 27\text{ nm}$) and 870 nm ($sd = 35\text{ nm}$), were successfully etched at 35 and 40 V, respectively, with $J_{etch0} = 13.4\text{ mA cm}^{-2}$. A theoretical model was proposed, which allows experimental results to be interpreted in terms of an electric-field enhanced focusing of holes at the tip apex of the pores, with respect to the pore base, at high anodic voltages, which enables the etching of the pore tips to be preferentially initiated and steadily sustained over time and space.

The controlled anodic etching of submicrometer pores in low-doped n -type silicon envisages the possibility to scale the electrochemical micromachining (ECM) technology down to the mesoscale, through a better understanding of the silicon dissolution at high anodic biasing and by further optimization of the etching conditions, in terms of composition of the etching solution. This would open noteworthy applications in the fields of (though not limited to) nanomedicine, nanoelectromechanical systems (NEMS), and nanoelectronics.

AUTHOR CONTRIBUTIONS

CC and GP carried out the experiments. LS designed the theoretical model. GB conceived the idea and supervised the research. All authors analyzed and discussed the results and wrote the manuscript.

FUNDING

This work was financially supported by ECSEL Joint Undertaking through the R2POWER300 project (Grant no. 653933).

SUPPLEMENTARY MATERIAL

The Supplementary Material for this article can be found online at: <https://www.frontiersin.org/articles/10.3389/fchem.2018.00582/full#supplementary-material>

REFERENCES

- Barillaro, G. (2015). Silicon electrochemical micromachining technology: the good, the bad, and the future. *ECS Trans.* 69, 39–46. doi: 10.1149/06902.0039ecst
- Barillaro, G., Diligenti, A., Nannini, A., and Strambini, L. M. (2005). Gas sensors based on silicon devices with a porous layer. *Phys. Stat. Sol. C* 2, 3424–3428. doi: 10.1002/pssc.200461202
- Barillaro, G., Nannini, A., and Pieri, F. (2002b). Dimensional constraints on high aspect-ratio silicon microstructures fabricated by HF photoelectrochemical etching. *J. Electrochem. Soc.* 149, C180–C185. doi: 10.1149/1.1449953
- Barillaro, G., Nannini, A., and Piotta, M. (2002a). Electrochemical etching in HF solution for silicon micromachining. *Sens. Actuators A* 102:195–201. doi: 10.1016/S0924-4247(02)00385-0
- Barillaro, G., and Pieri, F. (2005). A self-consistent theoretical model for macropore growth in n -type silicon. *J. Appl. Phys.* 97:116105. doi: 10.1063/1.1915534
- Barillaro, G., and Strambini, L. M. (2010). Controlling macropore formation in patterned n -type silicon: existence of a pitch-dependent etching current density lower bound. *Electrochem. Commun.* 12, 1314–1317. doi: 10.1016/j.elecom.2010.07.008
- Bassu, M., Surdo, S., Strambini, L. M., and Barillaro, G. (2012). Electrochemical micromachining as an enabling technology for advanced silicon microstructuring. *Adv. Funct. Mater.* 22, 1222–1228. doi: 10.1002/adfm.201102124
- Cozzi, C., Polito, G., Kolasinski, K., and Barillaro, G. (2017). Controlled microfabrication of high-aspect-ratio structures in silicon at the highest etching rates: the role of H_2O_2 in the anodic dissolution of silicon in acidic electrolytes. *Adv. Funct. Mater.* 7:1604310. doi: 10.1002/adfm.201604310
- Cozzi, C., Polito, G., Strambini, L. M., and Barillaro, G. (2015). Electrochemical preparation of in-silicon hierarchical networks of regular out-of-plane macropores interconnected by secondary in-plane pores through controlled inhibition of breakdown effects. *Electrochim. Acta* 187, 552–559. doi: 10.1016/j.electacta.2015.11.006
- Delalat, B., Cozzi, C., Ghaemi, S. R., Polito, G., Kriel, F. E., Michl, T. D., et al. (2018). Microengineered bioartificial liver chip for drug toxicity screening. *Adv. Funct. Mater.* 28:1801825. doi: 10.1002/adfm.201801825

- Föll, H., Christophersen, M., Carstensen, J., and Hasse, G. (2002). Formation and application of porous silicon. *Mat. Sci. Eng. R.* 39, 93–141. doi: 10.1016/S0927-796X(02)00090-6
- Harding, F. J., Surdo, S., Delalat, B., Cozzi, C., Elnathan, R., Gronthos, S., et al. (2016). Ordered silicon pillar arrays prepared by electrochemical micromachining: substrates for high-efficiency cell transfection. *ACS Appl. Mater. Interface* 8, 29197–29202. doi: 10.1021/acsami.6b07850
- Kemell, M., Ritala, M., Leskelä, M., Ossei-Wusu, E., Carstensen, J., and Föll, H. (2007). Si/Al₂O₃/ZnO:Al capacitor arrays formed in electrochemically etched porous Si by atomic layer deposition. *Microelectron. Eng.* 84, 313–318. doi: 10.1016/j.mee.2006.10.085
- Lehmann, V. (1993). The physics of macropore formation in low doped *n*-type silicon. *J. Electrochem. Soc.* 140, 2836–2843. doi: 10.1149/1.2220919
- Lehmann, V., and Föll, H. (1990). Formation mechanism and properties of electrochemically etched trenches in *n*-type silicon. *J. Electrochem. Soc.* 137, 653–659. doi: 10.1149/1.2086525
- Matthias, S., Müller, F., Schilling, J., and Gösele, U. (2005). Pushing the limits of macroporous silicon etching. *Appl. Phys. A* 80, 1391–1396. doi: 10.1007/s00339-004-3193-x
- Muller, R. S., and Kamins, T. I. (1977). *Device Electronics for Integrated Circuits*. New York, NY: John Wiley & Sons.
- Polito, G., Surdo, S., Robbiano, V., Tregnano, G., Cacialli, F., and Barillaro, G. (2013). Two-dimensional array of photoluminescent light-sources by selective integration of conjugated luminescent polymers into three-dimensional silicon microstructures. *Adv. Optical Mater.* 1, 894–898. doi: 10.1002/adom.201300288
- Rönnebeck, S., Carstensen, J., Ottow, S., and Föll, H. (1999). Crystal orientation dependence of macropore growth in *n*-type silicon. *Electrochem. Solid State Lett.* 2, 126–128. doi: 10.1149/1.1390756
- Surdo, S., Carpignano, F., Silva, G., Merlo, S., and Barillaro, G. (2013). An all-silicon optical platform based on linear array of vertical high-aspect-ratio silicon/air photonic crystals. *Appl. Phys. Lett.* 103:171103. doi: 10.1063/1.4826146
- Surdo, S., Carpignano, F., Strambini, L. M., Merlo, S., and Barillaro, G. (2014). Capillarity-driven (Self-Powered) one-dimensional photonic crystals for refractometry and (Bio)sensing. *RSC Adv.* 4, 51935–51914. doi: 10.1039/C4RA09056J
- Surdo, S., Merlo, S., Carpignano, F., Strambini, L. M., Trono, C., Giannetti, A., et al. (2012). Optofluidic microsystems with integrated vertical one-dimensional photonic crystals for chemical analysis. *Lab Chip* 12, 4403–4415. doi: 10.1039/c2lc40613f
- Uhlir, A. (1956). Electrolytic shaping of germanium and silicon. *Bell Syst. Tech. J.* 35, 333–347. doi: 10.1002/j.1538-7305.1956.tb02385.x

Conflict of Interest Statement: The authors declare that the research was conducted in the absence of any commercial or financial relationships that could be construed as a potential conflict of interest.

Copyright © 2018 Cozzi, Polito, Strambini and Barillaro. This is an open-access article distributed under the terms of the Creative Commons Attribution License (CC BY). The use, distribution or reproduction in other forums is permitted, provided the original author(s) and the copyright owner(s) are credited and that the original publication in this journal is cited, in accordance with accepted academic practice. No use, distribution or reproduction is permitted which does not comply with these terms.



Hyperspectral and Color Imaging of Solvent Vapor Sorption Into Porous Silicon

Soohyun Chun and Gordon M. Miskelly*

School of Chemical Sciences, University of Auckland, Auckland, New Zealand

A porous silicon thin film photonic crystal (rugate) sample with both a radial gradient in the rugate reflectance band wavelength and two spatially separated pore-wall surface chemistries (methylated and oxidized) was monitored by hyperspectral and color imaging while it was dosed with vapors of acetone, ethanol, heptane, 2-propanol, and toluene at concentrations ranging from 100 to 3,000 mg m⁻³. The shift in the wavelength of the rugate reflectance band maximum at each position along a transect across the two surface chemistries, as derived from the hyperspectral imaging, could discriminate between the different solvents and concentrations of solvents, while the change in hue derived from the color camera data along an analogous transect did not provide discrimination. The discrimination between solvents was mainly due to the two different surface chemistries, and the gradient associated with the change in the rugate reflectance band wavelength did not affect the selectivity significantly. There was spatial variability in the spectral and color responses along the transect independent of the overall rugate reflectance band wavelength gradient and pore-wall surface chemistries, and this was attributed to factors such as the presence of striations in the silicon wafer from which the porous silicon was prepared.

Keywords: porous silicon, hyperspectral imaging, sensor, vapor sensing, surface modification

OPEN ACCESS

Edited by:

Nicolas Hans Voelcker,
Monash University, Australia

Reviewed by:

Klemens Rumpf,
Karl-Franzens-Universität, Austria
Martin Jay Sweetman,
University of South Australia, Australia

*Correspondence:

Gordon M. Miskelly
g.miskelly@auckland.ac.nz

Specialty section:

This article was submitted to
Chemical Engineering,
a section of the journal
Frontiers in Chemistry

Received: 01 October 2018

Accepted: 27 November 2018

Published: 11 December 2018

Citation:

Chun S and Miskelly GM (2018)
Hyperspectral and Color Imaging of
Solvent Vapor Sorption Into Porous
Silicon. *Front. Chem.* 6:610.
doi: 10.3389/fchem.2018.00610

INTRODUCTION

Porous silicon photonic crystal (rugate) substrates can act as optical transducers for the detection of volatile organic compounds (VOCs) that sorb or capillary condense within the pores. Most previous studies have monitored the response of porous silicon photonic crystal substrates to environmental conditions either via point measurements (e.g., Ruminski et al., 2010, 2011; Kelly et al., 2011b; Jalkanen et al., 2014) or using measurements integrated across an area of the porous silicon (e.g., Ariza-Avidad et al., 2014). An alternative approach is to individually monitor selected spatial areas across the substrate, and then combine those individual responses using multivariate analysis techniques. This approach can probe variability in the response due to deliberately imposed changes (e.g., surface chemistry or pore-size gradients) or other causes of heterogeneity (e.g., uncontrolled pore-size variations due to the substrate or experimental conditions).

Several recent papers have reported the use of porous silicon substrates with step changes in pore surface modification chemistry to obtain selectivity in response toward analytes which penetrate the pores. Thus, Wu et al. (2013) prepared uniformly-etched porous silicon and then used a masking technique to prepare sensors that were methylated on one half and oxidized

on the other. The response of these sensors to solution analytes of differing polarity were then examined by monitoring the visible reflectance spectrum of a small disc-shaped region of the substrate that included similar proportions of the two surface chemistries. A similar experimental design was reported by Murguía et al. (2013), except that they used a sinusoidally varying current when preparing their porous silicon thin film, to prepare one-dimensional photonic crystals (rugate porous silicon). These authors monitored a small region that included their two surface chemistries (oxidized silicon and hydrosilylated silicon), and then analyzed the temporal data using wavelets. In a third example, Sweetman and Voelcker (2012) used photoresist patterning to prepare porous silicon films with different surface chemistries, and then monitored a region of the porous silicon that included the two surface chemistries (modified with pentafluorophenylsilyl and aminopropylsilyl groups). In this case the hydrophobic and hydrophilic nature of the surface modification was designed so that the two analytes (toluene and ethanol) were preferentially sorbed by the hydrophobic layer while the hydrophilic layer provided a fiducial spectral marker.

The stability and relative response toward organic vapors of porous silicon sensors with different surface modifications was described by Ruminski et al. (2010). Of relevance to the current study, they noted that thermally-oxidized silicon and methylated silicon had good stability in ambient air, and that the oxidized surface responded strongly to isopropanol, with a shift in the wavelength of the rugate reflectance band of over 10 nm. In contrast, exposure of the oxidized porous silicon to heptane resulted in a <2 nm shift, while exposure of 2-propanol or heptane to the methylated porous silicon caused very similar shifts, both <2 nm.

An example of imaging porous silicon where the response signal was determined by integrating over a large region of the porous silicon was a study by Ariza-Avidad et al. (2014) on the degradation of porous silicon samples when immersed in aqueous solutions. This study reported that the hue of the samples had a non-monotonic behavior during the degradation process and therefore preprocessing was performed to extract a “hue-like parameter” that changed in a monotonic way with the sample degradation.

Hyperspectral imaging of porous silicon has been conducted by Leacock-Johnson et al. (2013), who prepared porous silicon with a pore wall surface chemistry gradient from hydrophobic (methyl terminated) to hydrophilic (pentyl alcohol terminated) and then monitored the spectral response as ethanol was titrated into water covering the porous silicon. This study demonstrated that there was an overall monotonic change in the extent to which the alcohol-water solution penetrated the porous silicon along the transect, but some of the data reported in that paper also show small deviations from the overall trend along the transect that could be ascribed to factors such as the presence of striations in the initial silicon used to form the porous silicon. The solution infiltration experiment caused large spectral changes, with the wavelength of the rugate reflectance maximum moving 30–50 nm. This change is sufficiently large that smaller scale variations due to factors such as striations did not cause significant effects on plots of the observed wavelength maxima

vs. time. Steady state hyperspectral imaging of porous silicon was also reported by Miskelly (2016).

The current study extends the above examples. The porous silicon was prepared using a temporally sinusoidal etching current so that it has a prominent rugate reflectance band (Lorenzo et al., 2005), but also has measurable interference fringes to the red (longer wavelengths) of the rugate peak. Furthermore, preparation of the porous silicon used a spatially varying current density so that there is a radial gradient in wavelength of the rugate reflectance band across the porous silicon. Two pore-wall surface modifications were performed on adjacent sections of the porous silicon, using the strategy reported by Wu et al. (2013). The change in the wavelength of the rugate reflectance band or in the hue was then monitored as the sample was exposed to organic solvent vapors. This resulted in much smaller wavelength or hue shifts than were observed in the Leacock-Johnson et al. (2013) solution immersion study, which meant that drift and porous silicon inhomogeneities had a relatively greater impact on the data than was reported by those authors. A comparison of data collected under almost identical conditions with a line-scan hyperspectral imager (Sigernes et al., 2000) and with a color camera allowed the comparison of the sensitivity of measurements using the two imaging modes.

MATERIALS AND METHODS

A silicon wafer (Siltronix, 100 single side polished B doped, 0.8–1.2 m Ω -cm, thickness 500–550 μ m) was cut into approximately 2 \times 2 cm pieces, which were immersed in 2-propanol (LR) and placed in an ultrasonic bath for 10 min. The samples were then dried using nitrogen and mounted into a Teflon etch cell using procedures based on those of Sailor (2012). All electrochemical procedures used a PAR EG&G Model 173 potentiostat/galvanostat. Where necessary, sinusoidal waveforms created using Tektronix ArbExpress AXW100 version 2.0.2005.30 software were input to a Tektronix AFG3021 single channel Arbitrary/Function generator, with the output applied to the PAR 173 input. A pre-etch was performed using 3:1 (v/v) 48% HF: ethanol and a platinum (Aldrich, 99.99%) ring counter electrode. A current density of 46.9 mA cm $^{-2}$ was applied for 30 s with the silicon as the anode to create a thin sacrificial porous layer. The silicon was then rinsed with ethanol three times and the thin sacrificial porous layer was removed by treatment with 1 M aqueous KOH containing 10% (v/v) ethanol for 2 min. The sample was then rinsed with ethanol two times.

The porous silicon samples were prepared using electrochemical etching with a straight Pt wire counter electrode (Aldrich, 99.99%), placed perpendicularly to the silicon anode so that the wire end was about 2 mm above the center of the silicon. Etching was performed using 3:1 (v/v) 48% HF: ethanol solution. Etching used a sinusoidal waveform of 40 cycles in which the current density varied between 35.2 and 48.9 mA cm $^{-2}$ and was applied for 750 s. After the etching, the sample was rinsed with absolute ethanol two to three times, and dried using nitrogen while still within the etch cell.

Two pore-wall surface chemistries were imposed on a single sample of porous silicon using a recently reported masking method (Wu et al., 2013). First, a KSL-1100X-S compact muffle furnace (MTI Corporation) with a programmable controller was used to partially thermally oxidize the porous silicon. The furnace temperature was ramped to 300°C over 60 min at 5°C min⁻¹ then the temperature was held at 300°C for 30 min before the furnace was allowed to cool to room temperature. The porous silicon sample was placed inside a small open crucible and was in the furnace for the complete thermal cycle. A small drop of 13% (w/w) polystyrene ($M_w \sim 280,000$) dissolved in toluene was then painted onto half of the porous silicon sample using a small flat paint brush. The sample was then immersed in HF:ethanol (1:1 v/v) for 2 min to dissolve the exposed oxidized porous silicon and then rinsed with ethanol prior to selective chemistry being performed on the unmasked side as described below.

The masked porous silicon sample was mounted into the same electrochemical cell as was used for porous silicon etching, with an adapter that allowed white light irradiation of the porous silicon during electrochemistry under an inert atmosphere. The solution used for electrochemical methylation was prepared by transferring 0.27 g of lithium iodide, 10 mL of anhydrous acetonitrile, and 0.44 mL of iodomethane into a round bottom flask and then freeze-pump-thawing the solution three times. The electrochemical cell was evacuated then filled with nitrogen three times before the electrochemical methylation solution was introduced under nitrogen. A current density of 10.16 mA cm⁻² was applied with the porous silicon as the cathode for 1 min, while the porous silicon was illuminated through the glass adapter with white light from a Rofin PL-10 Polilight. The electrochemical cell was then disassembled and the porous silicon was immediately acidified using glacial acetic acid. The porous silicon was then rinsed three times with glacial acetic acid, three times with acetonitrile, and then three times with ethanol. The electrochemical cell was then disassembled and the sample was immersed in a solution of pentane before air drying. Finally, the polystyrene masking was removed by immersing the sample in toluene for at least 30 min. The sample was then rinsed three times with toluene, followed by ethanol. The sample was then immersed in a solution of pentane before drying.

A Philips XL30S Field Emission Gun Scanning Electron Microscope (FEG SEM) with a SiLi Super Ultra-Thin Window detector was used to obtain cross sectional and surface images of the fabricated porous silicon samples. The SEM images were taken using the high resolution and ultra-high resolution modes operating at electron accelerating voltages of 5 kV in a vacuum.

A Perkin Elmer Spectrum Two 100 FT-IR Spectrometer with attenuated total reflectance (ATR) attachment was used to collect Fourier transform infrared spectroscopy (FT-IR) absorbance spectra. Perkin Elmer spectrum 10TM software was used to collect and analyse the spectra, which were averages of 32 scans with a resolution of 4 cm⁻¹ over the range 600 to 4,000 cm⁻¹. The background was collected with the ATR crystal exposed to air.

A KSV Cam 100 tensiometer with Attension Theta analysis software was used to determine the water contact angles for the porous silicon samples. Measurements were performed three

times for each different surface, and the average water contact angle is reported with calculated standard deviation.

A scientific charge coupled detector camera (QICAM, Q-Imaging) with Varispec Liquid Crystal Tunable Filter (LCTF) (CRI Ltd) was used to obtain a hyperspectral image cube of the complete surface of a modified porous silicon sample from 450 to 720 nm at 5 nm intervals (55 bands). In-house code in the V++ program (version 5.0.0.301 Digital Optics Ltd[®]) was used to control image collection. An image cube of a specular reflectance standard was also collected to allow determination of reflectance. The saved images were averages of 4 images with a constant shutter time of 30 ms. A Fiber-Light DC-950 illuminator (Dolan Jenner) with a Fiber-Lite Diffuse Axial Illuminator (Edmund Scientific Optics) was used as the light source. The collected images were processed using the Matlab software[®] R2014a (The MathWorks, Inc.). The image cubes for the sample, reference standard, and dark image were first imported and cropped to isolate the porous silicon. The same cropping coordinates were used for the reference standard and dark images. One dimension of the cropped image cube corresponds to a spectrum at each image pixel, and these spectra were processed to determine the wavelength of the rugate band at each position of the hyperspectral image using a modified version of the Matlab function findpeaks.m, (O'Haver, 2018).

Two different imaging systems were used to image the porous silicon samples during vapor dosing. A Point Gray Research[®] Flea 2G 13S2C-C model camera (F2G) with a 50 mm double Gauss lens (Edmund Scientific Optics) was used for color (RGB) imaging. A line-scan hyperspectral imager constructed with a Point Gray Research[®] Flea 2-03S2M grayscale camera and a 50 mm double Gauss imaging lens was used for hyperspectral imaging during vapor dosing, and this system was calibrated using an HG-1 mercury-argon lamp (Ocean Optics, Inc.). The porous silicon was mounted in the vapor dosing cell so that the porous silicon surface was perpendicular to the selected imaging system. The position of the vapor dosing cell was arranged to provide maximum reflectance for the hyperspectral imaging, and so that the porous silicon filled the field of view for the RGB imaging. The vapor dosing cell was constructed of Teflon, with an A48-927 anti-reflection coated glass slide (Edmund Optics) as the window.

An automated vapor dosing system was used to generate pulses of vapor at known concentrations for known periods of time. The vapor dosing system used in this research was designed and developed in-house at the University of Auckland and characterized by Wong (2012). Vapors of five solvents: acetone, ethanol, heptane, 2-propanol, and toluene were generated using the automated vapor dosing system. The concentrations used were 100, 300, 700, 1,000, 1,500, and 2,000 mg m⁻³ for acetone and 2-propanol, 100, 300, 700, 900, 1,100, and 1,500 mg m⁻³ for ethanol, 200, 400, 800, 1,500, 2,000, and 2,500 mg m⁻³ for heptane, and 200, 400, 800, 1,600, 2,000, 2,500, and 3,000 mg m⁻³ for toluene. A pre-dose of the system with 1,000 mg m⁻³ of the next solvent followed by a purge period was performed prior to measurement with each solvent. The purge periods during dosing for hyperspectral imaging was 20 min while the dose period was 30 min. The purge period for RGB imaging was

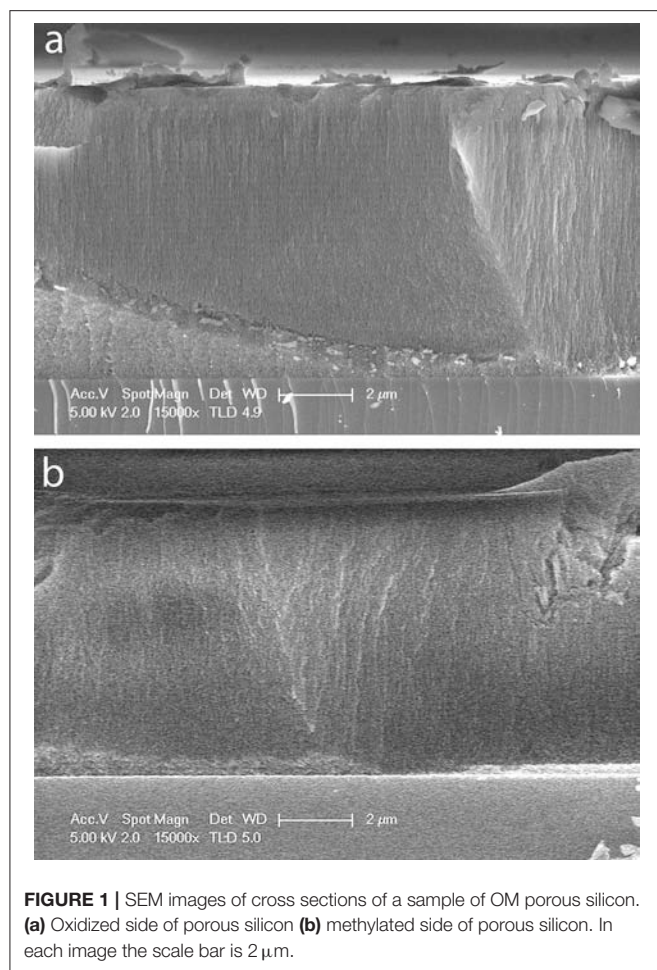


FIGURE 1 | SEM images of cross sections of a sample of OM porous silicon. **(a)** Oxidized side of porous silicon **(b)** methylated side of porous silicon. In each image the scale bar is 2 μm .

40 min with dosing for 30 min. A Baseline[®]-MOCON[®] PID-TECH[®] plus photoionization detector was connected to the outlet of the vapor dosing cell to independently monitor the solvent vapor concentration. TRAQ-WARE software recorded the concentration (ppm) of the vapor every 2 s.

The hyperspectral images were collected every 30 s during the dosing cycle for each solvent, with ten images being averaged at each time point. Images for each dosing experiment were saved directly to a computer, and were analyzed off-line using Matlab. The region of interest of each image corresponding to the porous silicon was selected, resulting in cropped images of 221 by 370 pixels. The hyperspectral images were corrected for the estimated spectral envelope of the system response, using the obtained raw image cube data. First, the minimum value of the image cube was subtracted from all the other values. The column means of the resulting matrix were calculated, and then the row means of these column means were calculated. This calculation resulted in a vector of average brightness with respect to wavelength. This vector of average brightness was then normalized and replicated to create a hyperspectral cube that contained the normalized mean spectrum for every pixel position and every time point. The raw image data was then

divided by this mean spectrum, and this corrected data matrix was either used directly in subsequent multivariate data analyses or the wavelength of the rugate reflectance maximum in each spectrum was extracted, and these wavelengths were used in the multivariate analyses.

Color (RGB) images of the porous silicon during vapor dosing were collected by averaging 10 RGB images every 60 s and saving the average images directly to a computer. The images were imported into Matlab, and a 801 by 21 pixel region of interest corresponding to a transect down the center of each porous silicon image was isolated by cropping. The row means of each of the red, green, and blue channels for this transect were calculated and then used to calculate the hue for each transect position, using the following equation

$$\text{hue} = \cos^{-1} \left[\frac{0.5 \times (\text{red} - \text{green}) + (\text{red} - \text{blue})}{[(\text{red} - \text{green})^2 + (\text{red} - \text{blue})(\text{green} - \text{blue})]^{1/2}} \right]$$

The difference in hue at a given point and time compared to the initial hue at that point was then calculated. The RGB hue difference data required spatial filtering to improve the signal to noise ratio of the processed data. This was performed using the 3 X 3 median filtering function of Matlab “medfilt2.” Following this preprocessing the data were analyzed using principal component analysis and linear discriminant analysis in Matlab.

RESULTS

Preparation and Characterization

The porous silicon was prepared using a sinusoidal etching current density and with a thin Pt wire counter electrode placed perpendicularly above the center of the silicon wafer, so that the resulting porous silicon was a rugate filter (photonic crystal) with a radial gradient wavelength of the rugate reflection band (Li et al., 2005). The average pore size in such porous silicon structures has also been shown to vary with current density (Collins et al., 2002; Clements et al., 2012) so that there should also be a radial gradient in pore size. The porous silicon was then modified with two different pore-wall surface chemistries as described by Wu et al. (2013). The porous silicon was partially thermally oxidized, and then half of the porous silicon was impregnated with polystyrene. The oxidized porous silicon was removed from the non-protected half using dilute HF solution, and then the exposed hydrogen-terminated porous silicon was immediately methylated via the electrochemical reduction of iodomethane with the porous silicon as the cathode (Gurtner et al., 1999). Finally, the polystyrene was dissolved to expose the remaining oxidized porous silicon. This procedure gave porous silicon samples that had an oxidized (hydrophilic) portion and a methylated (hydrophobic) portion and also had a radial gradient in pore-size. These are referred to as OM samples in the following text.

A cross-sectional SEM image of a small region of the oxidized portion of an OM porous silicon sample prepared as described above is shown in **Figure 1a**. The thickness of $8.7 \pm 0.1 \mu\text{m}$ appears constant across the image with faint horizontal banding

due to the periodic change in porosity caused by the rugate filter formation. A cross-sectional SEM image of part of the methylated portion of sample OM is shown in **Figure 1b**. The calculated average thickness of the methylated side ($8.1 \pm 0.1 \mu\text{m}$) is slightly smaller than that of the oxidized side at a similar position along the radial gradient.

The ATR-FTIR spectrum of the oxidized portion of OM porous silicon (**Figure 2a**) shows a large Si-O stretching band with a maximum at $1,038 \text{ cm}^{-1}$. The methylated portion of OM porous silicon should mainly be CH_3 terminated, and the ATR-FTIR spectrum shows a sharp rocking band of the methyl groups at 763 cm^{-1} with two weak bands at $1,403$ and $1,252 \text{ cm}^{-1}$, which are associated with $-\text{CH}_x$ deformation modes (**Figure 2b**). The spectral position of the rocking band is similar to that reported earlier (Canaria et al., 2002). The difference in the pore wall surface chemistry for the two halves of OM porous silicon is also shown by water contact angles. The oxidized portion gave a water contact angle of $70.8 \pm 1.4^\circ$ ($n = 3$) while the methylated portion had a contact angle of $131.2 \pm 0.8^\circ$ ($n = 3$).

The UV-Visible reflectance spectra at selected points along a transect of the OM porous silicon sample are shown in **Figure 3**. The wavelength of the maximum of the rugate reflectance band on the oxidized side varied from 550 to 620 nm, while the wavelength of the maximum of the rugate reflectance band on the methylated side varied from 500 to 550 nm. These differences in wavelength on the two sides are due to the fabrication process of the sample. The removal of pore wall material prior to the methylation of the porous silicon has resulted in a blue shift of the rugate band. The magnitude of the rugate reflectance band for this OM sample were not much larger than the heights of the thin film interference fringes also observed in the UV-Vis spectra. However, the rugate peak can be identified as the significant peak with the shortest wavelength.

A false color map showing the wavelength of the maximum in the rugate reflectance band at all positions of an OM porous silicon sample is shown in **Figure 4**. The wavelength of the rugate peak maximum had approximately radial symmetry across each half of the porous silicon sample, with the longest wavelength near the center. The magnitude of the reflectance between the two surfaces were different from each other, and so the transition line between the surfaces could be distinguishable in single waveband images and the color difference could be observed by eye.

Vapor Dosing Results

The optical responses of the porous silicon samples during exposure to solvent vapors were monitored using hyperspectral and RGB imaging techniques. Hyperspectral images were collected using a custom built line scan imager (Sigernes et al., 2000; Leacock-Johnson et al., 2013), while the RGB images were acquired with a scientific color camera. The wavelength and spatial calibration of the hyperspectral imager were performed using an atomic line calibration light source and a precision ruler, respectively. The hyperspectral images were processed to determine the wavelength of the maximum of the rugate reflectance band at each point along the transect, and changes in these wavelengths were used to monitor the exposure of the porous silicon to organic solvent vapors.

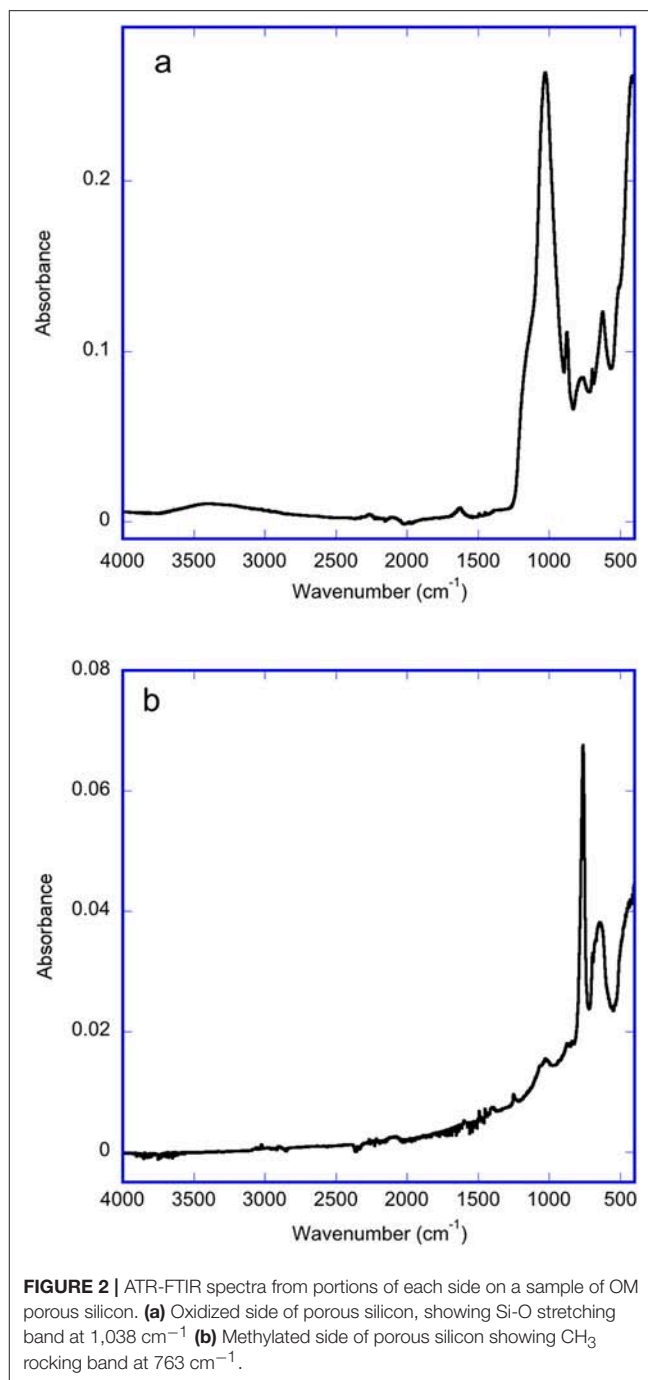


FIGURE 2 | ATR-FTIR spectra from portions of each side on a sample of OM porous silicon. **(a)** Oxidized side of porous silicon, showing Si-O stretching band at $1,038 \text{ cm}^{-1}$. **(b)** Methylated side of porous silicon showing CH_3 rocking band at 763 cm^{-1} .

A slight drift was sometimes seen in the rugate peak wavelength values (for the hyperspectral image data) and the values of the hue (for the RGB image data) during a given vapor dosing experiment, and different experiments showed different patterns and magnitudes of the drift. The drift on the two sides could differ. For example, during 2-propanol dosing the wavelength of the maximum in the rugate reflectance band on the oxidized side decreased by up to 1 nm while on the methylated side it increased by up to 0.5 nm. All the drifts

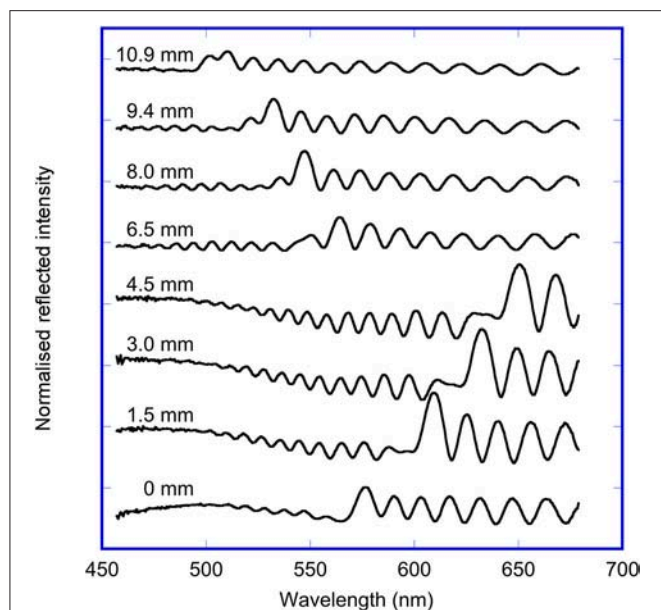


FIGURE 3 | Reflected light spectra measured at specified points along a transect across the OM sample, starting at the oxidized side (0–4.5 mm) and ending on the methylated side (6.5–10.9 mm).

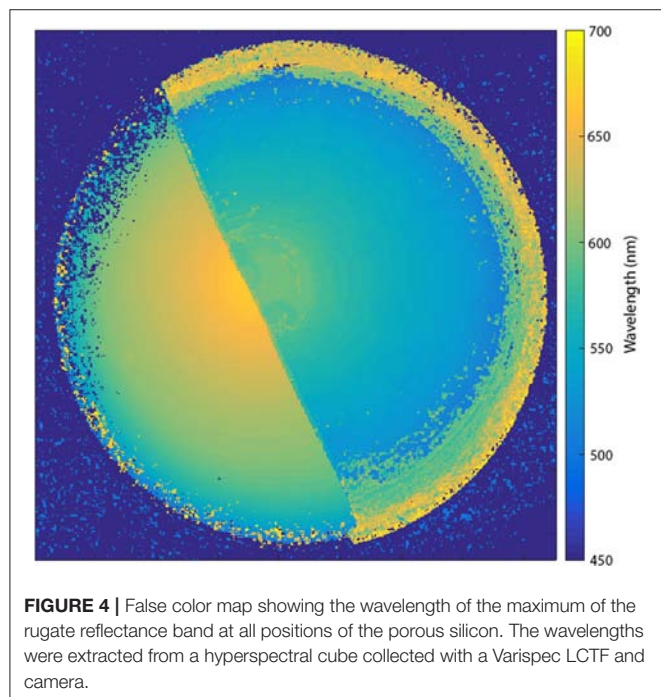


FIGURE 4 | False color map showing the wavelength of the maximum of the rugate reflectance band at all positions of the porous silicon. The wavelengths were extracted from a hyperspectral cube collected with a Varispec LCTF and camera.

for the hyperspectral data were <1 nm, however this change was sometimes significant compared to the observed changes resulting from a vapor concentration change. Thus, the largest change in the wavelength of the rugate reflectance band due to dosing for the methylated side of sample OM during dosing of 2-propanol vapor was about 0.5 nm. It was therefore important to

correct this background drift prior to any multivariate analysis. Separate monitoring of the temperature next to the porous silicon indicated that the drift was not caused by the small changes in temperature (up to 1°C) of the sample during dosing experiments. Although the actual cause of the drift was not determined, one possibility is that it was due to a slight change in the intensity or temperature of the light source, which could affect the observed wavelength of the rugate peak. Baseline correction was performed using the Matlab function `bf.m` applied to time points during the known purge periods. Since the dose and purge timing for the dosing experiments was always the same this background correction could be readily implemented. For most baseline corrections two points of the purge period were selected; one timepoint early in the purge period, and one timepoint near the end of the purge period. For 2-propanol, only one value toward the end of the purge period was selected to define the background, due to the slow desorption of 2-propanol from the oxidized porous silicon during the purge periods.

The data matrices containing the changes in the rugate peak wavelength (for hyperspectral image data) and median filtered change in hue (for RGB and Mode 0 image data) during vapor dosing with five different solvents were represented as false color maps, where the vertical axis is the distance along the transect, the horizontal axis is time, and the color represents either the change in wavelength or the change in hue at a given position compared to the initial value. The upper portion of each false color map represented the oxidized side of the porous silicon and the lower portion represented the methylated side. Depending on the polarity of the vapor and the polarity of the porous silicon surface, the magnitude of the response to a given solvent and concentration were different for each side of the porous silicon. Solvents with higher polarity showed higher responses on the oxidized (hydrophilic) side than on the methylated (hydrophobic) side.

The false color maps generated from hyperspectral and RGB imaging during 2-propanol vapor dosing are shown in **Figures 5a, 6a**, respectively. 2-Propanol was dosed in the order; 100, 300, 700, 1,000, 1,500, and 2,000 mg m^{-3} , so 13 vertical bands (7 purge bands, and 6 dose bands) can be seen in the false color map for RGB imaging. The false color map for the hyperspectral imaging only shows 12 bands because the image collection was stopped near the start of the final purge. The false color map for the hyperspectral imaging (**Figure 5a**) and the plot of wavelength changes at selected pixels in **Figure 5b** shows that the shift in wavelength of the rugate peak during vapor dosing of 2-propanol on the oxidized side is larger than on the methylated side. The change is the greatest during the final dose period, which is when the concentration of the 2-propanol vapor is the highest. The first (lowest) dose resulted in a rugate peak wavelength shift of about 2.5 nm on the oxidized side, while the last (highest) dose caused a rugate wavelength shift of about 6 nm. The wavelength shift on the methylated side of the porous silicon is much smaller than for the oxidized side with the change being around 0.1 to 0.5 nm over the vapor dosing experiment. The transition between the two pore wall surface chemistries can be clearly observed by this difference in response. This result shows that 2-propanol is sorbed by the oxidized (hydrophilic) side more

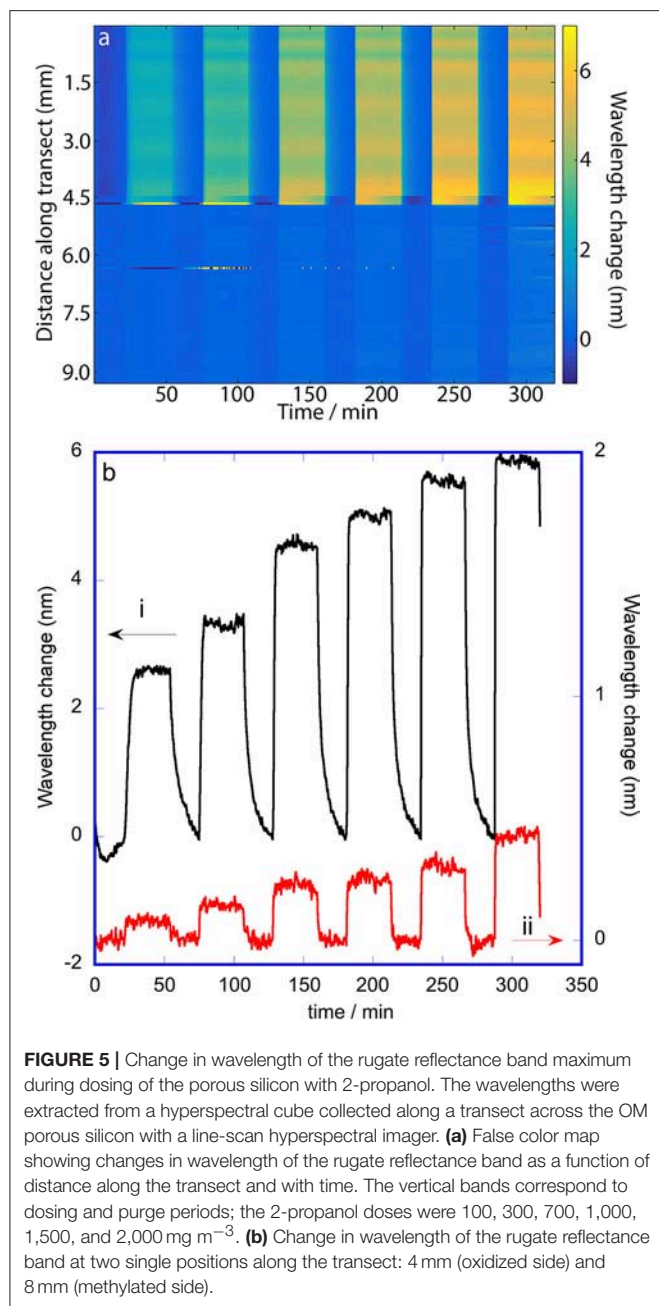


FIGURE 5 | Change in wavelength of the rugate reflectance band maximum during dosing of the porous silicon with 2-propanol. The wavelengths were extracted from a hyperspectral cube collected along a transect across the OM porous silicon with a line-scan hyperspectral imager. **(a)** False color map showing changes in wavelength of the rugate reflectance band as a function of distance along the transect and with time. The vertical bands correspond to dosing and purge periods; the 2-propanol doses were 100, 300, 700, 1,000, 1,500, and 2,000 mg m^{-2} . **(b)** Change in wavelength of the rugate reflectance band at two single positions along the transect: 4 mm (oxidized side) and 8 mm (methylated side).

than the methylated (hydrophobic) side. On the oxidized side of the OM porous silicon, additional variation in the response appearing as horizontal bands across the color map in **Figure 5a** are due to differences in pore sizes or other pore properties at different points across the porous silicon surface. The plots in **Figure 5** also show tailing of the response on the oxidized side after the higher concentration dosing periods, as the 2-propanol slowly desorbs.

The false color map of the change in hue for the RGB image data during 2-propanol dosing (**Figure 6a**) shows that some portions of the oxidized side are responsive with small changes in hue while the methylated side shows very slight evidence of

vertical bands corresponding to very small changes in hue. The oxidized side has a change in hue near the edge of the porous silicon that is opposite in direction to the change in hue near the transition line between the two pore wall surface chemistries. This non-monotonic behavior of hue with respect to change in the rugate wavelength was also noted by Ariza-Avidad et al. (2014). Since the change in hue on the oxidized side is greater than on the methylated side, the transition between the two pore wall surface chemistries can again be seen. The small hue change resulted in a much smaller signal to noise ratio compared to the wavelength changes determined with the hyperspectral imager. Thus, the plot of the response at a single position on the oxidized half of the porous silicon (**Figure 6b**) is much noisier than the similar plot in **Figure 5b**, and the hue change at 100 positions on the methylated side were averaged to obtain the smaller plot in **Figure 6b**, which still has a poor signal to noise ratio.

Dosing with the other solvent vapors led to similar false color maps, with decreased responses at the same concentration. Dosing with heptane led to the smallest responses, and the responses to this solvent on the oxidized and methylated sides of the porous silicon were very similar.

Multivariate Analysis of the Images of Sample OM During Vapor Dosing

The data matrices of the changes in the rugate peak wavelength upon dosing with each solvent were concatenated into a combined data matrix. Each row of the individual matrices matched in spatial position, and the combined matrix contained all the dosing pulses (as a function of time) in the order: acetone, ethanol, heptane, 2-propanol and toluene. Principal component analysis was performed on the transposed combined data matrix. The first three principal components explained 98.9, 0.78, and 0.08% of the variance in the data respectively. Plots of the scores and loadings for the first two principal components (labeled PC1 and PC2 respectively) are shown in **Figure 7**. The PC loadings, **Figure 7a**, are related to the contribution of changes in the wavelength of the rugate reflectance band at each position along transect to each principal component. The abrupt change in plots of the PC1 and PC2 loadings vs. pixel position is due to transition between the two pore-wall surface modifications, where the first part corresponds to the oxidized side, and the second part corresponds to the methylated side. The loadings of PC1 are higher for the oxidized side than the methylated side, while the loadings for PC2 are higher for the methylated side than the oxidized side. The PC3 plot loadings showed little difference in average magnitude between the two sides, however the values on the oxidized varied more than on the methylated side. The plots of the PC1 and PC2 scores for the change in the rugate peak wavelength during dosing are shown in **Figures 7b,c**. The PC1 score plot shows pulses due to the dosing of acetone, ethanol, heptane, 2-propanol and then toluene. The first six pulses represent acetone at six concentrations, the next six pulses represent ethanol at six concentrations and so on. The PC1 scores for 2-propanol are the highest, and then ethanol, acetone, toluene, with heptane showing the lowest PC1 scores. The PC2 scores also show a set of pulses with time, but heptane shows the

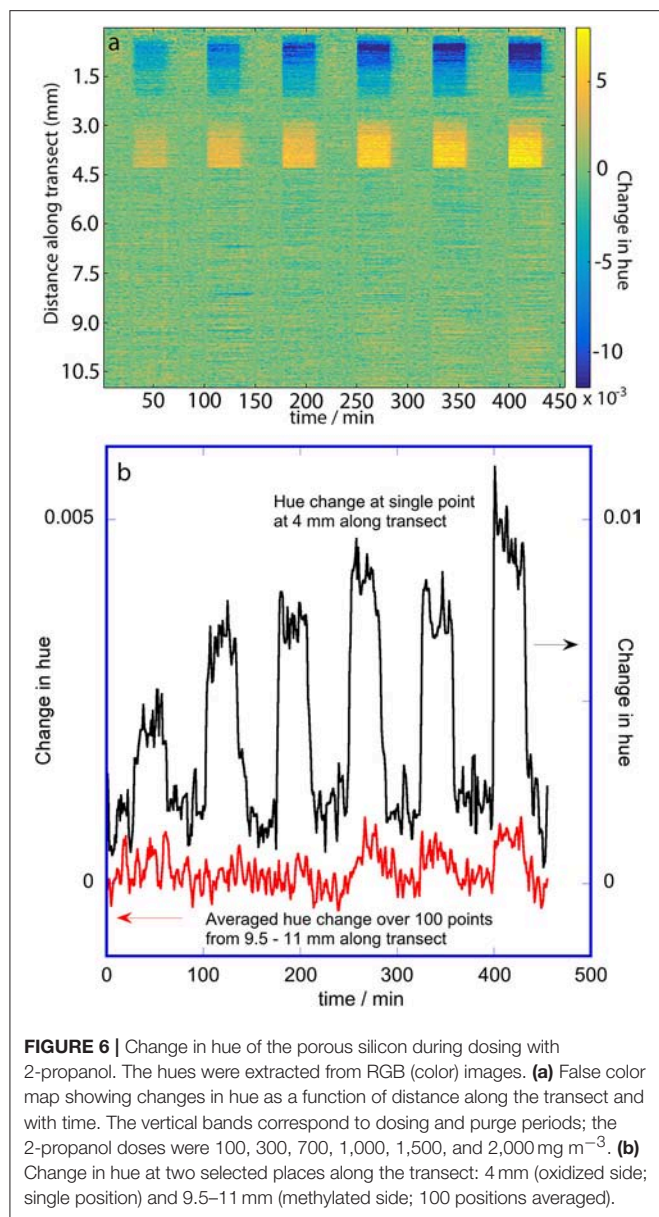


FIGURE 6 | Change in hue of the porous silicon during dosing with 2-propanol. The hues were extracted from RGB (color) images. **(a)** False color map showing changes in hue as a function of distance along the transect and with time. The vertical bands correspond to dosing and purge periods; the 2-propanol doses were 100, 300, 700, 1,000, 1,500, and 2,000 mg m^{-3} . **(b)** Change in hue at two selected places along the transect: 4 mm (oxidized side; single position) and 9.5–11 mm (methylated side; 100 positions averaged).

greatest values followed by toluene and propan-2-ol, with ethanol being only slightly higher than acetone. Most of the scores for principal component 3 (PC3) were near zero, with some large spikes which corresponded to when the system was transitioning between purge and dose periods.

Apart from the two pore-wall surface chemistries, the porous silicon also had a radial gradient in pore sizes. The PC1 loadings show a very small magnitude trend which may correspond to this radial gradient on the oxidized side underlying the more obvious short-scale variability. The PC3 loadings also showed longer- scale as well as shorter-scale changes in response over the oxidized side. From **Figure 7** it appears that small-scale variations (e.g., due to the striations which originate from different dopant densities in the silica substrate (Jastrzebski et al., 1980; Fusegawa

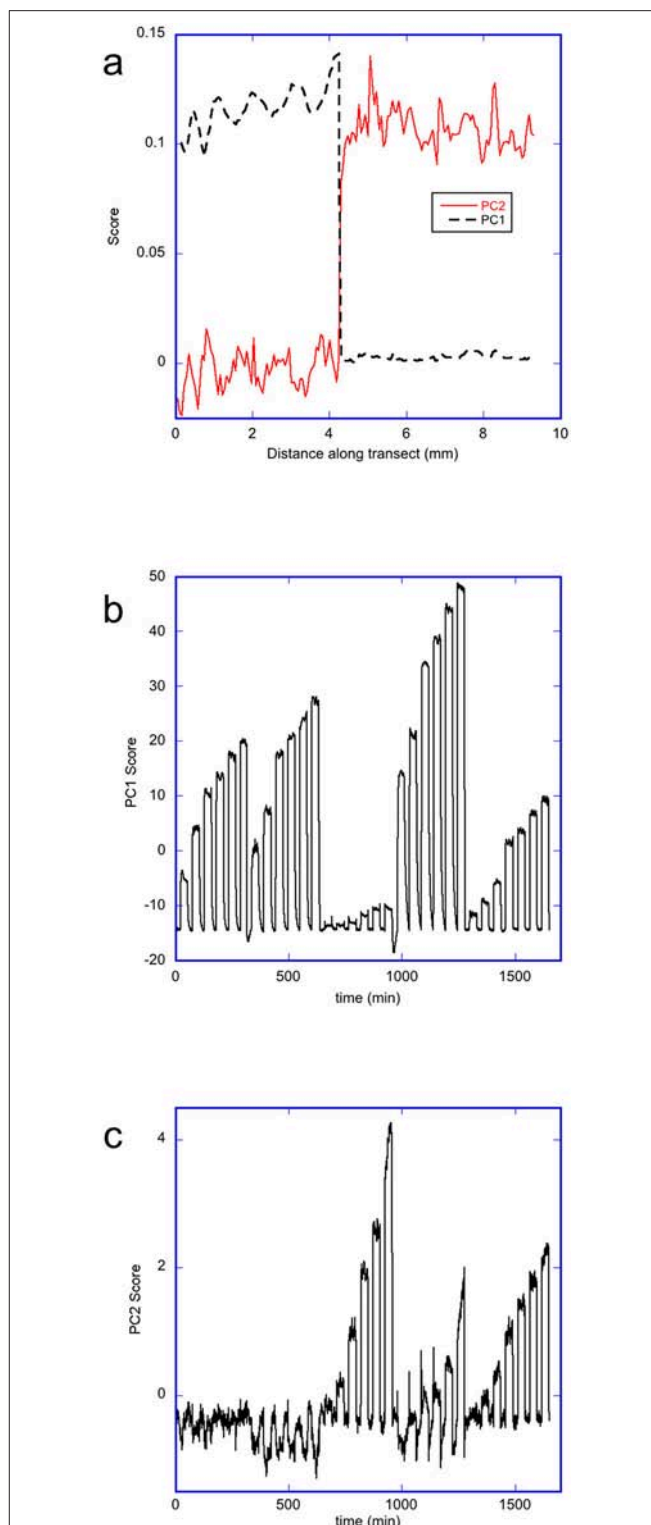


FIGURE 7 | Principal component analysis of the changes in wavelength of the rugate reflectance band as the porous silicon OM sample was dosed with 5 different solvents in the order acetone, ethanol, heptane, 2-propanol, and toluene. **(a)** Plot showing loadings of PC1 and PC2 along a transect across the OM porous silicon **(b)** Plot showing the scores for PC1 with time during dosing **(c)** Plot showing the scores for PC2 with time during dosing.

and Yamagishi, 1992; Schweizer et al., 2010), dominate over effects due to the radial porosity gradient.

The initial principal component analysis had significant contributions from changes occurring during the transitions from purge to dosing and from dosing to purge, particularly for PC3. In order to avoid the responses during the transition periods dominating or perturbing the analysis, the PCA was repeated using just selections of 40 data points obtained during the steady-state phase of each solvent dosing pulse at each pixel position. A plot of the PC2 scores vs. the PC1 scores from this analysis, **Figure 8**, shows clear separation of heptane, toluene and the other three solvents—acetone, ethanol, and 2-propanol. The most hydrophobic solvent, heptane, has lower PC1 scores but large PC2 scores, while the opposite is true for the more hydrophilic vapors (acetone, ethanol, and 2-propanol). Toluene is more hydrophilic than heptane, but is also more hydrophobic than acetone, ethanol and 2-propanol, so the score values of toluene are located between the data corresponding to heptane and the other three solvents. For each solvent, all concentrations could be distinguished. However, acetone, ethanol and 2-propanol all lie on similar curves. A similar plot of PC3 scores against PC1 scores for the change in rugate peak wavelength upon dosing with all the solvents (not shown) showed some separation of the data for ethanol from the data for acetone and 2-propanol.

Following these principal component analyses, the supervised data classification method of linear discriminant analysis (LDA) was performed on the rugate wavelength data. The wavelength shifts of the rugate reflectance band recorded during each solvent dosing period were combined into one matrix. The 40 columns corresponding to the steady state part of each of the dosing periods and the 10 columns corresponding to the first purge periods for each solvent were selected and combined into a new dataset. This combined matrix was transposed so that time was set as the observation variable and pixel positions were set as the properties to explain each observation. LDA was performed on this transposed dataset, and the first three linear discriminants were investigated.

A 3D plot with the scores from the first three linear discriminant axes was generated to capture the variation due to these components (**Figure 9**). The 3D plot has been rotated to optimize the visible separation between each solvent and each concentration. The plot shows separation due to both solvent identity and concentration, and all solvents are distinguished without any overlap. All the data for each solvent fall on a curve that starts near where the data representing the purge periods occur. The plot indicates that most of the variation in the data is explained by LD1 and LD2, however LD3 distinguishes acetone and ethanol from 2-propanol.

Principal component analysis on all the data, and principal component and linear discriminant analysis on just the data at the steady-state times of dosing and purging were also conducted on the hue data obtained from the color images. The loadings for PC1 of the complete dataset showed an abrupt change corresponding to the transition between the two pore-wall surface modifications, with the loadings being close to zero for the methylated side. The loadings for the oxidized side varied almost linearly from positive to negative, consistent

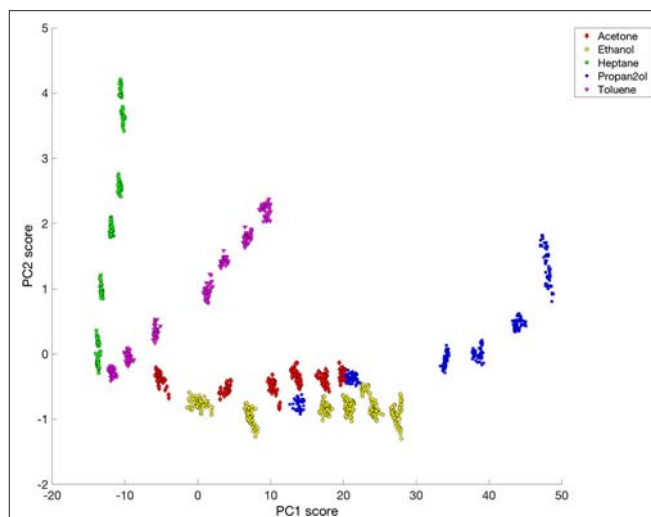


FIGURE 8 | Plot of PC2 vs. PC1 for rugate reflectance band wavelength shift data corresponding to steady-state dosing or purging of acetone, ethanol, heptane, 2-propanol and toluene.

with the observed change in direction of the hue change evident in the false color map in **Figure 6**. The scores plot for PC1 clearly showed the dosing for the oxygen-containing solvents acetone, ethanol, and 2-propanol with smaller responses for toluene and no responses for heptane. PC2 and PC3 did not contain chemically-interpretable variations. LDA was also unable to distinguish between the solvent vapors using the hue information.

DISCUSSION AND CONCLUSIONS

Previous studies have investigated enhancing the selectivity of porous silicon sensors to detect and discriminate a wide range of vapors. Different solvent vapors were used in this study, and were easily grouped into hydrophilic and hydrophobic vapors. A previous study of porous silicon optical sensors had shown that 2-propanol vapor had stronger adsorption on hydrophilic surfaces, while toluene vapor had stronger adsorption on hydrophobic surfaces (Kelly et al., 2011a). A separate study with stacked layers of porous silicon showed that non-polar analytes (such as cyclohexane, heptane, and toluene) did not interact with the silica surface (hydrophilic) while polar molecules were strongly adsorbed. That study also noted that Knudsen diffusion was the primary mode of mass transport of the vapor within the pores of porous silicon (Kelly et al., 2011b). The results reported in this paper are consistent with observations of interactions of 2-propanol and heptane with thermally oxidized and methyl porous silicon by Ruminski et al. (2010).

An aim of the present research was to investigate whether porosity gradients can provide added selectivity for vapor sensing. Gao et al. (2002) had proposed that decreased pore sizes offered greater sensitivity, since smaller pores offer greater surface areas, therefore the optical response for a given vapor concentration should be higher. This was tested by creating

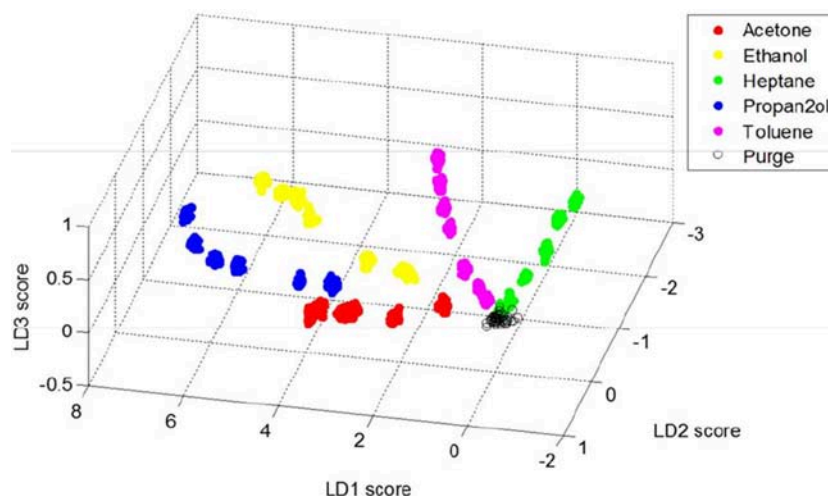


FIGURE 9 | Plot showing the first three linear discriminant scores for rugate reflectance band wavelength shift data corresponding to steady-state dosing or purging of acetone, ethanol, heptane, 2-propanol and toluene.

porous silicon samples with a gradient in pore sizes across the sample during the fabrication step, using a thin wire counter electrode placed above the center of the exposed silicon wafer. This method delivers different current densities at different positions on the porous silicon sample, since the center of the silicon is closest to the counter electrode, therefore the current density at the center is larger than at the edges, and this current density gradient can cause a gradient in pore sizes porous silicon (Collins et al., 2002). The pore size gradient was not measured directly in this study, but the UV-Vis reflectance characterization experiments confirmed the gradient in rugate reflectance band wavelength across the porous silicon sample (Li et al., 2005). The present investigation showed that the optical and spectral changes of the porous silicon upon dosing did not correlate with the rugate reflectance band wavelength across the porous silicon surface. If the smaller pore sizes expected to be associated with the shorter wavelengths of the rugate reflectance band had increased the optical response of the porous silicon, and if the optical response change is captured by the camera, we would have expected greater sensitivity at the edges of the porous silicon sample and this was not observed. Moreover, the variations in sensitivity and selectivity that were observed across the porous silicon were more localized than if they had been caused by the current density gradient, showing that other factors were controlling the adsorption to a greater extent.

The response of the porous silicon sample was investigated using a color camera and a hyperspectral imager. Rugate filter porous silicon samples have been previously studied by monitoring the wavelength shift of the rugate peak using reflectance spectra measured at a single point on the surface (e.g., King et al., 2007; Ruminski et al., 2008). These and similar studies have shown that the wavelength of the rugate reflectance band shifts to the red upon solvent exposure and have also shown that the porous silicon sensor can selectively detect different vapors; however these papers only reported measurements at a single

point (or several points) on the porous silicon sensor and not the whole sample.

As noted in the introduction, a previous study of the degradation of porous silicon used digital imaging combined with calculation of hue and a hue-related parameter (Ariza-Avidad et al., 2014). Those authors also noted that the apparent color of a rugate filter of wavelength lower than 560 nm was dependent on the white balance value of the color camera. This behavior is consistent with the observations in the current paper, where the change in hue upon dosing with solvent vapors had different signs depending on the initial hue or spectrum of the porous silicon at that position.

Finally, a recent study used color camera images to monitor the response of porous silicon under different concentrations of ethanol vapor (Park et al., 2010). That paper reported the color, current and photoluminescence responses of porous silicon as a function of ethanol vapor concentration. The authors reported that the color difference of the porous silicon was an efficient way of monitoring the optical response of the porous silicon. The color response of that study was observed under fluorescent lighting, whereas our study was conducted using broad-band white light. It is very likely that the sensitivity observed in the prior study is mainly due to the use of the fluorescent light source with its narrow band emissions in the red and green. The effect of different light sources on the information that can be obtained from photonic crystal sensors needs further study.

In the present research hyperspectral and RGB images of a transect across the whole porous silicon were captured during vapor dosing. These images were used to monitor the changes in reflectance of the porous silicon sample under as similar conditions as possible, so that these imaging techniques could be compared. The results showed that the hyperspectral imager was better at detecting small changes in optical response compared to RGB imaging for these porous silicon samples. In addition, it provided wavelength change information along a complete

transect of the porous silicon sample, whereas the RGB images only showed measurable responses at some positions of the porous silicon samples. The capability of color images to collect changes in optical reflectance of porous silicon can be further explored by using variables other than hue.

There are many methods for the multivariate image analysis of time series such as images obtained during our dosing of porous silicon. However, there is no particular method to analyse image data that has been shown to be optimal for such situations in terms of sensitivity, selectivity, speed, and use of computer resources. In this study, two common multivariate statistical methods were used. One method (principal component analysis, PCA) was used for exploratory analysis, and the other method (linear discriminant analysis, LDA) was used in attempts to distinguish between already known classes (solvents and concentrations) and so further distinguish the groupings within the data. The results of the multivariate analysis showed that LDA provided better separation of solvent and dosing concentration classes using the hyperspectral imaging data than did PCA. The main reason that LDA did not work well for the color imaging data is that some dosing pulses resulted in no hue changes while the small changes meant that other dosing pulses had very similar hue changes. The discrimination was

also adversely affected by there being little to no hue change on the methylated side of the OM porous silicon. This is likely to be due to the small shift in the spectral response, the initial wavelength of the rugate reflectance band, and the contribution from the interference fringes to the red of the rugate band.

AUTHOR CONTRIBUTIONS

SC conducted the experiments and data analysis and drafted part of the manuscript. GM designed the project, advised on the experiments and data analysis, and completed the manuscript.

FUNDING

This project was supported by funding from the University of Auckland.

ACKNOWLEDGMENTS

The authors acknowledge advice from Prof. M Sailor of UCSD, and thank A. Garcia-Sega and A. Sharief who constructed the vapor dosing system.

REFERENCES

- Ariza-Avidad, M., Nieto, A., Salinas-Castillo, A., Capitan-Vallvey, L. F., Miskelly, G. M., and Sailor, M. J. (2014). Monitoring of degradation of porous silicon photonic crystals using digital photography. *Nanoscale Res. Lett.* 9:410. doi: 10.1186/1556-276X-9-410
- Canaria, C. A., Lees, I. N., Wun, A. W., Miskelly, G. M., and Sailor, M. J. (2002). Characterization of the carbon-silicon stretch in methylated porous silicon – observation of an anomalous isotope shift in the FTIR spectrum. *Inorg. Chem. Commun.* 5, 560–564. doi: 10.1016/S1387-7003(02)00465-3
- Clements, L. R., Wang, P.-Y., Tsai, W.-B., Thissen, H., and Voelcker, N. H. (2012). Electrochemistry-enabled fabrication of orthogonal nanotopography and surface chemical gradients for high-throughput screening. *Lab Chip* 12, 1480–1486. doi: 10.1039/c2lc20732j
- Collins, B. E., Dancil, K. S., Abbi, G., and Sailor, M. J. (2002). Determining protein size using an electrochemically machined pore gradient in silicon. *Adv. Funct. Mater.* 12, 187–191.
- Fusegawa, I., and Yamagishi, H. (1992). Evaluation of interstitial oxygen along striations in CZ silicon single crystals with a micro-FTIR mapping system. *Semicond. Sci. Tech.* 7, A304–A310.
- Gao, J., Gao, T., Li, Y. Y., and Sailor, M. J. (2002). Vapor sensors based on optical interferometry from oxidized microporous silicon films. *Langmuir* 18, 2229–2233. doi: 10.1021/la015568f
- Gurtner, C., Wun, A. W., and Sailor, M. J. (1999). Surface modification of porous silicon by electrochemical reduction of organohalides. *Angew. Chem. Int.* 38, 1966–1968.
- Jalkanen, T., Torres-Costa, V., Mäkilä, E., Kassalainen, M., Koda, R., Sakka, T., et al. (2014). Selective optical response of hydrolytically stable stratified Si rugate mirrors to liquid infiltration. *ACS Appl. Mater. Interf.* 6, 2884–2892. doi: 10.1021/am405436d
- Jastrzebski, L., Levine, P. A., Cope, A. D., Henry, W. N., and Battson, D. F. (1980). Material limitations which cause striations in CCD imagers. *IEEE J. Solid State Circ.* 15, 759–766. doi: 10.1109/JSSC.1980.1051466
- Kelly, T. L., Gao, T., and Sailor, M. J. (2011a). Carbon and carbon/silicon composites templated in rugate filters for the adsorption and detection of organic vapors. *Adv. Mater.* 23, 1776–1781. doi: 10.1002/adma.201004142
- Kelly, T. L., Garcia-Sega, A., and Sailor, M. J. (2011b). Identification and quantification of organic vapors by time-resolved diffusion in stacked mesoporous photonic crystals. *Nano Lett.* 11, 3169–3173. doi: 10.1021/nl201385p
- King, B. H., Ruminski, A. M., Snyder, J., and Sailor, M. J. (2007). Optical-fiber-mounted porous silicon photonic crystals for sensing organic vapor breakthrough in activated carbon. *Adv. Mater.* 19, 4530–4534. doi: 10.1002/adma.200701294
- Leacock-Johnson, A., Garcia-Sega, A., Sharief, A., Sailor, M. J., and Miskelly, G. M. (2013). Real-time 1D hyperspectral imaging of porous silicon-based photonic crystals with one-dimensional chemical composition gradients undergoing pore-filling-induced spectral shifts. *Sensors Actuators A* 203, 154–159. doi: 10.1016/j.sna.2013.08.047
- Li, Y. Y., Kim, P., and Sailor, M. J. (2005). Painting a rainbow on silicon – a simple method to generate a porous silicon band filter gradient. *Phys. Stat. Sol.* 202, 1616–1618. doi: 10.1002/pssa.200461200
- Lorenzo, E., Oton, C. J., Capuj, N. E., Ghulinyan, M., Navarro-Urrios, D., Gaburro, Z., et al. (2005). Fabrication and optimization of rugate filters based on porous silicon. *Phys. Stat. Sol.* 2, 3227–3231. doi: 10.1002/pssc.200461125
- Miskelly, G. M. (2016). “Methods to evaluate spatial uniformity in porous silicon,” in *Handbook of Porous Silicon*, eds L. Canham (Springer, Cham), 1–18. doi: 10.1007/978-3-319-04508-5_123-1
- Murguía, J. S., Vergara, A., Vargas-Olmos, C., Wong, T. J., Fonollosa, J., and Huerta, R. (2013). Two-dimensional wavelet transform feature extraction for porous silicon chemical sensors. *Anal. Chim. Acta.* 785, 1–15. doi: 10.1016/j.aca.2013.04.024
- O’Haver, T. (2018). *Peak Finding and Measurement*. Available online at: <https://terpconnect.umd.edu/%7Etoh/spectrum/PeakFindingandMeasurement.htm> (Accessed September 21, 2018).
- Park, S. H., Seo, D., Kim, Y. Y., and Lee, K. W. (2010). Organic vapor detection using a color-difference image technique for distributed Bragg reflector structured porous silicon. *Sens. Actuators, B Chem.* 147, 775–779. doi: 10.1016/j.snb.2010.03.075

- Ruminski, A. M., Barillaro, G., Chaffin, C., and Sailor, M. J. (2011). Internally referenced remote sensors for HF and Cl₂ using reactive porous silicon photonic crystals. *Adv. Funct. Mater.* 21, 1511–1525. doi: 10.1002/adfm.201002037
- Ruminski, A. M., King, B. H., Salonen, J., Snyder, J. L., and Sailor, M. J. (2010). Porous silicon-based microsensors for volatile organic analytes: effect of surface chemistry on stability and specificity. *Adv. Funct. Mater.* 20, 2874–2883. doi: 10.1002/adfm.201000575
- Ruminski, A. M., Moore, M. M., and Sailor, M. J. (2008). Humidity-compensating sensor for volatile organic compounds using stacked porous silicon photonic crystals. *Adv. Funct. Mater.* 18, 3418–3426. doi: 10.1002/adfm.200701494
- Sailor, M. J. (2012). *Porous Silicon in Practice: Preparation, Characterization and Applications*. Weinheim: Wiley-VCH.
- Schweizer, S. L., von Rhein, A., Geppert, T. M., and Wehrspoon, R. B. (2010). Reduced pore diameter fluctuations of microporous silicon fabricated from neutron-transmutation-doped material. *Phys. Stat. Sol. R.* 4, 148–150. doi: 10.1002/pssr.201004115
- Sigernes, F., Lorentzen, D. A., Heia, K., and Svenøe, T. (2000). Multipurpose spectral imager. *Appl. Opt.* 39, 3143–3153. doi: 10.1364/AO.39.003143
- Sweetman, M. J., and Voelcker, N. H. (2012). Chemically patterned porous silicon photonic crystals .internally referenced organic vapor sensors. *RSC Adv.* 2, 4620–4622. doi: 10.1039/c2ra20232h
- Wong, A. (2012). *Analysis of VOCs Using Different Sampling Methods Followed by Gas Chromatography-Flame Ionization Detector (GC-FID)*. MSc thesis, University of Auckland.
- Wu, C.-C., Chen, M. Y., and Sailor, M. J. (2013). Differential adsorption of small molecules in spatially functionalized porous silicon nanostructures. *Langmuir* 29, 11802–11808. doi: 10.1021/la402261v

Conflict of Interest Statement: The authors declare that the research was conducted in the absence of any commercial or financial relationships that could be construed as a potential conflict of interest.

Copyright © 2018 Chun and Miskelly. This is an open-access article distributed under the terms of the Creative Commons Attribution License (CC BY). The use, distribution or reproduction in other forums is permitted, provided the original author(s) and the copyright owner(s) are credited and that the original publication in this journal is cited, in accordance with accepted academic practice. No use, distribution or reproduction is permitted which does not comply with these terms.



Impregnation of High-Magnetization FeCo Nanoparticles in Mesoporous Silicon: An Experimental Approach

Mathieu Lepesant^{1,2}, Benjamin Bardet^{3,4}, Lise-Marie Lacroix^{2*}, Pierre Fau¹, Cyril Garnero^{1,2}, Bruno Chaudret², Katerina Soulantica², Thomas Defforge³, Damien Valente³, Caroline Andreazza⁵, Jérôme Billoué³, Patrick Poveda⁴ and Gaël Gautier^{3*}

¹ LCC-CNRS, Laboratoire de Chimie de Coordination, CNRS, UPS, Toulouse, France, ² Laboratoire de Physique et Chimie de Nano-Objets, UMR 5215 INSA-CNRS-UPS, Université de Toulouse, Toulouse, France, ³ Groupe de Recherche en Matériaux, Microélectronique, Acoustique et Nanotechnologies, UMR CNRS 7347, INSA-CVL, Université de Tours, Tours, France, ⁴ ST Microelectronics, Tours, France, ⁵ Interfaces, Confinement, Matériaux et Nanostructures, CNRS, UMR 7374, Université d'Orléans, Orléans, France

OPEN ACCESS

Edited by:

Thierry Djenizian,
École des Mines de Saint-Étienne,
France

Reviewed by:

Petra Granitzer,
University of Graz, Austria
Jinmyoung Joo,
Ulsan National Institute of Science
and Technology, South Korea

*Correspondence:

Lise-Marie Lacroix
lmlacroix@insa-toulouse.fr
Gaël Gautier
gael.gautier@univ-tours.fr

Specialty section:

This article was submitted to
Chemical Engineering,
a section of the journal
Frontiers in Chemistry

Received: 18 October 2018

Accepted: 27 November 2018

Published: 18 December 2018

Citation:

Lepesant M, Bardet B, Lacroix L-M,
Fau P, Garnero C, Chaudret B,
Soulantica K, Defforge T, Valente D,
Andreazza C, Billoué J, Poveda P and
Gautier G (2018) Impregnation of
High-Magnetization FeCo
Nanoparticles in Mesoporous Silicon:
An Experimental Approach.
Front. Chem. 6:609.
doi: 10.3389/fchem.2018.00609

This paper deals with the synthesis of high-magnetization porous silicon-based nanocomposites. Using well-controlled organometallic synthesis of ferromagnetic FeCo nanoparticles, the impregnation of mesoporous silicon has been performed by immersion of porous silicon in a colloidal solution. The technique was optimized by controlling the temperature, the immersion duration, and the solvent nature. The characterization of the nanocomposites showed a homogeneous filling of the pores and a high magnetization of 135 emu/cm³. Such composites present a great interest for many applications including data storage, medical instrumentations, catalysis, or electronics.

Keywords: impregnation, magnetic nanoparticles, mesoporous silicon, nanocomposite, magnetic properties

INTRODUCTION

Magnetic materials such as iron alloys or iron oxides (FePt, FeCo, Fe₂O₃, etc.) present a great interest in data storage (Sun et al., 2000), drug delivery (Anglin et al., 2008; Zhu et al., 2009), medical instruments (ex: for magnetic resonance imaging; Bomati-Miguel et al., 2005; Thomas et al., 2006) or catalysis (Manova et al., 2006; Li et al., 2011; Bordet et al., 2016). For instance, the Fischer–Tropsch process is a widely studied method that uses magnetic metals such as iron or cobalt as catalysts to produce synthetic fuel (Bordet et al., 2016). Due the progressive disappearance of fossil fuels, this catalysis process appears nowadays as an attractive way to produce “green” synthetic fuels from biomass or natural gas sources. More specifically, employment of nanosized magnetic materials show an improved reactive surface area and their insertion in a porous medium is one of the solutions to prevent their mutual aggregation and sintering during reaction (Lu et al., 2004; Bomati-Miguel et al., 2005). Porous substrates made of different materials such as PEGDA (polyethylene glycol diacrylate; Allia et al., 2011), silicon (Anglin et al., 2008; Granitzer et al., 2010; Harraz, 2013) or silica (Lu et al., 2004; Nakamura et al., 2006; Kockrick et al., 2007; Zhu et al., 2009; Liu et al., 2011; Kim et al., 2013) can be used as supports. In particular, porous silicon (PS) is one of the most interesting media because it is a versatile material with tunable surface chemistry, pore size or surface area (Loni et al., 2015) and shows interesting behavior concerning biodegradability issues (Xia et al., 2017). However, the methods employed to fill such porous material with nanoparticles (NPs) remain very challenging. Two strategies of filling are reported in

the literature. In the case of *in situ* synthesis techniques, precursors are introduced by impregnation within the porous template and then directly reduced. However, this technique suffers from a poor renewing of precursors, a low in-depth homogeneity and strongly depends on silicon surface chemistry (Yiu et al., 2008; Fukami et al., 2009; Bardet et al., 2017). Another technique consists in impregnating the porous material with *ex situ* synthesized and stabilized NPs. In this way, a better control of the NP properties is achieved (Granitzer et al., 2013, 2015; Rumpf et al., 2013). However, the influence of the *ex situ* loading with regard to previous particle synthesis has not been widely studied and reported in the literature.

In this paper, we propose to load FeCo magnetic NPs with a regular cubic geometry into mesoporous silicon. This study aims at providing an experimental procedure to impregnate PS to high loadings and to characterize the in-depth homogeneity and the magnetic properties of the nanocomposite.

EXPERIMENTAL

Synthesis of FeCo Nanoparticles

FeCo NPs were synthesized by adaptation of a previously reported organometallic approach (Lacroix et al., 2009). Depending on the synthesis conditions, the size of the particles can be varied from 5 to 15 nm. In this work, we prepared FeCo NPs of 9.0 ± 0.6 nm. Fe and Co silylamides, (- Fe(N(Si(CH₃)₃)₂)₂)₂ and Co(N(Si(CH₃)₃)₂)₂(THF) -) were reduced under 3 bars of H₂ at 150°C for 48 h in mesitylene and in the presence of long chain surfactants (hexadecylamine—HDA, and palmitic acid—PA). The precursors concentrations were kept at 20 mmol/L. The HDA and PA concentrations were 80 and 55 mmol/L, respectively. After reaction, the excess of surfactant was removed by magnetically-assisted separation under inert atmosphere to prevent any oxidation. The particles were then kept as powder in the glove box. Chemical analyses were performed on FeCo NPs by inductively coupled plasma mass spectrometry (ICP-MS) revealing a global composition of Fe₅₂Co₄₈.

Synthesis of Porous Silicon

Porous silicon templates were synthesized by anodization of a highly-doped n-type silicon wafer with a resistivity of 10–20 mΩ.cm in an electrochemical cell containing concentrated hydrofluoric acid diluted in water (5 vol. %) and Triton X-100 (0.2 mmol/L). A current density of 25 mA/cm² was applied in order to form large and straight pores (Harras, 2013). The anodization duration was adapted in order to form a PS layer with a thickness of 18 μm. An average pore diameter of 100 nm was estimated by Scanning Electron Microscopy (SEM). A mean porosity (ratio of pore volume and overall volume) of around 66% was calculated from optical FTIR (Fourier Transform Infra-Red spectroscopy) measurements. After the anodization, the samples were thoroughly rinsed in ultrapure water and dried on a hot plate at 120°C. PS wafers were then singulated in 4 × 4 mm² square dices.

Impregnation Technique

The magnetic cubic NPs were loaded in the PS template by a simple immersion of the substrate in a FeCo colloidal solution at a concentration of 1.3 g/l. The setup is quite similar to the one proposed by Granitzer et al. (2013). However, the role of the solvent and the impregnation temperature is highlighted in this study and will be addressed in the next sections. After impregnation, the substrates were washed with a flow of tetrahydrofuran (THF) in order to eliminate most of the NPs aggregates left on the surface.

Structural and Morphological Characterization

The particles were characterized by SEM and Transmission Electron Spectroscopy (TEM), using a 100 kV Jeol JEM 1011 and a 200 kV FEI CM20. In order to characterize the particles, they were re-dispersed in toluene and a drop was deposited on a carbon coated copper grid. The nanocomposites were also characterized by Energy Dispersive X-Ray Spectroscopy (EDX) in order to estimate the in-depth homogeneity of the pore filling. Cross section samples were also prepared in order to observe by TEM the NPs impregnation along the PS pores.

Magnetic Characterization

Magnetic measurements were performed using a Quantum Design Physical Property Measurement System (PPMS) with a Vibrating Sample Magnetometer (VSM). PS substrates filled with NPs were characterized after immobilization on a quartz support using adhesive Kapton film. Hysteresis loops were recorded at 300 and 5 K applying induction field of ±3T. The exchange bias H_{ex} was determined from the hysteresis loop recorded at 5 K after cooling the sample from 300 K down to 5 K under an external field of 3T.

$$H_{ex} = \frac{H_c^- + H_c^+}{2} \quad (1)$$

where H_c^- is the coercive field observed during the demagnetization process (second quadrant, experimentally: -125 mT) and H_c^+ the coercive field observed during the magnetization (fourth quadrant, experimentally: 126 mT).

The pore filling factor Q , which characterizes the mass of NP loaded over a given surface area, was determined following Equation (2):

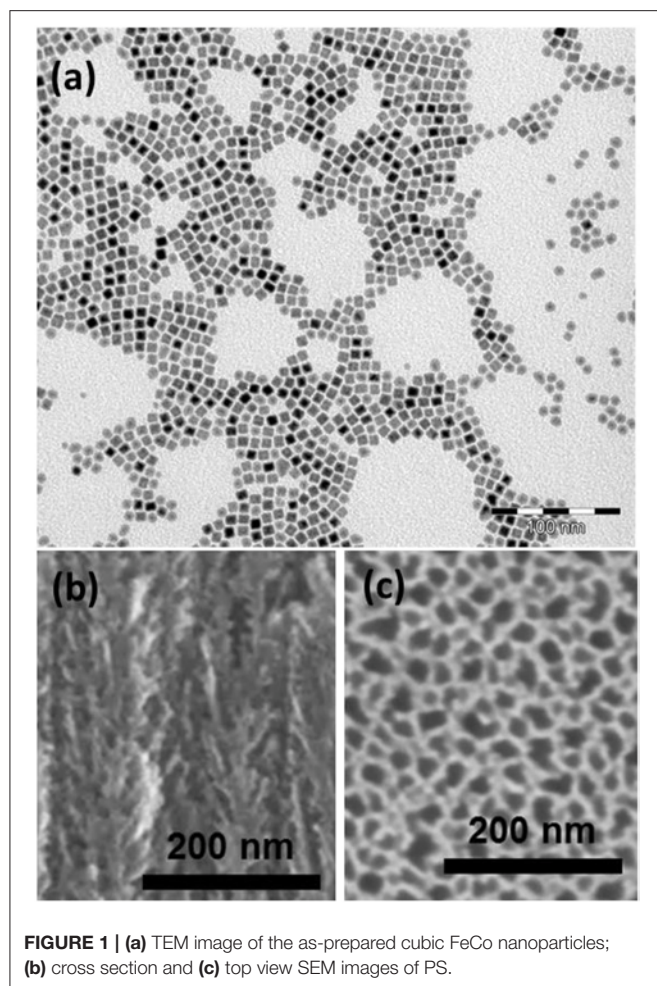
$$Q \text{ (g/m}^2\text{)} = \frac{M_s}{\Gamma \times S} \quad (2)$$

With Γ the saturation magnetization of the NPs (224 emu/g_{FeCo}), M_s the saturation magnetization of the composite determined experimentally as the magnetization at 3T, and S the footprint area of the substrate, i.e., 16 mm².

RESULTS

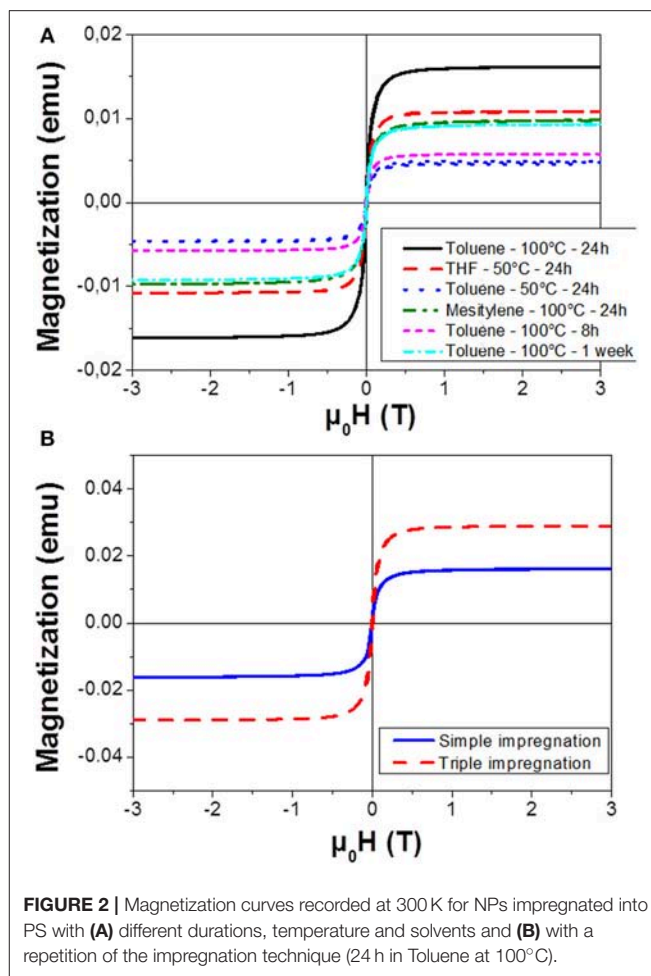
Material Structural Characterization

FeCo NPs were prepared following an organometallic approach. The Co and Fe precursors were decomposed in presence of dihydrogene leading to monodisperse NPs exhibiting a cubic



shape as shown in **Figure 1a**. The particle mean size of 9.0 ± 0.6 nm was well controlled thanks to the stabilization of the surface with a mixture of carboxylic acid and alkylamine ligands. The particles displayed a magnetization at high field (3T) of 204 emu/g_{FeCo} and 217 emu/g_{FeCo}, at 300 and 5 K, respectively, both values being close to the bulk saturation magnetization (230 emu/g_{FeCo}, **Figure S1**). The particles are not oxidized as revealed by the absence of any exchange bias at low temperature. This result was further confirmed by Mössbauer spectroscopy (Garnero, 2016).

The PS substrate was also characterized by electron microscopy. The **Figures 1b,c** show the PS layer before the NPs impregnation. The thickness of the PS layer is about 18 μ m. As we can observe in the **Figure 1b**, the structure is composed of primary pores oriented perpendicularly to the surface with a size in the range of 25–30 nm and secondary smaller branches which is typical of mesoporous silicon etched from highly doped wafers (Garnero, 2016). It is assumed that this secondary porosity is susceptible to bring an improved anchoring surface for the NPs. It is noteworthy that mesoporous silicon obtained by electrochemical etching produces non-interconnected pores (Lehmann et al., 2000). In other words, the only direction for



particle impregnation in each pore is from the surface toward the PS/silicon interface.

Optimization of Pore Filling

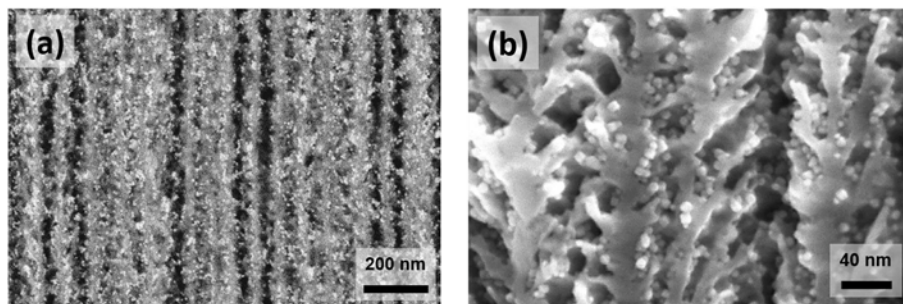
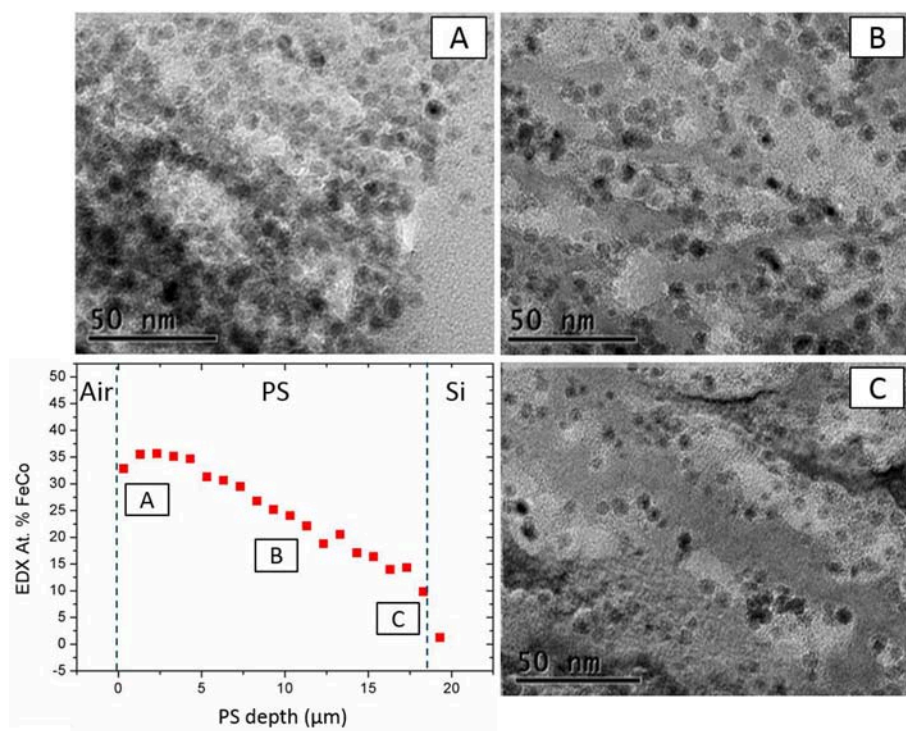
In this paper, we investigate the impact of multiple parameters: the temperature of the colloidal solution, the nature of the solvent and the impregnation duration. The pore filling factor Q , calculated from the magnetic response of the filled PS (**Figure 2**), is shown in **Table 1**.

Impregnations were initially carried out using toluene as solvent, keeping the impregnation duration constant at 24 h. Increasing the temperature of the colloidal solution from 50 to 100°C allowed improving the filling of the pores as revealed by the higher saturation magnetization obtained. This phenomenon can be attributed to a better diffusion of the particles along the pores.

In order to study the influence of the solvent, we compared the magnetic properties of the filled PS using mesitylene (previously used during NPs synthesis) and THF, which is also a good solvent for the colloidal dispersion of the FeCo NPs. As observed in **Figure 2A**, the impregnation in toluene gave the best overall result. The superiority of toluene compared to mesitylene could

TABLE 1 | Summary of saturation magnetization (M_s) and pore filling factor (Q) for different experimental conditions of **Figure 2**.

Duration	24 h				8 h	1 week	3 × 24 h
Temperature (°C)	50		100		100	100	100
Solvent	Toluene	THF	Toluene	Mesitylene	Toluene	Toluene	Toluene
M_s (memu)	4.9	10.8	16.2	9.8	5.8	12.6	38.9
Filling Factor Q (g/m ³)	1.4	3.0	4.5	2.7	1.6	2.6	10.9

**FIGURE 3** | SEM images of PS/FeCo nanocomposites observed with back-scattered electrons detector **(a)**, and with secondary electrons detector **(b)**.**FIGURE 4** | TEM images at different depths: near the Air/PS interface **(A)**, at the middle of the PS layer **(B)**, and near the PS/Si interface **(C)** in perspective with FeCo at % (EDX) in-depth profile.

be explained by a lower viscosity of the former, 0.59 and 0.66 cP at 25°C, respectively (Rumpf et al., 2013). The THF is a good solvent for NPs dispersion and moreover, it presents the lowest viscosity of all tested solvents (0.55 cP at 25°C). It shows a better impregnation performance than toluene at the

low temperature (50°C). However, a low boiling point (66°C) limits the maximum temperature reachable, and consequently the diffusion of the particles. The impregnation into the pores was therefore reduced compared to the results obtained at 100°C in toluene.

The experimental condition of solvent and temperature being optimized, the effect of impregnation duration was studied from 8 h to 1 week. Eight hours of contact was not a sufficient duration to fully fill the pores, as revealed by the low saturation magnetization and the limited filling factor ($Q = 1.6 \text{ g/m}^2$). After a 24 h impregnation, a filling factor of 4.5 g/m^2 was reached. Extending further the impregnation from 24 h up to a week did not promote a better loading (Figure S2). On the contrary, a decrease of the Q factor was observed following a non-monotonic trend, probably due to a dynamic process of release of the NPs initially hanged on the PS pores back to the colloidal solution. As a result, the best impregnation condition was obtained after an impregnation of 24 h in toluene at 100°C .

As it was not possible to increase the impregnation duration without a loss of NP material, we experimented the repetition of the impregnation procedure three times in the same porous host sample. We observe on Figure 2B an increase of the saturation magnetization and thus of the filling factor, after these three consecutive impregnations. This result highlights the benefit of the re-introduction of fresh NPs within the solution in order to improve the PS filling.

Structural Characterization of the Nanocomposite

SEM associated to EDX, TEM, and VSM techniques were employed to characterize the PS impregnated under optimized conditions. SEM images of the impregnated substrate are shown in the Figures 3a,b. These pictures show a cross section of impregnated PS, the white spots corresponding to FeCo NPs (electron back-scattering). As we can see, these nanoparticles are homogeneously dispersed along the pores. The homogeneity of the filling was evaluated by the EDX measurements correlated with TEM micrographs taken at different depths and presented in the Figure 4. In the graph (Figure 4 bottom left), we estimate the atomic percentage of iron and cobalt at different depths from the PS surface down to the Si/PS interface. The results show a quite good homogeneity of the NPs filling, with metal loading from 35% near the PS surface to 15% at the interface. A slight increase of the amount of FeCo is evidenced at the very near surface. This phenomenon can be attributed to the variation of PS morphology with the depth. The pores are indeed less branched at the Si/PS interface, thus leading to lower local specific surface area and less NP anchorage sites. The EDX analysis was confirmed by TEM imaging at different depths (cf. Figures 4A–C) showing a filling along the entire PS pores length. The slight modification of the NPs shape, from cubic like to spheroid, could be attributed to the extended oxidation induced by the TEM sample preparation.

The magnetization curves have been obtained by VSM measurements performed at two temperatures, 300 and 5 K (Figure 5). The room temperature measurement allows confirming the filling factor at 10.9 g/m^2 from the saturation magnetization. The low temperature hysteresis curve was recorded after a 3T field cooling procedure. At 5 K, the NPs appear to be in a blocked state, as revealed by the appearance of a coercive field. The hysteresis loop being symmetric, no exchange

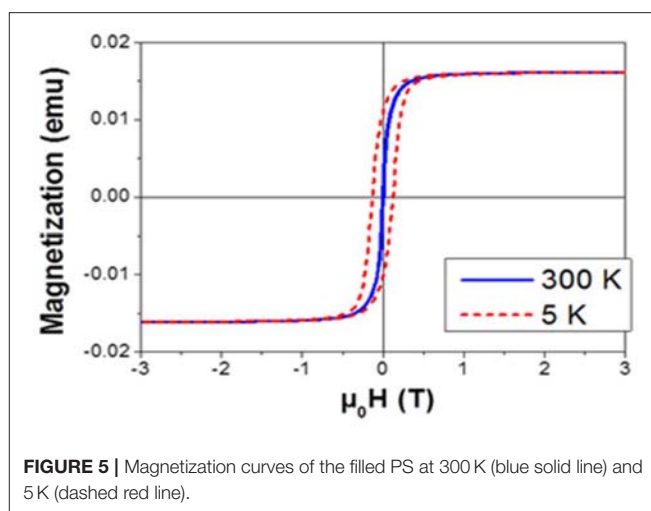


FIGURE 5 | Magnetization curves of the filled PS at 300 K (blue solid line) and 5 K (dashed red line).

bias was detected. One can therefore conclude that the FeCo NPs remained purely metallic, the impregnation technique and the adsorption into PS did not lead to the oxidation of the highly sensitive NPs.

CONCLUSION

In this paper, we report the *ex-situ* impregnation of 9 nm FeCo nanoparticles in an $18 \mu\text{m}$ -thick mesoporous silicon substrate with a pore diameter of about 30 nm. The optimization of the impregnation process parameters allowed defining the optimal conditions to get the best filling factor of the pores and the highest magnetization level. Toluene, heated up to a temperature of 100°C , was found to be the most suitable solvent. Furthermore, an impregnation duration of 24 h was assessed in order to obtain the amount of NPs in the substrate. This step can be repeated several times with fresh colloidal solutions in order to increase the density of nanoparticles embedded in the material. A maximum saturation magnetization around 39 memu (135 emu/cm^3) is obtained when the impregnation is repeated 3 times with an intermediate rinsing and drying step. We have characterized these samples by electron microscopy (SEM, TEM, and EDX) and found evidences of a high homogeneity of filling in depth. Finally, we showed that these nanoparticles do not exhibit significant oxidation after impregnation thus retaining their metallic nature and magnetic properties for future applications. The next step of this study will be to upscale these experiments on larger surfaces in order to bring this new composite material toward industrial applications.

AUTHOR CONTRIBUTIONS

JB, PP and GG designed the project and performed the overall supervisions of the experimental work. All authors discussed the results and revised the manuscript.

FUNDING

This work was performed in the frame of TOURS 2015, a project supported by the French Programme de l'économie numérique des Investissements d'Avenir.

REFERENCES

- Allia, P., Tiberto, P., Coisson, M., Chiolerio, A., Celegato, F., Vinai, F., et al. (2011). Evidence for magnetic interactions among magnetite nanoparticles dispersed in photoreticulated PEGDA-600 matrix. *J. Nanoparticle Res.* 13, 5615–5626. doi: 10.1007/s11051-011-0249-7
- Anglin, E. J., Cheng, L., Freeman, W., and Sailor, M. J. (2008). Porous silicon in drug delivery devices and materials. *Adv. Drug Deliv. Rev.* 60, 1266–1277. doi: 10.1016/j.addr.2008.03.017
- Bardet, B., Defforge, T., Negulescu, B., Valente, D., Billoué, J., Poveda, P., et al. (2017). Shape-controlled electrochemical synthesis of mesoporous Si/Fe nanocomposites with tailored ferromagnetic properties. *Mater. Chem. Front.* 1, 190–196. doi: 10.1039/C6QM00040A
- Bomati-Miguel, O., Leconte, Y., Morales, M. P., Herlin-Boime, N., and Veintemillas-Verdaguer, S. (2005). Laser pyrolysis preparation of SiO₂-coated magnetic nanoparticles for biomedical applications. *J. Magn. Magn. Mater.* 290–291 PA, 272–275. doi: 10.1016/j.jmmm.2004.11.207
- Bordet, A., Lacroix, M., Soulantica, K., and Chaudret, B. A. (2016). A new approach to the mechanism of fischer-tropsch syntheses arising from gas phase NMR and mass spectrometry. *ChemCatChem* 8, 1727–1731. doi: 10.1002/cctc.201600245
- Fukami, K., Tanaka, Y., M. L., Chourou, Sakka, T., and Ogata, Y. H. (2009). Filling of mesoporous silicon with copper by electrodeposition from an aqueous solution. *Electrochim. Acta* 54, 2197–2202. doi: 10.1016/j.electacta.2008.10.024
- Garnero, C. (2016). *Synthèse Organométallique de Nanoparticules de FeCo Pour l'intégration sur Inductance*. Thèse de l'Université de Toulouse.
- Granitzer, P., Rumpf, K., Gonzalez-Rodriguez, R., Coffey, J. L., and Reissner, M. (2015). The effect of nanocrystalline silicon host on magnetic properties of encapsulated iron oxide nanoparticles. *Nanoscale* 7, 20220–20226. doi: 10.1039/C5NR05232G
- Granitzer, P., Rumpf, K., Tian, Y., Akkaraju, G., Coffey, J., Pölt, P., et al. (2013). Fe₃O₄-nanoparticles within porous silicon: magnetic and cytotoxicity characterization. *Appl. Phys. Lett.* 102, 1–5. doi: 10.1063/1.4807421
- Granitzer, P., Rumpf, K., Venkatesan, M., Roca, A., G., Cabrera, L., et al. (2010). Magnetic study of Fe₃O₄ nanoparticles incorporated within mesoporous silicon. *J. Electrochem. Soc.* 157, K145–151. doi: 10.1149/1.3425605
- Harraz, F. A. (2013). Synthesis and surface properties of magnetite (Fe₃O₄) nanoparticles infiltrated into porous silicon template. *Appl. Surf. Sci.* 287, 203–210. doi: 10.1016/j.apsusc.2013.09.123
- Kim, D. J., Pal, M., and Seo, W. S. (2013). Confined growth of highly uniform and single bcc-phased FeCo/graphitic-shell nanocrystals in SBA-15. *Microporous Mesoporous Mater.* 180, 32–39. doi: 10.1016/j.micromeso.2013.06.006
- Kockrick, E., Krawiec, P., Schnelle, W., Geiger, D., Schappacher, F. M., Poettgen, R. S. et al. (2007). Space-confined formation of FePt nanoparticles in ordered mesoporous silica SBA-15. *Adv. Mater.* 19, 3021–3026. doi: 10.1002/adma.200601367
- Lacroix, L.-M., Lachaize, S., Falqui, A., and Chaudret, B. (2009). Iron nanoparticles growth in organic super-structures. *J. Am. Chem. Soc.* 131, 549–557. doi: 10.1021/ja805719c
- Lehmann, V., Stengl, R., and Luigart, A. (2000). On the morphology and the electrochemical formation mechanism of mesoporous silicon. *Mater. Sci. Eng. B* 69, 11–22. doi: 10.1016/S0921-5107(99)00286-X
- Li, Y., Kim, Y. J., Kim, A. Y., Lee, K., Jung, M. H., Hur, N., et al. (2011). Highly stable and magnetically recyclable mesoporous silica spheres embedded with FeCo / graphitic shell nanocrystals for supported catalysts highly stable and magnetically recyclable mesoporous silica spheres embedded with FeCo / graphitic shell nanocryst. *Chem. Mater* 23, 5398–5403. doi: 10.1021/cm202451n
- Liu, J., Qiao, S. Z., Hu, Q. H., and Lu, G. Q. (2011). Magnetic nanocomposites with mesoporous structures: synthesis and applications. *Small* 7, 425–443. doi: 10.1002/smll.201001402
- Loni, A., Canham, L. T., Defforge, T., and Gautier, G. (2015). Supercritically-dried porous silicon powders with surface areas exceeding 1000 m²/g. *ECS J. Solid State Sci. Technol.* 4, P289–P292. doi: 10.1149/2.0031508js
- Lu, A. H., Li, W. C., Kiefer, A., Schmidt, W., Bill, E., Fink, G., et al. (2004). Fabrication of magnetically separable mesostructured silica with an open pore system. *J. Am. Chem. Soc.* 126, 8616–8617. doi: 10.1021/ja0486521
- Manova, E., Tsoncheva, T., Estournes, C., Paneva, D., Tenchev, K., Mitov, I., et al. (2006). Nanosized iron and iron-cobalt spinel oxides as catalysts for methanol decomposition. *Appl. Catal. A Gen.* 300, 170–180. doi: 10.1016/j.apcata.2005.11.005
- Nakamura, T., Yamada, Y., and Yano, K. (2006). Novel synthesis of highly monodispersed γ -Fe₂O₃/SiO₂ and ϵ -Fe₂O₃/SiO₂ nanocomposite spheres. *J. Mater. Chem.* 16, 2417–2419. doi: 10.1039/B604025J
- Rumpf, K., Granitzer, P., Poelt, P., and Reissner, M. (2013). Specific loading of porous silicon with iron oxide nanoparticles to achieve different blocking temperatures. *Thin Solid Films* 543, 56–58. doi: 10.1016/j.tsf.2013.02.122
- Sun, S., Murray, C. B., Weller, D., Folks, L., and Moser, A. (2000). Monodisperse FePt nanoparticles and ferromagnetic FePt nanocrystal superlattice. *Science* 287, 1989–1992. doi: 10.1126/science.287.5460.1989
- Thomas, J. C., Pacholski, C., and Sailor, M. J. (2006). Delivery of nanogram payloads using magnetic porous silicon microcarriers. *Lab Chip* 6, 782–787. doi: 10.1039/b516121e
- Xia, B., Li, J., Shi, J., Zhang, Y., Zhang, Q., Chen, Z., et al. (2017). Biodegradable and magnetic-fluorescent porous silicon@iron oxide nanocomposites for fluorescence/magnetic resonance bimodal imaging of tumor *in vivo*. *ACS Biomater. Sci. Eng.* 3, 2579–2587. doi: 10.1021/acsbomaterials.7b00467
- Yiu, H., Keane, M. A., Lethbridge, Z. A., Lees, M. R., El Haj, A. J., and Dobson, J. (2008). Synthesis of novel magnetic iron metal-silica (Fe-SBA-15) and magnetite-silica (Fe₃O₄-SBA-15) nanocomposites with a high iron content using temperature-programed reduction. *Nanotechnology* 19:255606. doi: 10.1088/0957-4484/19/25/255606
- Zhu, Y., Kaskel, S., Ikoma, T., and Hanagata, N. (2009). Magnetic SBA-15/poly(N-isopropylacrylamide) composite: preparation, characterization and temperature-responsive drug release property. *Microporous Mesoporous Mater.* 123, 107–112. doi: 10.1016/j.micromeso.2009.03.031

SUPPLEMENTARY MATERIAL

The Supplementary Material for this article can be found online at: <https://www.frontiersin.org/articles/10.3389/fchem.2018.00609/full#supplementary-material>

Conflict of Interest Statement: The authors declare that the research was conducted in the absence of any commercial or financial relationships that could be construed as a potential conflict of interest.

Copyright © 2018 Lepesant, Bardet, Lacroix, Fau, Garnero, Chaudret, Soulantica, Defforge, Valente, Andreazza, Billoué, Poveda and Gautier. This is an open-access article distributed under the terms of the Creative Commons Attribution License (CC BY). The use, distribution or reproduction in other forums is permitted, provided the original author(s) and the copyright owner(s) are credited and that the original publication in this journal is cited, in accordance with accepted academic practice. No use, distribution or reproduction is permitted which does not comply with these terms.



Structural and Optical Properties of Silicon Nanowire Arrays Fabricated by Metal Assisted Chemical Etching With Ammonium Fluoride

Kirill A. Gonchar^{1*}, Veronika Y. Kitaeva¹, George A. Zharik¹, Andrei A. Eliseev^{2,3} and Liubov A. Osminkina^{1,4}

¹ Physics Department, Lomonosov Moscow State University, Moscow, Russia, ² Chemistry Department, Lomonosov Moscow State University, Moscow, Russia, ³ Faculty of Materials Science, Lomonosov Moscow State University, Moscow, Russia, ⁴ Institute for Biological Instrumentation of Russian Academy of Sciences, Pushchino, Russia

OPEN ACCESS

Edited by:

Thierry Djenizian,
École des Mines de Saint-Étienne,
France

Reviewed by:

Kui-Qing Peng,
Beijing Normal University, China
Jeffery L. Coffey,
Texas Christian University,
United States

*Correspondence:

Kirill A. Gonchar
k.a.gonchar@gmail.com

Specialty section:

This article was submitted to
Chemical Engineering,
a section of the journal
Frontiers in Chemistry

Received: 20 October 2018

Accepted: 14 December 2018

Published: 04 January 2019

Citation:

Gonchar KA, Kitaeva VY, Zharik GA, Eliseev AA and Osminkina LA (2019) Structural and Optical Properties of Silicon Nanowire Arrays Fabricated by Metal Assisted Chemical Etching With Ammonium Fluoride. *Front. Chem.* 6:653. doi: 10.3389/fchem.2018.00653

Here we report on the metal assisted chemical etching method of silicon nanowires (SiNWs) manufacturing, where the commonly used hydrofluoric acid (HF) has been successfully replaced with ammonium fluoride (NH₄F). The mechanism of the etching process and the effect of the pH values of H₂O₂: NH₄F solutions on the structural and optical properties of nanowires were studied in detail. By an impedance and Mott-Schottky measurements it was shown that silver-assisted chemical etching of silicon can be attributed to a facilitated charge carriers transport through Si/SiO_x/Ag interface. It was shown that the shape of nanowires changes from pyramidal to vertical with pH decreasing. Also it was established that the length of SiNW arrays non-linearly depends on the pH for the etching time of 10 min. A strong decrease of the total reflectance to 5–10% was shown for all the studied samples at the wavelength <800 nm, in comparison with crystalline silicon substrate (c-Si). At the same time, the intensities of the interband photoluminescence and the Raman scattering of SiNWs are increased strongly in compare to c-Si value, and also they were depended on both the length and the shape of SiNW: the biggest values were for the long pyramidal nanowires. That can be explained by a strong light scattering and partial light localization in SiNWs. Hereby, arrays of SiNWs, obtained by using weakly toxic ammonium fluoride, have great potential for usage in photovoltaics, photonics, and sensorics.

Keywords: silicon nanowires, impedance, total reflectance, photoluminescence, Raman scattering

INTRODUCTION

In recent decades, the possibility of using silicon nanowires (SiNWs) in sensorics (Cui et al., 2001; Wang and Ozkan, 2008; Cao et al., 2015; Georgobiani et al., 2018), photovoltaics (Kelzenberg et al., 2008; Stelzner et al., 2008; Sivakov et al., 2009), photonics (Brönstrup et al., 2010), and micro-and optoelectronics (Föll et al., 2010; Yang et al., 2010) has been shown. Nanowires are usually obtained as a result of anisotropic growth of a 1D crystal on a nanometer scale. The first SiNWs were fabricated via bottom-up approach by vapor-liquid-solid (VLS) method with different noble metals (mostly gold) as catalyst (Wagner and Ellis, 1964). Metal-assisted chemical etching (MACE) of silicon was observed for the first time in the 1990s, when a cleaning solution HF-H₂O₂-H₂O was used to remove metal impurities from the silicon substrate (c-Si) (Morinaga et al., 1995). Then this method was adapted for luminescent porous silicon formation (Gorostiza et al., 1999;

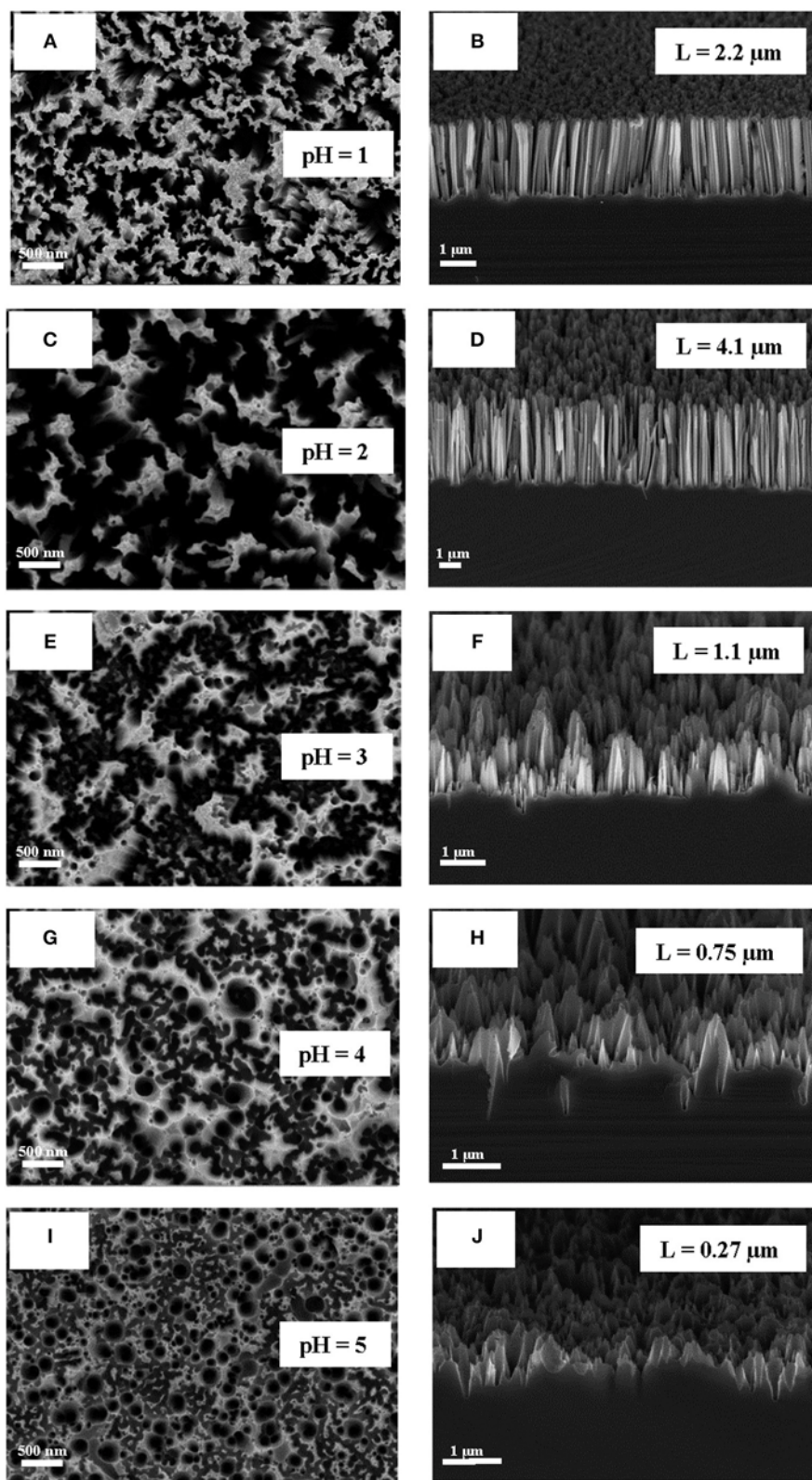


FIGURE 1 | (A,C,E,G,I) SEM micrographs of SiNWs with different pH of $\text{H}_2\text{O}_2:\text{NH}_4\text{F}$ (view from above); **(B,D,F,H,J)** SEM cross-sectional micrographs of SiNWs with different pH of $\text{H}_2\text{O}_2:\text{NH}_4\text{F}$.

Li and Bohn, 2000; Chattopadhyay et al., 2002). In 2002, Peng et al. for the first time adapted it for high aspect ratio SiNWs fabrication and systematically investigated the mechanism and further develop it into a new micro/nanofabrication method (Peng et al., 2002, 2006, 2008). Also MACE method of SiNWs fabrication was systematically investigated in Nahidi and Kolasinski (2006), Sivakov et al. (2010), Bai et al. (2012), and Dawood et al. (2012). Usually in MACE such catalysts, as nanoparticles of Au (Li and Bohn, 2000; Dawood et al., 2012), Ag (Sivakov et al., 2010), or Pt (Li and Bohn, 2000; Chattopadhyay et al., 2002) and such oxidizing agents as H_2O_2 (Li and Bohn, 2000; Sivakov et al., 2010; Dawood et al., 2012), KMnO_4 (Bai et al., 2012; Jiang et al., 2017), or $\text{Fe}(\text{NO}_3)_3$ (Nahidi and Kolasinski, 2006), are used in the process. SiNWs, which were fabricated by a standard MACE procedure, are found to possess such optical properties as extremely low total reflection (Gonchar et al., 2012), enhancement of Raman scattering and interband photoluminescence (PL) (Gonchar et al., 2014). However, HF, that is surely used in the MACE, is toxic and dangerous, and may also lead to hypocalcemia and hypomagnesemia (Bertolini, 1992). Therefore, it is very important, with a view to the future large-scale production of SiNWs, to study the possibilities of modifying the MACE method using safer and less toxic chemicals.

It is well-known that aqueous solutions of ammonium fluoride (NH_4F) can be used to dissolve SiO_2 , and the etching rate depends on the concentration of NH_4F and the pH of the solutions (Judge, 1971). Thus, NH_4F is shown can be used as an alternative to HF in the method of electrochemical etching in the manufacture of porous silicon, and the structural properties of the resulting porous silicon depend on the pH of the NH_4F solution used: at $\text{pH} = 4.5$ a pebble-like surface was formed, and at lower PH a nanoporous silicon layers were formed (Dittrich et al., 1995). Recently, the possibility of using NH_4F in the MACE process has been also shown, and optical properties of SiNW, formed using NH_4F , differed little from nanowires formed by

standard MACE technology with HF (Gonchar et al., 2016). However, the mechanism of the etching process and the influence of the pH of the etching solution on the structural and optical properties of SiNW remain open.

In this work, the etching process mechanism and the effect of pH values of $\text{H}_2\text{O}_2:\text{NH}_4\text{F}$ solutions on the structural and optical properties of SiNWs were studied using impedance measurements and Mott-Schottky analysis, as well as total reflectance, interband photoluminescence and Raman scattering intensities measurements.

METHODS

The samples of SiNWs were produced by MACE of (100)-oriented p-type c-Si wafer with resistivity of $10\text{--}20\ \Omega\cdot\text{cm}$. HF was replacement on NH_4F in all reactions. The PH value was

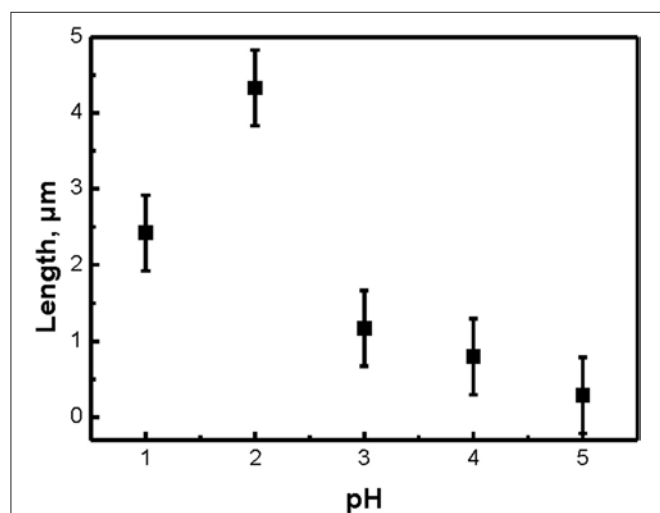


FIGURE 2 | The dependence of the length of SiNWs with different pH value of $\text{H}_2\text{O}_2:\text{NH}_4\text{F}$.

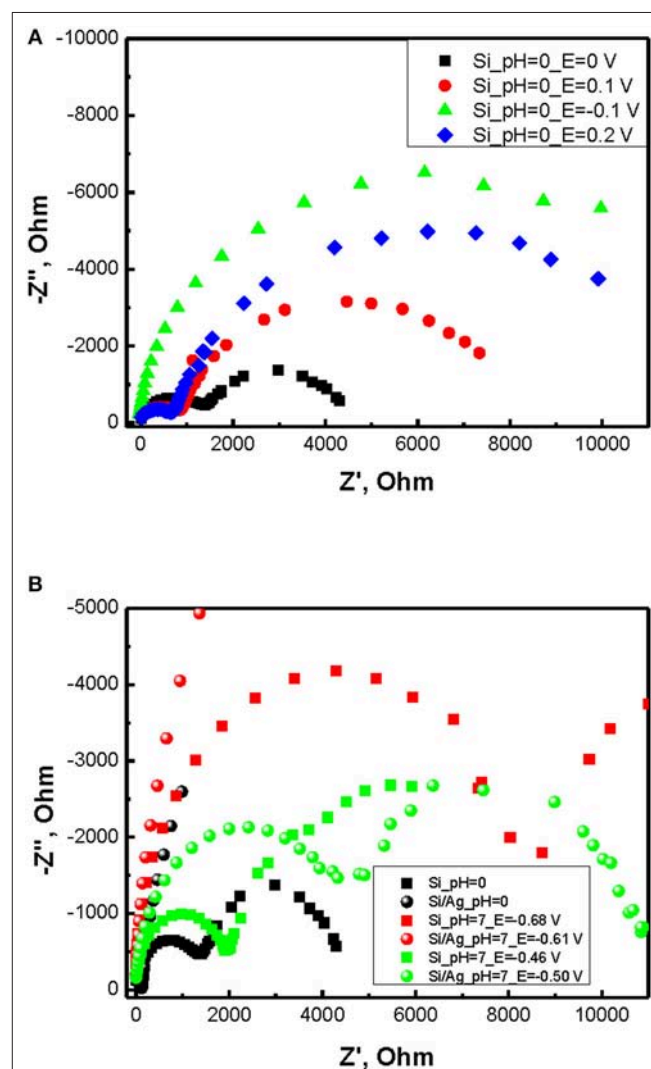
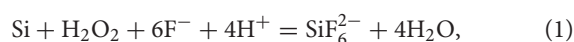


FIGURE 3 | (A) Impedance spectra of p-doped silicon in $\sim 5\text{M}$ $\text{NH}_4\text{F}/1\text{M}$ H_2SO_4 electrolyte containing 30% of H_2O_2 . **(B)** impedance spectra for different interfaces and pH.

controlled by PH indicator. Prior to the MACE procedure, c-Si wafers were rinsed in 2% HF solution for 1 min to remove a native silicon oxide. In the first stage of MACE process, c-Si wafers were placed in the aqueous solution of 0.02 M of silver nitrate (AgNO_3) and 5 M of NH_4F in the volume ratio of 1:1 for 30 s and a thin (~ 100 nm) layers of Ag nanoparticles were deposited on the surface of the wafers. In the second stage, c-Si wafers with Ag nanoparticles were placed in the etching solution containing 5 M of NH_4F and 30% H_2O_2 in the volume ratio of 10:1 for 10 min. The PH value of the NH_4F aqueous solution was changed by adding of H_2SO_4 droplets and varied in the range from 1 to 5. All the etching stages were carried out at room temperature. After the etching process all the samples were rinsed in de-ionized water and dried at room temperature. The main etching reaction the same that was described in Zhang et al. (2008):



however in our case the ions of F^- and H^+ were obtained not from the dissociation of HF as in standard MACE procedure, but from the dissociation of NH_4F and H_2SO_4 . Ag nanoparticles played the role of catalysts for the etching process. The removal of Ag nanoparticles from SiNW arrays was performed by immersing in concentrated (65%) nitric acid (HNO_3) for 15 min.

The structures of SiNWs were studied by a scanning electron microscope (SEM) of Carl Zeiss SUPRA 40 FE-SEM. Impedance spectra and Mott-Schottky measurements were performed using Solartron 1287 electrochemical interface and Solartron 1255B frequency response analyzer. All the measurements were carried out in three-electrode teflon cell using Ag/AgCl reference electrode joined through polypropylene Luggin capillary. The total reflectance (which includes both diffuse and specular components) spectra at the wavelength from 250 to 850 nm were studied with an integrating sphere on a Perkin Elmer spectrometer Lambda 950. The interband PL and Raman spectra were measured in a back scattering geometry with a Fourier-transform infrared (FTIR) spectrometer of Bruker IFS 66v/S equipped with a FRA-106 unit. Excitation was carried out by cw Nd:YAG laser at the wavelength $1.064 \mu\text{m}$ (excitation intensity was 100 mW and spot size was 2 mm). All experiments were carried out in air at room temperature.

TABLE 1 | Open circuit potential (OCP) and flat band potential for different interfaces and pH.

Sample	Open circuit potential, V	Flat band potential, V
Si_pH = 0–1	−0.17	−0.26
Si_pH = 2–3	−0.25	−0.34
Si_pH = 4–5	−0.34	−0.46
Si_pH = 6–7	−0.55	−0.75
Si/Ag_pH = 0–1	−0.14	−0.32
Si/Ag_pH = 2–3	−0.30	−0.38
Si/Ag_pH = 4–5	−0.33	−0.39
Si/Ag_pH = 6–7	−0.42	−0.50

RESULTS AND DISCUSSION

Typical SEM microphotographs of SiNW layers, which were obtained by using different pH of the etching solution $\text{H}_2\text{O}_2:\text{NH}_4\text{F}$ are presented in **Figure 1**. Note, that for pH = 6 or 7 the etching rate was very slow and the optical properties of SiNWs are slightly different from c-Si substrate. It is seen from the **Figure 1**, that the shape of SiNW is changing from vertical cylinders to pyramidal like structures with pH increasing. **Figure 2** presented the dependence of the length of SiNWs from the pH value. The length of SiNW is maximum at pH = 2 and then decreases with increasing pH. SiNW porosity was calculated by using Bruggeman model (Bruggeman, 1935) and was approximately 50–60% for all samples.

Impedance spectra of p-doped silicon in 5M $\text{NH}_4\text{F}/1\text{M}$ H_2SO_4 electrolyte containing 30% of H_2O_2 illustrate two semicircles with series resistance close to zero (**Figure 3A**). Thus, an equivalent circuit for the cell can be represented by parallel RC circuits connected in series. Applying positive bias vs. open circuit potential (OCP) leads to a first element resistivity decrease while increasing the radius of the second semicircle. Applying negative potential leads to first semicircle radius growth. As soon as Warburg resistance can be considered negligible in concentrated $\text{NH}_4\text{F}/\text{H}_2\text{SO}_4$ solution, the presence of the second semicircle can be referred to an electric double layer with non-equilibrium silicon oxide formed at the surface

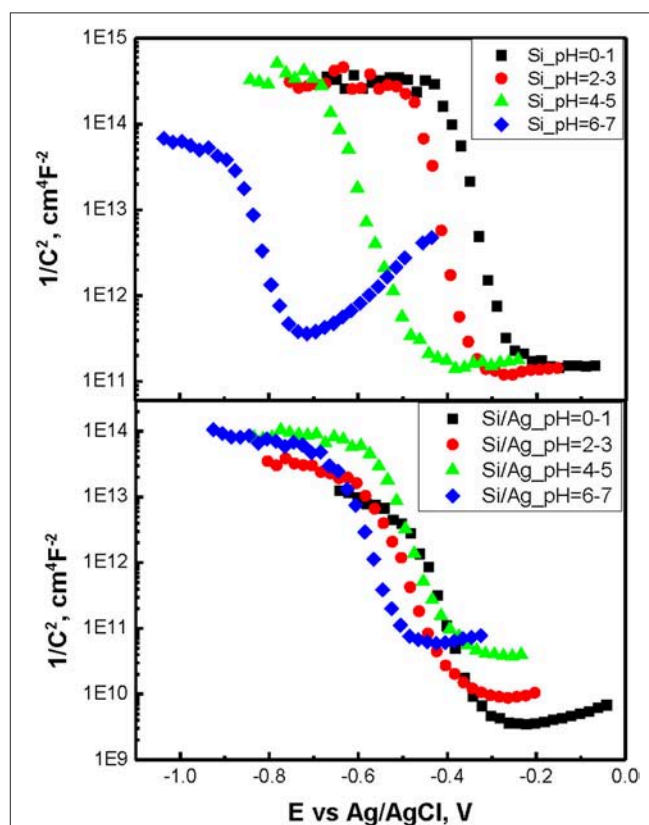


FIGURE 4 | Mott-Schottky measurements at 1,000 Hz.

of Si electrode. Resistivity of SiO_x layer predictably increases with shifting to positive potentials vs. Ag/AgCl reference due to growing layer thickness. As soon as first semicircle appear at higher frequencies (typically $>1,000$ Hz) it can only correspond to the processes at Si/SiO_x interface. This parallel RC element can be ascribed to the accumulation layer in Si resulting in downward bending of the valence and the conduction bands. Decreasing the radius of this semicircle with shifting to positive potentials is than well-explained by band flattening in p-doped silicon.

Notably both the SiO_x layer thickness and electrolyte potential are strongly affected by pH. With increasing pH of electrolyte OCP of the cell decreases reducing silicon oxidation rate (Figure 3B, Table 1). However, the radius of the second RC elements grows due to lower dissolution rate of silicon dioxide resulting in higher capacitance of the layer (Figure 3B).

Addition of silver particles to the system introduces a number of changes to the impedance spectra. First, Z'' at high frequencies strongly decreases implying lowering of the capacitance at Si/SiO_x interface. Secondly, the radius of the second semicircle greatly increases indicating larger thickness of SiO_x layer. These effects are associated with inhomogeneous nature of Ag/Si electrodes where both silver coated and uncoated regions contribute the impedance spectra. Probably Si/SiO_x/Ag/Ag₂O/H₂O₂ electrochemical chain provides smaller barrier as compared to direct electric double layer contact Si/SiO_x/H₂O₂. However, in case of low frequencies the depletion of charge carriers from Ag/Si results in limitation of carrier transport and SiO_x layer capacitance growth.

To determine flat band potentials of p-doped Si and Ag/Si electrodes Mott-Schottky measurements were performed at 1,000 Hz. The choice of the frequency was dictated by the necessity to attain depletion of the charge carriers while avoiding diffusion limitations. Resulting plots for different pH of etching solutions and derived flat band potential values are summarized

in Figure 4 and Table 1. One can see, the flat band potentials being pH dependent in case of etching of p-doped silicon converge into closely the same value in case of Ag/Si. On the other hand, OCP values stay very close in both p-Si and Ag/Si, with only small shift of OCP in case of Ag/Si. This effect corresponds well to smaller band bending and smaller capacitance of the interface layers. Thus, silver assisted chemical etching of silicon can be ascribed to facilitated transport through Si/SiO_x/Ag interface.

Total reflectance spectra of SiNW layers are presented in Figure 5. All samples exhibit a strong decrease of the total reflectance to 5–10% at the wavelength <850 nm in comparison to c-Si substrate (50%). At pH >3 , the total reflection spectra of nanowires have a very similar form with c-Si, since for a weak submicron length SiNW, the c-Si substrate has a significant effect on the reflection value. Also in this case, reflection peaks appear at 280 and 370 nm, which are associated with the c-Si direct band gap. Low total reflection of SiNW layers can be explained by the

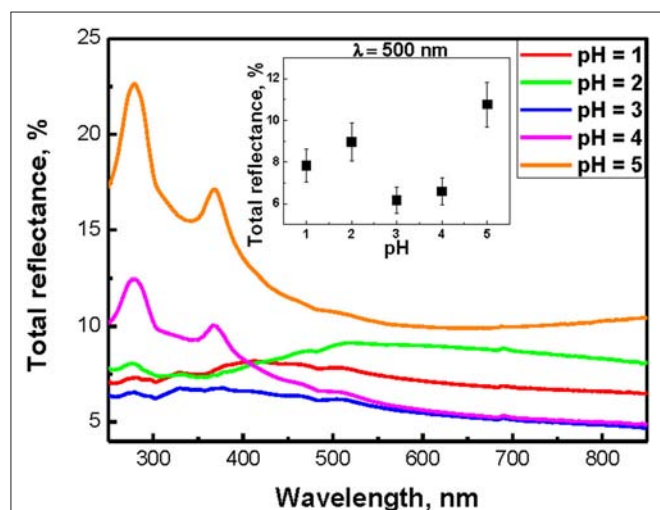


FIGURE 5 | Total reflectance spectra of SiNWs with different pH of $\text{H}_2\text{O}_2:\text{NH}_4\text{F}$; inset shows the dependence of total reflection of SiNWs from the pH value of $\text{H}_2\text{O}_2:\text{NH}_4\text{F}$.

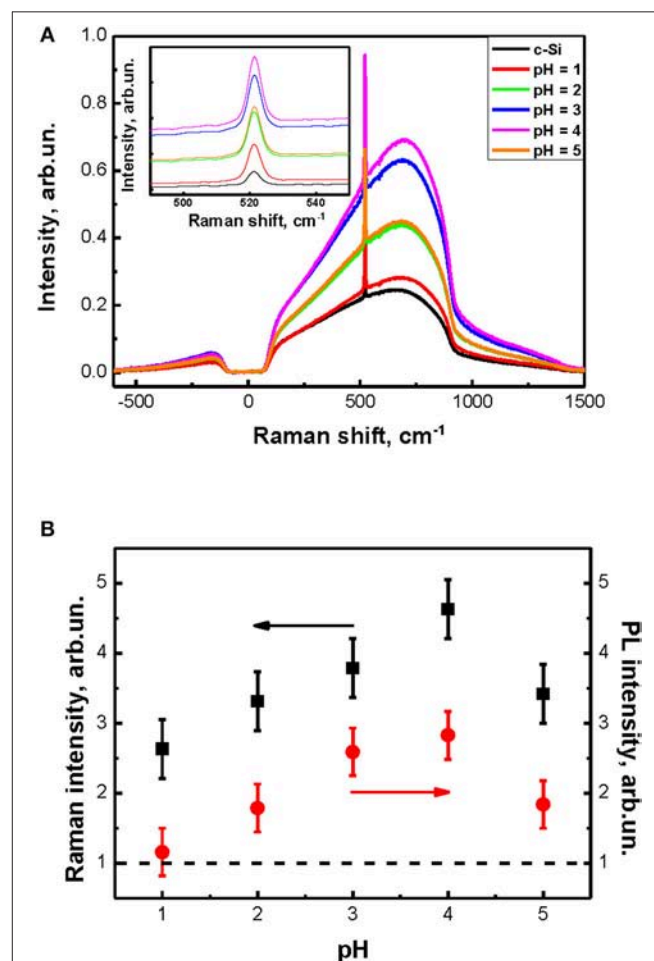


FIGURE 6 | (A) Spectra of interband PL and Raman scattering of c-Si substrate and SiNWs with different pH of $\text{H}_2\text{O}_2:\text{NH}_4\text{F}$; inset shows Raman scattering peaks of c-Si substrate and SiNWs with different pH of $\text{H}_2\text{O}_2:\text{NH}_4\text{F}$. **(B)** The dependence of intensities of Raman scattering and interband PL of SiNWs from the pH value of $\text{H}_2\text{O}_2:\text{NH}_4\text{F}$.

strong scattering and absorption of light in the visible region of the spectrum, which can lead to a partial localization of light in nanowires (Gonchar et al., 2012). The inset in **Figure 5** shows the dependence of the total reflection of SiNWs at 500 nm from the pH value of $\text{H}_2\text{O}_2\text{:NH}_4\text{F}$. It is seen that for this wavelength, all samples have the same low values of the total reflectance (5–10%).

The spectra of interband PL (broad peak) and Raman scattering (sharp peak at 520 cm^{-1}) of the c-Si substrate and a number of SiNW grown at different pH values are shown in **Figure 6A**. The inset in **Figure 6A** shows a close view of the Raman scattering peaks. SiNW's diameter is about 50–200 nm and far from the quantum confinement regime. That's why peaks and shapes of the interband PL and Raman scattering for all samples are similar to c-Si. At the same time the intensities of interband PL and Raman scattering for SiNWs increase strongly as opposed to corresponding value for c-Si. This effect can be explained by the light localization in such inhomogeneous optical medium as SiNW layers (Gonchar et al., 2014).

Figure 6B shows the calculated from **Figure 6A** dependence of SiNW's Raman scattering and interband PL intensities from the pH value. The signal intensity of the samples here was normalized to the signal intensity of c-Si substrate (dash line). Thus, the intensity of Raman scattering and interband PL increases by 3–5 times and 3 times, respectively, for all SiNWs layers in comparison with c-Si. Let's remember, that the shape and length of SiNWs is changed with the increasing of pH value of $\text{H}_2\text{O}_2\text{:NH}_4\text{F}$: the length is decrease and the shape is changing from vertical cylinders to pyramidal like structures (see **Figure 1**). Based on this, we can conclude that the intensity of Raman scattering and interband PL depends not only on the length of SiNW, but also on their shape.

CONCLUSION

The structural and optical properties of SiNWs, prepared by the metal assisted chemical etching method, where the commonly used hydrofluoric acid (HF) has been successfully replaced with ammonium fluoride (NH_4F), and their dependence from the pH of the etching $\text{H}_2\text{O}_2\text{:NH}_4\text{F}$ solutions were studied in detail for

the first time. It is shown that as the pH of $\text{H}_2\text{O}_2\text{:NH}_4\text{F}$ decrease, the shape of the nanowires changes from pyramidal to vertical. The length of SiNW arrays demonstrated non-linearly pH dependence. By impedance and Mott-Schottky measurements it was shown that the SiO_x layer thickness and electrolyte potential are strongly affected by pH. With increasing pH of electrolyte OCP of the cell decreases reducing silicon oxidation rate. Silver assisted chemical etching of silicon can be ascribed to facilitated charge carriers transport through Si/ SiO_x /Ag interface. All samples exhibit a strong decrease of the total reflectance to 5–10% at the wavelength $<800\text{ nm}$ in comparison to c-Si substrate. Also the intensities of interband PL and Raman scattering for SiNWs increase strongly as opposed to corresponding value for c-Si, but depends both from the length and the shape of SiNWs: they were larger for long pyramidal nanowires. This effect can be explained by the light localization in such inhomogeneous optical medium as SiNW layers. Thus, SiNW, manufactured using weakly toxic NH_4F , have great potential for applications in the field of photovoltaics, photonics, and sensorics.

AUTHOR CONTRIBUTIONS

KG and VK performed SiNWs fabrication, optical measurements, and data analysis. GZ performed the SEM measurements. AE performed impedance and Mott-Schottky measurements. KG and LO performed the general data analysis and discussion of the obtained data. All authors read and approved the final manuscript.

FUNDING

This work was supported by the Russian Science Foundation (Grant No. 17-12-01386).

ACKNOWLEDGMENTS

The equipment of the Educational and Methodical Center of Lithography and Microscopy, M. V. Lomonosov Moscow State University Research Facilities Sharing Center was used.

REFERENCES

- Bai, F., Li, M., Huang, R., Song, D., Jiang, B., and Li, Y. (2012). Template-free fabrication of silicon micropillar/nanowire composite structure by one-step etching. *Nanosci. Res. Lett.* 7:557. doi: 10.1186/1556-276x-7-557
- Bertolini, J. C. (1992). Hydrofluoric acid: a review of toxicity. *J. Emergency Med.* 10, 163–168. doi: 10.1016/0736-4679(92)90211-B
- Brönstrup, G., Jahr, N., Leiterer, C., Csáki, A., Fritzsche, W., and Christiansen, S. (2010). Optical properties of individual silicon nanowires for photonic devices. *ACS Nano* 4, 7113–7122. doi: 10.1021/nn101076t
- Bruggeman, D. A. G. (1935). Berechnung verschiedener physikalischer konstanten von heterogenen substanzen. *Ann. Phys.* 24, 636–679. doi: 10.1002/andp.19354160705
- Cao, A., Sudhölter, E. J., and de Smet, L. C. (2015). Silicon nanowire-based devices for gas-phase sensing. *Sensors* 14, 245–271. doi: 10.3390/s140100245
- Chattopadhyay, S., Li, X., and Bohn, P. W. (2002). In-plane control of morphology and tunable photoluminescence in porous silicon produced by metal-assisted electroless chemical etching. *J. Appl. Phys.* 91, 6134–6140. doi: 10.1063/1.1465123
- Cui, Y., Wei, Q., Park, H., and Lieber, C. M. (2001). Nanowire nanosensors for highly sensitive and selective detection of biological and chemical species. *Science* 293, 1289–1292. doi: 10.1126/science.1062711
- Dawood, M. K., Tripathy, S., Dolmanan, S. B., Ng, T. H., Tan, H., and Lam, J. (2012). Influence of catalytic gold and silver metal nanoparticles on structural, optical, and vibrational properties of silicon nanowires synthesized by metal-assisted chemical etching. *J. Appl. Phys.* 112:073509. doi: 10.1063/1.4757009
- Dittrich, T., Rauscher, S., Timoshenko, V. Y., Rappich, J., Sieber, I., Flietner, H., et al. (1995). Ultrathin luminescent nanoporous silicon on n-Si: pH dependent preparation in aqueous NH_4F solutions. *Appl. Phys. Lett.* 67, 1134–1136. doi: 10.1063/1.114985
- Föll, H., Hartz, H., Ossei-Wusu, E., Carstensen, J., and Riemenschneider, O. (2010). Si nanowire arrays as anodes in Li ion batteries. *Phys. Status Solidi RRL* 4, 4–6. doi: 10.1002/pssr.200903344

- Georgobiani, V. A., Gonchar, K. A., Zvereva, E. A., and Osminkina, L. A. (2018). Porous silicon nanowire arrays for reversible optical gas sensing. *Phys. Stat. Sol. A* 215:1700565. doi: 10.1002/pssa.201700565
- Gonchar, K. A., Osminkina, L. A., Galkin, R. A., Gongalsky, M. B., Marshov, V. S., Timoshenko, V. Y., et al. (2012). Growth, structure and optical properties of silicon nanowires formed by metal-assisted chemical etching. *J. Nanoelectr. Optoelectr.* 7, 602–606. doi: 10.1166/jno.2012.1401
- Gonchar, K. A., Osminkina, L. A., Sivakov, V., Lysenko, V., and Timoshenko, V. Y. (2014). Optical properties of nanowire structures produced by the metal-assisted chemical etching of lightly doped silicon crystal wafers. *Semiconductors* 48, 1613–1618. doi: 10.1134/S1063782614120082
- Gonchar, K. A., Zubairova, A. A., Schleusener, A., Osminkina, L. A., and Sivakov, V. (2016). Optical properties of silicon nanowires fabricated by environment-friendly chemistry. *Nanosci. Res. Lett.* 11:357. doi: 10.1186/s11671-016-1568-5
- Gorostiza, P., Diaz, R., Kulandainathan, M. A., Sanz, F., and Morante, J. R. (1999). Simultaneous platinum deposition and formation of a photoluminescent porous silicon layer. *J. Electroanal. Chem.* 469, 48–52. doi: 10.1016/S0022-0728(99)00189-8
- Jiang, Y., Shen, H., Zheng, C., Pu, T., Wu, J., Rui, C., et al. (2017). Nanostructured multi-crystalline silicon solar cell with isotropic etching by HF/KMnO₄. *Phys. Status Solidi A* 214:1600703. doi: 10.1002/pssa.201600703
- Judge, J. S. (1971). A study of the dissolution of SiO₂ in acidic fluoride solutions. *J. Electrochem. Soc.* 118, 1772–1775. doi: 10.1149/1.2407835
- Kelzenberg, M. D., Turner-Evans, D. B., Kayes, B. M., Filler, M. A., Putnam, M. C., Lewis, N. S., et al. (2008). Photovoltaic measurements in single-nanowire silicon solar cells. *Nano Lett.* 8, 710–714. doi: 10.1021/nl072622p
- Li, X., and Bohn, P. W. (2000). Metal-assisted chemical etching in HF/H₂O₂ produces porous silicon. *Appl. Phys. Lett.* 77, 2572–2574. doi: 10.1063/1.1319191
- Morinaga, H., Futatsuki, T., Ohmi, T., Fuchita, E., Oda, M., and Hayashi, C. (1995). Behavior of ultrafine metallic particles on silicon wafer. *Surface J. Electrochem. Soc.* 142, 966–970. doi: 10.1149/1.2048569
- Nahidi, M., and Kolasinski, K. W. (2006). Effects of stain etchant composition on the photoluminescence and morphology of porous silicon. *J. Electrochem. Soc.* 153, C19–C26. doi: 10.1149/1.2129558
- Peng, K. Q., Hu, J. J., Yan, Y. J., Wu, Y., Fang, H., Xu, Y., et al. (2006). Fabrication of single-crystalline silicon nanowires by scratching a silicon surface with catalytic metal particles. *Adv. Funct. Mater.* 16, 387–394. doi: 10.1002/adfm.200500392
- Peng, K. Q., Lu, A. J., Zhang, R. Q., and Lee, S. T. (2008). Motility of metal nanoparticles in silicon and induced anisotropic silicon etching. *Adv. Funct. Mater.* 18, 3026–3035. doi: 10.1002/adfm.200800371
- Peng, K. Q., Yan, Y. J., Gao, S. P., and Zhu, J. (2002). Synthesis of large-area silicon nanowire arrays via self-assembling nanoelectrochemistry. *Adv. Mater.* 14, 1164–1167. doi: 10.1002/1521-4095(20020816)14:16<1164::AID-ADMA1164>3.0.CO;2-E
- Sivakov, V., Andrä, G., Gawlik, A., Berger, A., Plentz, J., Falk, F., et al. (2009). Silicon nanowire-based solar cells on glass: synthesis, optical properties, and cell parameters. *Nano Lett.* 9, 1549–1554. doi: 10.1021/nl803641f
- Sivakov, V. A., Bronstrup, G., Pecz, B., Berger, A., Radnoczi, G. Z., Krause, M., et al. (2010). Realization of vertical and zigzag single crystalline silicon nanowire architectures. *J. Phys. Chem. C* 114, 3798–3803. doi: 10.1021/jp909946x
- Stelzner, T., Pietsch, M., Andrä, G., Falk, F., Ose, E., and Christiansen, S. H. (2008). *Nanotechnology* 19:295203. doi: 10.1088/0957-4484/19/29/295203
- Wagner, R. S., and Ellis, W. C. (1964). Vapor-liquid-solid mechanism of single crystal growth. *Appl. Phys. Lett.* 4, 89–90. doi: 10.1063/1.1753975
- Wang, X., and Ozkan, C. S. (2008). Multisegment nanowire sensors for the detection of DNA molecules. *Nano Lett.* 8, 398–404. doi: 10.1021/nl071180e
- Yang, P., Yan, R., and Fardy, M. (2010). Semiconductor nanowire: what's next? *Nano Lett.* 10, 1529–1536. doi: 10.1021/nl100665r
- Zhang, M. L., Peng, K. Q., Fan, X., Jie, J. S., Zhang, R. Q., Lee, S. T., et al. (2008). Preparation of large-area uniform silicon nanowires arrays through metal-assisted chemical etching. *J. Phys. Chem. C* 112, 4444–4450. doi: 10.1021/jp077053o

Conflict of Interest Statement: The authors declare that the research was conducted in the absence of any commercial or financial relationships that could be construed as a potential conflict of interest.

Copyright © 2019 Gonchar, Kitaeva, Zharik, Eliseev and Osminkina. This is an open-access article distributed under the terms of the Creative Commons Attribution License (CC BY). The use, distribution or reproduction in other forums is permitted, provided the original author(s) and the copyright owner(s) are credited and that the original publication in this journal is cited, in accordance with accepted academic practice. No use, distribution or reproduction is permitted which does not comply with these terms.



Crystallographically Determined Etching and Its Relevance to the Metal-Assisted Catalytic Etching (MACE) of Silicon Powders

Kurt W. Kolasinski^{1*}, Bret A. Unger¹, Alexis T. Ernst² and Mark Aindow²

¹ Department of Chemistry, West Chester University, West Chester, PA, United States, ² Department of Materials Science and Engineering, Institute of Materials Science, University of Connecticut, Storrs, CT, United States

OPEN ACCESS

Edited by:

Thierry Djenizian,
École des Mines de Saint-Étienne -
Campus Georges Charpak Provence,
France

Reviewed by:

Stefan Schweizer,
Martin Luther University of
Halle-Wittenberg, Germany
Michael J. Sailor,
University of California, San Diego,
United States

*Correspondence:

Kurt W. Kolasinski
kkolasinski@wcupa.edu

Specialty section:

This article was submitted to
Chemical Engineering,
a section of the journal
Frontiers in Chemistry

Received: 18 June 2018

Accepted: 13 December 2018

Published: 07 January 2019

Citation:

Kolasinski KW, Unger BA, Ernst AT
and Aindow M (2019)
Crystallographically Determined
Etching and Its Relevance to the
Metal-Assisted Catalytic Etching
(MACE) of Silicon Powders.
Front. Chem. 6:651.
doi: 10.3389/fchem.2018.00651

Metal-assisted catalytic etching (MACE) using Ag nanoparticles as catalysts and H₂O₂ as oxidant has been performed on single-crystal Si wafers, single-crystal electronics grade Si powders, and polycrystalline metallurgical grade Si powders. The temperature dependence of the etch kinetics has been measured over the range 5–37°C. Etching is found to proceed preferentially in a ⟨001⟩ direction with an activation energy of ~0.4 eV on substrates with (001), (110), and (111) orientations. A quantitative model to explain the preference for etching in the ⟨001⟩ direction is developed and found to be consistent with the measured activation energies. Etching of metallurgical grade powders produces particles, the surfaces of which are covered primarily with porous silicon (por-Si) in the form of interconnected ridges. Silicon nanowires (SiNW) and bundles of SiNW can be harvested from these porous particles by ultrasonic agitation. Analysis of the forces acting between the metal nanoparticle catalyst and the Si particle demonstrates that strongly attractive electrostatic and van der Waals interactions ensure that the metal nanoparticles remain in intimate contact with the Si particles throughout the etch process. These attractive forces draw the catalyst toward the interior of the particle and explain why the powder particles are etched equivalently on all the exposed faces.

Keywords: porous silicon, silicon nanowires, metallurgical grade silicon, etching, metal assisted catalytic etching, MACE, porous powder

INTRODUCTION

Silicon is poised to extend its range of application from primarily electronics and photovoltaics into drug delivery and energy storage. Nanostructured silicon has attracted significant interest for targeted delivery of multiple compounds in a theranostic setting (Salonen et al., 2008; Santos et al., 2011; Santos and Hirvonen, 2012). Porous silicon (por-Si) particles have been studied intensively for sustained release of drugs and used successfully to carry a wide variety of payloads from small-molecule drugs to therapeutic biomolecules, such as peptides, siRNA and DNA (Kaukonen et al., 2007; Anglin et al., 2008; Kilpeläinen et al., 2009; Ashley et al., 2011) as well as genes (Wareing et al., 2017). Nanostructured Si plays an increasingly important role in energy conversion and storage devices (Aricò et al., 2005; Kamat, 2007; Hochbaum and Yang, 2010; Micheli et al., 2013; Han et al., 2014; Mai et al., 2014).

Silicon nanowires (SiNW), and methods to produce them in industrial scale bulk quantities, are of particular interest in the realm of rechargeable lithium ion batteries (LIB). LIB have for all

practical purposes reached the theoretical capacity of 372 mA h g^{-1} with respect to their graphitic anodes (Lee et al., 2016). Silicon has the greatest specific capacity ($3,579 \text{ mA h g}^{-1}$) among elements that alloy with lithium; thus, it is particularly attractive for advanced battery designs (Kasavajjula et al., 2007; Bruce et al., 2008; Mai et al., 2014; Lee et al., 2016) and its introduction into commercial batteries has begun (Blomgren, 2017). However, the nearly 400% volume expansion of Si upon full lithiation destroys bulk Si anodes. Nanostructuring of Si anodes can alleviate pulverization, which increases dramatically the reversibility of lithiation/delithiation cycles (Aricò et al., 2005; Shin et al., 2005; Kang et al., 2008; Kim et al., 2008; Leisner et al., 2010; Han et al., 2014). Silicon pillars (as SiNW are sometimes referred to in this field) are of particular interest for LIBs (Chan et al., 2008; Armstrong et al., 2014) because crystalline pillars with a cross section below 150 nm (Liu et al., 2012) and amorphous pillars with a cross section below 870 nm (McSweeney et al., 2015) retain their structural integrity upon cycling. The cycling behavior of SiNW is improved by porosification (McSweeney et al., 2015).

The crystallinity, and whether preferential crystallographic orientation of SiNW can be controlled, is not merely of academic interest, but is also potentially important for applications. Swelling of Si upon lithiation is strongly dependent on crystallographic orientation (Lee et al., 2011), expanding preferentially in the $\langle 110 \rangle$ directions (Liu et al., 2012). Thus, SiNW with sidewalls terminated by $\{110\}$ planes will be particularly well-suited to lithiation/delithiation cycling with favorable kinetics and limited pulverization. SiNW with selected orientation along their long axis may be of interest for electronic devices since a significant enhancement of hole and electron mobilities was observed in $\langle 110 \rangle$ -oriented SiNW compared to $\langle 001 \rangle$ -oriented SiNWs with comparable diameters (Huang et al., 2009).

Metal-assisted catalytic etching (MACE) is a widely-used (Li, 2012; Han et al., 2014) method to produce either porous Si or SiNW. MACE takes advantage of the inherently faster kinetics of electron transfer at electrolyte/metal interfaces compared to semiconductor interfaces to catalyze etching of a semiconductor in the vicinity of a metal nanoparticle or patterned metal film deposited on the semiconductor surface (Li, 2012). Both local and remote etching can take place depending on reaction conditions (Chartier et al., 2008; Chiappini et al., 2010). Many aspects of the mechanism of catalysis remain unresolved because of uncertainties in the electronic structure of the metal/semiconductor interface and its role in electron transfer (Kolasinski, 2014, 2016). The vertical direction and its relationship to crystallographic axes are defined readily during the etching of flat single-crystal wafers. However, when etching powders, there is no obvious vertical direction because the particles not only exhibit roughness and irregularity of shape, but also they may be polycrystalline. A question that arises naturally is whether this difference will cause any differences in the structures that are etched in powders relative to wafers.

Pore formation by anodic etching is known to exhibit some degree of crystallographic preference. As demonstrated by Föll et al. (2002) a variety of pore geometries are accessible.

Key parameters for determining the pore morphology are the electrolyte type, e.g., whether it is aqueous vs. organic or possibly oxidizing, the HF concentration, doping level and type, and in some cases the illumination state (front side vs. back side). With macropores on n-type Si formed in an aqueous electrolyte with backside illumination, pores grow exclusively in $\langle 001 \rangle$ directions and (occasionally, if all available $\langle 001 \rangle$ directions are inclined steeply) in $\langle 113 \rangle$ directions. Their morphology is always describable as a main pore in one of these two directions and side pores or branches in some of the others. Mesopores with diameters $10 \text{ nm} \leq d \leq 50 \text{ nm}$ grow in $\langle 001 \rangle$ directions and branch at right angles to these into other $\langle 001 \rangle$ directions. However, at high current densities the geometrical shape of the pore walls is lost while the direction of the pore axis is still along a $\langle 001 \rangle$ direction.

The crystallographic orientations of etch track pores and SiNW produced by MACE were originally thought to be determined solely by the substrate crystallography (Peng et al., 2005). However, the dependence is more complex (Peng et al., 2008), and reports of the crystallographic dependence of MACE are often contradictory, perhaps because analysis by cross-sectional scanning electron microscopy (SEM) is difficult to interpret unambiguously with regard to directionality unless cross sectional cleavages are made in more than one known direction. Whereas etching on Si(001) wafers, even on wafers with significant miscut angles (Ma et al., 2013), is reported to proceed along $\langle 001 \rangle$ directions (Peng et al., 2007) even when the temperature is varied from 0–50°C (Cheng et al., 2008), the results on wafers of other orientations are much more varied.

It was initially reported (Huang et al., 2009) that $[110]$ -oriented SiNW could not be obtained by electroless deposition of Ag on a Si(110) wafer, and that only a Ag film with a lithographically defined mesh of openings could be used to form $[110]$ -oriented SiNW. This was later reported not to be the case (Huang et al., 2010). Nonetheless, a metal film with holes always preferentially catalyzes etching along the vertical direction of a wafer (more accurately normal to the wafer surface) even on Si(113) (Peng et al., 2007) and polycrystalline wafers (Toor et al., 2016b).

The concentration of the oxidant was shown by Huang et al. (2010) to be an important factor affecting the etching direction on non- $\langle 001 \rangle$ oriented substrates, e.g., both (111) and (110). On (110) substrates at *low oxidant concentrations*, etching along an inclined $\langle 001 \rangle$ direction was found. However, the preferred etching direction is along the normal $[110]$ direction for *high oxidant concentration*. In metal-assisted anodic etching, the current density can be controlled to affect the same change in preferred etch direction, which facilitates the formation of zigzag orientation-modulated pores. Similar results were found for (111) substrates, which etch along the normal $[111]$ direction at *high concentration* but along the $\langle 001 \rangle$ directions for *low concentration* regardless of whether the etchant is H_2O_2 or $\text{Fe}(\text{NO}_3)_3$.

The opposite behavior has been reported for Ag-catalyzed etching of Si(111) in $\text{H}_2\text{O}_2 + \text{HF}$. Pei et al. (2017) found that $[111]$ -oriented nanowires are observed for 20 mM H_2O_2 but $[001]$ -oriented SiNWs are formed at 400 mM

H₂O₂. Ghosh and Giri (2016) similarly reported that the etch direction changed from the vertical $\langle 111 \rangle$ direction to slanted and eventually to wavy as H₂O₂ concentration is increased.

Temperature is also reported to be an important factor, increasing the rate of etching with an activation energy estimated to be 0.36 eV (Cheng et al., 2008) as well as affecting the direction of etching on non-(001) wafers. On Si(111) Pei et al. (2017) reported that $[111]$ -directed etching is favored by low T and $[001]$ -directed etching by high T . The higher the concentration of H₂O₂, the lower the transition temperature from $[111]$ to $[001]$. On the other hand, Bai et al. (2013) reported that for etching of Si(111) with AgNO₃ + HF solution, the etch direction could be switched from $\langle 112 \rangle$ at 10°C to $\langle 113 \rangle$ at 20°C to $\langle 111 \rangle$ above 30°C.

Below we investigate the etch direction on three types of substrates: flat single crystal wafers, single-crystal wafers textured with crystallographically-defined macropores, and silicon powder (both polycrystalline metallurgical grade and single-crystal wafer reclaim). Crystallographically-defined macropores are produced by methods that have been described previously (Mills and Kolasinski, 2005; Dudley and Kolasinski, 2008). These samples allow us to prepare bulk single-crystals that present simultaneously several well-defined surfaces with different orientations. Here we report on the crystallographic dependence of MACE and develop a model that addresses quantitatively aspects of this dependence. With the aid of this model, and analysis of the forces acting between the metal nanoparticle and the silicon substrate, we explain why the etching of powders can lead to similar etch-track-pore structures as those found on wafers.

EXPERIMENTAL

Laser Ablation and Macropore Formation

Si wafers (University Wafers: Si(001) prime grade, 0–100 Ω cm, B doped, p type; Si(110) prime grade 1–10 Ω cm, B doped, p type; Si(111) mechanical grade, unspecified doping) with 500 μ m thickness were ablated using a Spectra-Physics Quanta Ray INDI-HG-205 Nd:YAG laser producing radiation with 355 nm or 532 nm wavelengths, 6 ns pulsewidths, and 115–175 mJ pulse energies. Adjacent stripes (1.25–2.5 mm spacing) were irradiated along the Si wafers by translating the ablation stage with 0.04–0.16 mm s^{−1} scan rate. The beam was focused softly by placing the sample \sim 30–35 cm in front of the focal point of a $f = 50$ cm lens. The pressure of 5% SF₆ in N₂ (Praxair) was maintained in the range of 1–10 kPa in the ablation chamber. Pure N₂ or Ar can also be used, though these tend to make blunter pillars and less well-defined macropores. Prior to ablation, Si wafers were cleaned by sonication for 5 min in acetone and 5 min in ethanol. After ablation, wafers were etched chemically to form crystallographically-defined macropores by immersion for 100–140 s in 40% KOH(aq) solution held at 80°C (VWR ACS reagent grade). After chemical etching, samples are rinsed in 0.2 M HCl (Fisher ACS certified), deionized (DI) H₂O, and ethanol (Pharmco-Aaper anhydrous ACS/USP grade), then dried with a stream of Ar.

Metal Assisted Catalytic Etching of Wafers

MACE was performed with Ag nanoparticles deposited at a low enough density that they should be able to etch as individual particles, rather than as a continuous film. Wafers were placed in 4 mL HF (Acros Organics 49% ACS reagent) in separate containers. To the wafers was added a separate solution of 3 drops 50.4 mM AgNO₃ (Fisher ACS reagent), 2 mL concentrated acetic acid (Fisher ACS reagent), and 2 mL deionized (DI) H₂O. After 10 min, the wafers were transferred to a mixture of 5 mL concentrated HF, 2 mL acetic acid, and 3 mL DI H₂O. To this container was added a solution of 0.2 mL 35% H₂O₂ (Acros Organics 35% ACS reagent), 2.5 mL conc. HF, and 2.5 mL DI H₂O. The wafers were etched for 4 min, rinsed in DI H₂O and ethanol, and dried with Ar. The etchant is 0.15 M H₂O₂.

Metal Assisted Catalytic Etching of Powders

Etching of powders is performed using either polycrystalline metallurgical-grade particles from Elkem Silicon Materials or unpolished single crystal reclaimed wafer chunks from Dow Chemical. H₂O₂, HNO₃, FeCl₃•6H₂O, Fe(NO₃)₃, and V₂O₅ have all been used as the oxidant but all kinetics data were obtained using H₂O₂. Addition of oxidant can either be made all at the beginning of the etch cycle or at a steady rate with a syringe pump. Just as in regenerative electroless etching (ReEtching) (Kolasinski et al., 2017), addition of oxidant with a syringe pump leads to a more controlled etching process with improved thermal management, a steadier rate of etching, improved yield, and most importantly independent control of the rate and extent of etching (Kolasinski et al., 2018). To \sim 0.1 g Si is added 17.5 mL concentrated HF, 10 mL DI H₂O, 2.5 mL acetic acid, and 20 mL 0.06 M AgNO₃. After 10 min the contents are decanted and 17.5 mL concentrated HF, 18 mL DI H₂O, and 12.5 mL Fe(NO₃)₃ are added to the Si. After 1–2 min of etching, 2 mL 0.06 M AgNO₃ is added. The Si etches for 15 min with stirring, and the contents are decanted. A 1:1 mixture of HNO₃ (Fisher ACS reagent) and H₂O is used to dissolve Ag. The Si is rinsed with DI water and pentane (Alfa Aesar environmental grade 98+%), then dried in an evacuated desiccator.

A different etch procedure, performed at 0°C with slow addition of metal catalyst and oxidant, produces por-Si/SiNWs of different quality. This method allows for control of porous film morphology by varying the concentration of oxidant injected. To 0.1 g Si is added 17.5 mL conc. HF, 10 mL DI H₂O, 2.5 mL acetic acid, and 20 mL 0.06 M AgNO₃. The AgNO₃ is added over the course of 8 min, but nucleation occurs for an additional 6 min before the contents are decanted. To the Si is added 30 mL DI H₂O and 17.5 mL concentrated HF. About 0.65 mL 6% H₂O₂ is injected into the solution over 16 min, and an additional 2 mL 0.06 M AgNO₃ is added slowly to the container after about 5 min etching time. The contents are decanted, and the Si is rinsed with a 1:1 mixture of HNO₃ and H₂O as well as 0.2 M HCl, DI water and pentane. The Si is dried in an evacuated desiccator.

Electron Microscopy Sample Preparation

Microstructural data were collected using a combination of advanced electron microscopy techniques. Secondary electron

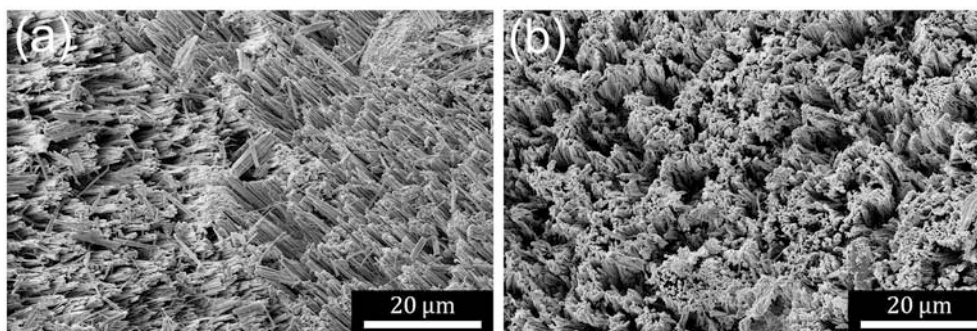


FIGURE 1 | (a) SE SEM micrograph showing a typical metallurgical grade powder particle after MACE. Etch track pores form structures in domains with different axial directions. Particles are porosified to expose several different morphologies. (b) SE SEM micrograph showing a typical single-crystal electronics grade powder particle after MACE. Domain sizes are much greater and the angle of the etching axis deviates less from the local normal than observed for metallurgical grade Si.

(SE) SEM images were acquired from MAC-etched shards of metallurgical and single-crystal electronics grade Si using an FEI Verios 460L SEM operating at an accelerating voltage of 2 kV. MAC-etched Si wafers were examined in an FEI Teneo LVSEM using an accelerating voltage of 5 kV. SE SEM images were acquired from cleaved samples to reveal the macropore geometry in cross-section. Cross-sectional TEM samples were produced from the MAC-etched silicon wafers using focused ion beam (FIB) techniques in an FEI Helios NanoLab 460F1 dual-beam FIB-SEM. TEM lamellae were prepared from the macropore by depositing a Pt layer *in-situ* to protect the near-surface region during Ga^+ ion milling. Parallel trenches were then milled on either side of the Pt strap to define a pre-thinned lamella. The lamella was then transferred to a Cu Omni grid using a micro-manipulator needle; final thinning was performed at 30 kV. The FIB lift-outs were then analyzed in an FEI Talos F200X scanning transmission electron microscopy (STEM) operating at an accelerating voltage of 200 kV.

RESULTS

Etching of Powders

MACE has been performed on Si powder, for which there is no unique upward, vertical or normal direction. As shown in **Figure 1**, domains of etch-track pores form that tend to point in the same direction within local domains. Some regions have the appearance of nanowires or blade-like ridges whereas other regions maintain the original flatness of the particle and etch porous regions with interconnected pore walls. Single-crystal powder particles tend to exhibit a single domain on each particle face with the axis of the etch track pores along a single direction. This can also occur on polycrystalline powder particles, particularly smaller ones. More typically, polycrystalline particles exhibit domains with etch axes that point in multiple directions with respect to the local surface normal. In some cases, structures on the same metallurgical-grade particle face can even be perpendicular to one another. The pores often exhibit a wavy character on single-crystal particles and are usually straighter on polycrystalline particles.

It has long been known that porous silicon films can be pulverized to form microparticles (Heinrich et al., 1992). Similarly it is known that capillary forces acting either during etching or drying (Campbell et al., 1995; Bellet and Canham, 1998) can change the structure of highly porous films. MAC-etched porosified particles are no different in this respect to MAC-etched porosified wafers. The ridge-like structures can be harvested from MAC-etched Si particles to produce individual SiNW and bundles of SiNW with lengths of several or even tens of micrometers.

Etching of Macropores

As previously reported (Mills et al., 2005; Dudley and Kolasinski, 2008), anisotropic KOH etching of laser ablation pillars leads to the formation of rectangular macropores on Si(001) substrates. On Si(111) substrates, macropores are initially hexagonal then progressively become triangular in shape. These results are confirmed in **Figures 2A,C**. Here we show, **Figure 2B**, that in addition parallelepiped macropores are formed when laser ablation pillars formed on Si(110) substrates are etched anisotropically.

The macropores represent single-crystal substrates with well-defined bulk orientations that also exhibit a variety of surface facets with well-defined but nonetheless very different orientations from the bulk orientation, as shown in the cross-sectional images in **Figures 2D–F**. Performing MACE on these substrates allows us to consider the influence of bulk orientation, surface orientation and, thus, whether etching along a local surface normal is different from etching along the normal to the macroscopic wafer surface. **Figure 2** demonstrates that most if not all exposed facets are porosified by the formation of etch track pores.

MAC-etched macropores in substrates with all three orientations were cross-sectioned by FIB to form electron-transparent specimens suitable for imaging with STEM. Three representative high-angle annular dark-field (HAADF) STEM images are displayed in **Figure 3**. For all three substrates the primary direction of etching is found along the $\langle 001 \rangle$ directions, with relatively few turns observed and only the occasional

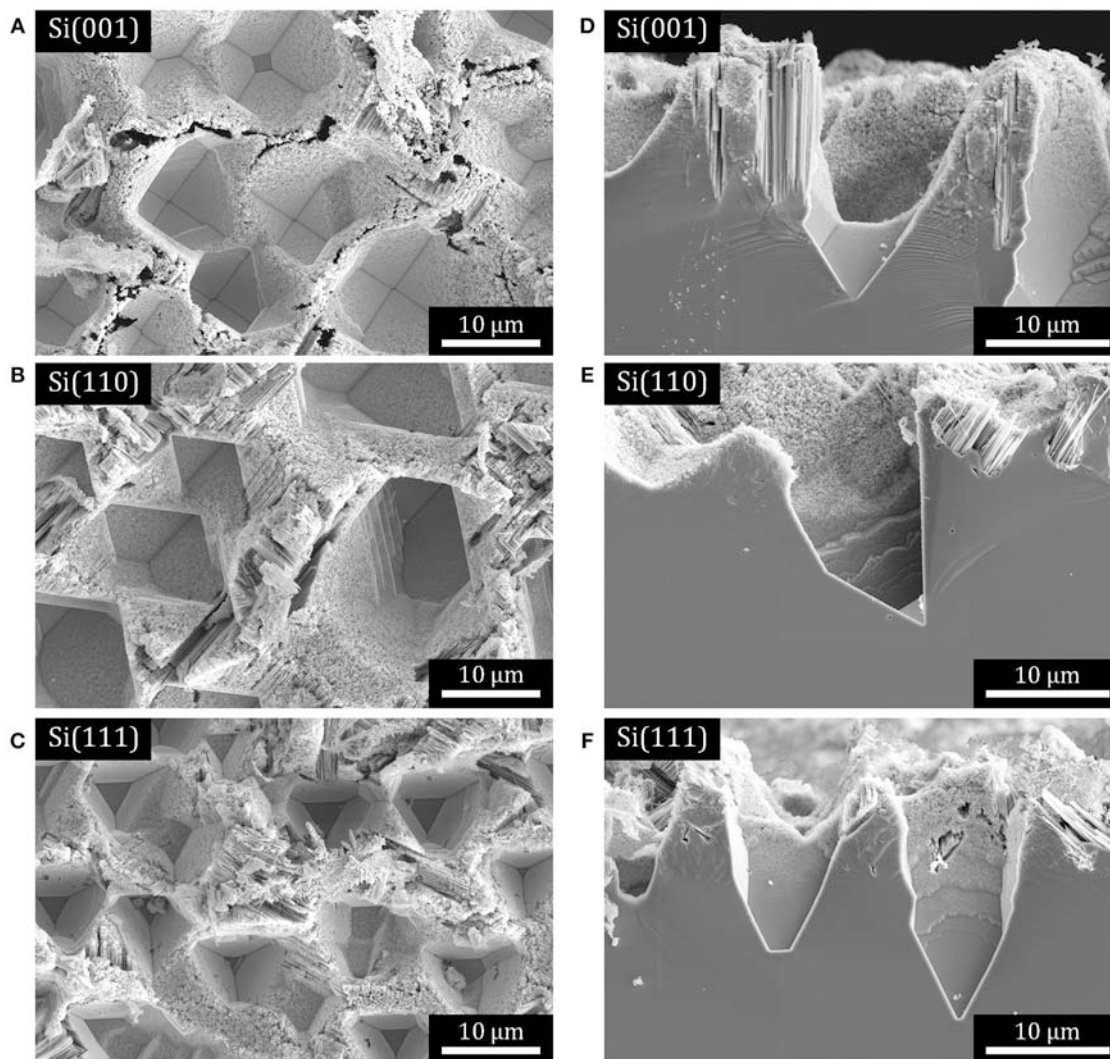


FIGURE 2 | SE SEM micrographs of macropores on Si substrates that have been subjected to Ag-catalyzed metal assisted etching in $\text{H}_2\text{O}_2 + \text{HF}$ solution. **(A–C)** Plan view micrographs of: **(A)** rectangular macropores on Si(001), **(B)** parallelepiped macropores on Si(110), and **(C)** triangular macropores on Si(111). **(D–F)** cross-sections of pores in the samples shown in **(A–C)**, respectively.

isolated meandering etch track. In each case, there are Ag nanoparticles found at the end of some of the etch track pores in these specimens. The Ag nanoparticles appear bright due to strong Z contrast in the HAADF images. We note that these nanoparticles were observed far more frequently than one would expect based upon random sampling of the etch track structure. The proximity of the Ag nanoparticles to one another is clear evidence that the MAC etching must involve some co-operative process.

In-depth analysis of the microstructure of MAC-etched wafers and particles will be presented elsewhere. Here we concentrate on the crystallographic dependence of the etch track pores. We note also that SEM images of MAC-etched wafers and particles often look as though SiNWs have been formed. Indeed, often a few SiNWs are observed at the edges of etched domains. However,

these SiNWs are most likely the result of cleavage caused either by H_2 bubble formation or during drying. The analysis of FIB cross sections reveals that the MAC-etched film is comprised predominantly of pores with interconnected walls rather than free-standing nanowires.

Temperature Dependence of Etch Rate

If the oxidant concentration remains constant during etching, we expect the etch depth to increase linearly in time, an observation that has been confirmed experimentally (Ghosh and Giri, 2016; Toor et al., 2016a). If we assume Arrhenius behavior and that the kinetic order is independent of temperature, the etch rate is given by the depth along the etch direction divided by time, and a plot of the etch rate vs. inverse temperature should yield a straight line as long as the concentration of the oxidant is

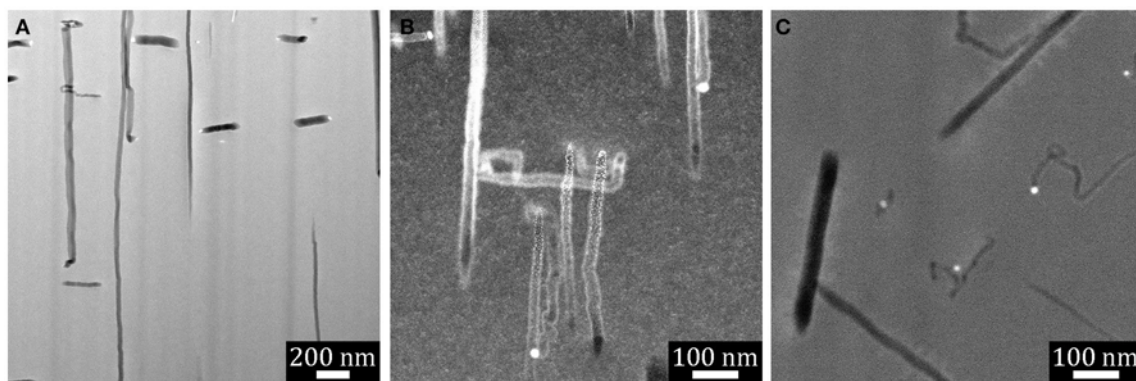


FIGURE 3 | HAADF STEM images of FIB-cut cross-sections taken from the walls of macropores on Si substrates that had been subjected to Ag-catalyzed metal assisted etching in $\text{H}_2\text{O}_2 + \text{HF}$ solution: **(A)** Si(001), **(B)** Si(110), **(C)** Si(111).

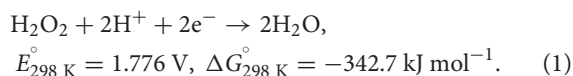
essentially invariant during the etch (as it is for wafer etching, but not necessarily for high-surface area powder etching). The results are shown in **Figure 4** and the expected linear behavior indicative of an activation energy $E_a = -k_B (\text{slope})$ is observed.

One measure of the uncertainty in the etch rate is obtained by averaging multiple measurements of the depth across the wafer as obtained from cross sectional SEM images. Generally this variance is less than the sample-to-sample variance between experiments run under identical conditions; hence, the reported experimental uncertainty likely underestimates the true uncertainty. Because etching is found to occur along $\langle 001 \rangle$ directions for all substrate orientations, one might expect the activation energy to be similar on each substrate orientation. The activation energy is found to be 0.44 ± 0.05 eV on Si(001), 0.34 ± 0.09 eV on Si(110), and 0.35 ± 0.05 eV on Si(111). The measured activation energies are insignificantly different on Si(110) and Si(111), but the larger value for Si(001) is on the border of statistical significance. Therefore, it appears that vertical as opposed to angled etching makes little, if any, difference to the mechanism of etching. These results are within the experimental uncertainty of the previously reported value of $E_a = 0.36$ eV (Cheng et al., 2008) for Si(001). The experimentally-determined activation energy is also similar in magnitude to the estimate of the etch energy of 0.31 eV from the model that will be developed below.

DISCUSSION

Modeling of Forces Between the Ag Nanoparticle and the Si Substrate

Figure 5 depicts schematically the chemical events that are occurring during MACE. H_2O_2 undergoes an electrochemical half-reaction that removes electrons from the Ag nanoparticle,



A hole injected into a Ag nanoparticle of side length l is more stable in the nanoparticle than at either the interface or in the

Si. There is a barrier (Kolasinski, 2014) to electron transfer from Ag to Si, and tunneling through this Schottky barrier has been implicated as the primary means of charge transfer between the metal and Si (Rezvani et al., 2016). Therefore, a steady-state electron imbalance builds up in the Ag nanoparticle. This effective positive charge is offset by the adsorption of anions such as F^- , which leads to an overall negative charge on the metal catalyst, as demanded by the negative voltage measured during etching by Rezvani et al. (2016).

Electrostatic Force

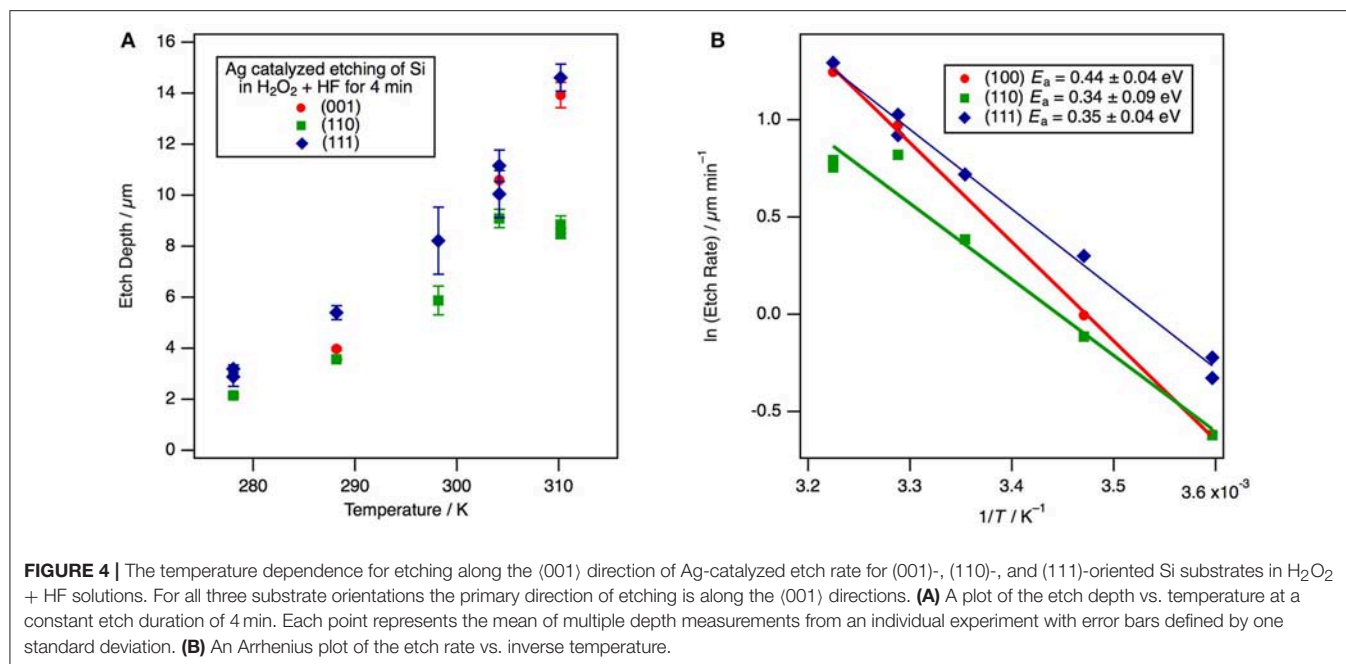
The charge imbalance on the Ag catalyst is modeled as a negative charge $-q$ at the center of the cubic nanoparticle. The charge polarizes the Si beneath it. The polarization is modeled as an image charge $+q_b$ located a distance $0.5l$ below the nanoparticle. The charges are related to one another by a ratio involving the susceptibility of Si (Griffiths, 1981),

$$q_b = \frac{\chi_e}{\chi_e + 2} q. \quad (2)$$

The susceptibility of Si is 10.9, thus $q_b = 0.845q$. It has been shown (Kolasinski et al., 2015) that the primary means of Si etching is a valence 2 process for catalysis by Ag and Au. That is, the primary means of Si atom removal is porous Si formation. Therefore, the effective voltage associated with the charge imbalance on the Ag nanoparticle must have a magnitude $< 2\text{ V}$, otherwise the etching would switch to electropolishing, a valence 4 process. This sets an upper bound on the net charge q on the nanoparticle that is consistent with the potential differences measured by Rezvani et al. of -0.5 V for Au and -0.2 V for Ag.

The voltage at the interface of the metal particle with the Si is given by

$$V = \frac{1}{4\pi\epsilon_0} \frac{q}{0.5l}. \quad (3)$$



The force generated by the attraction of this charge to its image charge is

$$F = \frac{1}{4\pi\epsilon_0} \frac{qq_b}{l^2} = \pi\epsilon_0 V^2 \frac{\chi_c}{\chi_c + 2}, \quad (4)$$

which is independent of the length of the particle. Upon substitution with $V = -0.2$ V, the electrostatic attraction between the Ag nanoparticle and the Si substrate is found to be 9×10^{-13} N. For a sense of scale, a nanoparticle with $l = 100$ nm has approximately 10^9 valence electrons. An excess of just 7 units of elementary charge is sufficient to engender an effective voltage of -0.2 V. The mass of this particle is 10^{-17} kg, which means that the electrostatic attraction is over 9,000 times larger than the force of gravity. Contrary to some assertions in the literature, the force of gravity is irrelevant for holding the catalyst in contact with the Si surface. The electrostatic force drives the nanoparticle toward the image charge and holds the catalyst tight against the Si surface irrespective of the orientation of the surface compared to the laboratory vertical direction.

Since pressure is force per unit area and the particles have a square contact with the Si, the effective pressure induced by the image force is

$$p = \frac{\pi\epsilon_0 V^2 \chi_c}{\chi_c + 2} \frac{1}{l^2}. \quad (5)$$

Thus, unlike force, pressure does scale with particle size. This amounts to 9.4 kPa at $r = 10$ nm but only 94 Pa at 100 nm. As we show below, the relative importance of van der Waals forces to electrostatic forces increases as particle size increases.

van der Waals Interaction

van der Waals forces, more specifically called Derjaguin and Landau, Verwey and Overbeek (DLVO) interactions, are non-linear and operate over a short distance; small changes in the gap distance or gap locations between the metal and Si will result in large changes in these attractive forces. However, the electrostatic forces calculated above are much less sensitive to surface roughness and gap variations. The combination of these two sets of forces ensures that the metal catalyst is always attracted strongly to the Si substrate and never loses contact with it as long as the metal is not pinned. This combination also enables the etching of all facets of powder particles irrespective of how the particles are oriented in the solution because these forces act to draw the metal catalyst toward the core of the Si particle.

Lai et al. (2013) have found that MACE was capable of deforming a pinned metal catalyst with a length of $2\mu\text{m}$ and a width of 315 nm. They estimated that the porous region below this catalyst was 2–4 nm thick and that the roughness of the Au catalyst surface was 5 nm at the Au/Si interface. The pressure required to deform the catalyst was 1–3 MPa, which they attributed to van der Waals forces.

Wong et al. (Hildreth et al., 2011, 2013; Rykaczewski et al., 2011) have also used pinned metal catalysts to estimate the forces experienced during MACE. The Pt catalysts had a width of $1\mu\text{m}$. They unequivocally showed that the electrophoretic model of Peng et al. (2008) cannot generate the forces required to deform their catalysts. They suggested that DLVO interactions were responsible for the attractive force between the catalyst and the Si substrate. They measured forces of 0.55–3.5 μN corresponding to pressure of 0.5–3.9 MPa.

To calculate the magnitude of DVLO interactions (Israelachvili, 2011), we start with the Hamaker constant,

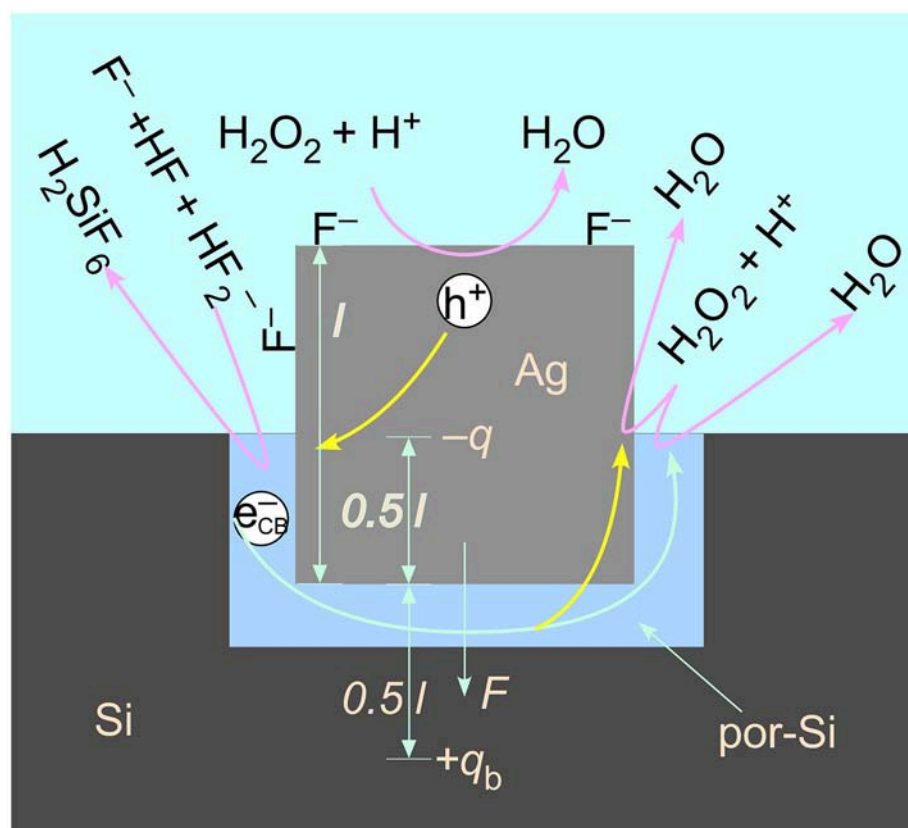


FIGURE 5 | A model of the electrostatic interaction of a charged particle and its image charge located in bulk Si across an intervening porous region. An excess of adsorbed anions, such as F^- , leads to a net negative charge on the metal catalyst. Reactions pertinent to valence band hole injection by H_2O_2 decomposition, Si etching by complexation of Si to H_2SiF_6 by fluoride species, and capture by H_2O_2 of the conduction band electron injected by F^- (which can occur either on the metal nanoparticle or on the Si) are also represented. The formation of a porous region in the immediate proximity of the metal/Si interface facilitates the transport of reactants into and products out of the reaction zone.

which is given by

$$A = \pi^2 C \rho_1 \rho_2 \quad (6)$$

where ρ_1 and ρ_2 are the number densities of the two materials and C is the London dispersion constant

$$C = \frac{3\alpha_0^2 I}{4(4\pi\epsilon_0)^2} \quad (7)$$

where α_0 is the polarizability, I is the ionization energy and ϵ_0 the vacuum permittivity. For the interaction of two flat surface separated by D , which we assume here to be the thickness of the porous region beneath the catalytic particle, the energy per unit area of interaction is

$$W_{vdW} = \frac{A}{12\pi D^2}, \quad (8)$$

and the pressure is

$$p_{vdW} = \frac{A}{6\pi D^3}. \quad (9)$$

At $D = 3$ nm, this amounts to $p_{vdW} = 542$ kPa independent of the particle size in terms of surface area. Therefore, since the pressure associated with the electrostatic force decreases with increasing particle size, as particle size increases, the relative importance of the van der Waals forces increases. On the other hand, whereas the electrostatic force is not affected by a change in the thickness of the sub-particle porous region, the van der Waals force depends strongly on this distance as D^3 . Consequently, p_{vdW} increases from 542 kPa at $D = 3$ nm to $p_{vdW} = 3.9$ MPa at $D = 1.55$ nm. The range $1.55 \text{ nm} \leq D \leq 3 \text{ nm}$ fits the range of pressures measured during MACE by Wong et al. (Hildreth et al., 2011, 2013; Rykaczewski et al., 2011). Clearly then, the net effect of the electrostatic and van der Waals forces is to adhere the Ag nanoparticle tightly to the Si particle surface at all stages throughout etching as long as the metal nanoparticle is not pinned by lithographic construction.

Etch Model

A wide variety of oxidants has been used in metal-assisted etching including H_2O_2 , V_2O_5 , HNO_3 , $Fe(NO_3)_3$, and dissolved O_2 among others. These species have different kinetics of

hole injection leading to, for example, different concentration dependences. However, once a hole has been injected into the Si valence band by any oxidant, the hole rapidly relaxes to the valence band maximum to initiate etching in a manner that is completely independent of the chemical identity of the oxidant. Dissolved V_2O_5 in HF has the advantage of being readily detected by absorption spectroscopy in both its oxidized $5+$ (VO_2^+) and reduced $4+$ (VO^{2+}) forms (Kolasinski and Barclay, 2013). This allowed Kolasinski et al. (2015) to establish that MACE catalyzed by both Ag and Au follows a valence two process. This demonstrates that the primary means of Si atom removal is porous Si formation through the current doubling pathway of the Gerischer mechanism (Kolasinski, 2003) rather than electropolishing. Electropolishing is a valence four process that involves SiO_2 formation followed by HF stripping of the oxide. This conclusion is strictly true for a low concentration (~ 20 mM) of VO_2^+ in 5 M HF. It is possible that at high oxidant concentration, the primary Si atom removal mechanism switches either to the valence four current quadrupling pathway of the Gerischer mechanism or else to electropolishing.

The results of these $V_2O_5 + HF$ experiments (Kolasinski et al., 2015) are consistent with the work of Chartier et al. (2008) who found that the structure of a Si substrate subjected to metal assisted etching depends on the oxidant concentration or, stated more precisely, the concentration ratio of oxidant to HF. At low oxidant concentration (i.e., high HF/ H_2O_2 ratio) they found no formation of oxide at the surface and etching localized to the catalyst, which results in the formation of meso- and macropores depending on the Ag nanoparticle size. This corresponds to the solution composition in the SiNW formation regime. At high oxidant concentration (low HF/ H_2O_2 ratio) the Si surface is oxidized, the injected holes are distributed homogeneously, and thus electropolishing occurs. Complete electropolishing is incompatible with etch track pore and SiNW formation. These results indicate clearly that etching beneath the metal catalyst depends on the oxidant concentration (and HF/ H_2O_2 ratio). Such dependence can lead to changes in the surface chemistry (a change in the adsorbates covering the surface as well as the etch mechanism), which could possibly lead to changes in the crystallographic dependence of MACE. A dependence of etch track pore direction on oxidant concentration was suggested by Huang et al. (2010).

Cooperative effects between metal particles influence MACE. This is evident, as noted above, from the frequent observation of Ag nanoparticles within lamellae produced for STEM imaging. In addition, cooperative effects are evinced by the observation that helical pores only occur with isolated metal particles [preferentially Pt (Tsujino and Matsumura, 2005)] and by the remarkably uniform etch depth and direction both across a wafer and across powder particles. Possible mechanisms for coordination include image forces between the metal particles, and/or the influence of band bending at the metal/Si interface from neighboring metal particles, which influences carrier transfer through the metal/Si interface (Huang et al., 2009). Another possibility is the diffusion of a chemical species such as F^- into Si in the wake of etching. Incorporation of F^- has been

observed by Rezvani et al. (2016) and could alter effective doping levels and band bending.

The planes most commonly mentioned as relevant to MACE of Si are the {111}, {110}, {112}, {113}, and {001}. The structures of these planes are shown in **Figure 6**.

A simple model to estimate the surface energy of various Si crystal faces has been described by Dabrowski and Müssig (2000). The cohesive energy of Si is $E_c = 4.63$ eV, which is the energy released when a crystal is formed from atoms. Si is tetravalent, that is, each Si atom forms $n_b = 4$ bonds and each bond is a two-center bond to which $n_a = 2$ atoms contribute. By microscopic reversibility, the energy released in making a bond is equal and opposite to the energy required to break that bond, $E = n_a E_c / n_b$. The surface energy E_{hkl} , i.e., the energy required to form a unit of surface area in the (hkl) plane, is estimated by the product of the bond dissociation energy E with the areal density of broken bonds. The number of broken bonds N_{hkl} divided by twice the surface area $2A_{hkl}$ (two surfaces are formed from cleaving the crystal) can be calculated from consideration of the unit cell for each plane (hkl). The surface energy is, therefore,

$$\gamma_{hkl} = \frac{E N_{hkl}}{2A_{hkl}} = \frac{E_c N_{hkl}}{4A_{hkl}} \quad (10)$$

Applying Equation (10) we obtain the results in **Table 1** for γ_{hkl} . Si(111) has a rhombohedral unit cell with equal side lengths a and apex angle $\alpha = 60^\circ$; hence, an area of $A = a^2 \sin \alpha$. All of the other planes have rectangular or square unit cells with side lengths a and b as indicated in **Figure 6** and **Table 1**. The stability of a clean surface scales as the inverse of the number of broken bonds per unit area. On this basis, the most stable surface is Si(111) and the least is Si(001). Semiconductor surfaces, of course, are known to reconstruct to minimize both the number of dangling bonds and the surface energy. We will not consider reconstructions here because H-termination is able to lift the reconstructions of the bare surface and relax them close to the bulk terminated structure. This is relevant because Si remains H-terminated throughout etching when etching follows the Gerischer mechanism (Kolasinski, 2003).

The energy cost per unit area of etching a plane of Si, $\gamma_{hkl}^{\text{etch}}$, is different than the surface energy. It is given by the energy required to break a Si-Si bond times the areal density of Si-Si bonds that must be etched to reveal the next surface unit cell

$$\gamma_{hkl}^{\text{etch}} = \frac{E N_{e,hkl}}{A_{hkl}} = \frac{E_c N_{e,hkl}}{2A_{hkl}} \quad (11)$$

A total of $N_{e,hkl}$ Si-Si bonds per unit cell are dissociated by etching as detailed in **Table 1**. These values are used to calculate the values of $\gamma_{hkl}^{\text{etch}}$ that appear in the last column of **Table 1**. $\gamma_{hkl}^{\text{etch}}$ is the energy per unit area required to remove one surface unit cell as atoms, which has a depth c_{hkl} that depends on the surface crystallography of the etch front. On the {001}, {113}, and {110} surfaces, this corresponds to removing the uppermost layer of surface atoms. On {111} and {112} planes, a bilayer must be removed.

The term $\gamma_{hkl}^{\text{etch}}$ has not been quantified previously. Nonetheless, previous explanations of the crystallographic

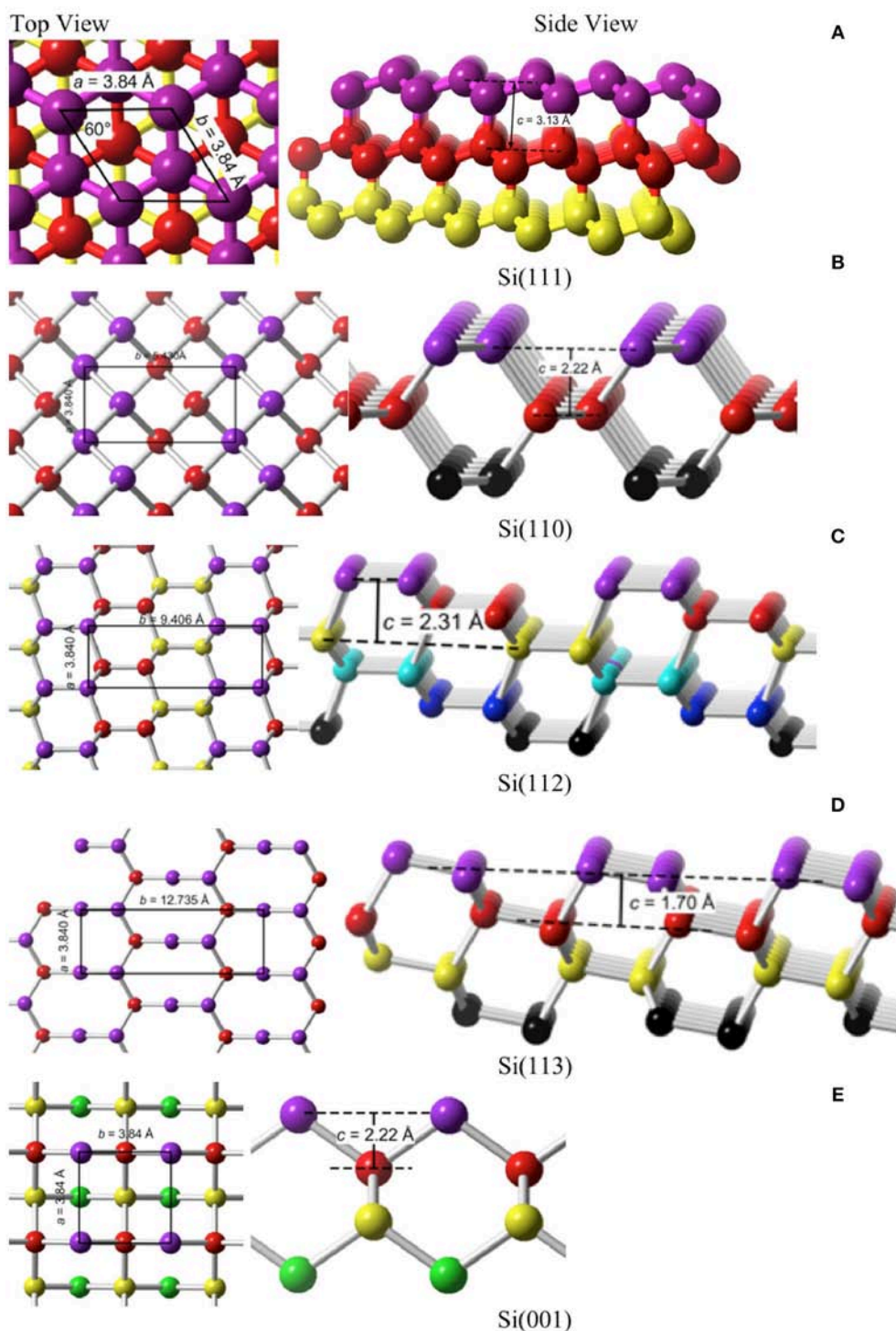


FIGURE 6 | Top and side views of the five planes that are most likely to be encountered in MACE. **(A)** Si(111), **(B)** Si(110), **(C)** Si(112), **(D)** Si(113), **(E)** Si(001).

dependence—sometimes loosely referred to as the back bond model (Peng et al., 2008; Huang et al., 2009, 2010, 2012; Bai et al., 2013; Ouertani et al., 2014; Ghosh and Giri, 2016; Jiang et al., 2016; Jiao et al., 2016; Li et al., 2016)—have attempted to

explain the crystallographic dependence of MACE with respect to this one term. A *misinterpretation that frequently appears in connection with the back bond model is that the back bond strength varies with crystallography*. This is false. The back bond

TABLE 1 | The parameters required for the calculation of the surface energy γ_{hkl} and etch energy $\gamma_{hkl}^{\text{etch}}$ are collected for the five most commonly encountered planes of Si in MACE.

Ideal surface	Unit cell dimensions Å	Cell area A Å ²	Broken bonds N per cell	Surface energy γ_{hkl} eV Å ⁻²	Bonds etched N_e per cell	Etch energy $\gamma_{hkl}^{\text{etch}}$ eV Å ⁻²
Si(111)	$a = 3.840, \alpha = 60^\circ, c = 3.13$	12.8	1	0.091	4	0.725
Si(110)	$a = 3.840, b = 5.430, c = 2.22$	20.9	2	0.111	4	0.444
Si(112)	$a = 3.840, b = 9.406, c = 2.31$	36.1	4	0.128	9	0.577
Si(113)	$a = 3.840, b = 12.735, c = 1.70$	48.9	6	0.142	8	0.379
Si(001)	$a = 3.840, b = 3.840, c = 2.22$	14.7	2	0.157	2	0.314

N is the number of dangling bonds formed per unit cell. The surface unit cell has area A . N_e is the number of Si-Si bonds broken by etching per unit cell.

strength does not possess a specific crystallographic dependence. Rather, the surface atoms experience different co-ordinations as the result of variations in surface crystallography. Therefore, the energy required to remove a specific surface atom can depend on the surface crystallography as well as on which of its neighbors have been removed previously. As shown by the final column in **Table 1**, the density of back bonds that must be broken per unit area varies with crystallographic plane. When averaged over the unit cell, an estimate of the energy required to etch the Si surface per unit area is simply the product of the mean bond energy and the number of bonds that have to be broken per unit area.

The term $\gamma_{hkl}^{\text{etch}}$ does not consider that the etched atom is coordinated, e.g., first as HSiF_3 , as it leaves the surface rather than as a Si atom. This will change the absolute energetics; however, all Si surfaces have the same etch product and, therefore, the relative etch energy will not be affected by the chemical nature of the etch product. Note also that $\gamma_{hkl}^{\text{etch}}$ is a thermodynamic rather than a kinetic parameter, i.e., it is not an activation energy but the difference in energy per unit area between the initial and final states. The expression does not take steric factors into account, which influence the kinetics but not thermodynamics of pore formation. The formation of a 5-fold transition state is commonly invoked to explain the crystallographic dependence of alkaline etching of Si (Hines et al., 1994; Baum and Schiffrin, 1998). An implicit assumption of the back bond model is that $E_{a,\text{etch}}$ scales with the value of $\gamma_{hkl}^{\text{etch}}$, in other words, that the activation energy follows a linear Brønsted-Evans-Polanyi relation as is often found in catalysis (Bligaard et al., 2004). Our experimentally measured values for the etching activation energy (0.34–0.44 eV) are comparable to the Si(001) value of $\gamma_{hkl}^{\text{etch}}$ reported in **Table 1** (0.31 eV), which lends credence to the model presented here.

Even without consideration of the effects of adsorbates or the final chemical form of the etch product, the term $\gamma_{hkl}^{\text{etch}}$ alone does not fully describe the energy required to form a pore or SiNW by etching. Etching one layer of Si atoms to reveal a new surface unit cell requires etching a depth c_{hkl} , that depends on the surface crystallography as shown in **Figure 6**. Thus, one must also consider the energy required to create the sidewalls of the pore/SiNW. It is important to recognize that etching is not an equilibrium process that is creating structures with the lowest possible surface energy. Rather, it is a kinetically-controlled process that is influenced by the trajectory that removes atoms along the minimum energy path.

We consider one metal catalyst particle, square in cross section with side length l , and the formation of one rectangular pore etched to a depth d_{etch} beneath it. We conceptualize etching as a stepwise process in which the depth of one surface unit cell c_{hkl} at a time is removed. We seek to derive an expression for the energy required to remove one such surface unit cell layer. The expression (assuming etching in only one direction and sidewalls of only one crystallographic orientation with sidewalls perpendicular to a planar etch front, as shown in **Figure 7**) is

$$E_{\text{pore}} = \gamma_{hkl}^{\text{etch}} A_{\text{cat}} + \gamma_{hkl}'^{\text{etch}} A_{\text{sw}} \quad (12)$$

where A_{cat} is the area beneath the catalyst

$$A_{\text{cat}} = l^2 = (\eta_1 a_{\text{Si}})^2 \quad (13)$$

which is expressed using the ratio of the length to the Si lattice constant $\eta_1 = l/a_{\text{Si}}$ and A_{sw} is the sidewall area

$$A_{\text{sw}} = 4lc_{hkl} = 4\eta_1 \eta_2 a_{\text{Si}}^2 \quad (14)$$

expressed in terms of the ratio $\eta_2 = c_{hkl}/a_{\text{Si}}$. The Si lattice constant is $a_{\text{Si}} = 5.43095$ Å (Sze and Ng, 2006).

The prime in Equation (12) indicates that the sidewalls will, in general, have a different crystallographic orientation than the etch front. The total energy to create a pore of some macroscopic depth d_{etch} would then be the sum of Equation (12) over the number of steps n_s required to etch to this depth, $d_{\text{etch}} = n_s c_{hkl}$, that is, $E_{\text{total}} = n_s E_{\text{pore}}$. Should etching reveal multiple sidewall orientations or the direction of etching change during etching, e.g., to form zigzag SiNW, then appropriate summations over surface energies and areas would have to be taken.

Substituting for the areas, the energy required to perform one step of pore formation is

$$E_{\text{pore}} = \eta_1 a_{\text{Si}}^2 \left[\eta_1 \gamma_{hkl}^{\text{etch}} + 4\eta_2 \gamma_{hkl}'^{\text{etch}} \right]. \quad (15)$$

The importance of the etch-front term $\eta_1 \gamma_{hkl}^{\text{etch}}$ compared to the sidewall term $4\eta_2 \gamma_{hkl}'^{\text{etch}}$ is determined by the ratio η_2/η_1 , which in turn is determined by the lateral size of the catalyst. For $l > 15$ nm, the sidewall term is <10% as large as the etch-front term, and can then be neglected. Only for small nanoparticle catalysts with $l < 15$ nm must the sidewall term be considered.

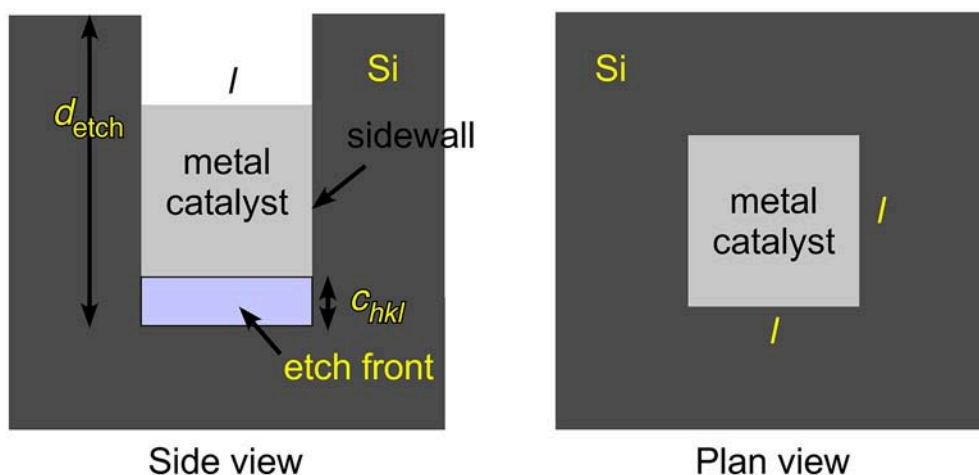


FIGURE 7 | Metal assisted catalyzed etching (MACE) is represented schematically for a cubic metal catalyst of side length l etching with a planar etch front that is perpendicular to the sidewalls. The sidewalls need not be perpendicular to the macroscopic normal to the wafer/particle that is being etched. The total etch depth d_{etch} is obtained by stepwise removal of one surface unit cell after another with a step depth c_{hkl} that depends on the surface crystallography of the plane that contains the etch front.

At this point it is interesting to compare to the “inverse problem,” that is, to the formation of SiNWs by growth rather than etching. Wu et al. (2004) have shown that SiNWs grown with a Au catalyst in a vapor-liquid-solid (VLS) process grow along the $\langle 111 \rangle$ direction for diameters above 20 nm, in the $\langle 112 \rangle$ direction for diameters between 10 and 20 nm, and along the $\langle 110 \rangle$ direction for diameters between 3 and 10 nm. They suggested that at large diameters, formation of the lowest surface energy plane, i.e., the (111) plane, in the growth front dominates the energetics. However, for the smallest diameters, sidewall energy becomes the dominant factor and leads to $\langle 110 \rangle$ -directed growth. For the intermediate region, $\langle 112 \rangle$ -directed growth occurs because the (112) plane, which can be thought of as a stepped surface intermediate between (111) and (110) planes, results from a balance between the growth front and sidewall terms. This line of reasoning is consistent with the etch model developed here and the results of Equation (15).

However, even if on energetic grounds the sidewall term can be neglected compared to the etch-front term, the influence of the sidewalls cannot be ignored. The crystallographic specificity of MACE is determined not only by the energy required to advance the etch front, but also by the combinations of planes that are allowed by crystallography. The sidewall term is always lowest for $\langle 001 \rangle$ - and $\langle 113 \rangle$ -directed facets. However, these cannot always be formed. The allowed combinations for sidewall facets that are perpendicular to the pore/NW axis are shown in **Figure 8**. First note that $\langle 113 \rangle$ -directed pillars cannot form pores/NW with all sidewalls perpendicular to the long axis. This is because only two $\{110\}$ -directed facets are perpendicular to the $\langle 113 \rangle$ -direction. The lowest energy sidewalls for $\langle 113 \rangle$ -directed pores/NW are $\{111\}$ -directed facets but these are inclined to the $\langle 113 \rangle$ direction by 71° . That Peng et al. (2008) did not observe $\langle 113 \rangle$ -directed pores when etching Si(113) substrates demonstrates that there are limits to the inclination of the sidewalls.

The results in **Table 1** show that the thermodynamic stability follows the order $\text{Si}(001) < \text{Si}(113) < \text{Si}(112) < \text{Si}(110) < \text{Si}(111)$. However, the susceptibility to etching follows the order $\text{Si}(001) > \text{Si}(113) > \text{Si}(110) > \text{Si}(112) > \text{Si}(111)$. Simple application of the back bond model predicts that $\langle 001 \rangle$ -directed pores/SiNW would be the most commonly observed, which is confirmed experimentally, and $\langle 111 \rangle$ -directed pores/SiNW should not be observed. $\langle 111 \rangle$ -directed pores/SiNW are observed when a perforated metal film is used as a catalyst, which demonstrates that a highly-correlated motion of metal catalyst is required to overcome the energetics of the $\gamma_{hkl}^{\text{etch}}$ term. Obviously, interpretation of the back bond model in terms only of the energy required to etch in a given crystallographic direction is overly simplistic as it does not include correlation between catalyst particles nor the dependence on the size of the catalyst particle. The above analysis does, however, show us that preferences for sidewall orientation are determined by the lowest barrier to etching rather than by selection of the most stable surface plane.

By combining the results in **Table 1** and **Figure 8**, we can determine the most likely sidewall terminations for each etching direction. Ideally $\langle 112 \rangle$ -directed etching is predicted to form square or rectangular pores/NW with $\{111\}$ - and $\{110\}$ -oriented facets.

Ideally, $\langle 111 \rangle$ -directed etching is predicted to form either hexagonal or rectangular pores/NW. However, the hexagonal pores/NW with $\{110\}$ -directed facets should have substantially lower formation energy than rectangular pores/NW that exhibit both $\{110\}$ - and $\{111\}$ -directed facets.

Similarly, $\langle 001 \rangle$ -directed etching is predicted to form either rectangular or octagonal pores/NW. Rectangular pores/NW with $\{001\}$ -directed facets should have substantially lower formation energy than rectangular pores/NW that exhibit $\{110\}$ -directed facets. The octagonal structure with a combination of both

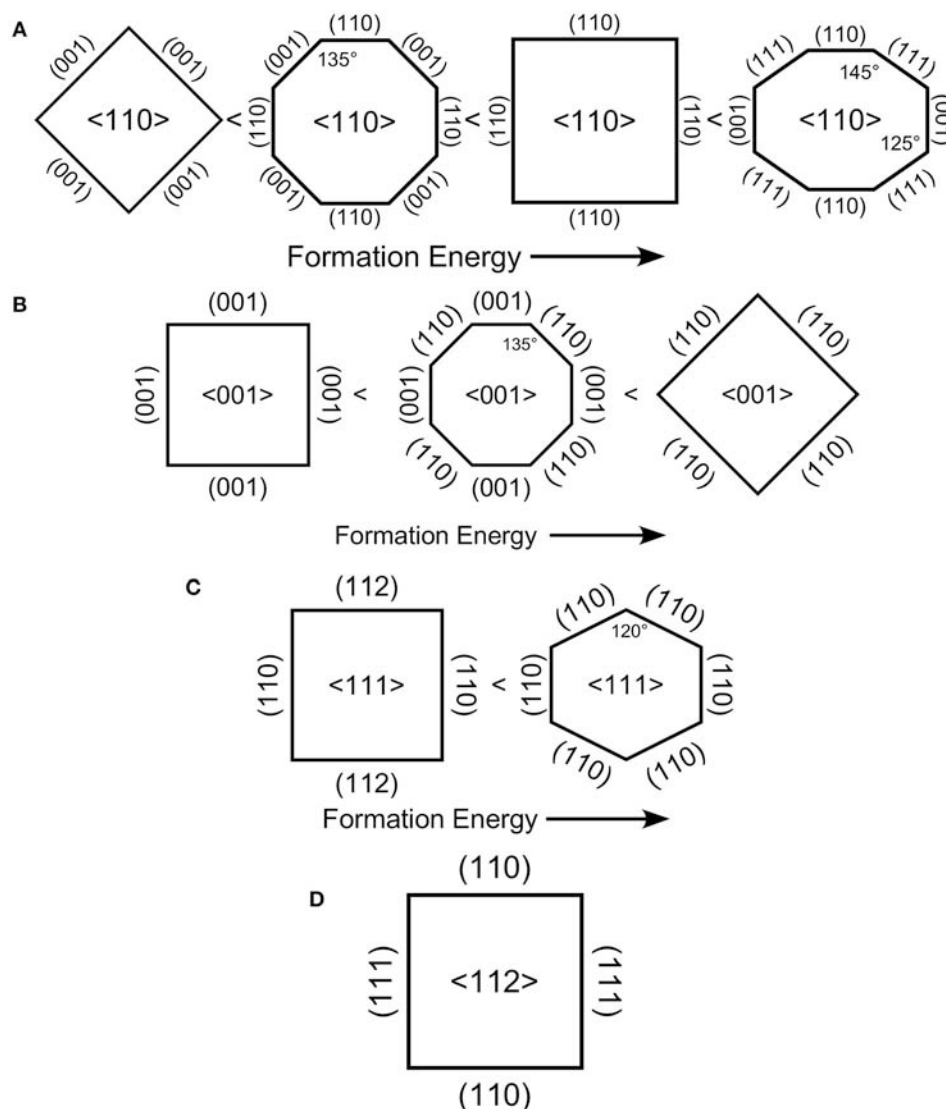


FIGURE 8 | Viewed down the long axis of a vertical pore (or pillar), the crystallography of the sidewalls is shown. For four directions **(A)** $\langle 110 \rangle$, **(B)** $\langle 001 \rangle$, **(C)** $\langle 111 \rangle$, **(D)** $\langle 112 \rangle$, vertical pores can be formed. Depending on the crystallography of the sidewall terminations, these ideal pores would exhibit facets that form either rectangular, hexagonal or octagonal cross-sections. A vertical pore in the direction is not possible as only two planes make right angles with it.

$\{110\}$ - and $\{001\}$ -directed facets has a formation energy averaged between these two.

Finally, $\{110\}$ -directed etching exhibits the richest variety of pore/NW structure. $\{111\}$ -directed facets have higher formation energy than $\{110\}$ -directed facets, which are higher than $\{100\}$ -directed facets. The $\{111\}$ facets can only form a closed structure with both $\{100\}$ and $\{111\}$ facets to form an irregular octagon as the highest energy structure. Next is a rectangular pore/NW with $\{110\}$ facets followed by an octagonal structure with a combination of both $\{110\}$ - and $\{100\}$ -directed facets. Rectangular pores/NW that exhibit $\{100\}$ -directed facets have by far the lowest formation energy.

Strong evidence for a porous region along the etch front has been presented. Geyer et al. (2012) reported extensive

experiments and high-resolution TEM images that reveal a porous Si region beneath a patterned Ag film etched with a solution consisting of 5.65 M HF and 0.10 M H_2O_2 . Lai et al. (2013) fitted extensive kinetic data to a cyclical process involving the formation of a porous etch front using Au catalyst and $\text{H}_2\text{O}_2 + \text{HF}$. Chourou et al. (2010) found a porous region subsequent to metal-assisted etching under anodic polarization.

Contradictory reports also exist. TEM has been interpreted as consistent with a solid etch front (Huang et al., 2010) for $\langle 111 \rangle$ -oriented SiNW etched at high H_2O_2 concentrations with Ag particles. A solid etch front was reported (Liu et al., 2013) for etching catalyzed by Au nanoparticles in $\text{H}_2\text{O}_2 + \text{HF}$ though it should be noted that the etched features were consistently larger than the nanoparticles and that a thin porous layer could easily

have been removed by the aqua regia used to dissolve the Au before microscopy was performed.

CONCLUSION

Metal-assisted catalytic etching (MACE) performed with Ag nanoparticles as catalysts and H_2O_2 as oxidant efficiently porosifies single-crystal Si wafers, single-crystal electronics grade Si powders and polycrystalline metallurgical grade silicon powders. Etching with 0.15 M H_2O_2 is found to preferentially proceed in a $\langle 001 \rangle$ direction with an activation energy of ~ 0.4 eV on substrates with (001) , (110) , and (111) orientations. A quantitative model based on the energy required to remove a surface unit cell through etching explains the preference for etching in the $\langle 001 \rangle$ directions, and is consistent with the measured activation energies. This model also predicts that catalyst particle size may influence the energetics of etch track pore formation. Etching of metallurgical grade powders produces particles covered primarily with porous silicon in the form of interconnected ridges. Capillary forces and ultrasonic agitation can be used to pulverize the porous layer to form silicon nanowires and bundles of nanowires. Strongly attractive electrostatic and van der Waals interactions adhere the nanoparticle catalyst to the Si surface ensuring that the nanoparticles remain in intimate contact with the Si surface throughout the etch process regardless of whether etching occurs on a wafer or on a powder particle. The attractive forces explain

why powder particles are etched equivalently on all exposed faces of powder particles because they draw the catalyst toward the interior of the particle irrespective of which direction is vertical.

AUTHOR CONTRIBUTIONS

KK was primarily responsible for the design of etching experiments, the development of the model, calculations and the writing of the first draft of the manuscript. BU performed the etching experiments and preliminary SEM characterization. MA designed the high-resolution microscopy characterization, which was performed by AE.

FUNDING

Funding provided by grant #1825331 from the National Science Foundation, West Chester University, and the resources of the Center for Microanalysis and Imaging Research and Training (CMIRT).

ACKNOWLEDGMENTS

The microscopy studies in this paper were performed using the facilities in the UConn/Thermo Fisher Scientific Center for Advanced Microscopy and Materials Analysis (CAMMA). Silicon provided by Elkem Silicon Materials and James Falcone.

REFERENCES

- Anglin, E. J., Cheng, L., Freeman, W. R., and Sailor, M. J. (2008). Porous silicon in drug delivery devices and materials. *Adv. Drug Deliver. Rev.* 60, 1266–1277. doi: 10.1016/j.addr.2008.03.017
- Aricò, A. S., Bruce, P., Scrosati, B., Tarascon, J. M., and Van Schalkwijk, W. (2005). Nanostructured materials for advanced energy conversion and storage devices. *Nat. Mater.* 4, 366–377. doi: 10.1038/nmat1368
- Armstrong, M. J., O'dwyer, C., Macklin, W. J., and Holmes, J. D. (2014). Evaluating the performance of nanostructured materials as lithium-ion battery electrodes. *Nano Res.* 7, 1–62. doi: 10.1007/s12274-013-0375-x
- Ashley, C. E., Carnes, E. C., Phillips, G. K., Padilla, D., Durfee, P. N., Brown, P. A., et al. (2011). The targeted delivery of multicomponent cargos to cancer cells by nanoporous particle-supported lipid bilayers. *Nat. Mater.* 10, 389–397. doi: 10.1038/nmat2992
- Bai, F., To, W. K., and Huang, Z. (2013). Porosification-induced back-bond weakening in chemical etching of n-Si(111). *J. Phys. Chem. C* 117, 2203–2209. doi: 10.1021/jp311999u
- Baum, T., and Schiffrin, D. J. (1998). Mechanistic aspects of anisotropic dissolution of materials etching of single-crystal silicon in alkaline solutions. *J. Chem. Soc. Faraday Trans.* 94, 691–694. doi: 10.1039/a707473e
- Bellet, D., and Canham, L. (1998). Controlled drying: the key to better quality porous semiconductors. *Adv. Mater.* 10, 487–490. doi: 10.1002/(SICI)1521-4095(199804)10:6<487::AID-ADMA487>3.0.CO;2-T
- Bligaard, T., Nørskov, J. K., Dahl, S., Matthiesen, J., Christensen, C. H., and Sehested, J. (2004). The brønsted-evans-polanyi relation and the volcano curve in heterogeneous catalysis. *J. Catal.* 224, 206–217. doi: 10.1016/j.jcat.2004.02.034
- Blomgren, G. E. (2017). The development and future of lithium ion batteries. *J. Electrochem. Soc.* 164, A5019–A5025. doi: 10.1149/2.0251701jes
- Bruce, P. G., Scrosati, B., and Tarascon, J. M. (2008). Nanomaterials for rechargeable lithium batteries. *Angew. Chem. Int. Ed. Engl.* 47, 2930–2946. doi: 10.1002/anie.200702505
- Campbell, S. D., Jones, L. A., Nakamichi, E., Wei, F. X., Zajchowski, L. D., and Thomas, D. F. (1995). Spectral and structural features of porous silicon prepared by chemical and electrochemical etching processes. *J. Vac. Sci. Technol. B* 13, 1184–1189. doi: 10.1116/1.588233
- Chan, C. K., Peng, H., Liu, G., Mcilwrath, K., Zhang, X. F., Huggins, R. A., et al. (2008). High-performance lithium battery anodes using silicon nanowires. *Nat. Nanotech.* 3, 31–35. doi: 10.1038/nnano.2007.411
- Chartier, C., Bastide, S., and Levy-Clement, C. (2008). Metal-assisted chemical etching of silicon in $\text{HF-H}_2\text{O}_2$. *Electrochim. Acta* 53, 5509–5516. doi: 10.1016/j.electacta.2008.03.009
- Cheng, S. L., Chung, C. H., and Lee, H. C. (2008). A study of the synthesis, characterization, and kinetics of vertical silicon nanowire arrays on $(001)\text{Si}$ substrates. *J. Electrochem. Soc.* 155, D711–D714. doi: 10.1149/1.2977548
- Chiappini, C., Liu, X., Fakhoury, J. R., and Ferrari, M. (2010). Biodegradable porous silicon barcode nanowires with defined geometry. *Adv. Func. Mater.* 20, 2231–2239. doi: 10.1002/adfm.201000360
- Chourou, M. L., Fukami, K., Sakka, T., Virtanen, S., and Ogata, Y. H. (2010). Metal-assisted etching of p-type silicon under anodic polarization in HF solution with and without H_2O_2 . *Electrochim. Acta* 55, 903–912. doi: 10.1016/j.electacta.2009.09.048
- Dabrowski, J., and Müssig, H. J. (2000). *Silicon surfaces and formation of interfaces: basic science in the industrial world*. Singapore; River Edge, NJ: World Scientific, 47–50.
- Dudley, M. E., and Kolasinski, K. W. (2008). Wet etching of pillar covered silicon surface: formation of crystallographically defined macropores. *J. Electrochem. Soc.* 155, H164–H171. doi: 10.1149/1.2826292
- Föll, H., Christophersen, M., Carstensen, J., and Hasse, G. (2002). Formation and application of porous silicon. *Mater. Sci. Eng. R* 39, 93–141. doi: 10.1016/S0927-796X(02)00090-6
- Geyer, N., Fuhrmann, B., Huang, Z. P., De Boor, J., Leipner, H. S., and Werner, P. (2012). Model for the mass transport during metal-assisted chemical etching with contiguous metal films as catalysts. *J. Phys. Chem. C* 116, 13446–13451. doi: 10.1021/jp3034227

- Ghosh, R., and Giri, P. K. (2016). Efficient visible light photocatalysis and tunable photoluminescence from orientation controlled mesoporous Si nanowires. *RSC Adv.* 6, 35365–35377. doi: 10.1039/C6RA05339D
- Griffiths, D. J. (1981). *Introductions to Electrodynamics*, Englewood Cliffs. New Jersey, NJ: Prentice-Hall.
- Han, H., Huang, Z. P., and Lee, W. (2014). Metal-assisted chemical etching of silicon and nanotechnology applications. *Nano Today* 9, 271–304. doi: 10.1016/j.nantod.2014.04.013
- Heinrich, J. L., Curtis, C. L., Credo, G. M., Kavanagh, K. L., and Sailor, M. J. (1992). Luminescent colloidal silicon suspensions from porous silicon. *Science* 255:66. doi: 10.1126/science.255.5040.66
- Hildreth, O. J., Brown, D., and Wong, C. P. (2011). 3D Out-of-plane rotational etching with pinned catalysts in metal-assisted chemical etching of silicon. *Adv. Func. Mater.* 21, 3119–3128. doi: 10.1002/adfm.201100279
- Hildreth, O. J., Rykaczewski, K., Fedorov, A. G., and Wong, C. P. (2013). A DLVO model for catalyst motion in metal-assisted chemical etching based upon controlled out-of-plane rotational etching and force-displacement measurements. *Nanoscale* 5, 961–970. doi: 10.1039/C2NR32293E
- Hines, M. A., Chabal, Y. J., Harris, T. D., and Harris, A. L. (1994). Measuring the structure of etched silicon surfaces with Raman spectroscopy. *J. Chem. Phys.* 101, 8055–8072. doi: 10.1063/1.468232
- Hochbaum, A. I., and Yang, P. (2010). Semiconductor nanowires for energy conversion. *Chem. Rev.* 110, 527–546. doi: 10.1021/cr900075v
- Huang, Z., Shimizu, T., Senz, S., Zhang, Z., Zhang, X., Lee, W., et al. (2009). Ordered arrays of vertically aligned [110] silicon nanowires by suppressing the crystallographically preferred etching directions. *Nano Lett.* 9, 2519–2525. doi: 10.1021/nl803558n
- Huang, Z., Wang, R., Jia, D., Maoying, L., Humphrey, M. G., and Zhang, C. (2012). Low-cost, large-scale, and facile production of Si nanowires exhibiting enhanced third-order optical nonlinearity. *ACS Appl. Mater. Interfaces* 4, 1553–1559. doi: 10.1021/am201758z
- Huang, Z. P., Shimizu, T., Senz, S., Zhang, Z., Geyer, N., and Gösele, U. (2010). Oxidation rate effect on the direction of metal-assisted chemical and electrochemical etching of silicon. *J. Phys. Chem. C* 114, 10683–10690. doi: 10.1021/jp911121q
- Israelachvili, J. N. (2011). *Intermolecular and Surface Forces*. Burlington, MA, Academic Press.
- Jiang, B., Li, M., Liang, Y., Bai, Y., Song, D., Li, Y., et al. (2016). Etching anisotropy mechanisms lead to morphology-controlled silicon nanoporous structures by metal assisted chemical etching. *Nanoscale* 8, 3085–3092. doi: 10.1039/C5NR07327H
- Jiao, X., Chao, Y., Wu, L., and Yao, A. (2016). Metal-assisted chemical etching of silicon 3D nanostructure using direct-alternating electric field. *J. Mater. Sci.* 27, 1881–1887. doi: 10.1007/s10854-015-3968-1
- Kamat, P. V. (2007). Meeting the clean energy demand: nanostructure architectures for solar energy conversion. *J. Phys. Chem. C* 111, 2834–2860. doi: 10.1021/jp066952u
- Kang, D. K., Corno, J. A., Gole, J. L., and Shin, H. C. (2008). Microstructured nanopore-walled porous silicon as an anode material for rechargeable lithium batteries. *J. Electrochem. Soc.* 155, A276–A281. doi: 10.1149/1.2836570
- Kasavajjula, U., Wang, C., and Appleby, A. J. (2007). Nano- and bulk-silicon-based insertion anodes for lithium-ion secondary cells. *J. Power Sour.* 163, 1003–1039. doi: 10.1016/j.jpowsour.2006.09.084
- Kaukonen, A. M., Laitinen, L., Salonen, J., Tuura, J., Heikkilä, T., Limnell, T., et al. (2007). Enhanced *in vitro* permeation of furosemide loaded into thermally carbonized mesoporous silicon (TCPSi) microparticles. *Euro. J. Pharm. Biopharm.* 66, 348–356. doi: 10.1016/j.ejpb.2006.11.021
- Kilpeläinen, M., Riikonen, J., Vlasova, M. A., Huotari, A., Lehto, V. P., Salonen, J., et al. (2009). *In vivo* delivery of a peptide, ghrelin antagonist, with mesoporous silicon microparticles. *J. Control. Release* 137, 166–170. doi: 10.1016/j.jconrel.2009.03.017
- Kim, H., Han, B., Choo, J., and Cho, J. (2008). Three-dimensional porous silicon particles for use in high-performance lithium secondary batteries. *Angew. Chem. Int. Ed. Engl.* 47, 10151–10154. doi: 10.1002/anie.200804355
- Kolasinski, K. W. (2003). The mechanism of Si etching in fluoride solutions. *Phys. Chem. Chem. Phys.* 5, 1270–1278. doi: 10.1039/b212108e
- Kolasinski, K. W. (2014). The mechanism of galvanic/metal-assisted etching of silicon. *Nanoscale Res. Lett.* 9:432. doi: 10.1186/1556-276X-9-432
- Kolasinski, K. W. (2016). Electron transfer during metal-assisted and stain etching of silicon. *Semicond. Sci. Technol.* 31:014002. doi: 10.1088/0268-1242/31/1/014002
- Kolasinski, K. W., and Barclay, W. B. (2013). Stain etching of silicon with and without the aid of metal catalysts. *ECS Trans.* 50, 25–30. doi: 10.1149/05037.0025ecst
- Kolasinski, K. W., Barclay, W. B., Sun, Y., and Aindow, M. (2015). The stoichiometry of metal assisted etching of Si in $V_2O_5 + HF$ and $HOOH + HF$ solutions. *Electrochim. Acta* 158, 219–228. doi: 10.1016/j.electacta.2015.01.162
- Kolasinski, K. W., Gimbar, N. J., Yu, H., Aindow, M., Mäkilä, E., and Salonen, J. (2017). Regenerative electroless etching of silicon. *Angew. Chem.* 55, 624–627. doi: 10.1002/anie.201610162
- Kolasinski, K. W., Unger, B. A., Yu, H., Ernst, A. T., Aindow, M., Mäkilä, E., et al. (2018). Hierarchical porous silicon and porous silicon nanowires produced with regenerative electroless etching (ReEtching) and metal assisted catalytic etching (MACE). *ECS Trans.* 86, 65–70. doi: 10.1149/08601.0065ecst
- Lai, C. Q., Cheng, H., Choi, W. K., and Thompson, C. V. (2013). Mechanics of catalyst motion during metal assisted chemical etching of silicon. *J. Phys. Chem. C* 117, 20802–20809. doi: 10.1021/jp407561k
- Lee, J. K., Oh, C., Kim, N., Hwang, J. Y., and Sun, Y. K. (2016). Rational design of silicon-based composites for high-energy storage devices. *J. Mater. Chem. A* 4, 5366–5384. doi: 10.1039/C6TA00265J
- Lee, S. W., Mcdowell, M. T., Choi, J. W., and Cui, Y. (2011). Anomalous shape changes of silicon nanopillars by electrochemical lithiation. *Nano Lett.* 11, 3034–3039. doi: 10.1021/nl201787r
- Leisner, M., Cojocar, A., Ossei-Wusu, E., Carstensen, J., and Föll, H. (2010). New applications of electrochemically produced porous semiconductors and nanowire arrays. *Nanoscale Res. Lett.* 5, 1502–1506. doi: 10.1007/s11671-010-9669-z
- Li, M., Li, Y., Liu, W., Yue, L., Li, R., Luo, Y., et al. (2016). Metal-assisted chemical etching for designable monocrystalline silicon nanostructure. *Mater. Res. Bull.* 76, 436–449. doi: 10.1016/j.materresbull.2016.01.006
- Li, X. L. (2012). Metal assisted chemical etching for high aspect ratio nanostructures: a review of characteristics and applications in photovoltaics. *Curr. Opin. Solid State Mater. Sci.* 16, 71–81. doi: 10.1016/j.cossms.2011.11.002
- Liu, G., Young, K. L., Liao, X., Personick, M. L., and Mirkin, C. A. (2013). Anisotropic nanoparticles as shape-directing catalysts for the chemical etching of silicon. *J. Am. Chem. Soc.* 135, 12196–12199. doi: 10.1021/ja4061867
- Liu, X. H., Zhong, L., Huang, S., Mao, S. X., Zhu, T., and Huang, J. Y. (2012). Size-dependent fracture of silicon nanoparticles during lithiation. *ACS Nano* 6, 1522–1531. doi: 10.1021/nn204476h
- Ma, J., Wen, L., Dong, Z., Zhang, T., Wang, S., and Jiang, L. (2013). Aligned silicon nanowires with fine-tunable tilting angles by metal-assisted chemical etching on off-cut wafers. *Rapid Res. Lett.* 7, 655–658. doi: 10.1002/psr.201307190
- Mai, L., Tian, X., Xu, X., Chang, L., and Xu, L. (2014). Nanowire electrodes for electrochemical energy storage devices. *Chem. Rev.* 114, 11828–11862. doi: 10.1021/cr500177a
- McSweeney, W., Geaney, H., and O'Dwyer, C. (2015). Metal-assisted chemical etching of silicon and the behavior of nanoscale silicon materials as Li-ion battery anodes. *Nano Res.* 8, 1395–1442. doi: 10.1007/s12274-014-0659-9
- Micheli, L., Sarmah, N., Luo, X., Reddy, K. S., and Mallick, T. K. (2013). Opportunities and challenges in micro- and nano-technologies for concentrating photovoltaic cooling: a review. *Renew. Sustain. Energy Rev.* 20, 595–610. doi: 10.1016/j.rser.2012.11.051
- Mills, D., and Kolasinski, K. W. (2005). A Non-lithographic method to form ordered arrays of silicon pillars and macropores. *J. Phys. D* 38, 632–636. doi: 10.1088/0022-3727/38/4/017
- Mills, D., Nahidi, M., and Kolasinski, K. W. (2005). Stain etching of silicon pillars and macropores. *Phys. Status Solidi A* 202, 1422–1426. doi: 10.1002/pssa.200461119
- Ouertani, R., Hamdi, A., Amri, C., Khalifa, M., and Ezzaouia, H. (2014). Formation of silicon nanowire packed films from metallurgical-grade silicon powder using a two-step metal-assisted chemical etching method. *Nanoscale Res. Lett.* 9:574. doi: 10.1186/1556-276X-9-574
- Pei, Z., Hu, H., Li, S., and Ye, C. (2017). Fabrication of orientation-tunable si nanowires on silicon pyramids with omnidirectional light absorption. *Langmuir* 33, 3569–3575. doi: 10.1021/acs.langmuir.6b04068

- Peng, K., Wu, Y., Fang, H., Zhong, X., Xu, Y., and Zhu, J. (2005). Uniform, axial-orientation alignment of one-dimensional single-crystal silicon nanostructure arrays. *Angew. Chem.* 44, 2737–2742. doi: 10.1002/anie.200462995
- Peng, K. Q., Lu, A. J., Zhang, R. Q., and Lee, S. T. (2008). Motility of metal nanoparticles in silicon and induced anisotropic silicon etching. *Adv. Func. Mater.* 18, 3026–3035. doi: 10.1002/adfm.200800371
- Peng, K. Q., Zhang, M. L., Lu, A. J., Wong, N. B., Zhang, R. Q., and Lee, S. T. (2007). Ordered silicon nanowire arrays via nanosphere lithography and metal-induced etching. *Appl. Phys. Lett.* 90:163123. doi: 10.1063/1.2724897
- Rezvani, S. J., Gunnella, R., Neilson, D., Boarino, L., Croin, L., Aprile, G., et al. (2016). Effect of carrier tunneling on the structure of Si nanowires fabricated by metal assisted etching. *Nanotechnology* 27:345301. doi: 10.1088/0957-4484/27/34/345301
- Rykaczewski, K., Hildreth, O. J., Wong, C. P., Fedorov, A. G., and Scott, J. H. (2011). Guided three-dimensional catalyst folding during metal-assisted chemical etching of silicon. *Nano Lett.* 11, 2369–2374. doi: 10.1021/nl200715m
- Salonen, J., Kaukonen, A. M., Hirvonen, J., and Lehto, V. P. (2008). Mesoporous silicon in drug delivery applications. *J. Pharm. Sci.* 97, 632–653. doi: 10.1002/jps.20999
- Santos, H. A., Bimbo, L. M., Lehto, V. P., Airaksinen, A. J., Salonen, J., and Hirvonen, J. (2011). Multifunctional porous silicon for therapeutic drug delivery and imaging. *Curr. Drug Discov. Tech.* 8, 228–249. doi: 10.2174/157016311796799053
- Santos, H. A., and Hirvonen, J. (2012). Nanostructured porous silicon materials: potential candidates for improving drug delivery. *Nanomedicine* 7, 1281–1284. doi: 10.2217/nnm.12.106
- Shin, H. C., Corno, J. A., Gole, J. L., and Liu, M. L. (2005). Porous silicon negative electrodes for rechargeable lithium batteries. *J. Power Sour.* 139, 314–320. doi: 10.1016/j.jpowsour.2004.06.073
- Sze, S. M., and Ng, K. K. (2006). *Physics of Semiconductor Devices*. New York, NY: Wiley-Interscience.
- Toor, F., Miller, J. B., Davidson, L. M., Duan, W., Jura, M. P., Yim, J., et al. (2016a). Metal assisted catalyzed etched (MACE) black Si: optics and device physics. *Nanoscale* 8, 15448–15466. doi: 10.1039/C6NR04506E
- Toor, F., Miller, J. B., Davidson, L. M., Nichols, L., Duan, W., Jura, M. P., et al. (2016b). Nanostructured silicon via metal assisted catalyzed etch (MACE): chemistry fundamentals and pattern engineering. *Nanotechnology* 27:412003. doi: 10.1088/0957-4484/27/41/412003
- Tsujino, K., and Matsumura, M. (2005). Helical nanoholes bored in silicon by wet chemical etching using platinum nanoparticles as catalyst. *Electrochem. Solid State Lett.* 8, C193–C195. doi: 10.1149/1.2109347
- Wareing, N., Szymanski, K., Akkaraju, G. R., Loni, A., Canham, L. T., Gonzalez-Rodriguez, R., et al. (2017). *In-vitro* gene delivery with large porous silicon nanocrystals fabricated using cost effective metal-assisted etching. *Small* 13:1602739. doi: 10.1002/smll.201602739
- Wu, Y., Cui, Y., Huynh, L., Barrelet, C. J., Bell, D. C., and Lieber, C. M. (2004). Controlled growth and structures of molecular-scale silicon nanowires. *Nano Lett.* 4, 433–436. doi: 10.1021/nl035162i

Conflict of Interest Statement: Independently of the work presented in the present publication, one of the authors (KK) has provided expert advice to OneD Material LLC during proceedings related to patents held by Nexxon Ltd.

The remaining authors declare that the research was conducted in the absence of any commercial or financial relationships that could be construed as a potential conflict of interest.

Copyright © 2019 Kolasinski, Unger, Ernst and Aindow. This is an open-access article distributed under the terms of the Creative Commons Attribution License (CC BY). The use, distribution or reproduction in other forums is permitted, provided the original author(s) and the copyright owner(s) are credited and that the original publication in this journal is cited, in accordance with accepted academic practice. No use, distribution or reproduction is permitted which does not comply with these terms.



Electrodeposition of Polymer Electrolyte Into Porous $\text{LiNi}_{0.5}\text{Mn}_{1.5}\text{O}_4$ for High Performance All-Solid-State Microbatteries

Girish D. Salian¹, Chrystelle Lebouin¹, Alina Galejeva², Andrey P. Kurbatov² and Thierry Djenizian^{3*}

¹ Electrochemistry of Materials Research Group, Aix Marseille Univ, CNRS, MADIREL, Marseille, France, ² Department of Chemistry and Chemical Technology, Al Farabi Kazakh National University, Alma Ata, Kazakhstan, ³ Mines Saint-Etienne, Department of Flexible Electronics, Center of Microelectronics in Provence, Gardanne, France

OPEN ACCESS

Edited by:

Jose Luis Sanchez,
Universidad de Zaragoza, Spain

Reviewed by:

Galstyan Vardan,
Università degli Studi di Brescia, Italy
Gregorio F. Ortiz,
Universidad de Córdoba, Spain

*Correspondence:

Thierry Djenizian
thierry.djenizian@mines-stetienne.fr

Specialty section:

This article was submitted to
Chemical Engineering,
a section of the journal
Frontiers in Chemistry

Received: 25 October 2018

Accepted: 27 December 2018

Published: 23 January 2019

Citation:

Salian GD, Lebouin C, Galejeva A,
Kurbatov AP and Djenizian T (2019)
Electrodeposition of Polymer
Electrolyte Into Porous
 $\text{LiNi}_{0.5}\text{Mn}_{1.5}\text{O}_4$ for High Performance
All-Solid-State Microbatteries.
Front. Chem. 6:675.
doi: 10.3389/fchem.2018.00675

We report the electrodeposition of polymer electrolyte (PMMA-PEG) in porous lithium nickel manganese oxide ($\text{LiNi}_{0.5}\text{Mn}_{1.5}\text{O}_4$) cathode layer by cyclic voltammetry. The cathode-electrolyte interface of the polymer-coated LNMO electrode has been characterized by scanning electron microscopy and electrochemical techniques. Electrochemical measurements consisting of galvanostatic cycling tests and electrochemical impedance spectroscopy revealed a significant improvement of the capacity values and the increase of the operating voltage. These effects are attributed to the total filling of pores by the electrodeposited polymer that contributes to improve the reversible insertion of Li^+ . A complete all-solid-state microbattery consisting of electropolymerized LNMO as the cathode, a thin polymer layer as the electrolyte, and TiO_2 nanotubes as the anode has been successfully fabricated and tested.

Keywords: electropolymerization, lithium nickel manganese oxide, porous materials, polymer electrolyte, Li-ion microbatteries

INTRODUCTION

Due to the highest electrochemical performance of the known energy storage systems, Lithium Ion Batteries (LIBs) have attracted attention to provide energy for low power microelectronic devices like Microelectromechanical Systems (MEMS), smart cards, radio-frequency identification (RFID) tags, biomedical *in vivo* micromachines, etc. However, downscaling the size of batteries alters their properties as the technology relies on the successive deposition of dense thin-films. In order to circumvent this issue, several strategies have been investigated including the use of nanostructured and porous materials (Shaijumon et al., 2010; Arthur et al., 2011; Roberts et al., 2011; Ellis et al., 2014; Ferrari et al., 2015) as well as the modification of the electrode surfaces (Lopez et al., 2014; Ortiz et al., 2016a,b). To improve the energy density of LIB microbatteries, thin-film cathodes with large capacity and/or high working voltage have to be envisioned. Among them, $\text{LiNi}_{0.5}\text{Mn}_{1.5}\text{O}_4$ (LNMO) is interesting due to its high capacity, good cycling stability, and good rate capability, which make it promising as thin-film positive electrode for microbatteries (Kang et al., 2006; Sun et al., 2009, 2012; Fergus, 2010; Ohzuku et al., 2011).

Miniaturizing LIBs also requires the use of solid electrolyte (polymers or glassy materials) because liquid counterparts are responsible for leakage risks and safety issues (Fergus, 2010). Reports of gel polymer electrolyte (GPE) used as electrolytes with LNMO have been reported previously (Bernhard et al., 2013; Sun et al., 2014; Chen et al., 2015). The main objective for the usage of gel polymer electrolyte is to limit the decomposition of the liquid electrolytes and the formation of a Solid Electrolyte Interphase (SEI) at the electrode surfaces hindering the electrochemical reactions. Moreover, manganese present in the cathode materials tends to dissolve in organic liquid electrolyte, especially at elevated temperature (Prabakar et al., 2012; Li et al., 2013). Hence, the high chemical stability of GPEs is interesting to be used as electrolyte materials particularly for cells involving LNMO.

Due to the stability in a wide potential window, polyethylene oxide (PEO) based electrolytes have been identified as potential polymer electrolytes for all-solid-state batteries (Goodenough and Singh, 2015; Long et al., 2016; Cheng et al., 2018). Of late polymethyl methacrylate–polyethylene glycol (PMMA-PEG) has been reported to be an efficient polymer electrolyte for the fabrication of complete all-solid-state microbatteries (Plylahan et al., 2014). Here, PEG serves as the ionic medium for the Li ion conduction while PMMA contributes to the mechanical stability. To improve the performance of the LIBs that employ polymer electrolytes, it is crucial to enhance the surface contact established between the porous electrodes and the electrolyte. The electrodeposition technique is an effective bottom-up approach to optimize the electrode/electrolyte interface. Previous reports have reported the conformal electrodeposition of this polymer electrolyte in self-organized titania nanotubes (TiO₂ nts) and its benefit on the capacity of the microbattery (Kyeremateng et al., 2011; Plylahan et al., 2012, 2015). We recently showed the positive influence of this approach for a microbattery based on polymer electropolymerized in TiO₂ nts and LNMO (Salian et al., 2017). While the electrodeposition of the polymer electrolyte in TiO₂ nts allows the improvement of the cell capacity, applying the same treatment to the LNMO cathode revealed the doubling of the capacity and an increase of the energy density due to a slight increase of the operating voltage. In this work, we study in details the electrodeposition of PMMA-PEG in porous LNMO to get a better insight into the key role of the interface on the performance of all-solid-state Li-ion microbatteries.

EXPERIMENTAL

Synthesis of LNMO Cathode and TiO₂ nts Anode

Porous LNMO serving as cathode was synthesized by a sol-gel technique as described by Cui et al. (2011). The synthesized LNMO was then mixed with carbon black (Super P) and Polyvinylidene fluoride (PVDF) in the ratio of 75:15:10 and grounded in a mortar for 15 min. The ground powder was then mixed with N-methyl-2-pyrrolidone (NMP) to obtain a paste that was subsequently spread on an aluminum disk with a diameter of 8 mm. The electrode was dried under vacuum at 110°C for 8 h.

The TiO₂ nts serving as anode was synthesized by the anodization of a titanium foil. Before anodization, the Ti foils (99.6% purity Goodfellow and 0.125 mm thickness) were cleaned and sonicated in acetone, isopropanol, and methanol for 10 min each. After drying the foils under compressed air, anodization of the cleaned Ti foil was carried out in an electrolyte containing 96.7 wt. % glycerol, 1.3 wt. % NH₄F, and 2 wt. % water. A constant voltage of 60 V was applied between the Ti substrate and a Pt foil (counter electrode) for 3 h using a generator (ISO-TECH IPS-603). Then, the sample was washed with deionized water and dried using compressed air. The as-formed TiO₂ nts were annealed in air at 450°C for 3 h to form the anatase phase. The TiO₂ nts obtained with these parameters exhibit a thickness of *c.a.* 1.5 μm and an outer diameter of 100 nm as it has been reported elsewhere (Plylahan et al., 2015).

Electropolymerization (EP) of the Electrolyte Into LNMO

The electrodeposition of PMMA-PEG in porous LNMO was performed by cyclic voltammetry (CV) in a three-electrode system using a VersaSTAT 3 potentiostat (Princeton Applied Research), Ag/AgCl (3M KCl) as the reference and Pt electrode as the counter electrode in an aqueous solution containing 0.5 M of bis(trifluoromethanesulfone)imide (LiTFSI) and 0.5 M MMA-PEG (methyl methacrylate–polyethylene glycol) with an average molecular weight of 500 g mol^{−1} [MMA-PEG (500)]. Prior to electropolymerization, the aqueous solution containing the polymer electrolyte was purged with Argon gas for 10 min to remove dissolved oxygen. The cyclic voltammetry experiments were carried out at room temperature for 5, 10, 25, 50, and 100 cycles at the scan rate of 10 mV s^{−1} in the potential window of −0.35 to −1 V vs. Ag/AgCl (3 M KCl). The electropolymerized LNMO electrode was then dried in vacuum at 70°C for 18 h. In this work, the number of electropolymerization cycle will be referred to as “x EP cycles.” The electropolymerized LNMO at “x EP cycles” is designated as LNMO_(xEP), where x = 5, 10, 25, 50, and 100 EP cycles.

Material and Electrochemical Characterizations

For electrochemical experiments performed in Swagelok-type half cells, the electrolyte consisted in two sheets of gel polymer that were prepared by soaking a Whatman paper disk in 70 μL of a solution of 0.5 M LiTFSI in 2 ml MMA-PEG (500) and then drying them overnight at 70°C under vacuum. For the CV and Electrochemical Impedance Spectroscopy (EIS) measurements on bare and electropolymerized LNMO, the samples were assembled in a three-electrode configuration with two lithium foils serving as reference and counter electrodes. CV measurements were performed in the range of 2.7–4.8 V at different scan rates (0.1, 0.2, 0.75, and 1 mV s^{−1}) successively for 5 cycles each. EIS measurements were performed in the range of 10 mHz–100 kHz with an amplitude of 10 mV at Open Circuit Voltage (OCV). For electrochemical experiments performed in Swagelok-type full cells, electropolymerized LNMO and as-formed TiO₂ nts electrodes were assembled in a two-electrode

configuration using a Whatman paper soaked with the polymer electrolyte. To fabricate the full all-solid-state microbattery, 7 μl of the polymer electrolyte was drop casted at the surface of the TiO_2 nts electrode. The sample was then dried again at 70°C for 18 h to obtain a homogeneous polymer thin film. The electropolymerized LNMO that was prior deposited on the aluminum disk was then pressed together with the polymer-coated TiO_2 nts. The wire connections were established at the backside of each current collector using a silver conductive paste. All electrochemical cells were assembled in an argon filled glovebox (MBraun, Germany) with <0.5 ppm H_2O and <0.5 ppm O_2 atmosphere.

Galvanostatic charge/discharge profiles and EIS measurements were performed using a VMP3 potentiostat-galvanostat (Bio Logic). The Scanning Electron Microscopy (SEM) images were obtained using a CARL ZEISS/Ultra 55 Scanning electron microscope.

RESULTS AND DISCUSSIONS

Figure 1A shows the SEM images of the as synthesized LNMO powder. The particle size varies from 100 nm to $1\ \mu\text{m}$. The powder is characterized by porous morphology. This is an advantage as pores promote the percolation of the electrolyte (polymer/liquid) in the bulk material. The electropolymerization of MMA-PEG (500) monomer in the presence of the LiTFSI salt was carried out by cyclic voltammetry. The cyclic voltammograms recorded for LNMO composite cathode electropolymerized up to 100 cycles are shown in **Figure 1B**. The cathodic current density measured at $-1\ \text{V}$ vs. Ag/AgCl decreases with the number of cycles. The polymer deposition occurs due to the formation of hydrogen free radicals generated by the reduction of protons as it has been reported for electropolymerization on TiO_2 nanotubes by our research group (Cram et al., 2002; Plylahan et al., 2012; Salian et al., 2017). Thus, the decrease of the cathodic current density with increment in cycle number can be attributed to the formation of successive thin polymer layers acting as an electronic insulator.

The relative high cathodic current densities observed for the first cycles are in accordance with the high rugosity of the cathode. This suggests that the polymer layer formed at the initial

EP cycles (up to 10 cycles) follows the rugosity of the LNMO electrode (**Figure 2A**), which is in agreement with the SEM images given in **Figures 2B,C**. But a thin polymer layer filling the pores has grown beyond 25 EP cycles (**Figures 2D,E**). For 100 EP cycles, the SEM image reveals that the porous LNMO electrode is completely covered by a smooth layer of polymer (**Figure 2F**). It can be noted that compared to TiO_2 nts, the cathodic current density recorded for porous LNMO shows a decrease (ca. 80%) with the increasing number of cycles (Salian et al., 2017), which may indicate that the electropolymerization results in a thicker layer than that grown on nanotubes.

The electrochemical reactions of $\text{LNMO}_{(\text{EP})}$ samples with Li were studied by cyclic voltammetry. **Figure 3** shows the 1st CV curves obtained in a potential range of $2.7\text{--}4.8\ \text{V}$ vs. Li^+/Li at a scan rate of $0.1\ \text{mV s}^{-1}$. For the bare LNMO sample, the two oxidation peaks appear at 2.9 V and 4.06 V while the reduction peaks are visible at 4.26 V and 3.93 V. These results are similar to the behavior of LNMO in liquid electrolyte for which a main peak attributed to the transition of $\text{Mn}^{3+}/\text{Mn}^{4+}$ is observed at around 4 V and another small peak corresponding to $\text{Ni}^{2+}/\text{Ni}^{4+}$ transition can be found at around 4.7 V (Kunduraci and Amatucci, 2008). The shift in the peaks could be attributed to the lower ionic conductivity of the polymer electrolyte compared to that of liquid electrolyte resulting in ohmic drop effects (Nayak et al., 2014). The CV curves for $\text{LNMO}_{(5\text{EP})}$, $\text{LNMO}_{(10\text{EP})}$, $\text{LNMO}_{(25\text{EP})}$, and $\text{LNMO}_{(50\text{EP})}$ show a reduction peak at $\sim 2.95\ \text{V}$, which fades as the number of EP cycles increases. There is an oxidation signal that also fades with the increasing number of EP cycles but no peak is present. Moreover, the $\text{LNMO}_{(100\text{EP})}$ shows no significant redox peaks in the CV. The decrease in current densities with increase of the number of EP cycles is consistent with the ohmic drop effect, which is due to the increase of the polymer thickness.

Bare LNMO and $\text{LNMO}_{(\text{EP})}$ electrodes were characterized by EIS tests at OCV. **Figure 4** shows the EIS plots obtained in a frequency range of 100 kHz–10 mHz at an amplitude of 10 mV. The experimental data were fitted using the equivalent circuit mentioned in **Table 1**. Here, R_{elec} is the electrolyte resistance that can be expressed by Equation (1):

$$R_{\text{elec}} = R_{\text{EP}} + R_{\text{separator}} \quad (1)$$

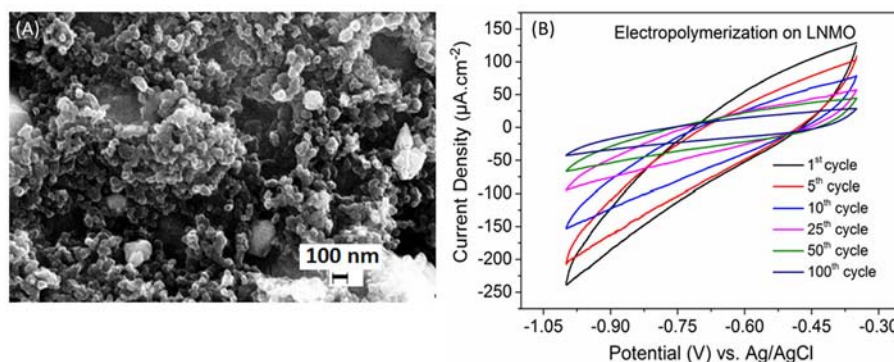


FIGURE 1 | (A) SEM image of the synthesized porous LNMO powder. **(B)** Cyclic voltammograms of the PMMA-PEG electropolymerization on LNMO in the potential window -0.35 to $-1\ \text{V}$ at a scan rate of $10\ \text{mV s}^{-1}$.

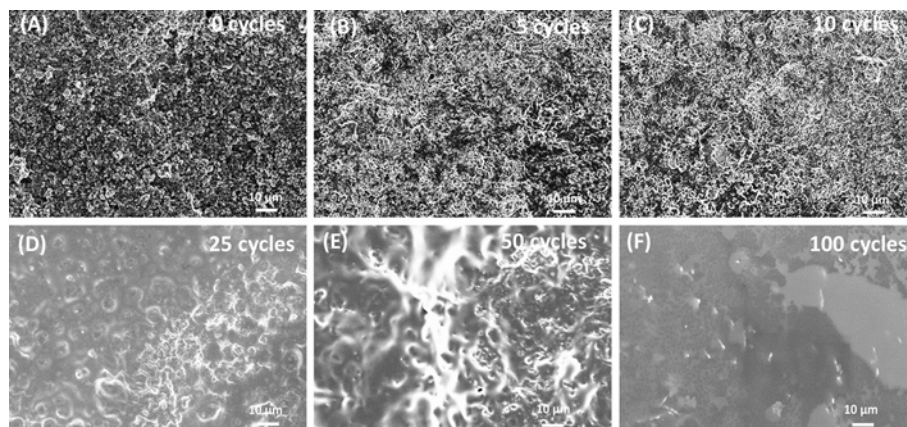


FIGURE 2 | SEM images of electrodeposited PMMA-PEG on porous LNMO by CV at (A) 0 cycle; (B) 5 cycles; (C) 10 cycles; (D) 25 cycles; (E) 50 cycles; (F) 100 cycles.

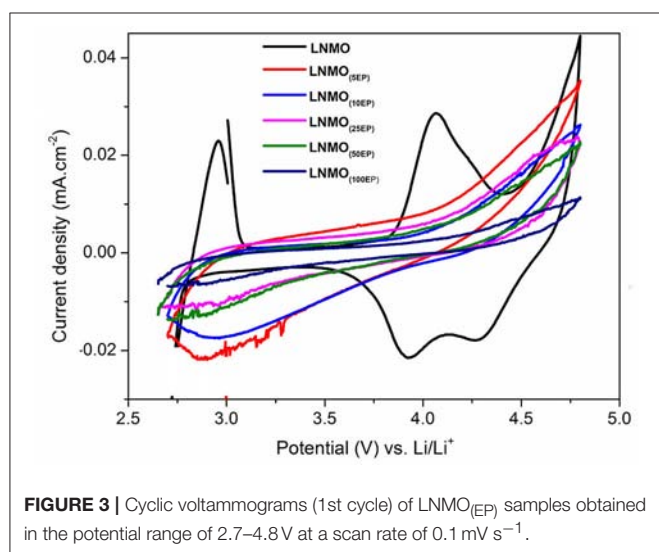


FIGURE 3 | Cyclic voltammograms (1st cycle) of LNMO_(EP) samples obtained in the potential range of 2.7–4.8 V at a scan rate of 0.1 mV s⁻¹.

where R_{EP} and $R_{separator}$ are the respective contributions of the electrodeposited polymer thin layer and the separator (i.e., the polymer embedded in the Whatman paper). R_{CEI} takes into account the formation of a SEI thin film on the LNMO surface, so-called cathode electrolyte interphase (CEI) (Nayak et al., 2014; Kohs et al., 2017). R_{CT} refers to the interfacial property of the charge transfer resistance. Q_{CEI} , Q_{DL} , and Q are the associated constant phase elements (CPE) with the respective resistances, used in order to account for the porous nature of the electrodes. The equivalent circuit for the EIS spectra of bare LNMO, LNMO_(5EP), LNMO_(10EP), and LNMO_(25EP) (Figure 4A) is $[R_{elec} + Q_{CT}/(R_{CT}+Q)]$. The high frequency limit of the impedance intercepts the x-axis and corresponds to the electrolyte resistance. Still at high frequencies, when it decreases, a short slope change is observed (Figure 4B). This might be due to the porous nature of the material or to contact resistances (current collector, interparticles) in the

electrode (Lasia, 2002; Levi et al., 2014). The main semicircle in the medium frequency and the sloped line in the lower frequency are attributed, respectively, to the charge transfer resistance and the capacitive limit behavior. The equivalent circuit for the EIS spectra of LNMO_(50EP) and LNMO_(100EP) is $[R_{elec} + Q_{CEI}/R_{CEI} + Q_{DL}/R_{CT}]$. In addition to the previously mentioned high frequency features, there are 2 semicircles in the medium and low frequencies. The 1st semicircle can be attributed to the resistance due to the CEI formation while the 2nd semicircle can be attributed to the charge transfer resistance at the interface.

Figure 4E shows the evolution of R_{elec} with the number of EP cycles. It globally increases from bare LNMO to LNMO_(100EP). However, we note that there is a decrease of R_{elec} between the LNMO_(5EP) and LNMO_(25EP). For these latter layers, the porosity of the LNMO is not fully filled by the electropolymer. If we consider that $R_{separator}$ is constant, R_{elec} evolution should come from R_{EP} , the contribution of the electropolymer deposited after successive EP cycles. For LNMO_(10EP) and LNMO_(25EP), the electropolymer layer is still very thin so R_{EP} is negligible. But, as it tends to covers the active surface of LNMO, this probably decreases the resistance due to the interface between the electropolymer and the separator. Thereafter, as the electropolymer thin-film grows after the complete pore filling, its thickness becomes less negligible. Thus, R_{EP} and then R_{elec} steadily increases for the LNMO_(50EP) and LNMO_(100EP).

The semicircle corresponding to R_{CEI} is not seen for bare LNMO, LNMO_(5EP), LNMO_(10EP), and LNMO_(25EP). Or there could be a possible superposition of R_{CEI} with R_{CT} (Aurbach et al., 2002). Thus, very thin CEI layers could be grown on the rough LNMO surface without any specific features on the EIS spectra. In the case of LNMO_(50EP) and LNMO_(100EP), the first semicircle that appeared at high frequencies was associated to a more prominent contribution of the CEI. Indeed, the formation of CEI could occur as the active surface area of the LNMO is more coated by the polymer. Regarding the charge transfer resistance R_{CT} , it increases with the number of EP cycles. It

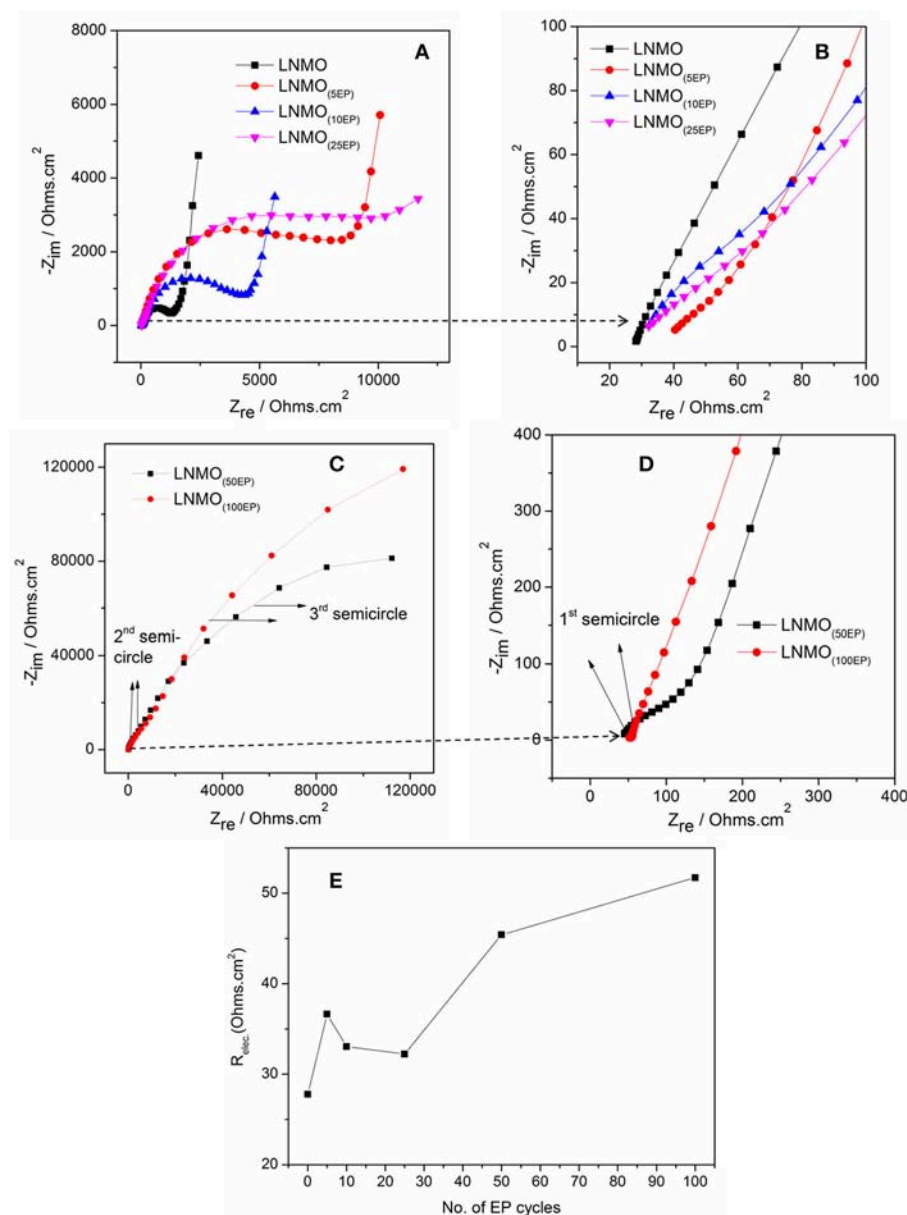


FIGURE 4 | EIS spectra of (A) bare LNMO, LNMO_(5EP), LNMO_(10EP), LNMO_(25EP); (B) 1st semicircles of the same samples at very high frequencies; (C) EIS spectra of LNMO_(50EP) and LNMO_(100EP); (D) 1st semicircles of the same samples at very high frequencies; (E) relationship between R_{elec} and the number of EP cycles. The EIS tests were performed at OCV in the frequency range of 100 kHz–10 mHz at an amplitude of 10 mV.

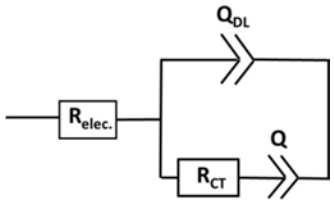
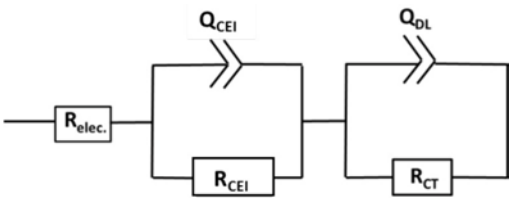
suggests that the kinetic reactions at the interface are limited by the electrodeposited polymer, which is coherent with the evolution of the CV peaks. The large increase in the charge transfer resistance R_{CT} for LNMO_(50EP) and LNMO_(100EP) could therefore be attributed to the gradual decomposition of the polymer with cycling as it has been suggested (Pylahan et al., 2015).

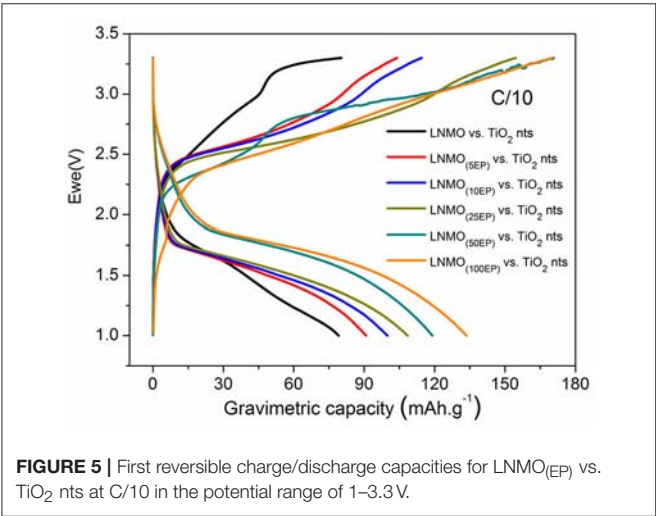
To investigate the performance of LNMO_(EP) electrodes in a full cell configuration, the different LNMO_(EP) electrodes were assembled with self-supported TiO₂ nts negative electrode.

Herein the mass limitation is controlled by the TiO₂ nts. **Figure 5** shows evolutions of the first reversible cycle of the full microbatteries.

We can clearly see that the polymer electrolyte deposition has a gradual positive influence on the discharge capacity values of the complete cells. Indeed, the capacity increases from 80 mAh g⁻¹ for non-modified electrodes to 134 mAh g⁻¹ for LNMO_(100EP). Even if the internal resistance of the battery increases with the polymer thickness, the active surface of the material in contact with the electrolyte is significantly enhanced,

TABLE 1 | EIS parameters obtained after fitting with the equivalent circuits for the polymer-coated LNMO_(EP).

	$R_{elec.} (\Omega.cm^{-2})$	$R_{CEI} (\Omega.cm^{-2})$	$R_{CT} (\Omega.cm^{-2})$	Deviations	χ^2 value
Equivalent circuit					
Bare LNMO	27.79	—	1,387	0.5	0.03
LNMO _(5EP)	36.64	—	3,811	0.8	0.06
LNMO _(10EP)	33.06	—	3,097	1.1	0.03
LNMO _(25EP)	32.24	—	7,620	1.2	0.04
Equivalent circuit					
LNMO _(50EP)	45.41	1,718	240,000	0.5	0.02
LNMO _(100EP)	51.72	4,826	421,000	0.7	0.02



promoting the reversible insertion of Li⁺. Also remarkably, the operating voltage of the cell is slightly increasing. This effect contributes to the improvement of the energy and power densities.

The LNMO_(100EP) cathode was used to fabricate an all-solid-state microbattery. The microbattery is designated as TiO₂nts/Polymer/LNMO_(100EP). **Figure 6A** shows the galvanostatic charge/discharge profile of the all-solid-state microbattery in the potential window of 1–3.3 V at C/10 for 10 cycles. Such a microbattery shows an operating voltage at 1.8 V. As the limiting reactant material of the microbattery is TiO₂ nts, the capacity is reported vs. the anode mass and its

geometrical surface. The mass was calculated considering a density of 4.23 g cm⁻³ and a porosity of 60% (Pylahan et al., 2014). The microbattery shows a first discharge capacity of 122 mA h g⁻¹ (60 μAh cm⁻² μm⁻¹). The coulombic efficiency (CE) for the first cycle corresponds to 72%. The discharge capacity for the 10th cycles is 89 mA h g⁻¹ (44 μAh cm⁻² μm⁻¹). The corresponding CEs from 2nd to 10th cycle are about ~85%. The capacity retention of the microbattery up to the 10th cycle corresponds to 72%. The charge/discharge curves for this self-standing microbattery shows similar characteristic to that of the full cell swagelok tests as discussed in **Figure 5**. The irreversible capacity loss occurring in the first cycle could be due to the residual water content present in both LNMO and TiO₂ nts and/or the presence of structural defects trapping irreversibly Li⁺ (Ortiz et al., 2009). The capacity retention for the 10th cycle corresponds to 72%. **Figure 6B** shows the cross-section image of this microbattery consisting of TiO₂ nts (1.5 μm long) supported on the Ti foil (current collector), the drop cast of the polymer electrolyte layer (ca. 200 μm) and the LNMO_(100EP) cathode (ca. 20 μm). The Al cathode current collector was removed on top of the assembly to facilitate imaging of the cathode. The ohmic drop due to the electropolymer in the LNMO_(EP) increases the overvoltage and hence has an influence on the operating voltage of the microbattery.

Figure 7 shows the cycling performance of TiO₂ nts/Polymer/LNMO_(100EP) at different C-rates for 50 cycles. At C/10, though there is a capacity decrease rapidly, it comparatively stabilizes at 89 mAh g⁻¹ (41 μAh cm⁻² μm⁻¹). The microbattery delivers ~75 mA h g⁻¹ (29 μAh cm⁻² μm⁻¹) at C/5 rate and ~47 mAh g⁻¹ (15 μAh cm⁻² μm⁻¹) at C/2 rate.

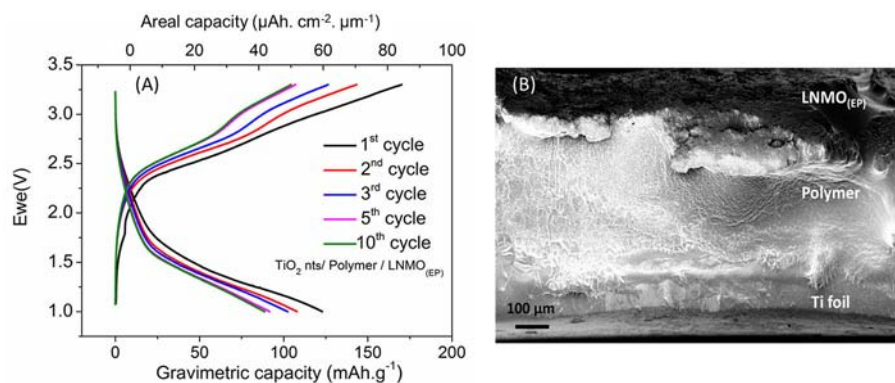


FIGURE 6 | (A) Galvanostatic charge/discharge profile of TiO_2 nts/Polymer/LNMO_(100EP) microbattery at C/10 rate; **(B)** cross-sectional SEM image of the all-solid-state battery composed of LNMO_(100EP)/Polymer/ TiO_2 nts.

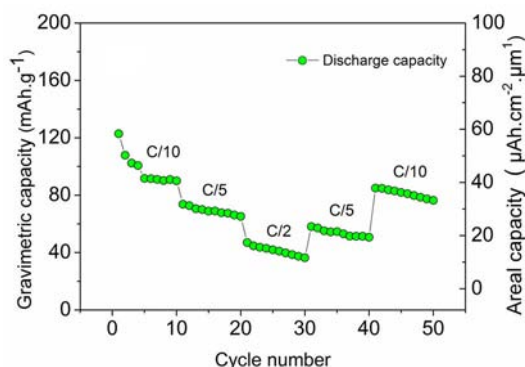


FIGURE 7 | Discharge capacity of the microbattery TiO_2 nts/Polymer/LNMO_(100EP) at multi-C rates.

The microbattery retains comparable capacities of $\sim 60 \text{ mAh g}^{-1}$ ($22 \mu\text{Ah cm}^{-2} \mu\text{m}^{-1}$) at C/5 and $\sim 85 \text{ mAh g}^{-1}$ ($37 \mu\text{Ah cm}^{-2} \mu\text{m}^{-1}$) at C/10 rates. The energy and power densities obtained from such microbatteries are comparable to the performance of the prevalent 3D electrodes based microbatteries and commercial products (Pikul et al., 2013).

CONCLUSIONS

Electrodeposition of PMMA-PEG electrolyte is studied into porous LNMO cathode electrode. SEM images reveal that the deposition follows and fills the porosity of the layer. These results

have been supported by the impedance measurements suggesting the increase in the overall impedance with the formation of the insulating polymer thin layer with successive cycles of electropolymerization. Swagelok full-cell tests of the LNMO_(EP) vs. TiO_2 nts revealed the capacity increase with the polymer thickness, a clear indication of a significant improvement of the electrode-electrolyte interface. Finally an all-solid-state microbattery has been fabricated using the polymer-coated LNMO_(100EP) as the cathode and TiO_2 nts as the anode. Such a microbattery delivered an initial capacity of 122 mA h g^{-1} ($57 \mu\text{Ah cm}^{-2} \mu\text{m}^{-1}$), with a capacity retention of 72% up to 10 cycles. These kind of microbatteries are stable and can be tested at different kinetics over 50 cycles. The electrochemical performances of these microbatteries are comparable with other micropower sources involving different 3D nanostructured electrodes.

AUTHOR CONTRIBUTIONS

GS did experimental works, AG and AK discussed the results and participated to the writing, CL and TD supervised the work.

ACKNOWLEDGMENTS

This work has been carried out thanks to the support of the A*MIDEX project (n° ANR-11-IDEX-0001-02) funded by the Investissements d'Avenir French government program, managed by the French National Research Agency (ANR).

REFERENCES

- Arthur, T. S., Bates, D. J., Cirigliano, N., Johnson, D. C., Malati, P., Mosby, J. M., et al. (2011). Three-dimensional electrodes and battery architectures. *MRS Bull.* 36, 523–531. doi: 10.1557/mrs.2011.156
- Aurbach, D., Nimberger, A., Markovsky, B., Levi, E., Sominski, E., and Gedanken, A. (2002). Nanoparticles of SnO produced by sonochemistry as anode materials for rechargeable lithium batteries. *Chem. Mater.* 14, 4155–4163. doi: 10.1021/cm021137m
- Bernhard, R., Latini, A., Panero, S., Scrosati, B., and Hassoun, J. (2013). Poly(ethyleneglycol)dimethylether-lithium bis(trifluoromethanesulfonyl) imide, PEG500DME-LiTFSI, as high viscosity electrolyte for lithium ion batteries. *J. Power Sour.* 226, 329–333. doi: 10.1016/j.jpowsour.2012.10.059

- Chen, T., Liao, Y., Yang, L., Li, X., and Li, W. (2015). Improved performance of $\text{LiNi}_0.5\text{Mn}_1.5\text{O}_4$ cathode for high-voltage lithium-ion battery at elevated temperature by using gel polymer electrolyte. *Ionics* 21, 2457–2463. doi: 10.1007/s11581-015-1424-0
- Cheng, X., Pan, J., Zhao, Y., Liao, M., and Peng, H. (2018). Gel Polymer Electrolytes for Electrochemical Energy Storage. *Adv. Energy Mater.* 8:201702184. doi: 10.1002/aenm.201702184
- Cram, S. L., Spinks, G. M., Wallace, G. G., and Brown, H. R. (2002). Mechanism of electropolymerisation of methyl methacrylate and glycidyl acrylate on stainless steel. *Electrochim. Acta* 47, 1935–1948. doi: 10.1016/S0013-4686(02)00097-X
- Cui, Y. L., Sun, Z., and Zhuang, Q. C. (2011). Electrochemical properties of a 4.7 V-class $\text{LiNi}_0.5\text{Mn}_1.5\text{O}_4$ positive electrode material for high power Li-ion battery. *J. Inorg. Organomet. Polym. Mater.* 21, 893–899. doi: 10.1007/s10904-011-9523-5
- Ellis, B. L., Knauth, P., and Djenizian, T. (2014). Three-dimensional self-supported metal oxides for advanced energy storage. *Adv. Mater.* 26, 3368–3397. doi: 10.1002/adma.201306126
- Fergus, J. W. (2010). Recent developments in cathode materials for lithium ion batteries. *J. Power Sour.* 195, 939–954. doi: 10.1016/j.jpowsour.2009.08.089
- Ferrari, S., Loveridge, M., Beattie, S. D., Jahn, M., Dashwood, R. J., and Bhagat, R. (2015). Latest advances in the manufacturing of 3D rechargeable lithium microbatteries. *J. Power Sour.* 286, 25–46. doi: 10.1016/j.jpowsour.2015.03.133
- Goodenough, J. B., and Singh, P. (2015). Review—solid electrolytes in rechargeable electrochemical cells. *J. Electrochem. Soc.* 162, A2387–A2392. doi: 10.1149/2.0021514jes
- Kang, K., Meng, Y. S., Bréger, J., Grey, C. P., and Ceder, G. (2006). Electrodes with high power and high capacity for rechargeable lithium batteries. *Science* 311, 977–980. doi: 10.1126/science.1122152
- Kohs, W., Kahr, J., Ahniyaz, A., Zhang, N., and Trifonova, A. (2017). Electrolyte-cathode interactions in 5-V lithium-ion cells. *J. Solid State Electrochem.* 21, 3389–3401. doi: 10.1007/s10008-017-3701-5
- Kunduraci, M., and Amatucci, G. G. (2008). The effect of particle size and morphology on the rate capability of 4.7 V $\text{LiMn}_1.5+\delta\text{Ni}_0.5-\delta\text{O}_4$ spinel lithium-ion battery cathodes. *Electrochim. Acta* 53, 4193–4199. doi: 10.1016/j.electacta.2007.12.057
- Kyeremateng, N. A., Dumur, F., Knauth, P., Pecquenard, B., and Djenizian, T. (2011). Electropolymerization of copolymer electrolyte into titania nanotube electrodes for high-performance 3D microbatteries. *Electrochem. Commun.* 13, 894–897. doi: 10.1016/j.elecom.2011.03.026
- Lasia, A. (2002). *Electrochemical Impedance Spectroscopy and its Applications*. New York, NY: Springer. doi: 10.1007/0-306-46916-2_2
- Levi, M. D., Dargel, V., Shilina, Y., Aurbach, D., and Halalay, I. C. (2014). Impedance spectra of energy-storage electrodes obtained with commercial three-electrode cells: some sources of measurement artefacts. *Electrochim. Acta* 149, 126–135. doi: 10.1016/j.electacta.2014.10.083
- Li, B., Xing, L., Xu, M., Lin, H., and Li, W. (2013). New solution to instability of spinel $\text{LiNi}_0.5\text{Mn}_1.5\text{O}_4$ as cathode for lithium ion battery at elevated temperature. *Electrochem. Commun.* 34, 48–51. doi: 10.1016/j.elecom.2013.05.022
- Long, L., Wang, S., Xiao, M., and Meng, Y. (2016). Polymer electrolytes for lithium polymer batteries. *J. Mater. Chem. A* 4, 10038–10039. doi: 10.1039/c6ta02621d
- Lopez, M. C., Ortiz, G. F., Gonzalez, J. R., Alcantara, R., and Tirado, J. L. (2014). Improving the performance of titania nanotube battery materials by surface modification with lithium phosphate. *ACS Appl. Mater. Inter.* 6, 5669–5678. doi: 10.1021/am500189h
- Nayak, P. K., Grinblat, J., Levi, M., and Aurbach, D. (2014). Electrochemical and structural characterization of carbon coated $\text{Li}_1.2\text{Mn}_0.56\text{Ni}_0.16\text{Co}_0.08\text{O}_2$ and $\text{Li}_1.2\text{Mn}_0.6\text{Ni}_0.2\text{O}_2$ cathode materials for Li-ion batteries. *Electrochim. Acta* 137, 546–556. doi: 10.1016/j.electacta.2014.06.055
- Ohzuku, T., Nagayama, M., Tsuji, K., and Ariyoshi, K. (2011). High-capacity lithium insertion materials of lithium nickel manganese oxides for advanced lithium-ion batteries: toward rechargeable capacity more than 300 mA h g⁻¹. *J. Mater. Chem.* 21, 10179–10188. doi: 10.1039/c0jm04325g
- Ortiz, G. F., Cabello, M., Lopez, M. C., Tirado, J. L., McDonald, M. J., and Yang, Y. (2016a). Exploring a Li-ion battery using surface modified titania nanotubes versus high voltage cathode nanowires. *J. Power Sour.* 303, 194–202. doi: 10.1016/j.jpowsour.2015.10.104
- Ortiz, G. F., Hanzu, I., Djenizian, T., Lavela, P., Tirado, J. L., and Knauth, P. (2009). Alternative Li-ion battery electrode based on self-organized titania nanotubes. *Chem. Mater.* 21, 63–67. doi: 10.1021/cm801670u
- Ortiz, G. F., Lopez, M. C., Li, Y. X., McDonald, M. J., Cabello, M., Tirado, J. L., et al. (2016b). Enhancing the energy density of safer Li-ion batteries by combining high-voltage lithium cobalt fluorophosphate cathodes and nanostructured titania anodes. *Sci. Rep.* 6:20656. doi: 10.1038/srep20656
- Pikul, J. H., Gang Zhang, H., Cho, J., Braun, P. V., and King, W. P. (2013). High-power lithium ion microbatteries from interdigitated three-dimensional bicontinuous nanoporous electrodes. *Nat. Commun.* 4:2747. doi: 10.1038/ncomms2747
- Pylahan, N., Kyeremateng, N. A., Eyraud, M., Dumur, F., Martinez, H., Santinacci, L., et al. (2012). Highly conformal electrodeposition of copolymer electrolytes into titania nanotubes for 3D Li-ion batteries. *Nanoscale Res. Lett.* 7, 1–11. doi: 10.1186/1556-276X-7-349
- Pylahan, N., Letiche, M., Barr, M. K. S., and Djenizian, T. (2014). All-solid-state lithium-ion batteries based on self-supported titania nanotubes. *Electrochem. Commun.* 43, 121–124. doi: 10.1016/j.elecom.2014.03.029
- Pylahan, N., Letiche, M., Samy Barr, M. K., Ellis, B., Maria, S., Phan, T. N. T., et al. (2015). High energy and power density TiO_2 nanotube electrodes for single and complete lithium-ion batteries. *J. Power Sour.* 273, 1182–1188. doi: 10.1016/j.jpowsour.2014.09.152
- Prabakar, S. J. R., Han, S. C., Singh, S. P., Lee, D. K., Sohn, K. S., and Pyo, M. (2012). W-doped $\text{LiW}_x\text{Ni}_{0.5}\text{Mn}_{1.5-x}\text{O}_4$ cathodes for the improvement of high rate performances in Li ion batteries. *J. Power Sour.* 209, 57–64. doi: 10.1016/j.jpowsour.2012.02.053
- Roberts, M., Johns, P., Owen, J., Brandell, D., Edstrom, K., El Enany, G., et al. (2011). 3D lithium ion batteries - from fundamentals to fabrication. *J. Mater. Chem.* 21, 9876–9890. doi: 10.1039/c0jm04396f
- Salian, G. D., Lebouin, C., Demoulin, A., Lepihin, M. S., Maria, S., Galeyeva, A. K., et al. (2017). Electrodeposition of polymer electrolyte in nanostructured electrodes for enhanced electrochemical performance of thin-film Li-ion microbatteries. *J. Power Sour.* 340, 242–246. doi: 10.1016/j.jpowsour.2016.11.078
- Shaijumon, M. M., Perre, E., Daffos, B., Taberna, P. L., Tarascon, J. M., and Simon, P. (2010). Nanoarchitected 3D cathodes for Li-ion microbatteries. *Adv. Mater.* 22, 4978–4981. doi: 10.1002/adma.201001922
- Sun, P., Liao, Y., Xie, H., Chen, T., Rao, M., and Li, W. (2014). Poly(methyl methacrylate-acrylonitrile-ethyl acrylate) terpolymer based gel electrolyte for $\text{LiNi}_0.5\text{Mn}_1.5\text{O}_4$ cathode of high voltage lithium ion battery. *J. Power Sour.* 269, 299–307. doi: 10.1016/j.jpowsour.2014.07.014
- Sun, Y. K., Chen, Z., Noh, H. J., Lee, D. J., Jung, H. G., Ren, Y., et al. (2012). Nanostructured high-energy cathode materials for advanced lithium batteries. *Nat. Mater.* 11, 942–947. doi: 10.1038/nmat3435
- Sun, Y. K., Myung, S. T., Park, B. C., Prakash, J., Belharouak, I., and Amine, K. (2009). High-energy cathode material for long-life and safe lithium batteries. *Nat. Mater.* 8, 320–324. doi: 10.1038/nmat2418

Conflict of Interest Statement: The authors declare that the research was conducted in the absence of any commercial or financial relationships that could be construed as a potential conflict of interest.

Copyright © 2019 Salian, Lebouin, Galeyeva, Kurbatov and Djenizian. This is an open-access article distributed under the terms of the Creative Commons Attribution License (CC BY). The use, distribution or reproduction in other forums is permitted, provided the original author(s) and the copyright owner(s) are credited and that the original publication in this journal is cited, in accordance with accepted academic practice. No use, distribution or reproduction is permitted which does not comply with these terms.



Magnetic Characteristics of Ni-Filled Luminescent Porous Silicon

Petra Granitzer^{1*}, Klemens Rumpf¹, Peter Poelt² and Michael Reissner³

¹ Institute of Physics, University of Graz, Graz, Austria, ² Institute for Electron Microscopy, University of Technology Graz, Graz, Austria, ³ Institute of Solid State Physics, Vienna University of Technology, Vienna, Austria

OPEN ACCESS

Edited by:

Thierry Djenizian,
École des Mines de Saint-Étienne -
Campus Georges Charpak Provence,
France

Reviewed by:

Guido Mula,
Università degli Studi di Cagliari, Italy
Nobuyoshi Koshida,
Tokyo University of Agriculture and
Technology, Japan

*Correspondence:

Petra Granitzer
petra.granitzer@uni-graz.at

Specialty section:

This article was submitted to
Chemical Engineering,
a section of the journal
Frontiers in Chemistry

Received: 20 September 2018

Accepted: 14 January 2019

Published: 29 January 2019

Citation:

Granitzer P, Rumpf K, Poelt P and
Reissner M (2019) Magnetic
Characteristics of Ni-Filled
Luminescent Porous Silicon.
Front. Chem. 7:41.
doi: 10.3389/fchem.2019.00041

The aim of the presented work is to combine luminescent porous silicon (PSi) with a ferromagnetic metal (Ni) to modify on the one hand the photoluminescence by the presence of metal deposits and on the other hand to influence the optical properties by an external magnetic field. The optical properties are investigated especially with respect to the wavelength-shift of the photoluminescence due to the metal filling. With increasing metal deposits within PSi the photoluminescence peak is blue-shifted and furthermore an increase of the intensity is observed. Photoluminescence spectra of bare PSi show a maximum around 620 nm whereas in the case of Ni filled samples the peak is blue-shifted to around 580 nm for a deposition time of 15 min. Field dependent magnetic measurements performed with an applied field parallel and perpendicular to the surface, respectively, show a magnetic anisotropy which is in agreement with a thin film. This film-like behavior is caused by the interconnected Ni structures due to the branched porous silicon morphology. The coercivity increases with increasing metal deposition from about 150 Oe to about 450 Oe and also the magnetic anisotropy is enhanced with the growth of metal deposits. Within this work the influence of the magnetic metal filling on the optical properties and the magnetic characterization of the nanocomposites are discussed. The presented systems give not only rise to optoelectronics applications but also to magneto optical integrated devices.

Keywords: porous silicon, photoluminescence, metal deposition, magnetic nanostructures, magnetic behavior

INTRODUCTION

Porous silicon in the nanoporous regime with pore diameters of 2–5 nm is known to emit light in the visible since 1990 (Canham, 1990) and it is still under intense investigation (Joo et al., 2016). The light emission can be classified mainly in three bands, the red-, the blue, and the infrared band (Canham, 1995). The origin of the red emission is explained by quantum confinement (Lehmann and Gösele, 1991), the blue emission occurs in oxidized samples (Kanemitsu et al., 1993) and is attributed either to defects in SiO₂ (Ito et al., 1992) or to OH groups adsorbed on structural defects in SiO₂ (Tamura et al., 1994). The infrared luminescence which is investigated less extensive is explained by mid-gap dangling bonds on the silicon nanocrystals (Koch et al., 1992).

Electroluminescence of porous silicon has been investigated (Koshida and Koyama, 1992) shortly after the observation of its photoluminescence (Canham, 1990), offering a similar spectrum to the light emission. The high surface area of this nanostructured material which depends on the morphology (nanoporous silicon ~1,000 m²/cm³, mesoporous silicon ~100 m²/cm³, macroporous silicon ~1 m²/cm³) makes it suitable for pore filling using various materials with specific properties

which opens the possibility to fabricate new nanocomposite materials with desired physical behavior. Metal filling of porous silicon firstly has been used in the 1990s to improve electrical contact to enhance the efficiency of the electroluminescence (Koshida et al., 1993; Li et al., 1994).

The main intention is to enhance the quantum yield of the photoluminescence. The efficiency of the luminescence generally is in the range of 1–10% without any further treatment of the samples. In the case of electroluminescence it is even reduced due to the absorption in the semitransparent metal layer. To enhance the luminescence of porous silicon various post-treatments of the samples have been performed such as high pressure water vapor annealing (HWA) a technique which is well-controlled (Gelloz et al., 2005) and can be used to get stable and highly efficient visible light emission. In this case the quantum efficiency is higher than 23%. Furthermore, it has been shown that this method leads to sufficiently passivated surfaces with low non-radiative defect density resulting in a stabilization of the samples. A further approach to influence the luminescence is the exploitation of surface plasmons of metal particles on the porous silicon surface as e.g., Au particles (De la Mora et al., 2014). Generally an emitter in the direct vicinity of a metal-dielectric interface couples to the plasmon mode because of the high optical density of states (Huck and Anderson, 2016). A blue shift of the porous silicon photoluminescence has been observed with decreasing particle size of Au nanoparticles which are deposited within the porous silicon (Amran et al., 2013).

Also the incorporation of Ni particles has been used to create new luminescent centers to achieve a luminescence enhancement (Amdouni et al., 2015). In the case of the utilization of magnetic particles not only the plasmon resonance of the metal can be used but also the magnetic properties can be utilized to explore magneto-optical properties of the nanocomposite. Systems for magneto-optical devices should offer on the one hand non-reciprocity which means that the time inverse symmetry is broken and on the other hand they should exhibit a memory effect. In the case of ferromagnetic structures the data can be memorized (Hu et al., 2016). Therefore, it is important to overcome a superparamagnetic behavior. Ni particles have been investigated with respect to the plasmon resonance showing its dependence on the size and shape but also on the surrounding medium (Sharma et al., 2017). This work aims to merge the optical properties of luminescent porous silicon and the magnetic properties of deposited magnetic nanostructures. Therefore, Ni is deposited within the porous silicon layer to exploit the plasmon resonance of the metal deposits to influence, especially to increase the photoluminescence. The photoluminescence as well as the magnetic properties are investigated with respect to the metal filling.

EXPERIMENTAL METHODS

The porous silicon is fabricated by anodization in a double tank cell of a moderately doped p-silicon wafer (8–12 Ωcm). The electrolyte consists of a hydrofluoric acid solution, consisting of distilled water, HF and ethanol in the ratio 1:1:2. A current

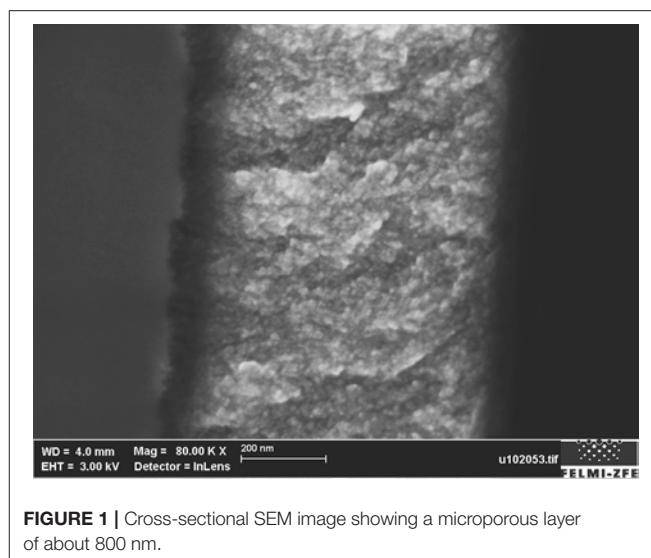


FIGURE 1 | Cross-sectional SEM image showing a microporous layer of about 800 nm.

density of 10 mAcm^{-2} is applied for 15 min resulting in a microporous layer with a thickness of about 800 nm (**Figure 1**). A mean pore diameter of about 5 nm is estimated from the optical investigations in using the following equation (Ossicini et al., 2003):

$$E = E_g + \frac{h^2}{8d^2} \left[\frac{1}{m_e^*} + \frac{1}{m_h^*} \right]$$

E , peak position of the photoluminescence

E_g , energy band gap of bulk silicon

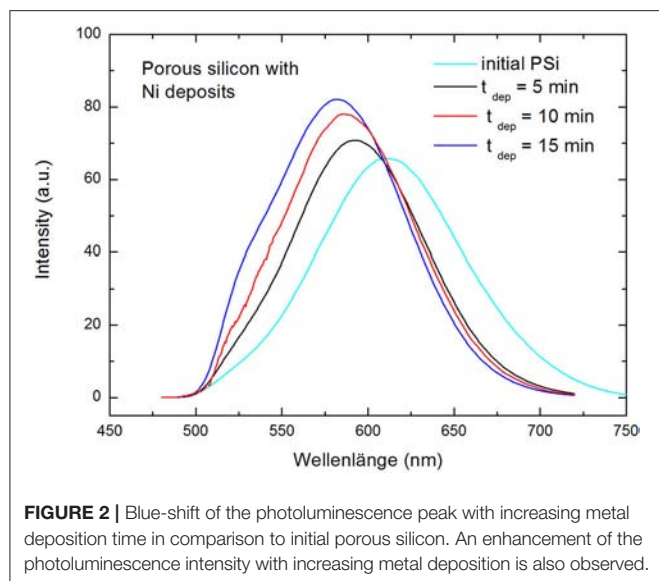
h , Planck's constant

m_e^* , effective mass of electron

m_h^* , effective mass of hole

The metal deposition (Ni) within the porous layer is performed by pulsed electrodeposition in using in the case of Ni a solution consisting of NiCl_2 and NiSO_4 , whereat H_3BO_3 acts as buffer. The Ni-deposition is carried out on different porous silicon samples offering an equal morphology by varying the deposition time between 5 min and 15 min. A current density of 10 mA/cm^2 with a frequency of 2 Hz is applied. The size of the deposited metal structures corresponds to the pore size of the porous silicon. Due to the interconnected morphology of microporous silicon also the Ni deposits offer interconnections rather than separated particles. From the knowledge of the Energy Dispersive X-Ray (EDX) spectra taken along the cross-section of porous silicon samples filled for 15 min with Ni the metal is deposited down to the pore tips.

First the optical properties of the luminescent PSi are investigated, especially the photoluminescence and the corresponding decay times, second Ni is electrochemically deposited in the porous silicon samples and subsequently the nanocomposite specimens are characterized optically and magnetically. The samples are structurally characterized by scanning electron microscopy (SEM) and Energy Dispersive



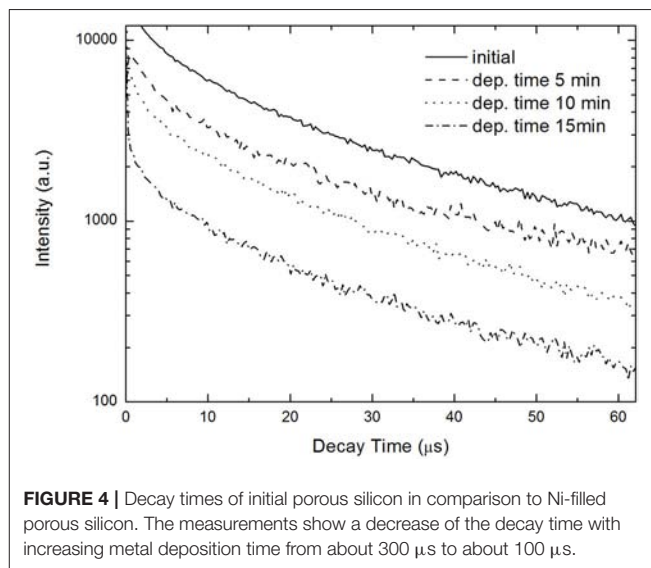
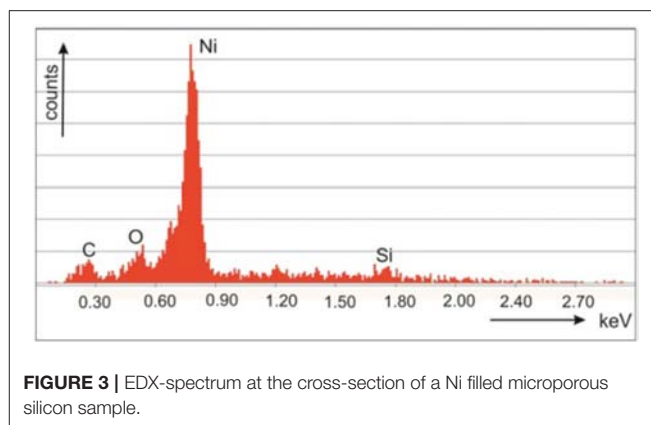
X-ray diffraction (EDX). The magnetic measurements are performed with a vibrating sample magnetometer (PPMS, Quantum Design).

RESULTS AND DISCUSSION

The optical properties are investigated especially with respect to the wavelength-shift of the photoluminescence (PL) due to the metal filling. Photoluminescence spectra of the used bare PSi show a maximum around 620 nm whereas in the case of Ni filled samples the peak can be blue-shifted to around 580 nm in using a metal deposition time of 15 min and the luminescence intensity is increased. **Figure 2** shows the comparison of the photoluminescence of initial porous silicon and Ni-filled samples with different metal deposition times. After a deposition time of 15 min EDX-spectra evidence Ni is deposited down to the bottom of the porous layer. All used samples offer the equal morphology which has been proved by investigating the photoluminescence before the Ni deposition. For the Ni deposition with various times always a current density of 10 mA/cm² with a frequency of 2 Hz is applied.

In **Figure 3** a cross-sectional EDX spectrum showing the Ni content of a sample prepared with a 15 min deposition time is presented. The decay times of the samples are measured with an excitation wavelength of 440 nm. The measurements show that the decay times of Ni-filled samples are faster than for the bare porous silicon (**Figure 4**) which indicates a decrease in the radiative life time with increasing metal filling. The decay time for initial porous silicon is around 300 μ s, for the sample filled with Ni for 5 min around 250 μ s, for a sample filled with Ni for 10 min about 150 μ s and for a 15 min Ni filled sample about 100 μ s.

In addition to the blue-shift of the PL-peak an increase of the luminescence intensity with increasing deposition time is observed which is shown in **Figure 5**. This result strongly indicates the involvement of Ni plasmons.



Concerning the magnetic properties of the nanocomposite the embedded Ni structures can be superparamagnetic from the size of the pore diameters which are around 5 nm (gained from optical measurements). Small separated magnetic particles of a few nanometers in size offer superparamagnetic behavior which can be figured out by temperature dependent measurements. From such measurements the transition temperature between superparamagnetic and blocked state can be determined. The transition temperature strongly depends on the particle size as well as on the proximity of the particles and thus their magnetic coupling. The investigated samples offer a branched morphology and therefore the achieved deposits tend to be interconnected and thus do not offer necessarily a superparamagnetic behavior. Temperature dependent magnetization measurements of the samples give no hint for superparamagnetism of the nanocomposite.

Field dependent magnetization measurements have been performed with a magnetic field applied parallel and perpendicular to the surface. In the case of isolated magnetic structures such measurements show a magnetic anisotropy

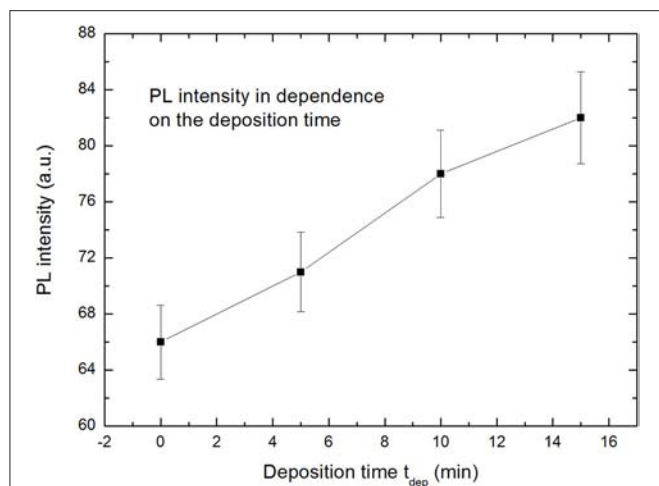


FIGURE 5 | With increasing metal (Ni) deposition time an increase of the photoluminescence intensity is observed which is attributed to the coupling between the emitter and the deposited metal structure (Granitzer et al., 2018).

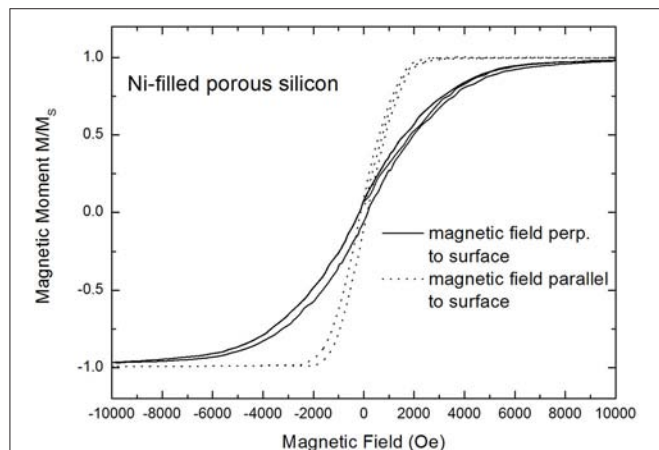


FIGURE 6 | Magnetization curves performed with an external magnetic field applied parallel (dotted line) and perpendicular to the surface (full line), respectively. The measurements show a magnetic anisotropy between these two magnetization directions exhibiting the easy axis for an applied field parallel to the surface (Granitzer et al., 2018).

which mainly depends on the shape anisotropy of the deposits. Elongated magnetic nanostructures offer a magnetic anisotropy with a magnetic easy axis along the long axis and a magnetic hard axis perpendicular to this one. The investigated samples offer in the case of the magnetic field applied perpendicular to the sample surface a low coercivity of about 200 Oe and a squareness (magnetic remanence/saturation magnetization) of about 0.2. Magnetization measurements performed with an external field applied parallel to the surface clearly show that the easy-axis of the sample coincides with this direction. **Figure 6** shows the magnetic anisotropy between these two magnetization directions with the easy axis for an applied external magnetic field parallel to the surface. It can be seen that in the case of a parallel applied

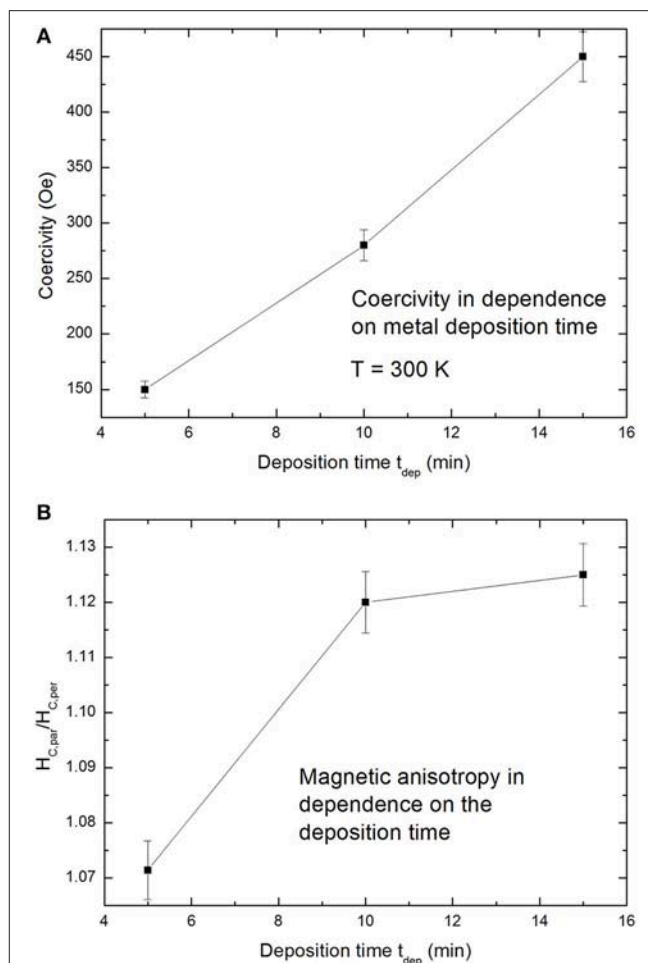


FIGURE 7 | (A) The coercivity, obtained from measurements with an applied field parallel to the surface, in dependence on the deposition time. **(B)** The magnetic anisotropy ($H_{C,\text{par}}/H_{C,\text{per}}$) in dependence on the deposition time (Granitzer et al., 2018).

magnetic field the saturation magnetization is reached at about 1,000 Oe, whereas in the case of a perpendicular applied field to the sample surface the saturation magnetization is reached at about 9,000 Oe.

The film-like behavior, offering an in-plane easy axis within the film, shown in **Figure 6** is caused by the interconnected Ni structures due to the branched morphology of the porous silicon template. **Figure 7A** shows an increase of the coercivity with increasing metal deposition time, whereat the measurements have been performed with an applied magnetic field parallel to the surface. The dependence of the magnetic anisotropy on the deposited Ni amount within the pores is presented in **Figure 7B**.

The optical properties, especially the photoluminescence and the decay times are varied by the amount of metal deposits within the porous silicon layer. The deposition of Ni within the porous silicon leads to a blue shift of the photoluminescence peak. Furthermore, an increase of the metal deposition time results in an enhancement of the photoluminescence intensity

and a decrease of the photoluminescence life time which can be interpreted by a decrease in the radiative life time. The enhancement of the photoluminescence intensity is interpreted by the coupling of the silicon emitter to the Ni plasmons. Due to the direct vicinity of the emitter and the metal structure, only separated by a thin SiO₂ native layer, coupling of the plasmonic modes with the emitter can occur. The magnetic properties of the Ni filled samples also show a dependence on the amount of metal deposits. An increase of the deposition time meaning an increase of the metal amount within the porous layer leads to more interconnected metal deposits. This behavior is evidenced by the enhancement of the coercivity from about 150 Oe to about 450 Oe with increasing deposition time from 5 to 15 min. Furthermore, a magnetic film-like behavior is observed which becomes more distinct with increased metal amount due to more interconnections. A magnetic anisotropy between the two magnetization directions parallel and perpendicular to the sample surface is observed which is typically for a magnetic film. In this case the magnetic easy axis corresponds to the parallel direction.

CONCLUSIONS

In the frame of this work the optical characteristics of luminescent PSi compared with Ni filled porous silicon is discussed especially with respect to the position of the photoluminescence peak and its intensity. The PL peak is blue-shifted and the luminescence intensity is increased with increasing metal filling within the pores which is attributed to the coupling of the silicon emitter with the plasmons of the

metal structures. Field dependent magnetization measurements of the nanocomposites are performed with an applied field parallel and perpendicular to the sample surface. A strong magnetic anisotropy between these two magnetization directions is observed, showing the easy axis for an applied field parallel to the surface. This film-like magnetic behavior is due to the interconnected metal structures which are present because of the branched morphology of the porous silicon. The coercivity of the samples decreases with decreasing metal filling and approximates to a superparamagnetic behavior which occurs in the case of separated magnetic nanoparticles. The presented systems which merge optical and magnetic properties are of interest for optoelectronics and magneto optical integrated devices.

AUTHOR CONTRIBUTIONS

KR and PG fabricated the porous silicon samples by anodization and subsequent electrodeposition and carried out the optical and magnetization measurements. PP performed the SEM investigations. MR supported the work with discussions. All authors discussed the data and prepared the manuscript.

ACKNOWLEDGMENTS

We thank the Institute for Electron Microscopy at the University of Technology Graz for SEM investigations and the Institute of Solid State Physics at the Vienna University of Technology for the possibility to perform magnetization measurements. Partly reproduced with permission from Granitzer et al. (2018).

REFERENCES

- Amdouni, S., Rahmani, M., Zaibi, M.-A., and Oueslati, M. J. (2015). Enhancement of porous silicon photoluminescence by electroless deposition of nickel. *J. Luminesc.* 157, 93–197. doi: 10.1016/j.jlumin.2014.08.041
- Amran, T. S. T., Hashim, R., Al-Obaidi, N. K. A., and Yazid, H. (2013). Optical absorption and photoluminescence studies of gold nanoparticles deposited on porous silicon. *Nanoscale Res. Lett.* 8:35. doi: 10.1186/1556-276X-8-35
- Canham, L. (1990). Silicon quantum wire array fabrication by electrochemical and chemical dissolution of wafers. *Appl. Phys. Lett.* 57, 1046–1048. doi: 10.1063/1.103561
- Canham, L. T. (1995). Luminescence bands and their proposed origins in highly porous silicon. *Phys. Stat. Sol. B* 190, 9–14. doi: 10.1002/pssb.2221900102
- De la Mora, M. B., Bornacelli, J., Nava, R., Zanella, R., and Reyes-Esqueda, J. A. (2014). Porous silicon photoluminescence modification by colloidal gold nanoparticles: plasmonic, surface and porosity roles. *J. Luminesc.* 146, 247–255. doi: 10.1016/j.jlumin.2013.09.053
- Gelloz, B., Kojima, A., and Koshida, N. (2005). Highly efficient and stable luminescence of nanocrystalline porous silicon treated by high-pressure water vapour annealing. *Appl. Phys. Lett.* 87:031107. doi: 10.1063/1.2001136
- Granitzer, P., Rumpf, K., Pölt, P., and Reissner, M. (2018). Optical properties of nanoporous silicon in the presence of magnetic nanostructures. *ECS Trans.* 85, 1329–1334. doi: 10.1149/08513.1329ecst
- Hu, J., Sun, X. Y., Du, Q., Onbasli, M., and Ross, C. A. (2016). “Monolithic on-chip nonreciprocal photonics based on magneto-optical thin films,” in *Proceedings of SPIE, 9750* (San Francisco, CA).
- Huck, A., and Anderson, U. L. (2016). Coupling single emitters to quantum plasmonic circuits. *Nanophotonics* 5:1. doi: 10.1515/nanoph-2015-0153
- Ito, T., Ohta, T., and Hiraki, A. (1992). Light emission from microcrystalline Si confined in SiO₂ matrix through partial oxidation of anodized porous silicon. *Jpn. J. Appl. Phys.* 31, L1–L3.
- Joo, J., Defforge, T., Loni, A., Kim, D., Li, Z. Y., Sailor, M. J., et al. (2016). Enhanced quantum yield of photoluminescent porous silicon prepared by supercritical drying. *Appl. Phys. Lett.* 108, 153111. doi: 10.1063/1.4947084
- Kanemitsu, Y., Matsumoto, T., Futagi, T., and Mimura, H. (1993). “Silicon based optoelectronic materials,” in *Materials Research Society Symposium Proceedings*, eds M. A. Tischler, R. T. Collins, M. L. W. Thewalt, and G. Abstreiter (New York, NY: Cambridge University Press), 298–205.
- Koch, F., Petrova-Koch, V., Muschik, T., Nikolov, A., Gavrilenko, V. (1992). “Microcrystalline semiconductors: materials science and devices,” in *Materials Research Society Symposium Proceedings*, eds P. M. Fauchet, C. C. Tsai, L. T. Canham, T. Shimizu, Y. Aoyagi (Boston, MA), 197.
- Koshida, N., and Koyama, H. (1992). Visible electroluminescence from porous silicon. *Appl. Phys. Lett.* 60, 347–349. doi: 10.1063/1.106652
- Koshida, N., Koyama, H., Yamamoto, Y., and Collins, G. J. (1993). Visible electroluminescence from porous silicon diodes with an electropolymerized contact. *Appl. Phys. Lett.* 63, 2655–2657. doi: 10.1063/1.10411
- Lehmann, V., and Gösele, U. (1991). Porous silicon formation: a quantum wire effect. *Appl. Phys. Lett.* 58, 856–858. doi: 10.1063/1.104512
- Li, K., Diaz, D. C., He, Y., Campbell, J. C., and Tsai, C. (1994). Electroluminescence from porous silicon with conducting polymer

- film contacts. *Appl. Phys. Lett.* 64, 2394–2396. doi: 10.1063/1.111625
- Ossicini, S., Pavesi, L., and Priolo, F. (2003). *Light Emitting Silicon for Microelectronics*. Berlin; Heidelberg: Springer.
- Sharma, V., Chotia, C., Tarachand, T., Ganesan, V., Okram, G. S. (2017). Influence of particle size and dielectric environment on the dispersion behaviour and surface plasmon in nickel nanoparticles. *Phys. Chem.Chem. Phys.* 19, 14096–14106. doi: 10.1039/C7CP01769C
- Tamura, H., Rückschloss, M., Wirschem, T.h., and Veprek, S. (1994). Origin of the green/blue luminescence from nanocrystalline silicon. *Appl. Phys. Lett.* 65, 1537–1539. doi: 10.1063/1.112035

Conflict of Interest Statement: The authors declare that the research was conducted in the absence of any commercial or financial relationships that could be construed as a potential conflict of interest.

Copyright © 2019 Granitzer, Rumpf, Poelt and Reissner. This is an open-access article distributed under the terms of the Creative Commons Attribution License (CC BY). The use, distribution or reproduction in other forums is permitted, provided the original author(s) and the copyright owner(s) are credited and that the original publication in this journal is cited, in accordance with accepted academic practice. No use, distribution or reproduction is permitted which does not comply with these terms.



TiO₂ ALD Coating of Amorphous TiO₂ Nanotube Layers: Inhibition of the Structural and Morphological Changes Due to Water Annealing

Siowwoon Ng¹, Hanna Sopha^{1,2}, Raul Zazpe^{1,2}, Zdenek Spotz¹, Vijay Bijalwan¹, Filip Dvorak², Ludek Hromadko^{1,2}, Jan Prikryl² and Jan M. Macak^{1,2*}

¹ Central European Institute of Technology, Brno University of Technology, Brno, Czechia, ² Faculty of Chemical Technology, Center of Materials and Nanotechnologies, University of Pardubice, Pardubice, Czechia

OPEN ACCESS

Edited by:

Nicolas Hans Voelcker,
Monash University, Australia

Reviewed by:

Xiao-Yu Wu,
Massachusetts Institute of
Technology, United States
Gael Gautier,
Institute National des Sciences
Appliquées Centre Val de Loire,
France

*Correspondence:

Jan M. Macak
jan.macak@upce.cz

Specialty section:

This article was submitted to
Chemical Engineering,
a section of the journal
Frontiers in Chemistry

Received: 20 October 2018

Accepted: 14 January 2019

Published: 01 February 2019

Citation:

Ng S, Sopha H, Zazpe R, Spotz Z,
Bijalwan V, Dvorak F, Hromadko L,
Prikryl J and Macak JM (2019) TiO₂
ALD Coating of Amorphous TiO₂
Nanotube Layers: Inhibition of the
Structural and Morphological
Changes Due to Water Annealing.
Front. Chem. 7:38.
doi: 10.3389/fchem.2019.00038

The present work presents a strategy to stabilize amorphous anodic self-organized TiO₂ nanotube layers against morphological changes and crystallization upon extensive water soaking. The growth of needle-like nanoparticles was observed on the outer and inner walls of amorphous nanotube layers after extensive water soakings, in line with the literature on water annealing. In contrary, when TiO₂ nanotube layers uniformly coated by thin TiO₂ using atomic layer deposition (ALD) were soaked in water, the growth rates of needle-like nanoparticles were substantially reduced. We investigated the soaking effects of ALD TiO₂ coatings with different thicknesses and deposition temperatures. Sufficiently thick TiO₂ coatings (≈ 8.4 nm) deposited at different ALD process temperatures efficiently hamper the reactions between water and F⁻ ions, maintain the amorphous state, and preserve the original tubular morphology. This work demonstrates the possibility of having robust amorphous 1D TiO₂ nanotube layers that are very stable in water. This is very practical for diverse biomedical applications that are accompanied by extensive contact with an aqueous environment.

Keywords: TiO₂, nanotubes, atomic layer deposition, coating, water annealing

INTRODUCTION

Various morphologies of TiO₂ with nano scale dimensions have been extensively investigated as photo catalysts for H₂ evolution, dye-sensitized solar cells (DSSCs), degradation of organic compounds, methanol oxidation, CO₂ reduction, self-cleaning and anti-fogging, and many other applications (Chen and Mao, 2007; Schneider et al., 2014; Wang et al., 2014). Particularly in the last 15 years, the anodic self-organized TiO₂ nanotube layers have attracted scientific interests in the mentioned areas. This is mainly attributed to the controllable geometry and large specific surface area of the anodic TiO₂ nanotube layers which allow higher reaction activities as well as the one-dimensional (1D) orientation which offers unidirectional charge transport from the tubes to the supporting Ti substrate (Macak et al., 2007; Lee et al., 2014; Wang et al., 2014).

Generally, the as-anodized TiO₂ nanotube layers in the amorphous state are not favored in semiconducting applications such as photo catalysts and DSSCs, primarily due to their low conductivity and a significant number of recombination centers which impede efficient charge transport (Roy et al., 2011; Krbal et al., 2016). As the electronic properties are influenced by

the structural quality of the nanotube layers (Tsuchiya et al., 2007), post-thermal annealing in temperature range of 280–600°C for 1–3 h (Varghese et al., 2003; Tighineanu et al., 2010) or hydrothermal treatment (Yu et al., 2010) needs to be carried out to crystallize the nanotube layers.

For a long time, only crystalline TiO₂ nanomaterials have been comprehensively studied, whereas its amorphous counterparts have not received much attention so far. In spite of the strong focus on crystalline TiO₂ forms (anatase or rutile) that show higher performance in diverse applications, amorphous TiO₂ structures have increasingly showcased its popular role in various semiconductor applications as well (Lu et al., 2008; Ortiz et al., 2008; Djenizian et al., 2011; Xiong et al., 2011; Bi et al., 2013; Wang et al., 2015; Jiang et al., 2016; Liang et al., 2018; Liu et al., 2018). TiO₂ has been long recognized as excellent biocompatible material owing to its low cytotoxicity, high stability, and antibacterial properties (Fu and Mo, 2018). Its amorphous state is particularly preferred in biomedical applications, including carrier for magnetic nanoparticles for protein purification (Kupcik et al., 2017), supporting layer for enhanced hydroxyapatite (Hap) deposition in Osseo integration (Kar et al., 2006; Crawford et al., 2007), supporting layer for epithelial cells and fibroblasts viability (Mei et al., 2014) and improved magnetic resonance contrast for molecular receptor targeted imaging (Chandran et al., 2011). In the case of TiO₂ nanotube layers, controllable nano-geometry, surface modification, topography, and roughness are crucial for tissue and cell vitality (seeding, spreading, and proliferation) (Park et al., 2007; Peng et al., 2009; Fu and Mo, 2018). On top of its hemocompatibility (Huang et al., 2017), the tubular morphology is an added advantage for genes, drugs, and therapeutic carrier or reservoirs, for example, gentamicin sulfate, chitosan, bone morphogenetic protein 2, and tumor necrosis factor-related apoptosis-inducing ligand (Hu et al., 2012; Feng et al., 2016; Kaur et al., 2016).

For the mentioned biomedical applications, the TiO₂ nanotube layers are frequently used in an aqueous environment. Nevertheless, the soaking of the as-anodized amorphous TiO₂ nanotube layers in a water bath transform them to polycrystalline anatase structure via so-called water annealing effect or low-temperature crystallization approach (Liao et al., 2011; Wang et al., 2011; Krengvirat et al., 2013; Lamberti et al., 2015; Cao et al., 2016). These water annealing processes are accompanied by a strong morphological transformation. As a result, the unique tubular morphology cannot be sustained in the case of prolonged soaking. Additional particle-like deposits grow on the surface of the amorphous nanotubes and may completely block them, reducing drastically the accessibility of various species inside the nanotubes and reducing also the overall available surface area. Eventually, in certain cases, the amorphous nanotubes were first transformed to double-wall nanotubes, then to core-shell wires/rods-within-tubes and finally full transformation into crystallized nanowires/rods after different soaking durations took place (Wang et al., 2011; Lamberti et al., 2015; Cao et al., 2016). The water annealed nanotubes or nanowires/rods possess much rougher surface as compared to the amorphous nanotube layers. Interestingly, when the similar soaking experiment was carried

out in a cell culture environment, such as in fetal bovine serum and phosphate buffered saline (PBS) media, the amorphous TiO₂ nanotube layers did not experience any structural or morphological changes (Cao et al., 2016).

To incorporate the aforementioned advantages of anodic 1D TiO₂ nanotube layers in the biomedical applications, it is crucial to maintain the amorphous state and preserve the tubular morphology. In fact, it is quite common that the addition of a shell (an outer layer) serves as a protective layer for the inner core structure (Yan et al., 2012; Hu et al., 2014; Kwiatkowski et al., 2015). For instance, an ultrathin Al₂O₃ coating was employed to improve the chemical, mechanical, and thermal stability of TiO₂ nanotube layers in extreme environments (Zazpe et al., 2017) such as for Li-ion batteries (Sopha et al., 2017a). On the other hand, a SiO₂ insulating layer was utilized to encapsulate TiO₂ nanoparticles to inhibit the photo catalytic activity, which undesirably darkens the white pigment of TiO₂ (Guo et al., 2017), and also to improve the cell compatibility and photo-killing ability (Feng et al., 2013).

To achieve ultrathin and continuous coatings that completely enfold a high aspect ratio structure such as TiO₂ nanotube layers, ALD technique is viable to provide such homogeneous and conformal coatings due to its self-saturating surface reactions (Leskelä and Ritala, 2002; Leskelä et al., 2007; Zazpe et al., 2016, 2018). Tupala et al. first performed an ALD amorphous TiO₂ coating within crystalline TiO₂ nanotube layers. It is worth noting that with a 5 nm amorphous TiO₂ layer, the conductivity of the coated nanotube layer is substantially increased. (Tupala et al., 2012) We have also demonstrated that additional ALD crystalline TiO₂ coatings within crystalline TiO₂ nanotube layers passivate defects within TiO₂ and enhance the charge carrier separation towards improved photo electrochemical and photo catalytic performance (Sopha et al., 2017b).

Despite other materials such as ZnO, Fe₃O₄, and CuO may potentially serve as a protective coating, we deliberately select an identical coating material (TiO₂) for the core nanotube layers due to the fact that (i) the biocompatible TiO₂ coating is required to be robust in extreme environments, and (ii) the stacking of two different materials (different densities) creates a gradient at the interface between outer and inner layers, which complicates the reactants transfer and interaction process. In the present work, we extend the application of ALD TiO₂ coatings as a protective coating of amorphous TiO₂ nanotube layers to prevent their morphological changes, known as water annealing effect. The longest soaking duration shown in previous works was up to 7 days (Wang et al., 2011; Cao et al., 2016). We significantly prolong the soaking duration up to 28 days to show the extreme stability of these ultrathin TiO₂ coated TiO₂ nanotube layers in order to broaden their functional range specifically in the aqueous environments for biomedical applications.

MATERIALS AND METHODS

Self-organized TiO₂ nanotube layers with thicknesses of $\approx 5\ \mu\text{m}$ and inner diameters $\approx 230\ \text{nm}$ were produced via electrochemical anodization as described in our previous works (Das et al.,

2017). Atomic layer deposition (ALD, TFS200, Benes) of TiO₂ was carried out at 150°, 225°, and 300°C using TiCl₄ (electronic grade 99.9998%, STREM) and Millipore deionized water (15 MΩ) as the titanium precursor and the oxygen source, respectively. Temperature of both precursors was kept at 20°C. High purity N₂ (99.9999%) was the carrier and purging gas at a flow rate of 400 standard cubic centimeters per minute sccm (Standard Cubic Centimeters per Minute). Under these deposition conditions, one ALD growth cycle was defined by the following sequence: TiCl₄ pulse (500 mS)-N₂ purge (3 s)-H₂O pulse (500 mS)-N₂ purge (4 s). The as-anodized amorphous TiO₂ nanotube layers were coated by TiO₂ applying different ALD cycles, N_{ALD} = 10, 50, and 150, yielding nominal thicknesses of 0.56, 2.8, and 8.4 nm, respectively. The thickness is obtained according to the growth rate per ALD cycle, evaluated from TiO₂ thin layers deposited on Si wafers using variable angle spectroscopic ellipsometry using VASE[®] ellipsometer, J.A. Woollam.

For water soaking, the blank and TiO₂ coated TiO₂ nanotube layers were soaked in deionized water (18 MΩ.cm) and phosphate buffered saline (PBS) for different durations, i.e., 1, 7, 14, or 28 day(s) in a still environment at room temperature. The morphology of the blank, coated, and soaked TiO₂ nanotube layers was imaged by field-emission scanning electron microscope (SEM, JEOL JSM 7500F, FEI Verios 460L). The structural evaluation was based on X-ray diffraction (XRD) measured by diffractometer (SmartLab 3kW from Rigaku). The diffractometer was set up in Bragg-Brentano geometry using Cu Kα radiation ($\lambda = 1.54 \text{ \AA}$) equipped by 1D-detector Dtex-Ultra. Cu lamp was operated at current 30 mA and voltage 40 kV. Phase analysis was performed based on chemical composition using databases PDF2 and ICSD. The chemical state of the blank and TiO₂ coated (N_{ALD} = 150 at 300°C) amorphous nanotube layers was examined by X-ray photoelectron spectroscopy (XPS, ESCA2SR, Scienta-Omicron) using a monochromatic Al Kα (1486.7 eV) X-ray source. The survey spectra were acquired using 250 W power of X-ray source with pass energy set to 150 eV. The quantitative analysis was based on sensitivity factors provided by the manufacturer. It is noteworthy to point out that the quantitative analysis was performed in order to provide a relative comparison between a chemical composition of blank and TiO₂ coated nanotube layers. The absolute values of the atomic concentration of elements are in great extent affected by the surface sensitivity of XPS.

RESULTS AND DISCUSSION

The blank (as-anodized) TiO₂ nanotube layers and TiO₂ coated (N_{ALD} = 150 at 300°C) TiO₂ nanotube layers are imaged by SEM in two regions of the nanotube layer, i.e., the top (water/nanotubes opening interface, **Figures 1a,c**) and the bottom (bottom of nanotubes/Ti interface, **Figures 1b,d**). At the top of the tubes, the blank nanotube layer clearly presents an inner diameter of $\approx 230 \text{ nm}$. It is obvious that the ALD TiO₂ ($\approx 8.4 \text{ nm}$) coated nanotube layer shows slightly thicker tube walls compared to the blank nanotube layer. In addition, at

the bottom of the tubes, the ALD coated nanotube layer has a smaller inner diameter. These images evidence that the coating is uniform across the entire tube walls. The layer thicknesses are $\approx 5 \mu\text{m}$ as shown in **Figure 1e**. The coating thickness is confirmed by the thickness measurement on the identical TiO₂ coating deposited on a flat substrate. It is an utmost challenge to differentiate the TiO₂ coating and TiO₂ tube wall due to the identical material, as they are of the same mass and contrast. This fact disables microscopists to distinguish them. Nevertheless, in a previous work, it was shown that the walls of 400 ALD cycles ($\approx 22 \text{ nm}$) TiO₂ coated TiO₂ nanotube layer is visibly much thicker than the blank nanotube layer (Sopha et al., 2017b). Thus, from the ALD principle, the thickness of the present coatings follows the same trend: the higher number of ALD cycles, the thicker is the coating.

The blank and TiO₂ coated TiO₂ nanotube layers were then soaked in deionized water for different durations from 1 to 28 days. No modification in physical appearance such as changes in color was noticed. We first proceeded to investigate the structural properties on (i) blank nanotube layers soaked for all durations; (ii) nanotube layers with different ALD coating thickness (N_{ALD} = 10, 50, 150) deposited at 300°C and (iii) nanotube layers with N_{ALD} = 150 deposited at different temperatures (150°, 225°, and 300°C), the latter two cases were soaked for 28 days. The resulting XRD patterns are depicted in **Figure 2**. The blank nanotube layers remain amorphous after extensive soaking in deionized water up to 28 days, as only the diffraction peaks of hexagonal Ti (from the substrate) are present in the obtained diffraction patterns as shows in **Figure 2A**. Similarly, all ALD cycles and temperatures coated nanotube layers are in amorphous state after the identical soaking experiments. The only exception is credited to the TiO₂ coating deposited with N_{ALD} = 150 at 300°C with polycrystalline anatase structure. The corresponding diffraction peaks of anatase are labeled in **Figure 2B**. Note that the crystallization is not induced by the water soaking; instead, it occurred during the ALD deposition process because the coating with a thickness of 8.4 nm becomes crystalline due to the deposition temperature of 300°C. This is supported by the XRD data of the amorphous nanotube layer, and the same layer then coated with N_{ALD} = 150 at 300°C prior to the soaking experiment, as shown in **Figure 2C**. The anatase diffraction peaks are very similar before and after soaking. Furthermore, previous studies reported that the initiation of crystallization process is influenced by the ALD deposition temperature and coating thickness (Aarik et al., 2001; Nie et al., 2015). This means that initially an amorphous coating is formed on the substrate until a (thermodynamical) threshold thickness is achieved for the nucleation of crystals. The threshold thickness reduces with the increase of deposition temperature (Aarik et al., 2001; Nie et al., 2015). Certainly, the selection of Ti and O₂ precursors is another important factor due to the different activation kinetics for different precursors. Several works have suggested that the crystallization process is initiated at the temperature range of 165–250°C (Aarik et al., 1995, 2013; Saha et al., 2014; Chiappim et al., 2016). For example, an 11 nm thin anatase TiO₂ film was obtained at deposition temperature of 225°C when TiCl₄ and H₂O were employed as precursors (Aarik et al., 2013). The whole

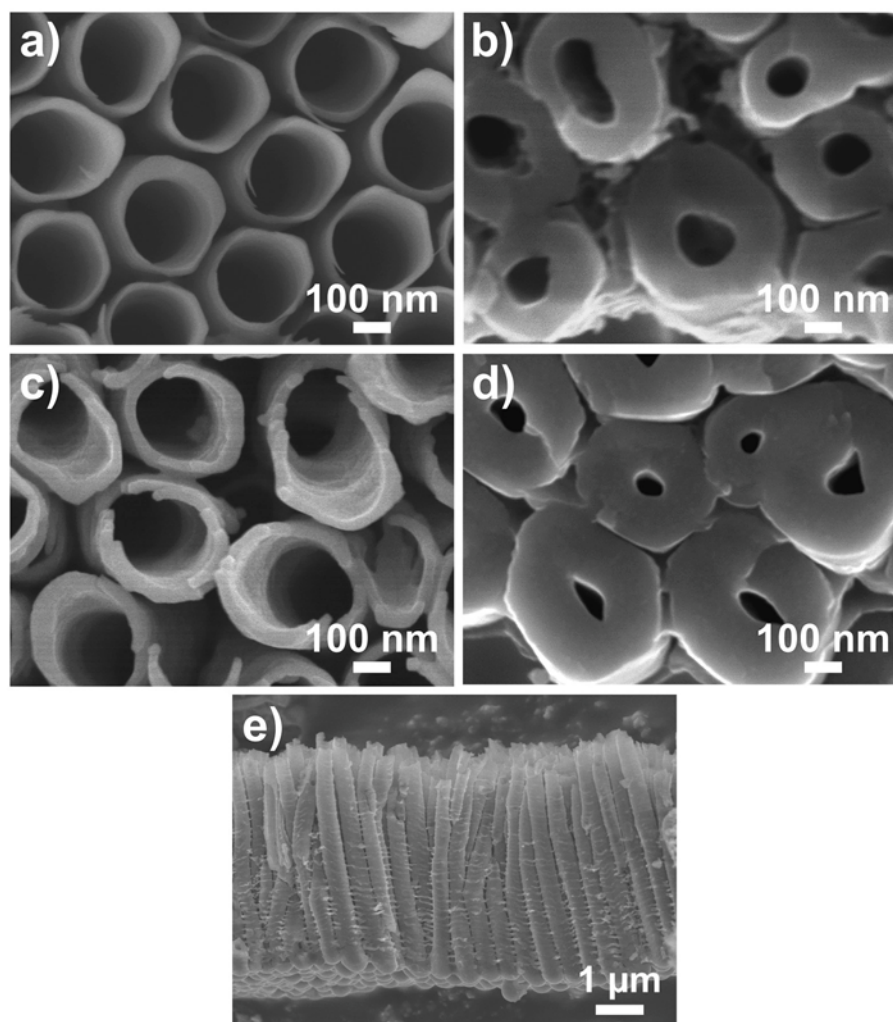


FIGURE 1 | SEM images of (a,b) blank and (c,d) TiO₂ coated ($N_{\text{ALD}} = 150 \approx 8.4 \text{ nm}$) TiO₂ nanotube layers. (a,c) Are taken at top of the nanotube layer (water/nanotubes opening interface) (b,d) Are taken at the bottom of the nanotube layer (bottom of nanotubes/Ti interface). (e) Shows the entire nanotube layer with thickness $\approx 5 \mu\text{m}$.

set of samples was analyzed by XRD, all others were amorphous except for $N_{\text{ALD}} = 150$ at 300°C , and selected patterns are shown in **Figure 2**. Thus, we can state that all nanotube layers with lower coating thicknesses or at lower deposition temperatures remain amorphous after soaking experiments with the duration up to 28 days.

The soaked blank nanotube layers were further inspected for their morphologies. **Figure 3** presents the SEM images of the nanotube layers taken at their top (water/nanotubes opening interface) and bottom (bottom of nanotubes/Ti interface). The larger inner diameter at the top than the bottom featuring a conical shape is a typical type of double-walled nanotube layers (Zazpe et al., 2016). It can be seen that the soaked nanotube layers experience a gradual change. After 1 day of soaking, the blank nanotube layer remains similar to the as-anodized nanotube layer in **Figure 1a**. When the soaking duration was extended to 7 and 14 days, needle-like particles were observed on the tube walls. A pronounced effect was observed after 28 days of soaking, where

the tube walls were completely occupied by the nanoparticles, which is drastically different from the as-anodized nanotube layers. The coalescence of nanoparticles has resulted in rather rough outer and inner tube walls and the nanoparticles were found over the entire nanotubes from the top to the bottom of the tube layers, as visualized in **Figure 3** (soakings for 28 days). This confirms that the morphological changes occurred over the entire available nanotube surface that was in contact with the water molecules. And it also confirms very good wettability of these nanotube layers. The final morphology very well-resembles the one reported in the literature (Wang et al., 2011; Liu et al., 2012). The transformation mechanism will be discussed later in this section.

Similar water soaking procedures were performed on the TiO₂ coated TiO₂ nanotube layers, where the coatings were deposited by ALD at different deposition temperatures and different coating cycles. For these coated nanotube layers, careful inspection did not reveal any noticeable morphological

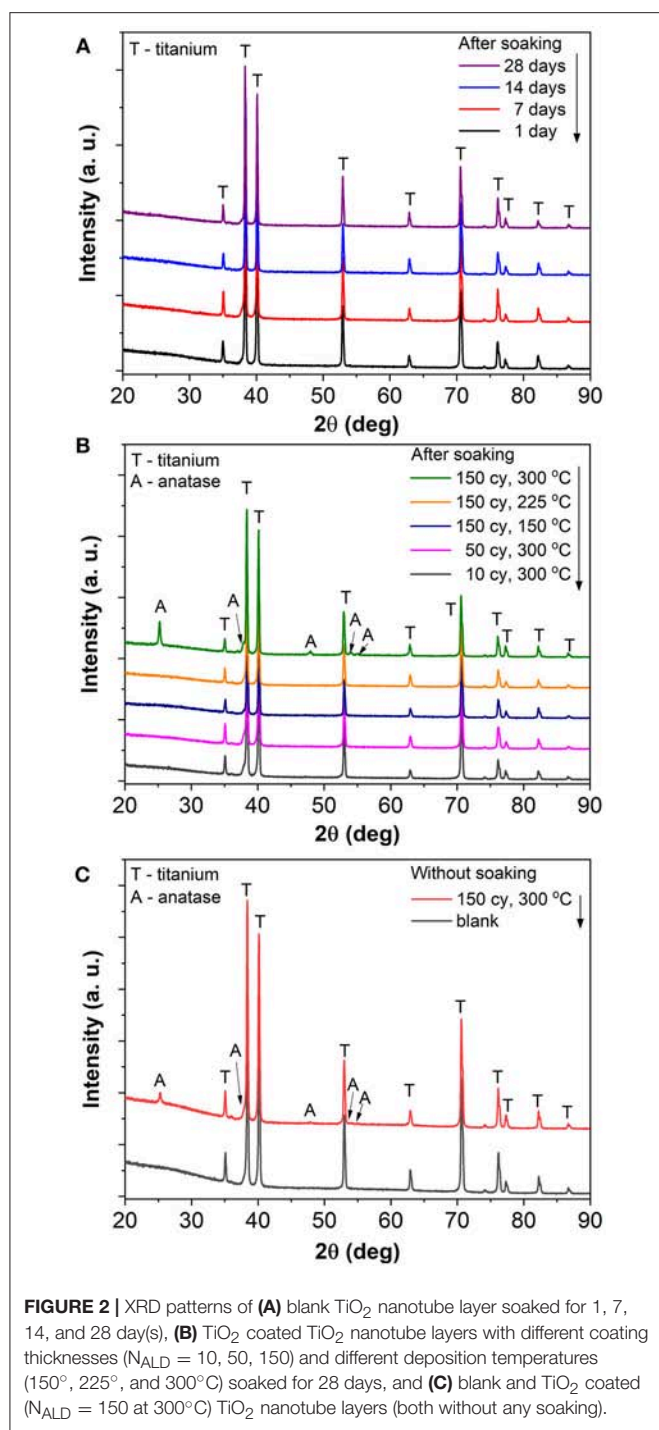


FIGURE 2 | XRD patterns of (A) blank TiO₂ nanotube layer soaked for 1, 7, 14, and 28 day(s), (B) TiO₂ coated TiO₂ nanotube layers with different coating thicknesses ($N_{\text{ALD}} = 10, 50, 150$) and different deposition temperatures (150°, 225°, and 300°C) soaked for 28 days, and (C) blank and TiO₂ coated ($N_{\text{ALD}} = 150$ at 300°C) TiO₂ nanotube layers (both without any soaking).

change for soakings up to 14 days, as shown in **Figure 4**. This implies that the nanotube layers were well-protected by the additional TiO₂ coatings. Thicker tube walls are observed with the increase of ALD coating cycles (and thickness), but the increase of deposition temperature does not yield any detectable morphological difference in **Figure 4**.

When the soakings were extended to 28 days, a considerable amount of needle-like nanoparticles were grown on the tube

walls with low coating thickness ($N_{\text{ALD}} = 10$). The amount of nanoparticles gradually decreased with thicker coatings ($N_{\text{ALD}} = 50, 150$), as shown in **Figure 5**. However, in comparison to the blank nanotube layers [**Figure 3** (28 days)], the amount of needles grown in the coated nanotube layers is significantly lower. The only exception lies in the nanotube layer with TiO₂ coating of $N_{\text{ALD}} = 150$ at 300°C, which did not undergo any visible changes (i.e., no needles were grown). This is in good agreement with the XRD analysis in **Figure 2B** that this ALD TiO₂ coating was crystalline. As anatase is thermodynamically stable, the anatase coating completely prevents reaction between water and the TiO₂ nanotube wall at room temperature (Wang et al., 2011).

Other works on water treated TiO₂ nanotube layers suggested that the formation of nanoparticles on the tube walls is closely related to the growth of anatase crystals, due to the structural rearrangement of TiO₆²⁻ octahedral induced by water (Liao et al., 2011; Wang et al., 2011; Cao et al., 2016). Under extreme conditions (extensive soaking periods) it may eventually result in the transformation of hollow nanotubes to solid nanowires, or completely collapsed nanotube walls. Interestingly, the solid-state growth and dissolution-precipitation mechanism were proposed based on Yanagisawa and Ovenstone's model (Yanagisawa and Ovenstone, 1999), but it took more than 10 years to reveal this effect also for the amorphous anodic TiO₂ nanotube layers (Liao et al., 2011; Wang et al., 2011).

Somewhat surprisingly, in the present work, the morphological changes of blank nanotube layers in **Figure 3** are not accompanied by structural modification (amorphous to anatase) as of those reported in the literature. To understand the present phenomena, it is helpful to revisit the formation mechanism of the anodic TiO₂ nanotube layer in fluoride-containing electrolytes (Macak et al., 2007; Lee et al., 2014). Briefly, the presence of F⁻ ions enables the formation of the fluoride-complex [TiF₆]²⁻ ions, and the formation of tubular TiO₂ is a competition between the solvation of Ti⁴⁺ to [TiF₆]²⁻ and the oxide formation. However, under the absence of an electric field (driven by an applied voltage), at the oxide/water interface, the reaction turns to a self-induced oxide formation, which translates into the nucleation of needle-like nanoparticles observed in **Figure 3** (7 days). Apparently, the dissolution-precipitation mechanism is now inclined to the precipitation process, and the continuous precipitation leads to the copious quantity of nanoparticles as seen in **Figure 3** (28 days). Dissimilar to Wang et al. (2011) and Cao et al. (2016) where the dissolution process gradually dissolved the tube walls, in **Figure 3** (28 days), distinguished walls are identified even though the nanotubes are covered by the nanoparticles. This further affirms that the process is dominated by a surface precipitation process without structural modification.

Compositional analyses were carried out on the blank amorphous and TiO₂ ($N_{\text{ALD}} = 150$ at 300°C) coated TiO₂ nanotube layers by XPS. Besides Ti and O, the survey spectra in **Figure 6** reveals the presence of F, C, and N in the nanotube layers. It has been pointed out that amorphous nanotube layers contain a considerable amount of F and C species from the anodization performed in the electrolyte consists of ethylene glycol and NH₄F, specifically for double-walled nanotube layers

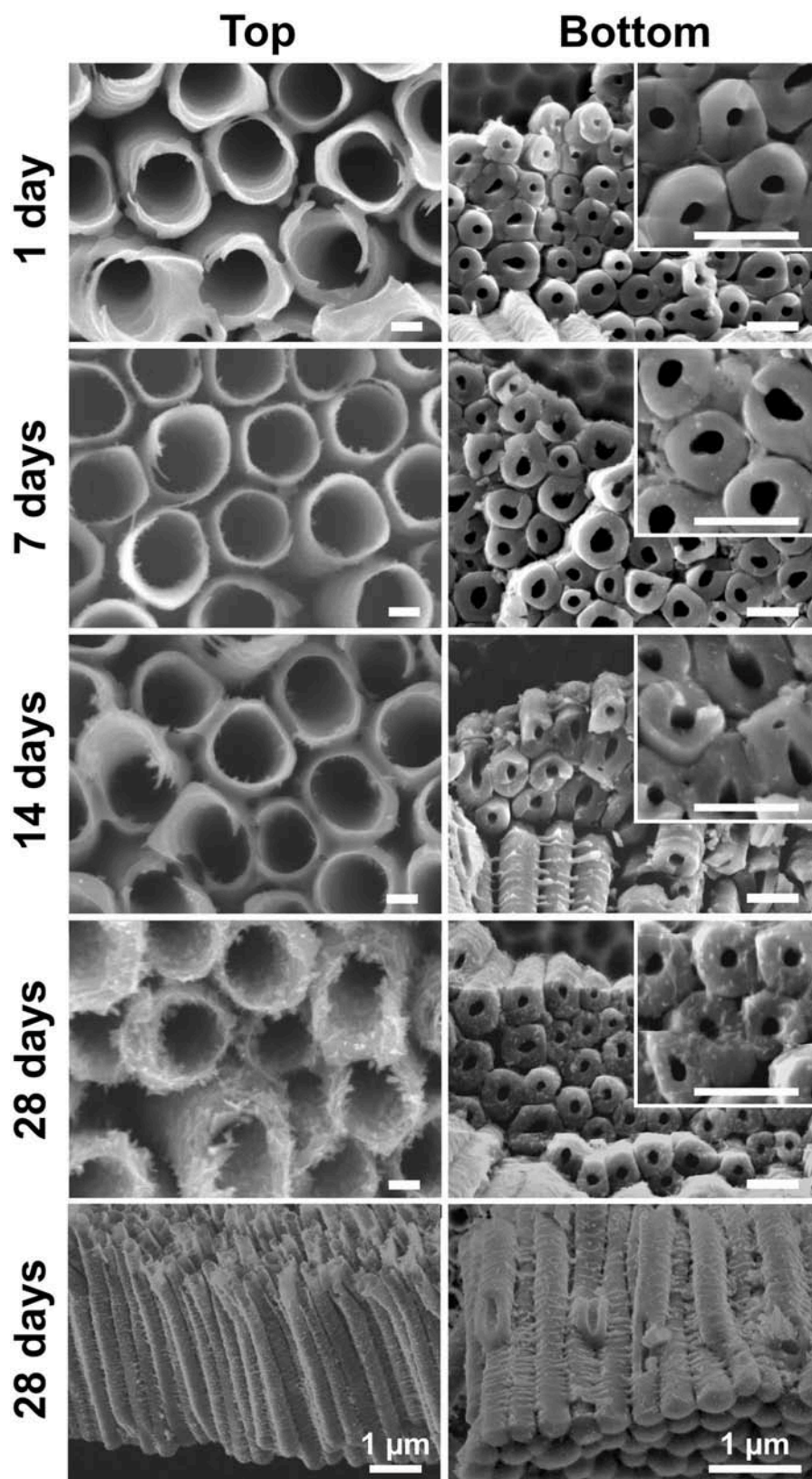
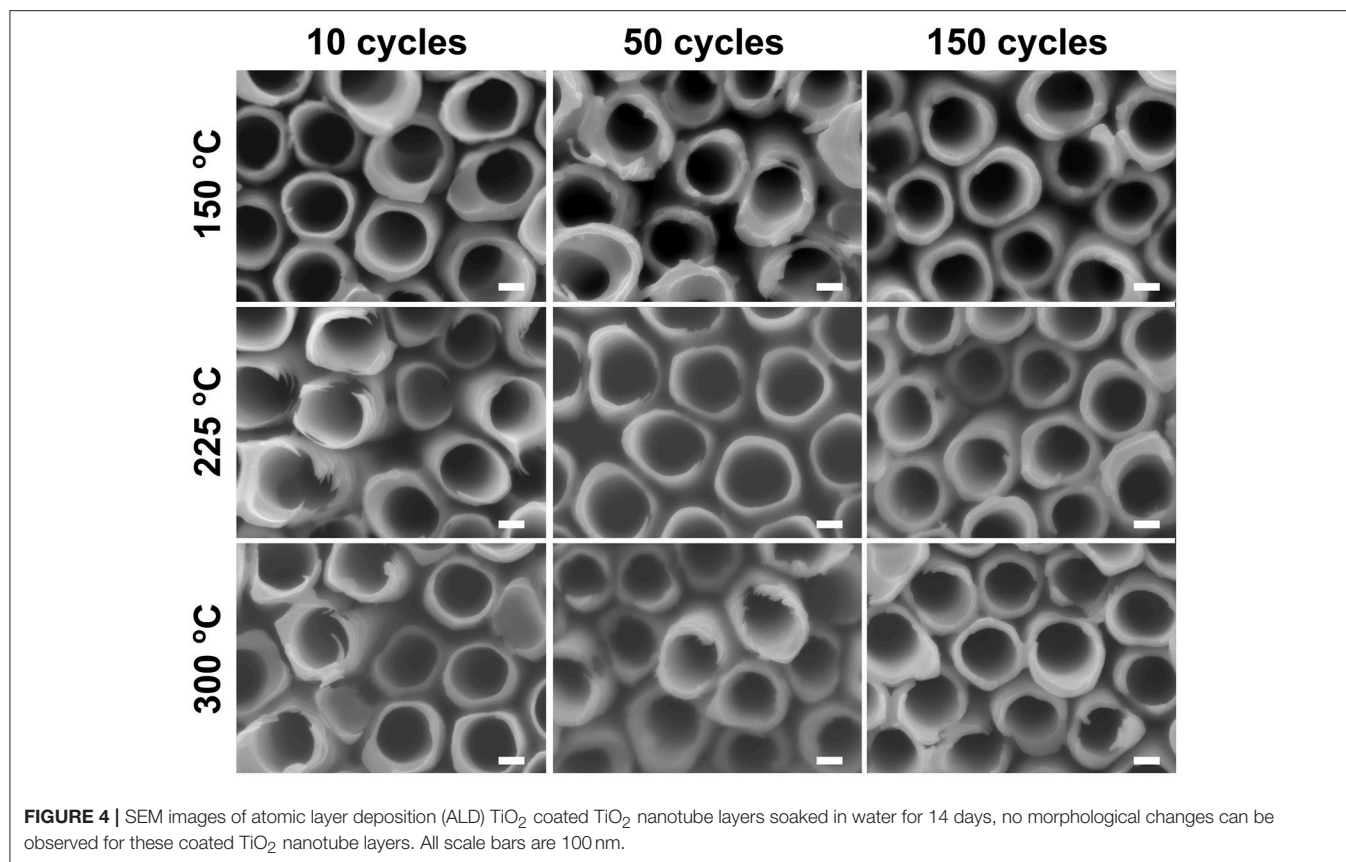


FIGURE 3 | SEM images of blank TiO₂ nanotube layers soaked in water for 1, 7, 14, and 28 day(s). Scale bars in the left column are 100 nm, in the right column and respective inset are 500 nm, unless stated otherwise.



(Albu et al., 2008) that were used also in this work. In particular, the presence of F content is associated with the high-field migration of electrolyte anions and the competition between small F⁻ ions and O²⁻ ions migration. For the successful formation of nanotubes, the inwards migration rate of F⁻ is twice to that of O²⁻, therefore accumulating a fluoride-rich inner layer especially toward the bottom of the tubes (Habazaki et al., 2007; Albu et al., 2008). In addition, an ultrathin fluoride-rich layer is also present at the outer walls, i.e., between individual tube walls, caused by the plastic-flow mechanism which pushes the nanotubes upward from the bottom of nanotubes/Ti interface during the tubes formation, hence promotes the F⁻ along the tube walls (Berger et al., 2011). The fluoride-rich, double-walled morphology is well-documented with the support by EDX, XPS, High Resolution Transmission Electron Microscope (HR-TEM), High Angle Annular Dark Field Scanning TEM (HAADF-STEM) Auger Electron Spectroscopy (AES) and Time-of-Flight Secondary-ion Mass Spectrometry (ToF SIMS) depth-profiling measurements (Albu et al., 2008; Berger et al., 2011; So et al., 2017; Dronov et al., 2018).

As a result, the as-anodized nanotube layers are usually subjected to thermal annealing at elevated temperatures for crystallization as well as for the removal of the F and C species (Albu et al., 2008). A clear double-walled morphology is visible after appropriate annealing process due to the removal of C in the form of CO₂ that leads to the separation of the inner and

outer walls, which have been shown in our previous works (Sopha et al., 2017b; Motola et al., 2018) and in other reports (Albu et al., 2008; So et al., 2017; Mohajernia et al., 2018). Without the annealing process, a substantial amount of C is noted in the amorphous nanotube layer as shown in **Figure 6**. The inner and outer walls remain intact and thus, the double-wall effect cannot be visualized in the images in **Figure 1**.

Comparing the blank and coated nanotube layers, the breakdown of the atomic concentration of each element tabulated in the inset of **Figure 6** shows that the amount of F, C, and N is significantly reduced as a result of the ALD TiO₂ coating. The C contamination can be partially assigned to the adventitious C resulting from the exposure to the air ambient. Whereas, the presence of F and N in the TiO₂ coating is related to the diffusion of these two elements from the nanotube walls to the coating during the ALD process at elevated temperature (performed at 300°C). Nevertheless, the traces of F (2.0%) and N (0.7%) are almost negligible. Therefore, without sufficient F⁻ ions on the surface of anatase TiO₂ coating (N_{ALD} = 150 at 300°C) at the water/coating interface, water annealing effect was not observed even after prolonged soakings. The same conclusion was reached by Cao et al. (2016) where the presence of a higher amount of F⁻ ions accelerated the growth of TiO₂ nanoparticles.

When an amorphous TiO₂ coating was added to the nanotube layer, forming nanotube/coating/water configuration, the additional coatings prepared by ALD (without F⁻ ions)

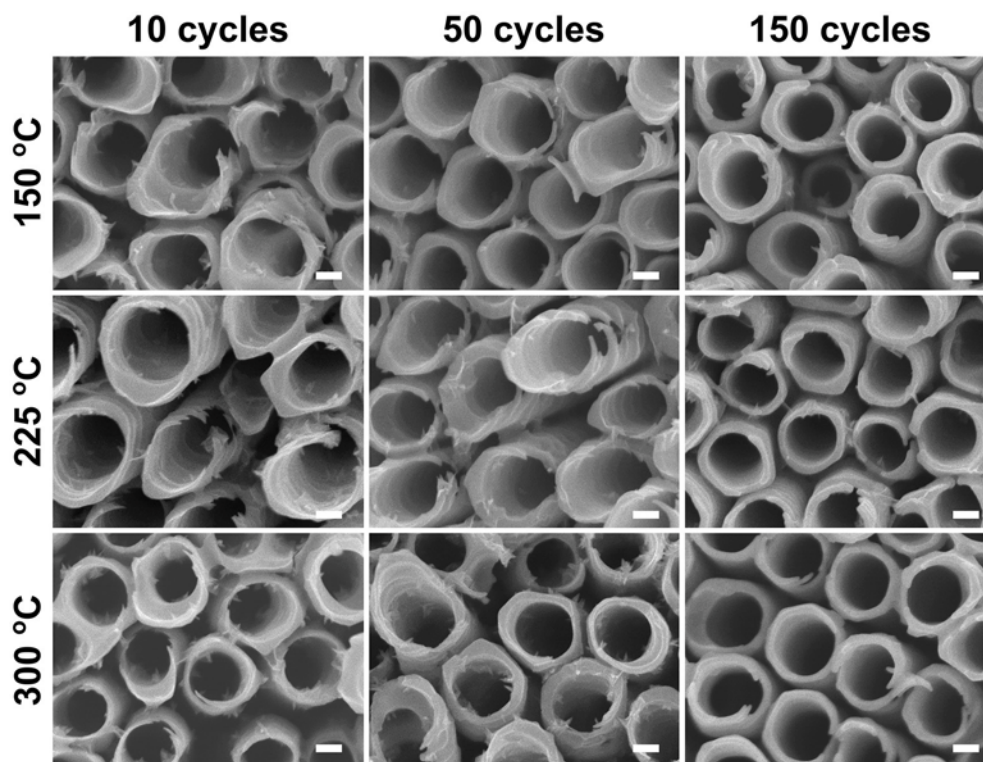


FIGURE 5 | SEM images of ALD TiO₂ coated TiO₂ nanotube layers soaked in water for 28 days. All scale bars are 100 nm.

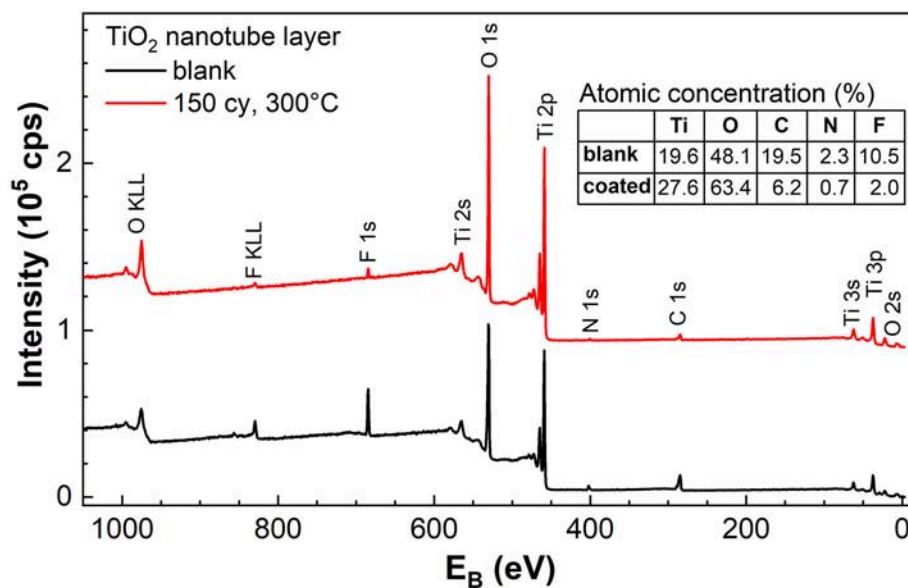


FIGURE 6 | XPS survey spectra of blank amorphous and TiO₂ coated ($N_{\text{ALD}} = 150$ at 300°C) TiO₂ nanotube layers. The table in the inset shows the atomic concentration of the elements found in the survey spectra. Spectra were offset for better clarity.

served as a protective layer (similar function as the anatase coating discussed above) to separate the tube walls and water. Due to the great adhesion of the coatings to the nanotubes,

there is no direct contact between F[−] ions ([TiF₆]^{2−} ions) and water. Hence, we observed in **Figure 4** that nanoparticles were not formed on the tube walls up to 14 days of soaking. However,

at the nanotube/coating interface, the F⁻ ions gradually attack both sides of TiO₂ and the thinner coatings are more prone to F⁻ ions transport across the entire coating, as the F⁻ ions are very small and mobile. The thinner coatings may be eventually consumed by the F⁻ ions, and the tube walls may be partially exposed to the water which may result in higher precipitation and growth of more nanoparticles. As the self-induced precipitation process occurs in a slow manner, an extended duration is required to observe the soaking effect. After 28 days of soaking (**Figure 5**), the most prominent effect (highest amount of nanoparticles) is credited to the thinnest coatings of $N_{\text{ALD}} = 10$, followed by $N_{\text{ALD}} = 50$. For these two coating thicknesses, the deposition temperatures did not have a significant effect. However, for $N_{\text{ALD}} = 150$, the amorphous coating deposited at 225°C has fewer nanoparticles than that at 150°C.

Further inspection of the bottoms of the TiO₂ coated nanotube layers was carried out. At first, we inspected TiO₂ coated ($N_{\text{ALD}} = 10$ at 150°C TiO₂) nanotube layer, which is the lowest coating thickness deposited at the lowest temperature applied in this work, as a representative one for all coated TiO₂ nanotube layers soaked for 14 days. The corresponding SEM image is shown in **Figure 7a** which confirms that no needles were grown for soakings up to 14 days. Note that the images shown in **Figure 7** are representative image based on the extensive analyses on a broad range of nanotube samples produced by the corresponding conditions.

For further verification, we compared the bottoms of the TiO₂ coated nanotube layers for $N_{\text{ALD}} = 150$ at 150° and 225°C and reached the same conclusion. Limited needles were discovered for 150°C in **Figure 7b** and almost no needle was detected for 225°C in **Figure 7c**. This is ascribed to the different densities of the TiO₂ coating during the ALD process as higher deposition temperature generally promotes the interconnection between the grains (Aarik et al., 1995; Saha et al., 2014). Thus, for identical thicknesses of $N_{\text{ALD}} = 150$, the film density is higher at 225°C and it can better resist the attack of F⁻ ions.

Similar morphology of TiO₂ nanoparticles coated TiO₂ nanotube layer in **Figure 3** (28 days) is observed for the renowned “TiCl₄ treatment” often carried out to decorate the TiO₂ nanotube layer by additional TiO₂ nanoparticles for DSSCs (Meen et al., 2012; So et al., 2015). Likewise, the as-deposited TiO₂ nanoparticles produced via hydrolysis of TiCl₄ are amorphous and conventional thermal annealing is required to crystallize the nanoparticles. A major difference between TiCl₄ treatment and water soaking is that the growth rate of TiO₂ nanoparticles is much slower in the present case. We have presented that the nanotube layer was completely decorated by nanoparticles after 30 min of treatment in a TiCl₄ bath (Sopha et al., 2017b), in line with other works (Meen et al., 2012; So et al., 2015). This is ascribed to the very reactive TiCl₄ precursor and considerably high reaction (chemical bath) temperature at 70°C, which accelerate the growth process. As for water soaking, the precipitation is a self-induced process and much longer duration is required to accumulate a comparable quantity of nanoparticle deposits. It has also been confirmed that higher soaking temperature and longer reaction time promote the growth rate of TiO₂ nanoparticles in a water bath (Krengvirat et al., 2013; Cao et al., 2016).

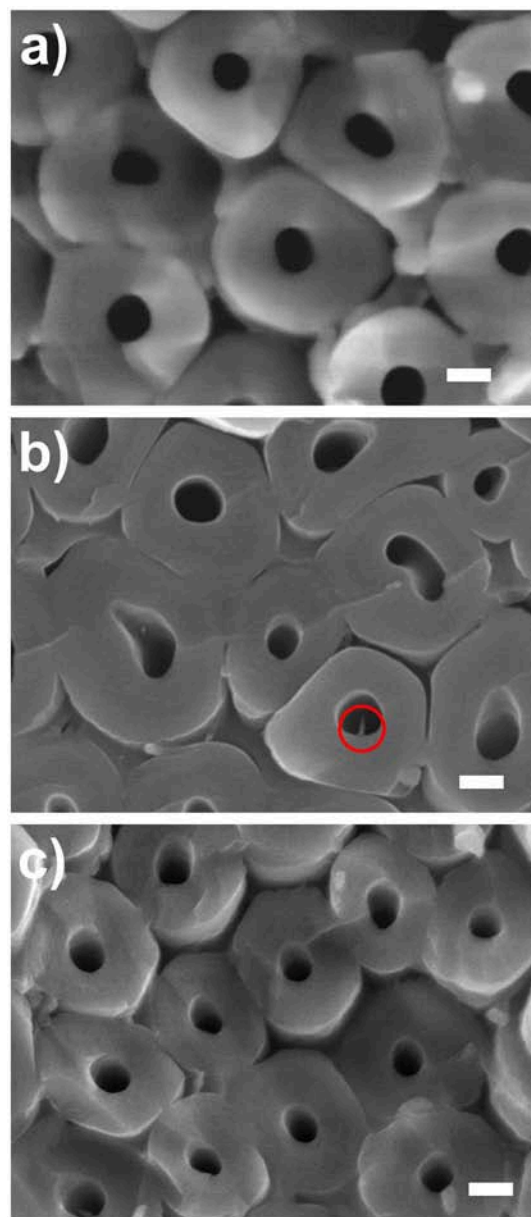


FIGURE 7 | SEM images of bottom parts of the TiO₂ nanotube layers taken close to the Ti substrate. **(a)** $N_{\text{ALD}} = 10$ at 150°C soaked for 14 days, $N_{\text{ALD}} = 150$ at **(b)** 150°C and **(c)** 225°C soaked for 28 days. All scale bars are 100 nm. The circle in **(b)** shows a needle found in an inner tube wall.

Altogether, these results indicate that the thin TiO₂ coatings act as a protective layer to maintain the smooth tubular morphology of the as-anodized nanotube layers in the amorphous state for more than 14 days, while the unprotected nanotube layers hardly sustain 7 days of soaking. This generously increases more than twice of the initial lifespan of the smooth amorphous TiO₂ nanotube layers which offers a stable platform for cell culturing and drug delivery testing typically carried out in the time scale from 3 to 20 days (Peng et al., 2009; Hu et al., 2012; Feng et al., 2016; Kaur et al., 2016). Moreover, it should be emphasized that a smooth morphology is usually favored for

cell culturing, as the cell spreading and the cell survival rate is influenced by the morphology of TiO₂ supporting layer (Park et al., 2007; Peng et al., 2009; Tian et al., 2015). In addition to the water soaking experiments, we also performed soakings in PBS with identical conditions (temperature, duration) for all blank and ALD TiO₂ coated TiO₂ nanotube layers. All these nanotube layers have revealed extreme stability in PBS. As shown in **Supplementary Figures 1 and 2**, no structural and morphological changes were observed even after 28 days due to the disruption of the precipitation kinetics by the inorganic species in the buffer solution. Although the full mechanism is not well-understood yet, this observation is in accord with Cao et al. (2016).

Overall, we recommend performing 150 ALD cycles of TiO₂ coating, equivalent to 8.4 nm thicknesses at 225°C which is sufficiently thick for effective protection for the nanotube layers whilst keeping the amorphous state. Among all the amorphous coatings after 28 days of soaking, this condition has the fewest nanoparticles on the nanotube walls, evidenced in **Figures 5 and 7**.

CONCLUSION

We proposed the utilization of thin ALD TiO₂ coatings to protect 1D TiO₂ nanotube layers against morphological changes within prolonged water soaking experiments. Thin and conformal TiO₂ coating of $N_{\text{ALD}} = 10, 50$, and 150 corresponding to 0.56, 2.8, and 8.4 nm in thickness, respectively, were deposited by ALD at temperatures 150°, 225°, and 300°C within 5 μm amorphous TiO₂ nanotube layers, which yielded amorphous and anatase coatings. The uncoated nanotube layers underwent significant morphological changes with additional nanoparticles formed on the nanotube walls after extensive soakings up to 28 days. The formation of the nanoparticles was related to the reaction between residual F[−] ions (present in the

nanotube walls) and water in a self-induced precipitation mechanism. The additional TiO₂ coatings delayed the soaking effect and preserved the nanotube walls for a minimum of 14 days. Overall, the optimum coating was credited to $N_{\text{ALD}} = 150$ (8.4 nm) deposited at 225°C. The combination of identical materials by different preparation techniques sustains the amorphous state and tubular morphology of 1D TiO₂ nanotube layers for biomedical applications as an example.

AUTHOR CONTRIBUTIONS

SN carried out the soakings and wrote the manuscript. HS synthesized the nanotubes and helped with the soakings. RZ and JP deposited the coatings. LH and VB carried out the SEM measurements. ZS measured and analyzed the XRD results. FD measured and evaluated the XPS results. JM designed the experiments, advised the results, corrected the manuscript and obtained the funding. All authors discussed, read, and approved the manuscript.

FUNDING

We gratefully acknowledge support from the European Research Council (project No. 638857) and the Ministry of Education, Youth and Sports of the Czech Republic (projects No. LM2015082, LM2015041, LQ1601). Part of the work was carried out with the support of CEITEC Nano Research Infrastructure (MEYS CR, 2016–2019).

SUPPLEMENTARY MATERIAL

The Supplementary Material for this article can be found online at: <https://www.frontiersin.org/articles/10.3389/fchem.2019.00038/full#supplementary-material>

REFERENCES

- Aarik, J., Aidla, A., Mändar, H., and Uustare, T. (2001). Atomic layer deposition of titanium dioxide from TiCl₄ and H₂O: Investigation of growth mechanism. *Appl. Surf. Sci.* 172, 148–158. doi: 10.1016/S0169-4332(00)00842-4
- Aarik, J., Aidla, A., Uustare, T., and Sammelselg, V. (1995). Morphology and structure of TiO₂ thin films grown by atomic layer deposition. *J. Cryst. Growth*. 148, 268–275. doi: 10.1016/0022-0248(94)00874-4
- Aarik, L., Arroval, T., Rammula, R., Mändar, H., Sammelselg, V., and Aarik, J. (2013). Atomic layer deposition of TiO₂ from TiCl₄ and O₃. *Thin Solid Films* 542, 100–107. doi: 10.1016/j.tsf.2013.06.074
- Albu, S. P., Ghicov, A., Aldabergenova, S., Drechsel, P., LeClere, D., Thompson, G. E., et al. (2008). Formation of double-walled TiO₂ nanotubes and robust anatase membranes. *Adv. Mater.* 20, 4135–4139. doi: 10.1002/adma.200801189
- Berger, S., Albu, S. P., Schmidt-Stein, F., Hildebrand, H., Schmuki, P., Hammond, J. S., et al. (2011). The origin for tubular growth of TiO₂ nanotubes: a fluoride rich layer between tube-walls. *Surf. Sci.* 605, L57–L60. doi: 10.1016/j.susc.2011.06.019
- Bi, Z., Paranthaman, M. P., Menchhofer, P. A., Dehoff, R. R., Bridges, C. A., Chi, M., et al. (2013). Self-organized amorphous TiO₂ nanotube arrays on porous Ti foam for rechargeable lithium and sodium ion batteries. *J. Power Sour.* 222, 461–466. doi: 10.1016/j.jpowsour.2012.09.019
- Cao, C., Yan, J., Zhang, Y., and Zhao, L. (2016). Stability of titania nanotube arrays in aqueous environment and the related factors. *Sci. Rep.* 6:23065. doi: 10.1038/srep23065
- Chandran, P., Sasidharan, A., Ashokan, A., Menon, D., Nair, S., and Koyakutty, M. (2011). Highly biocompatible TiO₂:Gd³⁺ nano-contrast agent with enhanced longitudinal relaxivity for targeted cancer imaging. *Nanoscale* 3, 4150–4161. doi: 10.1039/c1nr10591d
- Chen, X., and Mao, S. S. (2007). Titanium dioxide nanomaterials: synthesis, properties, modifications and applications. *Chem. Rev.* 107, 2891–2959. doi: 10.1021/cr0500535
- Chiappim, W., Testoni, G. E., de Lima, J. S. B., Medeiros, H. S., Pessoa, R. S., Grigorov, K. G., et al. (2016). Effect of process temperature and reaction cycle number on atomic layer deposition of TiO₂ thin films using TiCl₄ and H₂O precursors: correlation between material properties and process environment. *Brazilian J. Phys.* 46, 56–69. doi: 10.1007/s13538-015-0383-2
- Crawford, G. A., Chawla, N., Das, K., Bose, S., and Bandyopadhyay, A. (2007). Microstructure and deformation behavior of biocompatible TiO₂ nanotubes on titanium substrate. *Acta Biomater.* 3, 359–367. doi: 10.1016/j.actbio.2006.08.004
- Das, S., Sopha, H., Krbal, M., Zazpe, R., Podzemna, V., Prikrýl, J., et al. (2017). Electrochemical infilling of CuInSe₂ within TiO₂ nanotube layers and subsequent photoelectrochemical studies. *ChemElectroChem* 4, 495–499. doi: 10.1002/celec.201600763

- Djenizian, T., Hanzu, I., and Knauth, P. (2011). Nanostructured negative electrodes based on titania for Li-ion microbatteries. *J. Mater. Chem.* 21, 9925–9937. doi: 10.1039/c0jm04205f
- Dronov, A., Gavrilin, I., Kirilenko, E., Dronova, D., and Gavrilov, S. (2018). Investigation of anodic TiO₂ nanotube composition with high spatial resolution AES and ToF SIMS. *Appl. Surf. Sci.* 434, 148–154. doi: 10.1016/j.apsusc.2017.10.132
- Feng, W., Geng, Z., Li, Z., Cui, Z., Zhu, S., Liang, Y., et al. (2016). Controlled release behaviour and antibacterial effects of antibiotic-loaded titania nanotubes. *Mater. Sci. Eng. C* 62, 105–112. doi: 10.1016/j.msec.2016.01.046
- Feng, X., Zhang, S., and Lou, X. (2013). Controlling silica coating thickness on TiO₂ nanoparticles for effective photodynamic therapy. *Colloids Surf. B Biointerfaces* 107, 220–226. doi: 10.1016/j.colsurfb.2013.02.007
- Fu, Y., and Mo, A. (2018). A review on the electrochemically self-organized titania nanotube arrays: synthesis, modifications, and biomedical applications. *Nanoscale Res. Lett.* 13:187. doi: 10.1186/s11671-018-2597-z
- Guo, J., Yuan, S., Yu, Y., van Ommen, J. R., Van Bui, H., and Liang, B. (2017). Room-temperature pulsed CVD-grown SiO₂ protective layer on TiO₂ particles for photocatalytic activity suppression. *RSC Adv.* 7, 4547–4554. doi: 10.1039/C6RA27976G
- Habazaki, H., Fushimi, K., Shimizu, K., Skeldon, P., and Thompson, G. E. (2007). Fast migration of fluoride ions in growing anodic titanium oxide. *Electrochem. Commun.* 9, 1222–1227. doi: 10.1016/j.elecom.2006.12.023
- Hu, S., Shaner, M. R., Beardslee, J. A., Lichterman, M., Bruntschwig, B. S., and Lewis, N. S. (2014). Amorphous TiO₂ coatings stabilize Si, GaAs, and GaP photoanodes for efficient water oxidation. *Science* 344, 1005–1009. doi: 10.1126/science.1251428
- Hu, Y., Cai, K., Luo, Z., Xu, D., Xie, D., Huang, Y., et al. (2012). TiO₂ nanotubes as drug nanoreservoirs for the regulation of mobility and differentiation of mesenchymal stem cells. *Acta Biomater.* 8, 439–448. doi: 10.1016/j.actbio.2011.10.021
- Huang, Q., Yang, Y., Zheng, D., Song, R., Zhang, Y., Jiang, P., et al. (2017). Effect of construction of TiO₂ nanotubes on platelet behaviors: structure-property relationships. *Acta Biomater.* 51, 505–512. doi: 10.1016/j.actbio.2017.01.044
- Jiang, J., Tang, X., Zhou, S., Ding, J., Zhou, H., Zhang, F., et al. (2016). Synthesis of visible and near infrared light sensitive amorphous titania for photocatalytic hydrogen evolution. *Green Chem.* 18, 2056–2062. doi: 10.1039/C5GC02170G
- Kar, A., Raja, K. S., and Misra, M. (2006). Electrodeposition of hydroxyapatite onto nanotubular TiO₂ for implant applications. *Surf. Coatings Technol.* 201, 3723–3731. doi: 10.1016/j.surfcoat.2006.09.008
- Kaur, G., Willmore, T., Gulati, K., Zinonos, I., Wang, Y., Kurian, M., et al. (2016). Titanium wire implants with nanotube arrays: a study model for localized cancer treatment. *Biomaterials* 101, 176–188. doi: 10.1016/j.biomaterials.2016.05.048
- Krbal, M., Kucharik, J., Sopha, H., Nemec, H., and Macak, J. M. (2016). Charge transport in anodic TiO₂ nanotubes studied by terahertz spectroscopy. *Phys. Status Solidi - Rapid Res. Lett.* 10, 691–695. doi: 10.1002/pssr.201600179
- Krengvirat, W., Sreekantan, S., Mohd Noor, A. F., Negishi, N., Kawamura, G., Muto, H., et al. (2013). Low-temperature crystallization of TiO₂ nanotube arrays via hot water treatment and their photocatalytic properties under visible-light irradiation. *Mater. Chem. Phys.* 137, 991–998. doi: 10.1016/j.matchemphys.2012.11.013
- Kupcik, R., Rehulka, P., Bilkova, Z., Sopha, H., and Macak, J. M. (2017). New interface for purification of proteins: one-dimensional TiO₂ nanotubes decorated by Fe₃O₄ nanoparticles. *ACS Appl. Mater. Interfaces* 9, 28233–28242. doi: 10.1021/acsami.7b08445
- Kwiatkowski, M., Bezverkhyy, I., and Skompska, M. (2015). ZnO nanorods covered with a TiO₂ layer: simple sol-gel preparation, and optical, photocatalytic and photoelectrochemical properties. *J. Mater. Chem. A* 3, 12748–12760. doi: 10.1039/C5TA01087J
- Lamberti, A., Chiodoni, A., Shahzad, N., Bianco, S., Quaglio, M., and Pirri, C. F. (2015). Ultrafast room-temperature crystallization of TiO₂ nanotubes exploiting water-vapor treatment. *Sci. Rep.* 5:7808. doi: 10.1038/srep07808
- Lee, K., Mazare, A., and Schmuki, P. (2014). One-dimensional titanium dioxide nanomaterials: nanotubes. *Chem. Rev.* 114, 9385–9454. doi: 10.1021/cr500061m
- Leskelä, M., Kemell, M., Kukli, K., Pore, V., Santala, E., Ritala, M., et al. (2007). Exploitation of atomic layer deposition for nanostructured materials. *Mater. Sci. Eng. C* 27, 1504–1508. doi: 10.1016/j.msec.2006.06.006
- Leskelä, M., and Ritala, M. (2002). Atomic layer deposition (ALD): from precursors to thin film structures. *Thin Solid Films* 409, 138–146. doi: 10.1016/S0040-6090(02)00117-7
- Liang, H., Meng, Q., Wang, X., Zhang, H., and Wang, J. (2018). Nanoplasmonically engineered interfaces on amorphous TiO₂ for highly efficient photocatalysis in hydrogen evolution. *ACS Appl. Mater. Interfaces* 10, 14145–14152. doi: 10.1021/acsami.8b00677
- Liao, Y., Que, W., Zhong, P., Zhang, J., and He, Y. (2011). A facile method to crystallize amorphous anodized TiO₂ nanotubes at low temperature. *ACS Appl. Mater. Interfaces* 3, 2800–2804. doi: 10.1021/am200685s
- Liu, H. Y., Hsu, Y. L., Su, H. Y., Huang, R. C., Hou, F. Y., Tu, G. C., et al. (2018). A comparative study of amorphous, anatase, rutile, and mixed phase TiO₂ films by mist chemical vapor deposition and ultraviolet photodetectors applications. *IEEE Sens. J.* 18, 4022–4029. doi: 10.1109/JSEN.2018.2819700
- Liu, N., Albu, S. P., Lee, K., So, S., and Schmuki, P. (2012). Water annealing and other low temperature treatments of anodic TiO₂ nanotubes: a comparison of properties and efficiencies in dye sensitized solar cells and for water splitting. *Electrochim. Acta* 82, 98–102. doi: 10.1016/j.electacta.2012.06.006
- Lu, H. F., Li, F., Liu, G., Chen, Z. G., Wang, D. W., Fang, H. T., et al. (2008). Amorphous TiO₂ nanotube arrays for low-temperature oxygen sensors. *Nanotechnology* 19:405504. doi: 10.1088/0957-4484/19/40/405504
- Macak, J. M., Tsuchiya, H., Ghicov, A., Yasuda, K., Hahn, R., Bauer, S., et al. (2007). TiO₂ nanotubes: self-organized electrochemical formation, properties and applications. *Curr. Opin. Solid State Mater. Sci.* 11, 3–18. doi: 10.1016/j.cossms.2007.08.004
- Meen, T. H., Jhuo, Y. T., Chao, S. M., Lin, N. Y., Ji, L. W., Tsai, J. K., et al. (2012). Effect of TiO₂ nanotubes with TiCl₄ treatment on the photoelectrode of dye-sensitized solar cells. *Nanoscale Res. Lett.* 7:579. doi: 10.1186/1556-276X-7-579
- Mei, S., Wang, H., Wang, W., Tong, L., Pan, H., Ruan, C., et al. (2014). Antibacterial effects and biocompatibility of titanium surfaces with graded silver incorporation in titania nanotubes. *Biomaterials* 35, 4255–4265. doi: 10.1016/j.biomaterials.2014.02.005
- Mohajerania, S., Mazare, A., Hwang, I., Gaiaschi, S., Chapon, P., Hildebrand, H., et al. (2018). Depth elemental characterization of 1D self-aligned TiO₂ nanotubes using calibrated radio frequency glow discharge optical emission spectroscopy (GDOES). *Appl. Surf. Sci.* 442, 412–416. doi: 10.1016/j.apsusc.2018.02.185
- Motola, M., Sopha, H., Krbal, M., Hromádka, L., Zmrhalová, Z. O., Plesch, G., et al. (2018). Comparison of photoelectrochemical performance of anodic single- and double-walled TiO₂ nanotube layers. *Electrochem. Commun.* 97, 1–5. doi: 10.1016/j.elecom.2018.09.015
- Nie, X., Ma, F., Ma, D., and Xu, K. (2015). Thermodynamics and kinetic behaviors of thickness-dependent crystallization in high-k thin films deposited by atomic layer deposition. *J. Vac. Sci. Technol. A* 33:01A140. doi: 10.1116/1.4903946
- Ortiz, G. F. G., Hanzu, I., Djenizian, T., Lavela, P., Tirado, J. L., and Knauth, P. (2008). Alternative Li-ion battery electrode based on self-organized titania nanotubes. *Chem. Mater.* 21, 63–67. doi: 10.1021/cm801670u
- Park, J., Bauer, S., Von Der Mark, K., and Schmuki, P. (2007). Nanosize and vitality: TiO₂ nanotube diameter directs cell fate. *Nano Lett.* 7, 1686–1691. doi: 10.1021/nl070678d
- Peng, L., Eltgroth, M. L., LaTempa, T. J., Grimes, C. A., and Desai, T. A. (2009). The effect of TiO₂ nanotubes on endothelial function and smooth muscle proliferation. *Biomaterials* 30, 1268–1272. doi: 10.1016/j.biomaterials.2008.11.012
- Roy, P., Berger, S., and Schmuki, P. (2011). TiO₂ nanotubes: synthesis and applications. *Angew. Chemie Int. Ed.* 50, 2904–2939. doi: 10.1002/anie.201001374
- Saha, D., Ajimsha, R. S., Rajiv, K., Mukherjee, C., Gupta, M., Misra, P., et al. (2014). Spectroscopic ellipsometry characterization of amorphous and crystalline TiO₂ thin films grown by atomic layer deposition at different temperatures. *Appl. Surf. Sci.* 315, 116–123. doi: 10.1016/j.apsusc.2014.07.098
- Schneider, J., Matsuoka, M., Takeuchi, M., Zhang, J., Horiuchi, Y., Anpo, M., et al. (2014). Understanding TiO₂ photocatalysis: mechanisms and materials. *Chem. Rev.* 114, 9919–9986. doi: 10.1021/cr5001892

- So, S., Hwang, I., and Schmuki, P. (2015). Hierarchical DSSC structures based on “single walled” TiO₂ nanotube arrays reach a back-side illumination solar light conversion efficiency of 8%. *Energy Environ. Sci.* 8, 849–854. doi: 10.1039/C4EE03729D
- So, S., Riboni, F., Hwang, I., Paul, D., Hammond, J., Tomanec, O., et al. (2017). The double-walled nature of TiO₂ nanotubes and formation of tube-in-tube structures – a characterization of different tube morphologies. *Electrochim. Acta* 231, 721–731. doi: 10.1016/j.electacta.2017.02.094
- Sopha, H., Krbal, M., Ng, S., Prikryl, J., Zazpe, R., Yam, F. K., et al. (2017b). Highly efficient photoelectrochemical and photocatalytic anodic TiO₂ nanotube layers with additional TiO₂ coating. *Appl. Mater. Today* 9, 104–110. doi: 10.1016/j.apmt.2017.06.002
- Sopha, H., Salian, G. D., Zazpe, R., Prikryl, J., Hromadko, L., Djenizian, T., et al. (2017a). ALD Al₂O₃-coated TiO₂ nanotube layers as anodes for lithium-ion batteries. *ACS Omega* 2, 2749–2756. doi: 10.1021/acsomega.7b00463
- Tian, A., Wu, A., Zhang, H., Xing, D., Yang, H., Qiu, B., et al. (2015). Nanoscale TiO₂ nanotubes govern the biological behavior of human glioma and osteosarcoma cells. *Int. J. Nanomed.* 10, 2423–2439. doi: 10.2147/IJN.S71622
- Tighineanu, A., Ruff, T., Albu, S., Hahn, R., and Schmuki, P. (2010). Conductivity of TiO₂ nanotubes: influence of annealing time and temperature. *Chem. Phys. Lett.* 494, 260–263. doi: 10.1016/j.cplett.2010.06.022
- Tsuchiya, H., Macak, J. M., Ghicov, A., Räder, A. S., Taveira, L., and Schmuki, P. (2007). Characterization of electronic properties of TiO₂ nanotube films. *Corros. Sci.* 49, 203–210. doi: 10.1016/j.corsci.2006.05.009
- Tupala, J., Kemell, M., Härkönen, E., Ritala, M., and Leskelä, M. (2012). Preparation of regularly structured nanotubular TiO₂ thin films on ITO and their modification with thin ALD-grown layers. *Nanotechnology* 23:125707. doi: 10.1088/0957-4484/23/12/125707
- Varghese, O. K., Gong, D., Paulose, M., Grimes, C. A., and Dickey, E. C. (2003). Crystallization and high-temperature structural stability of titanium oxide nanotube arrays. *J. Mater. Res.* 18, 156–165. doi: 10.1557/JMR.2003.0022
- Wang, D., Liu, L., Zhang, F., Tao, K., Pippel, E., and Domen, K. (2011). Spontaneous phase and morphology transformations of anodized titania nanotubes induce by water at room temperature. *Nano Lett.* 11, 3649–3655. doi: 10.1021/nl2015262
- Wang, Q., Chen, M., Zhu, N., Shi, X., Jin, H., Zhang, Y., et al. (2015). Preparation of AgI sensitized amorphous TiO₂ as novel high-performance photocatalyst for environmental applications. *J. Colloid Interface Sci.* 448, 407–416. doi: 10.1016/j.jcis.2015.01.085
- Wang, X., Li, Z., Shi, J., and Yu, Y. (2014). One-dimensional titanium dioxide nanomaterials: nanowires, nanorods, and nanobelts. *Chem. Rev.* 114, 9346–9384. doi: 10.1021/cr400633s
- Xiong, H., Slater, M. D., Balasubramanian, M., Johnson, C. S., and Rajh, T. (2011). Amorphous TiO₂ nanotube anode for rechargeable sodium ion batteries. *J. Phys. Chem. Lett.* 2, 2560–2565. doi: 10.1021/jz2012066
- Yan, X., Zou, C., Gao, X., and Gao, W. (2012). ZnO/TiO₂ core-brush nanostructure: processing, microstructure and enhanced photocatalytic activity. *J. Mater. Chem.* 22, 5629–5640. doi: 10.1039/c2jm15477c
- Yanagisawa, K., and Ovenstone, J. (1999). Crystallization of anatase from amorphous titania using the hydrothermal technique: effects of starting material and temperature. *J. Phys. Chem. B* 103, 7781–7787. doi: 10.1021/jp990521c
- Yu, J., Dai, G., and Cheng, B. (2010). Effect of crystallization methods on morphology and photocatalytic activity of anodized TiO₂ nanotube array films. *J. Phys. Chem. C* 114:19378–79385. doi: 10.1021/jp106324x
- Zazpe, R., Knaut, M., Sopha, H., Hromadko, L., Albert, M., Prikryl, J., et al. (2016). Atomic layer deposition for coating of high aspect ratio TiO₂ nanotube layers. *Langmuir* 32, 10551–10558. doi: 10.1021/acs.langmuir.6b03119
- Zazpe, R., Prikryl, J., Gärtnerova, V., Nechvilova, K., Benes, L., Strizik, L., et al. (2017). Atomic layer deposition Al₂O₃ coatings significantly improve thermal, chemical, and mechanical stability of anodic TiO₂ nanotube layers. *Langmuir* 33, 3208–3216. doi: 10.1021/acs.langmuir.7b00187
- Zazpe, R., Sopha, H. I., Prikryl, J., Krbal, M., Mistrík, J., Dvorak, F., et al. (2018). A 1D conical nanotubular TiO₂/CdS heterostructure with superior photon-to-electron conversion. *Nanoscale* 10, 16601–16612. doi: 10.1039/C8NR02418A

Conflict of Interest Statement: The authors declare that the research was conducted in the absence of any commercial or financial relationships that could be construed as a potential conflict of interest.

Copyright © 2019 Ng, Sopha, Zazpe, Spitz, Bijalwan, Dvorak, Hromadko, Prikryl and Macak. This is an open-access article distributed under the terms of the Creative Commons Attribution License (CC BY). The use, distribution or reproduction in other forums is permitted, provided the original author(s) and the copyright owner(s) are credited and that the original publication in this journal is cited, in accordance with accepted academic practice. No use, distribution or reproduction is permitted which does not comply with these terms.



Optical and Electrochemical Properties of Self-Organized TiO₂ Nanotube Arrays From Anodized Ti–6Al–4V Alloy

Henia Fraoucene¹, Vinsensia Ade Sugawati², Djedjiga Hatem¹, Mohammed Said Belkaid¹, Florence Vacandio^{2*}, Marielle Eyraud², Marcel Pasquinelli³ and Thierry Djenizian⁴

¹ Laboratory of Advanced Technologies of Genie Electrics, Faculty of Electrical and Computer Engineering Mouloud Mammeri University, Tizi-Ouzou, Algeria, ² Electrochemistry of Materials Research Group, Aix-Marseille Université, CNRS, MADIREL, UMR 7246, Marseille, France, ³ Optoelectronics and Photovoltaics (OPTO-PV) Team, Institute of Microelectronic Materials Nanosciences of Provence (IM2NP), St Jérôme Center, University of Provence, Marseille, France, ⁴ Mines Saint-Etienne, Department of Flexible Electronics, Center of Microelectronics in Provence, Gardanne, France

OPEN ACCESS

Edited by:

Jean-Michel Lavoie,
Université de Sherbrooke, Canada

Reviewed by:

Xiao-Yu Wu,
Massachusetts Institute of
Technology, United States
Zhibao Huo,
Shanghai Jiao Tong University, China

*Correspondence:

Florence Vacandio
florence.vacandio@univ-amu.fr

Specialty section:

This article was submitted to
Chemical Engineering,
a section of the journal
Frontiers in Chemistry

Received: 25 October 2018

Accepted: 23 January 2019

Published: 08 February 2019

Citation:

Fraoucene H, Sugawati VA, Hatem D, Belkaid MS, Vacandio F, Eyraud M, Pasquinelli M and Djenizian T (2019) Optical and Electrochemical Properties of Self-Organized TiO₂ Nanotube Arrays From Anodized Ti–6Al–4V Alloy. *Front. Chem.* 7:66. doi: 10.3389/fchem.2019.00066

Due to their high specific surface area and advanced properties, TiO₂ nanotubes (TiO₂ NTs) have a great significance for production and storage of energy. In this paper, TiO₂ NTs were synthesized from anodization of Ti–6Al–4V alloy at 60 V for 3 h in fluoride ethylene glycol electrolyte by varying the water content and further annealing treatment. The morphological, structural, optical and electrochemical performances of TiO₂ NTs were investigated by scanning electron microscope (SEM), energy dispersive X-ray spectroscopy (EDS), X-ray diffraction (XRD), UV-Visible spectroscopy and electrochemical characterization techniques. By varying the water content in the solution, a honeycomb and porous structure was obtained at low water content and the presence of ($\alpha + \beta$) phase in Ti–6Al–4V alloy caused not uniform etching. With an additional increase in water content, a nanotubular structure is formed in the ($\alpha + \beta$) phases with different morphological parameters. The anatase TiO₂ NTs synthesized with 20 wt% H₂O shows an improvement in absorption band that extends into the visible region due the presence of vanadium oxide in the structure and the effective band gap energy (E_g) value of 2.25 eV. The TiO₂ NTs electrode also shows a good cycling performance, delivering a reversible capacity of 82 mAh.g⁻¹ (34 μ Ah.cm⁻². μ m⁻¹) at 1 C rate over 50 cycles.

Keywords: TiO₂ nanotubes, Ti–6Al–4V alloy, anodization, Li-ion microbatteries, negative electrode

INTRODUCTION

Rechargeable batteries play an important role in powering the electronic devices and in storing energy due to their high energy and power density which are expected to be a solution for the future energy storage requirements (Li et al., 2017). Due to the lack of suitable on-board power sources, the advances in the miniaturization of microelectronics is growing, opening opportunities to explore the both cathode and anode materials as thin-films (Sugawati et al., 2016) and nanostructured electrodes by utilizing various synthesis and deposition techniques (Djenizian et al., 2011; Pikul et al., 2013; Ellis et al., 2014; Xiong et al., 2014; Sugawati et al., 2018).

Titanium dioxide (TiO₂) is a semiconductor material that has been studied extensively in the last few decades due to its chemical stability, non-toxicity and biocompatibility (Morozová et al., 2012; Pansila et al., 2012; Reszczynska et al., 2014). In Li-ion microbatteries, the electrochemical performances of anode materials are highly dependent on their morphologies, surface characteristics, and particle sizes. Many researchers proposed to reduce the size of TiO₂ anode material to the nanometer scale in order to increase not only the number of reaction sites, but also gives new properties to the materials (Armstrong et al., 2005). Among these nanostructured materials, self-organized TiO₂ nanotubes (TiO₂ NTs) obtained by anodization of Ti foil can give a high porosity and larger specific area offering an enhancement in the cell capacity and cycle life (Ortiz et al., 2008, 2009; Fang et al., 2009; Panda et al., 2012; Kyeremateng et al., 2013b; Plylahan et al., 2014; Chang et al., 2015; Salian et al., 2017).

In addition, physical and electrochemical performance of TiO₂ NTs can be enhanced by chemical modification of the surface (Plylahan et al., 2012; Kyeremateng et al., 2013a; Sopha et al., 2017) and by incorporation of foreign ions into TiO₂ lattice such as Sn⁴⁺ (Kyeremateng et al., 2013b), Fe³⁺ (Das et al., 2011), Ni²⁺ (Choi et al., 2009), Nb⁵⁺ (Salian et al., 2018), and V³⁺ (Lin et al., 2013). The electrical conductivity and electrochemical kinetics of TiO₂ NTs electrodes can be improved by doping with Ti³⁺ ions due to a Li⁺ diffusion coefficient of $1.09 \times 10^{-12} \text{ cm}^2 \text{ s}^{-1}$ which is almost one order of magnitude higher than that of TiO₂ NTs ($1.39 \times 10^{-13} \text{ cm}^2 \text{ s}^{-1}$) (Duan et al., 2016). Yu et al. also demonstrated that 5 at.% Sn doped TiO₂ NTs exhibits the best cycling stability with specific capacity of 386 mAh.g⁻¹ and coulombic efficiency of 99.2% after 50 cycles at 0.1C (Yu et al., 2014).

Ternary titanium alloy (Ti-6Al-4V, with 6 wt% Aluminum and 4 wt% Vanadium) have also been utilized to synthesize the self-organized TiO₂ NTs, notably for their use in a wide range of applications such as bone substitute applications, including orthopedic and dental implants due to their superior compatibility, mechanical resistance, excellent corrosion resistance, and good thermal stability (Long and Rack, 1998; Black and Hastings, 2013). Furthermore, research works focused to improve the osseointegration and stability of the TA6V implant in the human body (Jo et al., 2013). However, to the best of our knowledge, there have been no reports to date on the use of the anodized TA6V alloy as electrode for Li-ion microbatteries. The basic objective of this work is therefore to study the electrochemical performance and optical properties of the anodized TA6V alloy produced through electrochemical anodization in fluoride-containing ethylene glycol electrolyte.

EXPERIMENTAL

Synthesis of TiO₂ Nanotubes

The Ti–6Al–4V (TA6V) alloy (0.1 mm thickness, 25% tolerance, Goodfellow) were cut into square shape ($1.2 \times 1.2 \text{ cm}$) with a selected work area of 0.6 cm^2 . Before anodization, the Ti–6Al–4V foils were degreased by sonication in acetone, 2-propanol and methanol for 10 min each, rinsed with ultrapure water and dried in a stream of compressed air. The anodization

was performed in a two-electrode electrochemical cell with Ti–6Al–4V foil as the anode and platinum foil as the cathode. At room temperature, all anodization experiments were carried out under a constant voltage of 60 V using a generator (ISO-TECH IPS-603) for 3 h. Ethylene glycol (EG) solution containing 0.3 wt% ammonium fluoride (NH₄F) was used as electrolyte, and the water content was varied at 2, 5, 10, 15, and 20 wt%. After anodization, the samples were soaked in ultrapure water for 10 min and then dried in an oven at 50°C for 10 min. In order to transform the amorphous crystallographic structure obtained just after electrochemical anodization into crystalline structure, the samples were annealed at 500°C for 3 h with a heating and cooling rate of 5°C/min.

Characterization of the Samples

Morphological characterization of the TiO₂ NTs was investigated by scanning electron microscopy (SEM) using a PHILIPS XL30. The chemical composition was analyzed by energy dispersive X-ray spectroscopy (EDS). The crystalline phases were characterized by X-ray diffraction (XRD) analysis. The diffraction patterns were obtained by a X'Pert Philips MPD with a Panalytical X'Celerator detector using a graphite monochromized CuK α radiation ($\lambda = 1.5418 \text{ \AA}$). The measurements were performed within the range of 2θ from 20° to 70°. The optical properties were investigated using a UV-Visible spectroscopy from 250 to 800 nm.

The electrochemical performance tests were performed using two-electrode Swagelok cells assembled in an argon-filled glove box in which the oxygen and moisture contents were <2 ppm. A 9 mm diameter Li foil was used as the counter electrode and two sheets of Whatman glass microfiber separator were soaked in the electrolyte of lithium hexafluorophosphate in ethylene carbonate and diethylene carbonate electrolyte (1M LiPF₆ in EC/DEC of 1:1 w/w) purchased from Sigma-Aldrich prior to assembling the cell. The cycling experiments were performed using a VMP3 potentiostat-galvanostat (Biologic, France). For all experiments, no additives such as poly (vinyl difluoride) as binder and carbon black as conductive agent were utilized. Cyclic voltammetry (CV) measurements were performed in the range voltage of 1–3 V vs. Li/Li⁺ at a scan rate of 0.05, 0.1 and 0.5 mV.s⁻¹, respectively. For galvanostatic discharge-charge tests, a constant current density of 3.23 $\mu\text{A.cm}^{-2}$ (C/10), 6.47 $\mu\text{A.cm}^{-2}$ (C/5), 16.18 $\mu\text{A.cm}^{-2}$ (C/2), and 32.35 $\mu\text{A.cm}^{-2}$ (1C), respectively, was applied to the assembled cells with a cut-off potential of 1–3 V vs. Li/Li⁺.

EXPERIMENTAL RESULTS

Morphological and Chemical

Characterization

Surface Morphology

Figure 1 shows the SEM images of the different morphologies of TA6V alloy anodized at 60 V for 3 h in Ethylene Glycol (EG) solution containing 0.3 wt% NH₄F with different water contents. It should be noticed that the ternary titanium alloy studied in the present work consist of two metallurgical phases, the α phase being enriched in Al and the β phase in V (Macak et al., 2005). We noted a great influence of the water content on

the formation of the self-organized TiO₂ NTs, both randomly arranged porous structure and uniformly arranged nanotubes. The formation of the porous structure depends on the underlying

phase (α or β) and the anodization parameters. As seen in **Figure 1A**, a honeycomb is obviously formed on the surface at water content of 2 wt%, however not on the entire surface.

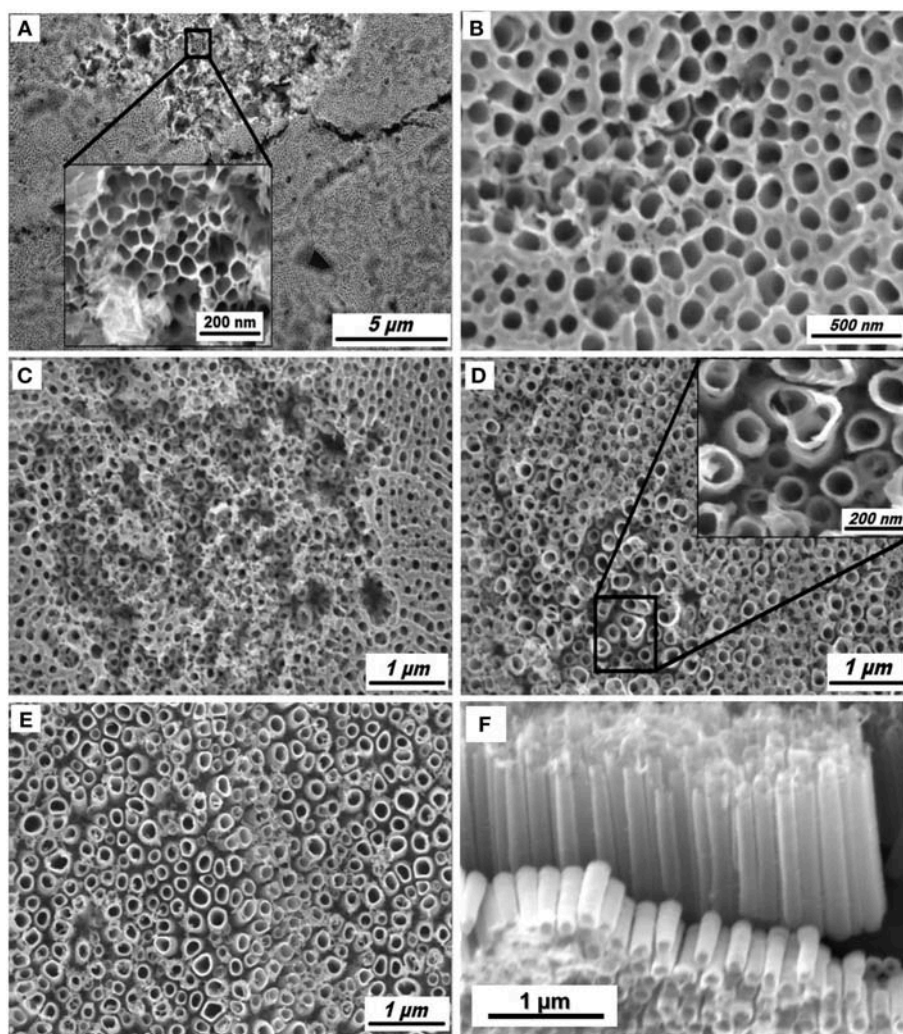


FIGURE 1 | SEM images of TiO₂ NTs obtained from anodization of TA6V alloy in fluoride ethylene glycol electrolyte with different water contents: 2 wt% (A), 5 wt% (B), 10 wt% (C), 15 wt% (D), and 20 wt% (E). Tilted view of TiO₂ NTs synthesized in 20 wt% H₂O (F).

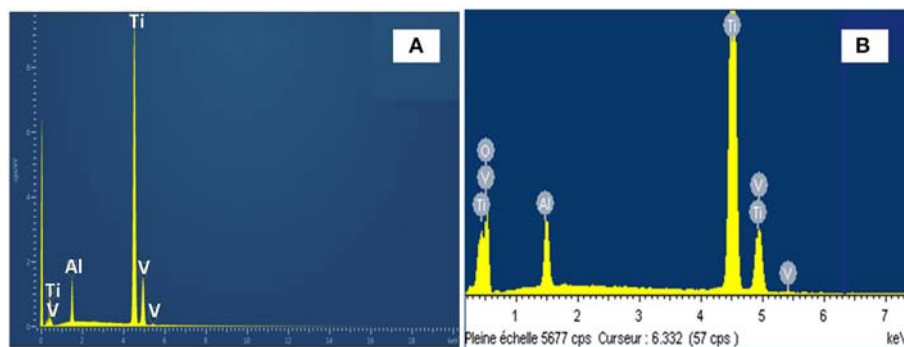


FIGURE 2 | EDS spectra of: pristine TA6V alloy (A) and anodized TA6V alloy in fluoride ethylene glycol electrolyte with 20 wt% H₂O content (B).

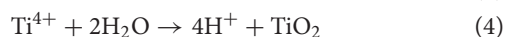
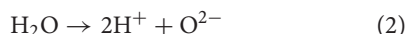
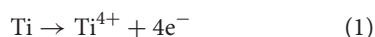
TABLE 1 | Elemental composition of the pristine TA6V alloy and the anodized TA6V alloy obtained in fluoride ethylene glycol electrolyte carrying 20 wt% H₂O content.

Element	% Weight		% Atomic	
	Pristine TA6V alloy	Anodized TA6V alloy	Pristine TA6V alloy	Anodized TA6V alloy
Al	6.41	3.61	10.87	3.95
V	3.21	2.68	2.88	1.55
O	–	29.93	–	55.21
Ti	90.37	63.78	86.25	39.29

Figures 1B–D exhibits the positive influence of the improved water content, from 5 to 15 wt%. The β phase is preferentially etched as the amount of water in the solution increases, indicating the enhanced solubility of the vanadium oxides. A similar phenomenon has been previously reported for the TiO₂ NTs grown from anodization of TA6V alloy in different electrolytes (sulphuric/hydrofluoric acid and ammonium sulfate with 0.2 wt% NH₄F, respectively) at controlled voltage and anodization time (Matytkina et al., 2011; Moravec et al., 2016). According to **Figures 1E,F**, a well-separated TiO₂ NTs with an inner diameter varying between 97 and to 206 nm and a length of 1.25 μ m can be formed in the fluoride-containing EG electrolyte carrying 20 wt% H₂O. At this percentage, the nanotubular structure is formed in the two phases ($\alpha + \beta$) via the formation of an oxide layer (TiO₂) and the chemical dissolution of this layer assisted by an electric field. The formation mechanism of TiO₂ NTs from alloys is similar to that of the pristine TiO₂ NTs obtained from anodization of pure Ti.

Composition Analysis

Figure 2 shows the EDS spectra of TiO₂ NTs grown from anodization of TA6V alloy with 20 wt% H₂O content in the fluoride EG. The energy dispersive X-ray characterization values are summarized in **Table 1**. After anodization, there is a slight difference of wt% for each element and the strong presence of oxygen confirming the formation of oxides. In fact, the wt% of Ti in the anodized TA6V alloy is lower compared to that of the pristine TA6V alloy. This result suggests that Ti anode is oxidized into TiO₂ through the oxidation of Ti to form Ti⁴⁺ according to Equation (1).



The dissociation of H₂O takes place at the cathode (Equation 2) and the overall reaction leads to the formation of the titanium dioxide (Equations 3 and 4) (Ortiz et al., 2009). TiO₂ NTs formed in the fluoride electrolyte are characterized by different morphological parameters (diameter, thickness, length,...) that can be confirmed from **Figures 1E,F**.

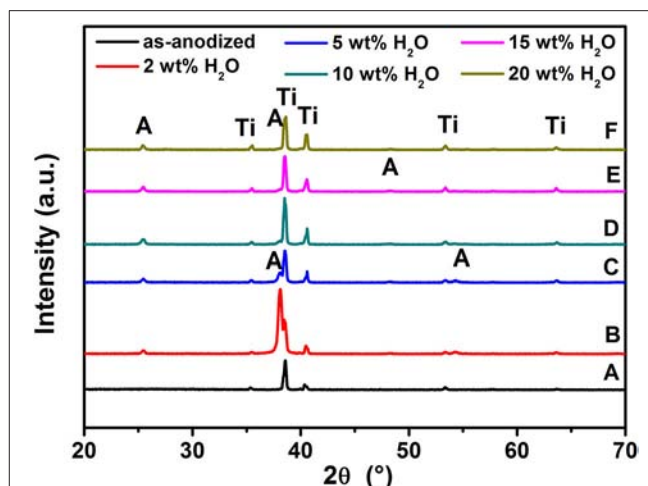


FIGURE 3 | XRD patterns of TiO₂ NTs grown on TA6V alloy: as-anodized (A), films annealed at 500°C for 3 h with the water content in the electrolyte is: 2 wt% H₂O (B), 10 wt% H₂O (C), 5 wt% H₂O (D), 15 wt% H₂O (E), and 20 wt% H₂O (F). "A" is Anatase, "Ti" is substrate of film.

The EDS analysis also shows that Al and V values are lower compared to the TA6V alloy, which can be explained by the oxidation of these elements to form the thin oxide layers of Al₂O₃ and V₂O₅ (or VO₂), respectively (Gibran et al., 2018). Note that Al and V signals may come also from the bulk alloy, not only from the surface oxide layer (Benea et al., 2014). The presence of these layers improves the osseointegration and enhances the biocompatibility of the implant material (Jo et al., 2013). It can be noted that no trace of F can be detected suggesting that this element is not incorporated into the oxides during the anodization process.

Structural Properties

After anodization, the as-formed TiO₂ NTs at various water contents were annealed at 500°C for 3 h to convert the amorphous compound into a crystalline structure. **Figure 3** shows the XRD patterns of these films. Compared to the as-anodized TiO₂ NTs using 20 wt% H₂O, the crystallizations of the TiO₂ NTs films are mainly composed of anatase phase, as evidenced by the diffraction peaks at $2\theta = 25.50, 37.80, 48.30$, and 55.10° . The diffraction peaks can be indexed to the (101), (004), (200), and (211) planes, respectively (JCPDS Pattern no 00-021-1272). Furthermore, the XRD patterns give no indication of the presence of the Al₂O₃ and V₂O₅ (or VO₂) peaks due to their low percentage in the samples and the high dispersion of metal ions in the nanotubular lattice (Li et al., 2009; Tang et al., 2014).

Optical Properties

Figures 4A–E shows the optical absorption spectra of the annealed TiO₂ NTs at 500°C for 3 h obtained from anodization of TA6V alloy in fluoride EG electrolyte at different water contents. The strong absorptions of these films in the range of 250–336 nm correspond to the electron-transition from the valence band (VB) to the conduction band (CB) with creation of two very

reactive species, an electron in the CB and a hole in the VB (Hoffmann et al., 1995). The UV absorption edge of samples prepared using 2, 5, 10, 15, and 20 wt% H₂O that are around 332, 335, 340, 380, and 410 nm, respectively, correspond to the maximum absorption edge for each curves that are projected on the wavelength axis (nm). By increasing the water content in the solution, the absorption band extends into the visible region. This behavior explained by the increase of the active surface (number of reaction sites) with the formation of TiO₂ NTs characterized by an improvement of their morphological parameters (diameter, thickness, length...) confirmed by the SEM images given in **Figures 1E,F**. In addition, the presence of vanadium oxide in the structure is responsible for additional impurity states in the band gap near the CB or the VB altering the optical properties of the material (Li et al., 2009; Nešić et al., 2013; Chen et al., 2015). The same behavior was obtained by the study of Luo et al. suggesting that the extends of absorption edge into the visible region is attributed to the quantum size effects (Luo et al., 2008).

Evaluation of the TiO₂ NTs band gap (E_g) grown from anodization of Ti–6Al–4V alloy can be obtained from the absorption coefficient α given in Equation (5) (Mane et al., 2005)

$$\alpha = (h\nu - E_g)^{0.5}/h\nu \quad (5)$$

$\alpha = A / l$, where A is the absorption film, l is the tubes length ($l = 1.25 \mu\text{m}$) and $h\nu$ is the photon energy. **Figure 4F** shows the variations of $(\alpha h\nu)^2$ vs. photon energy ($h\nu$) for the film synthesized using 20 wt% H₂O in the electrolyte. The extrapolation of the straight line to zero absorption gives the effective band gap energy (E_g) value of approximately 2.25 eV, which is significantly lower than that of TiO₂ anatase (~ 3.2 eV) (Li et al., 2013). The low band gap value is explained by the presence of vanadium oxide that can extend the absorption band into the visible region. Compared to the color of as-formed Ti–6Al–4V alloy in **Figure 5A**, this result is in agreement with the EDS analysis and the appearance of yellow-green color in the annealed sample at 500°C for 3 h as shown in **Figure 5B**. The color reflected on the annealed TiO₂ NTs sample at 20 wt% H₂O can be determined through the UV absorption spectra. As seen, the lowest absorption spectra is approximately 500 nm, reflecting a yellow-green color. In the agreement with the previous findings, the V-doped TiO₂ materials were prepared by both sol-gel technique and liquid phase deposition (LPD) reported that the presence of V can widen the absorption threshold wavelength to 650 nm (Gu et al., 2007; Zhou et al., 2010). In **Figure 5A** is presented a photo of the sample before annealing.

Electrochemical Performance

In this work, self-organized TiO₂ NTs fabricated from TA6V alloy containing α and β phase are investigated as a potential anode materials for Li-ion microbatteries. The electrochemical performance of TiO₂ NTs synthesized using ethylene glycol electrolyte containing 20 wt% H₂O is elucidated through cyclic voltammetry (CV) to analyse the charging and discharging mechanisms during cycling. The anodic and cathodic peaks obtained during the measurements represent the possible phase

transformations or redox reactions with the electrodes (Heinze, 1984). The TiO₂ NTs on TA6V alloy was tested at various scanning rates (0.05, 0.1 and 0.5 mV.s^{−1}) between 1 and 3 V vs. Li/Li⁺ at room temperature, as displayed in **Figure 6A**. Two distinct cathodic and anodic peaks are observed for all scan rates, corresponding to the lithium insertion (Ti⁴⁺ → Ti³⁺) and extraction (Ti³⁺ → Ti⁴⁺) in anatase (Li et al., 2012). At a scan rate of 0.05 mV.s^{−1}, the cathodic peak centered at ~ 1.74 V vs. Li/Li⁺ and the anodic peak centered at 1.96 V vs. Li/Li⁺ show a peak potential separation (ΔE_p) of 0.22 V. The cathodic and anodic peak slightly shifted to 1.73 V vs. Li/Li⁺ and 1.97 V vs. Li/Li⁺, respectively at 0.1 mV.s^{−1}, showing the ΔE_p of 0.24 V. Further higher scan rate of 0.5 mV.s^{−1}, the cathodic and anodic peaks are significantly shifted to ~ 1.71 V vs. Li/Li⁺ and ~ 2.03 V vs. Li/Li⁺, respectively with the ΔE_p of 0.32 V. Obviously, as the scan rate was increased, the displacement current increased due to the fact that the over potential become higher.

The separation between the cathodic and anodic peaks indicated the extent of polarization. Hence, the slow scan rate is selected to establish an electrochemical equilibrium between the active species due to the fast scan rate might provoke peak identification more difficult (Plylahan et al., 2015). In addition to the main peaks, an additional peak pair at a potential of ~ 2.55 V vs. Li/Li⁺ with a low current density is showed up in the reduction and oxidation potential at three different scan rates. It is due to the presence of an electrochemically active vanadium oxide with low valence state of vanadium such as VO₂ phase (Mai et al., 2010; Mattelaer et al., 2017). The formation of nanotubes on two phases ($\alpha + \beta$) titanium alloys leads to the selective dissolution of the elements and the different reactions rates at different phases, yielding VO₂ and Al₂O₃ phases. Considering the peak intensity of VO₂ with respect to anatase TiO₂ NTs, it is assumed that the VO₂ phase might not contribute significantly to the storage performance of the electrode. Apart from both peak pairs, no additional peak for the Al₂O₃ phase can be detected in the CVs curves as this phase is probably to be electrochemically inactive. Furthermore, cyclic voltammograms at low scan rate of both 0.05 and 0.1 mV.s^{−1} for 10 cycles reveal a good stability of the electrode which is attested by no peak shifting (see **Figures 6B,C**). The main cathodic and anodic peaks can be clearly identified up to the 10th cycle.

The charge-discharge behaviors of the alloyed TiO₂ NTs were examined by galvanostatic tests between cut-off voltages of 1 and 3 V vs. Li/Li⁺. The results are shown in **Figure 7A**. It is found that in the first discharge process, there is a short plateau at ~ 2.55 V which indicates a very small amount of Li ions inserted into VO₂ phase with a low storage capacity. This plateau is in good accordance with the cyclic voltammogram curve. The potential continuously drops and reaches the large constant plateau at ~ 1.77 V which is attributed to homogeneous Li insertion into the bulk anatase with a lithium insertion capacity of about 85 mAh.g^{−1} (36 $\mu\text{Ah.cm}^{-2}.\mu\text{m}^{-1}$). The slope after the plateau, started from ~ 1.77 V to 1 V has the insertion capacity of 183 mAh.g^{−1} (77 $\mu\text{Ah.cm}^{-2}.\mu\text{m}^{-1}$), which is attributed to the energy capacity accumulated on the surface of anatase. The lithium extraction capacity is solely about 20 mAh.g^{−1} within

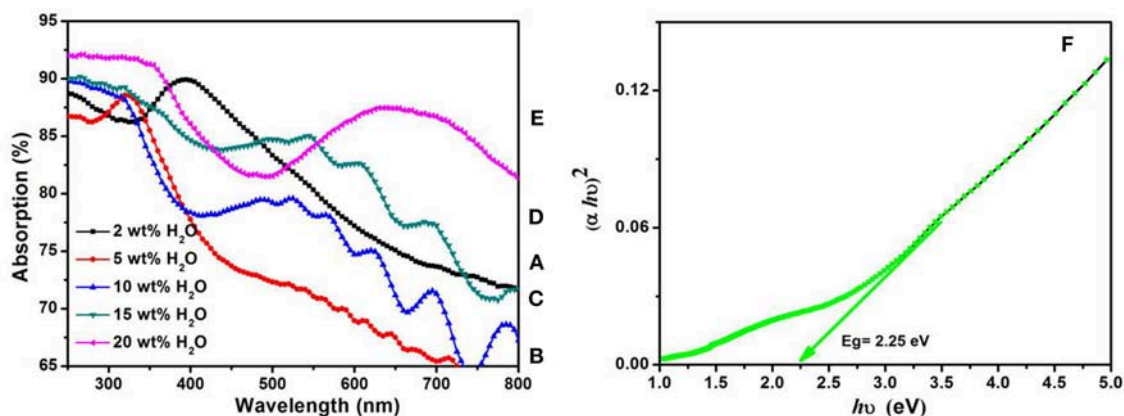


FIGURE 4 | UV-Vis absorption spectra of annealed TiO₂ NTs layers grown from anodization of TA6V alloys at 60 V for 3 h in fluoride ethylene glycol electrolyte with different water contents: 2wt%H₂O (A), 5wt%H₂O (B), 10wt%H₂O (C), 15wt%H₂O (D), and 20wt%H₂O (E). Variations of $(\alpha h\nu)^2$ vs. photon energy ($h\nu$) of TiO₂ NTs synthesized with 20 wt% H₂O in the fluoride ethylene glycol electrolyte (F).

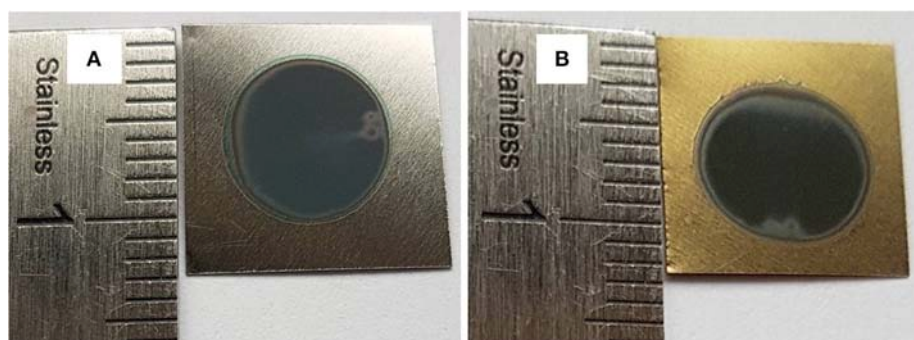


FIGURE 5 | Ti-6Al-4V alloys anodized in fluoride ethylene glycol electrolyte with 20 wt%H₂O at 60V for 3 h: as-formed (A) and annealed at 500 °C for 3 h (B).

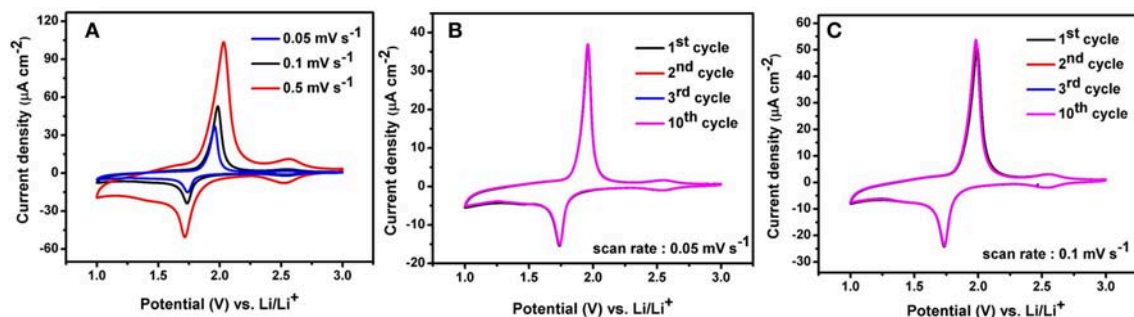


FIGURE 6 | Cyclic voltammograms of anatase TiO₂ NTs on Ti-6Al-4V alloy performed in the potential range 1–3 V at a scan rate of 0.05 mV s⁻¹, 0.1 mV s⁻¹, and 0.5 mV s⁻¹ (A), 10 cycles CVs at scan rate of 0.05 mV s⁻¹ (B) and 10 cycles CVs at scan rate of 0.1 mV s⁻¹ (C).

the charging potential window of 1–1.84 V in the first cycle, which is smaller than the capacity in the discharging potential region of 1.77–1 V. This results indicates that the irreversible capacity mainly occurs within the sloped region between 1.77 and 1 V. However, the main voltage plateaus consist of the discharge plateau at ~ 1.77 V vs. Li/Li⁺ and a charge plateau

at ~ 1.84 V vs. Li/Li⁺, resulting in a very small polarization of 0.07 V at C/10 rate. In a good agreement with previous results, the charge plateau at ~ 1.89 V vs. Li/Li⁺ and discharge plateau at ~ 1.75 V vs. Li/Li⁺ with a higher polarization of 0.14 V at C/10 rate are obtained for the self-organized TiO₂ NTs synthesized in a solution of ethylene glycol containing 1.0 wt% H₂O and

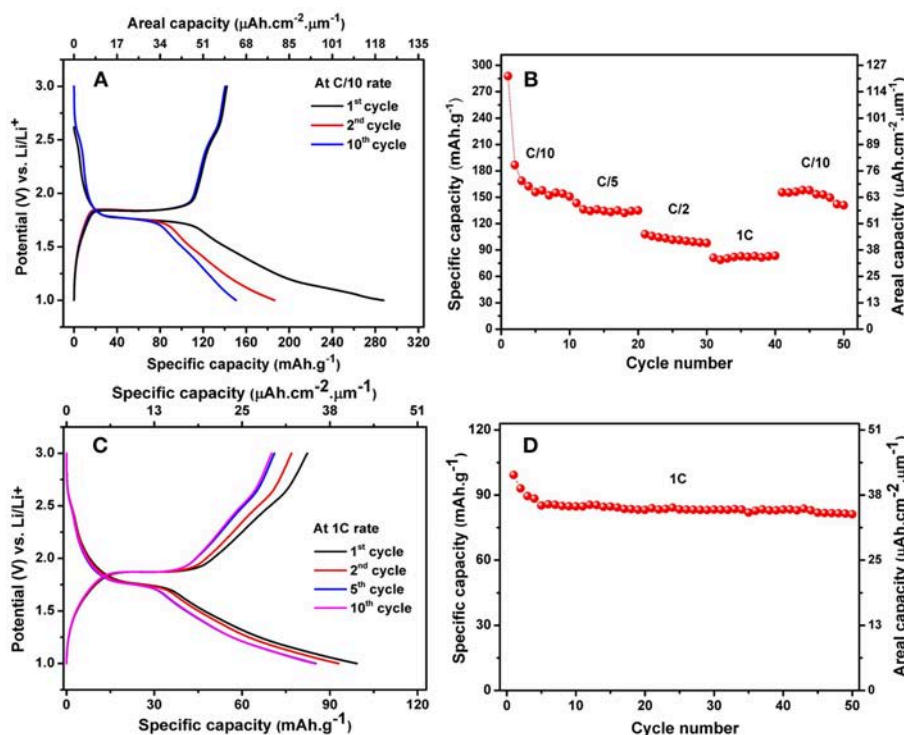


FIGURE 7 | Charge-discharge profile of anatase TiO₂ NTs on Ti–6Al–4V alloy at C/10 rate (A) and the discharge capacity vs. cycle number at multiple C-rates (B), Charge-discharge profile of anatase TiO₂ NTs on Ti–6Al–4V alloy at 1C rate (C) and cycling performance of anatase TiO₂ NTs on Ti–6Al–4V alloy at 1C rate (D).

2 wt% NH₄F (Prosini et al., 2013). The smaller difference of the charge and discharge plateaus indicates the better electrode reaction kinetics and better rate performance. The reversible Li⁺ insertion into TiO₂ NTs can be written according to Equation (6) (Djenizian et al., 2011).



Taking the middle points between these two plateaus, the average working potentials of cell were determined to be ~1.80 V vs. Li/Li⁺. The high working potential of the nanotubes is an advantage to avoid the electrolyte reduction and limit the formation of a solid electrolyte interphase (SEI) layer on the surface of the electrode (Xu et al., 2007).

The electrochemical reaction at the anode is based on the reduction of Ti⁴⁺ to Ti³⁺ and the Li⁺ insertion into the TiO₂ NTs. Lithium ions can be inserted reversibly into anatase TiO₂ to form Li_{0.5}TiO₂, giving a theoretical specific capacity of 168 mAh.g⁻¹ while the theoretical capacity of amorphous TiO₂ NTs is 335 mAh.g⁻¹ for the insertion of one Li per Ti unit (Auer et al., 2018). In this study, the obtained initial discharge and charge capacities of the electrodes are 288 mAh.g⁻¹ (122 μAh.cm⁻².μm⁻¹) and 142 mAh.g⁻¹ (60 μAh.cm⁻².μm⁻¹), corresponding to the lithium insertion coefficient of 0.86 and 0.42, respectively with a relatively low initial coulombic efficiency of 49.30%. A high capacity of anatase TiO₂ NTs in the first few

initial cycles is probably due to the presence of the remaining amorphous nanotubes (Prosini et al., 2013).

For the subsequent cycles, the discharge capacity values recorded in the 2nd and 10th cycles are 186 and 150 mAh.g⁻¹ with an improved coulombic efficiency of 76.34 and 94.67%, respectively. The capacity fading from the 2nd to the 10th cycle can be attributed to an irreversible reaction of Li⁺ ions with OH groups existing on the surface of nanotubes at low voltages (Ferrari et al., 2017). In addition, the initial capacity loss may also be caused by the interfacial reaction between the residual traces of water on the surface of the nanotubes and lithium salt in the electrolyte combined with the presence of structural defects (Hanzu et al., 2011; Chung et al., 2015). However, the cycling retention continuously improved after first few cycles, thereby coulombic efficiency approaches 100%.

The cells were cycled at multiple C-rates as presented in Figure 7B. TiO₂ NTs electrode gives a stable capacity of 150 mAh.g⁻¹ (63 μAh.cm⁻².μm⁻¹) at C/10, 134 mAh.g⁻¹ (56 μAh.cm⁻².μm⁻¹) at C/5, 101 mAh.g⁻¹ (43 μAh.cm⁻².μm⁻¹) at C/2 and 83 mAh.g⁻¹ (35 μAh.cm⁻².μm⁻¹) at 1C. The capacity can be recovered after cycling at C/10 rate over 50 cycles. We noted that the capacity loss at C/10 rate after cycling at fast kinetic rates is attributed to the hindered migration of Li⁺ ions within the TiO₂ NTs system due to the presence of other crystalline phases. However, it can be observed that the capacity of two last cycles are enough stable at C/10 rate, hence we assumed the discharge capacities stabilize

after few initial cycles. To prove the cycling stability of the TiO₂ NTs, galvanostatic charge-discharge were performed at 1C rate up to 50 cycles (Figures 7C,D). The results thus clearly show a good cycling stability of the TiO₂ NTs electrodes that can deliver a reversible capacity of 82 mAh.g⁻¹ (34 $\mu\text{Ah.cm}^{-2}.\mu\text{m}^{-1}$).

CONCLUSION

In summary, self-organized TiO₂ NTs have been successfully synthesized via anodization of Ti–6Al–4V alloy at 60 V for 3 h in fluoride ethylene glycol electrolyte at various water contents (2 wt% up to 20 wt% H₂O). Significant differences in morphological structure of TiO₂ NTs were obtained. At low water content, a honeycomb and porous structure is formed on the surface due to the presence of both α and β phases in the Ti–6Al–4V alloy leading to a dissimilar non-uniform etching. Remarkably, self-organized TiO₂ NTs could be formed uniformly across both α and β phases at 20 wt% H₂O. The optical properties and electrochemical performance of the anodized TiO₂ NTs carrying 20 wt% H₂O have been investigated. The anatase TiO₂ NTs offers a low band gap value equal to 2.25 eV due to the presence

of vanadium oxide in the structure that widens the threshold of absorption wavelength into the visible region. Moreover, galvanostatic charge-discharge tests exhibited a good capacity of 82 mAh.g⁻¹ (34 $\mu\text{Ah.cm}^{-2}.\mu\text{m}^{-1}$) at 1C rate over 50 cycles. These results show that the self organized TiO₂ NTs grown from TA6V alloy can be considered as competitive anode materials for Li-ion microbatteries, as well as other potential applications in gas sensors, solar cells, and photocatalysis.

AUTHOR CONTRIBUTIONS

HF and VS performed experiments, analyzed the experimental results, and wrote the manuscript. DH, MB, FV, ME, MP, and TD discussed experimental results. All the authors contributed to the reading of paper and gave advice on the revision of the manuscript.

FUNDING

This work is carried out with the contribution of the cooperation project No: 16 MDU 970; Mixed Evaluation and Prospective Commission-Hubert Curien Program (CMEP-PHC) TASSILI.

REFERENCES

- Armstrong, A. R., Armstrong, G., Canales, J., García, R., and andBruce, P. G. (2005). Lithium-ion intercalation into TiO₂-B nanowires. *Adv. Mater.* 17, 862–865. doi: 10.1002/adma.200400795
- Auer, A., Steiner, D., Portenkirchner, E., and Kunze-Liebhäuser, J. (2018). Nonequilibrium phase transitions in amorphous and anatase TiO₂ nanotubes. *ACS Appl. Energy Mater.* 1, 1924–1929. doi: 10.1021/acsaem.7b00319
- Benea, L., Mardare-Danaila, E., Mardare, M., and Celis, J.-P. (2014). Preparation of titanium oxide and hydroxyapatite on Ti–6Al–4V alloy surface and electrochemical behaviour in bio-simulated fluid solution. *Corros. Sci.* 80, 331–338. doi: 10.1016/j.corsci.2013.11.059
- Black, J., and Hastings, G. (2013). *Handbook of Biomaterial Properties*. London: Chapman & Hall; Springer Science and Business Media.
- Chang, Y. C., Peng, C. W., Chen, P. C., Lee, C. Y., and Chiu, H. T. (2015). Bio-ingredient assisted formation of porous TiO₂ for Li-ion battery electrodes. *RSC Adv.* 5, 34949–34955. doi: 10.1039/C5RA04896F
- Chen, Y. W., Chang, J. Y., and Moongraksathum, B. (2015). Preparation of vanadium-doped titanium dioxide neutral sol and its photocatalytic applications under UV light irradiation. *J. Taiwan Inst. Chem. Eng.* 52, 140–146. doi: 10.1016/j.jtice.2015.02.006
- Choi, J., Park, H., and Hoffmann, M. R. (2009). Effects of single metal-ion doping on the visible-light photoreactivity of TiO₂. *J. Phys. Chem. C*, 114, 783–792. doi: 10.1021/jp908088x
- Chung, D. Y., Chung, Y.-H., Kim, S., Lim, J. W., Lee, K. J., Jung, N., et al. (2015). Understanding interface between electrode and electrolyte: organic/inorganic hybrid design for fast ion conductivity. *J. Phys. Chem. C*, 119, 9169–9176. doi: 10.1021/acs.jpcc.5b02075
- Das, S. K., Gnanavel, M., Patel, M. U. M., Shivakumara, C., and Bhattacharyya, A. J. (2011). Anomolously high lithium storage in mesoporous nanoparticulate aggregation of Fe³⁺ doped anatase titania. *J. Electrochem. Soc.* 158:A1290. doi: 10.1149/2.029112jes
- Djenizian, T., Hanzu, I., and Knauth, P. (2011). Nanostructured negative electrodes based on titania for Li-ion microbatteries. *J. Mater. Chem.* 21, 9925–9937. doi: 10.1039/C0JM04205F
- Duan, J., Hou, H., Liu, X., Yan, C., Liu, S., Meng, R., et al. (2016). In situ Ti³⁺-doped TiO₂ nanotubes anode for lithium ion battery. *J. Porous Mater.* 23, 837–843. doi: 10.1007/s10934-016-0139-6
- Ellis, B. L., Knauth, P., and Djenizian, T. (2014). Three-dimensional self-supported metal oxides for advanced energy storage. *Adv. Mater.* 26, 3368–3397. doi: 10.1002/adma.201306126
- Fang, H. T., Liu, M., Wang, D. W., Sun, T., Guan, D. S., Li, F., et al. (2009). Comparison of the rate capability of nanostructured amorphous and anatase TiO₂ for lithium insertion using anodic TiO₂ nanotube arrays. *Nanotechnology* 20:225701. doi: 10.1088/0957-4484/20/22/225701
- Ferrari, I. V., Braglia, M., Djenizian, T., Knauth, P., and Di Vona, M. L. (2017). Electrochemically engineered single Li-ion conducting solid polymer electrolyte on titania nanotubes for microbatteries. *J. Power Sources* 353, 95–103. doi: 10.1016/j.jpowsour.2017.03.141
- Gibran, K., Ibadurrahman, M., and Slamet. (2018). Effect of electrolyte type on the morphology and crystallinity of TiO₂ nanotubes from Ti–6Al–4V anodization. *IOP Conf. Ser. Earth Environ. Sci.* 105:012038. doi: 10.1088/1755-1315/105/1/012038
- Gu, D.-E., Yang, B.-C., and Hu, Y.-D. (2007). A novel method for preparing V-doped titanium dioxide thin film photocatalysts with high photocatalytic activity under visible light irradiation. *Catal. Lett.* 118, 254–259. doi: 10.1007/s10562-007-9179-5
- Hanzu, I., Djenizian, T., and Knauth, P. (2011). Electrical and point defect properties of TiO₂ nanotubes fabricated by electrochemical anodization. *J. Phys. Chem. C*, 115, 5989–5996. doi: 10.1021/jp1111982
- Heinze, J. (1984). Cyclic voltammetry—“Electrochemical Spectroscopy”. new analytical methods(25). *Angew. Chem. Int. Ed. Engl.* 23, 831–847. doi: 10.1002/anie.198408313
- Hoffmann, M. R., Martin, S. T., Choi, W., and Bahnemann, D. W. (1995). Environmental applications of semiconductor photocatalysis. *Chem. Rev.* 95, 69–96. doi: 10.1021/cr00033a004
- Jo, C.-I., Jeong, Y.-H., Choe, H.-C., and Brantley, W. A. (2013). Hydroxyapatite precipitation on nanotubular films formed on Ti–6Al–4V alloy for biomedical applications. *Thin Solid Films.* 549, 135–140. doi: 10.1016/j.tsf.2013.09.095
- Kyeremateng, N. A., Plylahan, N., dos Santos, A. C., Taveira, L. V., Dick, L. F., and Djenizian, T. (2013a). Sulfidated TiO₂ nanotubes: a potential 3D cathode material for Li-ion micro batteries. *Chem. Commun.* 49, 4205–4207. doi: 10.1039/c2cc36857a
- Kyeremateng, N. A., Vacandio, F., Sougrati, M. T., Martinez, H., Jumas, J. C., Knauth, P., et al. (2013b). Effect of Sn-doping on the electrochemical behaviour

- of TiO₂ nanotubes as potential negative electrode materials for 3D Li-ion micro batteries. *J. Power Sources*. 224, 269–277. doi: 10.1016/j.jpowsour.2012.09.104
- Li, H., Martha, S. K., Unocic, R. R., Luo, H., Dai, S., and Qu, J. (2012). High cyclability of ionic liquid-produced TiO₂ nanotube arrays as an anode material for lithium-ion batteries. *J. Power Sources* 218, 88–92. doi: 10.1016/j.jpowsour.2012.06.096
- Li, J., Du, Z., Ruther, R. E., An, S. J., David, L. A., Hays, K., et al. (2017). Toward low-cost, high-energy density, and high-power density lithium-ion batteries. *JOM-US69*, 1484–1496. doi: 10.1007/s11837-017-2404-9
- Li, L., Liu, C. Y., and Liu, Y. (2009). Study on activities of vanadium (IV/V) doped TiO₂ (R) nanorods induced by UV and visible light. *Mater. Chem. Phys.* 113, 551–557. doi: 10.1016/j.matchemphys.2008.08.009
- Li, Z., Ding, D., Liu, Q., and Ning, C. (2013). Hydrogen sensing with Ni-doped TiO₂ Nanotubes. *Sensors* 13, 8393–8402. doi: 10.3390/s130708393
- Lin, S.-H., Ou, C.-C., Su, M.-D., and Yang, C.-S. (2013). Photo-catalytic behavior of vanadia incorporated titania nanoparticles. *Catal. Sci. Technol.* 3, 2081–2091. doi: 10.1039/c3cy00053b
- Long, M., and Rack, H. J. (1998). Titanium alloys in total joint replacement—a materials science perspective. *Biomaterials* 19, 1621–1639. doi: 10.1016/s0142-9612(97)00146-4
- Luo, B., Yang, H., Liu, S., Fu, W., Sun, P., Yuan, M., et al. (2008). Fabrication and characterization of self-organized mixed oxide nanotube arrays by electrochemical anodization of Ti–6Al–4V alloy. *Mater. Lett.* 62, 4512–4515. doi: 10.1016/j.matlet.2008.08.015
- Macak, J. M., Tsuchiya, H., Taveira, L., Ghicov, A., and Schmuki, P. (2005). Self-organized nanotubular oxide layers on Ti-6Al-7Nb and Ti-6Al-4V formed by anodization in NH₄F solutions. *J. Biomed. Mater. Res. Part A* 75, 928–933. doi: 10.1002/jbm.a.30501
- Mai, L., Xu, L., Han, C., Xu, X., Luo, Y., Zhao, S., et al. (2010). Electrospun ultralong hierarchical vanadium oxide nanowires with high performance for lithium ion batteries. *Nano Lett.* 10, 4750–4755. doi: 10.1021/nl103343w
- Mane, R. S., Lee, W. J., Pathan, H. M., and Han, S. H. (2005). Nanocrystalline TiO₂/ZnO thin films: fabrication and application to dye-sensitized solar cells. *J. Phys. Chem. B* 109, 24254–24259. doi: 10.1021/jp0531560
- Mattelaer, F., Geryl, K., Rampelberg, G., Dendooven, J., and Detavernier, C. (2017). Amorphous and crystalline vanadium oxides as high-energy and high-power cathodes for three-dimensional thin-film lithium ion batteries. *ACS Appl. Mater. Interfaces* 9, 13121–13131. doi: 10.1021/acsami.6b16473
- Matytkina, E., Hernandez-López, J. M., Conde, A., Domingo, C., de Damborenea, J. J., and Arenas, M. A. (2011). Morphologies of nanostructured TiO₂ doped with F on Ti–6Al–4V alloy. *Electrochim. Acta* 56, 2221–2229. doi: 10.1016/j.electacta.2010.11.069
- Moravec, H., Vandrovčova, M., Chotova, K., Fojt, J., Pruchova, E., Joska, L., et al. (2016). Cell interaction with modified nanotubes formed on titanium alloy Ti-6Al-4V. *Mater. Sci. Eng. C*. 65, 313–322. doi: 10.1016/j.msec.2016.04.037
- Morozová, M., Kluson, P., Krysa, J., Vesely, M., Dzik, P., and Solcova, O. (2012). Electrochemical properties of TiO₂ electrode prepared by various methods. *Procedia. Eng.* 42, 573–580. doi: 10.1016/j.proeng.2012.07.450
- Nešić, J., Manojlović, D. D., Andelković, I., Dojčinović, B. P., Vulić, P. J., Krstić, J., and et Roglić, G. M. (2013). Preparation, characterization and photocatalytic activity of lanthanum and vanadium co-doped mesoporous TiO₂ for azo-dye degradation. *J. Mol. Catal. A: Chem.* 378, 67–75. doi: 10.1016/j.molcata.2013.05.018
- Ortiz, G. F., Hanzu, I., Djenizian, T., Lavela, P., Tirado, J. L., and Knauth, P. (2008). Alternative Li-ion battery electrode based on self-organized titania nanotubes. *Chem. Mater.* 21, 63–67. doi: 10.1021/cm801670u
- Ortiz, G. F., Hanzu, I., Knauth, P., Lavela, P., Tirado, J. L., and Djenizian, T. (2009). TiO₂ nanotubes manufactured by anodization of Ti thin films for on-chip Li-ion 2D microbatteries. *Electrochim. Acta* 54, 4262–4268. doi: 10.1016/j.electacta.2009.02.085
- Panda, S. K., Yoon, Y., Jung, H. S., Yoon, W. S., and Shin, H. (2012). Nanoscale size effect of titania (anatase) nanotubes with uniform wall thickness as high performance anode for lithium-ion secondary battery. *J. Power Sources*. 204:162167. doi: 10.1016/j.jpowsour.2011.12.048
- Pansila, P., Witit-Anun, N., and Chaiyakun, S. (2012). Influence of sputtering power on structure and photocatalyst properties of DC magnetron sputtered TiO₂ thin film. *Procedia. Eng.* 32, 862–867. doi: 10.1016/j.proeng.2012.02.024
- Pikul, J. H., Zhang, H. G., Cho, J., Braun, P. V., and King, W. P. (2013). High-power lithium ion microbatteries from interdigitated three-dimensional bicontinuous nanoporous electrodes. *Nat. Commun.* 4:1732. doi: 10.1038/ncomms2747
- Pylahan, N., Demoulin, A., Chrystelle Lebouin, C. L., Knauth, P., and Djenizian, T. (2015). Mechanism study of Li⁺ insertion into titania nanotubes. *RSC Adv.* 5, 28474–28477. doi: 10.1039/c5ra03759j
- Pylahan, N., Kyremateng, N. A., Eyraud, M., Dumur, F., Martinez, H., Santinacci, L., et al. (2012). Highly conformal electrodeposition of copolymer electrolytes into titania nanotubes for 3D Li-ion batteries. *Nanoscale Res. Lett.* 7:349. doi: 10.1186/1556-276x-7-349
- Pylahan, N., Letiche, M., Barr, M. K. S., and Djenizian, T. (2014). All-solid-state lithium-ion batteries based on self-supported titania nanotubes. *Electrochem. Commun.* 43, 121–124. doi: 10.1016/j.elecom.2014.03.029
- Prosini, P. P., Cento, C., and Pozio, A. (2013). Lithium-ion batteries based on titanium oxide nanotubes and LiFePO₄. *J. Solid State Electrochem.* 18, 795–804. doi: 10.1007/s10008-013-2324-8
- Reszczynska, J., Grzyb, T., Sobczak, J. W., Lisowski, W., Gazda, M., Ohtani, B., et al. (2014). Lanthanide co-doped TiO₂: the effect of metal type and amount on surface properties and photocatalytic activity. *Appl. Surf. Sci.* 307, 333–345. doi: 10.1016/j.apsusc.2014.03.199
- Salian, G. D., Koo, B. M., Lefevre, C., Cottineau, T., Lebouin, C., Tesfaye, A. T., et al. (2018). Niobium alloying of self-organized TiO₂ nanotubes as an anode for lithium-ion microbatteries. *Adv. Mater. Technol.* 3 :1700274. doi: 10.1002/admt.201700274
- Salian, G. D., Lebouin, C., Demoulin, A., Lepihin, M. S., Maria, S., Galeyeva, A. K., et al. (2017). Electrodeposition of polymer electrolyte in nanostructured electrodes for enhanced electrochemical performance of thin-film Li-ion microbatteries. *J. Power Sources*, 340, 242–246. doi: 10.1016/j.jpowsour.2016.11.078
- Sopha, H., Salian, G. D., Zazpe, R., Prikryl, J., Hromadko, L., Djenizian, T., et al. (2017). ALD Al₂O₃-coated TiO₂ nanotube layers as anodes for lithium-ion batteries. *ACS Omega* 2, 2749–2756. doi: 10.1021/acsomega.7b00463
- Sugiawati, V. A., Vacandio, F., Eyraud, M., Knauth, P., and Djenizian, T. (2016). Porous NASICON-Type Li₃Fe₂(PO₄)₃ thin film deposited by rf sputtering as cathode material for li-ion microbatteries. *Nanoscale Res. Lett.* 11:365. doi: 10.1186/s11671-016-1574-7
- Sugiawati, V. A., Vacandio, F., Knauth, P., and Djenizian, T. (2018). Sputter-deposited amorphous LiCuPO₄ thin film as cathode material for li-ion microbatteries. *Chem. Select* 3, 405–409. doi: 10.1002/slct.201702429
- Tang, D., Wang, Y., Zhao, Y., Yang, Y., Zhang, L., and Mao, X. (2014). Effect of the composition of Ti alloy on the photocatalytic activities of Ti-based oxide nanotube arrays prepared by anodic oxidation. *Appl. Surf. Sci.* 319, 181–188. doi: 10.1016/j.apsusc.2014.07.149
- Xiong, W., Xia, Q., and Xia, H. (2014). Three-dimensional self-supported metal oxides as cathodes for microbatteries. *Funct. Mater. Lett.* 7:1430003. doi: 10.1142/S1793604714300035
- Xu, J., Jia, C., Cao, B., and Zhang, W. F. (2007). Electrochemical properties of anatase TiO₂ nanotubes as an anode material for lithium-ion batteries. *Electrochim. Acta*, 52, 8044–8047. doi: 10.1016/j.electacta.2007.06.077
- Yu, C., Bai, Y., Yan, D., Li, X., and Zhang, W. (2014). Improved electrochemical properties of Sn-doped TiO₂ nanotube as an anode material for lithium ion battery. *J. Solid State Chem.* 18, 1933–1940. doi: 10.1007/s10008-014-2436-9
- Zhou, W., Liu, Q., Zhu, Z., and Zhang, J. (2010). Preparation and properties of vanadium-doped TiO₂ photocatalysts. *J. Phys. D: Appl. Phys.* 43, 035301. doi: 10.1088/0022-3727/43/3/035301

Conflict of Interest Statement: The authors declare that the research was conducted in the absence of any commercial or financial relationships that could be construed as a potential conflict of interest.

Copyright © 2019 Fraoucene, Sugiawati, Hatem, Belkaid, Vacandio, Eyraud, Pasquinielli and Djenizian. This is an open-access article distributed under the terms of the Creative Commons Attribution License (CC BY). The use, distribution or reproduction in other forums is permitted, provided the original author(s) and the copyright owner(s) are credited and that the original publication in this journal is cited, in accordance with accepted academic practice. No use, distribution or reproduction is permitted which does not comply with these terms.



Formation of Si/SiO₂ Luminescent Quantum Dots From Mesoporous Silicon by Sodium Tetraborate/Citric Acid Oxidation Treatment

Maxim B. Gongalsky^{1,2*}, Julia V. Kargina¹, Jose F. Cruz², Juan F. Sánchez-Royo³, Vladimir S. Chirvony³, Liubov A. Osminkina^{1,4} and Michael J. Sailor²

¹ Faculty of Physics, Lomonosov Moscow State University, Moscow, Russia, ² Department of Chemistry and Biochemistry, University of California, San Diego, San Diego, CA, United States, ³ Institute of Material Sciences, University of Valencia, Valencia, Spain, ⁴ Institute for Biological Instrumentation of Russian Academy of Sciences, Moscow, Russia

OPEN ACCESS

Edited by:

Thierry Djenizian,
École des Mines de Saint-Étienne -
Campus Georges Charpak Provence,
France

Reviewed by:

Frederique Cunin,
Centre National de la Recherche
Scientifique (CNRS), France
Ester Segal,
Technion Israel Institute of Technology,
Israel

*Correspondence:

Maxim B. Gongalsky
mgongalsky@gmail.com

Specialty section:

This article was submitted to
Chemical Engineering,
a section of the journal
Frontiers in Chemistry

Received: 18 October 2018

Accepted: 04 March 2019

Published: 29 March 2019

Citation:

Gongalsky MB, Kargina JV, Cruz JF,
Sánchez-Royo JF, Chirvony VS,
Osminkina LA and Sailor MJ (2019)
Formation of Si/SiO₂ Luminescent
Quantum Dots From Mesoporous
Silicon by Sodium Tetraborate/Citric
Acid Oxidation Treatment.
Front. Chem. 7:165.
doi: 10.3389/fchem.2019.00165

We propose a rapid, one-pot method to generate photoluminescent (PL) mesoporous silicon nanoparticles (PSiNPs). Typically, mesoporous silicon (meso-PSi) films, obtained by electrochemical etching of monocrystalline silicon substrates, do not display strong PL because the silicon nanocrystals (nc-Si) in the skeleton are generally too large to display quantum confinement effects. Here we describe an improved approach to form photoluminescent PSiNPs from meso-PSi by partial oxidation in aqueous sodium borate (borax) solutions. The borax solution acts to simultaneously oxidize the nc-Si surface and to partially dissolve the oxide product. This results in reduction of the size of the nc-Si core into the quantum confinement regime, and formation of an insulating silicon dioxide (SiO₂) shell. The shell serves to passivate the surface of the silicon nanocrystals more effectively localizing excitons and increasing PL intensity. We show that the oxidation/dissolution process can be terminated by addition of excess citric acid, which changes the pH of the solution from alkaline to acidic. The process is monitored *in situ* by measurement of the steady-state PL spectrum from the PSiNPs. The measured PL intensity increases by 1.5- to 2-fold upon addition of citric acid, which we attribute to passivation of non-radiative recombination centers in the oxide shell. The measured PL quantum yield of the final product is up to 20%, the PL activation procedure takes <20 min, and the resulting material remains stable in aqueous dispersion for at least 1 day. The proposed phenomenological model explaining the process takes into account both pH changes in the solution and the potential increase in solubility of silicic acid due to interaction with sodium cations.

Keywords: silicon nanoparticles (SiNPs), photoluminescence, biomedical application, theranostics, porous silicon (PS)

INTRODUCTION

Porous silicon nanoparticles (PSiNPs) are promising agents for therapy and diagnostics (theranostics) of various diseases due to their biocompatibility (Canham, 1995; Durnev et al., 2010) and biodegradability (Canham, 2007). Therapeutic modalities include sensitizing of light (Osminkina et al., 2011) and ultrasound (Sviridov et al., 2017) resulting in oxidative stress,

hyperthermia, or other cell/tissue damage mechanisms, in addition to targeted drug delivery (Park et al., 2009). The dissolution of the material can be tuned over a wide temporal range, allowing sustained release of drug over periods of several minutes to several months (Low et al., 2009; Park et al., 2009). Diagnostic modalities include fluorescent labeling (Gu et al., 2013) and contrast agents for magnetic resonance (Erogbogbo et al., 2012; Gongalsky et al., 2015). Fluorescence labeling with photoluminescent PSiNPs benefits from the near-IR emission of the material, which coincides with the infrared transparency window of human tissues, and from the long luminescence lifetime (in microsecond range), which allows suppression of tissue autofluorescence by time-gated imaging (Gu et al., 2013). The combination of its drug loading capabilities and its infrared photoluminescence properties presents interesting opportunities for theranostics (Kumeria et al., 2017).

Mesoporous silicon prepared by electrochemical etch of highly doped p-type Si typically requires an activation step in order to display strong photoluminescence (PL), because the silicon nanocrystals generated in the etch are too large to exhibit quantum confinement effect (Cullis et al., 1997). Reduction of the silicon core size is usually accomplished by oxidation of the PSi surface to generate silicon oxide phases (Park et al., 2009; Pavlikov et al., 2012; Joo et al., 2014). The process is accompanied by formation of an electronically insulating oxide shell, which improves confinement of charge carriers in the silicon nanocrystals and partially eliminates non-radiative recombination centers. As a result highly luminescent Si/SiO₂ core/shell quantum dots are formed inside the porous matrix. The oxidation reaction retains the mesoporous morphology and thus allows subsequent drug loading (Park et al., 2009).

Activation of PL can be achieved by either liquid (Park et al., 2009; Joo et al., 2014) or gas phase oxidation chemistries (Pavlikov et al., 2012). A convenient and rapid means to induce oxidation is with a mildly basic aqueous solution of sodium borate (Joo et al., 2014). In that case, the optimal core size can be reached after between 50 and 400 min of oxidation, depending on borate and nanoparticle concentration; further dissolution results in loss of material and decrease in net PL signal. A drawback of the approach is that it is difficult to terminate the oxidation reaction in a reproducible manner. Usually the reaction is terminated by sudden dilution into excess deionized water, but this does not give consistent results. There is a tradeoff between speed of reaction and reproducibility: the faster the reaction, the more difficult it is to terminate the reaction at the point where quantum yield is maximum.

In this study we present a rapid, one-pot procedure to prepare photoluminescent PSiNPs that combines 2 stages: (i) oxidation in concentrated borax solutions, and (ii) instant termination of the reaction by addition of citric acid to rapidly change the pH to the acidic range where the rate of oxide dissolution is negligible.

MATERIALS AND METHODS

Materials

Silicon wafers were obtained from Virginia Semiconductors Inc., sodium tetraborate decahydrate, citric acid, and rhodamine 6G were purchased from Sigma Aldrich Chemicals.

Preparation of PSiNPs

Perforated mesoporous silicon films (Perf-PSi) were prepared by electrochemical etch of highly doped (specific resistivity ~ 0.001 to $0.005 \text{ Ohm}\cdot\text{cm}$) p-type Si wafers. A 3:1 by volume mixture of 48% aqueous HF and absolute ethanol was used. We used perforated etching, by application of a current density waveform consisting of $400 \text{ mA}/\text{cm}^2$ for 0.36 s followed by $50 \text{ mA}/\text{cm}^2$ for 1.8 s, repeated for 200 cycles (Qin et al., 2014). The resulting PSi films were then lifted off the substrate by etching in dilute HF solution (1:20 by volume mixture of aqueous 48% HF and absolute ethanol), for 5 min under an applied bias of 8 V. The freestanding films were then placed in deionized water and PSiNPs were obtained by subjecting the dispersion to ultrasonic fracture (50T, VWR international) for 24 h. Operating frequency was 35 KHz, ultrasonic power was 48 W in a 1.9 L tank, which corresponded to a power density of approximately $25 \text{ mW}/\text{cm}^3$. The nanoparticles were then purified: the larger microparticles were removed by allowing the suspension to sit undisturbed for 24 h and the sediment (consisting of larger particles) was removed from the nanoparticle suspension and discarded. The smaller nanoparticles were then removed by subjecting the supernatant to 3 cycles of centrifugation (15 min, 15,000 rpm). For this stage of the process, the supernatant was discarded after each cycle, and the sedimented pellet of nanoparticles was re-suspended by brief ultrasonication. The resulting size-selected nanoparticles were then activated for PL by exposure to sodium tetraborate decahydrate (borax) Na₂B₄O₇·10H₂O solutions. The borax concentration was varied in the range from 0.2 to 16 mM in order to evaluate the dependence of borax concentration on the oxidation reaction rate.

Characterization

PL of the suspensions was monitored *in situ* in the spectral range from 500 to 1,000 nm using an OceanOptics QE-65 spectrometer fitted with a 460 nm long-pass emission filter. The suspensions were placed in UV-transparent parallelepipedal cuvettes with length and width equal to 1 cm. The excitation source was a 365 nm light emitting diode (LSM-365A) with emission power about 10 mW and full width at half maximum (FWHM) about 12 nm. All elements of PL setup were coupled by optical fiber with SMA 905 connectors. The cuvettes were set into cuvette holder with 4 ports located on the 4 sides. Emission light beam was focused into the center of the cuvette via direct port. PL signal was collected by using of condenser also focused into the center of the cuvette, which was connected via side port of the holder. Typical exposure time was 3 s.

The quantum yield (QY) of PSiNPs was measured by the comparative method, using Rhodamine 6G as a standard (Kubin and Fletcher, 1982). In this approach integrated PL intensity/absorption ratio is compared for the investigated and reference samples. At least 3 different concentrations of Rhodamine 6G and PSiNPs were used to confirm linearity of the dependency. Optical absorbance was <0.2 at 365 nm for all QY measurements. Excitation and absorption wavelengths must coincide (365 nm in this study). QY of Rhodamine 6G was assumed to be 95%. PL was measured using the setup described above. Absorbance measurements were made using a SpectraMax 340PC384 reader from Molecular Devices in the same cuvettes as

were used for PL measurements. Spectra were measured in the range from 300 to 850 nm, but only values at 365 nm were used in the analysis. Optical depth was measured in the range from 0 to 4 with 0.006 accuracy.

Dynamic light scattering (Malvern Instruments Zetasizer ZS90) was used to determine average size (hydrodynamic diameter) of PSiNPs. The setup uses a 633 nm, 4 mW laser backscattered from suspended nanoparticles in the same cuvette that was used for PL and absorbance measurements. Precise photon counting was used for continuous measurements of the scattering intensity, calculation of the auto-correlation function, and final hydrodynamic distribution weighted by volume of nanoparticles. The mathematical model was based on the Smoluchowski diffusion equation.

Structural investigations of the samples were carried out with a field emission scanning electron microscope (Carl Zeiss ULTRA 55 FE-SEM) operated at an acceleration voltage of 10 kV. Transmission and reflection Fourier-transform infrared (FTIR) spectra of PSi layers were measured with a Bruker IFS 66 v/S FTIR spectrometer. TEM images were obtained with a LEO 912 AB Omega transmission electron microscope (Zeiss, Oberkochen, Germany) operated at an acceleration voltage of 120 kV. Size distributions (in the insets of **Figures 1B,D**) were obtained from the electron microscope images using ImageJ software. Each image was modified by contrast enhancement in GIMP software and then dark/bright spots corresponding to pores/crystallites were outlined and fitted by ellipses. Each ellipse gave us two values, i.e., major and minor axes, which both were used for calculation of pore/crystallite diameter distribution.

Raman scattering spectrum were measured with a Horiba Jobin-Yvon HR800 spectrometer with an He-Ne cw laser (wavelength of 633 nm, 5 mW) for the excitation.

X-ray Photoelectron Spectroscopy (XPS) investigations of Si nanoparticles were performed in an ultrahigh vacuum system ESCALAB210 (base pressure 1.0×10^{-10} mbar) from Thermo VG Scientific. The nanoparticles in suspension were dripped onto a Cu substrate just before the XPS measurements. The measurements were taken over an area of 1 mm² of the densely covered Cu substrate. Photoelectrons were excited by using the Mg K α line (1253.6 eV).

The pore diameter distribution was determined by using N₂ adsorption/desorption isotherms (Quantachrome NOVA 4200e, Quantachrome Instruments). The specific pore area was determined from the adsorption branch using BET theory (Brunauer et al., 1938), and the pore size distribution was calculated from the desorption branch using BJH theory (Barrett et al., 1951). Samples were subjected to degasation at 300°C before measurements.

Porosity of PSi films was measured by spectroscopic liquid infiltration method (SLIM), which is based on comparison of 2 optical interferograms for dry film and film with pores filled by methanol, which alternates effective medium refractive index (Segal et al., 2007).

RESULTS AND DISCUSSION

PSiNPs were prepared using the perforated-etching procedure (Qin et al., 2014). The perforated etch generated Perf-PSi films

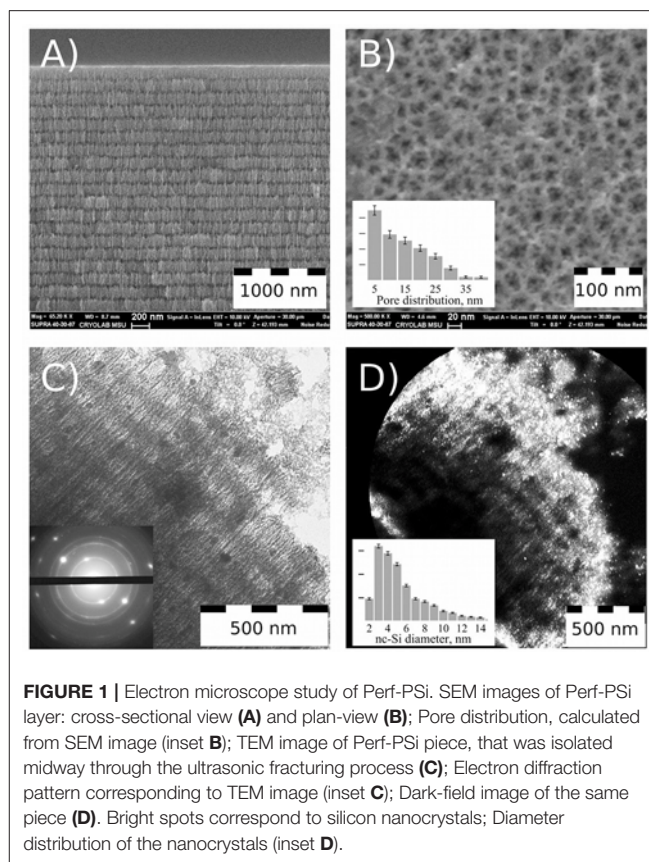


FIGURE 1 | Electron microscope study of Perf-PSi. SEM images of Perf-PSi layer: cross-sectional view (**A**) and plan-view (**B**); Pore distribution, calculated from SEM image (inset **B**); TEM image of Perf-PSi piece, that was isolated midway through the ultrasonic fracturing process (**C**); Electron diffraction pattern corresponding to TEM image (inset **C**); Dark-field image of the same piece (**D**). Bright spots correspond to silicon nanocrystals; Diameter distribution of the nanocrystals (inset **D**).

with a multilayered periodic structure consisting of alternating high and low porosity, as revealed by scanning electron microscope (SEM) images (**Figure 1A**). Thickness of the primary layers (those with the lower porosity—about 45%) was in the range of 150–200 nm, while the perforation layers were 50 nm thick and had a porosity of ~80%. Thickness of the primary layers determines the final size of the PSiNPs. A plan-view SEM image (**Figure 1B**) reveals the pore morphology of the top primary layer, which exhibits hierarchical branching from larger (15–40 nm) to smaller (5 nm or less) pores. The quantitative pore distribution is given in the inset of **Figure 1B**, which was obtained using ImageJ software (details in **Figure S1**). The majority of the pores exhibited sizes in the range of 2.5–15 nm. It should be noted that the spatial resolution of the SEM is such that pores smaller than 2 nm would not be observable.

TEM images were acquired from a piece of Perf-PSi that was isolated midway through the ultrasonic fracturing process, after sedimentation from aqueous suspension (**Figure 1C**). The sample displays the layered structure of the parent Perf-PSi material, and cracking of the highly porous “perforating” layer is evident on the right top corner of **Figure 1C** (Full TEM image is shown in **Figure S2**). The electron diffraction pattern (inset of **Figure 1C**) displays several bright, distinct diffraction spots corresponding to bulk Si, confirming the presence of crystalline silicon in the Perf-PSi sample. The diffraction spots are attributed to Si nanocrystals that inherited their preferred orientation from the initial c-Si wafer. The diffraction rings present in the image can be attributed to other randomly oriented Si nanocrystals.

Figure 1D shows a dark-field image of the same Perf-PSi piece, where bright spots correspond to diffraction from nanocrystalline silicon selected by special positioning of the TEM diaphragm. The brightest regions correspond to the periphery of the Perf-PSi piece. Quantitative analysis yielded the distribution of silicon nanocrystallite diameters (inset to **Figure 1D**, detail—also in **Figure S3**) According to the analysis, the mean diameter of silicon nanocrystallites was $5.5 \text{ nm} \pm 0.5 \text{ nm}$, but a substantial quantity of larger silicon nanocrystallites (7–14 nm) is also present.

Digital photos of Perf-PSi layers and suspensions are shown in **Figures S5A–C**. Sequential sedimentation and centrifugation steps after ultrasonic fracturing gave the specified 200 nm sized PSiNPs; the average size and the size distribution of the resulting nanoparticles were confirmed by TEM and DLS measurements (**Figure 2A** and **Figure S6**). **Figure 2A** shows the network of pores was maintained after the ultrasonic fracture process. Each PSiNP can be thought of as an assembly of many smaller silicon nanocrystals (nc-Si). Measured Zeta potential of the PSiNPs was $\sim 30 \text{ mV}$ (**Figure S7**), which imparted reasonable stability to the colloidal suspension.

The mean diameter of the silicon nanocrystallites was estimated from Raman and PL measurements from the peak position governed by the quantum confinement effects. **Figure 2B** shows the Raman spectra of the initial Perf-PSi film prior to oxidation (colored red), the Perf-PSi film after oxidation in aqueous borate solution (colored green) and bulk crystalline silicon (c-Si—black color) as a reference. The calculations (shown in **Supplementary Material**) give $d_R = 5 \text{ nm} \pm 0.5 \text{ nm}$ for the initial Perf-PSi film. Oxidation of the sample results in a slight shift of the band to lower wavenumbers, which is attributed to a further decrease in the mean diameter of the silicon nanocrystallites. More importantly, oxidation modifies the higher energy shoulder of the band, which lies beneath the shoulder of the initial Perf-PSi Raman band. This suggests that the oxidation process reduces the diameter of the larger ($>7 \text{ nm}$) nanocrystallites.

Figure 2C shows the pore diameter distribution for a powder of initial PSiNPs deposited from the aqueous suspension. Corresponding low-temperature nitrogen adsorption/desorption isotherms (BET/BJH isotherms) are shown in **Figure S8**. The mean pore diameter was about 8 nm, which is in good agreement with data presented in the inset of **Figure 1B**. However, the pore distribution in **Figure 2C** revealed low volume of micropores and mesopores smaller than 4 nm. According to BET model the specific surface of PSiNPs was $480 \pm 20 \text{ m}^2/\text{g}$. Assuming spherical shape of nc-Si their mean diameter can be estimated from the value of surface area as $5.4 \pm 0.5 \text{ nm}$, which is also in a good agreement with TEM and Raman results.

Neither the initial mesoporous Perf-PSi film nor the PSiNPs generated from ultrasonic fracture exhibited efficient PL. This is consistent with the microscopic and Raman data, which indicated that the average diameter of the majority of the silicon nanocrystallites in these samples were $>5 \text{ nm}$ (**Figure 1D**), too large to exhibit substantial quantum-confinement effects (Canham, 1990). In addition, the surface of the silicon nanocrystallites in these samples likely do not have a barrier

silicon oxide layer sufficient to passivate non-radiative surface traps (Cullis et al., 1997).

Two criteria are necessary to activate efficient PL: the average nanocrystallite size must be reduced into the quantum size regime, and the surface coating must be sufficiently passivated to inhibit non-radiative carrier recombination. In this work surface passivation was achieved with an SiO₂ shell, which has been well-established to generate good surface passivation in PSiNPs. In this work we followed the aqueous borate oxidation/dissolution protocol previously reported (Joo et al., 2014). **Figure 3A** shows the time evolution of the PL spectrum from nanoparticles during treatment with an aqueous borax solution (concentration 6.5 mM). Initially, PL was not detected. Digital photo of luminescent suspension of PSiNPs under UV excitation is shown in **Figure S5D**. For the next 10–30 min in the borax solution, the PL spectrum appeared and grew in intensity. After a period of time the PL intensity reached a maximum, and then it decreased again (**Figure 3B**—black curve). The data are consistent with a model in which the borax solution induces both oxidation of the Si skeleton and dissolution of this oxide (Joo et al., 2014), simultaneously shrinking the nc-Si core and passivating the nc-Si surface, as outlined in **Figure 3C**: Starting from thick silicon nanowires (colored green) in borax solution (colored light blue) through to complete oxidation of the silicon nanocrystallites to non-emissive silicon oxide (colored yellow). The black circles on the picture represent the relative number of luminescent nanocrystallites present in the sample. In this model, PL intensity is approximately proportional to the number of emissive Si nanocrystals. As-prepared PSiNPs and nanoparticles at the early stages of oxidation may contain some silicon nanocrystallites that meet the quantum-confinement criteria (see **Figure 1D**), but they do not have sufficient barrier oxide layer (shown as yellow) to display efficient emission due to non-radiative exciton recombination (Cullis et al., 1997). Once the oxide layer is sufficiently passivating, the silicon nanocrystallites begin to emit PL. Small silicon nanocrystallites are known to have a smaller quantum yield, because of increasing singlet-triplet state splitting and increasing non-radiative recombination processes (Ledoux et al., 2002). Continuation of the oxidation process eventually leads to a decrease in the amount of silicon nanocrystallites present, and ultimately to complete oxidation of the sample, which is accompanied by the disappearance of PL.

The PL spectra presented in **Figure 3A** can be used to estimate the mean diameter of luminescent silicon nanocrystallites in the samples. The PL energy E_{PL} is roughly determined from the nc-Si diameter d_{PL} by:

$$E_{PL} = E_g + \frac{3.73}{d_{PL}^{1.39}}, \quad (1)$$

where E_g is band gap of bulk Si (Ledoux et al., 2000). The peak position of 810 nm yields $d_{PL} = 5 \text{ nm} \pm 0.5 \text{ nm}$, which is consistent with the values obtained from Raman and TEM data. The shift of the PL peak position is $<20 \text{ nm}$, indicative of a relatively broad distribution of nc-Si sizes (**Figure 1D**).

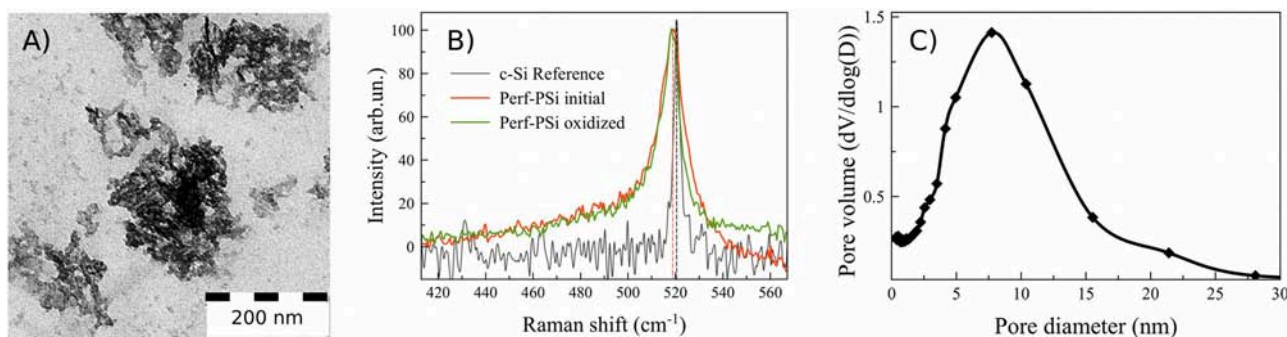


FIGURE 2 | TEM image of PSINPs, sedimented from aqueous suspension (A); Raman spectra of initial Perf-PSi (red), oxidized Perf-PSi (green), and reference c-Si (black) (B). Pore diameter distribution of PSINPs sedimented from the aqueous suspensions by using the low-temperature adsorption technique (C).

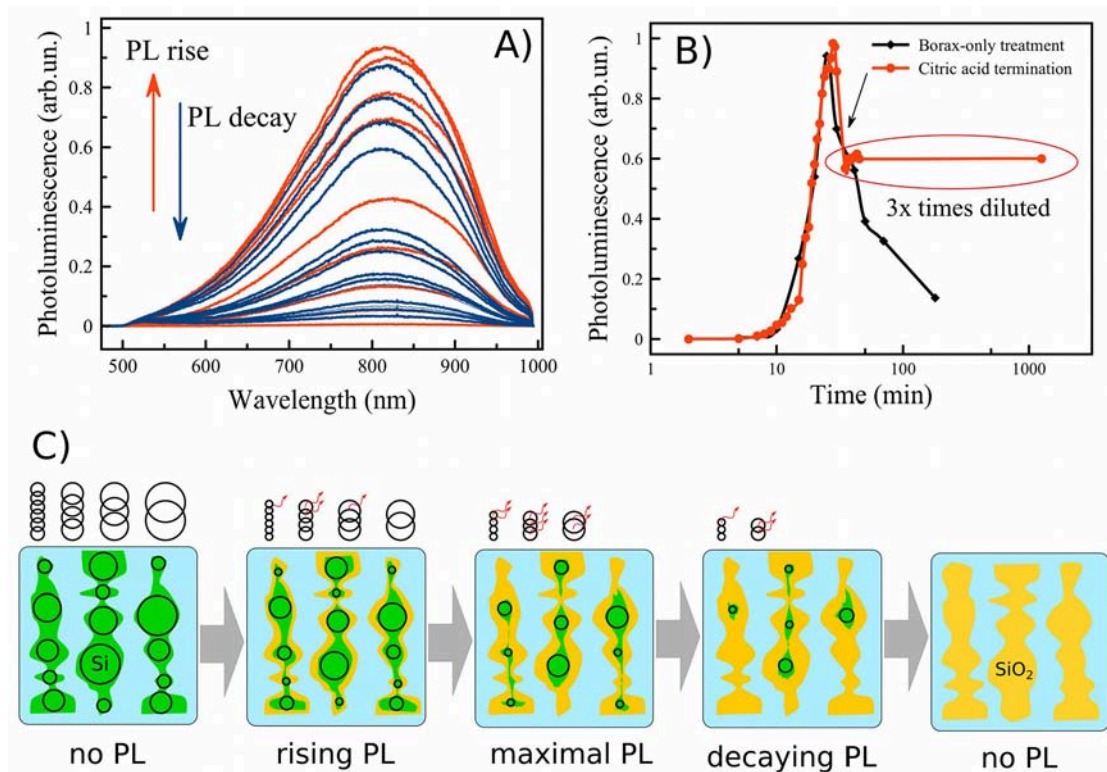


FIGURE 3 | Family of PL spectra of porous silicon nanoparticles obtained during aqueous borax oxidation (A); evolution of the PL intensity (measured at the emission maximum) during borax oxidation without (black curve—B) and with termination by citric acid (red curve—B); schematic view of the oxidation process starting from as-prepared PSINPs through maximal emissive state to complete oxidation in borax (C). Green—Si skeleton, yellow— SiO_2 shell, black circles—silicon nanocrystals (nc-Si) indicating the size of the nanocrystals, some of which fit the quantum confinement criteria for efficient emission, indicated with the red arrows.

Thus, during the nc-Si oxidation process, the smaller end of the nanocrystal ensemble becomes fully oxidized and non-emissive, while the larger end of the nanocrystal ensemble becomes smaller and begins to contribute to the PL spectra. Ensembles with narrower size distributions of nanocrystallites might be expected to generate a more pronounced blue shift in the overall emission spectrum according to formula (2), as was seen in Joo et al. (2014).

Since efficient PL is desirable for many applications, it is important to capture the oxidation/dissolution process at the moment of maximal PL. On the one hand, borax oxidation is a rapid and convenient process, but on the other hand, it is difficult to terminate at the point where the PL emission is maximal. As is shown in Figure 3B, just a few minutes is sufficient to lose PL efficiency several-fold. Rapid dilution of the solution slows but does not stop the oxidation/dissolution process. We reasoned

that acidification to change the pH of the solution from alkaline to acidic might be a more effective means to instantaneously terminate dissolution and freeze the overall process. When excess citric acid (CA) was used for this purpose, we found that pH changed from 9.3 to ~3 very rapidly, and PL was stabilized. The process is shown in the red trace of **Figure 3B**, and the moment of CA addition is indicated with an arrow. PL was stabilized within 1 min of CA addition. Under these conditions, PL intensity was stable for 1 day after CA addition.

The citric acid solution was added to the PSiNPs/borax suspension in a 2:1 ratio by volume. PL intensity remained approximately the same, even though the concentration of PSiNPs dropped by 3-fold upon dilution. This suggests that CA treatment induced an overall increase in the PL QY of PSiNPs. The origin of this enhancement is unclear at this time, though it is possible that CA contributed to passivation of the surface and elimination of non-radiative recombination centers for excitons in nc-Si. QY of PSiNPs in such suspensions measured after 1 day of storage in CA ranged from 15 to 20% depending on borax concentration (see QY values pointed by arrows in **Figure 4A**).

The time needed to activate PL in borax solutions can be tuned by changing borax concentration (**Figure 4A**). One can see that the higher the concentration of borax, the faster the PL evolved to its maximum and then subsequently decayed. Activation times could be varied over a wide range: from 10 min to several hours. It was shown in previous work that 6 days are required to activate PL in deionized water (Park et al., 2009). The result obtained from the PL measurements was verified by measurement of optical absorbance of a PSiNP suspension also during oxidation in borax (**Figure 4B**). Absorbance measurements at 365 nm showed similar activation times as well as a drastic drop in absorbance after the point in time where PL was at a maximum. This also points to oxidation/dissolution of the Si skeleton, since neither silicon dioxide nor silicic acid absorb light of 365 nm wavelength. The data can thus be used to track the phase composition of partially oxidized PSiNPs. Although absorbance values for all samples were out of range in the beginning, useful data were obtained in the range 0.1 to 3 cm⁻¹. The absorbance value corresponding to maximum PL was ~ 0.35 cm⁻¹. Different concentrations of borax yielded different PL activation times, but the final QY after termination of the reaction with CA was similar and could be as high as 12%. That result differs from the observations in a previous study (Joo et al., 2014), where high concentrations of borax did not correspond to maximal QY. Therefore, we believe the use of CA provides a more reliable means to produce photoluminescent Si, although there is still the requirement to closely monitor the process *in situ*.

The reaction rate was estimated from the initial time dependences in **Figures 4A,B** assuming a single-exponential first order rate law and using the following data thresholds: for the PL evolution (**Figure 4A**), data from time = 0 to the time point at which PL intensity was half of its maximum value was used for the fit; for the Si absorbance data (**Figure 4B**), measured absorbance values between 3 and 0.5 were fit by linear function and the values of time corresponding to threshold shown as the dotted line (1.25) were used. The result is presented in **Figure 5** for both PL (red curve) and absorbance (black curve). Both

dependences appear similar, i.e., they show a linear dependence of rate on borax concentration at low values (increasing rate with increasing borax concentration) and saturation of the rate at high borax concentrations. The data are consistent with the strong pH dependence of silica dissolution. Silica is stable at low pH but it readily dissolves at high pH. In the borate-induced oxidation/dissolution process, borate acts as a buffer, maintaining the pH at ~9, where dissolution of the formed oxide can occur. At low concentration of borate, the buffer capacity is low and thus readily exceeded by the silica dissolution reaction, which can consume hydroxide ions to form [Si(O)(OH)₃]⁻ ion (pKa = 10, Equation 3). As the pH drops, the dissolution of SiO₂ will slow down, and because the SiO₂ layer acts as a protective coating for the Si skeleton, the oxidation of silicon will also slow. Thus, increasing the borax concentration increases the rate of Si dissolution.

Saturation of the reaction rate can be explained by diffusion limitation of sodium tetraborate inside the pore network of PSiNPs. Borax depletes deep inside PSiNPs, thus the reaction slows down. Diffusion of new borax from the solution to the depth of PSiNPs is required for maintenance of the process, which is limited by diffusion through porous network. The diffusion coefficient of small molecules may vary in the wide range depending on pore diameter (Carbonaro et al., 2004). However, partial dissolution of PSiNPs may enlarge the pores and increase diffusion of reagents through the porous network.

The rate of Si dissolution was also measured indirectly by measurement of photoluminescence from the PSiNPs. PL QY showed a strong dependence on borax concentration (**Figure 6A**). An example of dependences of PL on absorbance used for calculation of QY is shown in **Figure S9**. High concentrations of borax (>1 mM) activated PL more quickly and provided the larger QYs (~10%). Low borax concentrations (<1 mM) led to loss of QY as well as a slowing of the oxidation process as described above. The optimal borax concentration from a perspective of experimental convenience and maximization of QY was between 2 and 20 mM.

The oxidation/dissolution process induced by borax could be interrupted by rapid acidification with citric acid (CA). **Figure 6A** shows the dependence of final measured QY after termination of the reaction with CA, presented as a function of borax concentration in the initial solution. The data are also presented as a function of optical absorbance of the sample in **Figure 6B**. The points from **Figure 6B** can be considered as the same sample subjected to the same oxidation process, but interrupted by CA addition at various times. As discussed above, absorbance correlated both with the overall amount of Si in the sample and the average diameter of nc-Si in the sample. Indeed, strong absorbance corresponds to larger nc-Si with a thin SiO₂ shell and weak absorbance corresponds to smaller nc-Si inside an SiO₂ shell. For these samples the larger nc-Si displayed a relatively low QY (below 1%). The QY rose if oxidation was allowed to proceed for a longer time. Surprisingly, QY did not drop substantially upon further oxidation (after PL intensity passed its maximum and began to degrade). This is interpreted to indicate that late stages of oxidation reduce the total amount of luminescent nc-Si, but the PL efficiency of individual silicon

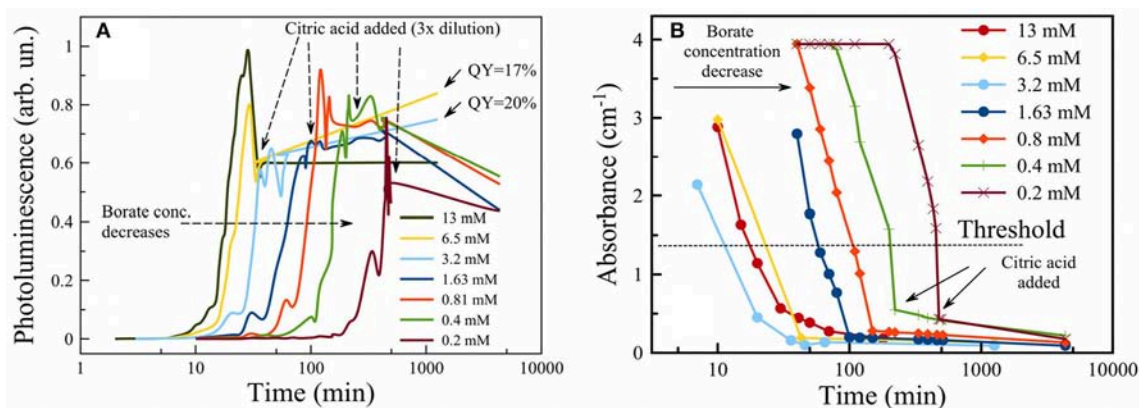


FIGURE 4 | Photoluminescence of PSiNPs during oxidation in aqueous borax with addition of citric acid to terminate the reaction (showed by vertical arrows) (A). Initial borate concentrations for each trace are given in the legend. Absorbance of PSiNPs during the same process (B).

nanocrystallites is retained. Thus, the late stages of oxidation reduce the overall mass yield of PSiNPs, but not the PL QY. Furthermore, **Figure 6A** shows that addition of CA resulted in enhancement of the PL QY, by factors of 2–3 times for all the borax concentration conditions tested. This result suggests that CA plays an additional role in enhancing PL, possibly via passivation of surface defects rather than changing the nc-Si sizes. Note that all measurements in this phase of the experiments were performed when PL reached its maximum for a given borax concentration.

Based on the above results, we propose that the mechanism of PSiNP oxidation/dissolution follows the mechanism depicted in **Figure 3C**: after extensive borax treatment the nanostructure is converted completely into SiO_2 without any Si core inside. Concomitant with the oxidation process is the dissolution of the SiO_2 shell. This interpretation is consistent with prior reports; however the data reported here and below indicate that the process is slightly more complicated.

To further investigate the borax-induced oxidation/dissolution process, PSi films (shown in **Figure 1B**) were subjected to the same borax oxidation conditions and then analyzed by Fourier transform infrared (FTIR) spectroscopy.

The spectrum of oxidized PSi (**Figure 7**; red curve) showed a strong absorption band at $1,070\text{ cm}^{-1}$ corresponding to stretching vibrations of Si-O-Si bonds in the SiO_2 phase (Theiss, 1997). As-prepared PSi is characterized by strong Si-H stretching bands associated with surface Si-H, SiH_2 , and SiH_3 species at $2,088\text{ cm}^{-1}$, $2,114\text{ cm}^{-1}$, and $2,137\text{ cm}^{-1}$, respectively (Gupta et al., 1991), along with other Si-H bands at 625 cm^{-1} , 660 cm^{-1} (wagging $\text{Si}_3\text{-Si-H}$, $\text{Si}_2\text{-Si-H}_2$), 910 cm^{-1} (scissors $\text{Si}_2\text{-Si-H}_2$) (Ogata, 1995; Theiss, 1997). As-prepared porous silicon is well-known to have a hydrogen-terminated surface. Surface hydrides were still detected after borax oxidation, although a new band associated with Si-H species that contain back-bonded Si-O was also present ($2,258\text{ cm}^{-1}$, depicted as $\text{O}_3\text{-Si-H}$ in **Figure 7**). The data indicate that borate oxidation did not remove surface hydrides, or if it did, the silicon skeleton generated new surface hydrides via the chemical reduction of water.

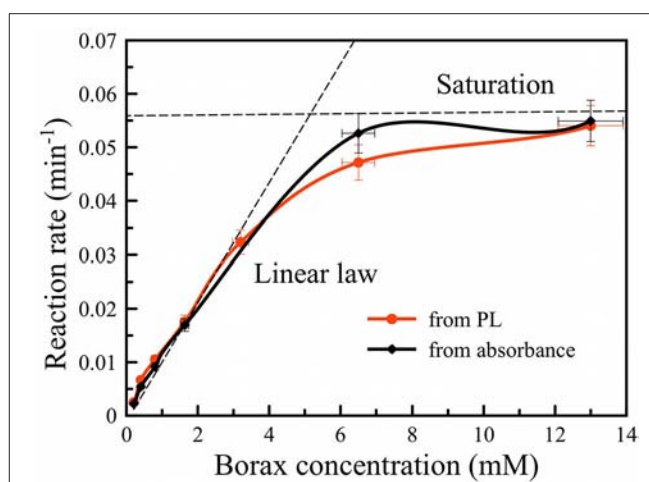


FIGURE 5 | Oxidation rate of PSiNPs vs. borax concentration in suspension obtained from photoluminescence (red curve) and absorbance (black curve) measurements. Dashed line traces are included as a guide to the eye.

Figure 7 exhibits a narrow band at $\sim 3,740\text{ cm}^{-1}$ for oxidized Perf-PSi, which indicates the presence of isolated/free silanols (Morrow and Mcfarlan, 1992) as opposed to extensively hydrogen-bonded silanols (broad band centered at $3,500\text{ cm}^{-1}$). The intensity of the band was decreased after addition of CA, which may refer to the partial hydrolysis of the surface in acidic medium (**Figure S10**). Coexistence of both initial Si-H_x and oxidized $\text{O}_3\text{-Si-H}$ groups points to a non-homogeneous oxidation process. Previous data show that oxidation takes place easier on convex regions, while smooth regions are less affected (Secret et al., 2015).

As discussed above, the mechanisms involved in PL activation need to take into account two simultaneous processes, i.e., oxidation of the Si core (nc-Si) and dissolution of the SiO_2 shell. Oxidation can be induced by water or oxygen molecules (Ogata, 1995). Both molecules can attack Si-Si bonds forming Si-O-Si bonds as a result. The SiO_2 shell is permeable to small molecules

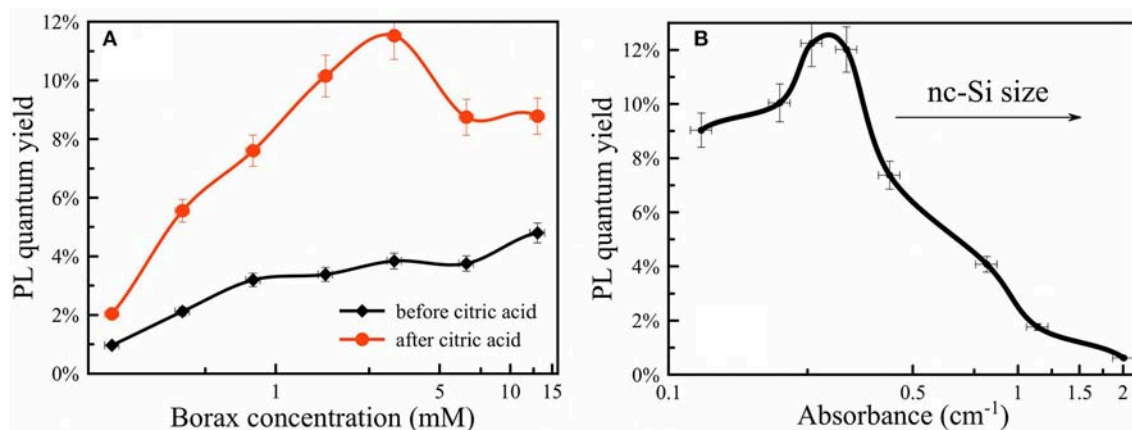


FIGURE 6 | PL quantum yield of PSiNPs vs. borax concentration **(A)** before (black curve) and after CA termination (red curve); PL quantum yield of PSiNPs vs. their absorbance at 365 nm **(B)**. Higher absorbance corresponds to both a larger quantity of silicon and larger silicon nanocrystals.

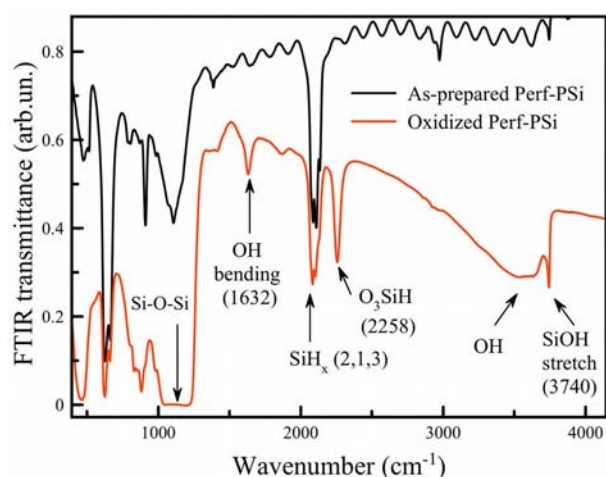
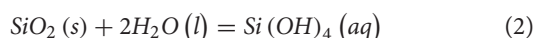


FIGURE 7 | FTIR transmission spectra of as-prepared (black curve) and borax-oxidized (red curve) PSi films.

such as H₂O and O₂, because they can penetrate through small voids between irregularly positioned SiO₄ tetrahedrons (Doremus, 1976). This process is strongly diffusion limited, therefore such an oxide layer is unlikely to be thicker than 1–2 nm to still allow molecular diffusion at room temperature.

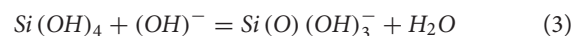
Dissolution of silica in water is a very complex process characterized by numerous silicon-containing species and a strong pH dependence. A simplified representation of the process can be given with the following chemical reaction (Rimstidt and Barnes, 1980):



where (s), (l) and (aq) mean “solid,” “liquid,” and “aqueous,” respectively. The process is reversible, so precipitation of solid silica from oversaturated silicic acid solution is possible.

Equilibrium constants are different for different polymorphs, i.e., quartz, α -cristobalite, β -cristobalite, amorphous silica, etc. For example, the solubility of quartz is 35 times lower than amorphous silica (Walther and Helgeson, 1977; Rimstidt and Barnes, 1980). The kinetics of the reaction depends on the exposed specific surface area of the nanomaterial, which for the investigated samples was about $5 \cdot 10^5 \text{ m}^2/\text{kg}$.

A significant increase (up to 50 times) in the solubility of SiO₂ was observed for pH > 9 (Alexander et al., 1954). This is explained by deprotonation of the Si(OH)₄ (silicic acid) product of Equation 3:



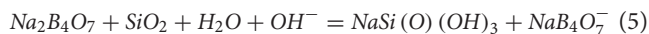
The solubility of silicic acid is also affected by the chemical composition of the solution, not only by the value of pH (Piryutko, 1959). Borax increases the solubility of silica in proportion to its concentration in solution (Seward, 1974). For high borax concentrations there is 5- to 10-fold enhancement. We believe that factor thus accelerates PL activation, which is supported by the observed dependence on borax concentration shown in Figure 5.

The mechanism of the solubility enhancement has been proposed (Seward, 1974) to involve formation of ion pairs between sodium ions and the monovalent orthosilicate ion formed in Equation 4.



The reaction of Equation 5 is reversible and the system eventually reaches equilibrium, when concentrations of the various silicic acid species saturate. In porous structures like PSiNPs the saturation point is important, because local saturation can be achieved very quickly due to the high surface area of the material. Thus, the oxidation of silicon and the dissolution of silica in aqueous media depends on a number of factors, in particular

the concentration of so-called “spectator” ions like sodium, the concentration of all the silicon-containing species, and the pH of the solution.



The state of the surface oxide may be a crucial determinant of the oxidation/dissolution rate. A thick oxide layer can protect against borax-induced corrosion of PSi. For instance, we verified that PSiNPs obtained by high energy mechanical milling and aged in aqueous solution for about 1 year were not affected by borax oxidation even in highly concentrated borax solutions. A similar effect has been observed for PSiNPs subjected to prior oxidation in H₂O₂ solutions. However, complete removal of the native oxide layer by rinsing in diluted HF solutions restored the ability of PSiNPs to be efficiently oxidized by the aqueous borax solution. This is likely related to the polymorphism of SiO₂: for example, crystalline SiO₂ is 10–100 times less soluble than amorphous silica or silicate glass (Walther and Helgeson, 1977).

The presence of defects in the silica shell nanostructure likely also influences solubility of PSiNPs. Dissolution of silicon dioxide (SiO₂) has been described in terms of the two processes of hydration and hydrolysis; that is, diffusion of molecular water into the oxide and hydrolysis of surface species (Bunker, 1994). In general silica is a network of interconnected SiO₄ tetrahedrons, and in the perfect situation each tetrahedron is connected to 4 others creating regular lattice such as in quartz. In quartz all oxygen atoms are connected with two silicon atoms, therefore they are called bridging oxygen. In amorphous silica there can also exist non-bridging oxygen groups, that is, oxygen atoms connected to only one silicon atom and having a charge of –1, and divalent oxide ions, i.e., oxygen atoms without any covalent connection to the SiO₂ network with a charge of –2. Such non-bridging oxygen centers can exert substantial influence in the dissolution process (Bunker, 1994; Nesbitt et al., 2011).

In order to gain more insight into the nature of the oxide shell in these materials, we acquired XPS spectra on both “fresh” and “aged” PSiNPs (Figure 8). The “fresh” PSiNPs were prepared as described above, that is perforated etching with subsequent ultrasonic fracture without any borax oxidation and the “aged” PSiNPs were prepared as described above (prepared from high energy mechanical milling and aged in aqueous solution for 1 year with concentration of approximately 20 mg/ml). Gaussian deconvolution of the Si 2p spectral region of fresh PSiNPs indicated the presence of three bands corresponding to completely oxidized silicon (Si⁴⁺–SiO₂, ~103 eV), partially oxidized silicon (Si²⁺–SiO, ~101 eV) and unoxidized silicon (Si⁰–nc-Si, 99 eV). For aged PSiNPs, the latter band assigned to zerovalent silicon was absent (Grunthaner et al., 1979). This points to stronger oxidation of the “aged” PSiNPs, a thicker oxide shell and/or a stoichiometry close to SiO₂. The O 1s spectra showed an abundance of free oxygen dianions (O^{2–}, ~528 eV) in the “fresh” PSiNPs and an absence of free oxygen dianions in the “aged” PSiNPs. At the same, time both non-bridging (O^{1–}, ~530 eV) and bridging (O⁰, ~533 eV) oxygen centers were detected in both samples (Nesbitt et al., 2011). The presence of

free oxygen anions and the abundance of elemental, zerovalent silicon point to a non-homogeneous, disordered oxide shell in the “fresh” PSiNPs by comparison with the “aged” ones, which is consistent with the dissolution behavior and the differences in photoluminescence intensity observed. The oxide shell of the “aged” PSiNPs was more ordered and dense, containing fewer sites that might be subject to accelerated hydrolysis, consistent with the low susceptibility of this material to the aqueous borax solution. As mentioned above, removal of the protective layer by rinsing in aqueous HF completely recovered the ability of the “aged” material to be activated by borax oxidation.

As a summary we present a phenomenological model for borax-induced oxidation/dissolution of porous Si based on the experimental data reported above. Figure 9 depicts the morphology of PSiNPs subjected to aqueous borax oxidation/dissolution. The scheme represents a cross-section of a silicon nanocrystallite (colored green) with an SiO₂ shell (colored yellow) submerged in borax solution (colored blue), and with some of the mesopores in the PSiNPs infiltrated with the aqueous solution. Approximate sizes of regions are also given in the scheme. There is a diffusion limitation to the process, because locally high concentrations of silicic acid can slow the dissolution of SiO₂ in the vicinity of the saturation. Creation of ion pairs between Na⁺ and Si(O)(OH)₃[–] accelerates the dissolution process. Diffusion of OH[–] into the micropores is also important, because it drives the dissolution of silica. Depletion of OH[–] ions inside the micropores leads to a local pH drop, which slows the overall process. A protective insoluble layer (not always present) is depicted as the red region on the surface of the SiO₂ shell. Notionally, this could be adsorbed polymer, protein, or some other species. In this model, if a protective layer covers the entire surface of PSiNPs, it will stop the oxidation/dissolution process completely.

The chemical oxidation of Si takes place at the Si/SiO₂ interface (black line between the yellow and green regions in the diagram), which is known to be a typical location for point defects, such as dangling bonds, responsible for non-radiative recombination of quantum-confined excitons (shown as “+” and “–” in the scheme) (von Bardeleben et al., 1993). Reaction between the Si core and H₂O or O₂ leads to migration of the interface toward the center of the Si core, growing the SiO₂ shell and shrinking the Si core. In the absence of defects an “atomic pore” layer characterized by highly restricted molecular diffusion partially protects the excitons from interaction with charged ions in the liquid phase, which determines the high quantum yield of PSiNPs. We propose that addition of citric acid terminates the growth of these micropores, allowing a thicker protective layer to grow that can increase quantum yield of the PSiNP.

CONCLUSIONS

A new, relatively rapid and one-pot method was proposed for formation of highly luminescent porous silicon nanoparticles. The procedure can be accomplished in <20 min, and it generates Si-SiO₂ core-shell nanoparticles with quantum yields up to 20% that remain stable in aqueous suspensions for at least 1 day. The time required for photoluminescence activation varies in a wide range depending on concentration of borax. Rapid addition

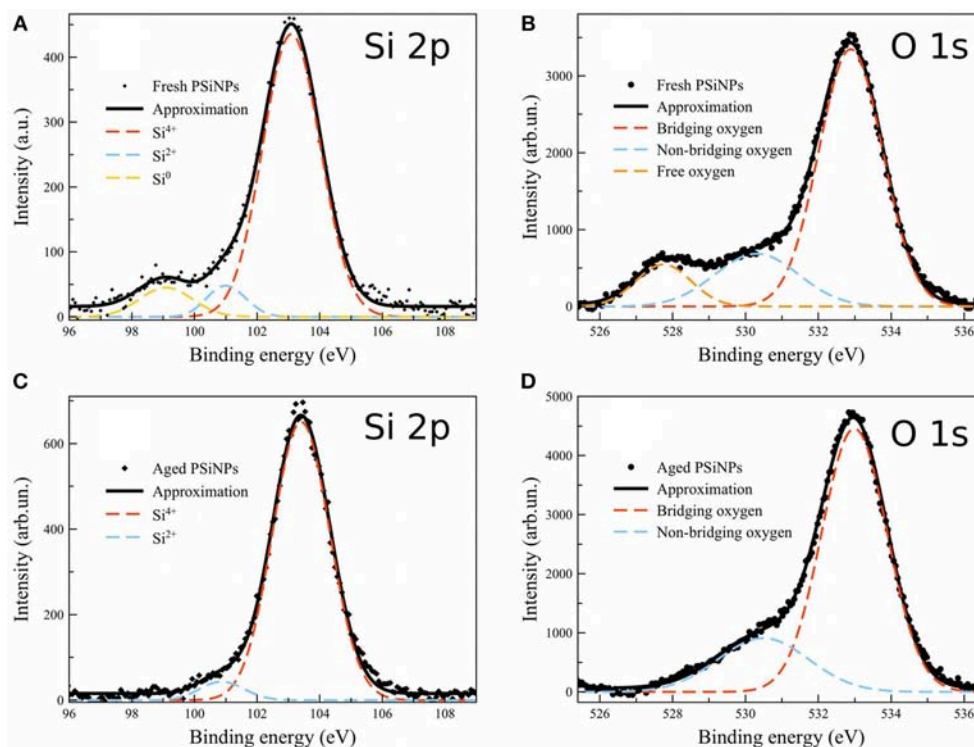


FIGURE 8 | XPS spectra of “fresh” and “aged” PSiNPs. Dots: experimental data for “fresh” (A,B) and “aged” (C,D) PSiNPs; Solid lines: approximation; Dashed: deconvolution into Gaussians.

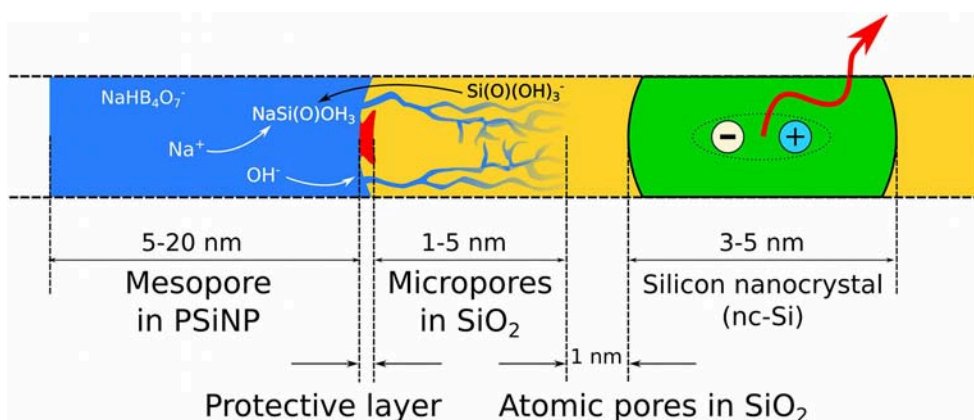


FIGURE 9 | Schematic cross-section of a PSiNP subjected to borax-induced oxidation/dissolution. Borax solution (blue) penetrates into the SiO_2 shell (yellow), which covers the silicon core silicon nanocrystallite (green). An exciton confined in the silicon nanocrystallite is shown as $\ll + \gg$ and $\ll - \gg$ in circles and photoluminescence is indicated with the red arrow. A notional insoluble protective surface layer is shown as a red region.

of citric acid was found not only to instantly terminate the oxidation/dissolution of silicon, but it also increased quantum yield 2- to 3-fold depending on borax concentration. This was explained as the efficient passivation of non-radiative recombination centers by the acidic medium. Dependence of the reaction rate on borax concentration was linear at low values, but the rate tended to saturate at high values.

We propose that oxidation takes place via formation of micropores in the silica shell, which provides a supply of reagent

to the silicon core, rather than uniform layer-by-layer dissolution. The constraints of diffusion inside narrow micropores may slow the overall rate of oxidation/dissolution. Borax plays a dual role in that it (i) sets up an alkaline medium with $\text{pH} \sim 9$ that accelerates dissolution of silica, and (ii) increases solubility of silicic acid. The latter effect is attributed to formation of ion pairs that prevents saturation of silicate ions in the pores. The reaction rate becomes constant in highly concentrated borax solutions, due to the pH buffering effect and mass transport

limitations associated with removal of silicic acid from the spatially confined micropores.

DATA AVAILABILITY

All datasets generated for this study are included in the manuscript and/or the **Supplementary Material**.

AUTHOR CONTRIBUTIONS

MG performed the majority of the experiments, analysis and wrote the manuscript. JK and JC assisted in PL measurements and sample characterization. JS-R and VC performed XPS experiments. LO and MS provided guidance for the research and editing of the manuscript.

FUNDING

MG is grateful to Fulbright FFDP-2016 and Russian Science Foundation Grant N 17-72-10200. The majority

of experiments, manuscript writing were performed under support of the RSF Grant, whereas preliminary PL and absorption experiments were supported by the Fulbright Fund. JC and MS acknowledge support from the National Science Foundation, from grant No. CBET-1603177.

ACKNOWLEDGMENTS

The authors are grateful to I. Bozhev for assistance in SEM, A. V. Pavlikov for assistance in FTIR measurements, A. Eliseev for assistance in BET/BJH measurements. MG is also grateful to T. Perova and V. Timoshenko for endorsements made to the Fulbright Council.

SUPPLEMENTARY MATERIAL

The Supplementary Material for this article can be found online at: <https://www.frontiersin.org/articles/10.3389/fchem.2019.00165/full#supplementary-material>

REFERENCES

- Alexander, G. B., Heston, W. M., and Iler, R. K. (1954). The solubility of amorphous silica in water. *J. Phys. Chem.* 58, 453–455. doi: 10.1021/j150516a002
- Barrett, E. P., Joyner, L. G., and Halenda, P. (1951). The determination of pore volume and area distributions in porous substances. I. Computations from nitrogen isotherms. *J. Am. Chem. Soc.* 1896, 373–380. doi: 10.1021/ja01145a126
- Brunauer, S., Emmett, P. H., and Teller, E. (1938). Adsorption of gases in multimolecular layers. *J. Am. Chem. Soc.* 407, 309–319. doi: 10.1021/ja01269a023
- Bunker, B. C. (1994). Molecular mechanisms for corrosion of silica and silicate glasses. *J. Non. Cryst. Solids* 179, 300–308. doi: 10.1016/0022-3093(94)90708-0
- Canham, L. T. (1990). Silicon quantum wire array fabrication by electrochemical and chemical dissolution of wafers. *Appl. Phys. Lett.* 57, 1046–1048. doi: 10.1063/1.103561
- Canham, L. T. (1995). Bioactive silicon structure fabrication through nanoetching techniques. *Adv. Mater.* 7, 1033–1037. doi: 10.1002/adma.19950071215
- Canham, L. T. (2007). Nanoscale semiconducting silicon as a nutritional food additive. *Nanotechnology* 18:185704. doi: 10.1088/0957-4484/18/18/185704
- Carbonaro, A., Walczak, R., Calderale, P. M., and Ferrari, M. (2004). Nano-pore silicon membrane characterization by diffusion and electrical resistance. *J. Memb. Sci.* 241, 249–255. doi: 10.1016/j.memsci.2004.04.039
- Cullis, A. G., Canham, L. T., and Calcott, D. J. (1997). The structural and luminescence properties of porous silicon. *J. Appl. Phys.* 82, 909–965. doi: 10.1063/1.366536
- Doremus, R. H. (1976). Oxidation of silicon by water and oxygen and diffusion in fused silica. *J. Phys. Chem.* 80, 1773–1775. doi: 10.1021/j100557a006
- Durnev, A. D., Solomina, A. S., Shreder, E. D., Nemova, E. P., Shreder, O. V., Dauge, N. O. L., et al. (2010). *In vivo* study of genotoxicity and teratogenicity of silica nanocrystals. *Int. J. Biomed. Nanosci. Nanotechnol.* 1:70. doi: 10.1504/IJBNN.2010.034126
- Erogbogbo, F., Chang, C. W., May, J. L., Liu, L., Kumar, R., Law, W. C., et al. (2012). Bioconjugation of luminescent silicon quantum dots to gadolinium ions for bioimaging applications. *Nanoscale* 4, 5483–5489. doi: 10.1039/c2nr31002c
- Gongalsky, M. B., Kargina, Y. V., Osminkina, L. A., Perepukhov, A. M., Gulyaev, M. V., Vasiliev, A. N., et al. (2015). Porous silicon nanoparticles as biocompatible contrast agents for magnetic resonance imaging. *Appl. Phys. Lett.* 107:233702. doi: 10.1063/1.4937731
- Grunthaner, F. J., Grunthaner, P. J., Vasques, R. P., Lewis, B. F., Masejigan, J., and Madhuhar, A. (1979). Local atomic and electronic structure of oxide/GaAs and SiO₂/Si interfaces using high-resolution XPS. *J. Vac. Sci. Tech.* 16:1443.
- Gu, L., Hall, D. J., Qin, Z., Anglin, E., Joo, J., Mooney, D. J., et al. (2013). *In vivo* time-gated fluorescence imaging with biodegradable luminescent porous silicon nanoparticles. *Nat. Commun.* 4:2326. doi: 10.1038/ncomms3326
- Gupta, P., Dillon, A. C., Bracker, A. S., and George, S. M. (1991). FTIR studies of I-I, O and I and O decomposition silicon surfaces. *Surf. Sci.* 245, 360–372. doi: 10.1016/0039-6028(91)90038-T
- Joo, J., Cruz, J. F., Vijayakumar, S., Grondek, J., and Sailor, M. J. (2014). Photoluminescent porous Si/SiO₂ core/shell nanoparticles prepared by borate oxidation. *Adv. Funct. Mater.* 24, 5688–5694. doi: 10.1002/adfm.201400587
- Kubin, R. F., and Fletcher, A. N. (1982). Fluorescence quantum yields of some rhodamine dyes. *J. Luminescence* 27, 455–462. doi: 10.1016/0022-2313(82)90045-X
- Kumeria, T., McInnes, S. J. P., Maher, S., and Santos, A. (2017). Porous silicon for drug delivery applications and theranostics: recent advances, critical review and perspectives. *Expert Opin. Drug Deliv.* 14, 1407–1422. doi: 10.1080/17425247.2017.1317245
- Ledoux, G., Gong, J., Huiskens, F., Guillois, O., and Reynaud, C. (2002). Photoluminescence of size-separated silicon nanocrystals: confirmation of quantum confinement. *Appl. Phys. Lett.* 80, 4834–4836. doi: 10.1063/1.1485302
- Ledoux, G., Guillois, O., Porterat, D., Reynaud, C., Huiskens, F., Kohn, B., et al. (2000). Photoluminescence properties of silicon nanocrystals as a function of their size. *Phys. Rev. B* 62, 15942–15951. doi: 10.1103/PhysRevB.62.15942
- Low, S. P., Voelcker, N. H., Canham, L. T., and Williams, K. A. (2009). The biocompatibility of porous silicon in tissues of the eye. *Biomaterials* 30, 2873–2880. doi: 10.1016/j.biomaterials.2009.02.008
- Morrow, B. A., and McFarlan, A. J. (1992). Surface vibrational modes of silanol groups on silica. *J. Phys. Chem.* 96, 1395–1400. doi: 10.1021/j100182a068
- Nesbitt, H. W., Bancroft, G. M., Henderson, G. S., Ho, R., Dalby, K. N., Huang, Y., et al. (2011). Bridging, non-bridging and free (O²⁻) oxygen in Na₂O-SiO₂ glasses: an X-ray Photoelectron Spectroscopic (XPS) and Nuclear Magnetic Resonance (NMR) study. *J. Non. Cryst. Solids* 357, 170–180. doi: 10.1016/j.jnoncrysol.2010.09.031
- Ogata, Y. (1995). Oxidation of porous silicon under water vapor environment. *J. Electrochem. Soc.* 142, 1595–1601. doi: 10.1149/1.2.048619

- Osminkina, L. A., Gongalsky, M. B., Motuzuk, A. V., Timoshenko, V. Y., and Kudryavtsev, A. A. (2011). Silicon nanocrystals as photo- and sonosensitizers for biomedical applications. *Appl. Phys. B Lasers Opt.* 105, 665–668. doi: 10.1007/s00340-011-4562-8
- Park, J. H., Gu, L., von Maltzahn, G., Ruoslahti, E., Bhatia, S. N., and Sailor, M. J. (2009). Biodegradable luminescent porous silicon nanoparticles for *in vivo* applications. *Nat. Mater.* 8, 331–336. doi: 10.1038/nmat2398
- Pavlikov, A. V., Lartsev, A. V., Gayduchenko, I. A., and Yu Timoshenko, V. (2012). Optical properties of materials based on oxidized porous silicon and their applications for UV protection. *Microelectron. Eng.* 90, 96–98. doi: 10.1016/j.mee.2011.06.005
- Piryutko, M. M. (1959). the Solubility of silicic acid in salt solutions. *Russian Chem. Bull.* 8, 355–360. doi: 10.1007/BF00917687
- Qin, Z., Joo, J., Gu, L., and Sailor, M. J. (2014). Size control of porous silicon nanoparticles by electrochemical perforation etching. *Part. Part. Syst. Charact.* 31, 252–256. doi: 10.1002/ppsc.201300244
- Rimstidt, J. D., and Barnes, H. L. (1980). The kinetics of silica-water reactions. *Geochim. Cosmochim. Acta* 44, 1683–1699. doi: 10.1016/0016-7037(80)90220-3
- Secret, E., Wu, C. C., Chaix, A., Galarneau, A., Gonzalez, P., Cot, D., et al. (2015). Control of the pore texture in nanoporous silicon via chemical dissolution. *Langmuir* 31, 8121–8128. doi: 10.1021/acs.langmuir.5b01518
- Segal, E., Perelman, L. A., Cunin, F., Di Renzo, F., Devoisselle, J. M., Li, Y. Y., et al. (2007). Confinement of thermoresponsive hydrogels in nanostructured porous silicon dioxide templates. *Adv. Funct. Mater.* 17, 1153–1162. doi: 10.1002/adfm.200601077
- Seward, T. M. (1974). Determination of the first ionization constant of silicic acid from quartz solubility in borate buffer solutions to 350°C. *Geochim. Cosmochim. Acta* 38, 1651–1664. doi: 10.1016/0016-7037(74)90183-5
- Sviridov, A. P., Osminkina, L. A., Kharin, A. Y., Gongalsky, M. B., Kargina, J. V., Kudryavtsev, A. A., et al. (2017). Cytotoxicity control of silicon nanoparticles by biopolymer coating and ultrasound irradiation for cancer theranostic applications. *Nanotechnology* 28:105102. doi: 10.1088/1361-6528/aa5b7c
- Theiss, W. (1997). Optical properties of porous silicon. *Surf. Sci. Rep.* 29, 91–192. doi: 10.1016/S0167-5729(96)00012-X
- von Bardeleben, H. J., Chamarro, M., Grosman, A., Morazzani, V., Ortega, C., Siejka, J., et al. (1993). Pb-defects and visible photoluminescence in porous silicon. *J. Lumin.* 57, 39–43. doi: 10.1016/0022-2313(93)90103-T
- Walther, J. V., and Helgeson, H. C. (1977). walther1977.pdf. *Am. J. Sci.* 277, 1315–1351. doi: 10.2475/ajs.277.10.1315

Conflict of Interest Statement: The authors declare that the research was conducted in the absence of any commercial or financial relationships that could be construed as a potential conflict of interest.

Copyright © 2019 Gongalsky, Kargina, Cruz, Sánchez-Royo, Chirvony, Osminkina and Sailor. This is an open-access article distributed under the terms of the Creative Commons Attribution License (CC BY). The use, distribution or reproduction in other forums is permitted, provided the original author(s) and the copyright owner(s) are credited and that the original publication in this journal is cited, in accordance with accepted academic practice. No use, distribution or reproduction is permitted which does not comply with these terms.



Gold-Sensitized Silicon/ZnO Core/Shell Nanowire Array for Solar Water Splitting

Fu-Qiang Zhang, Ya Hu, Rui-Nan Sun, Haoxin Fu and Kui-Qing Peng*

Department of Physics and Beijing Key Laboratory of Energy Conversion and Storage Materials, Beijing Normal University, Beijing, China

OPEN ACCESS

Edited by:

Nicolas Hans Voelcker,
Monash University, Australia

Reviewed by:

Jia Hong Pan,
North China Electric Power University,
China

Girish Sallan,
Uppsala University, Sweden

*Correspondence:

Kui-Qing Peng
kq_peng@bnu.edu.cn

Specialty section:

This article was submitted to
Chemical Engineering,
a section of the journal
Frontiers in Chemistry

Received: 10 July 2018

Accepted: 18 March 2019

Published: 03 April 2019

Citation:

Zhang F-Q, Hu Y, Sun R-N, Fu H and
Peng K-Q (2019) Gold-Sensitized
Silicon/ZnO Core/Shell Nanowire
Array for Solar Water Splitting.
Front. Chem. 7:206.
doi: 10.3389/fchem.2019.00206

Solar water splitting represents one of the most promising strategies in the quest for clean and renewable energy. However, low conversion efficiency, use of sacrificial agents, and external bias for current water splitting system limit its practical application. Here, a gold-sensitized Si/ZnO core/shell nanowire photoelectrochemical (PEC) cell is reported for efficient solar water oxidation. We demonstrated gold-sensitized n-Si/n-ZnO nanowire arrays exhibited higher energy conversion efficiency than gold-sensitized p-Si/n-ZnO nanowire arrays due to the favorable energy-band alignment characteristics. Without any assistance from an external electrical source and sacrificial reagents, gold-sensitized n-Si/n-ZnO core/shell nanowire array photoanode achieved unbiased water splitting under simulated solar light illumination. This method opens a promising venue to cost-efficient production of solar fuels.

Keywords: silicon nanowire, ZnO, core/shell heterostructure, solar water splitting, photosensitization

INTRODUCTION

Solar water splitting has a long history and continued to stimulate great interest in scientist around the world due to its promising application in storing the energy of the sun in the form of chemical fuels (Fujishima and Honda, 1972; Bard and Fox, 1995; Chen et al., 2010). As compared to water reduction reaction for hydrogen generation, water oxidation involves complex proton-coupled electron transfer process and the generation of oxygen is even more difficult. In the past decades, metal oxide semiconductors with wide band-gap have been widely explored as oxygen evolving photoanode due to their excellent stability in oxidizing environments. However, these wide band-gap semiconductors only absorb a small portion of sunlight, resulting in the poor water splitting efficiency. To achieve high efficient water splitting, sunlight has to be efficiently absorbed and utilized. Although significant efforts have been devoted to questing for cost-effective water splitting photocatalysts in the past decades (Wagner and Somorjai, 1980; Khaselev and Turner, 1998; Grätzel, 2001; Zou et al., 2001; Maeda et al., 2006; Grimes et al., 2008; Kanan and Nocera, 2008; Hwang et al., 2009; Kudo and Miseki, 2009; Lisorti et al., 2009; Yang et al., 2009; Sun et al., 2010; Walter et al., 2010; Ingram and Linic, 2011; Linic et al., 2011; Paracchino et al., 2011; Reece et al., 2011; Brillet et al., 2012; Warren and Thimsen, 2012; Qi et al., 2013; Wang et al., 2014; Liu et al., 2015; Yu et al., 2015), but the solar energy conversion efficiency reported is relatively low.

In this work, we demonstrate that this challenge may be addressed by devising an n-Si/n-ZnO core/shell nanowire heterojunction photoanode sensitized with gold nanoparticles (AuNPs). Without any assistance from an external electrical source and sacrificial reagents, such gold-sensitized n-Si/n-ZnO core/shell nanowires array photoanode shows efficient sunlight-driven

water splitting ability. Moreover, such 3D dual-absorber water oxidation devices consist of earth-abundant materials can be prepared on an industrial scale with ease. The results also demonstrated that gold-sensitized n-Si/n-ZnO core/shell nanowire exhibited higher energy conversion efficiency than gold-sensitized p-Si/n-ZnO core/shell nanowires due to reduced recombination of photo-generated charge carriers.

MATERIALS AND METHODS

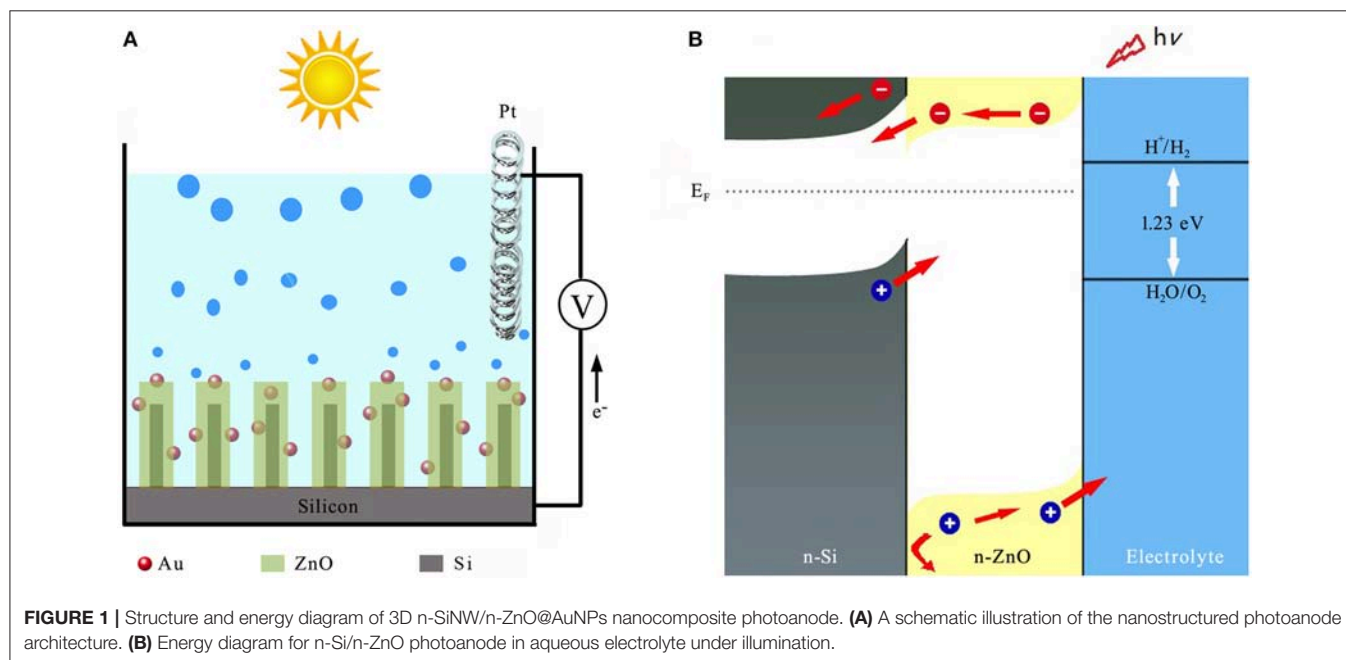
Despite its relative instability, however, ZnO is adopted here due to its excellent electrical conductivity for efficient charge transport when compared to TiO_2 , WO_3 , and $\alpha\text{-Fe}_2\text{O}_3$. Schematic illustration of the solar water splitting with n-Si/n-ZnO core/shell nanowire array sensitized with gold nanoparticles (AuNPs) is shown in **Figure 1A**. The n-Si/n-ZnO core/shell nanowire array significantly enhances light absorption over a wide solar spectral range, while reduces the photo-generated carrier loss due to the favorable energy-band alignment characteristics as illustrated in **Figure 1B**.

Figures 2A–C illustrate the fabrication process of the Si/n-ZnO core/shell nanowire heterojunction samples (for more details see the experimental section). Generally speaking, the silicon nanowire (SiNW) arrays are prepared by silver-catalyzed electroless etching of silicon wafer (Peng et al., 2002, 2003, 2006, 2008), then the SiNW arrays are impregnated with aqueous solutions containing mixed $\text{Zn}(\text{NO}_3)_2$ and HAuCl_4 precursors. In the last, the $\text{Zn}(\text{NO}_3)_2$ and HAuCl_4 wetted SiNW arrays are annealed in a vacuum tube furnace. The final n-SiNW/n-ZnO@AuNPs samples are yellowish black in color. The top-view scanning electron microscope (SEM) images of as-prepared SiNW array and n-SiNW/n-ZnO@AuNPs samples are shown in

Figures 2D,E, respectively, showing arrays of dense nanowires vertically aligned on the silicon surfaces.

The side-view SEM image of the Si/n-ZnO@AuNPs core/shell nanowire arrays (**Figure 3A**) were characterized by transmission electron microscopy (TEM). **Figures 3B–D** shows the low-magnification and high-magnification TEM images of Si/n-ZnO@AuNPs core/shell nanowires. It can be clearly seen that the SiNWs are uniformly coated with crystalline ZnO particle layer. The thickness of the crystalline ZnO layer coated on the SiNW depends on the density of SiNWs and varied in the range from 20 to 60 nm. The AuNPs are between 2 and 20 nanometers in size, most of which are embedded within the ZnO layer while some of which are exposed to the surface of the ZnO layer. High-resolution TEM image of the edge of a single nanowire shown in **Figure S1** clearly reveals the crystalline faceting at the Si/ZnO core/shell interface and the AuNPs loaded in the ZnO shell layer.

Figure 4A shows the X-ray diffraction (XRD) pattern of the as-prepared Si/ZnO@AuNPs photoanode. The diffraction peaks are well-matched with a mixture of the crystallographic structures of wurtzite zinc oxide, silicon, and gold. These results confirm that the solution immersion and annealing process is a facile route for large-scale fabrication of 3D composite photoelectrodes. The UV-visible absorption spectrum of as-prepared Si/n-ZnO@AuNPs core/shell nanowires photoanode is shown in **Figure 4B**, as a reference, the UV-visible absorption spectrum of Si/n-ZnO nanowires photoanode was included. It can be clearly seen that the Si/ZnO@AuNPs core/shell nanowires photoanode exhibits enhanced optical absorption in the wavelength range from 400 to 970 nm due to surface plasmon resonance (SPR) of AuNPs (Cushing et al., 2012; Li et al., 2013a,b). The enhanced light absorption due to SPR and photonic enhancement (Tian and Tatsuma, 2005; Li et al., 2013a) of AuNPs was further confirmed by electromagnetic



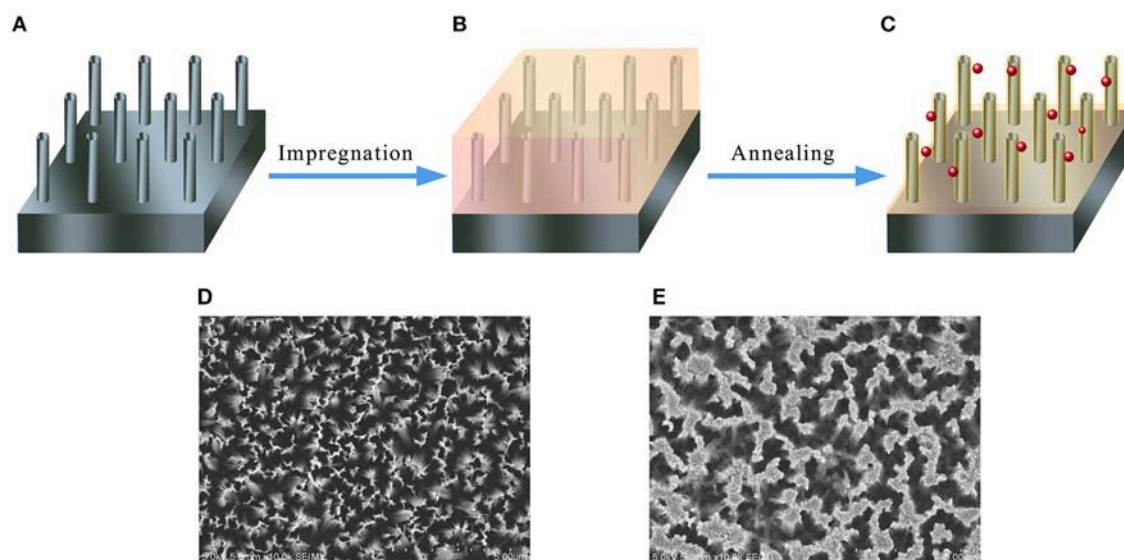


FIGURE 2 | Schematic illustration of the fabrication process for 3D n-SiNW/n-ZnO@AuNPs nanocomposite photoanode and corresponding SEM images. **(A)** SiNW array prepared by metal-catalyzed etching of silicon. **(B)** SiNW array is impregnated with aqueous solutions containing $\text{Zn}(\text{NO}_3)_2$ and HAuCl_4 precursors. **(C)** n-Si/n-ZnO@AuNPs nanowires photoanode by annealing the impregnated SiNW array at 500°C in a vacuum tube furnace. **(D)** Top-view SEM image of n-SiNW array. **(E)** Top-view SEM image of n-Si/n-ZnO@AuNPs nanowires photoanode.

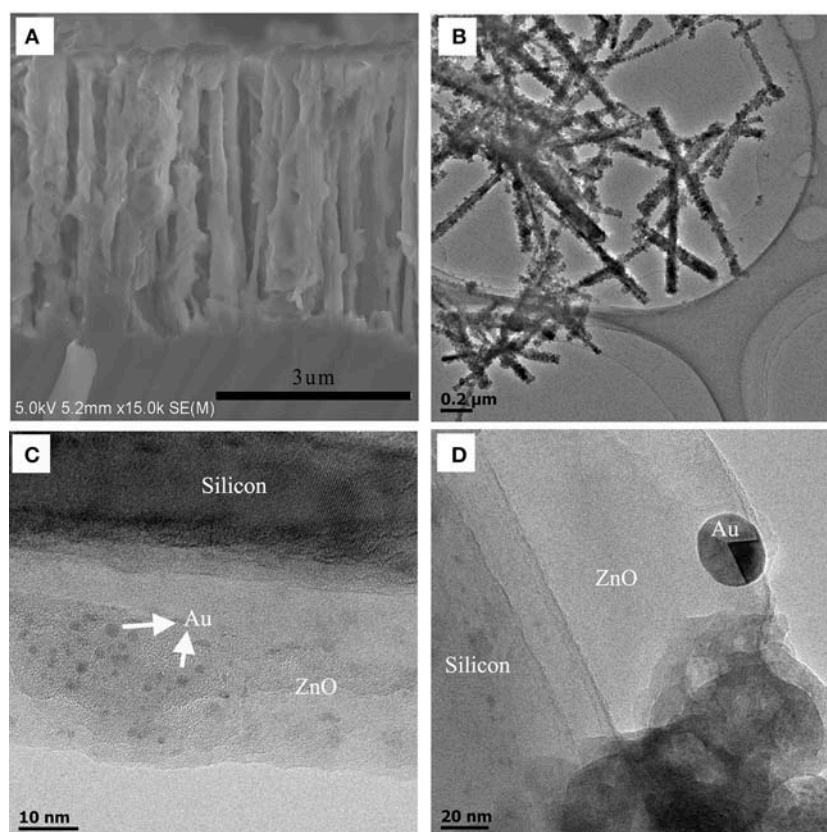


FIGURE 3 | Structural characterization of Si/ZnO@AuNPs core/shell nanocomposite photoanode. **(A)** Side-view SEM image of Si/n-ZnO@AuNPs core/shell nanowire array. **(B)** Low-magnification TEM image of Si/n-ZnO@AuNPs core/shell nanowires. **(C,D)** High-magnification TEM images of Si/n-ZnO@AuNPs core/shell nanowire.

simulation using finite-difference-time-domain (FDTD) method, as shown in **Figure S2**. The simulation geometry of the Si/ZnO@AuNPs core/shell nanowires photoanode is consistent

with the experiment result, the diameter of AuNPs is 5 nm and the thickness of ZnO layer is 20 nm. Under the incident wavelengths of 496–636 nm of the light, the FDTD results show

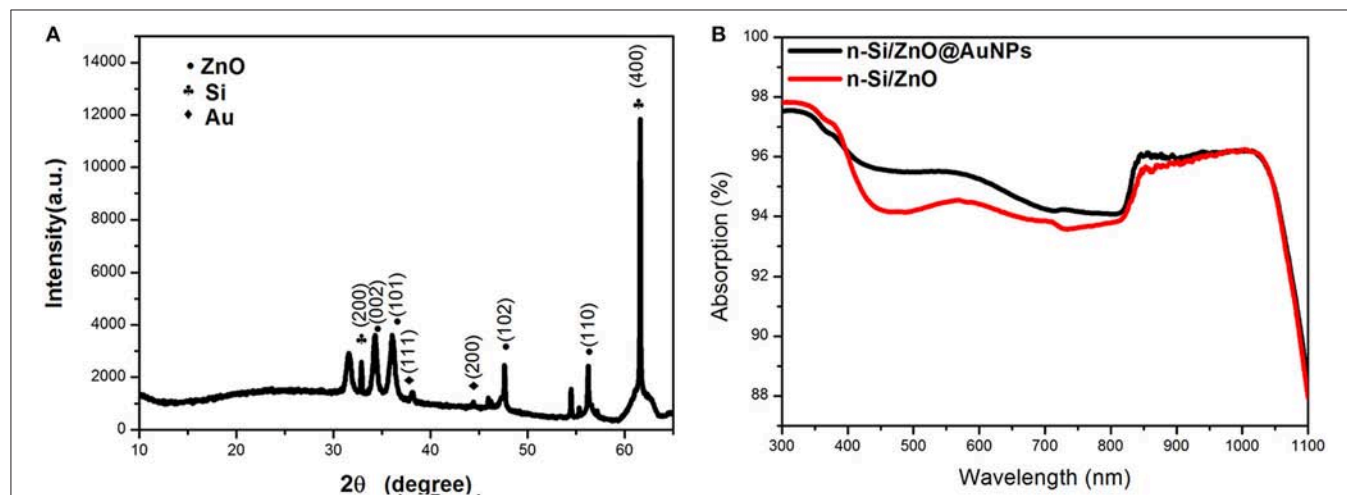


FIGURE 4 | (A) XRD pattern of Si/n-ZnO@AuNPs core/shell nanowires photoanode. (B) Absorption spectra of Si/n-ZnO core/shell nanowire photoanodes with and without AuNPs.

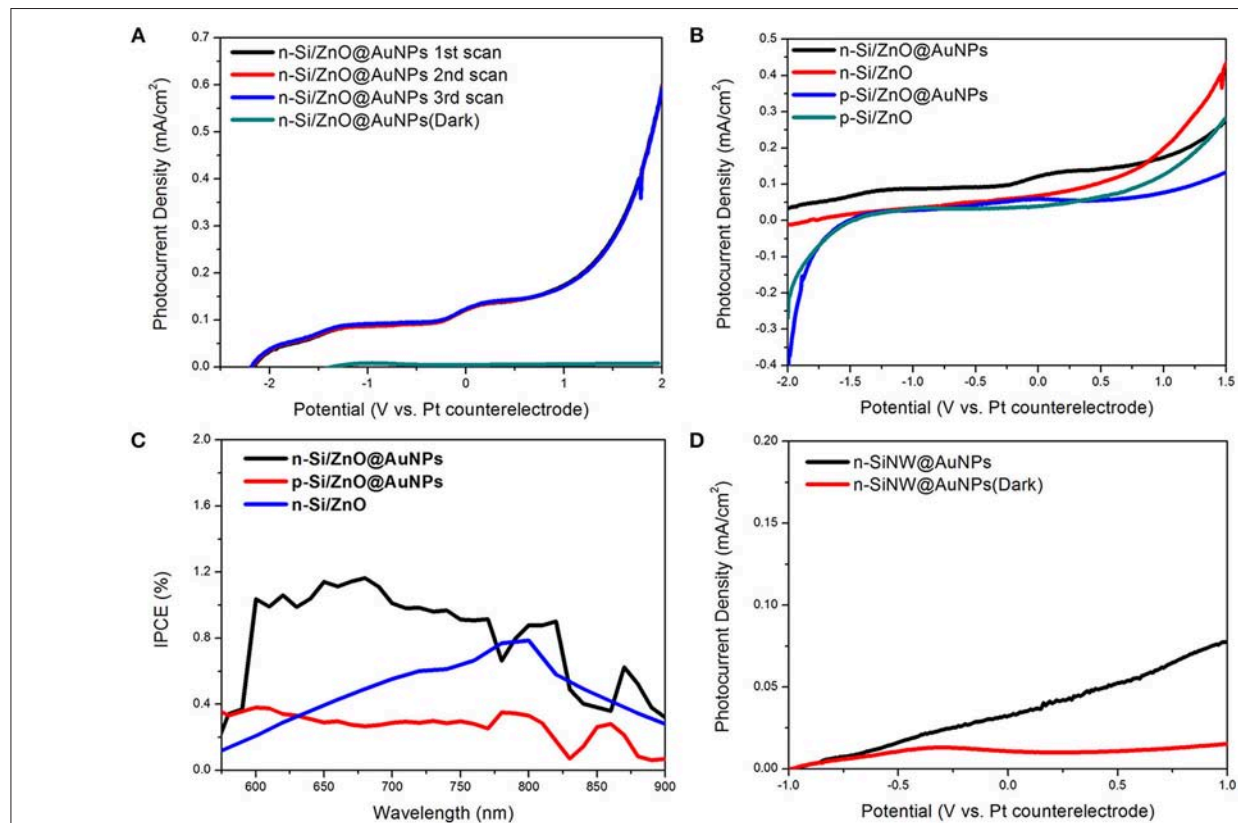


FIGURE 5 | Photoelectrochemical properties of as-prepared nanocomposite photoanodes in 0.5 M Na₂SO₄ mild aqueous electrolyte. (A) The consecutive multiple linear scan curve of the composite n-Si/n-ZnO@AuNPs core/shell nanowires photoanode under illumination and dark. (B) Photocurrent density vs. potential characteristics of n-Si/n-ZnO@AuNPs, n-Si/n-ZnO, p-Si/n-ZnO@AuNPs, and p-Si/n-ZnO core/shell nanowire photoanodes under illumination, respectively. (C) IPCE spectra of n-Si/n-ZnO@AuNPs, n-Si/n-ZnO, and p-Si/n-ZnO@AuNPs core/shell nanowire photoanodes. The IPCE spectra are recorded at zero applied bias. (D) Photocurrent density vs. potential characteristics of n-SiNW@AuNPs photoanode under illumination and in dark.

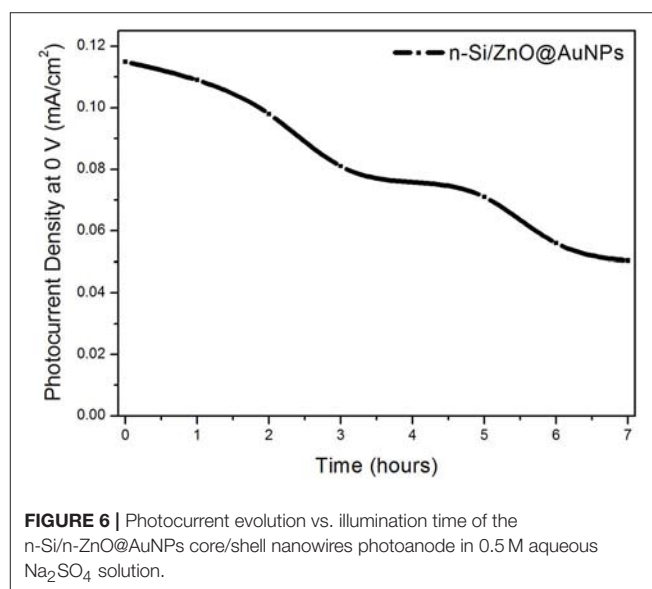
that the local electric fields near the AuNPs/n-ZnO interface are increased by about eight and 4 times, respectively. Thus, the generation rate of electron-hole pairs is expected to be greatly enhanced near the AuNPs/n-ZnO interface area due to the enhanced electric field intensity. In addition, the hot electrons due to the decay of plasmon transfer to the conduction band of ZnO result in photocurrent enhancement, as shown in **Figure S3**.

The photoelectrochemical (PEC) properties of the sample were characterized in a two-electrode configuration with platinum wire coil as the counter electrode. A 0.5 M Na₂SO₄ mild aqueous solution (PH~7) served as the electrolyte and no sacrificial reagents were used. All the tests were conducted under a.m. 1.5 G illumination with an intensity of 100 mW/cm². **Figure 5A** shows the consecutive multiple linear scan curve of the composite n-Si/n-ZnO@AuNPs core/shell nanowires photoanode under illumination and dark. The little difference of the curves in the linear scan indicate the repeatability and stability of the photoanode in solution. Moreover, the n-Si/n-ZnO@AuNPs core/shell nanowires photoanode shows 0.115 mA cm⁻² photocurrent density at 0 V, implying water oxidation activity without any assistance from an external electrical source. Moreover, the photocurrent density of the photoanode shows progress compared with previous results under zero applied bias (Lin et al., 2012; Guo et al., 2013), as shown in **Table S1**. We also use a three-electrode system to investigate the onset potential of the n-Si/ZnO@AuNPs photoanode for water oxidation as shown in **Figure S4**. It can be seen the onset potential in three-electrode system has about 1.1 V potential shift compare with two-electrode system, which means 1.71 V shift vs. RHE. The current-potential characteristics of the n-Si/n-ZnO, p-Si/n-ZnO@AuNPs and p-Si/n-ZnO core/shell nanowire photoanodes were also measured for comparison as shown in **Figure 5B**. The dark current density of these photoanode is shown in **Figure S5**. The dark current densities are negligible as compared to the photocurrent densities under illumination, revealing few chemical reactions occurred in dark. Under simulated solar illumination, the photocurrent density of n-Si/n-ZnO core/shell nanowires photoanode at 0 V is 0.064 mA cm⁻². The photocurrent density is about two times low and the open-circuit potential is higher as compared to the n-Si/ZnO@AuNPs core/shell nanowires photoanode. We suggest the AuNPs trigger the unbiased solar water splitting through surface plasmon resonance (SPR), plasmons decay induced hot electrons transfer and the plasmon resonance energy transfer (PRET). The PRET decreases the distance of the holes travel to the electrolyte and therefore improve the photocurrent density. We note that the photocurrent density at 0 V of p-Si/n-ZnO@AuNPs and p-Si/n-ZnO core/shell nanowire photoanodes is 0.042 mA cm⁻² and 0.014 mA cm⁻², respectively. More interestingly, the PEC water oxidation performance of n-Si/n-ZnO@AuNPs core/shell nanowires photoanode is higher than that of the p-Si/n-ZnO@AuNPs core/shell nanowires photoanode. This could be understood by the band bending characteristics of n-Si/n-ZnO (**Figure S6a**) and p-Si/n-ZnO junctions (**Figure S6b**). In p-Si/n-ZnO junctions, the photo generated holes in ZnO layer can move either to the p-Si or to the electrolyte for water oxidation. In contrast, the holes in the ZnO layer of n-Si/n-ZnO junctions can

only move to the electrolyte and the electrons in the silicon move to the electrode for a circuit.

The sunlight-driven water splitting performance of as-prepared composite photoanodes was further evaluated by the incident photo-to-current efficiency (IPCE). **Figure 5C** shows the IPCE spectra as a function of wavelength recorded at zero bias for n-Si/n-ZnO@AuNPs, n-Si/n-ZnO and p-Si/n-ZnO@AuNPs core/shell nanowire photoanodes. It is clearly observed that the n-Si/n-ZnO@AuNPs core/shell nanowire photoanode shows enhanced photoresponse in a wide wavelength range. In contrast, the photoresponse of p-Si/n-ZnO@AuNPs core/shell nanowires photoanode is relatively low in the same wavelength range due to the unfavorable energy-band alignment characteristics. The IPCE difference between n-Si/n-ZnO@AuNPs and n-Si/n-ZnO photoanode further confirms the effect of AuNPs. In order to certify the role of ZnO layer in improving the performance of n-Si/n-ZnO@AuNPs core/shell nanowires photoanode for water oxidation, we conducted the current-potential measurement of n-SiNW@AuNPs photoanode in 0.5 M Na₂SO₄ solution. **Figure 5D** shows the current-potential characteristics of n-SiNW@AuNPs photoanode under illumination and dark. The photocurrent density at 0 V is 0.02 mA cm⁻², which quantitatively shows the role of ZnO layer in promoting the performance of n-Si/n-ZnO@AuNPs core/shell nanowire photoanode.

The influence of the position of AuNPs in the ZnO layer upon the water splitting performance is evaluated. **Figure S7** illustrates the n-Si/ZnO core/shell nanowires photoanodes decorated with AuNPs in “mixed,” “outer,” and “inner” configurations. **Figure S8** shows the J-E curves of the n-Si/ZnO core/shell nanowires decorated with AuNPs in different position. All the tests are recorded in 0.5 M Na₂SO₄ solution. The photocurrent density at 0 V for the photoanodes decorated with AuNPs in outer and inner configurations are 0.073 and 0.080 mA/cm², respectively. The results clearly show that the nanowires photoanode decorated with AuNPs in mixed configuration



exhibited better water splitting performance. The suppressed plasmonic photosensitization for AuNPs in inner configuration limits the catalytic effect. And the lower electrical conductivity in the surface configuration limits the separation of electron-hole pairs. Such distinct performance implies that AuNPs play the roles of plasmonic photosensitization, co-catalyst for water splitting reaction, and electrical conductivity enhancement.

The stability of the n-Si/n-ZnO@AuNPs core/shell nanowires photoanode was assessed by measuring the photocurrent density at 0 V in 0.5 M Na₂SO₄ solution under a.m. 1.5 G illumination of 100 mW cm⁻². **Figure 6** shows the evolution of photocurrent density of n-Si/n-ZnO@AuNPs core/shell nanowires photoanode at 0 V with the illumination time. The photocurrent density gradually declined to ~70% of its initial value over 3 h. This is a good stability performance in comparison with previous reports (Qiu et al., 2012).

CONCLUSIONS

In summary, we have demonstrated an efficient solar water splitting system based on n-Si/n-ZnO core/shell nanowire array photosensitized with AuNPs. The n-Si/n-ZnO@AuNPs core/shell nanowires photoanode demonstrate much higher efficiency than p-Si/n-ZnO@AuNPs core/shell nanowires photoanode. We suggest that the ZnO shell and incorporated AuNPs play crucial catalytic and plasmonic photosensitization roles, while silicon

core absorbs light and generates photocarriers. AuNPs also may function as efficient co-catalyst for water splitting reaction. We believe such solar water splitting system represents a step toward the goal of cost-effective large-scale production of solar fuels.

AUTHOR CONTRIBUTIONS

All authors listed have made substantial, direct and intellectual contributions to the work: F-QZ performed all experiments and wrote the manuscript. YH, R-NS, and HF prepared the samples and analyzed the data. K-QP analyzed the data and wrote the manuscript. All authors discussed, reviewed and approved the manuscript.

ACKNOWLEDGMENTS

We acknowledge support through Beijing Natural Science Foundation (2172030), National Natural Science Foundation of China (91333208, 51072025), and the Interdisciplinary support from the Beijing Normal University.

SUPPLEMENTARY MATERIAL

The Supplementary Material for this article can be found online at: <https://www.frontiersin.org/articles/10.3389/fchem.2019.00206/full#supplementary-material>

REFERENCES

- Bard, A. J., and Fox, M. A. (1995). Artificial photosynthesis-solar splitting of water to hydrogen and oxygen. *Acc. Chem. Res.* 28, 141–145. doi: 10.1021/ar00051a007
- Brillet, J., Yum, J. H., Cornuz, M., Hisatomi, T., Solarska, R., Augustynski, J., et al. (2012). Highly efficient water splitting by a dual-absorber tandem cell. *Nat. Photon.* 6, 824–828. doi: 10.1038/NPHOTON.2012.265
- Chen, X., Shen, S., Guo, L., and Mao, S. S. (2010). Semiconductor-based photocatalytic hydrogen generation. *Chem. Rev.* 110, 6503–6570. doi: 10.1021/cr1001645
- Cushing, S. K., Li, J., Meng, F., Senty, T. R., Suri, S., Zhi, M., et al. (2012). Photocatalytic activity enhanced by plasmonic resonant energy transfer from metal to semiconductor. *J. Am. Chem. Soc.* 134, 15033–15041. doi: 10.1021/ja305603t
- Fujishima, A., and Honda, K. (1972). Electrochemical photolysis of water at a semiconductor electrode. *Nature* 238, 37–38. doi: 10.1038/238037a0
- Grätzel, M. (2001). Photoelectrochemical cells. *Nature* 414, 338–344. doi: 10.1038/35104607
- Grimes, C. A., Varghese, O. K. and Ranjan S., (2008). *Light Water Hydrogen: The Solar Generation of Hydrogen by Water Photoelectrolysis*. New York, NY: Springer.
- Guo, C. X., Dong, Y. Q., Yang, H. B., and Li, C. M. (2013). Graphene quantum dots as a green sensitizer to functionalize ZnO nanowire arrays on F-doped SnO₂ glass for enhanced photoelectrochemical water splitting. *Adv. Energy Mater.* 3, 997–1003. doi: 10.1002/aenm.201300171
- Hwang, Y., Bukai, A., and Yang, P. D. (2009). Highly aligned n-Si/n-TiO₂ core/shell nanowire arrays with enhanced photoactivity. *Nano Lett.* 9, 410–415. doi: 10.1021/nl8032763
- Ingram, D. B., and Linic, S. (2011). Water splitting on composite plasmonic-metal/semiconductor photoelectrodes: evidence for selective plasmon-induced formation of charge carriers near the semiconductor surface. *J. Am. Chem. Soc.* 133, 5202–5205. doi: 10.1021/ja200086g
- Kanan, M. W., and Nocera, D. G. (2008). *In situ* formation of an oxygen-evolving catalyst in neutral water containing phosphate and Co²⁺. *Science* 321, 1072–1075. doi: 10.1126/science.1162018
- Khaselev, O., and Turner, J. A. (1998). A monolithic photovoltaic-photoelectrochemical device for hydrogen production via water splitting. *Science* 280, 425–427. doi: 10.1126/science.280.5362.425
- Kudo, A., and Miseki, Y. (2009). Heterogeneous photocatalyst materials for water splitting. *Chem. Soc. Rev.* 38, 253–278. doi: 10.1039/b800489g
- Li, J., Cushing, S. K., Zheng, P., Meng, F., Chu, D., and Wu, N. (2013b). Plasmon-induced photonic and energy-transfer enhancement of solar water splitting by a hematite nanorod array. *Nat. Commun.* 4:2651. doi: 10.1038/ncomms3651
- Li, J. T., Cushing, S. K., Bright, J., Meng, F. K., Senty, T. R., Zheng, P., et al. (2013a). Ag@Cu₂O core-shell nanoparticles as visible-light plasmonic photocatalysts. *ACS Catal.* 3, 47–51. doi: 10.1021/cs300672f
- Lin, Y. G., Hsu, Y. K., Chen, Y. C., Wang, S. B., Jeffrey, T. M., Chen, L. C., et al. (2012). Plasmonic Ag@Ag₃(PO₄)_{1-x} nanoparticle photosensitized ZnO nanorod-array photoanodes for water oxidation. *Energy Environ. Sci.* 5, 8917–8922. doi: 10.1039/C2EE22185C
- Linic, S., Christopher, P., and Ingram, D. B. (2011). Plasmonic-metal nanostructures for efficient conversion of solar to chemical energy. *Nat. Mater.* 10, 911–921. doi: 10.1038/NMAT3151
- Lisorti, A., Durrant, J., and Barber, J. (2009). Artificial Photosynthesis: solar to fuel. *Nat. Mater.* 8, 929–930. doi: 10.1038/nmat2578
- Liu, J., Liu, Y., Liu, N. Y., Han, Y. Z., Zhang, X., Huang, H., et al. (2015). Metal-free efficient photocatalyst for stable visible water splitting via a two-electron pathway. *Science* 27, 970–974. doi: 10.1126/science.aaa3145
- Maeda, K., Teramura, K., Lu, D., Takata, T., Saito, N., Inoue, Y., et al. (2006). Photocatalyst releasing hydrogen from water. *Nature* 440:295. doi: 10.1038/440295a
- Paracchino, A., Laporte, V., Sivula, K., Grätzel, M., and Thimsen, E. (2011). Highly active oxide photocathode for photoelectrochemical water reduction. *Nat. Mater.* 10, 456–461. doi: 10.1038/NMAT3017

- Peng, K. Q., Hu, J. J., Yan, Y. J., Wu, Y., Fang, H., Xu, Y., et al. (2006). Fabrication of single-crystalline silicon nanowires by scratching a silicon surface with catalytic metal particles. *Adv. Funct. Mater.* 16, 387–394. doi: 10.1002/adfm.200500392
- Peng, K. Q., Lu, A. J., Zhang, R. Q., and Lee, S. T. (2008). Motility of metal nanoparticles in silicon and induced anisotropic silicon etching. *Adv. Funct. Mater.* 18, 3026–3035. doi: 10.1002/adfm.200800371
- Peng, K. Q., Yan, Y. J., Gao, S. P., and Zhu, J. (2002). Synthesis of large-area silicon nanowire arrays via self-assembling nanoelectrochemistry. *Adv. Mater.* 14, 1164–1167. doi: 10.1002/1521-4095(20020816)14:16<1164::AID-ADMA1164>3.0.CO;2-E
- Peng, K. Q., Yan, Y. J., Gao, S. P., and Zhu, J. (2003). Dendrite-assisted growth of silicon nanowires in electroless metal deposition. *Adv. Funct. Mater.* 13, 127–132. doi: 10.1002/adfm.200390018
- Qi, X., She, G., Wang, M., Mu, L., and Shi, W. (2013). Electrochemical synthesis of p-type Zn-doped α -Fe₂O₃ nanotube arrays for photoelectrochemical water splitting. *Chem. Commun.* 49, 5742–5744. doi: 10.1039/c3cc40599k
- Qiu, Y., Yan, K., Deng, H., and Yang, S. (2012). Secondary branching and nitrogen Doping of zn nanotetrapods: building a highly active network for photoelectrochemical water splitting. *Nano Lett.* 12, 407–413. doi: 10.1021/nl2037326
- Reece, S. Y., Hamel, J. A., Sung, K., Jarvi, T. D., Esswein, A. J., Pijpers, J. J., et al. (2011). Wireless solar water splitting using silicon-based semiconductors and earth-abundant catalysts. *Science* 334, 645–648. doi: 10.1126/science.1209816
- Sun, J., Zhong, D. K., and Gamelin, D. R. (2010). Composite photoanodes for photoelectrochemical solar water splitting. *Energy Environ. Sci.* 3, 1252–1261. doi: 10.1039/c0ee00030b
- Tian, Y., and Tatsuma, T. (2005). Mechanisms and applications of plasmon-induced charge separation at TiO₂ films loaded with gold nanoparticles. *J. Am. Chem. Soc.* 127, 7632–7637. doi: 10.1021/ja042192u
- Wagner, F. T., and Somorjai, G. A. (1980). Photocatalytic and photoelectrochemical hydrogen production on strontium titanate single crystals. *J. Am. Chem. Soc.* 102, 5494–5502. doi: 10.1021/ja00537a013
- Walter, M. G., Warren, E. L., McKone, J. R., Boettcher, S. W., Mi, Q., Santori, E. A., et al. (2010). Solar water splitting cells. *Chem. Rev.* 110, 6446–6473. doi: 10.1021/cr1002326
- Wang, X., Peng, K. Q., Hu, Y., Zhang, F. Q., Hu, B., Li, L., et al. (2014). Silicon/Hematite Core/Shell nanowire array decorated with gold nanoparticles for unbiased solar water oxidation. *Nano Lett.* 14, 18–23. doi: 10.1021/nl402205f
- Warren, S. C., and Thimsen, E. (2012). Plasmonic solar water splitting. *Energy Environ. Sci.* 5, 5133–5146. doi: 10.1039/c1ee02875h
- Yang, X., Wolcott, A., Wang, G., Sobo, A., Fitzmorris, R. C., Qian, F., et al. (2009). Nitrogen-doped ZnO nanowire arrays for photoelectrochemical water splitting. *Nano Lett.* 9, 2331–2336. doi: 10.1021/nl900772q
- Yu, X., Han, X., Zhao, Z. H., Zhang, J., Guo, W. B., Pan, C. F., et al. (2015). Hierarchical TiO₂ nanowire/graphite fiber photoelectrocatalysis setup powered by a wind-driven nanogenerator: A highly efficient photoelectrocatalytic device entirely based on renewable energy. *Nano Energy* 11, 19–27. doi: 10.1016/j.nanoen.2014.09.024
- Zou, Z., Ye, J., Sayama, K., and Arakawa, H. (2001). Direct splitting of water under visible light irradiation with an oxide semiconductor photocatalyst. *Nature* 414, 625. doi: 10.1038/414625a

Conflict of Interest Statement: The authors declare that the research was conducted in the absence of any commercial or financial relationships that could be construed as a potential conflict of interest.

Copyright © 2019 Zhang, Hu, Sun, Fu and Peng. This is an open-access article distributed under the terms of the Creative Commons Attribution License (CC BY). The use, distribution or reproduction in other forums is permitted, provided the original author(s) and the copyright owner(s) are credited and that the original publication in this journal is cited, in accordance with accepted academic practice. No use, distribution or reproduction is permitted which does not comply with these terms.



Emerging Functions of Nanostructured Porous Silicon—With a Focus on the Emissive Properties of Photons, Electrons, and Ultrasound

Nobuyoshi Koshida^{1*} and Toshihiro Nakamura²

¹ Graduate School of Engineering, Tokyo University of Agriculture and Technology, Fuchu, Japan, ² Department of Electrical and Electronic Engineering, Hosei University, Tokyo, Japan

OPEN ACCESS

Edited by:

Thierry Djenizian,
École des Mines de Saint-Étienne,
France

Reviewed by:

Petra Granitzer,
University of Graz, Austria
Jia Hong Pan,
North China Electric Power University,
China
Androula Galiouna Nassiopoulou,
National Centre of Scientific Research
Demokritos, Greece

*Correspondence:

Nobuyoshi Koshida
koshida@cc.tuat.ac.jp

Specialty section:

This article was submitted to
Chemical Engineering,
a section of the journal
Frontiers in Chemistry

Received: 18 January 2019

Accepted: 02 April 2019

Published: 24 April 2019

Citation:

Koshida N and Nakamura T (2019)
Emerging Functions of
Nanostructured Porous Silicon—With
a Focus on the Emissive Properties of
Photons, Electrons, and Ultrasound.
Front. Chem. 7:273.
doi: 10.3389/fchem.2019.00273

Recent topics of application studies on porous silicon (PS) are reviewed here with a focus on the emissive properties of visible light, quasiballistic hot electrons, and acoustic wave. By exposing PS in solvents to pulse laser, size-controlled nc-Si dot colloids can be formed through fragmentation of the PS layer with a considerably higher yield than the conventional techniques such as laser ablation of bulk silicon and sol-gel precursor process. Fabricated colloidal samples show strong visible photoluminescence (~40% in quantum efficiency in the red band). This provides an energy- and cost-effective route for production of nc-Si quantum dots. A multiple-tunneling transport mode through nc-Si dot chain induces efficient quasiballistic hot electron emission from an nc-Si diode. Both the efficiency and the output electron energy dispersion are remarkably improved by using monolayer graphene as a surface electrode. Being a relatively low operating voltage device compatible with silicon planar fabrication process, the emitter is applicable to mask-less parallel lithography under an active matrix drive. It has been demonstrated that the integrated 100 × 100 emitter array is useful for multibeam lithography and that the selected emission pattern is delineated with little distortion. Highly reducing activity of emitted electrons is applicable to liquid-phase thin film deposition of metals (Cu) and semiconductors (Si, Ge, and SiGe). Due to an extremely low thermal conductivity and volumetric heat capacity of nc-Si layer, on the other hand, thermo-acoustic conversion is enhanced to a practical level. A temperature fluctuation produced at the surface of nc-Si layer is quickly transferred into air, and then an acoustic wave is emitted without any mechanical vibrations. The non-resonant and broad-band emissivity with low harmonic distortions makes it possible to use the emitter for generating audible sound under a full digital drive and reproducing complicated ultrasonic communication calls between mice.

Keywords: porous silicon, nanocrystal, colloidal silicon, photoluminescence, ballistic electron emission, thermoacoustic

INTRODUCTION

As the scaling of integrated silicon devices approaches 10 nm or below, precise control of the physical and chemical properties of silicon becomes very important. In the quantum-size region of silicon (<4.7 nm), particularly, optimal processing is critical to enhance the optical, electrical, thermal, interfacial, and mechanical properties. Porous silicon (PS), prepared by electrochemical

anodization of crystalline silicon (c-Si) under the certain conditions, consists of a nanopore structure and residual quantum-sized nanocrystalline silicon (nc-Si). With appropriate surface passivation, nc-Si shows tunable properties in different ways from those of bulk c-Si and plays a role as a platform of functional devices in photonics, electronics, biometrics, biomedicine, acoustics, energetics, and so on (Sailor, 2012; Canham, 2017). From among these possibilities, the studies on the emission of photons, electrons, and ultrasound are discussed here.

Regarding the photonic applications, one key issue is to develop an efficient fabrication process of highly luminescent nc-Si colloids. For this purpose, some top-down and bottom-up approaches have been conducted to obtain colloidal nc-Si dots (Heath, 1992; Henderson et al., 2009; Shirahata et al., 2010). Typical techniques in the former are laser ablation of c-Si wafer and ultrasonic fragmentation of PS. Those in the latter are chemical vapor deposition (CVD), thermal decomposition treatment, and liquid-phase chemical reaction. In any case, an energy- and cost-effective process is strongly required for producing a practical amount of nc-Si dots or powder. Although the complicated nanostructure in PS layers seems to impede the electrical conduction, on the other hand, experimental and theoretical analyses of electron transport in arrayed nc-Si dots suggests the existence of a specific multiple-tunneling cascade mode therein (Koshida, 2017a). This leads to quasiballistic electron emission from an nc-Si diode. Its usefulness has been demonstrated not only in vacuum but also in atmospheric-pressure gases and solutions. Due to extremely low thermal conductivity and volumetric heat capacity of the nc-Si layer (Lysenko et al., 1999; Valalaki and Nassiopoulou, 2013, 2014, 2017; Koshida, 2017b), in addition, thermo-acoustic coupling with air is enhanced. Since no mechanical vibrations are involved, this thermally induced sound emission shows non-resonant flat frequency response (Koshida, 2017c). The nc-Si sound source can effectively reproduce complicated ultrasonic communication calls between mice.

These functional applications are different from the pursuit of scaling merits that have been sought in usual silicon device technology. The present status of technological exploration is summarized in the following sections and some recent developments are highlighted.

DIVERSIFYING STUDIES OF POROUS SILICON

While the minimum size of advanced large-scale integrated (LSI) circuit enters into the region below 10 nm, another viewpoint relating to environmental, social, and human issues has become important in pursuing the silicon device technology. Actually, the International Technology Roadmap for Semiconductors was recently reorganized¹ such that some new intentionality and keywords are contained [such as systems, beyond CMOS (complementary metal-oxide-semiconductor)

logic, emerging research materials, and so on] in addition to the conventional scaling activity “more Moore.” The silicon technology has reached the phase of evolutionary transformation from straightforward scaling to diversification, systematization, and functional combinations.

The scientific and technological evolution of PS materials is shown in **Figure 1**. Reflecting the versatile structures of PS, its research and development (R&D) have been conducted in many divergences. In the early stage just after finding of PS by Uhler (1956), the interests of PS were mainly in the formation mechanism and structural characterizations (Lehman, 2002). The application studies were field oxide formation for integrated device isolation (Watanabe et al., 1975) and use as substrates for epitaxial growth of compound and elemental semiconductors (Lin et al., 1987). Discovery of visible photoluminescence by Canham (1990) at 1990 led to the expansion of concern from the use as passive components to as an active quantum confinement material. Related investigations were also reported around that time on the photoelectrochemical solar cell (Koshida et al., 1985), photoconduction (Koshida et al., 1991), and electroluminescence (Koshida and Koyama, 1992), and optical effects (Thonissen et al., 1997). It was clarified that the physical and chemical properties of PS become radically different from those of single-crystalline bulk silicon. Then, the continuing studies paved the way for advanced surface chemistry (Coffinier and Boukherroub, 2016), biocompatibility (Canham, 1995), bio-sensors (Lin et al., 1997), biomedical therapy (Santos, 2014), quasiballistic electron emission (Koshida et al., 1999), thermal isolation (Nassiopoulou and Kaltsas, 2000; Nassiopoulou, 2014), and thermoacoustics (Shinoda et al., 1999). Recently the studies are further expanded to the field of energetics (Kouassi et al., 2012). Tunable optical, electrical, structural, surface, thermal, and chemical properties of PS meet the above-mentioned situation that silicon technology is rapidly evolving in a multilateral manner.

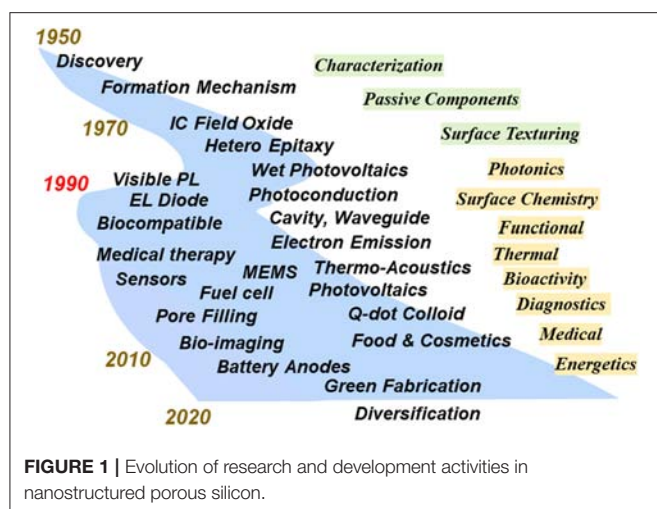
EMISSIVE PROPERTIES AND APPLICATIONS

Visible Luminescent Quantum Dots

Bottom-Up Fabrication Routes of Silicon Quantum Dot

Free-standing mono-dispersed colloidal particles of nc-Si (nc-Si dots) with diameter range of ~2–8 nm is well known to exhibit size-tunable visible luminescence. Both the dispersibility of nc-Si dots in solution and luminescence properties can be controlled by modifying their surface termination (Dohnalová et al., 2014). Recently, because of such interesting properties and the resultant compatibility of future solution-based luminescence devices, such as flexible electroluminescence diode (Choi et al., 2018), the nc-Si dot attracts a lot of attention. In addition, silicon dots are expected to apply in bio-technology, such as cellular imaging, due to non-toxicity of silicon (Cheng et al., 2014). For these applications, scalable production routes of the luminescent nc-Si dots are expected to develop. In this section, we review various routes for the nc-Si dots formation and the recent advances in the efficient production of the nc-Si dots,

¹IRDS. *IEEE International Roadmap for Devices and Systems (IRDS)*. Available online at: <https://irds.ieee.org>



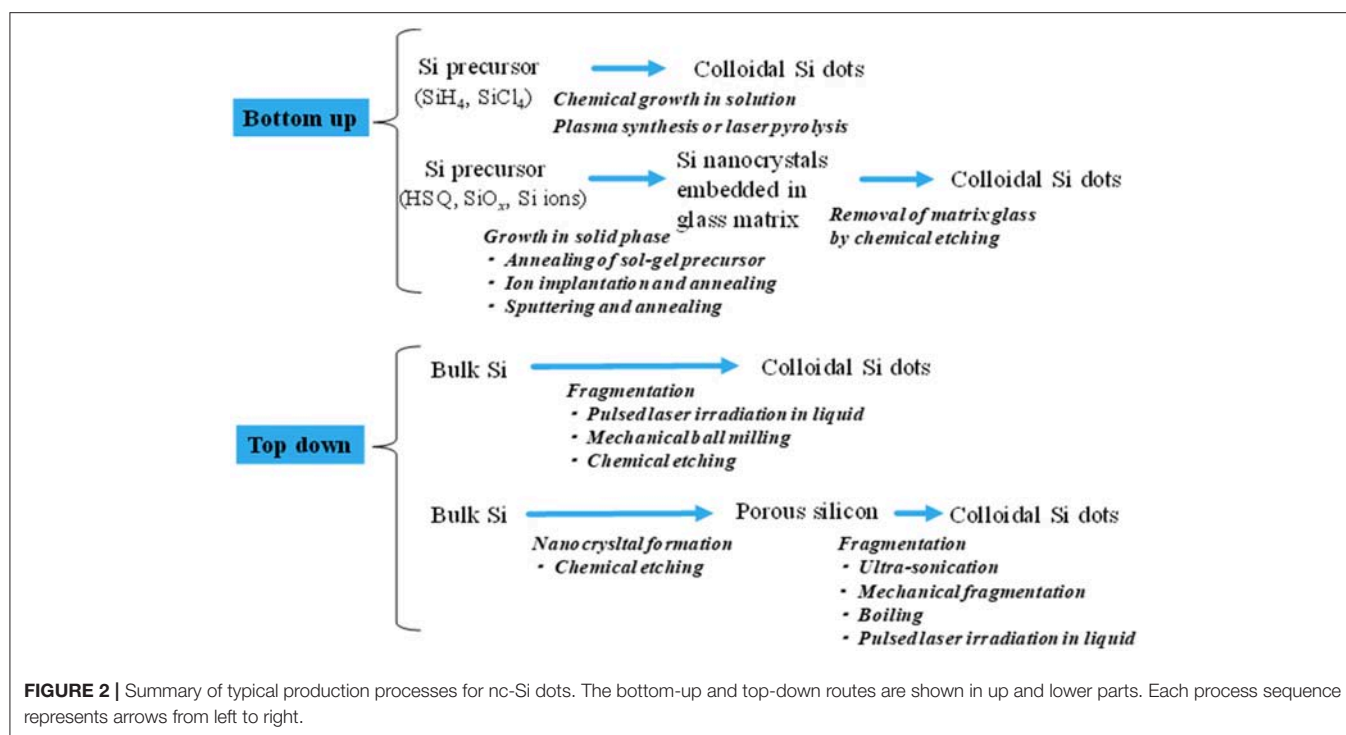
including the processes where PS (an assembly of nc-Si dots) is utilized as an intermediate material.

The nc-Si dots are prepared through the two types of preparation routes, i.e., top-down and bottom-up routes as summarized in **Figure 2**. A typical bottom-up process is the solution-phase chemical synthesis (Heath, 1992; Wilcoxon et al., 1999; Holmes et al., 2001; English et al., 2002; Zou et al., 2004; Liu et al., 2005; Dohnalová et al., 2012, 2013; Cheng et al., 2015; Debenedetti et al., 2015; Ghosh et al., 2018). In this method, the reduction of silicon precursors, such as SiCl_4 with Zintl salts (KSi , NaSi , Mg_2Si), at high temperature under high pressures forms colloidal nanocrystals. To render soluble the silicon colloids in arbitrary solvents (polar or nonpolar solvents), their surface termination usually modifies from initial termination (e.g., Br and Cl) to organic ligands. In some cases, further ligand exchanges from a ligand (e.g., alkene and thiol groups) to another ligand or biomolecules were performed for the organically-capped silicon colloids (Shiohara et al., 2010; Ruizendaal et al., 2011). The prepared colloids usually exhibit an emission in blue to green regions with nanosecond lifetimes, indicating the surface-related or direct gap recombination (Holmes et al., 2001; Dohnalová et al., 2012, 2013). Furthermore, by attaching adequate surface ligands, yellow to red luminescent colloids can be obtained. Interestingly their luminescent quantum efficiency increases up to $\sim 90\%$ (Qi et al., 2016). Note that the quantum efficiencies of typical nc-Si dots, where the quasi-direct electron-hole recombination occurs, were up to 60% (Jurbergs et al., 2006).

Another typical bottom-up process is laser pyrolysis (Ehbrecht et al., 1997; Ehbrecht and Huisken, 1999; Ledoux et al., 2002; Li et al., 2003, 2004; Hua et al., 2006) or plasma synthesis (Mangolini et al., 2005; Nozaki et al., 2007; Anthony and Kortshagen, 2009; Gupta et al., 2009; Shen et al., 2010; Miller et al., 2012; Askari et al., 2015) from the silicon precursor such as silane. In these methods, the treatment of a pulsed laser or an induction of high frequency power leads to the decomposition of precursor molecules and formation of Si clusters. Subsequently, the growth of the silicon nanoparticles occurs due to the aggregation of

the generated clusters. The obtained nanoparticles consist of the single phase crystalline core and the surrounding amorphous layer of SiO_x (Ledoux et al., 2002; Mangolini et al., 2005). Then, to adequately terminate the surfaces or further control the nanoparticle size, stain etching was performed in HF/HNO_3 aqueous solution, where the oxidation of the silicon surface of the nanoparticles occurs and the removal of the oxide layer leads to the decrease in the size (Li et al., 2003; Gupta et al., 2009). Subsequent organic capping may also be formed by an additional chemical treatment (Li et al., 2004; Hua et al., 2006). Due to such size control processes by stain-etching, the PL emission colors of the formed nanoparticles were tuned in all visible spectral regions (Gupta et al., 2009). The emission color of the nanoparticles also changes from blue to green by the total pressure of the plasma reactor (Shen et al., 2010). In the case of the laser pyrolysis, an excellent size separation was demonstrated by using a molecular-beam chopper synchronization of the irradiation pulsed laser combining the time-of-flight mass spectroscopy (Ehbrecht et al., 1997; Ehbrecht and Huisken, 1999). Formation of such size-separated nc-Si dots reveals the clear size-dependent PL data in a red spectral region (**Figure 3**), and an excellent agreement between the theory and data was shown (Ledoux et al., 2002). Typical PL quantum efficiencies of the nanoparticles prepared by laser pyrolysis are 1–30% depending on their size, i.e., the larger (smaller) nanoparticles with a diameter of 8 nm (3.5 nm) have lower (higher) efficiencies (Ledoux et al., 2002).

Recently, a new type of bottom-up process using sol-gel precursors for the formation of the nc-Si dots has been developed by Veinof's Group (Hessel et al., 2006, 2008; Henderson et al., 2009; Clark et al., 2010; Kelly et al., 2010). After the annealing of hydrogen silsesquioxane ($\text{HSiO}_{1.5}$) at high temperature (900–1400°C) under the H_2/Ar atmosphere, nanocrystalline silicon forms in the oxide matrix (Hessel et al., 2006). With varying annealing temperature and/or annealing time, the size of the nanocrystals can be controlled. After the nanocrystal formation, HF treatment of the nanocrystal embedded oxide liberates the nanocrystals as a freestanding form due to the etched removal of the oxides, i.e., the formation of the hydrogen-terminated colloidal silicon nanoparticles. The various organic termination can be formed by the subsequent photo- or thermally-induced hydrosilylation between the hydrogen surface of silicon nanoparticles and unsaturated organic species, which can make the colloidal nanoparticles soluble in desired types of solvents (Clark et al., 2010; Yu et al., 2013). The colloidal silicon nanoparticles prepared by this process exhibit usual quantum confinement induced size-dependent PL in the yellow to red region (Hessel et al., 2006). However, by attaching particular organic functional groups on the surface of the nanoparticles, the emission color can be tuned in all visible range (blue to red) without size control of dots, e.g., the diphenylamine functionalized dots shows the yellow emission (Dasog et al., 2014). These PL emission colors were independent on the polarity of the solvent and the excitation wavelength, indicating that the origin of the PL is the recombination at unknown surface states. The recombination lifetimes of such surface-related PL emission are much faster (several nanoseconds) than that of the usual quasi-direct electron-hole recombination due to quantum



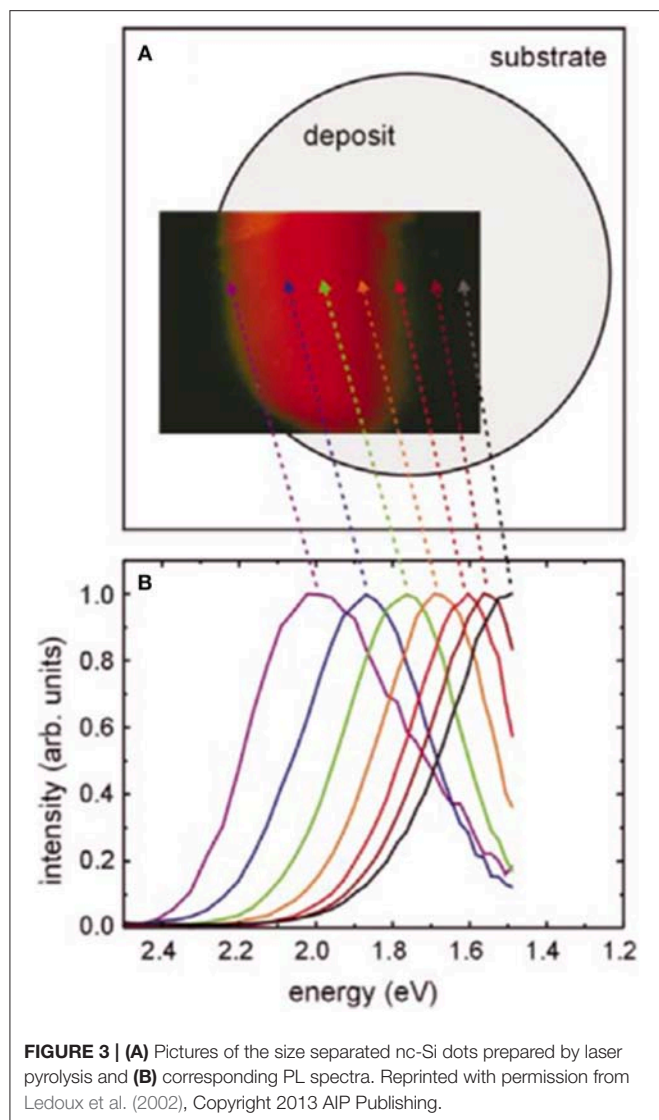
confinement effect. Note that their PL quantum efficiencies are 20–30% (Dasog et al., 2014). By using the silicon nanoparticles prepared by this sol-gel precursor process, solution-based multicolor light emitting diodes having high external quantum efficiencies $\sim 1.1\%$ were demonstrated (Figure 4) (Maier-Flaig et al., 2013) with combining the size separation technique (Mastronardi et al., 2011). Successful demonstration of such diode is thanks to the ease of the preparation handling and mass productivity as discussed below. Moreover, Ghosh et al. reported the improved sol-gel precursor process to form brighter silicon nanoparticles under mild condition, and fabricated white- (Ghosh et al., 2014) and red-emitting diodes (Ghosh et al., 2018). In addition to these sol-gel precursor process, the HF etching process of SiO_x films incorporated in crystalline silicon nanoparticles, which is prepared by radio-frequency sputtering method (Shinoda et al., 2006; Sugimoto et al., 2012) and subsequent thermal annealing, provides the formation of the colloidal nc-Si dot.

Top-Down Fabrication Routes of Silicon Quantum Dot

One of the most simple top-down processes is the mechanical fragmentation of bulk silicon and/or silica by a ball milling technique (Lam et al., 2000; Heintz et al., 2007). In particular, Heintz et al. (2007) demonstrated the formation of blue-emitting quantum dots with alkyl-termination by combining the high energy ball milling of a bulk silicon chunk and a simultaneous chemical reaction with unsaturated organic species. Furthermore, chemically size reducing technique by stain-etching of bulk silicon or silicon rich oxide powders have been reported (Sato and Swihart, 2006; Sato et al., 2009; Goller et al., 2010). Sato et al. demonstrated the PL color tuning (green

to red) of the quantum dots (2–3 nm) by stain-etching of the polycrystalline powder with an average diameter of 50 nm in HF/HNO_3 aqueous solution with ultrasound treatment which allows uniform etching (Sato et al., 2009). Furthermore, Goller et al. reveal that spherical quantum dots (3–10 nm) formed by stain-etching of silicon powder (25 nm), and they show a single exponential PL decay curves (Goller et al., 2010), in contrast to stretched exponential curves for usual silicon nanocrystals including PS (Pavesi and Ceschini, 1993). This is considered to be attributed to a uniform spherical shape of the dots.

Laser ablation of bulk silicon in liquid, such as water (Švrček et al., 2006; Umezū et al., 2007), organic solvent (Shirahata et al., 2010; Abderrafi et al., 2011), and supercritical fluid (Saitow and Yamamura, 2009) is a simple fabrication route for the nc-Si dots. Umezū et al. demonstrated that the irradiation of pulsed laser light (532 nm, 10 mJ/cm²) to a bulk silicon wafer in hexane and water generates blue-emitting oxide-capped colloidal silicon nanoparticles (Umezū et al., 2007). Švrček et al. revealed that the size of the nanoparticles depends on the irradiation laser power in the diameter range from 2 to 10 nm, and higher power laser irradiation causes the fragmentation of the aggregated nanoparticles (Švrček et al., 2016). Shirahata et al. demonstrated the pulsed laser irradiation to a bulk silicon wafer in unsaturated organic solvents such as 1-octene yields organically-capped silicon nanoparticles (Shirahata et al., 2010). The nanoparticle formation mechanism in these laser ablation methods in liquid is as follows: Intense pulsed laser light ablates bulk silicon target, resulting in the formation of the silicon vapors and/or clusters. Then, the ablated silicon vapor condensed into the silicon nanoparticles at the liquid/vapor interface. In particular, using the unsaturated organic solvent, chemical reaction between



the surface of the nanoparticles and unsaturated bonds of the organic solvent causes the efficient surface termination, resulting in a relatively higher PL quantum efficiency ($\sim 10\%$). However, in these pulsed laser ablation methods, the formed silicon nanoparticles have relatively larger size distribution and an exact size control are essentially difficult.

An important top-down process for nc-Si dots is the formation of the PS by electrochemical etching of silicon wafer and subsequent pulverization of the porous layer. As the porous layer consists of the assembly of nc-Si dots, a relatively *mild* pulverization treatment can render the porous layer free-standing nanoparticle form. Several pulverization techniques have been employed, such as ultra-sonification (Heinrich et al., 1992), and mechanical milling (Ryabchikov et al., 2012; Luna López et al., 2014). Heinrich et al. firstly demonstrated that the ultra-sonification of the PS layer in various solvents, such as methanol, toluene, and water, generates the colloidal silicon nanoparticles (Heinrich et al., 1992). However, the obtained



FIGURE 4 | Photographs of the multicolor light emitting diodes utilizing the size-separated silicon nanocrystals prepared by the thermal process of the sol-gel precursor (hydrogen silsesquioxane). Reprinted with permission from Maier-Flaig et al. (2013), Copyright 2013 ACS Publishing.

colloidal nanoparticles have a wide size distribution from several nanometers to hundreds of nanometers. Thus, to purely obtain light emitting nanoparticles (a diameter range from 2 to 10 nm) due to quantum confinement effect, additional size separation procedures are usually needed. For example, the subsequent filtering of the supernatant part of as-prepared colloidal solution was performed (Valenta et al., 2008). Furthermore, the additional chemical etching of the as-prepared colloidal nanoparticles was also employed to obtain colloidal samples having controllable visible PL emission from green to red (Choi et al., 2007; Kang et al., 2009). The surface of the obtained colloidal silicon nanoparticles prepared by this method are oxygen or hydrogen terminations. The silicon nanoparticles formed by the pulverization of the PS usually have the similar PL emission properties as original PS, although they exhibit a blue shift of the PL peak due to being free from matrix stress (Kusová et al., 2012) and the apparent increase in PL quantum yields (Credo et al., 1999). Organically capped nanoparticles can be also obtained by an additional chemical treatment, i.e., the photo-assisted hydrosilylation in organic solvent (Buriak, 2009). Kusová demonstrated the formation of yellow emitting organically capped nc-Si dots prepared by combining the sonification of porous layer and subsequent photo-assisted hydrosilylation treatments (**Figure 5**) (Kusová et al., 2010). Interestingly, these colloidal nanoparticles exhibit the nanosecond PL decay, due to electron-hole direct gap recombination induced by the crystalline strain and resultant modification of the electronic band structure (Kusová et al., 2014). Another simple process to pulverize the PS is boiling of the PS in an organic solvent with unsaturated bonding (Lie et al., 2002; Chao et al., 2007). This treatment leads to the formation of alkyl-capped silicon nanoparticles with a diameters of ~ 2.5 nm, resulting from the bubble formation by hydrosilylation between the unsaturated organic solvent and hydrogen-terminated silicon surface (Phatvej et al., 2018), and resultant pulverization of PS.

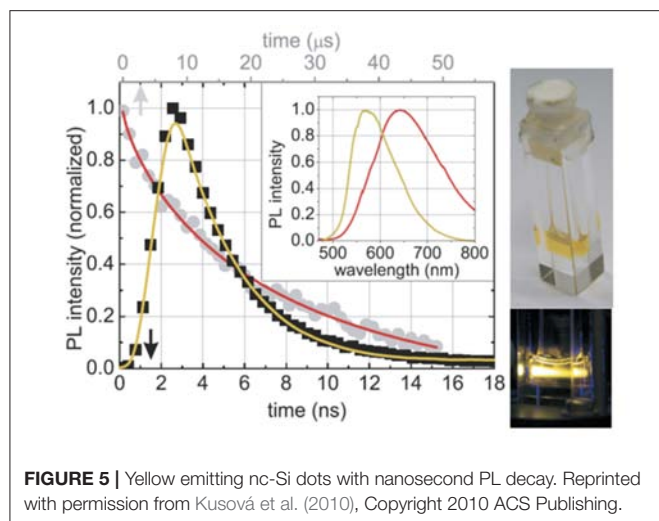


FIGURE 5 | Yellow emitting nc-Si dots with nanosecond PL decay. Reprinted with permission from Kusová et al. (2010), Copyright 2010 ACS Publishing.

Efficient Approaches for the Silicon Quantum Dot Production

There are various criteria to evaluate the productivity for the nc-Si dot fabrication. Askari et al. summarized the figure of merit such as absolute throughput (kg h^{-1}) and throughput density ($\text{kg h}^{-1} \text{m}^{-2}$), of above mentioned various processes (Askari et al., 2015). In this subsection, we summarize recent advances in the view of the production quantity per experimental batch. Zhong et al. produced ~ 10 g of green emitting green-quantum dots from ~ 100 g silicon precursor ($\text{C}_6\text{H}_{17}\text{NO}_3\text{Si}$) by solution-phase chemical process for 30 min (Zhong et al., 2015). Here, we define the production yield as the ratio of the weight of the produced quantum dots to that of original silicon material. The production yield per batch of Zhong's process is $\sim 10\%$. In the high annealing process of sol-gel precursor (~ 2 h per batch), typically 20 mg of the hydrogen terminated nc-Si dots were produced from 200 mg of HSQ silicon precursor, corresponding to the production yield of $\sim 10\%$ (Islam et al., 2017). Bose et al. demonstrated that the quantum dots can be prepared from the reduction of rice husk by rapid microwave heating (Bose et al., 2018). The production yield of this process is $\sim 5\%$, i.e., 0.1 g of nanoparticles from 2 g of rice husk per batch. Note that the plasma synthesis from silane precursor provides ~ 20 mg quantum dots per batch (~ 45 min) with almost 100% of production yield, representing the complete conversion from the silane precursor (Mangolini et al., 2005). We summarize the production yields for these processes in **Table 1**.

Very recently, Nakamura et al. demonstrated that the pulsed laser irradiation of the PS powder in organic solution efficiently generates the nc-Si dots and the formed quantum dots exhibited the multicolor PL emission in blue (Nakamura et al., 2014), white (Yuan et al., 2017a), and red (Nakamura et al., 2016; Yuan et al., 2017b) regions. The PL quantum efficiencies are much higher (~ 10 – 30%) than the original PS ($\sim 1\%$) (Nakamura et al., 2016). The prepared quantity of the quantum dots is more than ten times larger than the usual pulsed laser ablation method using the bulk silicon target (Nakamura et al., 2014). The

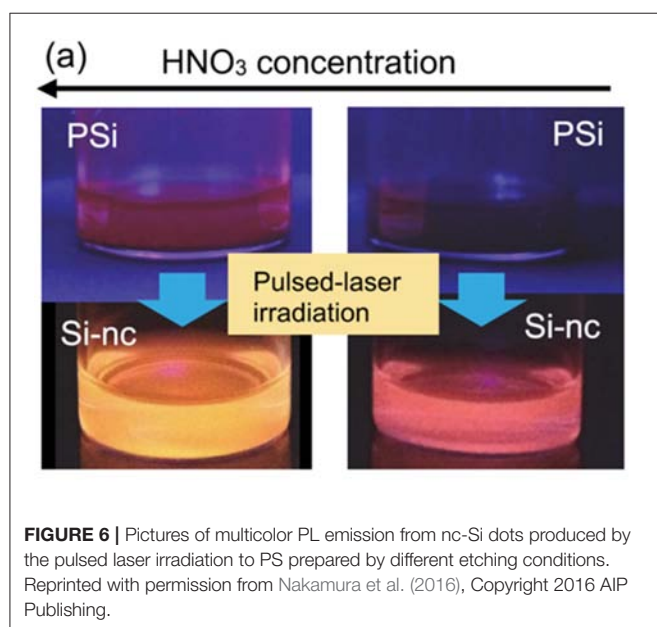
formation mechanisms depend on laser irradiation conditions, i.e., the ablation of porous layer and subsequent condensation into nanoparticles, or the pulverization of the porous layer resulting from the laser induced thermal stress. In the case of the pulverization induced formation of the dots, the PL emission color was able to be controlled via etching condition of the target PS (**Figure 6**) (Nakamura et al., 2016), i.e., the changes in the size of nanocrystalline porous network core. As described in the above subsection, such PL emission color control was usually difficult in the usual laser ablation process using bulk silicon target. This efficient fabrication of the nc-Si dots is attributed to unique thermal properties of PS. The PS has a much smaller thermal conductivity (in the range of 0.5–1.0 W/mK), which is comparative to insulators such as quartz glass and rubber (Lysenko et al., 1999; Valalaki and Nassiopoulou, 2013, 2014, 2017; Koshida, 2017b). In addition to the conductivity, heat capacities are also very low (0.2–0.6 MJ/m³K) in contrast to the insulators (Koshida, 2017b). These unique thermal properties of PS cause a local heating inside the porous layer when the pulse laser irradiated to it, and the efficient ablation or fragmentation occurs. By improved pulsed laser irradiation process for 10 mg of PS, ~ 8.5 mg of red emitting nc-Si dots has been produced (Nakamura et al., 2018). This production amount of the quantum dot per batch is much larger than the boiling process of PS, i.e., several hundred micro grams of dots from 1 cm² of silicon chip wafer (Dickinson et al., 2008; Alsharif et al., 2009). Moreover, the production yield of this process ($\sim 85\%$) is larger than the above mentioned chemical synthesis and high temperature annealing process of sol-gel precursor (Islam et al., 2017) (see **Table 1**). Thus, the demonstrated laser induced heating process of PS provides an energy- and cost-effective route for production of nc-Si dots.

Quasiballistic Electron Emission Emission Mechanism and Characteristics

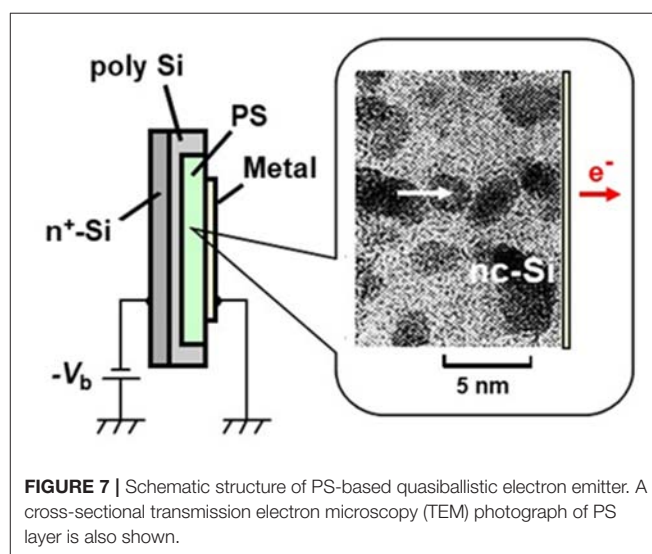
The device is composed of a thin film surface electrode, a PS layer ($\sim 1 \mu\text{m}$ thick), a silicon wafer substrate, and a back contact (**Figure 7**). As observed by transmission electron micrograph (TEM) shown in this figure, the PS layer prepared by galvanostatic anodization and additional oxidation includes nc-Si dots (~ 3 nm in mean diameter) interconnected with tunnel oxides. In this PS layer, there is a multiple-tunneling transport mode through nc-Si dot chain, and quasiballistic hot electrons are efficiently generated (Mori et al., 2011). Under the condition that a positive voltage is applied to the surface electrode with respect to the substrate, electrons are accelerated in the PS layer toward the outer surface, and then some of them are emitted through the surface electrode. The emission starts at an onset voltage corresponding to the work function potential of the surface electrode. The applied voltage dependence of the emission current follows the Fowler-Nordheim tunneling scheme. The emission efficiency η , defined as the ratio of the emission current density to the diode current density, depends on the nanostructure arrangement of nc-Si dots, quality of interfacial tunneling oxide, and the surface electrode material.

TABLE 1 | Typical production yields of nc-Si dot per batch in various processes.

	Bottom-up process			Top-down process	
	Sol-gel precursor thermal process (Islam et al., 2017)	Chemical synthesis (Zhong et al., 2015)	Plasma synthesis (Mangolini et al., 2005)	Reduction by microwave thermal process (Bose et al., 2018)	Improved pulsed laser irradiation (Nakamura et al., 2018)
Si precursor	HSQ	$C_6H_{17}NO_3Si$	Silane	Rice husk	PS
Nanocrystal formation process	High temperature annealing	Chemical reduction growth	Plasma decomposition	Thermal reduction	Chemical etching
Liberation process	Chemical etching	None	None	Milling and sedimentation	Pulsed laser irradiation
Amount of precursor [mg]	200	10^4	200	2000	10
Amount of quantum dots [mg]	20	10^3	200	100	8.5
Production yield [%]	10	10	100	5	85



When a monolayer graphene is used as a surface electrode, the typical η value is drastically enhanced to 6.3% at an applied voltage of 10 V (Kojima et al., 2018a) due to a high transparency of monolayer graphene for quasiballistic electrons. At that applied voltage, the mean energy of output electrons becomes higher than 2 eV. The corresponding electron temperature is far from the thermal equilibrium. The mean energy of emitted electrons can be tuned well by the applied voltage while keeping narrow energy dispersion. Both the output electron energy distribution and the emission angle dispersion become significantly narrow even at room temperature. The energy distribution becomes more monochromatic at a low temperature of around 150 K. The measured emission angle dispersion is just $\pm 8^\circ$ with respect to the surface normal (Kojima et al., 2018b). The relatively low operation voltages and the compatibility with silicon planar processing make it possible to drive the emitter array under an active-matrix mode.



Applications of Quasiballistic Electron Source

(i) Availability for varied media

Being the energetic, directional, planar, and uniform emission, the quasiballistic emission from PS is insensitive to vacuum pressure, in contrast to the conventional cold cathodes such as field emitters and metal-insulator-metal ones. Far from it, the PS emitter operates in gases and even in solutions. The application studies have been carried out in vacuum (flat panel display, multibeam parallel lithography, high-sensitivity image sensor), in atmospheric pressure gases (negative ion generation, non-discharge VUV emission), and in solutions (H_2 gas evolution, pH control, thin film deposition) (Koshida, 2017a). As specific approaches, two topics on the development that demonstrates the characteristic feature of the PS emitter are presented here.

(ii) Multibeam parallel lithography

In advanced silicon device technology, a high resolution (below 10 nm), high throughput, and cost-effective nanofabrication process is strongly required. Though electron beam (EB)

TABLE 2 | Developing studies of multibeam parallel EB lithography.

Group	EB Source	Mode	Demagnification	Beam	Voltage (kV)	Use	Reference
IMS ^a	Thermionic	Aperture blanking	1/200	512 × 512	50	Photo-mask writer	Klein et al., 2012; Platzgummer et al., 2013; Klein and Platzgummer, 2016
NuFlare ^b			1/200	512 × 512	50		Matsumoto et al., 2016
MAPPER ^c			1/1	13,260	5	Direct-write	Rio et al., 2010; Brandt et al., 2015
TU ^d and TUAT ^e	nc-Si ballistic emitter	Active-matrix drive	1/1000	100 × 100	5		Esashi et al., 2015

^aIMS Nanofabrication AG, Austria; ^bNuFlare Technology, Japan; ^cMAPPER Lithography, The Netherlands ^dTohoku Univ., Japan; ^eTokyo Univ. of Agri. and Tech., Japan.

is a very attractive exposure source from a viewpoint of the resolution, the conventional focused EB writer has a seriously limited throughput. If a practical multibeam exposure scheme could be possible, the usefulness of mask-less EB direct-write should be dramatically enhanced. Its major possible applications are photomask fabrication and mask-less direct-write exposure. Specifications of multibeam parallel lithography systems under development are summarized in **Table 2**.

In the conventional systems, thermionic emitter or thermally assisted field emitter is used as an electron source. Since the employment of active-matrix drive is difficult in that case, broadened electron beam is spatially switched by aperture blanking method for generating multibeam (Rio et al., 2010; Klein et al., 2012; Platzgummer et al., 2013; Brandt et al., 2015; Klein and Platzgummer, 2016; Matsumoto et al., 2016). In contrast, the PS approach is characterized by active-matrix drive of arrayed emitters (Esashi et al., 2015). The PS emitter array can be fabricated on a Si-wafer substrate by planar processes. The back contact of each electron emitter with an active area of $10 \times 10 \mu\text{m}^2$ is interconnected to an active matrix driving circuit using a through-silicon-via (TSV) technique (**Figure 8A**). A CMOS-based LSI circuit has been developed for the multibeam (100×100) parallel lithography.

The compatibility of the implemented LSI with the active-matrix operation was confirmed, including the basic function for the electron emitter process variation compensation and the test of integrated devices. The evaluation was performed with the 1:1 exposure test system, in which an EB-resist coated target wafer was placed at about 3 mm distance from the emitter surface (**Figure 8B**) and the exposed resist pattern is shown in **Figure 8C**. It has been demonstrated that the integrated nc-Si emitter array is compatible with the active-matrix drive for multi-beam massive parallel exposure, and that the selected emitter pattern is delineated corresponding to the activated emitters. In accordance with the results of beam optics simulation in the prototype system, the miniaturized electron optics is suitable for 10 nm order EB writing. For the practical use with a throughput comparable to extreme ultraviolet (EUV) lithography, criteria of the electron beam number and the resolution target to be pursued are 10^6 beams and 5 nm, respectively.

(iii) Reductive deposition of thin films

From a chemical viewpoint, the PS emitter can be regarded as a supplier of electrons with highly reducing activity. Its direct application is liquid-phase thin film deposition of metals and semiconductors under an electron incident mode (Suda et al., 2016). The deposition process is illustrated in **Figure 9**. Output of quasiballistic electrons of the nc-Si emitter impinges onto the target substrate on which an extremely small amount of salt solutions such as CuCl_2 , SiCl_4 , and GeCl_4 was coated in advance with a thickness of 100 nm. The spacing between the emitter and substrate was controlled in the range from 500 nm to $100 \mu\text{m}$ by a piezoelectric actuator, taking the relation between the electron mean free path and the vacuum pressure of used solution into account. The experiments were done in a N_2 -gas filled glove box.

After the emitter operation for a few minutes, residual solutions were removed, and then thin Cu, Si, and Ge films are formed on the incident area as shown in **Figure 10**. According to the structure and compositional characterizations of deposited thin films, every film consists of nanoclusters. No contaminations were detected by X-ray photoelectron spectroscopy (XPS). Obviously thin films are deposited with no byproducts. Thin films can be deposited at room temperature on varied substrates including insulating layers (i.e., oxidized c-Si wafer) and flexible polymers. In addition, a mixture solution such as $\text{SiCl}_4 + \text{GeCl}_4$ is available for deposition of thin SiGe films with a controllable composition.

Incident electrons with energy of 10 eV can penetrate 10 nm deep in solutions (Emfietzoglou et al., 2009), and reduce positive ions therein followed by the formation of nanoclusters and deposition. Thermodynamic investigation supports that the incident electron energy meets the requirement for preferential nucleation of atoms rather than their out-diffusion (Suda et al., 2017). The theoretical analysis based on the reaction diffusion equation suggests that the deposition rate depends mainly on the incident electron current density J_e , and that it reaches a stationary value within 0.1 s after electron incidence (Suda et al., 2018). At the typical condition of $J_e = 10\text{--}100 \mu\text{A}/\text{cm}^2$, the estimated stationary deposition rate of Cu, Si, and Ge films are around 0.2–2.0 nm/min. This is consistent with the experimental results.

Typical thin film deposition techniques are summarized in **Table 3**. The most widely used dry processes (chemical and

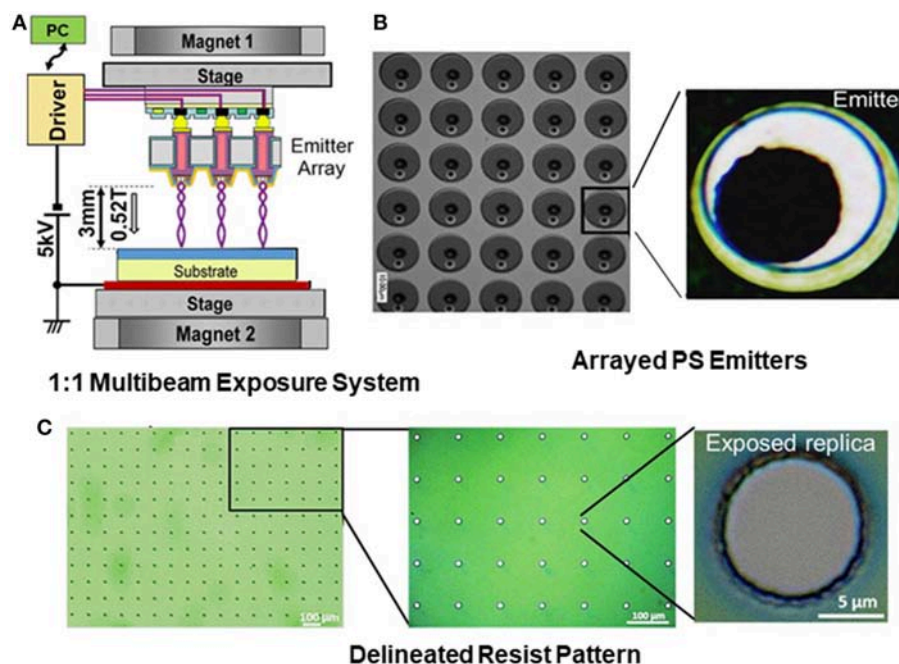


FIGURE 8 | (A) Schematic configuration of 1:1 electron multibeam exposure system using arrayed nanocrystalline PS emitters. (B) SEM photographs of emitter array. The emission area is 12 μm in diameter in this case. (C) Delineated resist patterns.

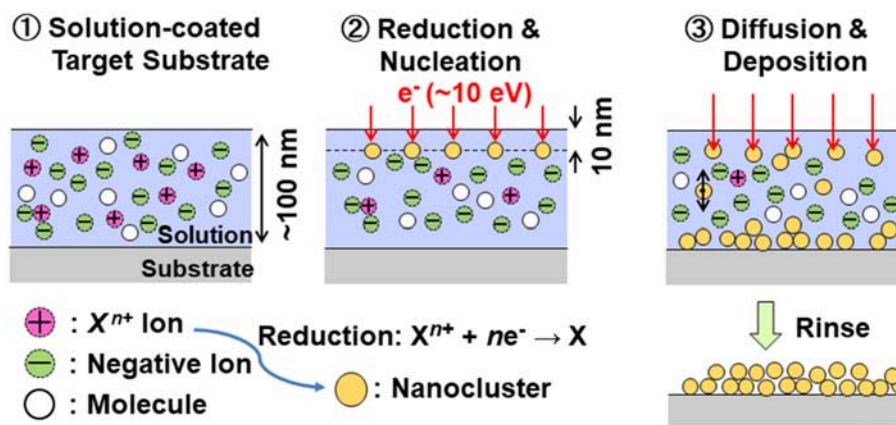


FIGURE 9 | Process of liquid-phase reductive thin-film deposition promoted by direct incidence of quasiballistic electrons emitted from nanocrystalline PS cold cathode.

physical vapor deposition) are established by precise control of temperature, vacuum pressure, and gas flow rate (Seshan, 2012). The wet electroplating, based on exchange of thermalized electrons at the working and counter electrodes, proceeds at room temperature with gas evolutions. It is mainly used to deposit thin metal films (Schlesinger and Paunovic, 2010). Electron-beam-induced deposition (EBID), on the other hand, has been studied to form cluster, metal nanowires, thin films, and nanostructures (Kiyohara et al., 2002; Adelung et al., 2004; Gazzadi and Frabboni, 2005; van Dorp et al., 2005; Randolph et al., 2006; Frabboni et al., 2008; Furuya, 2008; van Dorp and Hagen, 2008; Botman et al., 2009; de Boer et al., 2011; Vollnhals

et al., 2013; den Heijer et al., 2014; Leenheer et al., 2015). The focused electron beam with high-energies of 10–50 keV in the conventional scanning or transmission electron microscope is transmitted through membranes and then hits the absorbed gases or ionic liquids on the substrate leading to decomposition of molecules. The key issue is to reduce carbon and other contaminations in deposited thin films. The ballistic electron incidence mode mentioned above is based on the mechanism different from EBID. Unilateral reduction proceeds with neither gas evolution nor by-product generation. In addition, the deposition of thin metal and group IV semiconductor films is available for varied substrates.

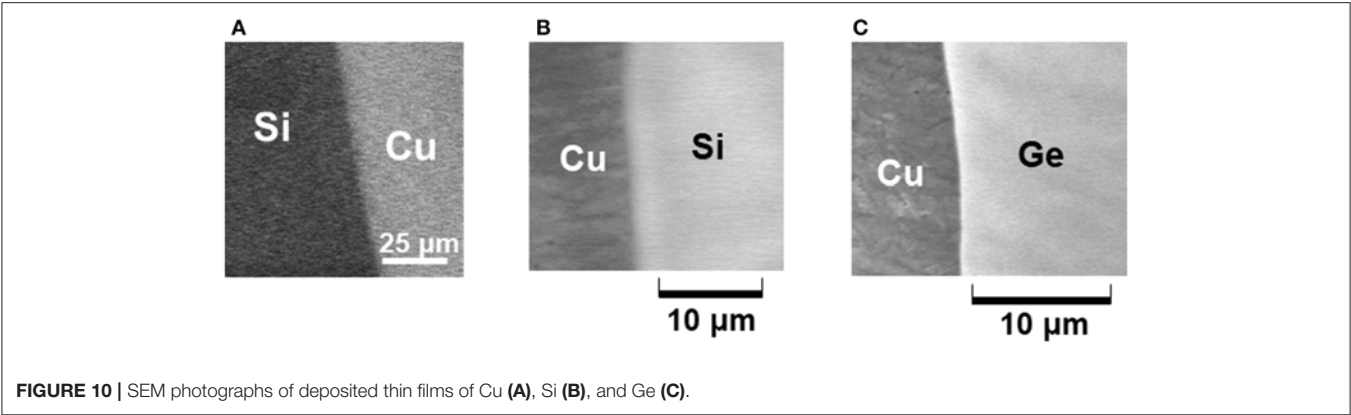


TABLE 3 | Comparative survey of thin film deposition processes.

Aspects	process	Dry process (CVD ^a and PVD ^b)	Electroplating	Electron Irradiation	
				EBID ^c (10~50 keV)	Ballistic incidence (~10 eV)
Phase		Vapor or vacuum	Liquid	Liquid or vapor	Liquid
Mode		Decomposition, sputtering, or evaporation	Redox reaction	Decomposition	Reduction
Temperature		High		Room temperature	
Contamination		< ppb	Gas evolution	C, O	<300 ppm

^aChemical Vapor Deposition, ^bPhysical Vapor Deposition, ^cElectron Beam Induced Deposition.

Thermo-Acoustic Emission and Applications

The PS acoustic devices are composed of a thin-film surface heater electrode, a PS layer, and a c-Si wafer. Due to a strong phonon confinement and interfacial scattering in PS, the thermal conductivity of PS layers, α , is drastically lowered in comparison to that of bulk silicon (Lysenko et al., 1999; Valalaki and Nassiopoulou, 2013, 2014, 2017; Koshida, 2017b). At the same time, its volumetric heat capacity C is also significantly decreased. In the case of high-porosity PS, particularly, both α and C values become close to the lower limit of solid state materials. Thus, the thermal diffusivity $\sqrt{\alpha C}$ is extremely decreased. When a temperature fluctuation is produced by electrical input to the heater electrode, a significant acoustic wave is generated near the surface, because the thermos-acoustic transfer effect is inversely proportional to $\sqrt{\alpha C}$ (Shinoda et al., 1999). A significant sound pressure amplitude is produced without any mechanical vibrations.

Due to the sound emission from still surface, the frequency response covering a fully wide range is free from the mechanical resonance. The theoretical limit of frequency response is 1 GHz. No resonant peaks are observed in the whole range of available frequency. The broad-band flat emissivity of the PS device is useful for reproducing complicated ultrasonic communication calls and male-female interactions between mice (Kihara et al., 2006; Uematsu et al., 2007). Conventional ultrasound emitters cannot be utilized for this application because of a resonant frequency response and a bulky size larger than mice. As previously demonstrated, mouse mothers were attracted by pup

ultrasonic vocalizations (USVs) reproduced by an nc-Si emitter, while they did not respond to other synthesized sounds. It was also found that the response to pup USVs was enhanced by social experiences (Okabe et al., 2013). Recent study on mutual recognition between mother and infant suggests that pup USVs looks to have an individual signature used in pup differentiation by mouse mothers, similar to acoustic communication between human mothers and their infants (Asaba et al., 2015; Mogi et al., 2017).

Regarding thin metal film heaters and underlying thermal insulators, many studies have been conducted by using varied combinations: suspended Al wires-air (Niskanen et al., 2009), Si nanowires-polymer or -glass (Tian et al., 2011a), indium-tin-oxide film-glass (Daschewski et al., 2015), Si nanoparticles-sapphire (Odagawa et al., 2010), conducting polymers-glass (Tian et al., 2011b), thin Au film-porous polymer (Chitnis et al., 2012), thin Ag-Pd film-glass-Al₂O₃ (Nishioka et al., 2015), carbon nanotube (CNT)-air (Xiao et al., 2011), or -grooved Si (Wei et al., 2013), graphene-polymer (Suk et al., 2012; Tian et al., 2014; Kim et al., 2016; Tao et al., 2016; Sbrockey et al., 2018), -porous Al₂O₃ (Tian et al., 2012), or -glass (Fei et al., 2015), CNT-laser-scribed graphene-polymer (Yeklangi et al., 2018), and W-Al₂O₃-polymer (Brown et al., 2016). The basic characteristics of these devices are consistent with the theoretical analyses of the thermo-acoustic effect and its key factors (Hu et al., 2010, 2012a,b, 2014; Vesterinen et al., 2010; Daschewski et al., 2013; Lim et al., 2013; Yang and Liu, 2013; Wang et al., 2015; Tong et al., 2017; Xing et al., 2017). Making use of the non-resonant and broad-band emissivity with no harmonic distortions, possible

applications have been pursued to audible compact speaker under a full digital drive, probing source for 3-dimensional object sensing in air, acoustic pressure generator for noncontact actuation, directivity control under phased array configuration, loud speaker, noise cancellation, thermoacoustic tomography, and thermoacoustic sound projector (Koshida, 2017c; Aliev et al., 2018; Bobinger et al., 2018; Julius et al., 2018; Liu et al., 2018; Song et al., 2018).

SUMMARY

Including photonic visible luminescence, emerging functions of nanostructured PS has extended to electronics, biometrics, biomedicine, acoustics, thermology, and energetics. In the quantum-size silicon, especially, the emissive properties of photons, electrons, and sound are activated. From a technological viewpoint, cost- and power-effective production of luminescent nc-Si powder or colloid is desired for wide applications. As one practical approach, high-yield fabrication of strongly luminescent colloidal nc-Si dots has been developed by employing *in-situ* self-regulated process for pulverization of anodized PS by pulsed laser irradiation. A multiplier tunneling transport through nc-Si dots, on the other hand, induces quasiballistic electron emission. The potential of nc-Si cold

cathode has been made clear by using monolayer graphene as a surface electrode. This makes the foundation more solid for applications to massively parallel EB lithography under an active-matrix drive and to reductive thin film deposition of metals and semiconductors. Based on specific thermal properties of PS, on the other hand, thermos-acoustic device has been developed. Observed broad-band non-resonant sound emission from a compact PS device provides standard ultrasound source for researches in the bio-acoustic communications. These studies meet in the direction and requirements for diversification of silicon technology.

AUTHOR CONTRIBUTIONS

NK: overview, ballistic electron emission, thermo-acoustic device. TN: visible luminescent Si quantum dots.

ACKNOWLEDGMENTS

The author NK would like to thank Prof. M. Esashi, Prof. K. Kikuchi, Dr. A. Kojima, and Dr. R. Suda for their support and cooperation. This work was partially supported by the Formation of Innovation Centers for Fusion of Advanced Technologies programs setup by MEXT, Japan.

REFERENCES

- Abderrafi, K., Calzada, R. G., Gongalsky, M. B., Suárez, I., Abarques, R., Chirvony, V. S., et al. (2011). Silicon nanocrystals produced by nanosecond laser ablation in an organic liquid. *J. Phys. Chem. C* 115, 5147–5151. doi: 10.1021/jp109400v
- Adelung, R., Ernst, F., Zheng, N., and Landau, U. (2004). In situ nanoscale observation and control of electron-beam-induced cluster formation. *J. Vac. Sci. Technol. B* 22, 1797–1802. doi: 10.1116/1.1767830
- Aliev, A. E., Codoluto, D., Baughman, R. H., Ovalle-Robles, R., Inoue, K., Romanov, S. A., et al. (2018). Thermoacoustic sound projector: exceeding the fundamental efficiency of carbon nanotubes. *Nanotech* 29:325704. doi: 10.1088/1361-6528/aac509
- Alsharif, N. H., Berger, C. E., Varanasi, S. S., Chao, Y., Horrocks, B. R., and Datta, H. K. (2009). Alkyl-capped silicon nanocrystals lack cytotoxicity and have enhanced intracellular accumulation in malignant cells via cholesterol-dependent endocytosis. *Small* 5, 221–228. doi: 10.1002/sml.200800903
- Anthony, R., and Kortshagen, U. (2009). Photoluminescence quantum yields of amorphous and crystalline silicon nanoparticles. *Phys. Rev. B* 80:115407. doi: 10.1103/PhysRevB.80.115407
- Asaba, A., Okabe, S., and Nagasawa, M. (2015). Determining ultrasonic vocalization preferences in mice using a two-choice playback test. *J. Vis. Exp.* 103:e53074/1–8. doi: 10.3791/53074
- Askari, S., Macias-Montero, M., Velusamy, T., Maguire, P., Svrcek, V., and Mariotti, D. (2015). Silicon-based quantum dots: synthesis, surface and composition tuning with atmospheric pressure plasmas. *J. Phys. D: Appl. Phys.* 48:314002. doi: 10.1088/0022-3727/48/31/314002
- Bobinger, M., La Torraca, P., Mock, J., Becherer, M., Cattani, L., Angeli, D., et al. (2018). Solution-processing of copper nanowires for transparent heaters and thermo-acoustic loudspeakers. *IEEE Trans. Nanotech.* 17, 940–947. doi: 10.1109/TNANO.2018.2829547
- Bose, S., Ganayee, M. A., Mondal, B., Baidya, A., Chennu, S., Mohanty, J. S., et al. (2018). Synthesis of silicon nanoparticles from rice husk and their use as sustainable fluorophores for white light emission. *ACS Sust. Chem. Eng.* 6, 6203–6210. doi: 10.1021/acssuschemeng.7b04911
- Botman, A., Hagen, C. W., Li, J., Thiel, B. L., Dunn, K. A., Mulders, J. J. L., et al. (2009). Electron postgrowth irradiation of platinum-containing nanostructures grown by electron-beam-induced deposition from Pt(PF₃)₄. *J. Vac. Sci. Technol. B* 27:2759. doi: 10.1116/1.3253551
- Brandt, P., Tranquillin, C., Wieland, M., Bayle, S., Milléquant, M., and Renault, G. (2015). Alternative stitching method for massively parallel e-beam lithography. *Proc SPIE* 9423:942312. doi: 10.1117/1.JMM.14.3.031203
- Brown, J. J., Moore, N. C., Supekar, O. D., Gertsch, J. C., and Bright, V. M. (2016). Ultrathin thermoacoustic nanobridge loudspeakers from ALD on polyimide. *Nanotechnol.* 27:475504. doi: 10.1088/0957-4484/27/47/475504
- Buriak, J. M. (2009). Organometallic chemistry on silicon and germanium surfaces. *Chem. Rev.* 102, 1271–1308. doi: 10.1021/cr000064s
- Canham, L. (1990). Silicon quantum wire array fabrication by electrochemical and chemical dissolution of wafers. *Appl. Phys. Lett.* 57:1046. doi: 10.1063/1.103561
- Canham, L. (1995). Bioactive silicon structure fabrication through nanoetching techniques. *Adv. Mater.* 7, 1033–1037. doi: 10.1002/adma.19950071215
- Canham, L. (2017). *Handbook of Porous Silicon*. 2nd Ed. New York, NY: Springer. 1017.
- Chao, Y., Siller, L., Krishnamurthy, S., Coxon, P. R., Bangert, U., Gass, M., et al. (2007). Evaporation and deposition of alkyl-capped silicon nanocrystals in ultrahigh vacuum. *Nat. Nano.* 2, 486–489. doi: 10.1038/nnano.2007.224
- Cheng, X., Hinde, E., Owen, D. M., Lowe, S. B., Reece, P. J., Gaus, K., et al. (2015). Enhancing quantum dots for bioimaging using advanced surface chemistry and advanced optical microscopy: application to silicon quantum dots (SiQDs). *Adv. Matter.* 27, 6144–6150. doi: 10.1002/adma.201503223
- Cheng, X., Lowe, S. B., Reece, P. J., and Gooding, J. J. (2014). Colloidal silicon quantum dots: from preparation to the modification of self-assembled monolayers (SAMs) for bio-applications. *Chem. Soc. Rev.* 43, 2680–2700. doi: 10.1039/C3CS60353A
- Chitnis, G., Kim, A., Song, S. H., Jessop, A. M., Bolton, J. S., and Ziaie, B. (2012). A thermophone on porous polymeric substrate. *Appl. Phys. Lett.* 101:021911. doi: 10.1063/1.4737005
- Choi, J., Wang, N. S., and Reipa, V. (2007). Photoassisted tuning of silicon nanocrystal photoluminescence. *Langmuir* 23, 3388–3394. doi: 10.1021/la062906+

- Choi, M. K., Yang, J., Hyeon, T., and Kim, D.-H. (2018). Flexible quantum dot light-emitting diodes for next-generation displays. *NPJ Flex. Electron.* 2:10. doi: 10.1038/s41528-018-0023-3.
- Clark, R. J., Dang, M. K., and Veinot, J. G. (2010). Exploration of organic acid chain length on water-soluble silicon quantum dot surfaces. *Langmuir* 26, 15657–15664. doi: 10.1021/la102983c
- Coffinier, Y., and Boukherroub, R. (2016). "Surface chemistry of porous silicon," in *Porous Silicon: From Formation to Application, Vol. 1*, eds. G. Korotcenkov (Boca Raton, FL: Taylor and Francis Group, CRC Press), 357–390.
- Credo, G. M., Mason, M. D., and Buratto, S. K. (1999). External quantum efficiency of single porous silicon nanoparticles. *Appl. Phys. Lett.* 74, 1978–1980. doi: 10.1063/1.123719
- Daschewski, M., Boehm, R., Prager, J., Kreutzbruck, M., and Harrer, A. (2013). Physics of thermo-acoustic sound generation. *J. Appl. Phys.* 114:114903. doi: 10.1063/1.4821121
- Daschewski, M., Kreutzbruck, M., and Prager, J. (2015). Influence of thermodynamic properties of a thermo-acoustic emitter on the efficiency of thermal airborne ultrasound generation. *Ultrasonics* 6, 16–22. doi: 10.1016/j.ultras.2015.06.008
- Dasog, M., De los Reyes, G. B., Titova, L. V., Hegmann, F. A., and Veinot, J. G. (2014). Size vs surface: tuning the photoluminescence of freestanding silicon nanocrystals across the visible spectrum via surface groups. *ACS Nano* 8, 9636–9648. doi: 10.1021/nn504109a
- de Boer, S. K., van Dorp, W. F., and De Hosson, J. T. M. (2011). Charging effects during focused electron beam induced deposition of silicon oxide. *J. Vac. Sci. Technol. B* 29:06FD01. doi: 10.1116/1.3659713
- Debenedetti, W. J. I., Chiu, C., Sheng-Kuei, C., Radlinger, C. M., Ellison, R. J., Manhat, B. A., et al. (2015). Conversion from red to blue photoluminescence in alcohol Dispersions of alkyl-capped silicon nanoparticles: insight into the origins of visible photoluminescence in colloidal nanocrystalline silicon. *J. Phys. Chem. C* 119, 9595–9608. doi: 10.1021/acs.jpcc.5b01137
- den Heijer, M., Shao, I., Radisic, A., Reuter, M. C., and Ross, F. M. (2014). Patterned electrochemical deposition of copper using an electron beam. *Appl. Phys. Lett.* Mater. 2:022101. doi: 10.1063/1.4863596
- Dickinson, F. M., Alsop, T. A., Al-Sharif, N., Berger, C. E., Datta, H. K., Siller, L., et al. (2008). Dispersions of alkyl-capped silicon nanocrystals in aqueous media: photoluminescence and ageing. *Analyst* 133, 1573–1580. doi: 10.1039/b801921e
- Dohnalová, K., Fucíková, A., Umesh, C. P., Humpolicková, J., Paulusse, J. M., Valenta, J., et al. (2012). Microscopic origin of the fast blue-green luminescence of chemically synthesized non-oxidized silicon quantum dots. *Small* 8, 3185–3191. doi: 10.1002/sml.201200477
- Dohnalová, K., Gregorkiewicz, T., and Kusová, K. (2014). Silicon quantum dots: surface matters. *J. Phys. Condens. Matter* 26:173201. doi: 10.1088/0953-8984/26/17/173201
- Dohnalová, K., Poddubny, A. N., Prokofiev, A. A., D. A. M., de Boer, W., Umesh, C. P., et al. (2013). Surface brightens up Si quantum dots: direct bandgap-like size-tunable emission. *Light Sci. Appl.* 2:e47. doi: 10.1038/lsa.2013.3
- Ehbrecht, M., and Huiskens, F. (1999). Gas-phase characterization of silicon nanoclusters produced by laser pyrolysis of silane. *Phys. Rev. B* 39, 2975–2985. doi: 10.1103/PhysRevB.39.2975
- Ehbrecht, M., Kohn, B., and Huiskens, F., Laguna, M. A., and Paillard, V. (1997). Photoluminescence and resonant Raman spectra of silicon films produced by size-selected cluster beam deposition. *Phys. Rev. B* 56, 6958–6964. doi: 10.1103/PhysRevB.56.6958
- Emfietzoglou, D., Kyriakou, I., Abril, I., Garcia-Molina, R., Petsalakis, I. D., Nikjoo, H., et al. (2009). Electron inelastic mean free paths in biological matter based on dielectric theory and local-field corrections. *Nucl. Inst. Methods Phys. Res. B* 267, 45–52. doi: 10.1016/j.nimb.2008.11.008
- English, D. S., Pell, L. E., Yu, Z., Barbara, P. F., and Korgel, B. A. (2002). Size tunable visible luminescence from individual organic monolayer stabilized silicon nanocrystal quantum dots. *Nano Lett.* 2, 681–685. doi: 10.1021/nl025538c
- Esashi, M., Kojima, A., Ikegami, N., Miyaguchi, H., and Koshida, N. (2015). Development of massively parallel electron beam direct write lithography using active-matrix nanocrystalline-silicon electron emitter arrays. *Microsyst. Nanoeng.* 1:15029. doi: 10.1038/micronano.2015.29
- Fei, W., Zhou, J., and Guo, W. (2015). Low-voltage driven graphene foam thermoacoustic speaker. *Small* 11, 2252–2256. doi: 10.1002/sml.201402982
- Frabboni, S., Gazzadi, G. C., Felisari, L., and Spessot, A. (2008). Fabrication by electron beam induced deposition and transmission electron microscopic characterization of sub-10-nm freestanding Pt nanowires. *Appl. Phys. Lett.* 88:213116. doi: 10.1063/1.2206996
- Furuya, K. (2008). Nanofabrication by advanced electron microscopy using intense and focused beam. *Sci. Technol. Adv. Mater.* 9:014110. doi: 10.1088/1468-6996/9/1/014110
- Gazzadi, G. C., and Frabboni, S. (2005). Fabrication of 5 nm gap pillar electrodes by electron-beam Pt deposition. *J. Vac. Sci. Technol. B* 23:L1. doi: 10.1116/1.1872015
- Ghosh, B., Hamaoka, T., Nemoto, Y., Takeguchi, M., and Shirahata, N. (2018). Impact of anchoring monolayers on the enhancement of radiative recombination in light-emitting diodes based on silicon nanocrystals. *J. Phys. Chem. C* 122, 6422–6430. doi: 10.1021/acs.jpcc.7b12812
- Ghosh, B., Masuda, Y., Wakayama, Y., Imanaka, Y., Inoue, J., Hashi, K., et al. (2014). Hybrid white light emitting diode based on silicon nanocrystals. *Adv. Func. Mater.* 24, 7151–7160. doi: 10.1002/adfm.201401795
- Goller, B., Polisski, S., Wiggers, H., and Kovalev, D. (2010). Freestanding spherical silicon nanocrystals: a model system for studying confined excitons. *Appl. Phys. Lett.* 97:041110. doi: 10.1063/1.3470103
- Gupta, A., Swihart, M. T., and Wiggers, H. (2009). Luminescent colloidal dispersion of silicon quantum dots from microwave plasma synthesis: exploring the photoluminescence behavior across the visible spectrum. *Adv. Func. Mater.* 19, 696–703. doi: 10.1002/adfm.200801548
- Heath, J. R. (1992). A liquid-solution-phase synthesis of crystalline silicon. *Science* 258:1131. doi: 10.1126/science.258.5085.1131
- Heinrich, J. L., Curtis, C. L., Credo, G. M., Sailor, M. J., and Kavanagh, K. L. (1992). Luminescent colloidal silicon suspensions from porous silicon. *Science* 255, 66–68. doi: 10.1126/science.255.5040.66
- Heintz, A. S., Fink, M. J., and Mitchell, B. S. (2007). Mechanochemical synthesis of blue luminescent alkyl/alkenyl-passivated silicon nanoparticles. *Adv. Mater.* 19, 3984–3988. doi: 10.1002/adma.200602752
- Henderson, E. J., Kelly, J. A., and Veinot, J. G. C. (2009). Influence of HSiO_{1.5} Sol-gel polymer structure and composition on the size and luminescent properties of silicon nanocrystals. *Chem. Mater.* 21, 5426–5434. doi: 10.1021/cm902028q
- Hessel, C. M., Henderson, E. J., Kelly, J. A., Cavell, R. G., Sham, T.-K., and Veinot, J. G. C. (2008). Origin of luminescence from silicon nanocrystals: a near edge X-ray absorption fine structure (NEXAFS) and X-ray excited optical luminescence (XEOL) study of oxide-embedded and free-standing systems. *J. Phys. Chem. C* 112, 14247–14254. doi: 10.1021/jp802095j
- Hessel, C. M., Henderson, E. J., and Veinot, J. G. C. (2006). Hydrogen silsesquioxane: a molecular precursor for nanocrystalline Si-SiO₂ composites and freestanding hydride-surface-terminated silicon nanoparticles. *Chem. Mater.* 18, 6193–6146. doi: 10.1021/cm0602803
- Holmes, J. D., Ziegler, K. J., Doty, R. C., Pell, L. E., Johnston, K. P., and Korgel, B. A. (2001). Highly luminescent silicon nanocrystals with discrete optical transitions. *J. Am. Chem. Soc.* 123, 3743–3748. doi: 10.1021/ja002956f
- Hu, H., Wang, D., and Wang, Z. (2014). Solution for acoustic field of thermo-acoustic emission from arbitrary source. *AIP Adv.* 4:107114. doi: 10.1063/1.4898149
- Hu, H., Wang, Y., and Wang, Z. (2012a). Wide band flat frequency response of thermo-acoustic emission. *J. Phys. D: Appl. Phys.* 45:345401. doi: 10.1088/0022-3727/45/34/345401
- Hu, H., Wang, Z., Wu, H., and Wang, Y. (2012b). Analysis of spherical thermo-acoustic radiation in gas. *AIP Adv.* 2:032106. doi: 10.1063/1.4738497
- Hu, H., Zhu, T., and Xu, J. (2010). Model for thermoacoustic emission from solids. *Appl. Phys. Lett.* 96:214101. doi: 10.1063/1.3435429
- Hua, F., Erogbogbo, F., Swihart, M. T., and Ruckenstein, E. (2006). Organically capped silicon nanoparticles with blue photoluminescence prepared by hydrosilylation followed by oxidation. *Langmuir* 22, 4363–4370. doi: 10.1021/la0529106
- Islam, M. A., Mobarok, M. H., Sinelnikov, R., Purkait, T. K., and Veinot, J. G. C. (2017). Phosphorus pentachloride initiated functionalization of silicon nanocrystals. *Langmuir* 33, 8766–8773. doi: 10.1021/acs.langmuir.7b00518

- Julius, S., Gold, R., Kleiman, A., Leizeronok, B., and Cukurel, B. (2018). Modeling and experimental demonstration of heat flux driven noise cancellation on source boundary. *J. Sound Vib.* 434, 442–455. doi: 10.1016/j.jsv.2018.02.007
- Jurbergs, D., Rogojina, E., Mangolini, L., and Kortshagen, U. (2006). Silicon nanocrystals with ensemble quantum yields exceeding 60%. *Appl. Phys. Lett.* 88:233116. doi: 10.1063/1.2210788
- Kang, Z., Liu, Y., Tsang, C. H. A., Ma, D. D. D., Fan, X., Wong, N. B., et al. (2009). Water-soluble silicon quantum dots with wavelength-tunable photoluminescence. *Adv. Mater.* 6, 661–664. doi: 10.1002/adma.200801642
- Kelly, J. A., Henderson, E. J., and Veinot, J. G. (2010). Sol-gel precursors for group 14 nanocrystals. *Chem. Comm.* 46:8704. doi: 10.1039/c0cc02609c
- Kihara, T., Harada, T., Kato, M., Nakano, K., Murakami, O., Kikusui, T., et al. (2006). Reproduction of mouse-pup ultrasonic vocalizations by nanocrystalline silicon thermoacoustic emitter. *Appl. Phys. Lett.* 88:043902. doi: 10.1063/1.2168498
- Kim, C. S., Hong, S. K., Lee, J. M., Kang, D. S., Cho, B. J., and Choi, J. W. (2016). Free-standing graphene thermophone on a polymer-mesh substrate. *Small* 12, 185–189. doi: 10.1002/smll.201501673
- Kiyohara, S., Takamatsu, H., and Mori, K. (2002). Microfabrication of diamond films by localized electron beam chemical vapour deposition. *Semicond. Sci. Technol.* 17, 1096–1100. doi: 10.1088/0268-1242/17/10/311
- Klein, C., Loeschner, H., and Platzgummer, E. (2012). 50 keV electron multibeam mask writer for the 11 nm HP node: first results of the proof of concept tool (eMET POC). *Proc SPIE* 8323:8323. doi: 10.1117/12.916613
- Klein, C., and Platzgummer, E. (2016). “MBMW-101: World’s 1st high-throughput multi-beam mask writer,” in *Proceedings SPIE 9985, Photomask Technology* (Bellingham, WA). doi: 10.1117/12.2243638
- Kojima, A., Suda, R., and Koshida, N. (2018a). Improved quasiballistic electron emission from a nanocrystalline Si cold cathode with a monolayer-graphene surface electrode. *Appl. Phys. Lett.* 112:133102. doi: 10.1063/1.5017770
- Kojima, A., Suda, R., and Koshida, N. (2018b). “Reduced energy-angle dispersion of output electrons from a nanocrystalline Si emitter with a monolayer-graphene surface electrode,” *Technical Digest of 31st Int. Vacuum Nanoelectronics Conference*. (2018, Kyoto), 38–39.
- Koshida, N. (2017a). “Porous silicon ballistic hot electron emitter,” in *Handbook of Porous Silicon, 2nd Edn.*, eds. L. Canham (New York, NY: Springer), 11.
- Koshida, N. (2017b). “Thermal properties of porous silicon,” in *Handbook of Porous Silicon, 2nd Edn.*, eds. L. Canham (New York, NY: Springer), 9.
- Koshida, N. (2017c). “Porous silicon acoustic devices,” in *Handbook of Porous Silicon, 2nd Edn.*, eds. L. Canham (New York, NY: Springer), 9.
- Koshida, N., Kiuchi, Y., and Yoshimura, S. (1991). Photoconduction effects of porous Si in the visible region. *Proceedings in Conference Photoelectrics Image Devices*. London, Sep. 1991, 377–384.
- Koshida, N., and Koyama, H. (1992). Visible electroluminescence from porous silicon. *Appl. Phys. Lett.* 60, 347–349. doi: 10.1063/1.106652
- Koshida, N., Nagasu, M., Sakusabe, T., and Kiuchi, Y. (1985). The current-voltage characteristics of a photoelectrochemical cell using p-type porous-Si. *J. Electrochem. Soc.* 132, 346–349. doi: 10.1149/1.2113835
- Koshida, N., Sheng, X., and Komoda, T. (1999). Quasiballistic electron emission from porous silicon diodes. *Appl. Surf. Sci.* 146, 371–376. doi: 10.1016/S0169-4332(99)00004-5
- Kouassi, S., Gautier, G., Thery, J., Desplombain, S., Borella, M., Ventura, L., et al. (2012). Proton exchange membrane micro fuel cells on 3D porous silicon gas diffusion layers. *J. Power Sources* 216, 15–21. doi: 10.1016/j.jpowsour.2012.05.046
- Kusová, K., Cibulka, O., Dohnalová, K., Pelant, I., Valenta, J., Fucíková, A., et al. (2010). Brightly luminescent organically capped silicon nanocrystals fabricated at room temperature and atmospheric pressure. *ACS Nano* 4, 4495–4504. doi: 10.1021/nn1005182
- Kusová, K., Hapala, P., Valenta, J., Jelínek, P., Cibulka, O., Ondič, L., et al. (2014). Direct bandgap silicon: tensile-strained silicon nanocrystals. *Adv. Mater. Inter.* 1:1300042. doi: 10.1002/admi.201300042
- Kusová, K., Ondič, L., Klimešová, E., Herynková, K., Pelant, I., Daniš, S., et al. (2012). Luminescence of free-standing versus matrix-embedded oxide-passivated silicon nanocrystals: the role of matrix-induced strain. *Appl. Phys. Lett.* 101:143101. doi: 10.1063/1.4756696
- Lam, C., Zhang, Y. F., Tang, Y. H., Lee, C. S., Bello, I., and Lee, S. T. (2000). Large-scale synthesis of ultrafine Si nanoparticles by ball milling. *J. Cryst. Grow.* 220, 466–470. doi: 10.1016/S0022-0248(00)00882-4
- Ledoux, G., Gong, J., Huiskena, F., Guillois, O., and Reynaud, C. (2002). Photoluminescence of size-separated silicon nanocrystals: confirmation of quantum confinement. *Appl. Phys. Lett.* 80, 4834–4836. doi: 10.1063/1.1485302
- Leenheer, A. J., Sullivan, J. P., Shaw, M. J., and Harris, C. T. (2015). A sealed liquid cell for in situ transmission electron microscopy of controlled electrochemical processes. *J. Microelectromech. Syst.* 24, 1061–1068. doi: 10.1109/JMEMS.2014.2380771
- Lehman, V. (2002). *Electrochemistry of Silicon: Instrumentation, Science, Materials and Applications*. Verlag GmbH: Wiley-VCH.
- Li, X., He, Y., and Swihart, M. T. (2004). Surface functionalization of silicon nanoparticles produced by laser-driven pyrolysis of silane followed by HF–HNO₃ etching. *Langmuir* 20, 4720–4727. doi: 10.1021/la036219j
- Li, X., He, Y., Talukdar, S. S., and Swihart, M. T. (2003). Process for preparing macroscopic quantities of brightly photoluminescent silicon nanoparticles with emission spanning the visible spectrum. *Langmuir* 19, 8490–8496. doi: 10.1021/la034487b
- Lie, L. H., Duerdin, M., Tuite, E. M., Houlton, A., and Horrocks, B. R. (2002). Preparation and characterisation of luminescent alkylated-silicon quantum dots. *J. Electroanal. Chem.* 538, 183–192. doi: 10.1016/S0022-0728(02)00994-4
- Lim, C. W., Tong, L. H., and Li, Y. C. (2013). Theory of suspended carbon nanotube thin film as a thermal-acoustic source. *J. Sound Vibration* 332, 5451–5461. doi: 10.1016/j.jsv.2013.05.020
- Lin, T. L., Sadwick, L., Wang, K. L., Kao, Y. C., Hull, R., Nieh, C. W., et al. (1987). Growth and characterization of molecular beam epitaxial GaAs layers on porous silicon. *Appl. Phys. Lett.* 51:814. doi: 10.1063/1.98821
- Lin, V. S., Motesheri, K., Dancil, K.-P., Sailor, M. J., and Ghadiri, M. R. (1997). A porous silicon-based optical interferometric biosensor. *Science* 278:840. doi: 10.1126/science.278.5339.840
- Liu, S. M., Sato, S., and Kimura, K. (2005). Synthesis of luminescent silicon nanopowders redispersible to various solvents. *Langmuir* 21, 6424–6429. doi: 10.1021/la050346t
- Liu, Y. S., Tong, L. H., and Lai, S. K. (2018). Thermo-acoustics generated by periodically heated thin line array. *J. Sound Vib.* 427, 28–40. doi: 10.1016/j.jsv.2018.04.034
- Luna López, J. A., Román, A., Gómez Barojas, E., Gracia, J. F., Martínez Juárez, J., and López, J. (2014). Synthesis of colloidal solutions with silicon nanocrystals from porous silicon. *Nano. Res. Lett.* 9:571. doi: 10.1186/1556-276X-9-571
- Lysenko, V., Perichon, S., Remaki, B., and Barbier, D. (1999). Thermal conductivity of thick meso-porous silicon layers by micro-Raman scattering. *J. Appl. Phys.* 86, 6841–6846. doi: 10.1063/1.371760
- Maier-Flaig, F., Rinck, J., Stephan, M., Bocksrocker, T., Bruns, M., Kübel, C., et al. (2013). Multicolor silicon light-emitting diodes (SiLEDs). *Nano Lett.* 13, 475–480. doi: 10.1021/nl3038689
- Mangolini, L., Thimsen, E., and Kortshagen, U. (2005). High-yield plasma synthesis of luminescent silicon nanocrystals. *Nano Lett.* 5, 655–659. doi: 10.1021/nl050066y
- Mastronardi, M. L., Hennrich, F., Henderson, E. J., Maier-Flaig, F., Blum, C., Reichenbach, J., et al. (2011). Preparation of monodisperse silicon nanocrystals using density gradient ultracentrifugation. *J. Am. Chem. Soc.* 133, 11928–11931. doi: 10.1021/ja204865t
- Matsumoto, H., Inoue, H., Yamashita, H., Morita, H., Hirose, S., Ogasawara, M., et al. (2016). Multi-beam mask writer MBM-1000 and its application field. *Proc SPIE*. 9984:998405. doi: 10.1117/12.2245177
- Miller, J. B., Van Sickle, A. R., Anthony, R. J., Kroll, D. M., Kortshagen, U. R., and Hobbie, E. K. (2012). Ensemble brightening and enhanced quantum yield in size-purified silicon nanocrystals. *ACS Nano* 6, 7389–7396. doi: 10.1021/nn302524k
- Mogi, K., Takakuda, A., Tsukamoto, C., Oyama, R., Okabe, S., Koshida, N., et al. (2017). Mother-infant recognition in mice: involvement of pup ultrasonic vocalizations. *Behav. Brain Res.* 325, 138–146. doi: 10.1016/j.bbr.2016.08.044
- Mori, N., Minari, H., Uno, S., Mizuta, H., and Koshida, N. (2011). Theory of quasi-ballistic transport through nanocrystalline silicon dots. *Appl. Phys. Lett.* 98:062104. doi: 10.1063/1.3553501

- Nakamura, T., Yuan, Z., and Adachi, S. (2014). High-yield preparation of blue-emitting colloidal Si nanocrystals by selective laser ablation of porous silicon in liquid. *Nanotechnology* 25:275602. doi: 10.1088/0957-4484/25/27/275602
- Nakamura, T., Yuan, Z., and Koshida, N. (2018). *Efficient Conversion From Porous Silicon to Luminescent Colloidal Silicon Nanoparticles by Pulsed Laser Irradiation in Liquid*. PSST 2018 Abstract Book, La Grande Motte, 433–434.
- Nakamura, T., Yuan, Z., Watanabe, K., and Adachi, S. (2016). Bright and multicolor luminescent colloidal Si nanocrystals prepared by pulsed laser irradiation in liquid. *Appl. Phys. Lett.* 108:023105. doi: 10.1063/1.4939902
- Nassiopoulou, A. G. (2014). "Thermal isolation with porous silicon," In *Handbook of Porous Silicon*, ed L. Canham (New York, NY: Springer), 753–765.
- Nassiopoulou, A. G., and Kaltsas, G. (2000). Porous silicon as an effective material for thermal isolation on bulk crystalline silicon. *Phys. Status Solidi A* 182, 307–311. doi: 10.1002/1521-396X(200011)182:1<307::AID-PSSA307>3.0.CO;2-#
- Nishioka, T., Teshima, Y., Mano, T., Sakai, K., Asada, T., Matsukawa, M., et al. (2015). Ultrasound radiation from a three-layer thermoacoustic transformation device. *Ultrasonics* 57, 84–89. doi: 10.1016/j.ultras.2014.10.019
- Niskanen, A. O., Hassel, J., Tikander, M., Maijala, P., Gronberg, L., and Helisto, P. (2009). Suspended metal wire array as a thermoacoustic sound source. *Appl. Phys. Lett.* 95:163102. doi: 10.1063/1.3249770
- Nozaki, T., Sasaki, K., Ogino, T., Asahi, D., and Okazaki, K. (2007). Microplasma synthesis of tunable photoluminescent silicon nanocrystals. *Nanotechnology* 18:235603. doi: 10.1088/0957-4484/18/23/235603
- Odagawa, A., Matsushita, A., and Hashimoto, M. (2010). Thermally induced ultrasound emission from printable semiconductor nanoparticles. *J. Appl. Phys.* 108:076104. doi: 10.1063/1.3483946
- Okabe, S., Nagasawa, M., Kihara, T., Kato, M., Harada, T., Koshida, N., et al. (2013). Pup odor and ultrasonic vocalizations synergistically stimulate maternal attention in mice. *Behav. Neurosci.* 127, 432–438. doi: 10.1037/a0032395
- Pavesi, L., and Ceschini, M. (1993). Stretched-exponential decay of the luminescence in porous silicon. *Phys. Rev. B* 48, 17625–17628. doi: 10.1103/PhysRevB.48.17625
- Phatvej, W., Datta, H. K., Wilkinson, S. M., Mutch, E., Daky, A. K., and Horrocks, B. R. (2018). *Endocytosis of Alkyl-Capped Silicon Quantum Dots Prepared From Porous Silicon*. PSST 2018 Abstract book, La Grande Motte, 415–416.
- Platzgummer, E., Klein, C., and Loeschner, H. (2013). Electron multibeam technology for mask and wafer writing at 0.1 nm address grid. *J. Micro. Nanolith. Mem.* 12:031108. doi: 10.1117/1.JMM.12.3.031108
- Qi, L., Luo, T.-Y., Zhou, M., Abroshan, H., Huang, J., Kim, H. J., et al. (2016). Silicon nanoparticles with surface nitrogen: 90% quantum yield with narrow luminescence bandwidth and the ligand structure based energy law. *ACS Nano*. 10, 8385–8393. doi: 10.1021/acsnano.6b03113
- Randolph, S., Fowlkes, J., and Rack, P. (2006). Focused, nanoscale electron-beam-induced deposition and etching. *Crit. Rev. Solid State Mater. Sci.* 31, 55–89. doi: 10.1080/10408430600930438
- Rio, D., Constancias, C., Martin, M., Icard, B., van Nieuwstadt, J., Vijverberg, J., et al. (2010). 5 kV multielectron beam lithography: MAPPER tool and resist process characterization. *J. Vac. Sci. Technol. B* 28, C6C14–C6C20. doi: 10.1116/1.3517664
- Ruizendaal, L., Pujari, S. P., Gevaerts, V., Paulusse, J. M., and Zuilhof, H. (2011). Biofunctional silicon nanoparticles by means of thiol-ene click chemistry. *Chem. Ascan J.* 6, 2776–2786. doi: 10.1002/asian.201100375
- Ryabchikov, Y. V., Alekseev, S. A., Lysenko, V. V., Bremond, G., and Bluet, J.-M. (2012). Luminescence behavior of silicon and carbon nanoparticles dispersed in low-polar liquids. *Nano. Res. Lett.* 7:365. doi: 10.1186/1556-276X-7-365
- Sailor, M. J. (2012). *Porous Silicon in Practice: Preparation, Characterization and Applications*. Weinheim: Wiley-VCH, 249.
- Saitow, K., and Yamamura, T. (2009). Effective cooling generates efficient emission: blue, green, and red light-emitting Si nanocrystals. *J. Phys. Chem. C* 113, 8465–8470. doi: 10.1021/jp900067s
- Santos, H. (2014). *Porous Silicon for Biomedical Applications, 1st Ed*, Cambridge, UK: Woodhead Publishing, 558.
- Sato, K., Tsuji, H., Hirakuri, K., Fukata, N., and Yamauchi, Y. (2009). Controlled chemical etching for silicon nanocrystals with wavelength-tunable photoluminescence. *Chem. Comm.* 25, 3759–3761. doi: 10.1039/b903313k
- Sato, S., and Swihart, M. T. (2006). Propionic-acid-terminated silicon nanoparticles: synthesis and optical characterization. *Chem. Mater.* 18, 4083–4088. doi: 10.1021/cm060750t
- Sbrockey, N. M., Salagaj, T., Tompa, G. S., and Kalkur, T. S. (2018). Synthesis and characterization of graphene based thermoacoustic devices. *J. Cryst. Growth* 493, 41–44. doi: 10.1016/j.jcrysgro.2018.04.019
- Schlesinger, M., and Paunovic, M. (2010). *Modern Electroplating, Electrochemical Society Series*, 5th ed, New York, NY: Wiley.
- Seshan, K. (2012). *Handbook of Thin Film Deposition*, 3rd ed. Waltham, MA: William Andrew Publishing.
- Shen, P., Uesawa, N., Inasawa, S., and Yamaguchi, Y. (2010). Stable and color-tunable fluorescence from silicon nanoparticles formed by single-step plasma assisted decomposition of SiBr₄. *J. Mater. Chem.* 20, 1669–1675. doi: 10.1039/b919412f
- Shinoda, H., Nakajima, T., Ueno, K., and Koshida, N. (1999). Thermally induced ultrasonic emission from porous silicon. *Nature* 400, 853–854. doi: 10.1038/23664
- Shinoda, K., Yanagisawa, S., Sato, K., and Hirakuri, K. (2006). Stability of nanocrystalline silicon particles in solution. *J. Cryst. Grow* 288, 84–86. doi: 10.1016/j.jcrysgro.2005.12.035
- Shiohara, A., Hanada, S., Prabakar, S., Fujioka, K., Lim, T. H., Yamamoto, K., et al. (2010). A general route to efficient functionalization of silicon quantum dots for high-performance fluorescent probes. *J. Am. Chem. Soc.* 132, 248–253. doi: 10.1021/ja906501v
- Shirahata, N., Hirakawa, D., and Sakka, Y. (2010). Interfacial-related color tuning of colloidal Si nanocrystals. *Green Chem.* 12, 2139–2141. doi: 10.1039/c0gc00502a
- Song, J. X., Li, Y. H., Li, Y. Y., and Liu, G. Q. (2018). Three-dimensional model of thermoacoustic tomography with electric excitation. *J. Appl. Phys.* 124:164902. doi: 10.1063/1.5045510
- Suda, R., Kojima, A., and Koshida, N. (2018). Mechanism of liquid-phase reductive thin-film deposition under quasiballistic electron incidence. *ECS J. Solid State Sci. Tech.* 7, Q222–Q227. doi: 10.1149/2.031181jss
- Suda, R., Yagi, M., Kojima, A., Mori, N., Shirakashi, J., and Koshida, N. (2016). Reductive deposition of thin Cu films using ballistic hot electrons as a printing beam. *J. Electrochem. Soc.* 163, E162–E165. doi: 10.1149/2.0921606jes
- Suda, R., Yagi, M., Kojima, A., Mori, N., Shirakashi, J., and Koshida, N. (2017). Liquid-phase deposition of thin Si and Ge Films based on ballistic hot electron printing. *Mater. Sci. Semicond. Process.* 70, 44–49. doi: 10.1016/j.mssp.2016.12.022
- Sugimoto, H., Fujii, M., Imakita, K., Hayashi, S., and Akamatsu, K. (2012). All-inorganic near-infrared luminescent colloidal silicon nanocrystals: high dispersibility in polar liquid by phosphorus and boron codoping. *J. Phys. Chem. C* 116, 17969–17974. doi: 10.1021/jp305832x
- Suk, J. W., Kirk, K., Hao, Y., Hall, N. A., and Ruoff, R. S. (2012). Thermoacoustic sound generation from monolayer graphene for transparent and flexible sound sources. *Adv. Mater.* 24, 6342–6347. doi: 10.1002/adma.201201782
- Švrček, V., and Sasaki, T., and Shimizu, Y., Koshizaki, N. (2006). Silicon nanocrystals formed by pulsed laser-induced fragmentation of electrochemically etched Si micrograins. *Chem. Phys. Lett.* 429, 483–487. doi: 10.1016/j.cplett.2006.08.022
- Švrček, V., Sasaki, T., Shimizu, Y., and Koshizaki, N. (2016). Blue luminescent silicon nanocrystals prepared by ns pulsed laser ablation in water. *Appl. Phys. Lett.* 89:213113. doi: 10.1063/1.2397014
- Tao, L. Q., Liu, Y., Tian, H., Ju, Z. Y., Xie, Q. Y., Yang, Y., et al. (2016). A novel thermal acoustic device based on porous graphene. *AIP Adv.* 6:015105. doi: 10.1063/1.4939935
- Thonissen, M., Kruger, M., Lerondel, G., and Romestain, R. (1997). "Optical applications of porous silicon," in *Properties of Porous Silicon (EMIS Datareview Series No. 18)*, eds. L. Canham, (London, UK: the Institution of Electrical Engineers), 349–355.
- Tian, H., Li, C., Mohammad, M. A., Cui, Y. L., Mi, W. T., Yang, Y., et al. (2014). Graphene earphones: entertainment for both humans and animals. *ACS Nano* 8, 5883–5890. doi: 10.1021/nn5009353
- Tian, H., Xie, D., Yang, Y., Ren, T. L., Feng, T. T., Wang, Y. F., et al. (2011b). Poly(3,4-ethylenedioxythiophene):poly(styrenesulfonate)-based organic, ultrathin, and transparent sound-emitting device. *Appl. Phys. Lett.* 99:233503. doi: 10.1063/1.3666224

- Tian, H., Xie, D., Yang, Y., Ren, T. L., Lin, Y. X., Chen, Y., et al. (2011a). Flexible, ultrathin, and transparent sound-emitting devices using silver nanowires film. *Appl. Phys. Lett.* 99:253507. doi: 10.1063/1.3671332
- Tian, H., Xie, D., Yang, Y., Ren, T. L., Wang, Y. F., Zhou, C. J., et al. (2012). Single-layer graphene sound-emitting devices: experiments and modeling. *Nanoscale* 4:2272. doi: 10.1039/c2nr11572g
- Tong, L. H., Lai, S. K., and Lim, C. W. (2017). Broadband signal response of thermo-acoustic devices and its applications. *J. Acoust. Soc. Am.* 141:2430–2439. doi: 10.1121/1.4979667
- Uematsu, A., Kikusui, T., Kihara, T., Harada, T., Kato, M., Nakano, K., et al. (2007). Maternal approaches to pup ultrasonic vocalizations produced by a nanocrystalline silicon thermo-acoustic emitter. *Brain Res.* 1163, 91–99. doi: 10.1016/j.brainres.2007.05.056
- Uhlir, A. Jr. (1956). Electrolytic shaping of germanium and silicon. *Bell Syst. Tech. J.* 35, 333–347. doi: 10.1002/j.1538-7305.1956.tb02385.x
- Umez, I., Minami, H., Seno, H., and Sugimura, A. (2007). Synthesis of photoluminescent colloidal silicon nanoparticles by pulsed laser ablation in liquids. *J. Phys. Conf.* 59, 392–395. doi: 10.1088/1742-6596/59/1/083
- Valalaki, K., and Nassiopoulou, A. G. (2013). Low thermal conductivity porous Si at cryogenic temperatures for cooling applications. *J. Phys. D: Appl. Phys.* 46:295101. doi: 10.1088/0022-3727/46/29/295101
- Valalaki, K., and Nassiopoulou, A. G. (2014). Thermal conductivity of highly porous Si in the temperature range 4.2 to 20 K. *Nanoscale Res. Lett.* 9:318. doi: 10.1186/1556-276X-9-318
- Valalaki, K., and Nassiopoulou, A. G. (2017). Improved approach for determining thin layer thermal conductivity using the 3ω method. application to porous Si thermal conductivity in the temperature range 77–300 K. *J. Phys. D Appl. Phys.* 50:195302. doi: 10.1088/1361-6463/aa69fa
- Valenta, J., Fucikova, A., Pelant, I., Kusová, K., Dohnalová, K., Aleknavicius, A., et al. (2008). On the origin of the fast photoluminescence band in small silicon nanoparticles. *New J. Phys.* 10:073022. doi: 10.1088/1367-2630/10/7/073022
- van Dorp, W. F., and Hagen, C. W. (2008). A critical literature review of focused electron beam induced deposition. *J. Appl. Phys.* 104:081301. doi: 10.1063/1.2977587
- van Dorp, W. F., van Someren, B., Hagen, C. W., Kruit, P., and Crozier, P. A. (2005). Approaching the resolution limit of nanometer-scale electron beam-induced deposition. *Nano Lett.* 5, 1303–1307. doi: 10.1021/nl050522i
- Vesterinen, V., Niskanen, A. O., Hassel, J., and Helistö, P. (2010). Fundamental efficiency of nanothermophones: modeling and experiments. *Nano Lett.* 10, 5020–5024. doi: 10.1021/nl1031869
- Vollnhals, F., Woolcot, T., Walz, M.-M., Seiler, S., Steinrück, H.-P., Thornton, G., et al. (2013). Electron beam-induced writing of nanoscale iron wires on a functional metal oxide. *J. Phys. Chem. C Nanomater. Interfaces.* 117, 17674–17679. doi: 10.1021/jp405640a
- Wang, D. D., Hu, H., and Wang, Z. (2015). Modeling of the acoustic field of thermally induced ultrasonic emission from a spherical cavity surface. *Ultrasonics* 56, 497–504. doi: 10.1016/j.ultras.2014.09.016
- Watanabe, Y., Arita, Y., Yokoyama, T., and Igarashi, Y. (1975). Formation and properties of porous silicon and its application. *J. Electrochem. Soc.* 122:1351. doi: 10.1149/1.2134015
- Wei, Y., Lin, X., Jiang, K., Liu, P., Li, Q., and Fan, S. (2013). Thermoacoustic Chips with Carbon Nanotube Thin Yarn Arrays. *Nano Lett.* 13, 4795–4801. doi: 10.1021/nl402408j
- Wilcoxon, J. P., Samara, G. A., and Provencio, P. N. (1999). Optical and electronic properties of Si nanoclusters synthesized in inverse micelles. *Phys. Rev. B* 60, 2704–2714. doi: 10.1103/PhysRevB.60.2704
- Xiao, L., Liu, P., Liu, L., Li, Q., Feng, Z., Fan, S., et al. (2011). High frequency response of carbon nanotube thin film speaker in gases. *J. Appl. Phys.* 110:084311. doi: 10.1063/1.3651374
- Xing, Q. H., Li, S., Fan, X. L., Bian, A. H., Cao, S. J., and Li, C. (2017). Influential factors on thermoacoustic efficiency of multilayered graphene film loudspeakers for optimal design. *J. Appl. Phys.* 122:125107. doi: 10.1063/1.5004124
- Yang, Y., and Liu, J. (2013). Computational characterization on the thermoacoustic thermophone effects induced by micro/nano-heating elements. *Microfluid Nanofluid* 14, 873–884. doi: 10.1007/s10404-012-1121-5
- Yeklangi, A. G., Khadem, S. E., and Darbari, S. (2018). Fabrication and investigation of a thermoacoustic loudspeaker based on carbon nanotube coated laser-scribed graphene. *J. Appl. Phys.* 124, 224501. doi: 10.1063/1.5038729
- Yu, Y., Hessel, C. M., Bogart, T. D., Panthani, M. G., Rasch, M. R., and Korgel, B. A. (2013). Room temperature hydrosilylation of silicon nanocrystals with bifunctional terminal alkenes *Langmuir* 29, 1533–1540. doi: 10.1021/la304874y
- Yuan, Z., Nakamura, T., Adachi, S., and Matsuishi, K. (2017a). Luminescence color control and quantum-efficiency enhancement of colloidal Si nanocrystals by pulsed laser irradiation in liquid. *Nanoscale* 9, 1193–1200. doi: 10.1039/C6NR08757D
- Yuan, Z., Nakamura, T., Adachi, S., and Matsuishi, K. (2017b). Improvement of laser processing for colloidal silicon nanocrystal formation in a reactive solvent. *J. Phys. Chem. C* 121, 8623–8629. doi: 10.1021/acs.jpcc.7b00288
- Zhong, Y., Sun, X., Wang, S., Peng, F., Bao, F., Su, Y., et al. (2015). Facile, large-quantity synthesis of stable, tunable-color silicon nanoparticles and their application for long-term cellular imaging. *ACS Nano*. 9, 5958–5967. doi: 10.1021/acsnano.5b00683
- Zou, J., Baldwin, R. K., Pettigrew, K. A., and Kauzlarich, S. M. (2004). Solution synthesis of ultrastable luminescent siloxane-coated silicon nanoparticles. *Nano Lett.* 4, 1181–1186. doi: 10.1021/nl0497373

Conflict of Interest Statement: The authors declare that the research was conducted in the absence of any commercial or financial relationships that could be construed as a potential conflict of interest.

Copyright © 2019 Koshida and Nakamura. This is an open-access article distributed under the terms of the Creative Commons Attribution License (CC BY). The use, distribution or reproduction in other forums is permitted, provided the original author(s) and the copyright owner(s) are credited and that the original publication in this journal is cited, in accordance with accepted academic practice. No use, distribution or reproduction is permitted which does not comply with these terms.



3D Patterning of Si by Contact Etching With Nanoporous Metals

Stéphane Bastide^{1*}, Encarnacion Torralba¹, Mathieu Halbwax², Sylvain Le Gall³, Elias Mpogui¹, Christine Cachet-Vivier¹, Vincent Magnin², Joseph Harari², Dmitri Yarekha² and Jean-Pierre Vilcot²

¹ Institut de Chimie et des Matériaux Paris-Est (UMR 7182), CNRS, UPEC, Université Paris Est, Thiais, France, ² Institut d'Électronique de Microélectronique et de Nanotechnologie (IEMN), UMR 8520, Université de Lille, Villeneuve d'Ascq, France, ³ Group of Electrical Engineering of Paris (GeePs), CNRS, Centralesupelec, Univ. Paris-Sud, Sorbonne Université, Gif sur Yvette, France

OPEN ACCESS

Edited by:

Thierry Djenizian,
École des Mines de
Saint-Étienne-Campus Georges
Charpak Provence, France

Reviewed by:

Bruno Azeredo,
Arizona State University, United States
Thomas Defforge,
UMR7347 Matériaux,
Microélectronique, Acoustique,
Nanotechnologies (GREMAN), France

*Correspondence:

Stéphane Bastide
bastide@icmpe.cnrs.fr

Specialty section:

This article was submitted to
Chemical Engineering,
a section of the journal
Frontiers in Chemistry

Received: 03 December 2018

Accepted: 01 April 2019

Published: 25 April 2019

Citation:

Bastide S, Torralba E, Halbwax M,
Le Gall S, Mpogui E, Cachet-Vivier C,
Magnin V, Harari J, Yarekha D and
Vilcot J-P (2019) 3D Patterning of Si
by Contact Etching With Nanoporous
Metals. *Front. Chem.* 7:256.
doi: 10.3389/fchem.2019.00256

Nanoporous gold and platinum electrodes are used to pattern n-type silicon by contact etching at the macroscopic scale. This type of electrode has the advantage of forming nanocontacts between silicon, the metal and the electrolyte as in classical metal assisted chemical etching while ensuring electrolyte transport to and from the interface through the electrode. Nanoporous gold electrodes with two types of nanostructures, fine and coarse (average ligament widths of ~ 30 and 100 nm, respectively) have been elaborated and tested. Patterns consisting in networks of square-based pyramids ($10 \times 10 \mu\text{m}^2$ base $\times 7 \mu\text{m}$ height) and U-shaped lines ($2, 5$, and $10 \mu\text{m}$ width $\times 10 \mu\text{m}$ height $\times 4 \mu\text{m}$ interspacing) are imprinted by both electrochemical and chemical ($\text{HF-H}_2\text{O}_2$) contact etching. A complete pattern transfer of pyramids is achieved with coarse nanoporous gold in both contact etching modes, at a rate of $\sim 0.35 \mu\text{m min}^{-1}$. Under the same etching conditions, U-shaped line were only partially imprinted. The surface state after imprinting presents various defects such as craters, pores or porous silicon. Small walls are sometimes obtained due to imprinting of the details of the coarse gold nanostructure. We establish that np-Au electrodes can be turned into “np-Pt” electrodes by simply sputtering a thin platinum layer (5 nm) on the etching (catalytic) side of the electrode. Imprinting with np Au/Pt slightly improves the pattern transfer resolution. 2D numerical simulations of the valence band modulation at the Au/Si/electrolyte interfaces are carried out to explain the localized aspect of contact etching of n-type silicon with gold and platinum and the different surface state obtained after patterning. They show that n-type silicon in contact with gold or platinum is in inversion regime, with holes under the metal (within 3 nm). Etching under moderate anodic polarization corresponds to a quasi 2D hole transfer over a few nanometers in the inversion layer between adjacent metal and electrolyte contacts and is therefore very localized around metal contacts.

Keywords: silicon, nanoporous gold, imprinting, MACE, contact etching, patterning

INTRODUCTION

Metal Assisted Chemical Etching (MACE) of silicon began in the mid-2000s. Its new remarkable characteristic was to allow a localized dissolution of silicon around metal catalysts whose typical size is in the range of 10 – 100 nm. Due to the possibility of easily forming silicon nanowires and mesopores in crystalline silicon substrates, MACE has aroused considerable interest among the

scientific community. Substantial efforts have been devoted to study the effects related to the nature of the metal catalyst and oxidizing agent, the crystal orientation of the silicon substrate and the concentration ratio “hydrofluoric acid/ oxidizing agent” (ρ) (Huang et al., 2011), as well as to produce ordered structures using films/metal grids of a larger characteristic size, typically a network of pillars of diameter and inter-distance of a few hundreds of nanometers (Huang et al., 2007).

More recently, a new research axis has developed around the imprinting of 3D structures in silicon by contact etching, based on the principles of MACE. *Imprinting* means that a macroscopic tool with the pattern to be transferred is brought into contact with the silicon substrate and removed, and can be reused several times. This tool is at least partly metallic in order to catalyze the dissolution of silicon in HF medium, with as oxidizing agent either a chemical species in solution or an anodic polarization using a potentiostat. This approach was first reported by the group of Kobayashi in 2011. Pattern transfer in (100) and (111) oriented c-Si was performed using as imprinting tool a NaOH texturized (100) c-Si substrate, (i.e., with square-based pyramids at the surface) covered by a SiNx layer and a platinum layer on the top acting as catalyst (Fukushima et al., 2011). The SiNx layer was meant to protect the silicon substrate of the etching tool to be self-etched by the platinum layer. Although the extent and quality of the pattern transfer appeared limited, inverted pyramids could be etched in (111) c-Si. This represented a remarkable achievement considering that this crystallographic orientation is incompatible with forming such structures.

Azeredo et al. reported on pattern transfer in porous silicon by contact etching in HF-H₂O₂ using macroscopic gold metallized pre-patterned stamps with a sinusoidal shape (Azeredo et al., 2016b). The shape transfer was impossible in silicon but easily obtained in porous silicon since the electrolyte could reach the metal interface through the porous silicon network. For silicon, this problem was partially alleviated by patterning with a 2.5D sinusoidal wave with sub-microscale dimensions (Azeredo et al., 2016a). The technique used a Cr/Au coated polyethylene sheet with a holographic surface (1 μ m pitch and 350 nm amplitude) rolled around a platinum rod, immersed into HF-H₂O₂ and pressed on silicon with a load of 9 N. This process achieved a millimeter-scale parallel patterning with sub-100 nm resolution with a mirror-finish quality. Problems pointed out by the authors were the limited etch rates (imprinting time of 10 min) and some porosification of the silicon wafer (from a few nanometers to a few hundred nanometers from center to edge). Regrading etch rate, the work of Azeredo et al. (2016b) has clearly demonstrated that imprinting is a process mainly determined by the mass-transport of reactants and products. The overall etch rate dependence on the local depletion of reactant is characterized by quantitative means for the first time, which reveals the importance of the volume of reactant initially confined between the stamp and the substrate.

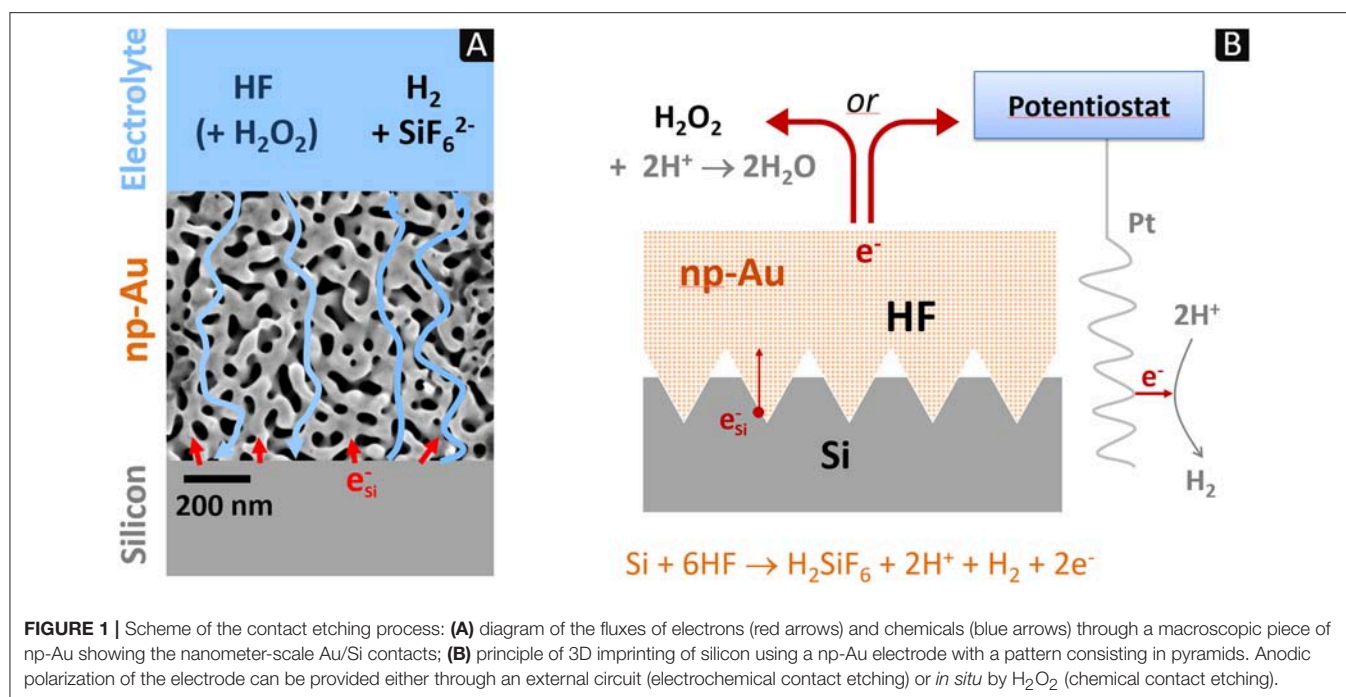
An electrochemical nanoimprint lithography (ECNL) approach based on MACE was also developed in the group of Zhan, for GaAs (Zhang et al., 2017a,b) and for silicon (Zhan et al., 2017). A review on electrochemical and nanomachining including ECNL is given in Zhan et al. (2017). In the case of

silicon, a platinum metallized PDMS mold with a nanopillar array was used to imprint a nanohole array in (111) c-Si. Diameter and height of nanopillars were ~ 350 and 544 nm, respectively, and the imprinted nanoholes depth ~ 116 nm. The reason for incomplete in-depth imprinting was also attributed to the consumption and blocked mass transfer of reactant and etching products in the ultrathin electrolyte layer between the platinum metallized imprint mold and the silicon wafer. Using metal catalyst-coated grayscale stamps and chemical etching (Ki et al., 2018), have also succeeded to imprint multilevel patterns in a single step. Large and complex eagle-shaped stamps (1×1 cm², micrometer sized patterns) could be repeatedly imprinted on Si substrates, only limited in depth (<1 μ m) by mass transport of the electrolyte.

Another category of direct imprinting of silicon based on MACE concerns macroscopic 3D structures, i.e., of tens of micrometers either laterally or in height. The first example of silicon contact etching using a macroscopic object has been given in 2009 by the group of Matsumura (Lee et al., 2009). They used a platinum wire, 50 μ m in diameter, anodically polarized against a counter-electrode in a HF solution and brought in contact with silicon to make cuts a few millimeters deep. Since then, grooves and through-holes have been etched using metal wires or tips as etching tools (Lee et al., 2009, 2011; Salem et al., 2010; Sugita et al., 2011, 2013). Another example of contact etching with a platinum needle has been given by Imamura et al. (2015). Takahashi et al. (2013) also reported on the use of platinum meshes (10 μ m wires and 50 μ m openings) attached to a sponge-like material to pattern arrays of macropores (10 μ m in size).

The major problem encountered with electrochemical contact etching at the macroscopic scale is the diffusion of the electrolyte. Because the metal and silicon phases must be in intimate contact, there is no room for the diffusion of the electrolyte and consequently, as reported by Sugita et al. (2011), etching must proceed laterally from the solution bulk to the center of the metal tool, which slows down the in-depth etch rate. This problem is not severe when imprinting a single element with a diffusion path length of a few tenths of μ m, (\sim wire diameter), but rather insurmountable for a “flat” contacting surface area of say a few cm².

We have recently reported a strategy specially defined to address this problem of large-scale electrolyte diffusion (Torralba et al., 2017). It is based on the use of nanoporous metal electrodes allowing both a “classical” MACE attack, i.e., with an interface consisting of nano-areas of metal and electrolyte in contact with silicon (for which the diffusion length is a few tens of nm) and a possible access of the electrolyte from the bulk of the solution to the interface. The principle of this configuration is represented in **Figure 1A**. The use of a nanoporous metal electrode to imprint patterns in silicon is a new concept. However, the well-known formation of silicon nanowires by MACE in HF-AgNO₃ medium, as initially developed by Peng et al. (2002) is actually operating on the same principle. In this system, the oxidation of silicon atoms (dissolution) is coupled with the reduction of silver ions (deposition). During the experiment, silver grows dendritically from the silicon substrate to form a silver foam (cf. **Figure 7A** in Nassiopoulou et al., 2011) which



reaches macroscopic dimensions (volume of $\sim 1 \text{ cm}^3$), much larger than the silicon substrate itself (*cf.* Materials and Methods and **Figure E** in **Supplementary Information**). This network of dendrites ($\sim 50 \text{ nm}$ in diameter) is *de facto* a “nanoporous silver electrode.” The extremely localized dissolution of silicon at the Ag/Si interface leads to the formation of nanowires that lengthen as the “nanoporous silver electrode” sinks into silicon. The silicon nanowires are smooth and well-defined over several tens of micrometers, without parasitic etching. This is due to the depletion of silver ions inside the foam. They are only present outside of the foam (dendritic growth) but promotes the anodic polarization (Ag^+/Ag redox couple) responsible for the electrochemical dissolution in HF of silicon at the Ag/Si interface. The anodic current corresponds to electrons injected (Si atom oxidation) at the bottom of the Ag foam and released at the tip of the dendrites (Ag deposition, *cf.* **Figure E3** in **Supplementary Information**). This well-known experiment thus demonstrates the possibility of etching silicon on a macroscopic scale with a nanoporous metal tool (silver foam) allowing both electrolyte diffusion and MACE. The aim is therefore to develop an equivalent process with nanoporous metals of controlled structure and patterns.

Our first etching tests with nanoporous metal electrodes focused on imprinting square-based pyramids as represented in **Figure 1B**. They were made with nanoporous gold (np-Au) electrodes by electrochemical contact etching. A network of inverted pyramids was partially imprinted in n-type silicon oriented (100) in this way (Torralba et al., 2017).

We show this time that a complete transfer of complex patterns can be obtained in n-type silicon by contact etching, either electrochemically or chemically. The effects of several parameters such as the type of pattern (pyramid vs. U-shaped line), the characteristic size of the metal nanostructure

(30 vs. 100 nm) and the nature of the catalytic metal (gold vs. platinum) with respect to etch rate, resolution of pattern transfer and formation of surface defects have been examined.

2D numerical simulations of the valence band modulation at the Au/Si/electrolyte interfaces have been performed to interpret the experimental results. The local modulations of silicon bands induced by metal nanocontacts were first studied by the group of Nakato (Nakato et al., 1988). This type of analysis subsequently benefited from numerical simulation methods and was reported by Rossi and Lewis for nanometer scale Ni arrays on Si electrodes (Rossi and Lewis, 2001) and by Huang et al. in the case of metal assisted electrochemical etching with silver nanoparticles on p-type silicon under anodic polarization in HF solutions (Huang et al., 2010). Recently, Torralba et al. studied MACE of p-type silicon with platinum nanoparticles using 2D numerical TCAD simulations based on a finite volume method (Torralba et al., 2016). The same type of modeling is developed here to determine the silicon band structure at adjacent metal and electrolytic contacts of nanometric size (20 nm). The assembly is connected so that metal contacts, which mimic the ligaments of the nanoporous metal electrode, can be anodically polarized with respect to the electrolyte through the silicon substrate (Metal/Silicon/Electrolyte). This allows to describe the band structure during etching.

MATERIALS AND METHODS

Chemicals

AuAg alloys in the form of 170 nm thick leaves (12 carats, $\text{Au}_{35}\text{Ag}_{65}$, $8 \times 8 \text{ cm}^2$, Noris) were used as source of material for the elaboration of np-Au electrodes. Imprinting experiments were performed in n-type (phosphorous doped at

$N_d \sim 10^{15} \text{ cm}^{-3}$) c-Si wafers oriented (100), 1–3 $\Omega \text{ cm}$, 400 μm (Sil'tronix). Analytical grade (VWR chemicals) 30% H_2O_2 , 96% H_2SO_4 , 40% HF, 65% HNO_3 , 60% HClO_4 and ultra-pure water (18.2 M $\Omega \text{ cm}$, Millipore) were used in all experiments.

Electrochemical Treatments

Dealloying and contact etching were performed with a PGSTAT20 Metrohm Autolab and Nova software, in a three-electrode PTFE cell. The np-Au electrode, a platinum wire and a $\text{Hg}/\text{Hg}_2\text{SO}_4$ electrode (SME) were used as working, counter and reference electrodes, respectively. The SME included a K_2SO_4 bridge with a glass frit (EC dealloying) or a K_2SO_4 agar-gel tip (etching in HF).

Instrumentation

Scanning electron microscopy (SEM) images, Energy Dispersive X-ray Spectroscopy (EDS) and Electron Back Scattered Diffraction (EBSD) were obtained with a Merlin FEG microscope from Zeiss equipped with AZtec systems (EDS Advanced, HKL Advanced Nordlys Nano, Oxford Instruments). Depth measurements of imprinted patterns were obtained by SEM from working distances measurements at different points of the patterns. AuAg powders were sintered using a Dr-Sinter 515S-Syntex Spark Plasma Sintering (SPS) machine.

Fabrication of Silicon Molds

Alkaline etching using a SiN_x mask was used to create arrays of square-based inverted pyramids of 10×10 and 7 μm depth, in p-type (100) silicon wafers (5–10 Ωcm). Cryogenic plasma etching was used for parallel lines of rectangular cross section (U-shaped line) with a height of 5 μm , a width of 2, 5, or 10 μm and a spacing of 4 μm . In both cases, etching mask were defined by E-beam lithography.

Patterned np-Au Electrodes

AuAg leaves were fragmented in water under simple magnetic stirring overnight and dried at 100°C. The obtained powder ($\sim 350 \text{ mg}$) was sintered against the silicon mold at 500°C under vacuum, with a uniaxial pressure of 50 MPa (3.3 kN/cm²) for 20 min, in a graphite die ($\varnothing = 10 \text{ mm}$) enclosed between two graphite punches. After dissolution of the mold in $\text{HF-HNO}_3\text{-H}_2\text{O}$ (44:16:40), $\text{Au}_{35}\text{Ag}_{65}$ disks of 10 mm diameter (0.35 mm thick) with a patterned central (79 mm²) were obtained. More details can be found in **Supplementary Information**.

Electrochemical Contact Etching

n-type silicon wafers were cleaved into $2 \times 2 \text{ mm}^2$ pieces, cleaned in $\text{H}_2\text{SO}_4\text{-H}_2\text{O}_2$ (3:1) and rinsed with ultra-pure water. Before etching, the np-Au electrode was also cleaned in $\text{H}_2\text{SO}_4\text{-H}_2\text{O}_2$ (5:1). This must be performed with great care because the disproportionation of H_2O_2 into H_2O and O_2 is catalyzed by the gold surface and hence results in a strong effervescence of the hot mixture (exothermic mixing): the np-Au electrode was first placed in a Pyrex-type glass beaker with a small amount of H_2SO_4 and second H_2O_2 was added drop by drop. The electrode was cleaned for 5 min and then rinsed thoroughly with ultrapure water.

After this, the np-Au electrode was placed on a platinum plate (fixed on the bottom of a Teflon cell) which is itself connected to the potentiostat. A cleaned silicon piece was placed in contact with np-Au and a pressure applied *via* a weight in gold of 4.5 g. The electrolyte was 5 M HF with 2 vol.% ethanol to favor the elimination of H_2 generated at the Si/metal interface.

Chemical Contact Etching

The cleaning procedure of the sample and the electrode was the same as described above. The electrode was maintained under pressure (corresponding to a weight of $\sim 0.4 \text{ g}$) using a gold wire connected to a micromanipulator. This is necessary due to H_2 evolution (Si dissolution) and O_2 evolution (disproportionation of H_2O_2 on Au) that may displace the electrode during imprinting. Etching was carried out in 5 mol L⁻¹ HF and 1 mol L⁻¹ H_2O_2 , the rho value ($[\text{HF}]/([\text{HF}] + [\text{H}_2\text{O}_2])$) being 0.83.

Use of Nanoporous Metal Electrodes

On the average, we could use 5 times np-Au electrodes with pyramids and 15 times those with U-shaped lines (for either chemical or electrochemical contact etching). With pyramids, “damaged tips” was the main reason for overruling an electrode. The second pattern is logically more robust, the damages originating more from handling. See **Supplementary Information** for more details.

Etch rate are most likely not constant during etching. We only have access to apparent etch rate, i.e., depth divided by etch time. For each set of etching condition, 3 to 4 experiments were used to calculate an average value of the apparent etch rates given in **Tables 2, 3**. The maximum deviation from the average value is between 10 and 20%.

Modeling

Numerical simulations in 2D of the valence band modulation at the Au/n-Si/electrolyte interfaces were performed using the commercial TCAD software [Atlas from Silvaco[®] (Torralba et al., 2016)] based on a finite volume method. This simulator solves the physical equations governing the electrostatics (Poisson, electro-neutrality) and the transport of e^- and h^+ (drift-diffusion) self-consistently on a 2D mesh.

The modeled structure is schemed in **Figure D** of **Supplementary Information**. It consists of a n-type silicon substrate with a thickness of 100 μm and a width of 1 μm , covered by 20 nm large gold pads, separated by two electrolyte contacts of the same length. The gold and electrolyte phases are separated by 1 nm of insulating vacuum to allow charge transfer only through the Si/Electrolyte and Si/Au interfaces. All the electrolyte contacts are short-circuited, so at the same potential, identically for the all gold pads. Silicon is doped n-type at a level of $3 \times 10^{15} \text{ cm}^{-3}$. The work functions of gold and the electrolyte are taken at $W_{\text{Au}} = 5.5 \text{ eV}$ (Hözl and Schulte, 1979) and $W_{\text{El}} = 4.5 \text{ eV}$ (determined in our experimental conditions, cf. Torralba et al., 2016 and its Supplementary Information). The Fermi level is set at 0 eV at the equilibrium. To mimic the MACE process, a positive polarization can be applied between gold and the electrolyte.

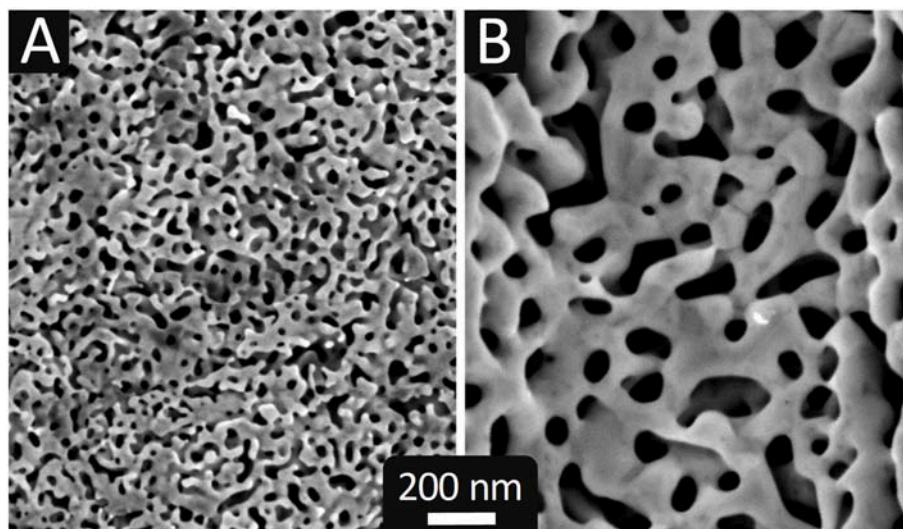


FIGURE 2 | SEM images of np-Au electrodes elaborated by: **(A)** electrochemical dealloying at 0.7 V_{SME} in $HClO_4$ (0.77 mol L^{-1}) at 60°C for 53 h; **(B)** chemical dealloying in HNO_3 (14.2 mol L^{-1} , 65 wt.%) at 80°C for 12 h.

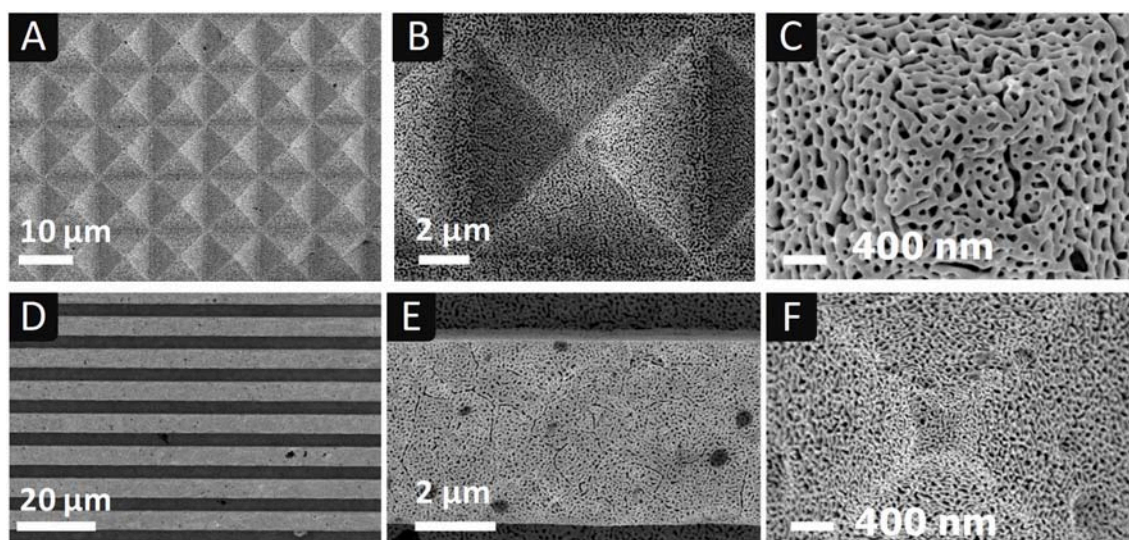


FIGURE 3 | SEM images at different magnification of np-Au electrodes dealloyed chemically **(A–E)** and electrochemically **(F)**, with two different surface patterns: **(A–C,F)** array of square based pyramids ($10 \times 10 \mu\text{m}^2 \times 7 \mu\text{m}$ depth); **(D,E)** parallel lines with rectangular cross section ($5 \times 5 \mu\text{m}^2$ (width \times height), spacing of $4 \mu\text{m}$).

RESULTS AND DISCUSSION

Elaboration of Patterned np-Au Electrodes Surface Patterns

The chosen strategy to elaborate patterned np-Au electrodes has been to design silicon molds using traditional microelectronics techniques and then sinter an $\text{Au}_{35}\text{Ag}_{65}$ powder in these molds to obtain their complementary shape (*cf.* experimental section). Experience has shown that the brittleness of silicon molds requires maintaining the pressure during sintering at the lowest

possible value (3.3 kN) and that it was necessary to cover the silicon substrate with a Si_3N_4 diffusion barrier layer to avoid the formation of an AuSi eutectic which appears at 363°C . Under these conditions, a temperature of 500°C was chosen and the sintering time adjusted to obtain a good powder densification. The final density is at least 95% of that of bulk $\text{Au}_{35}\text{Ag}_{65}$ after 20 min of sintering.

$\text{Au}_{35}\text{Ag}_{65}$ pellets, $300 \mu\text{m}$ thick, exhibiting arrays of square-based upright pyramids and U-shaped parallel lines on their surface were designed in this way. **Figures 2, 3** show

TABLE 1 | Characteristics of np-Au obtained by electrochemical and chemical dealloying.

Dealloying mode	+ 0.7 V _{SME} in HClO ₄	HNO ₃
Temperature, duration	60°C, 53 h	80°C, 12 h
Dissolved silver (wt. %)	87	100
Composition (EDS)—surface	Au ₉₅ Ag ₅	Au
Composition (EDS)—core	Au ₈₈ Ag ₁₂	Au
Average ligament width (nm)	28	95
Average pore area (nm ²)	698	7,146
2D surface porosity (%)	22	28
Denomination	fine np-Au	coarse np-Au

representative images of the patterned electrodes after being dealloyed as described below.

Au Nanostructures

Dealloying Au₃₅Ag₆₅, i.e., removing selectively silver, results in the formation of np-Au, a material consisting in a mixture of interconnected Au ligaments and pores which sizes can vary considerably (from 1 nm to 1 μm), depending on the dealloying conditions (Ding et al., 2004; Qian and Chen, 2007). The characteristic size of the nanostructure is a parameter that can influence the etching of patterns. Indeed, the dimensions of the ligaments determine the diffusion length that the electrolyte (reactants and dissolution products) must travel (parallel to the interface) to allow a complete dissolution of underlying silicon and thus the penetration rate of the electrode. The pore size may have an impact on the transport of the electrolyte but also on the escape of hydrogen bubbles formed by silicon dissolution in HF, when the dissolution valence n is <4 (low anodic current, high HF concentration), according to the reaction:



We therefore wanted to develop nanoporous electrodes with different characteristic sizes to determine whether a fine or coarse nanostructure is more suitable for etching.

From the literature and trials, we have determined two sets of dealloying conditions to obtain nanostructures with very different sizes: electrochemical dealloying at 60°C in HClO₄ at 0.7 V_{SME} for ~50 h and chemical dealloying in HNO₃ at 80°C for 12 h. Etching times were established by weighing the AuAg pellet between successive treatments, i.e., by monitoring the removal of silver until zero mass loss is reached. **Figure 2** shows SEM images of the pellets dealloyed with both treatments and **Table 1** gives some features of the so formed np-Au.

Electrochemical dealloying produces a fine nanostructure (**Figure 2A**) whereas that obtained by chemical dealloying is coarse (**Figure 2B**). The average pore area varies over one order of magnitude and the average ligament width varies by a factor of 3 (**Table 1**). In agreement with these features, these two types of nanostructures will be designated hereafter as fine and coarse np-Au.

The porosity is difficult to evaluate. If we assume neither shrinkage nor expansion of the pellet during dealloying, the

porosity of np-Au simply corresponds to the volume of dissolved Ag, which for Au₃₅Ag₆₅ is 65% (silver and gold having nearly identical atomic radius). Accordingly, the porosity would be 59 and 65% for fine and coarse np-Au, respectively. The surface porosity, calculated by image analysis as the area fraction of pore openings (*cf.* details in **Supplementary Information**), is higher by a factor of ~1.3 for coarse np-Au vs. fine np-Au (28 vs. 22%, respectively).

Mass loss values indicate that silver removal is not completed after electrochemical dealloying. An EDS analysis conducted on the surface but also in the core of the pellet (after cleavage, at ~180 μm below the surface) confirms the residual presence of silver with a positive gradient toward the core. On the contrary, silver is not detected, even in the core, after chemical dealloying.

Figure 3 shows SEM images of np-Au electrodes with two different patterns, pyramids (A-D) and U-shaped lines (E-F), obtained by chemical (A-E) or electrochemical dealloying (F).

It can be seen that np-Au electrodes reproduce well the initial patterns of the silicon molds. The tip of the pyramids seems better defined when the characteristic size of np-Au is in the order of 30 nm, i.e., for fine np-Au, as could be expected. However, on all the electrodes produced, the replication resolution appears to depend firstly on the sintering step rather than on the type of dealloying. Indeed, several problems can occur at this stage which degrade the quality of the replica of the silicon mold patterns: areas contaminated by foreign particles/impurities deposited on the surface of the mold coming from the graphite die and punches, incomplete filling of the pyramid tips with the Au₃₆Ag₆₅ powder or even small breaks of the Si mold due to the applied pressure.

Metal Catalysts

In MACE of silicon, it is known that the nature of the metal catalyst has a profound effect on both the localization of dissolution around the catalyst and the dissolution rate. Platinum is more efficient than silver or gold at catalyzing the reduction of H₂O₂, which results in higher etch rate. However, it has been shown (with p-type silicon) that platinum generates a lot of porous silicon as a result of delocalized etching, while silver does not at all, and this can influence the resolution of pattern transfer. Hence, we wanted to perform tests with other nanoporous metals such as silver or platinum. These metals can be obtained in a nanoporous form but in a more difficult way and with a limited range in terms of characteristic size and porosity, thus making comparison with np-Au delicate. A simple and direct solution to this problem is to consider that, since catalysis of etching occurs at Si/metal contacts, it is sufficient to cover the np-Au surface with the desired metal. This allows to work under exactly the same conditions (ligament sizes, diffusion of the electrolyte into the electrode) but with another catalyst. As alternative catalysts, we tested Pt, deposited as 5 nm thick layers by sputtering on coarse np-Au electrodes. The SEM images of these electrodes are very similar to those of np-Au in **Figures 2, 3** (not shown).

Electrochemical Contact Etching

Etchings of silicon substrates were performed electrochemically in HF by anodic polarization of np-Au electrodes. **Table 2**

TABLE 2 | Etching conditions and results obtained by electrochemical contact etching using np-Au electrodes with pyramids and U-shaped lines arrays as surface patterns (cf. **Supplementary Information** for more details on contact etching data).

Metal	Pattern	Au nanostructure Remaining Ag <ligament size>	Electrochemical contact etching in HF (5 mol L ⁻¹ HF + 2 vol.% EtOH) /apparent etch rate (depth/etch time)
np-Au	Pyramid	fine ^a 12 wt.% < 28 nm >	0.3 V _{SME} , 10 min → partial imprinting/0.36 μm min ⁻¹
	Line		0.3 V _{SME} , 20 min → 0.3 μm deep/0.015 μm min ⁻¹ <i>PSi^c traces + Ag deposition</i>
np-Au	Pyramid	coarse ^b 0 wt.% < 95 nm >	0.2 V _{SME} , 20 min → full imprint/0.35 μm min ⁻¹
	line		0.2 V _{SME} , 20 min → 1.5 μm deep/0.075 μm min ⁻¹

^a0.7 V_{SME}, 53 h; ^bHNO₃, 80°C, 12 h; ^cporous silicon.

summarizes the etching conditions tested and the corresponding results. The highlights that can be drawn from these results are presented in the following sections through SEM images of the imprinted surfaces.

Influence of the Nanostructure Size

Figure 4 shows examples of imprinted silicon surfaces with fine and coarse np-Au pyramids. With fine np-Au electrodes, inverted pyramids of $5 \times 5 \mu\text{m}^2$ (3.6 μm depth) were etched after 10 min at 0.3 V_{SME} (**Figures 4A,B**). With coarse np-Au electrodes, inverted pyramids of $9 \times 9 \mu\text{m}^2$ were patterned after 20 min at 0.3 V_{SME} (**Figure 4C**). In another experiment, conducted at 0.2 V_{SME} for 20 min with the same electrode, full pattern transfer was achieved (**Figure 4D**): the inverted pyramid base is 9.9 μm and the depth 7 μm at the tip. It results in a lack of flat spots between adjacent inverted pyramids. The maximum apparent etch rates (depth/etch time), after several experiments with both types of electrodes) are found to be relatively close (0.32–0.36 μm/min). Hence, the characteristic size of the gold nanostructure does not affect the apparent etch rate significantly.

A comparison of **Figures 4B,D** shows that the surface state is different depending on the type of np-Au (fine or coarse). The insert in **Figure 4B** is a zoom on an edge of the pyramid. The surface appears rough and there is silver deposited in the form of nanoparticles (as indicated by EDS). This deposit, also visible on the flat part of the substrate between pyramids (**Figure 4A**) must be related to the residual presence of silver in the electrodes (5–12 at.%, cf. **Table 1**). During etching, the anodic polarization of the electrode causes some dissolution of silver and the silver ions thus formed diffuse to the silicon substrate. Their reduction into silver nanoparticles is coupled with silicon dissolution, which causes craters to form around the nanoparticles and is thus at the origin of the surface roughness (Chemla et al., 2003; Chartier et al., 2008; Lee et al., 2008).

Inverted pyramids patterned with coarse np-Au (**Figure 4D**) have both smooth and rough areas, with some porous silicon visible on the upper edges. The absence of silver deposition

is consistent with the complete dealloying obtained chemically in HNO₃ at 80°C (cf. **Table 1**). It is interesting to note that a complete pattern transfer of the pyramid network is achieved after 20 min etching at 0.2 V_{SME} (**Figure 4D**) and quasi-complete at 0.3 V_{SME} (same electrode and etching time) (**Figure 4C**). Below 0.2 V_{SME}, imprinting was found to be much less effective (only the pyramid tips were visible on the silicon surface) due to a low oxidation current. The bias applied to etch at 0.2 V_{SME} was ~ 0.35 V (V_{OCp} ~ -0.15 V_{SME}).

Effect of the Pattern

An example of trenches patterned in silicon by electrochemical contact etching of np-Au electrodes with U-shaped lines is shown in **Figure 5**.

Almost no imprinting (0.3 μm in depth) was obtained with np-Au electrodes of fine nanostructure, as shown in **Figure 5A**. The surface is extremely damaged as a result of silver deposition, as clearly shown in the inset image at higher magnification of the etched surface. Deeper imprints were observed when using electrodes with coarse np-Au, and without silver deposition (**Figure 5B**), in agreement with the results obtained with pyramids. The etched bottom of the trenches exhibits the details of the electrode coarse nanostructure (upper inset of **Figure 5B**), the small silicon walls corresponding to pore openings. This indicates a high pattern transfer resolution. From these results, coarse np-Au seems to be more suitable than fine np-Au for imprinting.

In terms of imprinting depth, etching was more effective for the pyramid pattern (cf. **Figures 4, 5**). The maximum depth reached with U-shaped lines under identical etching conditions (0.2 or 0.3 V, 20 min) was 1.8 μm compared to 7 μm for pyramids. The penetration rate is therefore almost four times lower for the U-shaped line pattern. This difference could be related to the supply of electrolyte at the interface. However, the diffusion path of the electrolyte through a 300 μm thick nanoporous electrode is essentially the same regardless of the surface pattern (~10 μm in height). It is possible that the actual difference lies in the free volume of electrolyte around the patterns which is more confined in the case of U-shaped lines (flow only along the lines) than for the pyramids thanks to their truncated shape. This implies that despite the porous nature of the electrode there could be some limitation in electrolyte supply.

Chemical Contact Etching

Admittedly, the use of np-Au electrodes allows to apply a polarization externally and this offers a reproducible control of the potential, the ability to measure the dissolution current and avoids the use of an oxidizing agent. However, because in some cases it is simpler to use the purely chemical method of classical MACE, etching tests were conducted in HF-H₂O₂ solutions, as reported in **Table 3**.

Compared to electrochemical etching, we found that a higher gas evolution occurs in HF-H₂O₂. It is most probably related to the disproportionation of H₂O₂ on the gold surface of the electrode.

As for electrochemical contact etching, while fine np-Au electrodes did not provide a full pattern transfer (**Figure 6A**), a complete transfer was obtained with coarse np-Au electrodes

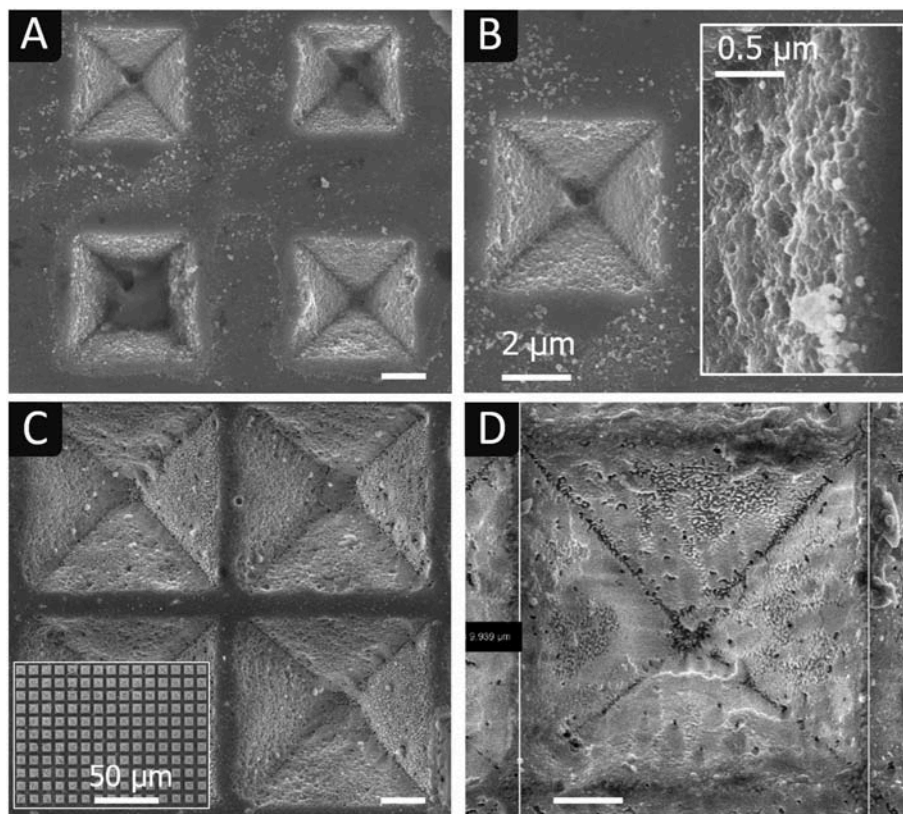


FIGURE 4 | SEM images of silicon surfaces after imprinting inverted pyramids with a fine (A,B) and a coarse (C,D) np-Au electrode. Electrochemical contact etching was carried at 0.3 V_{SME} for 10 min (A,B); at 0.3 V_{SME} for 20 min (C) and at 0.2 V_{SME} for 20 min (D). Insets: (B) inverted pyramid border at higher magnification; (C) inverted pyramid array at lower magnification. Electrolyte: HF 5 mol L^{-1} with 2 vol.% EtOH. Scale bars: 2 μm unless otherwise noted.

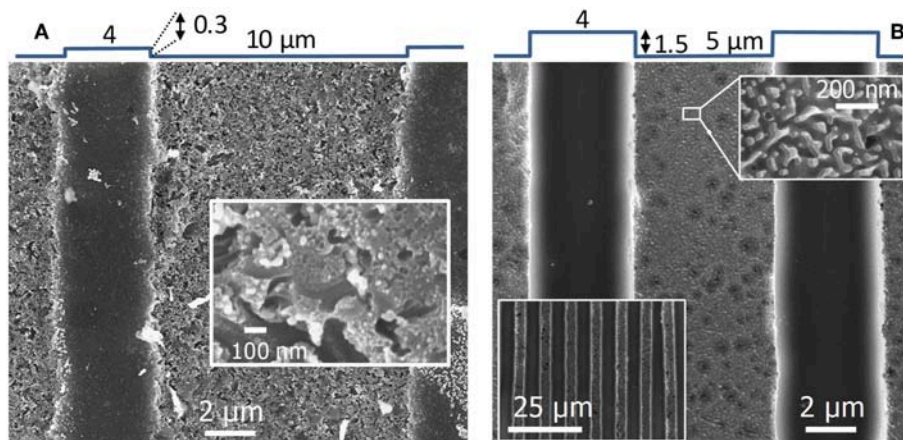


FIGURE 5 | SEM images of silicon surfaces after imprinting U-shaped lines with np-Au electrode: (A) fine nanostructure (0.3 V_{SME} , 20 min); (B) coarse nanostructure (0.2 V_{SME} , 20 min). Insets: (A, B-upper) high magnification image of the etched area; (B-bottom) U-shaped line array at a lower magnification. Electrolyte: HF 5 mol L^{-1} with 2 vol.% EtOH.

(Figure 6B). Inverted pyramids have sides of 10 μm and a depth of 7 μm , like their models. The surface is relatively rough and craters of ~ 500 nm in diameter and ~ 100 nm

deep are present everywhere. The intersections of facets are relatively rounded, indicating a partial delocalization of etching, probably due to porous silicon formation. SEM observations in

TABLE 3 | Etching conditions and results obtained by chemical contact etching using np-Au and np-Au/Pt electrodes with pyramid and U-shaped line arrays as surface patterns (cf. **Supplementary Information** for more details on contact etching data).

Metal	Pattern	Au nanostructure Remaining Ag <ligament size>	Chemical contact etching in HF/H ₂ O ₂ (5:1 mol L ⁻¹) /apparent etch rate (depth/etch time)
np-Au	Pyramid	fine 12 wt. %	20 min → partial imprinting/0.28 μm min ⁻¹
	Line	<28 nm>	20 min → no imprinting
np-Au	Pyramid		20 min → full imprint/0.35 μm min ⁻¹
	Line	coarse 0 wt. % <95 nm>	20 min → 2.8 μm deep/0.14 μm min ⁻¹
np-Au/Pt ^a	Pyramid		25 min → full imprint/0.28 μm min ⁻¹
	Line		25 min → 1.7 μm deep/0.07 μm min ⁻¹

^a5 nm coating on np-Au.

cross section confirm the rounded edge morphology and the presence of a porous silicon layer everywhere on the walls, with a thickness of ~50 nm measured at the bottom of an inverted pyramids (cf. **Figure G** in **Supplementary Information**). These defects were not observed after electrochemical contact etching. Delocalized etching with porous silicon formation is a well-known effect of MACE that explains the production of tapered and porous silicon nanowires with metal mesh as catalyst [(Azeredo et al., 2013) and (Geyer et al., 2012), respectively] or that of cone-shape pores with platinum nanoparticles (Torralba et al., 2016). However, delocalized etching is not expected with low doped n-type silicon and gold or platinum catalysts. This discrepancy is discussed in the Modeling section.

Trenches imprinted chemically with coarse np-Au (**Figure 6C**) exhibit a depth of 2.8 μm which is two times higher than what is obtained electrochemically (1.5 μm). Like with the inverted pyramids (**Figure 6B**) the etched surface (bottom) presents a high density of craters.

Effect of the Metal Catalyst

In order to study the influence of the metal catalyst, inverted pyramids and trenches were imprinted chemically with np-Au/Pt electrodes, under the conditions reported in **Table 3**. SEM images of the obtained inverted pyramids and trenches are given in **Figures 7A,B**, respectively.

The chemical apparent etch rate with coarse np-Au/Pt is lower than that obtained with coarse np-Au, the trench depth after 20 min being 1.7 μm and 2.8 μm, respectively. It should be noted though that the U-shaped lines with np-Au/Pt are five times larger than in the case of np-Au (10 μm instead of 2 μm, identical spacing of 4 μm). The volume of etched silicon is therefore five times more important, which is consistent with the difference in apparent etch rates.

Another difference lies in the quality of the pattern transfer, which seems slightly better with Pt: the facets of pyramids are flatter and their intersections better marked; very few craters are present although a significant amount of porous silicon appears in the form of particles detached from the surface. The surface state is also different, with the presence of “small walls” that appear to be a replica of the pores on the surface of the metal electrode. Such walls are also observable at some locations on the surface of silicon electrochemically etched by anodization with a np-Au electrode (see **Figures 4B, 5B**). Hence, their presence is not due to the intrinsic properties of gold and platinum (work functions), or to the contact etching mode, but to certain etching conditions that leads to a higher transfer resolution.

Figure 7B also shows that the trenches are not aligned with the <110> directions of the substrate because the electrode and silicon samples are contacted regardless of their orientation. These directions are those necessarily followed in the case of alkaline etching and lithography (Moreau, 1988). In the same vein, it should be stressed that the facets of the pyramids obtained by contact etching do not correspond to (111) planes as is the case with alkaline etching (Torralba et al., 2017). This independence from the crystallographic orientation is obviously an advantage for creating new or more complex patterns.

Modeling

To explain the results obtained experimentally, numerical simulations of the modulation of the silicon valence band induced by the metal (ligaments) and the electrolyte contacts (pores) were performed at the scale of a few tenths of nanometers. For that, we developed a 2D model representing a Si/Electrolyte interface over a distance of 1 μm with 3 gold pads at the center, 20 nm in size and interspacing and surrounded with electrolyte, as described in the experimental section (cf. **Figure D** in **Supplementary Information**). The size of the pads was chosen small enough to apply to both fine (30 nm) and coarse (100 nm) Au nanostructures. Modulations obtained with 20 nm plots and interspacing will only be accentuated at larger sizes. **Figure 8** shows the 2D variations of the valence band laterally and in depth (at low (A) and high magnification (B)) at equilibrium (0 V).

Figure 8A reveals that the silicon valence band is modulated by the gold contacts only at close distance to the surface (<0.1 μm). **Figure 8B** shows that most of this modulation follows the details of the “np-Au nanostructure” whose ligaments are represented by the gold pads.

Figure 9A gives the 1D band diagrams for three cut-lines, one centered under a gold pad ($x = 0.5 \mu\text{m}$), and the other under an electrolyte contact either between two gold pads ($x = 0.48 \mu\text{m}$) or far from them ($x = 0 \mu\text{m}$). From this figure, it can be seen that the two phases (gold and electrolyte) form nano-Schottky junctions of different barrier heights, with an intermediary situation between gold pads.

At the level of Au, the valence band exceeds the Fermi level, which results in a strong inversion regime with an accumulation of holes (valence band above E_F) within the first 3 nm, equivalent to a 2D hole gas. To simulate the electrochemical or chemical etching process, an anodic bias is applied to the np-Au pads with respect to the electrolyte. **Figure 9B** shows the lateral

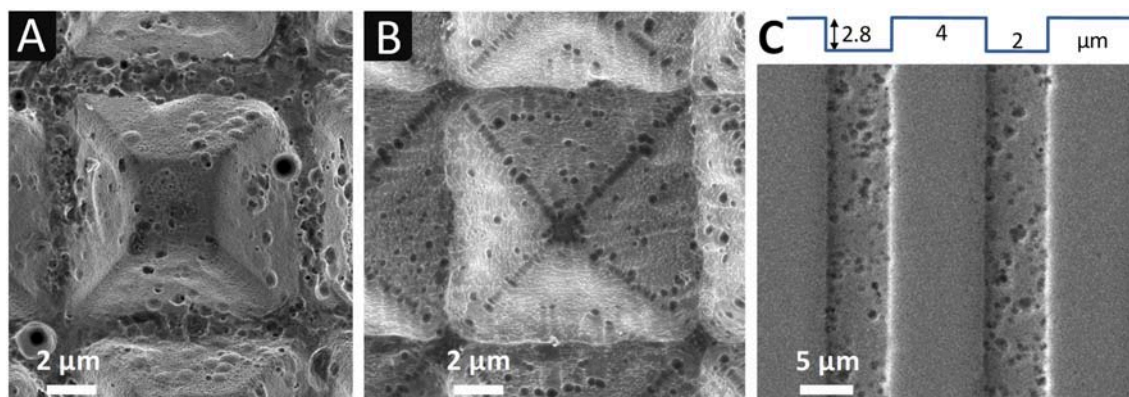


FIGURE 6 | SEM images of silicon surfaces after imprinting inverted pyramids in HF-H₂O₂ with (A) fine np-Au and (B) coarse np-Au, and U-shaped lines with (C) coarse np-Au/Pt electrodes. Electrolyte: HF 5 mol L⁻¹ - H₂O₂ 1 mol L⁻¹, with 2 vol.% EtOH.

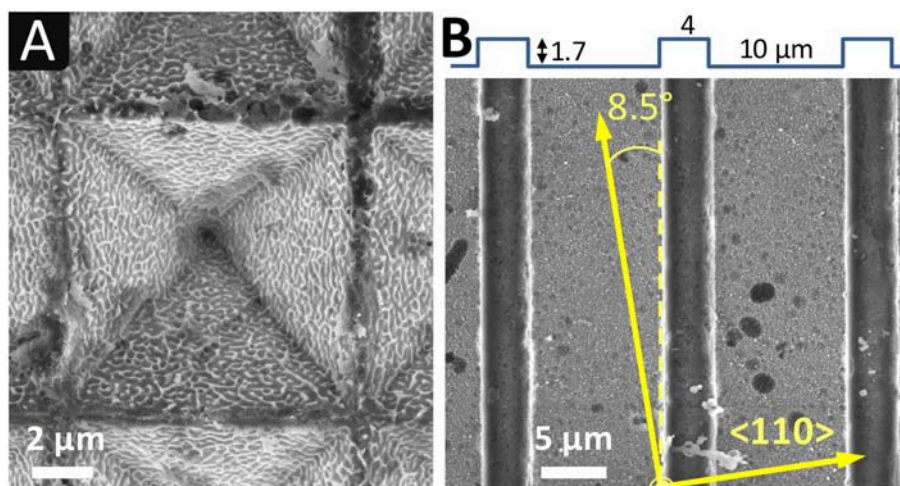


FIGURE 7 | SEM images of silicon surfaces after imprinting chemically (A) inverted pyramids and (B) U-shaped lines in HF-H₂O₂ with coarse np-Au/Pt electrodes. Electrolyte: HF 5 mol L⁻¹ - H₂O₂ 1 mol L⁻¹, with 2 vol.% EtOH. In (B): line offset with respect to <110> directions, as determined by EBSD.

modulations of the valence band energy at the border of the hole accumulation region (3 nm underneath the silicon surface) under positive polarization. The anodic bias of gold (0.1, 0.2 V, and 0.7 V) results in a potential drop occurring mostly at the n-Si/Au interface and slightly at the n-Si/electrolyte junction, especially at the edge of the gold pad (the potential barrier of the Si/Electrolyte junction remains nearly the same). At low applied bias, holes located under the gold pads face an energy barrier and can barely diffuse laterally whereas at high polarization (>0.7 V), this barrier almost disappears which induces a lateral hole flow. The *I*-*V* curves corresponding to the current flowing through the device (two interfaces in series, Au/n-Si/electrolyte) are reported in **Figure 9C**. These simulated curves makes it possible to determine that the etching current is due to a flow of holes despite the n-type doping of Si (holes being minority carriers in the bulk and majority carriers in the inversion layer at the surface).

The simulation results show that the current remains laterally confined very close to the surface, without exchange with the bulk, i.e., without delocalized etching next to the electrode or on the back side of the silicon sample. This agrees with the experimental results described previously. This effect, highly desired because it favors a localized etching around the gold ligaments, is mainly due to the n-type doping which does not lead to an ohmic but rectifying contact with Au, i.e., to a potential barrier that prevents holes from diffusing toward the bulk. Since W_{Pt} and W_{Au} are almost identical (5.7 vs. 5.5 eV, respectively), from a band bending and carrier transport point of view, the situation would be very similar with Pt, in agreement with the ability to imprint pyramids observed with both metal catalysts. On the contrary, in the case of a p-type silicon, the contact is ohmic with both gold and platinum, and therefore there is a delocalized etching, as described for the Pt/p-Si system (Torralba et al., 2016). The silicon walls observed

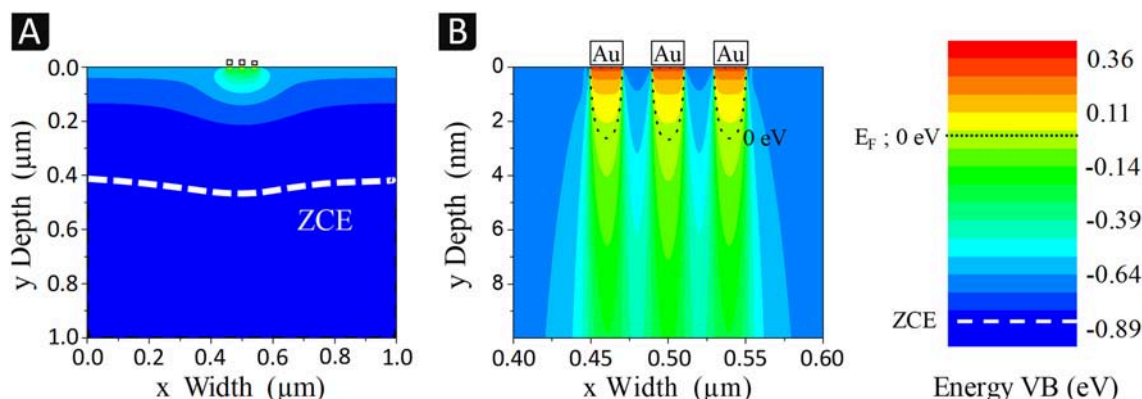


FIGURE 8 | Simulation of 3 gold ligaments (20 nm in size and interspace) surrounded by an electrolyte and in contact with n-type silicon ($3 \times 10^{15} \text{ cm}^{-3}$) through 2D profiles of the valence band energies (referenced to the Fermi level) at equilibrium, at low (A) and high (B) magnification. The VB energy color scale is given on the right-hand side.

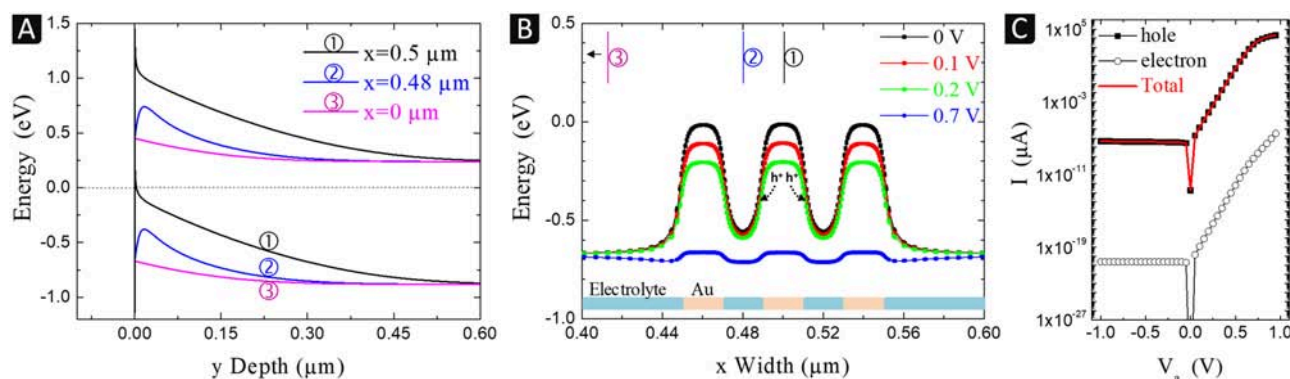


FIGURE 9 | Simulations of: (A) the band bending of n-Si/Au and n-Si/electrolyte junctions with cut-lines (y Depth) corresponding to a gold pad center ($x = 0.5 \mu\text{m}$), an electrolyte contact between two gold pads ($x = 0.48 \mu\text{m}$) and the electrolyte far from gold ($x = 0 \mu\text{m}$); (B) lateral modulations (x Width) of the valence band energies at 3 nm beneath the silicon surface, at 0 V (equilibrium) and under 0.1, 0.2, and 0.7 V bias applied to the gold contacts (cf. **Supplementary Information**); (C) *I*-*V* characteristics of the Au/n-Si/Electrolyte device.

in **Figure 7A**, for example, result from this localization of the etching under the ligaments and not (or less) between them (pores). The height of the walls is nevertheless limited by deeper ligaments in the electrode that come into contact with them as the electrode penetrates the substrate. Under higher positive bias (0.7 V), the lateral band bending at the interface between Au and electrolyte contacts can be canceled (**Figure 9B**) and the diffusion of holes away from n-Si/Au interfaces is possible. The presence of porous silicon observed after chemical etching may be related to this phenomenon. The high oxidative power and concentration of H_2O_2 combined with the large surface area of np-Au can result in a significantly reduced diffusion barrier and a high current of holes along the inversion layer, causing porous silicon to form in areas between or away from the metal ligaments. A more precise study of this effect is needed in future work.

CONCLUSION

The process of patterning silicon at the macroscopic scale by contact etching with nanoporous metal electrodes has been developed in several directions. We have shown that a complete transfer of complex patterns such as square-based pyramids can be obtained by electrochemical or chemical contact etching in n-type Si. The apparent etch rate depends on the type of imprinted patterns, being two to four times lower for U-shaped lines than for pyramids. Using np-Au electrodes of different characteristic sizes (30 and 100 nm) has revealed that this parameter has little influence on pattern transfer. Finally, the influence of the metal catalyzing the etching could be tested under identical conditions by covering the surface of a np-Au electrode with a platinum layer (5 nm). “np-Pt” is also suitable to transfer the pyramid pattern and seems to offer a better resolution.

The surface state after imprinting presents defects (roughness, pores, craters, porous silicon). When np-Au with a fine structure is used, the presence of residual silver in the electrode (related to the dealloying method used to produce this fine structure) strongly degrades the surface state due to silver deposition during etching (formation of craters or pores). With np-Au of coarse structure, the resolution is better, with even the formation of small walls due to imprinting of the gold nanostructure details (ligaments and pores). By simulating the modulation of the valence band on a scale of a few tens of nanometers, we have shown that there are holes under the metal (within 3 nm) because of the inversion regime established with n-type silicon in contact with gold or platinum. A lateral potential barrier in silicon between regions in contact with the metal and the electrolyte prevents these holes to diffuse. Under moderate anodic polarization, etching corresponds to a quasi 2D electron transfer from a metallic contact zone to the adjacent electrolytic zone and is therefore very localized, which explains the formation of small walls at the level of pores in np-Au/(Pt). If the anodic polarization (electrochemical or chemical) is higher, the band bending between the contacts and the electrolyte can be canceled and the dissolution becomes more delocalized without formation of walls.

All these results demonstrate the interest of imprinting 3D patterns in silicon using nanoporous metal electrodes. Further investigations are needed to increase the etch rate, improve the

surface quality and the tolerance to electrode's defects and to test new and more complex pattern transfers.

AUTHOR CONTRIBUTIONS

All authors participated in the design and planning of the research. MH, VM, JH, DY, and J-PV worked on the elaboration of Si molds. ET, EM, and SB performed the patterning experiments and SL the numerical simulations. SB and ET wrote the first draft of the manuscript. All authors provided feedback and participated to the final writing of the manuscript.

ACKNOWLEDGMENTS

The authors acknowledge the support of the French Agence Nationale de la Recherche (ANR), under grant ANR-14-CE07-0005-01 (project PATTERN) and of the French Renatech network for the use of clean room facilities. We are grateful to Rémy Pires for the EBSD analysis and Benjamin Villeroy for the SPS experiments.

SUPPLEMENTARY MATERIAL

The Supplementary Material for this article can be found online at: <https://www.frontiersin.org/articles/10.3389/fchem.2019.00256/full#supplementary-material>

REFERENCES

- Azeredo, B., Hsu, K., and Ferreira, P. (2016a). "Direct electrochemical imprinting of sinusoidal linear gratings into silicon," in *ASME 2016 11th International Manufacturing Science and Engineering Conference*. Blacksburg, VA.
- Azeredo, B. P., Lin, Y.-W., Avagyan, A., Sivaguru, M., Hsu, K., and Ferreira, P. (2016b). Direct imprinting of porous silicon via metal-assisted chemical etching. *Adv. Funct. Mater.* 26, 2929–2939. doi: 10.1002/adfm.201505153
- Azeredo, B. P., Sadhu, J., Ma, J., Jacobs, K., Kim, J., Lee, K., et al. (2013). Silicon nanowires with controlled sidewall profile and roughness fabricated by thin-film dewetting and metal-assisted chemical etching. *Nanotechnology* 24:225305. doi: 10.1088/0957-4484/24/22/225305
- Chartier, C., Bastide, S., and Lévy-Clément, C. (2008). Metal-assisted chemical etching of silicon in HF–H₂O₂. *Electrochimica Acta* 53, 5509–5516. doi: 10.1016/j.electacta.2008.03.009
- Chemla, M., Homma, T., Bertagna, V., Erre, R., Kubo, N., and Osaka, T. (2003). Survey of the metal nucleation processes on silicon surfaces in fluoride solutions: from dilute HF to concentrated NH₄F solutions. *J. Electroanal. Chem.* 559, 111–123. doi: 10.1016/S0022-0728(02)01280-9
- Ding, Y., Kim, Y.-J., and Erlebacher, J. (2004). Nanoporous gold leaf: ancient technology/advanced material. *Adv. Mater.* 16, 1897–1900. doi: 10.1002/adma.200400792
- Fukushima, T., Ohnaka, A., Takahashi, M., and Kobayashi, H. (2011). Fabrication of low reflectivity poly-crystalline si surfaces by structure transfer method. *Electrochem. Solid State Lett.* 14:B13. doi: 10.1149/1.3515990
- Geyer, N., Fuhrmann, B., Huang, Z., de Boor, J., Leipner, H. S., and Werner, P. (2012). Model for the mass transport during metal-assisted chemical etching with contiguous metal films as catalysts. *J. Phys. Chem. C* 116, 13446–13451. doi: 10.1021/jp3034227
- Hözl, J., and Schulte, F. K. (1979). *Solid Surface Physics*. Berlin Heidelberg: Springer-Verlag. Available online at: "www.springer.com/us/book/9783662158098" (accessed November 26, 2018).
- Huang, Z., Fang, H., and Zhu, J. (2007). Fabrication of silicon nanowire arrays with controlled diameter, length, and density. *Adv. Mater.* 19, 744–748. doi: 10.1002/adma.200600892
- Huang, Z., Geyer, N., Werner, P., de Boor, J., and Gösele, U. (2011). Metal-assisted chemical etching of silicon: a review: in memory of prof. Ulrich Gösele. *Adv. Mater.* 23, 285–308. doi: 10.1002/adma.201001784
- Huang, Z. P., Geyer, N., Liu, L. F., Li, M. Y., and Zhong, P. (2010). Metal-assisted electrochemical etching of silicon. *Nanotechnology* 21:465301. doi: 10.1088/0957-4484/21/46/465301
- Imamura, K., Akai, T., and Kobayashi, H. (2015). High aspect ratio Si micro-holes formed by wet etching using Pt needles. *Mater. Res. Express* 2:075901. doi: 10.1088/2053-1591/2/7/075901
- Ki, B., Song, Y., Choi, K., Yum, J. H., and Oh, J. (2018). Chemical imprinting of crystalline silicon with catalytic metal stamp in etch bath. *ACS Nano* 12, 609–616. doi: 10.1021/acsnano.7b07480
- Lee, C.-L., Kanda, Y., Hirai, T., Ikeda, S., and Matsumura, M. (2009). Electrochemical grooving of si wafers using catalytic wire electrodes in HF solution. *J. Electrochem. Soc.* 156:H134. doi: 10.1149/1.3033735
- Lee, C.-L., Kanda, Y., Ikeda, S., and Matsumura, M. (2011). Electrochemical method for slicing Si blocks into wafers using platinum wire electrodes. *Sol. Energy Mater. Sol. Cells* 95, 716–720. doi: 10.1016/j.solmat.2010.10.009
- Lee, C.-L., Tsujino, K., Kanda, Y., Ikeda, S., and Matsumura, M. (2008). Pore formation in silicon by wet etching using micrometre-sized metal particles as catalysts. *J. Mater. Chem.* 18, 1015–1020. doi: 10.1039/B715639A
- Moreau, W. M. (1988). *Semiconductor Lithography: Principles, Practices, and Materials*. Springer. Available online at: <https://www.springer.com/us/book/9781461282280> (accessed March 20, 2019).
- Nakato, Y., Ueda, K., Yano, H., and Tsubomura, H. (1988). Effect of microscopic discontinuity of metal overlayers on the photovoltages in metal-coated semiconductor-liquid junction photoelectrochemical cells for efficient solar energy conversion. *J. Phys. Chem.* 92, 2316–2324. doi: 10.1021/j100319a043
- Nassiopoulou, A. G., Gianneta, V., and Katsogridakis, C. (2011). Si nanowires by a single-step metal-assisted chemical etching process on

- lithographically defined areas: formation kinetics. *Nanoscale Res. Lett.* 6:597. doi: 10.1186/1556-276X-6-597
- Peng, K.-Q., Yan, Y.-J., Gao, S.-P., and Zhu, J. (2002). Synthesis of large-area silicon nanowire arrays via self-assembling nanoelectrochemistry. *Adv. Mater.* 14, 1164–1167. doi: 10.1002/1521-4095(20020816)14:16<1164::AID-ADMA1164>3.0.CO;2-E
- Qian, L. H., and Chen, M. W. (2007). Ultrafine nanoporous gold by low-temperature dealloying and kinetics of nanopore formation. *Appl. Phys. Lett.* 91:083105. doi: 10.1063/1.2773757
- Rossi, R. C., and Lewis, N. S. (2001). Investigation of the size-scaling behavior of spatially nonuniform barrier height contacts to semiconductor surfaces using ordered nanometer-scale nickel arrays on silicon electrodes. *J. Phys. Chem. B* 105, 12303–12318. doi: 10.1021/jp011861c
- Salem, M. S., Lee, C.-L., Ikeda, S., and Matsumura, M. (2010). Acceleration of groove formation in silicon using catalytic wire electrodes for development of a slicing technique. *J. Mater. Process. Technol.* 210, 330–334. doi: 10.1016/j.jmatprotec.2009.09.019
- Sugita, T., Hiramatsu, K., Ikeda, S., and Matsumura, M. (2013). Pore formation in a p-Type silicon wafer using a platinum needle electrode with application of square-wave potential pulses in HF solution. *ACS Appl. Mater. Interfaces* 5, 1262–1268. doi: 10.1021/am302314y
- Sugita, T., Lee, C.-L., Ikeda, S., and Matsumura, M. (2011). Formation of through-holes in Si wafers by using anodically polarized needle electrodes in HF solution. *ACS Appl. Mater. Interfaces* 3, 2417–2424. doi: 10.1021/am2003284
- Takahashi, M., Fukushima, T., Seino, Y., Kim, W.-B., Imamura, K., and Kobayashi, H. (2013). Surface structure chemical transfer method for formation of ultralow reflectivity Si surfaces. *J. Electrochem. Soc.* 160, H443–H445. doi: 10.1149/2.044308jes
- Torralba, E., Halbwax, M., El Assimi, T., Fouchier, M., Magnin, V., Harari, J., et al. (2017). 3D patterning of silicon by contact etching with anodically biased nanoporous gold electrodes. *Electrochem. Commun.* 76, 79–82. doi: 10.1016/j.elecom.2017.01.014
- Torralba, E., Le Gall, S., Lachau, R., Magnin, V., Harari, J., Halbwax, M., et al. (2016). Tunable surface structuration of silicon by metal assisted chemical etching with Pt nanoparticles under electrochemical bias. *ACS Appl. Mater. Interfaces* 8, 31375–31384. doi: 10.1021/acsami.6b09036
- Zhan, D., Han, L., Zhang, J., He, Q., Tian, Z.-W., and Tian, Z.-Q. (2017). Electrochemical micro/nano-machining: principles and practices. *Chem Soc Rev* 46, 1526–1544. doi: 10.1039/C6CS00735J
- Zhang, J., Zhang, L., Han, L., Tian, Z.-W., Tian, Z.-Q., and Zhan, D. (2017a). Electrochemical nanoimprint lithography: when nanoimprint lithography meets metal assisted chemical etching. *Nanoscale* 9, 7476–7482. doi: 10.1039/C7NR01777D
- Zhang, J., Zhang, L., Wang, W., Han, L., Jia, J.-C., Tian, Z.-W., et al. (2017b). Contact electrification induced interfacial reactions and direct electrochemical nanoimprint lithography in n-type gallium arsenate wafer. *Chem. Sci.* 8, 2407–2412. doi: 10.1039/c6sc04091h

Conflict of Interest Statement: The authors declare that the research was conducted in the absence of any commercial or financial relationships that could be construed as a potential conflict of interest.

Copyright © 2019 Bastide, Torralba, Halbwax, Le Gall, Mpogui, Cachet-Vivier, Magnin, Harari, Yarekha and Vilcot. This is an open-access article distributed under the terms of the Creative Commons Attribution License (CC BY). The use, distribution or reproduction in other forums is permitted, provided the original author(s) and the copyright owner(s) are credited and that the original publication in this journal is cited, in accordance with accepted academic practice. No use, distribution or reproduction is permitted which does not comply with these terms.



Cavitation Induced by Janus-Like Mesoporous Silicon Nanoparticles Enhances Ultrasound Hyperthermia

Andrey Sviridov^{1*†}, Konstantin Tamarov^{1,2†}, Ivan Fesenko^{1,3}, Wujun Xu², Valery Andreev¹, Victor Timoshenko^{1,3,4} and Vesa-Pekka Lehto²

¹ Faculty of Physics, M. V. Lomonosov Moscow State University, Moscow, Russia, ² Department of Applied Physics, University of Eastern Finland, Kuopio, Finland, ³ Institute of Engineering Physics for Biomedicine, National Research Nuclear University MEPhI, Moscow, Russia, ⁴ Lebedev Physical Institute of the Russian Academy of Sciences, Moscow, Russia

OPEN ACCESS

Edited by:

Thierry Djenizian,
École des Mines de
Saint-Étienne–Campus Georges
Charpak Provence, France

Reviewed by:

Rinat Esenaliev,
The University of Texas Medical
Branch at Galveston, United States
Arkadiusz Jozefczak,
Adam Mickiewicz University in
Poznan, Poland

*Correspondence:

Andrey Sviridov
asagittarius89@gmail.com

[†]These authors have contributed
equally to this work

Specialty section:

This article was submitted to
Chemical Engineering,
a section of the journal
Frontiers in Chemistry

Received: 04 February 2019

Accepted: 16 May 2019

Published: 05 June 2019

Citation:

Sviridov A, Tamarov K, Fesenko I,
Xu W, Andreev V, Timoshenko V and
Lehto V-P (2019) Cavitation Induced
by Janus-Like Mesoporous Silicon
Nanoparticles Enhances Ultrasound
Hyperthermia. *Front. Chem.* 7:393.
doi: 10.3389/fchem.2019.00393

The presence of nanoparticles lowers the levels of ultrasound (US) intensity needed to achieve the therapeutic effect and improves the contrast between healthy and pathological tissues. Here, we evaluate the role of two main mechanisms that contribute to the US-induced heating of aqueous suspensions of biodegradable nanoparticles (NPs) of mesoporous silicon prepared by electrochemical etching of heavily boron-doped crystalline silicon wafers in a hydrofluoric acid solution. The first mechanism is associated with an increase of the attenuation of US in the presence of NPs due to additional scattering and viscous dissipation, which was numerically simulated and compared to the experimental data. The second mechanism is caused by acoustic cavitation leading to intense bubble collapse and energy release in the vicinity of NPs. This effect is found to be pronounced for as-called Janus NPs produced via a nano-stopper technique, which allow us to prepare mesoporous NPs with hydrophobic inner pore walls and hydrophilic external surface. Such Janus-like NPs trap air inside the pores when dispersed in water. The precise measurement of the heating dynamics *in situ* enabled us to detect the excessive heat production by Janus-like NPs over their completely hydrophilic counterparts. The excessive heat is attributed to the high intensity cavitation in the suspension of Janus-like NPs. The present work elicits the potential of specifically designed Janus-like mesoporous silicon NPs in the field of nanotheranostics based on ultrasound radiation.

Keywords: porous silicon, nanoparticles, therapeutic ultrasound, hyperthermia, heating, selective modification, hydrophobic, hydrophilic

INTRODUCTION

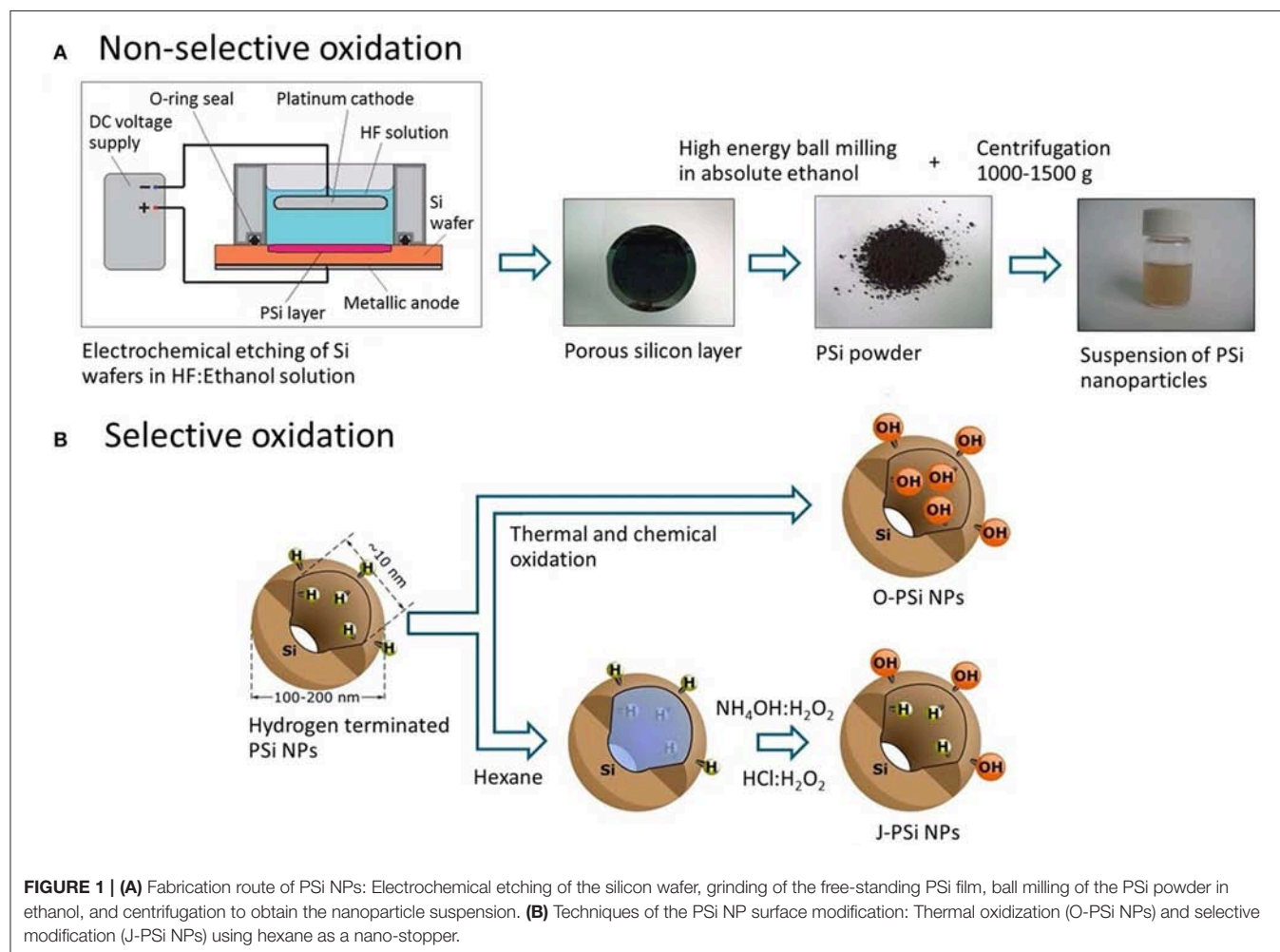
Hyperthermia is considered to be one of the most popular and well-studied treatment modalities in cancer therapy (Wust et al., 2002). This non-ionizing treatment is based on the temperature rise in the tumor, that makes cancer cells more susceptible to radio- and chemotherapy due to the heat-induced chemosensitization (Issels, 2008) and tumor tissue oxygenation (Song et al., 2001). Furthermore, some specific proteins provide healthy and malignant cells with different hyperthermal sensitivity leading to the selective destruction of the tumor (Setroikromo et al., 2007).

There are several methods to produce hyperthermia, but the general aim is to generate hyperthermia locally with external electromagnetic radiation (Tamarov et al., 2014) or ultrasound (US) (Diederich and Hynynen, 1999) sources. US, being widely used in modern medicine (Hill et al., 2005), is one of the most promising and effective external sources for the local hyperthermia. This is due to its numerous advantages over laser or electromagnetic wave sources: low invasiveness, precise focusing, and excellent penetration depth. These features are crucial for the local thermo-ablation of both benign and malignant tumors deep inside the body without causing serious harm to the skin or the adjacent healthy tissues (Bessonova et al., 2009; Miller et al., 2012).

Currently available US-mediated treatment techniques employ high-intensity focused ultrasound (HIFU) sources, which enable a relatively high degree of accuracy and agility (Frazier et al., 2006; Tempny et al., 2011). However, the utilization of HIFU has several drawbacks. In the technique, the precise and expensive focusing equipment is required to achieve the absorption contrast between the normal tissues and the lesion sites (Haar and Coussios, 2007). Due to the small focal region of

HIFU, the volume of the tissue to be ablated is limited leading to long exposure times, which can cause undesired thermal injuries and DNA mutations in the surrounding healthy tissues due to the US waves reflected from interfaces (Chatterjee et al., 2011).

Special micro- and nanoagents, sometimes referred as sonosensitizers (Deepagan et al., 2016), were proposed to overcome the limitations of HIFU ablation. Sonosensitizers can significantly enhance the therapeutic efficiency by reducing the US intensity and duration necessary for the therapeutic effect (Sviridov et al., 2015; Kosheleva et al., 2016). The recent advances in nanobiotechnology and nanomedicine have directed the researchers to create various types of sonosensitizers. For example, solid gold (Kosheleva et al., 2016), magnetic (Józefczak et al., 2016), and silicon (Sviridov et al., 2015) NPs, as well as highly heat-conducting graphene oxide nanosheets (Darabdhara et al., 2015), are good mediators for the US-induced hyperthermia because of significant energy release via the US absorption. Mesoporous silicon-based NPs enhance the cavitation effect of US (Kharin et al., 2015; Sviridov et al., 2015), which leads to the additional heating of the surroundings and initiation of sonochemical reactions and sonoluminescence, i.e.,



light generation (Qian et al., 2016). TiO_2 , polyhydroxy fullerene, alumina, and platinum NPs can respond to US by generating reactive oxygen species for the sonodynamic therapy (Serpe et al., 2012; Canavese et al., 2018; Pan et al., 2018). Furthermore, different nanocomposites and nanocontainers can be used to enhance synergistic effects of US treatment modalities as well (Qian et al., 2017).

Biomedical applications of solid sonosensitizers are usually limited due to their cytotoxicity and low biodegradability (Yildirim et al., 2011). In this regard, biocompatible and biodegradable porous silicon (PSi) NPs seem to be very promising material for various medical applications (Sviridov et al., 2017). We have previously demonstrated that the presence of NPs led to the temperature difference between the aqueous PSi NP suspensions and distilled water under US irradiation (Sviridov et al., 2013). There, the high heating efficiency was achieved in the acoustic resonator, which increased the US wave amplitude by several orders of magnitude. Unfortunately, the geometry of resonator is not applicable *in vivo*.

In our recent study, Janus-like PSi NPs were designed to be specifically employed with ultrasound. In these NPs, the pore walls were hydrophobic and the external surfaces of NPs were hydrophilic giving sustainability in aqueous solution while maintaining air inside the pores (Tamarov et al., 2017). The present work compares the enhanced heating effects produced by fully oxidized, hydrophilic PSi NPs (O-PSi NPs), and Janus-like PSi NPs (J-PSi NPs) in the field of the US traveling wave, and it explains the phenomenology behind the exceptional cavitation and heating capability of these NPs. The pronounced temperature rise in the area of the NP localization can be applied to the hyperthermia treatment of tumors, or for the purposes of drug release from PSi NPs coated with thermo-sensitive polymers (Tamarov et al., 2016).

MATERIALS AND METHODS

Materials

Si wafers (diameter 20 cm, p^+ (100), 0.01–0.02 $\Omega\cdot\text{cm}$, Okmetic Inc.), ethanol (EtOH, absolute, Altia Oyj), ammonium hydroxide (NH_4OH , 28%, VWR), hydrogen peroxide (H_2O_2 , >30% w/v, Fisher Scientific), n-hexane ($\geq 99\%$, Merck), toluene (anhydrous, 99.8%, Alfa Aesar), hydrofluoric acid (38%, Merck) were used as received.

Preparation of PSi NPs

First, free-standing PSi (pore size ~ 10 nm) films were prepared by anodizing p^+ -type silicon wafers (100) with the resistivity of 0.01–0.02 $\Omega\cdot\text{cm}$ in a HF (38%)-ethanol mixture (Bimbo et al., 2010). After drying at 65°C for 1 h, the obtained films were ground in a mortar and then ball milled in ethanol to produce PSi NPs. The overall sequence of preparation steps is depicted in Figure 1A.

In order to prepare J-PSi NPs, hexane was used as a nano-stopper (Xu et al., 2014; Tamarov et al., 2017) to protect hydrogen terminated (hydrophobic) pore walls that were the result of etching. Second, the unprotected outer surface was selectively oxidized in $\text{NH}_4\text{OH}:\text{H}_2\text{O}_2$ (30%): H_2O 1:1:6 at RT for 15 min and in $\text{HCl}:\text{H}_2\text{O}_2$ (30%): H_2O 1:1:6 for 15 min, subsequently. This is possible since hexane is a non-polar solvent and does not mix with aqueous solutions. Next, PSi NPs were washed in water and stored in absolute ethanol. As a reference sample, fully hydrophilic nanoparticles were prepared through non-selective oxidation of PSi nanoparticles as described previously (Näkki et al., 2015) and are denoted as O-PSi NPs. These ways of surface modification are shown in Figure 1B.

Characterization of PSi NPs

The surface composition after each step of the surface modification was verified with FTIR transmittance (Thermo Nicolet Nexus 8700) measurements of the KBr tablets containing the PSi NPs. The morphology of PSi NPs was imaged with

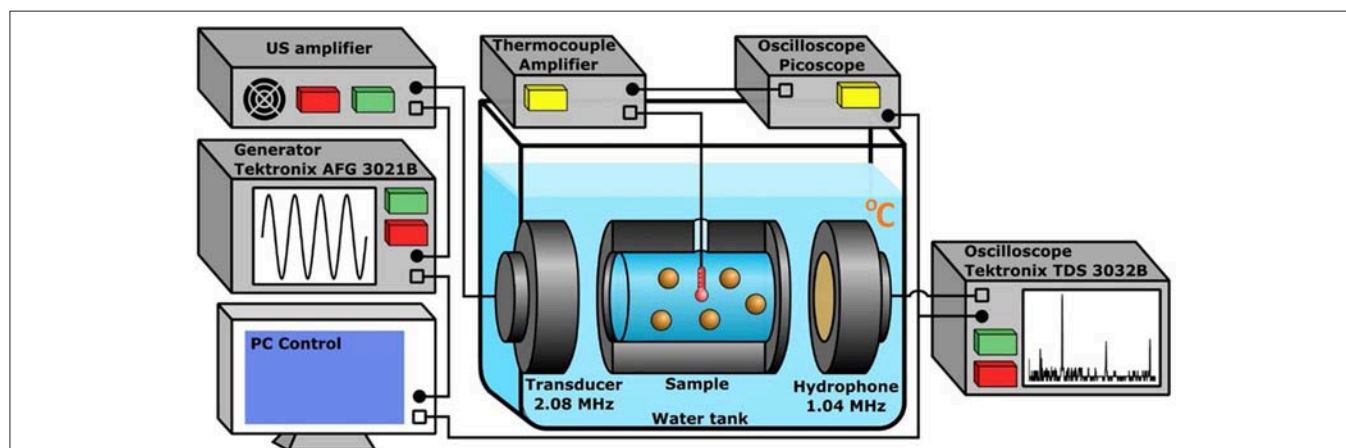


FIGURE 2 | The experimental setup used for the heating measurement and cavitation detection in aqueous suspensions of PSi NPs. The cuvette, US transducer, and hydrophone are immersed into the water tank. The amplified sinusoidal signal from the generator is irradiated by the transducer, the oscilloscope collects data from the hydrophone and performs FFT. The E-type thermocouple measures the heating. The PC reads data from the oscilloscopes and controls the generator.

transmission electron microscopy (TEM) in a JEOL JEM-2100F microscope. Dynamic light scattering (DLS, Malvern Instruments Zetasizer Nano ZS) was used to measure the hydrodynamic diameters of the NP samples in deionized water. Diluted suspensions (<0.2 mg/ml) were equilibrated at 25°C for 5 min prior to the measurements.

Measurements of Heating

A specific setup was developed for the measurement of heating in the suspensions of PSi NPs. The core part of the setup consisted of an aluminum cylindrical sample chamber (cuvette) with two US transparent windows located between a flat transducer and a hydrophone immersed into a water tank (**Figure 2**). The volume of the cuvette was ~15 ml. The transducer with a diameter of 10 mm emitted a low-divergence US beam of frequency 2,080 kHz, which heated the samples. The diameter of windows was 25 mm and coincided with the internal diameter of the cuvette of 30 mm length. The distance between the transducer and cuvette was 10 mm, while the distance from the cuvette to the hydrophone was 50 mm. The transducer was connected to a custom-made US amplifier (output power of 75 W at 50 Ohms load in the frequency band of 1–5 MHz), which amplified the sinusoidal signal from a generator (Tektronix AFG 3021B). The matching of the output impedance of the amplifier with the piezotransducer was provided by trimming inductance. Simultaneously with temperature, the cavitation intensity was measured by detecting the subharmonic magnitude of US wave passing through the cuvette. For this purpose, an oscilloscope (Tektronix TDS 3032B) recorded a signal from the hydrophone within 0.1 ms, averaged it over 32 successive realizations and calculated the spectrum of the averaged signal. Hamming function was chosen as a time interval window. The generator and oscilloscope were connected to a PC with a custom NI™ LabVIEW 2013 (National Instruments Corp., Austin, TX) program to control the experiment. The obtained spectra were recorded with a repetition rate of 3 Hz.

The temperature was measured with a highly sensitive chromel-constantan E-type thermocouple (TC, OMEGA Engineering) encased in the cylindrical sheath with a diameter of 0.25 mm. The TC was inserted into the cuvette center. The TC signal was amplified by a self-made amplifier powered by a battery, which significantly lowered the level of electromagnetic noise. The amplified TC signal was registered by an oscilloscope (PicoScope 5204) and then loaded into the PC memory for storage and subsequent processing. The TC was calibrated in advance for the temperature range of 20–40°C using a mercury thermometer. The used TC model (thermocouple in a thin metal tube with earthing, EMQSS-010G-12) has a minimum response time of 0.2 s (**Figure S1**), which makes it possible to measure not only slow temperature trends, but also its rapid fluctuations. Special control experiments were carried out to ensure that the metal tube with the TC itself did not enhance cavitation in the investigated ranges of US power and concentration of PSi NPs. The collapse of cavitation bubbles on the surface of PSi NPs creates their overheating, which in turn leads to local heating of the medium. Such temperature fluctuations are rather random, since their magnitude is defined by the number of cavitation

bubbles near the TC. The duration of local fluctuations is small, so a quick-response thermocouple is required to register them.

Cavitation Measurements

Cavitation is known to be an important factor which influences the process of heating in aqueous suspensions and biological media. The threshold and intensity of acoustic cavitation can be determined by the appearance of subharmonic component and its magnitude in the spectrum of the signal recorded by the hydrophone (Didenkulov et al., 2011). The setup described above (see **Figure 2**) enabled the initiation and detection of cavitation in the suspensions of PSi NPs. In order to specifically amplify the subharmonic signal, the resonance frequency of the hydrophone was half (1.04 MHz) of the resonance frequency of the transducer (2.08 MHz). The cavitation threshold was measured by detecting the pressure amplitude, which corresponded to an abrupt growth of subharmonic magnitude extracted from the spectrum along with the fundamental and high-order harmonics (**Figure S3A**). The voltage on the transducer was increased stepwise to provide a change of acoustic pressure in the range of 0.3–0.5 MPa (**Figure S4**). Such pressure amplitudes were beyond the cavitation thresholds for the suspensions of Si NPs and water (Tamarov et al., 2017), because the level of subharmonic (in dB) remained much higher than the noise level throughout the period of exposure (blue dashed line in **Figure S3B**). At each pressure, the harmonics were measured for 200 s and their average values for this period were calculated to obtain the mean magnitudes (red dashed line in **Figure S3B**). Relative errors for each pressure were calculated as mean square deviations of normal distributions of the subharmonic magnitude smoothed by 10 points (**Figure S3C**).

NUMERICAL CALCULATION OF TEMPERATURE GROWTH

The absorption of US energy in aqueous suspensions is associated with the relative motion of solid nanoparticles under the US wave field. In a viscous medium, the Stokes force is exerted on a particle leading to inconvertible heat losses, which depend on the ratio of the particle and medium densities, particle size and medium viscosity. The temperature T of the medium in which the US wave of intensity I propagates can be calculated using the heat transfer equation:

$$\frac{\partial T}{\partial t} = \chi \nabla^2 T + \frac{2\alpha I}{\rho_0 c_p}, \quad (1)$$

where t is the time variable, ∇^2 is Laplacian operator, $\chi = \kappa/\rho_0 c_p$ is the thermal diffusivity, κ is the thermal conductivity, α is the US absorption coefficient in the medium, I is the US intensity, ρ_0 and c_p are the medium density and the specific heat capacity, respectively.

To calculate the heating for a given set of parameters using Equation (1), one needs first to define the absorption coefficient α . The work of R. J. Urlick is considered to be a classic work which estimated the attenuation coefficient of nanoparticle suspensions

(Urlick, 1948). According to this work, the attenuation coefficient α_a of US wave of frequency ω in a medium with spherical particles of radius a can be written as a sum of two terms. The first term describes the process of wave scattering and is negligibly small for nano-sized particles, while the second one is associated directly with the absorption:

$$\alpha_a = \alpha_w + \frac{C}{2} \cdot \left[\frac{1}{6} k^4 a^3 + k(\theta - 1)^2 \frac{s}{s^2 + (\theta + \tau)^2} \right], \quad (2)$$

where the following notations are used:

$$s = \frac{9}{4\beta a} \left(1 + \frac{1}{\beta a} \right), \quad \tau = \frac{1}{2} + \frac{9}{4\beta a}, \quad \theta = \frac{\rho_1}{\rho_0}, \quad \beta = \left(\frac{\omega}{2\mu} \right)^{\frac{1}{2}},$$

$$C = \frac{4}{3} \pi a^3 n = \frac{v}{\rho_1},$$

$k = 2\pi f/c$ is the wavenumber, c is the speed of sound in the medium, μ is the kinematic viscosity coefficient, ρ_0 is the medium density, ρ_1 is the nanoparticle density, C is the volume concentration of nanoparticles. The absorption coefficient of water α_w for the MHz range of US frequencies f can be estimated using the following formula:

$$\alpha_w = \alpha_{1w} \cdot f^2, \quad (3)$$

where α_{1w} is the absorption coefficient of water for the frequency of 1 MHz, the frequency f is expressed in MHz.

The heating of an aqueous suspension exposed to US radiation during time t_1 can be calculated using a 1D heat transfer equation due to an axial symmetry of the experimental setup (see **Figure 2**; **Figure S2**):

$$\frac{\partial T}{\partial t} = \chi \frac{\partial^2 T}{\partial r^2} + \frac{2\alpha I}{\rho_0 c_p}, \quad 0 < r \leq R_{beam}, \quad (4)$$

$$\frac{\partial T}{\partial t} = \chi \frac{\partial^2 T}{\partial r^2}, \quad R_{beam} < r < R_{cuv},$$

where r is the radial coordinate, R_{beam} is the US beam radius, R_{cuv} is the radius of the cuvette filled with the suspension. The physical constants and model parameters are enumerated in **Table S1**. The initial and first-type (Dirichlet) boundary conditions are:

$$t = 0: T = T_0, \quad 0 \leq r \leq R_{cuv}; \quad (5a)$$

$$r = 0: -\chi \rho_0 c_p \frac{\partial T}{\partial r} = 0, \quad 0 < t \leq t_1; \quad (5b)$$

$$r = R_{cuv}: T = T_0, \quad 0 < t \leq t_1, \quad (5c)$$

where t_1 is the time of exposure, T_0 is the initial temperature of the sample equilibrated to the temperature of water in the tank.

Here, Equation (5b) takes into account the symmetry of the system and Equation (5c) assumes the thermostabilized

border of the cuvette wall made of aluminum with high thermal conductivity. It is also assumed that the presence of NPs at the studied concentrations negligibly changes the specific heat capacity and density of water. At the US beam-suspension border, the boundary conditions are the temperature and heat flux equality:

$$T_1|_{r=R_{beam}} = T_2|_{r=R_{beam}}; \quad (6a)$$

$$-\kappa \frac{\partial T_1}{\partial r} \Big|_{r=R_{beam}} = -\kappa \frac{\partial T_2}{\partial r} \Big|_{r=R_{beam}}. \quad (6b)$$

In case of the suspension cooling succeeding the US-induced heating, the problem is reduced to the following set of equations:

$$\frac{\partial T}{\partial t} = \chi \frac{\partial^2 T}{\partial r^2}, \quad 0 < r < R_{cuv}; \quad (7a)$$

$$t = t_1: T = T(t_1), \quad 0 \leq r \leq R_{cuv}; \quad (7b)$$

$$r = R_{cuv}: T = T_0, \quad t_1 < t \leq t_2, \quad (7c)$$

where $T(t_1)$ is the temperature distribution in the cuvette just after the heating phase, $(t_2 - t_1)$ is the time of cooling.

The effective attenuation coefficients α_{eff} of the polydisperse suspensions of PSi NPs were calculated for the distributions of particle sizes a , which were measured using the DLS technique (see section Characterization of PSi NPs) and approximated using lognormal functions $f(x)$ (Sviridov et al., 2013):

$$\alpha_{eff} = \frac{\int f(a) \alpha(a) da}{\int f(a) da}, \quad f(x) = A + \frac{B}{\sqrt{2\pi} x \sigma} e^{-(\ln x - m)^2 / 2\sigma^2}, \quad (8)$$

where the attenuation coefficient $\alpha(a)$ for each particle size can be calculated using Equation (2). The coefficients of lognormal functions for the size distributions of O-PSi NPs and J-PSi NPs are given at the bottom of **Table S1**.

Equation (4) was solved numerically using an implicit four-point difference scheme in MATLAB® (the Mathworks, Natick, MA) (Ames, 1992). The number of time and space mesh nodes was equal to 1,000 to provide an appropriate accuracy. An example of the radial temperature distribution calculated for the parameters specified in **Table S1** is given in **Figure S2** and is in accordance with the result one may predict: The heating effect dominates in the region of cuvette irradiated with the US and vanishes fast with the distance from the beam boundary.

Note, the temperature effect of US in the suspension of PSi NPs can be also analyzed by considering more sophisticated approaches, i.e., the Epstein, Carhart, Allegra, and Hawley (ECAH) theory, which takes into account the contributions from viscous and thermal transport processes at the interface

of inhomogeneities, as well as intrinsic absorption in the components of the heterogeneous system (Allegra and Hawley, 1972). The dipole (first-order) contribution from the relative motion of spheres in respect to the molecules in the suspending fluid is predominant in case of large density differences between the suspended matter and that of the suspending fluid (even for materials with mean porosity of 40–60%, as it is valid for mesoporous silicon matrix). This first-order term is incorporated both into the ECAH model by including shear waves and into the model of Urlick by using the Stokes calculation of the energy loss of a pendulum oscillating in a viscous fluid. At the other hand, the zero-order contribution, which takes into account the difference of attenuation between the substances comprising the suspension and heat flow between the particle and the suspending fluid, is 1–2 orders of magnitude smaller than the first-order contribution for rigid particles, by contrast with the case of emulsions, viscous suspending fluids and low-density particles like polystyrene (Allegra and Hawley, 1972). Therefore, we consider the results obtained by using the model of Urlick (1948) quite satisfactory to analyze the US-induced heating dynamics in aqueous suspensions of PSi NPs.

RESULTS AND DISCUSSION

Characterization of PSi NPs

Both the O-PSi and J-PSi NPs had irregular shapes (Figures 3A,B) due to the top-down fabrication method (Nissinen et al., 2016). The sizes of all the investigated NPs were in the range of 20–300 nm with the maximum close to 100 nm (Figure 3C), which are appropriate to provide temperature contrast with the surrounding medium under exposure to US, but are still small enough to reach distant tissues when considering their biomedical applications. FTIR measurements revealed that the pristine material of PSi displayed intense bands between 2,000 and 2,170 cm^{-1} due to the surface Si-H_x ($x = 1-3$) groups (Figure 3D) (Riikonen et al., 2012). After the complete surface oxidation (O-PSi), an intense peak at 1,000–1,200 cm^{-1} of Si-O_x bonds appeared, while the peak from Si-H_x disappeared completely. However, in the case of the J-PSi NPs, the intensity of Si-O_x was lower, and a small amount of Si-H_x bands was still present, indicating the success of production of J-PSi NPs to preserve Si-H groups on the inner pore surfaces.

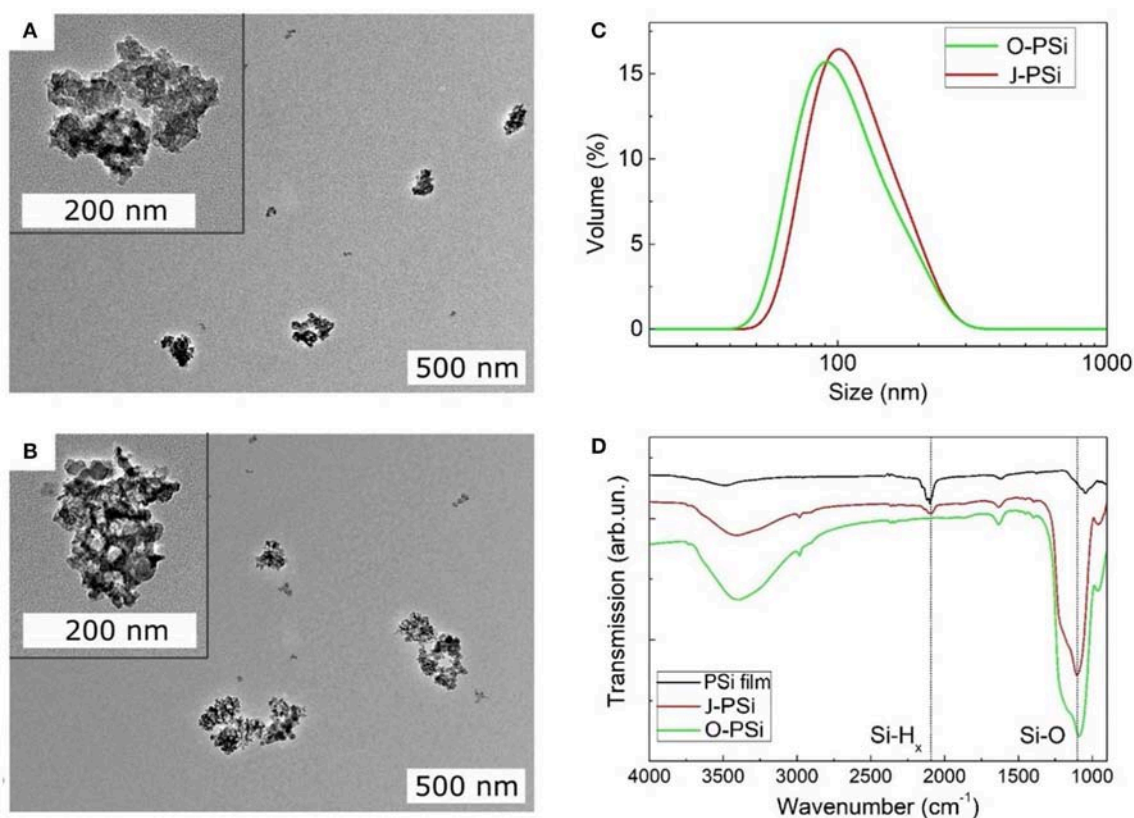
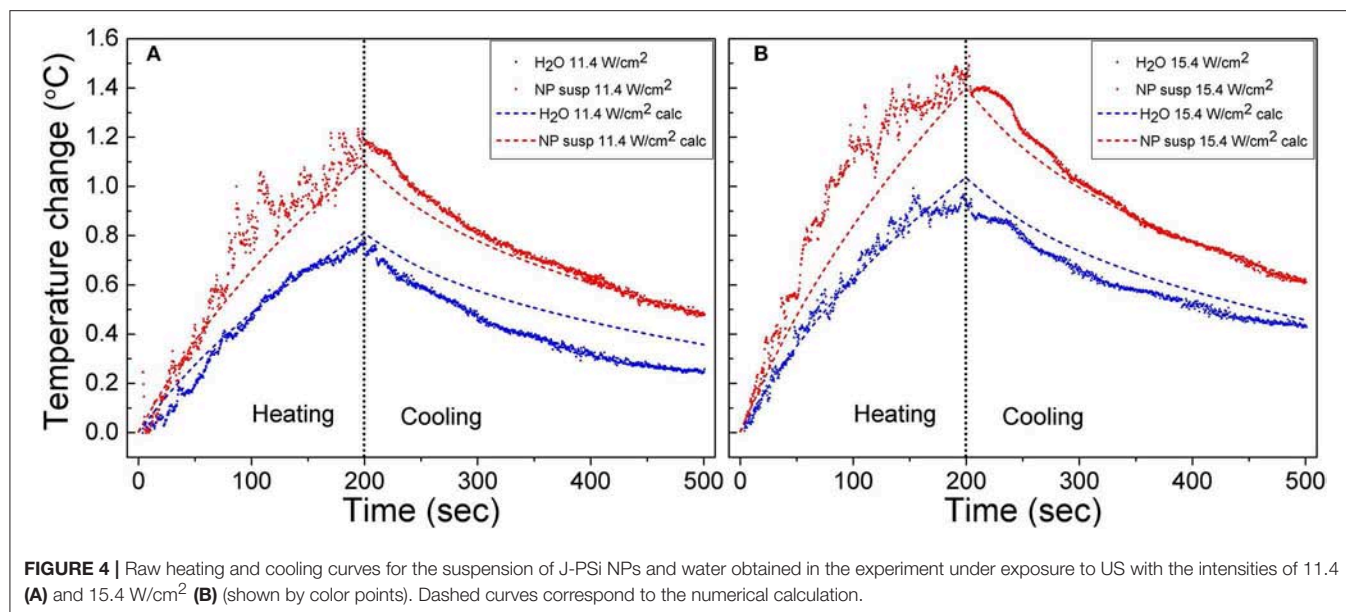


FIGURE 3 | Material characterization of the PSi NPs. **(A,B)** The TEM images of TO-PSi NPs and J-PSi NPs, respectively; the insets show the NPs at a smaller scale. **(C)** Hydrodynamic size distributions of O-PSi NPs (green line) and J-PSi NPs (red line) in water. **(D)** FTIR spectra of the hydrogen terminated pristine PSi NPs (black line), O-PSi NPs (green line), and J-PSi NPs (red line).



Measurement and Calculation of Temperature Evolution

The heating dynamics of the aqueous J-PSi NP suspensions was investigated under US radiation within 200 s, as well as the subsequent cooling dynamics for 300 s after the US radiation was turned off. The characteristic time of heat diffusion from a heated cylindrical volume of radius $R_{beam} = 5$ mm can be estimated as:

$$\tau_T \approx \frac{R_{beam}^2}{\chi} \approx 175 \text{ s.} \quad (9)$$

For the times considerably shorter than τ_T , the temperature at the center of the cuvette grows approximately linearly after the US radiation is turned on. The process of heat diffusion becomes significant at the times exceeding τ_T : The temperature increase slows down and its value reaches a constant level. As the US was turned off, the heated area spread over a distance comparable with R_{beam} , being less than $R_{cuv} = 12.5$ mm. This estimation justifies the boundary conditions Equations (5c, 7c) of the heat-transfer equation, where the influence of metallic wall is negligible. To study in detail all the characteristic features of the US-induced heating and subsequent cooling of the suspensions, the US exposure time of 200 s and cooling observation time of 300 s were selected. The values of the temperature changes in the suspensions under the experimental conditions were about 1°C. To ensure a minimal measurement error, the initial temperatures of the suspension in the cuvette and the water in the tank were equalized with an accuracy of 0.1°C. Data from the thermocouple were recorded synchronously with the spectrum of the US wave transmitted through the cuvette at the frequency of 3 Hz.

The raw experimental data and temperature curves calculated using Equation (4) for the suspensions of J-PSi NPs and

distilled water under exposure to US with the intensities of 11.4 and 15.4 W/cm² are given in **Figure 4**. The selected model describes the dynamics of heating with a sufficient degree of accuracy. At the US intensity of 11.4 W/cm², the temperature rise in water and the suspension of J-PSi NPs is consistent with the theoretical calculation. However, there are small discrepancies close to the moment of US turn-off, when the maximum heating is observed. The presence of J-PSi NPs led to additional heating of the suspension by an average of 0.15°C. The temperature fluctuations in the suspension due to cavitation at a specified intensity of 11.4 W/cm² were by 7–10% higher than fluctuations of the temperature in water. The decrease in temperature during the cooling phase occurred faster than it was predicted by the calculations both in the suspension and water (**Figure 4A**). Such behavior can be explained by the fact that the temperature in the tank was for some reason lower than the temperature of the suspension. As a result, there was a heat flow from the walls of the cuvette to its center, which resulted in faster cooling. The same effect led to a decrease in the peak temperature at the moment the US was switched off.

When the US intensity increases up to 15.4 W/cm², the temperature fluctuations in the stage of heating grew both in water and in the suspension. The maximum range of temperature fluctuations was 0.4 and 0.3°C for the suspension and water, respectively, being about 30% of the peak temperatures. Cavitation also led to an increase in the average heating of both the suspension and water. However, the intensity of cavitation in the suspension of J-PSi NPs was higher, therefore, the additional heating in the suspension was, on the average, 0.2°C higher than in distilled water (**Figure 4B**). A satisfactory agreement between the measured and calculated values of temperature in the cooling stage at $t > 300$ s indicates that the temperature of the suspension in

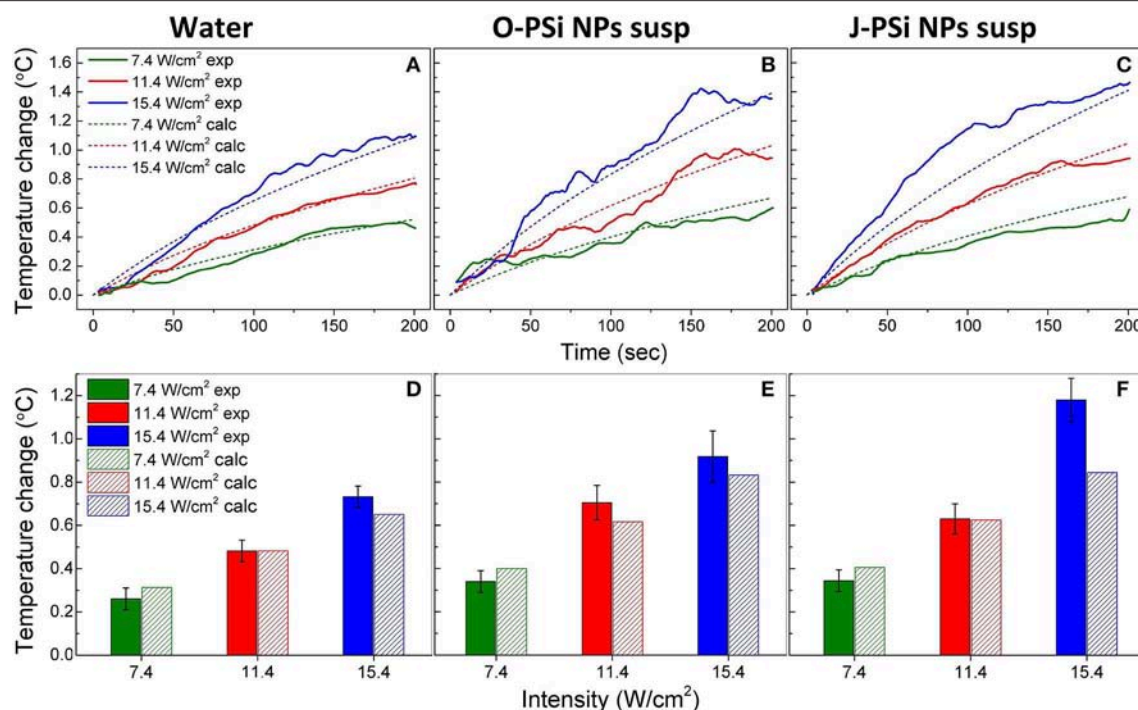


FIGURE 5 | The temperature rise in distilled water (A), the suspension of O-PSi NPs (B), and the suspension of J-PSi NPs (C) at the concentration of 1 g/l induced by US with the intensities of 7.4, 11.4, and 15.4 W/cm². Experimental results are shown by the solid lines, while the dashed lines represent the simulated data. Temperature increase in distilled water (D), the suspension of O-PSi NPs (E), the suspension and J-PSi NPs (F) after the first 100 s of exposure to US. The solid bars stand for the measured temperatures and the dashed bars for the calculated ones. The error bars indicate s.d. of the residual statistics obtained after non-linear fitting of the experimental heating curves (adj. *R*-squared > 0.98).

the cuvette and water in the tank were nearly equal at the initial time.

For a better interpretation of the obtained raw data, 30-point moving averages of the heating trends were plotted vs. time. **Figures 5A–C** shows the smoothed experimental and calculated time dependences of heating in distilled water (a), the suspensions of O-PSi NPs (b), and J-PSi NPs (c) at the concentration of 1 g/l induced by US with the intensities of 7.4, 11.4, and 15.4 W/cm². The initial temperature of all the samples was ~23°C. The simulated curves for water are in a good agreement with the experimental data given in **Figure 5A**. The maximum heating of water at 15.4 W/cm² amounted to 1.16°C and led to a negligible deviation from the calculated value of 1.09°C. Despite the smoothing, significant fluctuations of the experimental curves are still visible in **Figure 5B**. The most pronounced deviations from the results of simulation up to 0.1 and 0.2°C took place for the US intensities of 11.4 and 15.4 W/cm², respectively. As expected based on Equation (2) (see section Cavitation Measurements), the maximum heating for the suspension of O-PSi NPs was higher than the one for the distilled water at both 11.4 W/cm² (1.1°C) and 15.4 W/cm² (1.4°C). The highest heating among all the samples at 15.4 W/cm² was observed for the suspension of J-PSi NPs (**Figure 5C**) and amounted to 1.46°C. The maximum deviation from the simulated curve in 0.31°C was achieved 81 s after turning the US

on. The fluctuations of the experimental curve at 11.4 W/cm² were less pronounced and led to the difference of 0.1°C between the measured and calculated values.

For the further analysis, the temperature increase in water and the suspensions of O-PSi NPs and J-PSi NPs at the concentration of 1 g/l was plotted after 100 s of US exposure of different intensities (**Figures 5D–F**). The presented data unambiguously reveal contrast between the heating of distilled water and the suspensions of PSi NPs at the same US intensity, which could reach 0.4–0.6°C in the case of high intensity. Moreover, within the limits of error, the experimental values of heating at low intensities coincide with the simulated ones. However, at the highest intensity, the measured temperature increased significantly over the calculated values. In particular, for the suspension of J-PSi NPs the excess was 0.35°C, which can be explained by the prominent acoustic cavitation that led to the collapse of air bubbles accompanied by release of energy and additional heating (see section Cavitation Contribution to the Heating Effect).

Figure 6 represents the experimental and calculated time dependences of heating at different concentrations of nanoparticles in the suspensions of O-PSi NPs (a) and J-PSi NPs (b) at the US intensity of 11.4 W/cm². At this intensity, the additional heating from cavitation was negligible (**Figure 5E**) and made it possible to investigate the effect of the PSi NPs

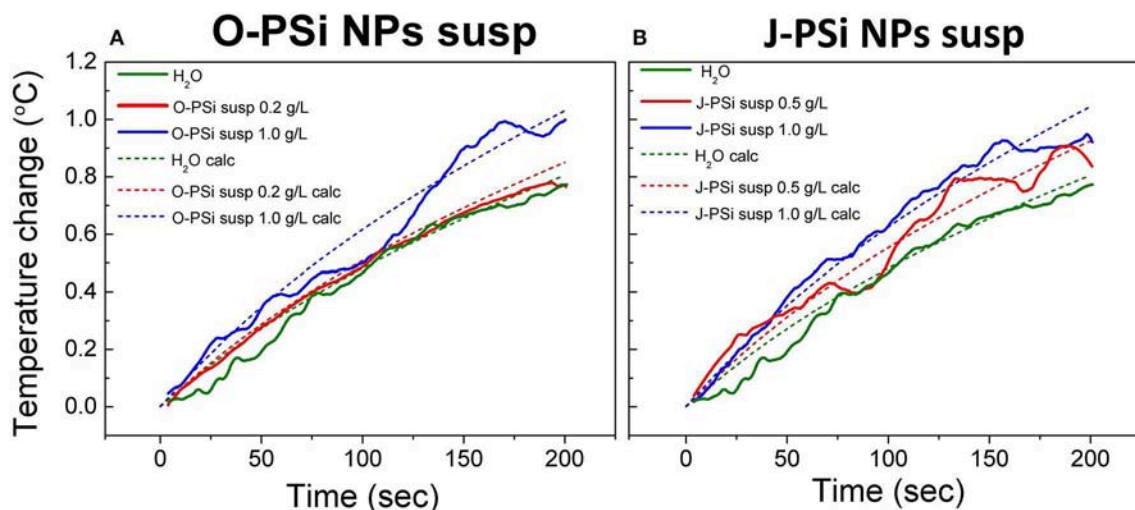


FIGURE 6 | Experimental (solid lines) and theoretically calculated (dashed lines) time dependences of heating in the suspensions of O-PSi NPs (A) and J-PSi NPs (B) exposed to the US with the intensity of 11.4 W/cm² at different NP concentrations.

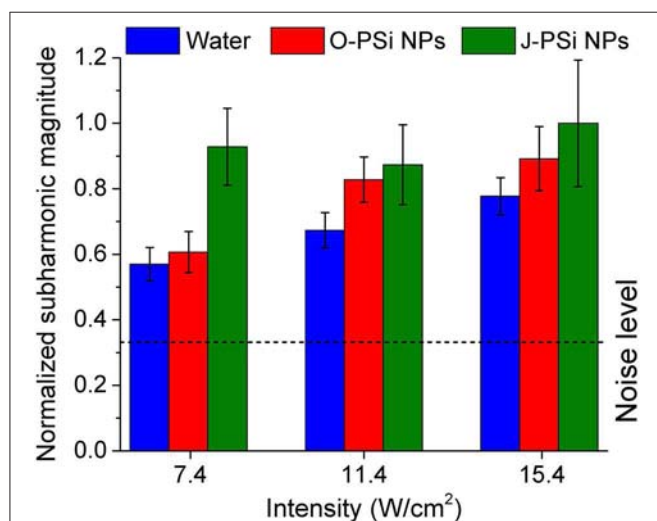


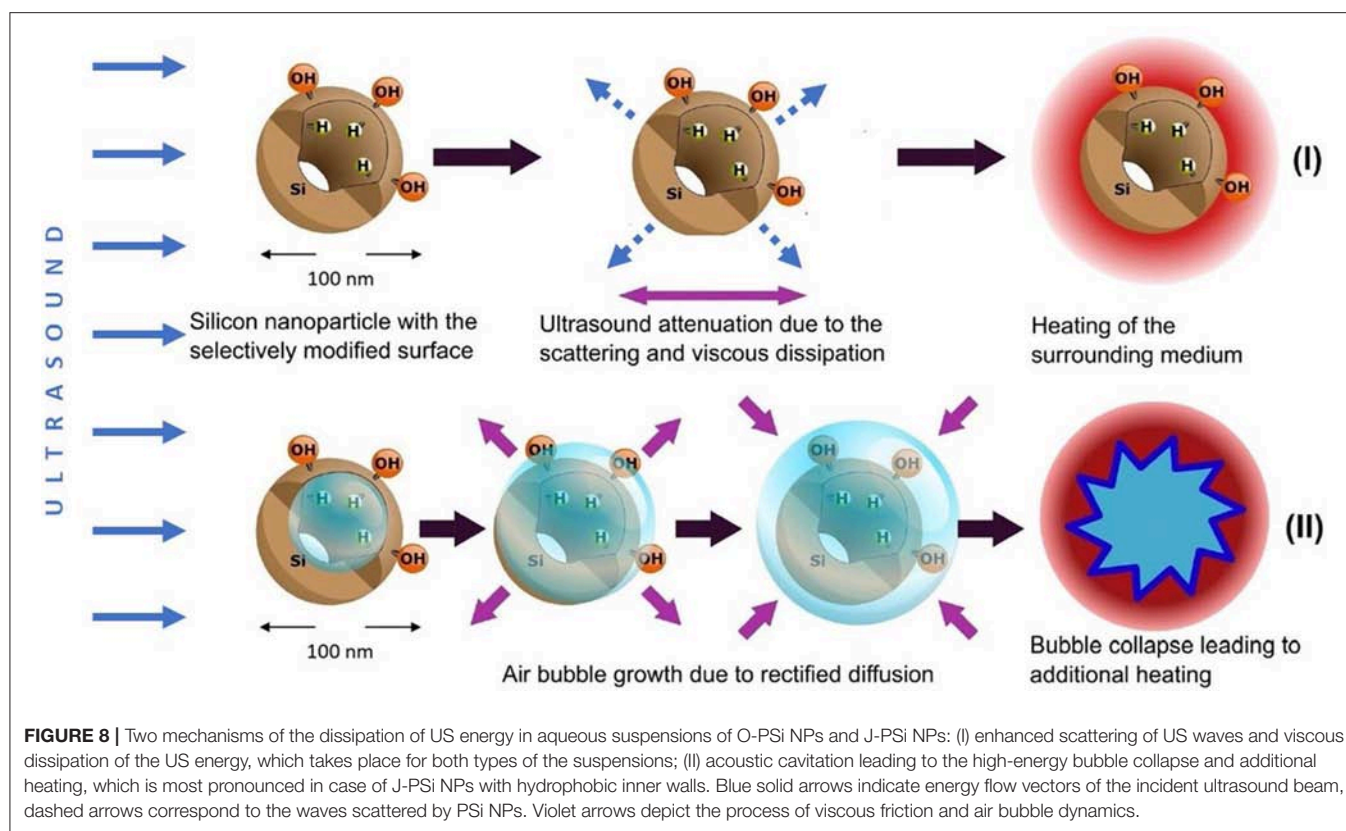
FIGURE 7 | Mean subharmonic magnitudes in distilled water and the suspensions of O-PSi NPs and J-PSi NPs during 200 s of exposure to US at three different intensities. The dashed line corresponds to the noise level. The error bars indicate s.d. (significance level $\alpha = 5\%$).

concentration on the heating tendency. The concentrations of 0.5 and 1 g/l led to the temperature difference between the suspension of J-PSi NPs and distilled water in 0.15 and 0.3°C, respectively. The temperature difference between the suspension of O-PSi NPs at the concentration of 0.2 g/l and distilled water was almost negligible, while the concentration of 1 g/l led to the result equal to the case of J-PSi NPs. Such temperature increase was in good agreement with the increase of the US absorption coefficient described by Urick (1948). The calculated values of US absorption coefficients for distilled water, the suspensions of O-PSi NPs, and J-PSi NPs at 1 g/l were 0.108, 0.138, and 0.140 m⁻¹, respectively. It should be noted, that these experiments were carried out with the concentration of PSi NPs

in the suspensions up to 1 g/l, which defines the upper limit of concentration levels that are non-toxic to organisms (Näkki et al., 2015; Sviridov et al., 2017). High concentration levels of PSi NPs in tissues necessary for the contrast enhancement of ultrasound can be provided by the targeted delivery of nanoparticles. Only in this case it is possible to reach the desired effect using PSi NPs as the activators together with US of relatively low intensity (as compared, for example, with HIFU).

Cavitation Contribution to the Heating Effect

Simultaneously with measuring the temperature during the heating process, the subharmonic magnitude in the spectrum of the transmitted signal was also measured, the generation of subharmonic characterizes the intensity of cavitation in the suspensions (Didenkulov et al., 2011). The values of mean subharmonic magnitudes for the distilled water and the NP suspensions during 200 s of exposure to US with the intensities of 7.4, 11.4, and 15.4 W/cm² are shown in Figure 7. The subharmonic magnitudes for all the samples were much higher than the noise level, which means that the intensities mentioned were far beyond the cavitation thresholds (Tamarov et al., 2017). The subharmonic magnitude in water grew gradually with the US intensity: It increased by more than 30% when the intensity was changed from 7.4 to 15.4 W/cm². The suspension of O-PSi NPs expressed also positive, but less progressive (as compared with water) trend in the subharmonic magnitude with the increase of US intensity. Furthermore, the magnitudes were higher as compared with such for the distilled water (0.89 against 0.78 μ V at 15.4 W/cm²), which was associated with the greater number of the bubble nucleation centers when nanoparticles are present (Tuziuti et al., 2005; Sviridov et al., 2015). The subharmonic magnitude at the intensity of 15.4 W/cm² was the highest one among for the J-PSi NPs. Here, the measured values of subharmonic magnitude in the suspension of J-PSi



NPs at all the employed intensities coincided within the margin of error. This saturation can be explained with two reasons. The first factor is that at some limit value of US intensity the number of cavitating air bubbles stops increasing and so does the subharmonic magnitude. The second one is associated with the transmission geometry used (Figure 2). Even though the number of the cavitation bubbles collapsing per time unit increases with the US intensity (Tamarov et al., 2017) the growing number of the air bubbles leads to the scattering of the US signal detected by the hydrophone resulting in reduced subharmonic magnitude. It should be noticed, that besides the subharmonic generation the inertial cavitation above a threshold intensity should generate broadband white noise and harmonic emissions, which can be also responsible for additional heating effect.

Figure 8 gives a schematic view on two possible ways of the dissipation of US energy in the suspension of PSi NPs. For rather low US intensities (regime I) the main mechanism is determined by the US attenuation in the aqueous medium and the additional attenuation due to the solid particle-induced scattering and viscous dissipation (Sviridov et al., 2013). At higher US intensities, the acoustic cavitation leads to the high-energy bubble collapse and additional heating (regime II). The averaged thermal effect in regime I is well-estimated by using the model described in section Cavitation Measurements. Indeed, in this case the smoothed experimental heating curves are accurately approximated by the simulated ones (see green and red lines and bars in Figure 5). The discrepancies become observable for the heating curves of the NP suspension and

distilled water (see red and blue lines in Figure 4, respectively). While the curve for water has weak oscillations at 11.4 W/cm², the presence of NPs in the aqueous medium leads to evident fluctuations. It became possible to observe such effects due to the usage of E-type thermocouple, which provided fast and precise control of temperature fluctuations with time resolution of ~200 ms evaluated using Equation (9). This value was close to the speed of data acquisition: the duration of a program cycle was ~300 ms.

The temperature fluctuations growing up to 0.1–0.3°C with the increase of the US intensity as well as the additional heating reaching the values of 0.3–0.4°C in the case of the high US intensities (see blue lines and bars in Figure 5), are attributed to the acoustic cavitation leading to vigorous bubble collapse and subsequent heat release. This phenomenon has a stochastic nature and threshold values, which depend on the number of cavitation nuclei (submicron air bubbles) (Li et al., 2017). PSi NPs are known to lower the thresholds of acoustic cavitation (Sviridov et al., 2015; Tamarov et al., 2017), which can be utilized to enhance the cell membrane permeability due to the effect of sonoporation (Mullin et al., 2013). The subharmonic magnitudes being the measure of cavitation activity (Figure 7) correlate well with the values of the heating: The heating trend exceeds the simulated curve because of the increase in the cavitation intensity. Moreover, the effect is stronger with J-PSi NPs, because the number of the cavitation nuclei in their suspension is the highest due to the residual air in hydrophobic pores when dispersed in water (Tamarov et al., 2017).

While the total thermal effect of PSi NPs under the employed NP concentration and US intensity is not enough to realize ultrasound hyperthermia itself, the cavitation related subsequences, which are induced by PSi NPs and especially the Janus-like ones, look promising for both the detection (by using the thermal and acoustic responses), and destruction of undesirable biological tissues and cells. The observed temperature fluctuations (see **Figure 4**) indicate the local heat release in the vicinity of the collapsing air bubbles growing from the pores of PSi NPs. The values of such cavitation-induced hyperthermia can exceed the average temperature of the surrounding medium (Zhou and Gao, 2013; Yoshizawa et al., 2017). This “nanoscalpel” effect (Osminkina et al., 2015) can be utilized for the targeted destruction of cancer cells, but in contrast to the HIFU technique, it employs clearly lower US intensities. Furthermore, outstanding opportunities for the surface modification of PSi NPs as US actuators open wide perspectives of auxiliary biomedical modalities like bioimaging (Kharin et al., 2015; Tolstik et al., 2016) and controlled drug release (Tamarov et al., 2016).

As for the ultrasound imaging, PSi NPs themselves are a weak contrast agent because they are too small to backscatter US waves at a detectable level. However, Janus-like PSi NPs look more promising for US imaging because they act as seeds for cavitation bubbles, which can be detected even with a standard US scanner (Tamarov et al., 2017).

CONCLUSIONS

We investigated mesoporous silicon nanoparticles with fully oxidized and Janus-type hydrophobic/hydrophilic surfaces as potential contrast agents to stimulate the temperature increase of their aqueous suspensions. To achieve that, we developed an experimental setup to simultaneously measure the heating of the nanoparticle suspensions and monitor the cavitation intensity by measuring the subharmonic magnitude. Based on the measurements, we evaluated two main mechanisms leading to the heating effect in nanoparticle suspensions. The first mechanism was associated with enhanced scattering and viscous dissipation of the ultrasound energy in the aqueous medium filled with solid nanoparticles. This mechanism dominated for low

ultrasound intensities and was numerically calculated using the model of heat transfer and ultrasound energy attenuation. The second mechanism was used to explain the discrepancies between the experimental and theoretical results at higher ultrasound intensities, as well as the differences between the suspensions of the oxidized and Janus-like nanoparticles. These discrepancies were because of the acoustic cavitation, which led to the high-energy bubble collapse. This contribution was observed by an apparent excess of the experimental heating curves over the simulated ones as well as strong temperature fluctuations. The increase of experimentally measured subharmonic magnitude in the spectrum of the acoustic signal transmitted through the cuvette correlated with the heating dynamics. The highest values of heating were obtained for the suspension of Janus nanoparticles, which inner pore walls were hydrophobic while the external surfaces were hydrophilic. Such surface modification made it possible to preserve nano-air seeds inside the pores of the nanoparticles, which acted as nuclei for the growth of the microbubbles and cavitation. The results of the present study obtained for the biocompatible and biodegradable porous silicon nanoparticles shed light on their behavior under ultrasonic radiation boosting comprehensively the development of inorganic nanoparticles for theranostic applications.

AUTHOR CONTRIBUTIONS

All authors listed have made a substantial, direct, and intellectual contribution to the work, and approved it for publication.

FUNDING

AS, IF, VA, and VT acknowledge the financial support from the Russian Science Foundation (Grant No. 16-13-10145). KT, WX, and V-PL acknowledge the financial support from the Academy of Finland (Grant Nos. 314552 and 314412).

SUPPLEMENTARY MATERIAL

The Supplementary Material for this article can be found online at: <https://www.frontiersin.org/articles/10.3389/fchem.2019.00393/full#supplementary-material>

REFERENCES

- Allegra, J. R., and Hawley, S. A. (1972). Attenuation of sound in suspensions and emulsions: theory and experiments. *JASA* 52, 1545–1564. doi: 10.1121/1.1912999
- Ames, W. F. (1992). *Numerical Methods for Partial Differential Equations*, 3rd Edn. Boston: Academic Press, Inc.
- Bessonova, O. V., Khokhlova, V. A., Bailey, M. R., Canney, M. S., and Crum, L. A. (2009). Focusing of high power ultrasound beams and limiting values of shock wave parameters. *Acoust. Phys.* 55, 463–473. doi: 10.1134/S1063771009040034
- Bimbo, L. M., Sarparanta, M., Santos, H. A., Airaksinen, A. J., Mäkilä, E., Laaksonen, T. L., et al. (2010). Biocompatibility of thermally hydrocarbonized porous silicon nanoparticles and their biodistribution in rats. *ACS Nano* 4, 3023–3032. doi: 10.1021/nn901657w
- Canavese, G., Ancona, A., Racca, L., Canta, M., Dumontel, B., F., Barbaresco, F., et al. (2018). Nanoparticle-assisted ultrasound: a special focus on sonodynamic therapy against cancer. *Chem. Eng. J.* 340, 155–172. doi: 10.1016/j.cej.2018.01.060
- Chatterjee, D. K., Diagaradjane, P., and Krishnan, S. (2011). Nanoparticle-mediated hyperthermia in cancer therapy. *Ther. Deliv.* 2, 1001–1014. doi: 10.4155/tde.11.72
- Darabdhara, G., Das, M. R., Turcheniuk, V., Turcheniuk, K., Zaitsev, V., Boukherroub, R., et al. (2015). Reduced graphene oxide nanosheets decorated with AuPd bimetallic nanoparticles: a multifunctional material for photothermal therapy of cancer cells. *J. Mater. Chem. B* 3, 8366–8374. doi: 10.1039/C5TB01704A
- Deepagan, V. G., You, D. G., Um, W., Ko, H., Kwon, S., Choi, K. Y., et al. (2016). Long-circulating Au-TiO₂ nanocomposite as a sonosensitizer for ROS-mediated eradication of cancer. *Nano Lett.* 16, 6257–6264. doi: 10.1021/acs.nanolett.6b02547
- Didenkulov, I. N., Martyanov, A. I., and Pronchatov-Rubtsov, N. V. (2011). “Experimental investigation of ultrasound cavitation in a

- flat open resonator," in *Proceedings of the XXIV Session of RAS* (Moscow).
- Diederich, C. J., and Hynynen, K. (1999). Ultrasound technology for hyperthermia. *Ultrasound Med. Biol.* 25, 871–887. doi: 10.1016/S0301-5629(99)00048-4
- Frazier, N., Payne, A., de Bever, J., Dillon, C., Panda, A., Subrahmanyam, N., et al. (2006). High intensity focused ultrasound hyperthermia for enhanced macromolecular delivery. *J. Control. Release* 241, 186–193. doi: 10.1016/j.jconrel.2016.09.030
- Haar, G., and Coussios, C. (2007). High intensity focused ultrasound: physical principles and devices. *Int. J. Hyperth.* 23, 89–104. doi: 10.1080/02656730601186138
- Hill, C. R., Bamber, J. C., and Haar, G. R. (2005). *Physical Principles of Medical Ultrasound*, 2nd Edn. Chichester: John Wiley & Sons, Ltd.
- Issels, R. D. (2008). Hyperthermia adds to chemotherapy. *Eur. J. Cancer* 44, 2546–2554. doi: 10.1016/j.ejca.2008.07.038
- Józefczak, A., Kaczmarek, K., Hornowski, T., Kubovčíková, M., Rozynek, Z., Timko, M., et al. (2016). Magnetic nanoparticles for enhancing the effectiveness of ultrasonic hyperthermia. *Appl. Phys. Lett.* 108:263701. doi: 10.1063/1.4955130
- Kharin, A., Syshchyk, O., Geloan, A., Alekseev, S., Rogov, A., Lysenko, V., et al. (2015). Carbon fluoroxide nanoparticles as fluorescent labels and sonosensitizers for theranostic applications. *Sci. Technol. Adv. Mater.* 16:44601. doi: 10.1088/1468-6996/16/4/044601
- Kosheleva, O. K., Lai, T. C., Chen, N. G., Hsiao, M., and Chen, C. H. (2016). Selective killing of cancer cells by nanoparticle-assisted ultrasound. *J. Nanobiotechnol.* 14, 1–11. doi: 10.1186/s12951-016-0194-9
- Li, B., Gu, Y., and Chen, M. (2017). An experimental study on the cavitation of water with dissolved gases. *Exp. Fluids* 58:164. doi: 10.1007/s00348-017-2449-0
- Miller, D. L., Smith, N. B., Bailey, M. R., Czarnota, G. J., Hynynen, K., and Makin, R. S. (2012). Overview of therapeutic ultrasound applications and safety considerations. *J. Ultrasound. Med.* 31, 623–634. doi: 10.7863/jum.2012.31.4.623
- Mullin, L. B., Phillips, L. C., and Dayton, P. A. (2013). Nanoparticle delivery enhancement with acoustically activated microbubbles. *IEEE Trans. Ultrason. Ferroelectr. Freq. Control* 60, 65–77. doi: 10.1109/TUFFC.2013.2538
- Näkki, S., Rytönen, J., Nissinen, T., Florea, C., Riikonen, J., Ek, P., et al. (2015). Improved stability and biocompatibility of nanostructured silicon drug carrier for intravenous administration. *Acta Biomater.* 13, 207–215. doi: 10.1016/j.actbio.2014.11.019
- Nissinen, T., Ikonen, T., Lama, M., Riikonen, J., and Lehto, V. P. (2016). Improved production efficiency of mesoporous silicon nanoparticles by pulsed electrochemical etching. *Powder Technol.* 288, 360–365. doi: 10.1016/j.powtec.2015.11.015
- Osminkina, L. A., Nikolaev, A. L., Sviridov, A. P., Andronova, N. V., Tamarov, K. P., Gongalsky, M. B., et al. (2015). Porous silicon nanoparticles as efficient sensitizers for sonodynamic therapy of cancer. *Microporous Mesoporous Mater.* 210, 169–175. doi: 10.1016/j.micromeso.2015.02.037
- Pan, X., Wang, H., Wang, S., Sun, X., Wang, L., Wang, W., et al. (2018). Sonodynamic therapy (SDT): a novel strategy for cancer nanotheranostics. *Sci. China Life Sci.* 61, 415–426. doi: 10.1007/s11427-017-9262-x
- Qian, X., Han, X., and Chen, Y. (2017). Insights into the unique functionality of inorganic micro/nanoparticles for versatile ultrasound theranostics. *Biomaterials* 142, 13–30. doi: 10.1016/j.biomaterials.2017.07.016
- Qian, X., Zheng, Y., and Chen, Y. (2016). Micro/nanoparticle-augmented sonodynamic therapy (SDT): Breaking the depth shallow of photoactivation. *Adv. Mater.* 28, 8097–8129. doi: 10.1002/adma.201602012
- Riikonen, J., Salomäki, M., Van Wonderen, J., Kemell, M., Xu, W., Korhonen, O., et al. (2012). Surface chemistry, reactivity, and pore structure of porous silicon oxidized by various methods. *Langmuir* 28, 10573–10583. doi: 10.1021/la301642w
- Serpe, L., Foglietta, F., and Canaparo, R. (2012). Nanosonotechnology: the next challenge in cancer sonodynamic therapy. *Nanotechnol. Rev.* 1, 173–182. doi: 10.1515/ntrev-2011-0009
- Setroikromo, R., Wierenga, P. K., Van Waarde, M. A. W. H., Brunsting, J. F., Vellenga, E., and Kampinga, H. H. (2007). Heat shock proteins and Bcl-2 expression and function in relation to the differential hyperthermic sensitivity between leukemic and normal hematopoietic cells. *Cell Stress Chaperones* 12, 320–330. doi: 10.1379/CSC-279.1
- Song, C. W., Park, H., Griffin, R. J., and Res, R. (2001). Improvement of tumor hyperthermia by mild oxygenation. *Radiat. Res.* 155, 515–528. Available online at: https://www.jstor.org/stable/3580354?seq=1#page_scan_tab_contents
- Sviridov, A. P., Andreev, V. G., Ivanova, E. M., Osminkina, L. A., Tamarov, K. P., and Timoshenko, V. Y. (2013). Porous silicon nanoparticles as sensitizers for ultrasonic hyperthermia. *Appl. Phys. Lett.* 103:193110. doi: 10.1063/1.4829148
- Sviridov, A. P., Osminkina, L. A., Kharin, A. Y., Gongalsky, M. B., Kargina, J. V., Kudryavtsev, A. A., et al. (2017). Cytotoxicity control of silicon nanoparticles by biopolymer coating and ultrasound irradiation for cancer theranostic applications. *Nanotechnology* 28:105102. doi: 10.1088/1361-6528/aa5b7c
- Sviridov, A. P., Osminkina, L. A., Nikolaev, A. L., Kudryavtsev, A. A., Vasiliev, A. N., and Timoshenko, V. Y. (2015). Lowering of the cavitation threshold in aqueous suspensions of porous silicon nanoparticles for sonodynamic therapy applications. *Appl. Phys. Lett.* 107:23107. doi: 10.1063/1.4931728
- Tamarov, K., Sviridov, A., Xu, W., Malo, M., Andreev, V., Timoshenko, V., et al. (2017). Nano air seeds trapped in mesoporous Janus nanoparticles facilitate cavitation and enhance ultrasound imaging. *ACS Appl. Mater. Interfaces* 9:35234–35243. doi: 10.1021/acsami.7b11007
- Tamarov, K., Xu, W., Osminkina, L., Zinovyev, S., Soininen, P., Kudryavtsev, A., et al. (2016). Temperature responsive porous silicon nanoparticles for cancer therapy – spatiotemporal triggering through infrared and radiofrequency electromagnetic heating. *J. Control. Release* 241, 220–228. doi: 10.1016/j.jconrel.2016.09.028
- Tamarov, K. P., Osminkina, L. A., Zinovyev, S. V., Maximova, K. A., Kargina, J. V., Gongalsky, M. B., et al. (2014). Radio frequency radiation-induced hyperthermia using Si nanoparticle-based sensitizers for mild cancer therapy. *Sci. Rep.* 4:7034. doi: 10.1038/srep07034
- Tempny, C. M. C., McDannold, N. J., Hynynen, K., and Jolesz, F. A. (2011). Focused ultrasound surgery in oncology: Overview and principles. *Radiology* 259, 39–56. doi: 10.1148/radiol.11100155
- Tolstik, E., Osminkina, L. A., Akimov, D., Gongalsky, M. B., Kudryavtsev, A. A., Timoshenko, V. Y., et al. (2016). Linear and non-linear optical imaging of cancer cells with silicon nanoparticles. *Int. J. Mol. Sci.* 17, 6–10. doi: 10.3390/ijms17091536
- Tuzziuti, T., Yasui, K., Sivakumar, M., Iida, Y., and Miyoshi, N. (2005). Correlation between acoustic cavitation noise and yield enhancement of sonochemical reaction by particle addition. *J. Phys. Chem. A* 109, 4869–4872. doi: 10.1021/jp0503516
- Urick, R. J. (1948). The absorption of sound in suspensions of irregular particles. *J. Acoust. Soc. Am.* 20, 283–289. doi: 10.1121/1.1906373
- Wust, P., Hildebrandt, B., Sreenivasa, G., Rau, B., Gellermann, J., Riess, H., et al. (2002). Hyperthermia in combined treatment of cancer. *Lancet Oncol.* 3, 487–497. doi: 10.1016/S1470-2045(02)00818-5
- Xu, W., Rytönen, J., Rönkkö, S., Nissinen, T., Kinnunen, T., Suvanto, M., et al. (2014). A nanostopper approach to selectively engineer the surfaces of mesoporous silicon. *Chem. Mater.* 26, 6734–6742. doi: 10.1021/cm503004b
- Yildirim, L., Thanh, N. T. K., Loizidou, M., and Seifalian, A. M. (2011). Toxicological considerations of clinically applicable nanoparticles. *Nano Today* 6, 585–607. doi: 10.1016/j.nantod.2011.10.001
- Yoshizawa, S., Takagi, R., and Umemura, S. (2017). Enhancement of high-intensity focused ultrasound heating by short-pulse generated cavitation. *Appl. Sci.* 7:288. doi: 10.3390/app7030288
- Zhou, Y., and Gao, X. W. (2013). Variations of bubble cavitation and temperature elevation during lesion formation by high-intensity focused ultrasound. *J. Acoust. Soc. Am.* 134, 1683–1694. doi: 10.1121/1.4812895

Conflict of Interest Statement: The authors declare that the research was conducted in the absence of any commercial or financial relationships that could be construed as a potential conflict of interest.

Copyright © 2019 Sviridov, Tamarov, Fesenko, Xu, Andreev, Timoshenko and Lehto. This is an open-access article distributed under the terms of the Creative Commons Attribution License (CC BY). The use, distribution or reproduction in other forums is permitted, provided the original author(s) and the copyright owner(s) are credited and that the original publication in this journal is cited, in accordance with accepted academic practice. No use, distribution or reproduction is permitted which does not comply with these terms.



Magnetic Nanoparticles Enhance Pore Blockage-Based Electrochemical Detection of a Wound Biomarker

Gayathri Rajeev^{1,2}, Allison J. Cowin¹, Nicolas H. Voelcker^{3,4,5,6*} and Beatriz Prieto Simon^{3,4,5*}

OPEN ACCESS

Edited by:

Thierry Djenizian,
École des Mines de Saint-Étienne -
Campus Georges Charpak Provence,
France

Reviewed by:

Abel Santos,
University of Adelaide, Australia
Alfredo De La Escosura-Muñiz,
Universidad de Oviedo, Spain

*Correspondence:

Nicolas H. Voelcker
nicolas.voelcker@monash.edu
Beatriz Prieto Simon
beatriz.prieto-simon@monash.edu

Specialty section:

This article was submitted to
Chemical and Process Engineering,
a section of the journal
Frontiers in Chemistry

Received: 20 October 2018

Accepted: 28 May 2019

Published: 12 June 2019

Citation:

Rajeev G, Cowin AJ, Voelcker NH and
Prieto Simon B (2019) Magnetic
Nanoparticles Enhance Pore
Blockage-Based Electrochemical
Detection of a Wound Biomarker.
Front. Chem. 7:438.
doi: 10.3389/fchem.2019.00438

¹ Future Industries Institute, University of South Australia, Mawson Lakes, SA, Australia, ² Faculty of Science, Institute for Biomedical Materials and Devices, University of Technology, Sydney, NSW, Australia, ³ Drug Delivery, Disposition and Dynamics, Monash Institute of Pharmaceutical Sciences, Monash University, Parkville, VIC, Australia, ⁴ Melbourne Centre for Nanofabrication, Victorian Node of the Australian National Fabrication Facility, Clayton, VIC, Australia, ⁵ Commonwealth Scientific and Industrial Research Organisation, Clayton, VIC, Australia, ⁶ Department of Materials Science and Engineering, Monash University, Clayton, VIC, Australia

A novel pore blockage-based electrochemical immunosensor based on the combination of 100 nm-magnetic nanoparticles (MNPs), as signal enhancers, and 200 nm-pore diameter nanoporous anodic alumina (NAA) membranes, as sensing platform, is reported. A peptide conjugate mimicking flightless I (Flii), a wound healing biomarker, was chosen as target analyte. The sensing platform consists of an anti-Flii antibody (Ab1)-modified NAA membrane attached onto a gold electrode. Anti-KLH antibody (Ab2)-modified MNPs (MNP-Ab2) were used to selectively capture the Flii peptide conjugate in solution. Sensing was based on pore blockage of the Ab1-modified NAA membrane caused upon specific binding of the MNP-Ab2-analyte complex. The degree of pore blockage, and thus the concentration of the Flii peptide conjugate in the sample, was measured as a reduction in the oxidation current of a redox species ($[\text{Fe}(\text{CN})_6]^{4-}$) added in solution. We demonstrated that pore blockage is drastically enhanced by applying an external magnetic field at the membrane backside to facilitate access of the MNP-Ab2-analyte complex into the pores, and thus ensure its availability to bind to the Ab1-modified NAA membrane. Combining the pore blockage-based electrochemical magnetoimmunosensor with an externally applied magnetic field, a limit of detection (LOD) of 0.5 ng/ml of Flii peptide conjugate was achieved, while sensing in the absence of magnetic field could only attain a LOD of 1.2 $\mu\text{g/ml}$. The developed sensing strategy is envisaged as a powerful solution for the ultra-sensitive detection of an analyte of interest present in a complex matrix.

Keywords: magnetic nanoparticles, porous anodic alumina membrane, pore blockage, electrochemical biosensor, chronic wound, nanoporous materials

INTRODUCTION

There is a growing demand for rapid, highly sensitive, simple-to-fabricate, and cost-effective biosensing platforms for the detection of biological targets in medical diagnostics. Conventional methods like enzyme-linked immunosorbent assays (ELISAs) are not desirable as diagnostic platforms in clinical setups as they require long analysis time, sample preparation and several incubation and rinsing steps prior to analysis.

Electrochemical biosensors translate the presence of analytes into electrical signals (Grieshaber et al., 2008) and are suitable to develop point-of-care (POC) handheld sensing devices since electrodes can be easily miniaturized by methods such as screen printing (Yamanaka et al., 2016), photolithography (Mir et al., 2010) or ink-jet printing (Silveira et al., 2016) which allow easy integration into electronic devices (Zhu et al., 2014).

With substantial advancements in nanotechnology, remarkable improvement in the sensing performance of electrochemical biosensors has been achieved using nanoparticle (NP)-based signal amplification (Zhu et al., 2014). Nowadays, different kinds of functional nanomaterials such as metal NPs, quantum dots, nanoporous materials, carbon-based nanomaterials, and magnetic NPs (MNPs) have been used to design ultra-sensitive biosensing platforms (Lei and Ju, 2012; Walcarius et al., 2013; Holzinger et al., 2014).

MNPs have been extensively used in magnetic separation of biomolecules from complex biological samples and as solid supports for performing immunoassays (Rocha-Santos, 2014). Advances in biosensing strategies that employ magnetic labels have resulted in platforms that push the limits of detection to very low levels resulting in devices that can be used for early disease detection in medical diagnostics (Dittmer et al., 2008). Nowadays, a variety of commercial MNPs are readily available with a wide range of sizes, magnetic properties, and surface functionalities that are used in biosensors. They have been used for capturing analytes from complex samples, leaving behind undesired molecules in the background matrix, and labeling analytes (Van Reenen et al., 2014).

The main advantages of using MNPs include their large surface area, ease of functionalization, lack of harmful effects to the human body, controllable size, and simple manipulation in magnetically actuated devices. Surface functionalities on MNPs allow their surface modification with biorecognition elements that feature high affinity to the analyte of interest, whereas the large surface-to-volume ratio increases the number of bioreceptors available to react with the analyte, contributing to increase the sensitivity of the device (Dittmer et al., 2008; Gijs et al., 2009; Peyman et al., 2009). The latter effect can be further enhanced by the feasibility of MNPs to facilitate pre-concentration of analytes prior to analysis, being key for applications that require ultra-sensitivity to detect minute concentrations of analyte. Additionally, biofunctionalized MNPs can isolate specific analytes of interest from complex biological samples by magnetic actuation, which can minimize matrix effects thereby reducing the occurrence of false positives.

Lab-on-chip technologies that integrate multiple analytical functions in a single chip are of great interest to scientists due to the growing demand for easy-to-use diagnostic devices (Huang and Mason, 2013). Such devices enable the end users to perform all the steps from sampling to obtaining easily readable results in a single platform. MNPs have been used in developing such bioassays (Rocha-Santos, 2014; Van Reenen et al., 2014). MNPs allow integration into microfluidic devices where they can be manipulated within the microfluidic channels by applying an external magnetic force (Giouroudi and Keplinger, 2013). This can lead to the design of miniaturized technologies based on MNPs which significantly reduce sample volume and analysis time.

After specific analyte capture using MNPs, a detection step is crucial to provide accurate and specific detection of the analyte-MNP complex. Several strategies have been explored by researchers for the detection of the analyte-MNP complexes (Gijs et al., 2009). Labeling strategies are commonly used, where the captured analyte is labeled with a fluorescent dye (Peyman et al., 2008, 2009; Tarn et al., 2010; Sasso et al., 2012), a chemiluminescent molecule or an enzyme, that enable further detection. Thorough washing or separation steps are required when using labeled strategies so that only the captured analytes are labeled and only the bound labels are detected. Using fluorescent molecules as labels results in high limits of detection (LODs) since the background fluorescence from the MNPs is significant and thus the fluorescence from the label itself is comparatively weak (Peyman et al., 2009). Chemiluminescent molecules are also commonly used as labels and are considered one of the most sensitive immunoassays where the intensity of luminescence emitted from chemical reactions is measured (Zhang et al., 2011; Kim and Lim, 2015). Although they exhibit very low LODs (Wang et al., 2012), chemiluminescent emission intensities are sensitive to environmental factors such as temperature, solvent ionic strength, pH, and other species present in the system. Moreover, emission intensity from the chemiluminescent reaction varies with time. Therefore, the emission versus time profile varies greatly from one compound to another (Baeyens et al., 1998). When enzymes are used as labels in enzyme-linked immunosorbent assays (ELISAs), addition of substrates that convert the enzymes into a measurable signal is required (Sista et al., 2008). Enzymatic labeling has the advantage that the signal is amplified by the enzymatic conversion process. However, several incubation and washing steps are required, which are not desirable. Alternatively, the use of MNPs as labels in surface binding assays has been explored where the analyte-MNP complexes bind specifically on a surface in a sandwich format (Morozov and Morozova, 2006; Dittmer et al., 2008). To this purpose, specific bioreceptors with affinity toward two different epitopes of the analyte are required to be immobilized on the MNPs and on the surface.

Nanoporous anodic alumina (NAA) membranes have been demonstrated as suitable substrates for developing biosensing platforms owing to their exceptional features such as highly ordered nanopores, tunable pore geometry, high surface-to-volume ratio, thermal and mechanical stability, biocompatibility, and chemical resistance (Jani et al., 2013; Santos et al., 2013;

Rajeev et al., 2018a). Various electrochemical biosensors have been developed using NAA as the sensing platform (Santos et al., 2013; Rajeev et al., 2018b). NAA membranes functionalized with specific bioreceptors have been used to electrochemically detect various analytes such as DNA (De La Escosura-Muñiz and Merkoçi, 2010), proteins (De La Escosura-Muñiz and Merkoçi, 2010), and pathogens (Cheng et al., 2012; Nguyen et al., 2012). Detection is carried out by monitoring changes either in impedance or current intensity upon specific analyte binding to the immobilized bioreceptor, which partially blocks the diffusion of a redox species through the nanopores toward the underlying electrode surface. De la Escosura-Muñiz et al. demonstrated the use of NAA membrane for *in situ* monitoring of parathyroid hormone-like hormone (PTHrP) secretion in cultured human cells using electrochemical detection (De La Escosura-Muñiz et al., 2018). Recently, De la Escosura-Muñiz et al. also developed a methodology for electrical monitoring of virulence factors secreted by bacterial pathogens using NAA membranes (De La Escosura-Muñiz et al., 2019). AuNP tags have been used by Merkoçi's group as pore blockage agents in NAA-based electrochemical biosensors. Signal enhancement using AuNPs in a sandwich immunoassay approach aimed to detect an IgG lowered the LOD to 50 ng/ml compared to a LOD of 500 µg/ml achieved by an equivalent NAA immunosensor based on direct detection (De La Escosura-Muñiz and Merkoçi, 2010, 2011).

In this work, we report a pore blockage-based electrochemical magnetoimmunosensor where the MNPs are demonstrated as pore blockage enhancers. Results show that simply applying a magnetic force to pull the analyte-MNP complex toward the sensor surface significantly pushes the LOD down, being 2,400-folds lower than that achieved in the absence of magnetic field. The combination of NAA pore blockage-based sensing systems along with the unique features of MNPs in immunosensing is highly promising to develop diagnostic platforms fulfilling the requirements of point-of-care devices. There have been other studies published in the past using gold or magnetic nanoparticles (MNP) as pore blockage enhancers on NAA-membranes. For example, in a work published by Ye et al. (2016), NAA membranes integrated into a PDMS chamber with a Pt electrode as working electrode were combined with the use of MNP as pore blockage enhancers for histamine detection in seafood. In another work published by De La Escosura-Muñiz and Merkoçi (2011), they used a NAA membrane on a screen-printed carbon electrode as sensor surface and AuNPs as pore blockage enhancers for the detection of proteins in whole blood. In this work, for the first time we demonstrated the use of magnetic field to concentrate MNP bound analytes on the sensor surface to enhance the pore blockage.

Flightless I is a negative regulator of wound healing which is present at high level in chronic, non-healing wounds (Ruzehaji et al., 2012). Flightless neutralizing antibodies (FnAb) have been developed by Cowin group. Use of these neutralizing antibodies show that Flii can be depleted from wound fluid and that they have a positive therapeutic effect on chronic wounds (Cowin et al., 2007; Kopecki et al., 2012; Ruzehaji et al., 2014). Detection of Flii proteins in chronic wounds is of great interest in chronic wound research since it may be an indication of the wound status in non-healing wounds. However, wound fluid is a complex

biological sample containing a plethora of biomolecules involved in wound healing which can cause significant matrix effects during biosensing. MNPs can help to tackle this issue, as they are known to isolate specific biomolecules from complex biological samples, eliminating or at least reducing potential interferences.

We aim here to develop a pore blockage-based biosensing platform with sensitivity enhancement via MNP-boosted pore blockage as a proof of concept for the electrochemical detection of Flii proteins. Isolated or recombinant whole Flii protein is not readily available. Hence, a synthetic peptide corresponding to the active region of Flii protein conjugated to a keyhole limpet hemocyanin (KLH) carrier protein is used in this study as a model analyte that facilitates a sandwich immunoassay. While FnAbs are used as immobilized antibodies on the NAA sensor surface, commercial polyclonal anti-KLH antibodies are used as the bioreceptors on the MNP surface. Anti-KLH antibodies displayed on the MNPs specifically capture the KLH-Flii peptide conjugate from solution. MNPs with bound analyte are then incubated onto the FnAb-modified NAA sensor surface to perform a sandwich assay within the nanopores. Partial blockage of the pores upon binding impedes free diffusion of a redox species, $[\text{Fe}(\text{CN})_6]^{4-}$, toward the underlying gold transducer surface, measured as a decrease in its oxidation current intensity. We compared the sensing performance in the presence and absence of magnetic field to study the effect of the magnetic attraction on facilitating the access of the KLH-Flii peptide conjugate-MNP immunocomplex into the pores and thus on the achieved sensitivity.

MATERIALS AND METHODS

Reagents

NAA membranes of 200 nm pore diameter (Whatman Anodisc Circles 13 mm, 200 nm) were purchased from Interpath services (Australia). Carboxyl-terminated MNPs (100 nm diameter, 25 mg/ml, fluidMAG-ARA) were purchased from Chemically (Germany). Potassium ferrocyanide ($\text{K}_4[\text{Fe}(\text{CN})_6]$), potassium ferricyanide ($\text{K}_3[\text{Fe}(\text{CN})_6]$), *N*-hydroxysuccinimide (NHS), *N*-(3-dimethylaminopropyl) *N'*-ethylcarbodiimide hydrochloride (EDC), ethanalamine, phosphate buffered saline (PBS) tablets, 3-(triethoxysilyl) propyl isocyanate (ICN) silane, 3,3',5,5'-tetramethylbenzidine (TMB) substrate, and 2-(*N*-morpholino)-ethanesulfonic acid (MES) were purchased from Sigma-Aldrich (Australia).

Polyclonal antibodies against KLH produced in rabbit and anti-human IgG antibodies (used as control) were purchased from Sapphire Bioscience (NBP1-30443, Australia). Monoclonal antibodies raised in mouse against the N-terminus of the LRR domain of the human Flii protein (FnAb) were developed and supplied by Cowin group (Jackson et al., 2012). Custom made KLH-Flii peptide conjugate was purchased from Mimotopes (Australia).

Preparation and Characterization of Antibody-Modified MNPs (MNP-Ab2)

Carboxyl-terminated MNPs were modified with anti-KLH antibodies (Ab2) via carbodiimide chemistry. One microliter of MNPs, which is equivalent to $4.5 \cdot 10^{10}$ particles, was added to 100

μl of MES buffer, pH 5. MNPs were washed by 5 min-incubation in MES buffer with good mixing in an orbital shaker, followed by 4 min-capture on a magnet to allow supernatant removal. This washing step was performed 3 times. Carboxyl groups on the washed MNPs were activated to form NHS ester groups by reacting with a 1:1 mixture of 100 μl of 0.4 M of EDC and 0.1 M of NHS in cold MES buffer. This reaction was conducted under good mixing in an orbital shaker for 30 min at room temperature. Then, the activated MNPs were captured on a magnet for 5 min and the supernatant was removed. Activated MNPs were incubated in 100 μl of 50 $\mu\text{g}/\text{ml}$ of Ab2 in 0.01 M PBS, pH 7.6, for 1 h at room temperature. Antibody-modified MNPs were washed 4 times in PBS containing 0.01% Tween 20, following the washing protocol previously described, to remove any non-specifically bound antibodies. Ab2-modified MNPs (MNP-Ab2) were incubated in 100 μl of 0.1 M ethanolamine in PBS for 1 h to block any remaining active ester groups on the MNPs surface. Modified MNPs were stored at 4°C until further use.

Fourier transform infrared (FTIR) spectroscopy was conducted after each surface modification step. FTIR spectra were obtained using a Vertex 70 Hyperion microscope Bruker in reflectance mode (Bruker Optics, Germany) over the range of 650–1,000 cm^{-1} at a resolution of 4 cm^{-1} and averaging 64 scans. Background spectra were taken on a gold-coated glass slide. Samples for FTIR characterization were prepared by placing a small drop of unmodified MNP solution, NHS ester-activated MNP solution, and Ab-modified MNP solution on the surface of the gold slide and drying them in a desiccator under vacuum to generate a thin layer of MNPs. Sample spectra were recorded and data analyzed using the OPUS 7.2 spectroscopy software (Bruker).

Preparation and Characterization of the NAA Immunosensing Surface

Isocyanate groups were introduced on the surface of the NAA membranes with 200 nm pores via silanization to facilitate further covalent immobilization of the bioreceptor FnAb. Briefly, NAA membranes were boiled in 30% H_2O_2 for 1 h to obtain fresh hydroxyl groups and remove any organic contaminants. Hydroxylated membranes were dried under a mild nitrogen flow and baked in an oven at 60°C for 2 h to remove any remaining water content. This is a key step since the silanes are highly reactive to water. Then, the membranes with active hydroxyl groups were immersed in a 5% solution of ICN silane in dry toluene in a sealed reaction vessel under nitrogen atmosphere. Silanization was carried out for 2 h under constant shaking at room temperature and inert atmosphere, which resulted in isocyanate groups ($-\text{N}=\text{C}=\text{O}$) displayed on the NAA surface. After silanization, the functionalized membranes were washed with fresh dry toluene and dried under a nitrogen stream. Finally, they were incubated with a 50 $\mu\text{g}/\text{ml}$ FnAb (Ab1) solution in 0.1 M PBS (pH 7.4) for 2 h under constant shaking. After incubation, membranes were washed thoroughly with copious amount of PBS, and stored in PBS at 4°C until they were used for sensing experiments.

FTIR spectroscopy was used to characterize the membranes surface after each step of modification. FTIR spectra were obtained using the method described in section Preparation and Characterization of Antibody-Modified MNPs (MNP-Ab2).

Scanning electron microscopy (SEM) was used to characterize the surface morphology of the NAA membranes.

Analyte (KLH-Flii-Conjugate) Isolation Using MNP-Ab2

MNPs-Ab2 were used to capture the KLH-Flii peptide conjugate from solution as shown in **Scheme 1**. MNPs-Ab2 were incubated in 100 μl of Flii peptide conjugate at various concentrations (2.5, 5, 10, 20, and 40 $\mu\text{g}/\text{ml}$) in PBS for 1 h at room temperature with good mixing. Afterwards, MNPs-Ab2 with captured analyte (MNP-Ab2-Flii) were washed 3 times in PBS solution containing 0.01% Tween 20 using the protocol previously described and the washed MNP-Ab2-Flii complex was re-suspended in fresh PBS and used for sensing experiments.

ELISA to Detect MNP-Ab2-Flii Complex

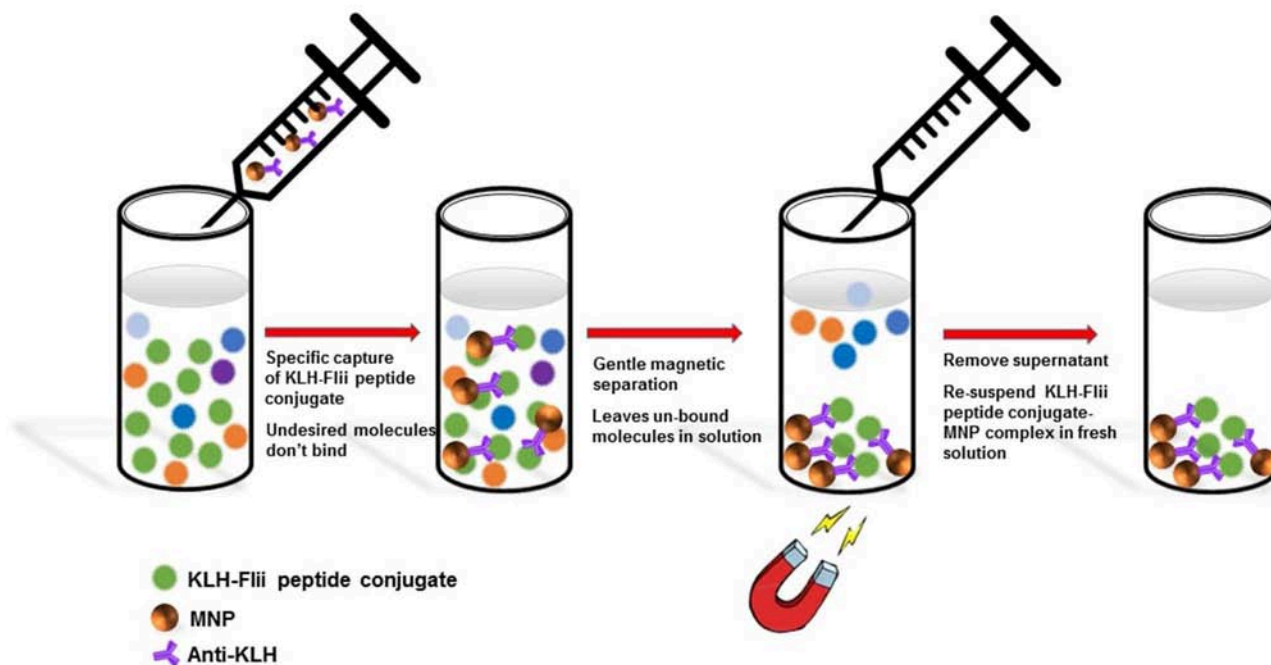
Detection of MNP-Ab2-Flii complex was initially carried out by colorimetric ELISA to confirm the feasibility to use the involved immunospecies in a sandwich assay and to compare the sensing performance of this colorimetric assay with that achieved by the novel NAA-based electrochemical immunosensor which uses MNPs as pore blockage enhancers. Briefly, isolated MNP-Ab2-Flii complex was incubated first in 100 μl of 50 $\mu\text{g}/\text{ml}$ Ab1 in PBS for 1 h followed by incubation in a 1:5,000 dilution of HRP-labeled anti-mouse IgG in PBS. Every incubation step was followed by 3 washing steps in PBS containing 0.01% Tween 20 followed by one washing step in PBS. One hundred μl of TMB were added as HRP substrate. The catalytic conversion of the chromogenic substrate TMB into a colored product by the enzyme used as label was followed by measuring the absorbance at 650 nm, allowing target quantification.

Electrochemical Detection of MNP-Ab2-Flii Complex on a NAA-Based Immunosensor

Electrochemical sensing was conducted using an electrochemical analyser (CH Instruments, model 600 D series, USA) and a three-electrode system in a Teflon cell. Ab1-modified NAA membrane mounted on a gold-coated glass slide (Au/NAA-Ab1) acted as the working electrode, a silver/silver chloride electrode (CH Instruments, USA) was the reference electrode and a platinum wire was the counter electrode. Electrochemical measurements were done using a 2 mM $\text{K}_4[\text{Fe}(\text{CN})_6]$ and 2 mM $\text{K}_3[\text{Fe}(\text{CN})_6]$ solution in 0.1 M PBS. Differential Pulse Voltammetry (DPV) was used as detection technique in which a series of regular voltage pulses were applied ranging from -0.3 to 0.8 V and the oxidation current of the redox species was measured at 0.18 V.

One hundred μl of MNP-Ab2-Flii complex in PBS, obtained upon incubation of MNP-Ab2 in solutions of different concentrations of Flii peptide conjugate (2.5, 5, 10, 20, and 40 $\mu\text{g}/\text{ml}$), were incubated on the immunosensor surface for 1 h at room temperature. DPV measurements were performed before and after incubating the MNP-Ab2-Flii complex solutions. Each experiment was performed in triplicate. Control experiments

Magnetic capture of analyte molecule using MNPs



SCHEME 1 | Isolation of KLH-Flii peptide conjugate using MNPs.

were done using an anti-human IgG-modified NAA-based sensor to evaluate whether the MNP-Ab2-Flii complex was non-specifically adsorbed on the membrane.

Sensitivity Enhancement Using External Magnetic Field

A strong external magnetic field using a large rare earth magnet made from neodymium, iron, and boron-NdFeB (Jaycar Electronics, Australia) was applied at the backside of the immunosensing surface to study its effect on the sensing performance by providing an additional force to attract the MNP-Ab2-Flii complex into the pores and thus facilitates its binding to the Ab1 immobilized on the NAA surface. We hypothesize that this novel approach can enhance MNP-Ab2-Flii complex binding by overcoming diffusion limitations that limit analytes entering the pores, and thus amplify the sensing signal and eventually enhance the sensitivity. In the absence of magnetic field, the MNP-Ab2-Flii complex enters the pores only by diffusion and gravitational forces. The externally applied magnetic field acts as an extra force to attract the MNP-Ab2-Flii complex which facilitates its effective path toward the sensor surface and thus its exposure and final binding to the immobilized Ab1, thereby acting as pore blockage enhancers. Stringent washing while placing the magnet on top of the sensor was required after the MNP-Ab2-Flii complex incubation under magnetic field to

remove any MNPs that may be non-specifically bound or trapped within the pores.

RESULTS AND DISCUSSION

Immobilization of Anti-KLH on MNPs and FnAb on NAA Membranes

MNPs were used to harvest KLH-Flii peptide conjugate from solution. To that purpose, first anti-KLH antibody (Ab2) was covalently bound to carboxyl-terminated MNPs. Carboxyl-terminated MNPs have a particle size of 100 nm, confirmed using TEM (**Figure 1A**). Carbodiimide chemistry is the most versatile method to activate carboxylic groups for their binding to primary amines, EDC being the most popular carbodiimide used for this purpose. NHS was used in the EDC coupling protocols to improve the efficiency of the reaction by creating an amine-reactive intermediate. EDC couples NHS to carboxyl groups and forms an NHS ester which is more stable than the O-acylisourea intermediate formed in the absence of NHS. The NHS ester intermediate reacts with the amine groups of the antibody to form stable amide bonds. **Figure 1B** presents the FTIR spectra at different modification steps of MNPs. The spectrum of the carboxyl-terminated MNPs before activation (black) shows a strong band at $1,624\text{ cm}^{-1}$ and a broad band at $3,400\text{ cm}^{-1}$ which are characteristic of C=O stretching and O-H stretching, respectively. This confirms the presence of carboxylic groups

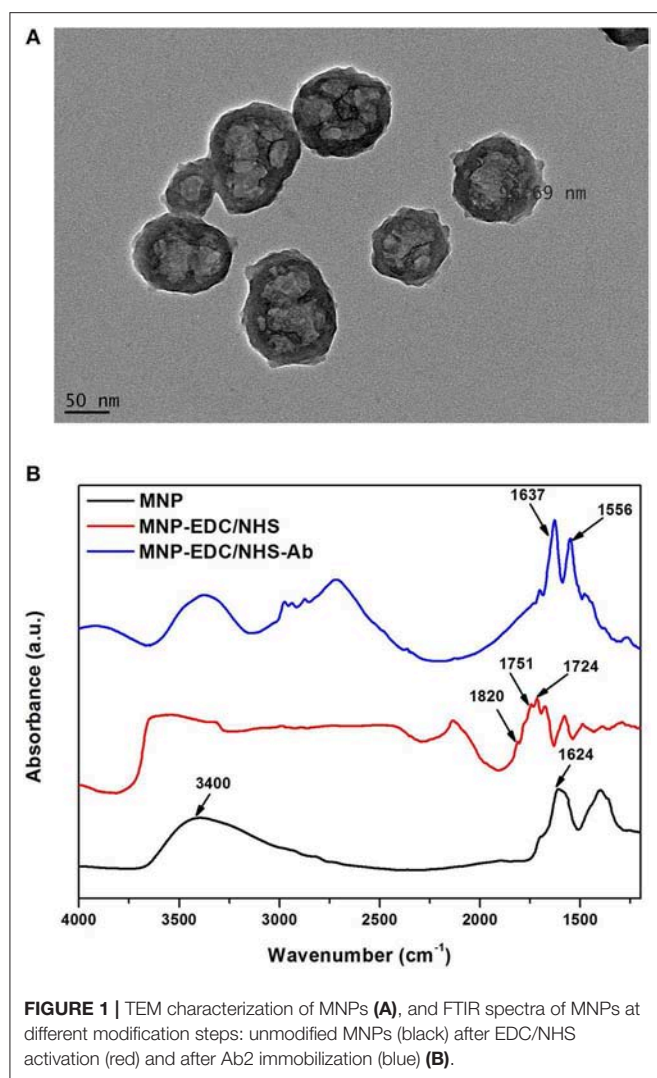


FIGURE 1 | TEM characterization of MNPs (A), and FTIR spectra of MNPs at different modification steps: unmodified MNPs (black) after EDC/NHS activation (red) and after Ab2 immobilization (blue) (B).

on the MNPs surface. EDC/NHS activation results in an NHS ester intermediate, reflected in the corresponding FTIR spectrum (red) as a characteristic triplet peak at 1,724, 1,751, and 1,820 cm⁻¹ (Böcking et al., 2008; Sam et al., 2009). The bands at 1,724 and 1,751 cm⁻¹ correspond to the C=O anti-symmetric and C=O symmetric stretching vibrational modes of the succinimidyl ring, respectively. The band at 1,820 cm⁻¹ corresponds to the C=O symmetric stretching vibrational mode and the C=O stretching vibrational mode of the succinimidyl ester. After antibody binding, the FTIR spectrum (blue) shows two bands at 1,556 and 1,637 cm⁻¹ that confirm the formation of amide bonds between the activated MNPs and the antibody. These bands correspond to the amine I and amine II vibrations, respectively.

The surface for immunosensing was prepared as detailed in the experimental section Preparation and Characterization of the NAA Immunosensing Surface. Silanization chemistry was used to immobilize FnAb within the porous layer. The NAA porous surface is characterized by a high density of native hydroxyl groups. These groups were activated by boiling in H₂O₂ at 70°C for 1 h. This step also removes any organic contaminants from

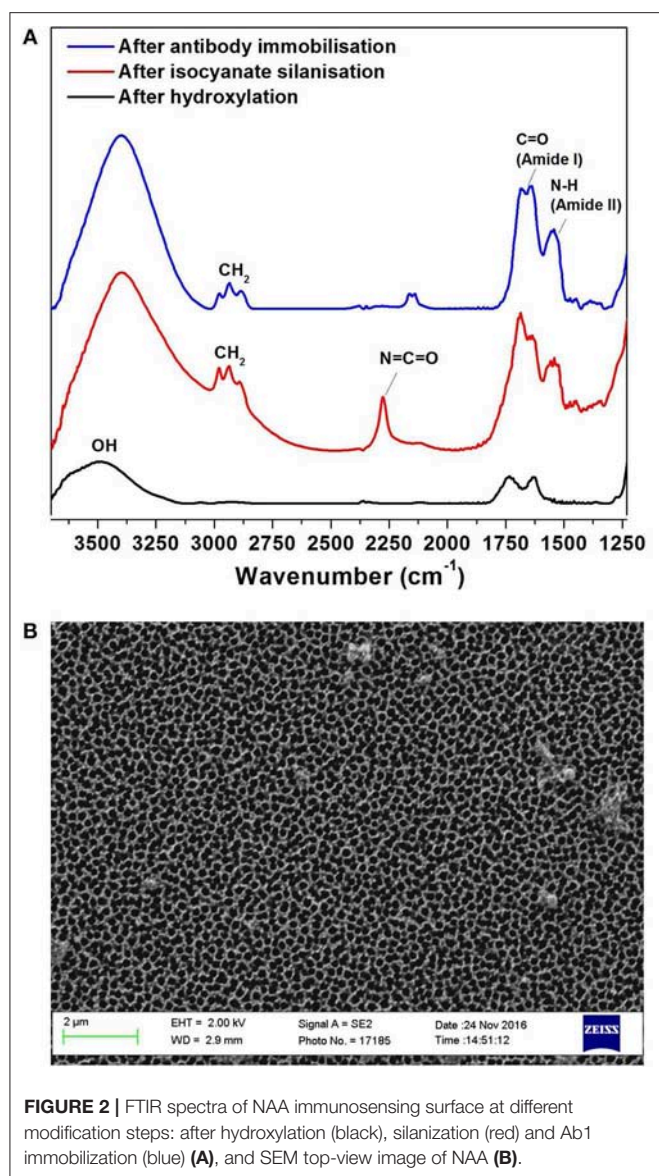
the surface and forms fresh hydroxyl groups. The hydroxylated surface was functionalized by means of silanization chemistry using ICN silane. This produced a dense monolayer of ICN silane with highly reactive isocyanate groups (N=C=O) on the NAA surface. This group readily reacted with the amine groups of FnAb. FTIR spectroscopy was used in reflectance mode to confirm the surface modification steps of the NAA membranes. **Figure 2A** presents the FTIR spectra at different NAA surface modification steps. The broad peak at 3,340 cm⁻¹ in the black spectrum in **Figure 2A** corresponds to hydroxyl groups on NAA surface after hydroxylation. The spectrum of the NAA surface after reacting the hydroxylated membrane with ICN silane (red spectrum in **Figure 2A**) showed a characteristic band at 2,250 cm⁻¹ representing N=C=O stretching vibration mode, confirming the successful silanization and presence of isocyanate groups on the surface. Bands at 2,925 and 2,854 cm⁻¹ were assigned to the stretching vibration modes of the aliphatic CH₂ groups in the silane (Dronov et al., 2011). In this same spectrum, bands at 1,550 and 1,650 cm⁻¹ were present which are characteristics of C=O stretching and N-H bending vibration modes. The presence of these bands is attributed to the fast hydrolysis undergone by some of the isocyanate groups upon reaction with residual water in the solvent or water vapor in the atmosphere. The blue spectrum in **Figure 2A** was obtained after covalent immobilization of FnAb on the silanized NAA surface. It confirms successful immobilization of antibodies via the disappearance of the isocyanate band at 2,250 cm⁻¹ and the presence of intense bands at 1,550 cm⁻¹ (N-H bending vibration mode) and 1,650 cm⁻¹ (C=O stretching vibration mode) from the peptide bonds formed between the antibodies and the isocyanate groups (Dronov et al., 2011).

Scanning SEM was used to characterize the surface morphology of the NAA membrane (**Figure 2B**). The top view of the membranes revealed that they had an average pore diameter of 207 ± 11 nm.

Detection of MNP-Ab2-Flii Complex on NAA Membranes

Before conducting electrochemical sensing experiments on the NAA immunosensing surface, initially we performed a colorimetric ELISA as described in the experimental section ELISA to Detect MNP-Ab2-Flii Complex, to confirm that the sandwich format works well and to compare its sensing performance with that of the NAA-based immunosensor. **Figure 3A** shows the scheme for the sandwich colorimetric ELISA. Absorbance was measured at 650 nm and plotted against the logarithm of KLH-Flii peptide conjugate concentrations (2.5, 5, 10, 20, and 40 µg/ml). The colorimetric ELISA detection based on a sandwich assay provided a LOD of 2.9 µg/ml, calculated using the equation 3Sa/b, where Sa is the standard deviation of the y-axis and b is the slope of the linear range of the calibration curve (**Figure 3B**). The sensitivity of this system was found to be 0.52 ml/µg.

The sensitivity achieved by the described ELISA is expected to be improved by the developed NAA-based electrochemical immunosensor combining the properties of MNPs, NAA



membrane and pore blockage-based electrochemical transduction method as explained previously.

As shown in **Scheme 2**, pore blockage was used as sensing principle to detect MNP-Ab2-Flii complex on a NAA-based immunosensor. Pore size is key to allow access of the immunocomplexes and maximize blockage, and thus sensitivity, upon binding to the immobilized antibodies. Formation of sandwich immunocomplexes within the pores partially blocks the diffusion of the redox species present in solution toward the gold transducer surface. This results in a reduction in the voltammetric oxidation signal of [Fe(CN)₆]⁴⁻ to [Fe(CN)₆]³⁻ used to quantify the concentration of KLH-Flii peptide conjugate.

The pore blockage sensing principle using NAA membranes has been demonstrated as an efficient label-free biomolecule detection approach (De La Escosura-Muñoz and Merkoçi, 2010; De La Escosura-Muñoz et al., 2013; Espinoza-Castañeda et al., 2015). We show here the advantages of using MNPs in

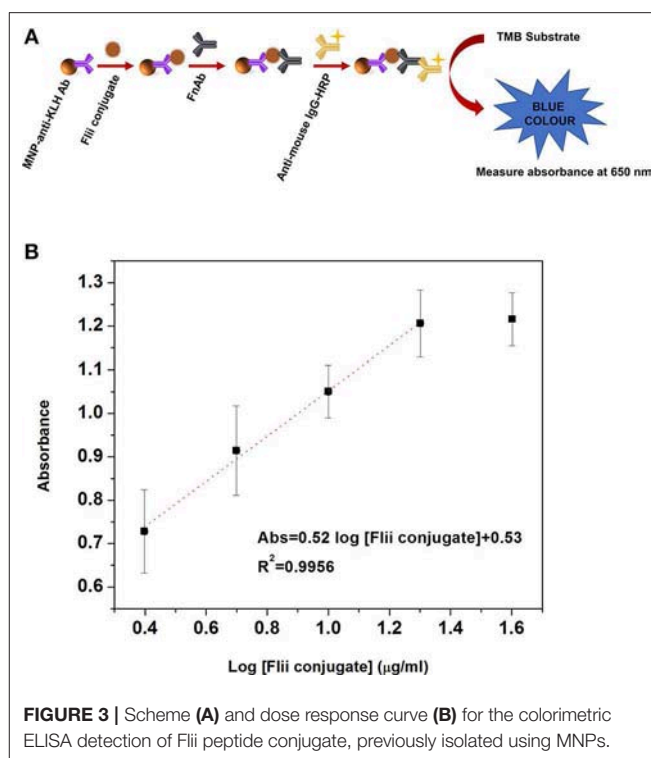


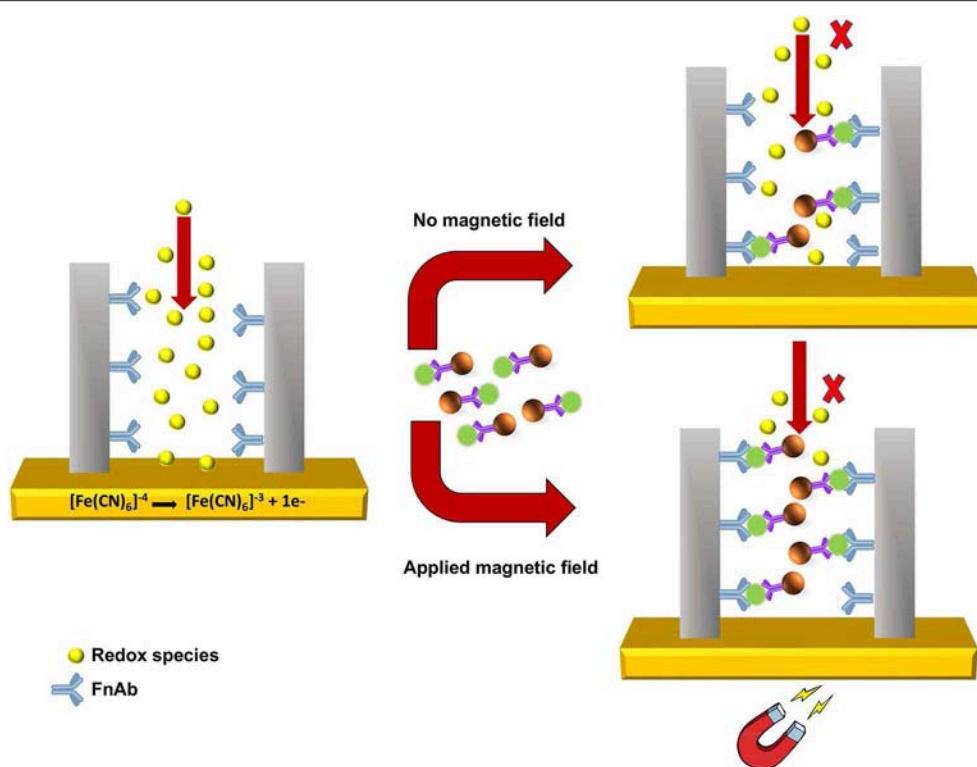
FIGURE 3 | Scheme (A) and dose response curve (B) for the colorimetric ELISA detection of Flii peptide conjugate, previously isolated using MNPs.

combination with a pore blockage-based immunosensor, not only to enhance the sensitivity, but also to capture the analyte from complex samples and thus avoid matrix effects caused by interfering compounds. Additionally, manipulation of MNPs by an external magnetic field can be utilized to facilitate the access of MNPs containing the immunocomplex into the pores to increase their availability for immunoreaction with the antibodies immobilized on the pores surface. This amplification strategy is expected to significantly improve the sensing sensitivity. Hence in this research, we demonstrate the use of MNPs as pore blockage enhancers and the possibility to further increase the sensitivity by applying an external magnetic field.

Figure 4A shows the DPV curves obtained after incubating the MNP-Ab2-Flii complex solutions, obtained upon incubation of MNP-Ab2 in various solutions with KLH-Flii peptide concentrations ranging from 2.5 to 40 μg/ml, on the NAA-based immunosensor in the absence of magnetic field. As expected, the oxidation current decreased with binding of the MNP-Flii complex obtained upon incubation with increasing concentrations of KLH-Flii peptide conjugate. To prove the specific binding between MNP-Flii peptide conjugate complex and the FnAb immobilized on the pores surface, a control experiment was performed using a NAA-based sensor modified with an anti-human IgG (**Figure 4B**).

To evaluate the sensing performance, current intensity changes were normalized using the following equation:

$$I_p = \frac{(I_0 - I_p)}{I_0} \times 100$$



SCHEME 2 | Sensing principle of pore blockage-based electrochemical detection using MNPs as enhancers.

where ΔI_p was the % current intensity change and I_0 and I_p were the current intensity values measured prior and after incubation with MNP-Ab2-Flii peptide conjugate. Calibration curves were obtained by plotting ΔI_p as a function of \log [Flii peptide conjugate] (maximum standard deviation of 4.4%; **Figure 4C**). The response from the control sensor (red triangles in **Figure 4C**) was negligible compared to the response from the Flii NAA immunosensor (black squares in **Figure 4C**), proving that the sensing response was due to specific binding between the MNP-Flii peptide conjugate complex and the Ab1 immobilized on the pores surface. The LOD was found to be 1.2 $\mu\text{g/ml}$, being only somewhat better than that obtained by ELISA (**Figure 3B**) which is 2.9 $\mu\text{g/ml}$. However, the sensitivity of the proposed sensing system was 76 times higher (40 $\text{ml}/\mu\text{g}$) than that of the ELISA which had a sensitivity of 0.52 $\text{ml}/\mu\text{g}$. The proposed NAA-based electrochemical immunosensor significantly improved the performance of the ELISA even in the absence of magnetic field. Reproducibility of the developed immunosensors was calculated as the relative standard deviation of the sensitivity of three individual sensors, being 3.8%. Encouraged by the outstanding improvement in sensitivity of the NAA-based immunosensor using MNPs as pore blockage enhancers, we then combined the same detection strategy with the application of an external magnetic field. We expect this approach to further improve the sensitivity by facilitating access of the immunocomplex into the pores, as described in the next section.

Sensitivity Enhancement Using External Magnetic Field

Our initial hypothesis was that the sensing performance of the developed pore blockage-based electrochemical immunosensor could be greatly enhanced in terms of sensitivity by applying an external magnetic field at the backside of the electrode. In the presence of the magnetic field, MNPs with bound analyte molecules are actuated in the direction of the magnetic field. This is an additional force for the MNPs to go through the pores apart from diffusion and gravitational pull when sensing is performed in the absence of magnetic field. This facilitates the binding of the MNP-Ab2-Flii complex to the bioreceptors (FcAb) immobilized on the pores surface and thus enhances the pore blockage effect. The immunosensor was placed on top of a large rare earth magnet made from neodymium, iron and boron-NdFeB during MNP-Ab2-Flii complex incubation. After that, thorough washing was performed with the magnet on top of the pores to magnetically drive any unbound MNPs stuck inside the pores outside the membrane by placing the magnet on top of the sensor.

Sensing experiments were performed by incubating MNP-Ab2-Flii complex solutions obtained upon MNP-Ab2 incubation in various KLH-Flii peptide conjugate solutions with concentrations ranging from 2.5 ng/mL to 2.5 $\mu\text{g/mL}$. DPV curves before and after incubation of MNP-Ab2-Flii complex on a NAA-based immunosensor and a control sensor, in the presence of an external magnetic force, are shown in

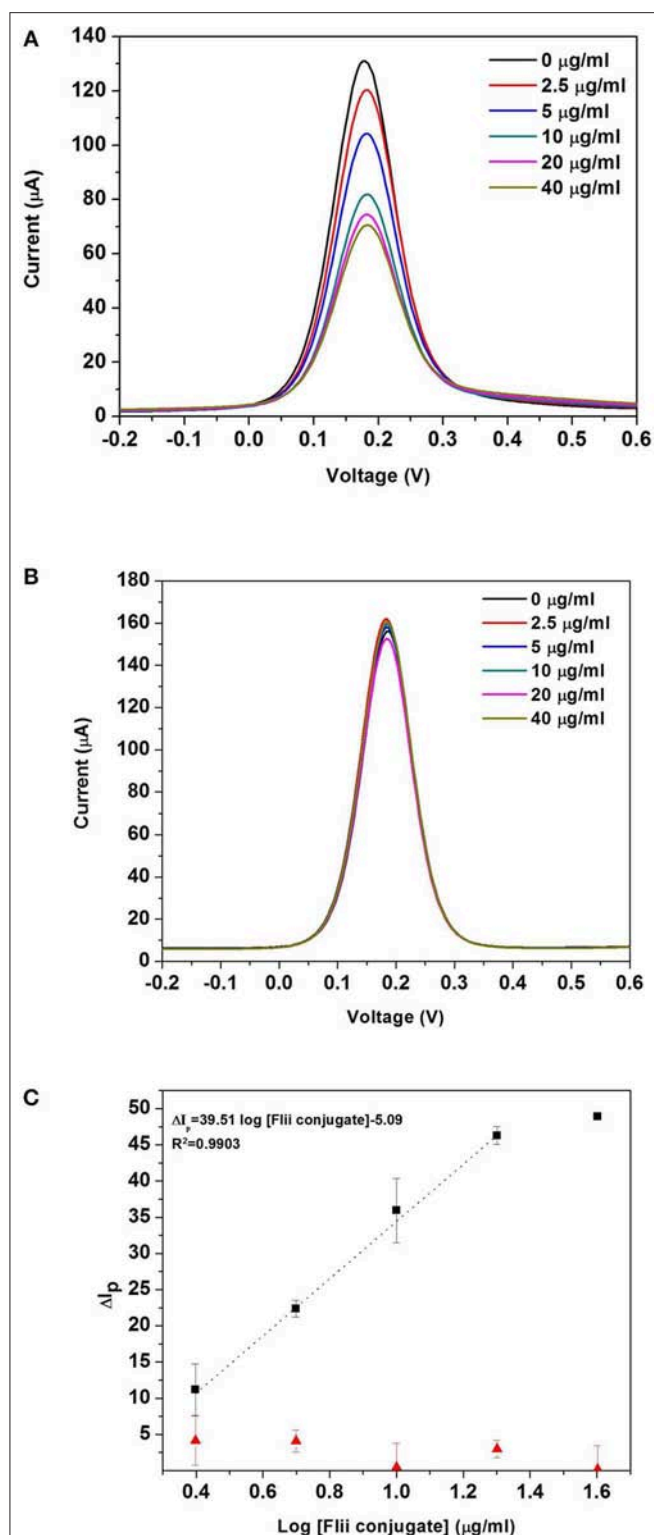


FIGURE 4 | DPV curves obtained with the NAA-based electrochemical immunosensor (A), and the control sensor (B) in the absence of magnetic field; dose response curves for the detection of KLH-Flii peptide conjugate plotted using the NAA-based electrochemical immunosensor and control sensor in the absence of magnetic field (C). Error bars are calculated as standard deviation from the average of three individual experiments.

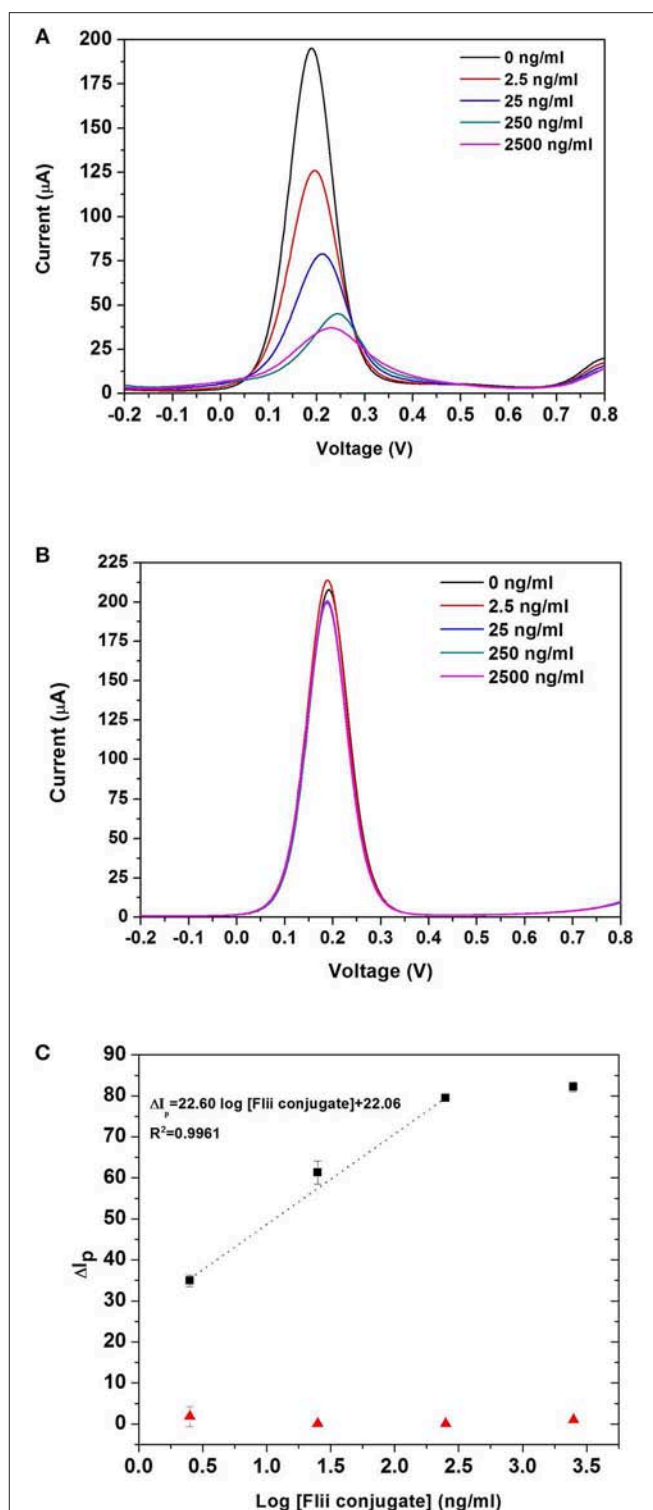


FIGURE 5 | DPV curves obtained with the NAA-based electrochemical immunosensor (A), and the control sensor (B) when an external magnetic field is applied during the analyte incubation step; dose response curves for the detection of KLH-Flii peptide conjugate plotted using the NAA-based electrochemical immunosensor and control sensor when an external magnetic field is applied during the analyte incubation step (C). Error bars are calculated as standard deviation from the average of three individual experiments.

Figures 5A,B, respectively. Calibration curves were plotted as explained previously to evaluate the sensing performance (maximum standard deviation of 2.8%; **Figure 5C**). The response from the control sensor (red triangles in **Figure 5C**) was negligible compared to that from the specific NAA immunosensor (black squares in **Figure 5C**). A LOD of 0.5 ng/mL was obtained, providing 5,800 and 2,400-fold enhancement, respectively, compared to the results obtained using ELISA and the same NAA-based immunosensor in the absence of magnetic field. A sensitivity of $27 \cdot 10^3 \text{ ml}/\mu\text{g}$ was achieved which is 673 times higher than that obtained by the immunosensor in the absence of magnetic field. Application of an external magnetic field to manipulate the particles seems to enhance the pore blockage effect as demonstrated by the ability to detect KLH-Flii peptide conjugate at concentrations 1,000-folds' lower than in the absence of magnetic field. The immunosensor performance in terms of sensitivity and LOD was greatly enhanced using the developed sensing strategy by magnetically manipulating the access of MNPs into the pores, while still showing an excellent reproducibility among sensors (2.8%).

These results confirm that by combining the use of MNPs as pore blockage agents and the application of an external magnetic field during analyte incubation, the NAA-based electrochemical immunosensor performance can be greatly improved when pore blockage is used as sensing mechanism. This sensing system has the potential to be extended to detect low concentrations of small molecules. Due to the ability of MNPs to isolate a target analyte from a complex biological sample, it may well be suitable to detecting biomarkers in samples with complex matrices.

CONCLUSIONS

We report here the development of a pore blockage-based biosensing platform with sensitivity enhancement via MNPs as a proof of concept for the electrochemical detection of Flii proteins. We have successfully demonstrated the proof-of-principle of the use of MNPs as signal enhancers in combination with FnAb-modified NAA platforms based on pore blockage

as sensing mechanism. A synthetic peptide corresponding to the active region of the wound biomarker Flii protein conjugated to a KLH carrier protein was used as a model analyte. MNPs were modified with an anti-KLH antibody to specifically capture the Flii-KLH conjugate. Then, the MNP-Ab2-Flii complex was subsequently captured by the FnAb antibodies within the NAA porous structure causing partial pore blockage. Pore blockage was used as sensing principle, being measured as a reduction in the voltammetric oxidation current of a redox species added in solution. Enhancement in pore blockage was achieved by applying an external magnetic field which pulled the MNP-Ab2-Flii complex more efficiently toward the sensor. This resulted in a significant enhancement in the analytical signal achieving a LOD of 0.5 ng/ml, while the LOD achieved in the absence of magnetic field was 1.2 $\mu\text{g}/\text{ml}$. Our results confirm that this novel sensing strategy can be used for developing biosensing platforms with enhanced sensing performance.

AUTHOR CONTRIBUTIONS

The experiments presented in this work were designed by GR, AC, NV, and BP. GR conducted the experimental work. GR, NV, and BP discussed the results obtained from the experiments. GR wrote the manuscript and the last version was revised by all authors (GR, AC, NV, and BP). All authors read and approved the final manuscript.

FUNDING

GR would like to thank UniSA and Wound Management Innovation CRC for PhD scholarship. This project was supported by Wound Management CRC.

ACKNOWLEDGMENTS

This work was performed in part at the Melbourne Center for Nanofabrication (MCN) in the Victorian Node of the Australian National Fabrication Facility (ANFF).

REFERENCES

- Baeyens, W., Schulman, S., Calokerinos, A., Zhao, Y., Campana, A. M. G., Nakashima, K., et al. (1998). Chemiluminescence-based detection: principles and analytical applications in flowing streams and in immunoassays. *J. Pharma. Biomed. Analysis* 17, 941–953. doi: 10.1016/S0731-7085(98)00062-4
- Böcking, T., Kilian, K. A., Gaus, K., and Gooding, J. J. (2008). Modifying porous silicon with self-assembled monolayers for biomedical applications: the influence of surface coverage on stability and biomolecule coupling. *Adv. Funct. Mater.* 18, 3827–3833. doi: 10.1002/adfm.200800640
- Cheng, M. S., Ho, J. S., Tan, C. H., Wong, J. P. S., Ng, L. C., and Toh, C.-S. (2012). Development of an electrochemical membrane-based nanobiosensor for ultrasensitive detection of dengue virus. *Anal. Chim. Acta* 725, 74–80. doi: 10.1016/j.aca.2012.03.017
- Cowin, A. J., Adams, D. H., Strudwick, X., Chan, H., Hooper, J., Sander, G. R., et al. (2007). Flightless I deficiency enhances wound repair by increasing cell migration and proliferation. *J. Pathol.* 211, 572–581. doi: 10.1002/path.2143
- De La Escosura-Muñiz, A., Chunglok, W., Surareungchai, W., and Merkoçi, A. (2013). Nanochannels for diagnostic of thrombin-related diseases in human blood. *Biosens. Bioelectron.* 40, 24–31. doi: 10.1016/j.bios.2012.05.021
- De La Escosura-Muñiz, A., Espinoza-Castañeda, M., Chamorro-García, A., Rodríguez-Hernández, C. J., De Torres, C., and Merkoçi, A. (2018). In situ monitoring of PTHLH secretion in neuroblastoma cells cultured onto nanoporous membranes. *Biosens. Bioelectron.* 107, 62–68. doi: 10.1016/j.bios.2018.01.064
- De La Escosura-Muñiz, A., Ivanova, K., and Tzanov, T. (2019). Electrical evaluation of bacterial virulence factors using nanopores. *ACS Appl. Mater. Interfaces* 11, 13140–13146. doi: 10.1021/acsami.9b02382
- De La Escosura-Muñiz, A., and Merkoçi, A. (2010). Nanoparticle based enhancement of electrochemical DNA hybridization signal using nanoporous electrodes. *Chem. Commun.* 46, 9007–9009. doi: 10.1039/c0cc02683b
- De La Escosura-Muñiz, A., and Merkoçi, A. (2011). A nanochannel/nanoparticle-based filtering and sensing platform for direct detection of a cancer biomarker in blood. *Small* 7, 675–682. doi: 10.1002/sml.201002349

- Dittmer, W., De Kievit, P., Prins, M., Vissers, J., Mersch, M., and Martens, M. (2008). Sensitive and rapid immunoassay for parathyroid hormone using magnetic particle labels and magnetic actuation. *J. Immunol. Methods* 338, 40–46. doi: 10.1016/j.jim.2008.07.001
- Dronov, R., Jane, A., Shapter, J. G., Hodges, A., and Voelcker, N. H. (2011). Nanoporous alumina-based interferometric transducers ennobled. *Nanoscale* 3, 3109–3114. doi: 10.1039/c0nr00897d
- Espinoza-Castañeda, M., De La Escosura-Muñiz, A., Chamorro, A., De Torres, C., and Merkoçi, A. (2015). Nanochannel array device operating through Prussian blue nanoparticles for sensitive label-free immunodetection of a cancer biomarker. *Biosens. Bioelectron.* 67, 107–114. doi: 10.1016/j.bios.2014.07.039
- Gijs, M. A., Lacharme, F., and Lehmann, U. (2009). Microfluidic applications of magnetic particles for biological analysis and catalysis. *Chem. Rev.* 110, 1518–1563. doi: 10.1021/cr9001929
- Giouroudi, I., and Keplinger, F. (2013). Microfluidic biosensing systems using magnetic nanoparticles. *Int. J. Mol. Sci.* 14, 18535–18556. doi: 10.3390/ijms140918535
- Grieshaber, D., Mackenzie, R., Voeroes, J., and Reimhult, E. (2008). Electrochemical biosensors-Sensor principles and architectures. *Sensors* 8, 1400–1458. doi: 10.3390/s80314000
- Holzinger, M., Le Goff, A., and Cosnier, S. (2014). Nanomaterials for biosensing applications: a review. *Front. Chem.* 2:63. doi: 10.3389/fchem.2014.00063
- Huang, Y., and Mason, A. J. (2013). Lab-on-CMOS integration of microfluidics and electrochemical sensors. *Lab Chip* 13, 3929–3934. doi: 10.1039/c3lc50437a
- Jackson, J. E., Kopecki, Z., Adams, D. H., and Cowin, A. J. (2012). Flii neutralizing antibodies improve wound healing in porcine preclinical studies. *Wound Repair Regenerat.* 20, 523–536. doi: 10.1111/j.1524-475X.2012.00802.x
- Jani, A. M. M., Losic, D., and Voelcker, N. H. (2013). Nanoporous anodic aluminum oxide: advances in surface engineering and emerging applications. *Prog. Mater. Sci.* 58, 636–704. doi: 10.1016/j.pmatsci.2013.01.002
- Kim, S., and Lim, H. (2015). Chemiluminescence immunoassay using magnetic nanoparticles with targeted inhibition for the determination of ochratoxin A. *Talanta* 140, 183–188. doi: 10.1016/j.talanta.2015.03.044
- Kopecki, Z., Ruzehaji, N., Turner, C., Iwata, H., Ludwig, R. J., Zillikens, D., et al. (2012). Topically applied flightless I neutralizing antibodies improve healing of blistered skin in a murine model of epidermolysis bullosa acquisita. *J. Invest. Dermatol.* 133, 1008–1016. doi: 10.1038/jid.2012.457
- Lei, J., and Ju, H. (2012). Signal amplification using functional nanomaterials for biosensing. *Chem. Soc. Rev.* 41, 2122–2134. doi: 10.1039/c1cs15274b
- Mir, M., Dondapati, S. K., Duarte, M. V., Chatzichristidi, M., Misiakos, K., Petrou, P., et al. (2010). Electrochemical biosensor microarray functionalized by means of biomolecule friendly photolithography. *Biosens. Bioelectron.* 25, 2115–2121. doi: 10.1016/j.bios.2010.02.012
- Morozov, V. N., and Morozova, T. Y. (2006). Active bead-linked immunoassay on protein microarrays. *Anal. Chim. Acta* 564, 40–52. doi: 10.1016/j.aca.2005.09.068
- Nguyen, B. T. T., Peh, A. E. K., Chee, C. Y. L., Fink, K., Chow, V. T., Ng, M. M., et al. (2012). Electrochemical impedance spectroscopy characterization of nanoporous alumina dengue virus biosensor. *Bioelectrochemistry* 88, 15–21. doi: 10.1016/j.bioelechem.2012.04.006
- Peyman, S. A., Iles, A., and Pamme, N. (2008). Rapid on-chip multi-step (bio) chemical procedures in continuous flow—manoeuvring particles through co-laminar reagent streams. *Chem. Commun.* 2008, 1220–1222. doi: 10.1039/b716532c
- Peyman, S. A., Iles, A., and Pamme, N. (2009). Mobile magnetic particles as solid-supports for rapid surface-based bioanalysis in continuous flow. *Lab Chip* 9, 3110–3117. doi: 10.1039/b904724g
- Rajeev, G., Prieto Simon, B., Marsal, L. F., and Voelcker, N. H. (2018a). Advances in nanoporous anodic alumina-based biosensors to detect biomarkers of clinical significance: a review. *Adv. Healthcare Mater.* 7:1700904. doi: 10.1002/adhm.201700904
- Rajeev, G., Xifre-Perez, E., Simon, B. P., Cowin, A. J., Marsal, L. F., and Voelcker, N. H. (2018b). A label-free optical biosensor based on nanoporous anodic alumina for tumour necrosis factor- α detection in chronic wounds. *Sens. Actuat. B Chem.* 257, 116–123. doi: 10.1016/j.snb.2017.10.156
- Rocha-Santos, T. A. (2014). Sensors and biosensors based on magnetic nanoparticles. *TrAC Trends Anal. Chem.* 62, 28–36. doi: 10.1016/j.trac.2014.06.016
- Ruzehaji, N., Grose, R., Krumbiegel, D., Zola, H., Dasari, P., Wallace, H., et al. (2012). Cytoskeletal protein Flightless (Flii) is elevated in chronic and acute human wounds and wound fluid: neutralizing its activity in chronic but not acute wound fluid improves cellular proliferation. *Eur. J. Dermatol.* 22, 740–750. doi: 10.1684/ejd.2012.1878
- Ruzehaji, N., Kopecki, Z., Melville, E., Appleby, S. L., Bonder, C. S., Arkell, R. M., et al. (2014). Attenuation of flightless I improves wound healing and enhances angiogenesis in a murine model of type 1 diabetes. *Diabetologia* 57, 402–412. doi: 10.1007/s00125-013-3107-6
- Sam, S., Touahir, L., Salvador Andres, J., Allongue, P., Chazalviel, J.-N., Gouget-Laemmel, A., et al. (2009). Semiquantitative study of the EDC/NHS activation of acid terminal groups at modified porous silicon surfaces. *Langmuir* 26, 809–814. doi: 10.1021/la902220a
- Santos, A., Kumeria, T., and Losic, D. (2013). Nanoporous anodic aluminum oxide for chemical sensing and biosensors. *TrAC Trends Anal. Chem.* 44, 25–38. doi: 10.1016/j.trac.2012.11.007
- Sasso, L. A., Johnston, I. H., Zheng, M., Gupte, R. K., Ündar, A., and Zahn, J. D. (2012). Automated microfluidic processing platform for multiplexed magnetic bead immunoassays. *Microfluid. Nanofluid.* 13, 603–612. doi: 10.1007/s10404-012-0980-0
- Silveira, C. M., Monteiro, T., and Almeida, M. G. (2016). Biosensing with paper-based miniaturized printed electrodes—a modern trend. *Biosensors* 6:51. doi: 10.3390/bios6040051
- Sista, R. S., Eckhardt, A. E., Srinivasan, V., Pollack, M. G., Palanki, S., and Pamula, V. K. (2008). Heterogeneous immunoassays using magnetic beads on a digital microfluidic platform. *Lab Chip* 8, 2188–2196. doi: 10.1039/b807855f
- Tarn, M. D., Peyman, S. A., Fakhruddin, R. F., Iles, A., Paunov, V. N., and Pamme, N. (2010). “Magnetically actuated particle-based procedures in continuous flow,” in *The 14th International Conference on Miniaturized Systems for Chemistry and Life Sciences*, Groningen.
- Van Reenen, A., De Jong, A. M., Den Toonder, J. M., and Prins, M. W. (2014). Integrated lab-on-chip biosensing systems based on magnetic particle actuation—a comprehensive review. *Lab Chip* 14, 1966–1986. doi: 10.1039/C3LC51454D
- Walcarius, A., Minter, S. D., Wang, J., Lin, Y., and Merkoçi, A. (2013). Nanomaterials for bio-functionalized electrodes: recent trends. *J. Mater. Chem. B* 1, 4878–4908. doi: 10.1039/c3tb20881h
- Wang, C., Wu, J., Zong, C., Xu, J., and Ju, H.-X. (2012). Chemiluminescent immunoassay and its applications. *Chin. J. Anal. Chem.* 40, 3–10. doi: 10.1016/S1872-2040(11)60518-5
- Yamanaka, K., Vestergaard, M. D. C., and Tamiya, E. (2016). Printable electrochemical biosensors: a focus on screen-printed electrodes and their application. *Sensors* 16:1761. doi: 10.3390/s16101761
- Ye, W., Xu, Y., Zheng, L., Zhang, Y., Yang, M., and Sun, P. (2016). A nanoporous alumina membrane based electrochemical biosensor for histamine determination with biofunctionalized magnetic nanoparticles concentration and signal amplification. *Sensors* 16:1767. doi: 10.3390/s16101767
- Zhang, Q.-Y., Chen, H., Lin, Z., and Lin, J.-M. (2011). Chemiluminescence enzyme immunoassay based on magnetic nanoparticles for detection of hepatocellular carcinoma marker glypican-3. *J. Pharma. Anal.* 1, 166–174. doi: 10.1016/j.jpba.2011.06.004
- Zhu, C., Yang, G., Li, H., Du, D., and Lin, Y. (2014). Electrochemical sensors and biosensors based on nanomaterials and nanostructures. *Anal. Chem.* 87, 230–249. doi: 10.1021/ac5039863

Conflict of Interest Statement: The authors declare that the research was conducted in the absence of any commercial or financial relationships that could be construed as a potential conflict of interest.

The handling editor is currently organizing a Research Topic with one of the authors, NV, and confirms the absence of any other collaboration.

Copyright © 2019 Rajeev, Cowin, Voelcker and Prieto Simon. This is an open-access article distributed under the terms of the Creative Commons Attribution License (CC BY). The use, distribution or reproduction in other forums is permitted, provided the original author(s) and the copyright owner(s) are credited and that the original publication in this journal is cited, in accordance with accepted academic practice. No use, distribution or reproduction is permitted which does not comply with these terms.

Advantages of publishing in Frontiers



OPEN ACCESS

Articles are free to read
for greatest visibility
and readership



FAST PUBLICATION

Around 90 days
from submission
to decision



HIGH QUALITY PEER-REVIEW

Rigorous, collaborative,
and constructive
peer-review



TRANSPARENT PEER-REVIEW

Editors and reviewers
acknowledged by name
on published articles

Frontiers

Avenue du Tribunal-Fédéral 34
1005 Lausanne | Switzerland

Visit us: www.frontiersin.org

Contact us: info@frontiersin.org | +41 21 510 17 00



REPRODUCIBILITY OF RESEARCH

Support open data
and methods to enhance
research reproducibility



DIGITAL PUBLISHING

Articles designed
for optimal readership
across devices



FOLLOW US

@frontiersin



IMPACT METRICS

Advanced article metrics
track visibility across
digital media



EXTENSIVE PROMOTION

Marketing
and promotion
of impactful research



LOOP RESEARCH NETWORK

Our network
increases your
article's readership